

Interaction of tectono-sedimentary processes in the south china sea and their implication for hazards

Edited by

Zhigang Li, Peizhen Zhang, Weiwei Ding, Shaohong Xia, Rafael Almeida and Hao Liang

Published in

Frontiers in Earth Science



FRONTIERS EBOOK COPYRIGHT STATEMENT

The copyright in the text of individual articles in this ebook is the property of their respective authors or their respective institutions or funders. The copyright in graphics and images within each article may be subject to copyright of other parties. In both cases this is subject to a license granted to Frontiers.

The compilation of articles constituting this ebook is the property of Frontiers.

Each article within this ebook, and the ebook itself, are published under the most recent version of the Creative Commons CC-BY licence. The version current at the date of publication of this ebook is CC-BY 4.0. If the CC-BY licence is updated, the licence granted by Frontiers is automatically updated to the new version.

When exercising any right under the CC-BY licence, Frontiers must be attributed as the original publisher of the article or ebook, as applicable.

Authors have the responsibility of ensuring that any graphics or other materials which are the property of others may be included in the CC-BY licence, but this should be checked before relying on the CC-BY licence to reproduce those materials. Any copyright notices relating to those materials must be complied with.

Copyright and source acknowledgement notices may not be removed and must be displayed in any copy, derivative work or partial copy which includes the elements in question.

All copyright, and all rights therein, are protected by national and international copyright laws. The above represents a summary only. For further information please read Frontiers' Conditions for Website Use and Copyright Statement, and the applicable CC-BY licence.

ISSN 1664-8714
ISBN 978-2-8325-2687-3
DOI 10.3389/978-2-8325-2687-3

About Frontiers

Frontiers is more than just an open access publisher of scholarly articles: it is a pioneering approach to the world of academia, radically improving the way scholarly research is managed. The grand vision of Frontiers is a world where all people have an equal opportunity to seek, share and generate knowledge. Frontiers provides immediate and permanent online open access to all its publications, but this alone is not enough to realize our grand goals.

Frontiers journal series

The Frontiers journal series is a multi-tier and interdisciplinary set of open-access, online journals, promising a paradigm shift from the current review, selection and dissemination processes in academic publishing. All Frontiers journals are driven by researchers for researchers; therefore, they constitute a service to the scholarly community. At the same time, the *Frontiers journal series* operates on a revolutionary invention, the tiered publishing system, initially addressing specific communities of scholars, and gradually climbing up to broader public understanding, thus serving the interests of the lay society, too.

Dedication to quality

Each Frontiers article is a landmark of the highest quality, thanks to genuinely collaborative interactions between authors and review editors, who include some of the world's best academicians. Research must be certified by peers before entering a stream of knowledge that may eventually reach the public - and shape society; therefore, Frontiers only applies the most rigorous and unbiased reviews. Frontiers revolutionizes research publishing by freely delivering the most outstanding research, evaluated with no bias from both the academic and social point of view. By applying the most advanced information technologies, Frontiers is catapulting scholarly publishing into a new generation.

What are Frontiers Research Topics?

Frontiers Research Topics are very popular trademarks of the *Frontiers journals series*: they are collections of at least ten articles, all centered on a particular subject. With their unique mix of varied contributions from Original Research to Review Articles, Frontiers Research Topics unify the most influential researchers, the latest key findings and historical advances in a hot research area.

Find out more on how to host your own Frontiers Research Topic or contribute to one as an author by contacting the Frontiers editorial office: frontiersin.org/about/contact

Interaction of tectono-sedimentary processes in the south china sea and their implication for hazards

Topic editors

Zhigang Li — Sun Yat-sen University, Zhuhai Campus, China

Peizhen Zhang — Sun Yat-sen University, China

Weiwei Ding — Second Institute of Oceanography, Ministry of Natural Resources, China

Shaohong Xia — South China Sea Institute of Oceanology, Chinese Academy of Sciences (CAS), China

Rafael Almeida — San Diego State University, United States

Hao Liang — Sun Yat-sen University, China

Citation

Li, Z., Zhang, P., Ding, W., Xia, S., Almeida, R., Liang, H., eds. (2023). *Interaction of tectono-sedimentary processes in the south china sea and their implication for hazards*. Lausanne: Frontiers Media SA. doi: 10.3389/978-2-8325-2687-3

Table of contents

- 05 **Editorial: Interaction of tectono-sedimentary processes in the South China Sea and their implication for hazards**
Zhigang Li, Peizhen Zhang, Weiwei Ding, Shaohong Xia, Rafael Almeida and Hao Liang
- 08 **Bathymetric Highs Control the Along-Strike Variations of the Manila Trench: 2D Numerical Modeling**
Letian Ma, Lin Chen, Zihua Cheng, Taras Gerya and Jiabiao Li
- 27 **Exhumation history of the Hengchun Ridge and its implications for Taiwan orogenic processes**
Pingchuan Tan, Weiwei Ding and Jiabiao Li
- 37 **An earthquake-triggered submarine mass failure mechanism for the 1994 Mindoro tsunami in the Philippines: Constraints from numerical modeling and submarine geomorphology**
Alec Benjamin G. Ramirez, Noelynna T. Ramos, Lyndon P. Nawanao Jr, Robelyn Z. Mangahas-Flores, Ishmael C. Narag, Toshitaka Baba, Naotaka Chikasada and Kenji Satake
- 57 **Magnetic anomaly lineations in the Northeastern South China Sea and their implications for initial seafloor spreading**
Zhaocai Wu, Jialing Zhang, Mingju Xu and Hailong Li
- 65 **Tectonic dynamics of the Zhongjiannan Basin in the western South China Sea since the late Miocene**
Zhengxin Yin, Zhourong Cai, Yongjian Yao, Qianru Huang and Zhengyuan Li
- 75 **Seismic stratigraphy and development of a modern isolated carbonate platform (Xuande Atoll) in the South China Sea**
Y. Liu, S. Wu, X. Li, W. Chen, X. Han, C. Yang, Y. Qin, X. Huang, Z. Yang, J. Sun and L. Zhu
- 87 **An approach to determine brittle upper crustal thinning: Insights into crustal extension discrepancy in the central part of Qiongdongnan Basin**
Chao He, Zhongxian Zhao, Eun Young Lee and Yulong Xue
- 102 **Hydrodynamic variations and human activities have influenced sediment fluxes in the pearl river delta since the late holocene**
Xiaoqiang Yang, Shuang Wu, Shentang Shang and Yan Chen
- 115 **Temporally varied coastal uplift rates north of the Littoral Fault Zone since the late Quaternary in the northern South China Sea: Insights from the wave-cut platform and cosmogenic exposure dating**
Hao Liang, Ke Zhang, Zhigang Li, Zhen Chen, Gege Hui, Ping Huang, Qingying Tian, Yongjie Tang, Cong Chen, Yipeng Zhang, Xiaohui He, Yonggang Yan, Xiangming Dai, Zhongyun Li, Weitao Wang and Peizhen Zhang

- 128 **Rifting/spreading propagation interacts with preexisting transform faults: 3D geodynamic modeling**
Hao Li, Jie Liao, Yongqiang Shen, Jiarong Qing, Yangming Wu, Zhongxian Zhao and Xiaobin Shi
- 144 **Characteristics and distribution of geohazards since the middle miocene of the Xisha sea area, South China Sea**
Jiao Zhou, Hongjun Chen, Jiale Chen, Shantang Yi, Lihua Guo, Xiaosan Hu, Wenbo Du and Meijing Sun
- 160 **Cenozoic evolution of the Yangjiang-Yitong'an-sha fault zone in the northern South China Sea: Evidence from 3D seismic data**
Huawang Zhan, Guangzeng Wang, Guangrong Peng, Yanhui Suo, Pengcheng Wang, Xiaodong Du, Jie Zhou, Sanzhong Li and Dingwei Zhu
- 179 **Overpressure characteristics and geological origin of the paleogene in Baiyun Sag, Pearl River Mouth Basin**
Ting Xiong, Leli Cheng, Dongming Guo, Lijun Guan, Qiangtao Jiang, Hu Zhangming, Senlin Yin and Gongyang Chen
- 190 **Frontal wedge variations and controls of submarine landslides in the Negros–Sulu Trench System, Philippines**
Lyndon P. Nawanao Jr and Noelynna T. Ramos
- 207 **Corrigendum: Frontal wedge variations and controls of submarine landslides in the Negros-Sulu Trench system, Philippines**
Lyndon P. Nawanao Jr and Noelynna T. Ramos
- 209 **An erosive neritic area of Shantou in coastal NE South China Sea since at least MIS 5 revealed by OSL dating of cores**
Jiemei Zhong, Bohui Liu, Yang Ou, Ruonan Tian, Jingxiang Shan, Yantian Xu, Feng Wang, Mahmoud Abbas, Ke Zhang and Zhongping Lai
- 218 **Soft-sediment deformation structures of mottled clay in Huizhou Quaternary basin, coastal South China**
Zhen Chen, Wen Wang, Ping Huang, Yongjie Tang, Jing Wang, Qiang Zeng and Cong Chen



OPEN ACCESS

EDITED AND REVIEWED BY

Sabine Schmidt,
Centre National de la Recherche
Scientifique (CNRS), France

*CORRESPONDENCE

Zhigang Li,
✉ lizhigang@mail.sysu.edu.cn

RECEIVED 17 May 2023

ACCEPTED 24 May 2023

PUBLISHED 30 May 2023

CITATION

Li Z, Zhang P, Ding W, Xia S, Almeida R and
Liang H (2023), Editorial: Interaction of
tectono-sedimentary processes in the
South China Sea and their implication
for hazards.
Front. Earth Sci. 11:1224049.
doi: 10.3389/feart.2023.1224049

COPYRIGHT

© 2023 Li, Zhang, Ding, Xia, Almeida and
Liang. This is an open-access article
distributed under the terms of the
[Creative Commons Attribution License
\(CC BY\)](#). The use, distribution or
reproduction in other forums is
permitted, provided the original author(s)
and the copyright owner(s) are credited
and that the original publication in this
journal is cited, in accordance with
accepted academic practice. No use,
distribution or reproduction is permitted
which does not comply with these terms.

Editorial: Interaction of tectono-sedimentary processes in the South China Sea and their implication for hazards

Zhigang Li^{1,2*}, Peizhen Zhang^{1,2}, Weiwei Ding³, Shaohong Xia⁴,
Rafael Almeida⁵ and Hao Liang^{1,2}

¹Guangdong Provincial Key Lab of Geodynamics and Geohazards, School of Earth Sciences and Engineering, Sun Yat-sen University, Zhuhai, China, ²Southern Marine Science and Engineering Guangdong Laboratory, Zhuhai, China, ³Second Institute of Oceanography, MNR, Hangzhou, China, ⁴South China Sea Institute of Oceanology, Chinese Academy of Sciences, Guangzhou, China, ⁵Department of Geological Sciences, San Diego State University, San Diego, CA, United States

KEYWORDS

South China Sea, tectonism, sedimentary process, geohazards, numerical modeling

Editorial on the Research Topic

[Interaction of tectono-sedimentary processes in the South China Sea and their implication for hazards](#)

Introduction

The South China Sea (SCS), one of the largest marginal seas in the western Pacific, has a distinct setting that superposes complex tectonic environments, such as subduction setting, continental rifting, and seafloor spreading. Even though the SCS is a well-studied marginal sea, there are a number of unsolved questions concerning its formation, evolution, geodynamic processes, and geohazards. With the expanding of seafloor infrastructure (submarine cables, oil platforms) and increasing coastal population, the SCS region is particularly vulnerable to marine geohazards, e.g., submarine earthquakes, landslides and their associated tsunami hazards. In this context, it is of great scientific significance to further study the tectonic and sedimentary processes that have taken place in the past, as well as the present, in the SCS, and to better characterize the geological hazards they may pose.

To address these Research Topic and advance our understanding of the SCS, we proposed this Research Topic in Frontiers in Earth Science and collected a total of 17 high-quality papers. The papers cover the following four subjects: 1) Tectonics around the SCS; 2) Sedimentary process in the northern margin of SCS; 3) Geohazards; and 4) Numerical modeling. The multiscale, interdisciplinary and thematic nature of the research will allow for a better assessment of geological processes, climate and environmental changes, and potential marine geo-hazards in the region. By bringing together cutting-edge research on the SCS, this Research Topic aims to provide a comprehensive and up-to-date understanding of the region's geology and help mitigate the impact of future hazards in this following.

Here we present a short review of the contributions organized by the main subjects.

Tectonics around the SCS

Tan et al. estimated the uplift rate of the Hengchun Ridge (ca. 0.3 km/Ma) based on a linear regression between the hyperstretched continental crust (HSCC) and the observed depth of the prism crest. They suggest a two-stage collision hypothesis for the Taiwan orogen: the first stage was dominated by structurally underplated HSCC, and the second is a combination of the arrival of the continental shelf and arc-continent collision.

Yin et al. proposed compressional tectonic stress field weakened gradually from south to north, while the northern Zhongjiannan basin was formed under the dextral strike-slip movement of the Red River Fault. The above knowledge provides a reference for studying the initiation time of dextral strike-slip along the Red River Fault Zone.

Wu et al. confirmed the initial spreading of the South China Sea was dominated by local punctiform break-up, with the oldest anomaly, C12n (~30.8 Ma), appearing at two turns of the continent-ocean boundary. The study also observes the opening of the northwestern Sub-basin was rotated around a fixed point at the west, with a fault at the eastern end formed by the trajectory of the conjugate point during seafloor spreading.

He et al. suggested that the value of fault deformation width is generally less than 80 km and mostly less than 50 km in the northern South China Sea margin. They analyzed an inverse discrepancy in the southeast of the Qiongdongnan basin, likely due to differences in syn-rift sediment thickness causing a transition between inverse and positive extension discrepancies.

Liang et al. mapped four wave-cut platforms in the southern Pearl River Delta and dated two of them, with results suggesting uplift rates ranging from 0.30 to 0.38 mm/a during 239–128 ka and 0.09 mm/a since 128 ka. A decrease in the uplift rate, may correspond to a weakened differential uplift onshore of the seismically active Littoral Fault Zone.

Zhan et al. proposed that the NW-trending Yanjiang-Yitong'an-sha strike-slip fault zone have initiated sinistral motion around 35 Ma and served as a transfer zone during the intense rifting in the Pearl River Mouth Basin from 65 to 35 Ma, and then became a sinistral transtensional fault from 35 Ma to 16.5 Ma.

Chen et al. confirmed mottled clay overlying fluvial deposits or embedding homogeneous aeolian yellow silt can provide useful information on paleo-earthquakes. They suggest that the mottled clay structure in the Huizhou Basin is a product of liquefaction-induced soft-sediment deformation structure, and provide a potential indicator of paleo-earthquakes in the coastal Quaternary basins of the northern South China Sea.

Sedimentary process in the northern margin of SCS

Yang et al. investigated weak and high energy deposition influenced by El Niño-Southern Oscillation (ENSO) activity and high-frequency tropical storms. Growing human activity during 1.0–1.6 kyr impacted sediment flux. Understanding these dynamics can inform sustainable development in the Pearl River Delta.

Liu et al. revealed the Xuande Atoll is a carbonate platform formed since the early Miocene followed by a final shrinking stage in the southern and western parts due to tectonic subsidence and increased sediment inputs.

Zhong et al. analyzed intensified erosion in the neritic region of the northeastern South China Sea occurred due to fluvial incision caused by sea-level decline during the last glacial period and strong transportation by coastal currents.

Xiong et al. evaluated the pore pressure profile and indicates that overpressure zone mainly develops from the middle of Zhujiang Formation to the upper member of Enping Formation due to fluid expansion from hydrocarbon generation.

Geohazards

Zhou et al. systematically studied the geological hazards in the Xisha Sea area since the Miocene using high-resolution seismic data and provide a guide for future exploration and disaster prevention in the Xisha Sea area.

Nawanao and Ramos identified more than 1,200 submarine landslides and found that small submarine landslides are mainly controlled by submarine canyon systems at shallow depths, while large submarine landslides cluster where seamount subduction induces slope steepening. The study highlights the importance of understanding spatial, geomorphological, and tectonic controls in identifying offshore areas susceptible to large submarine landslides and tsunamis in active margins.

Ramirez et al. compared two tsunami models—one with only an earthquake component and one with an additional submarine mass failure component based on the San Andres submarine mass failure, suggesting an earthquake-triggered submarine mass failure source mechanism for the 1994 Mindoro tsunami.

Numerical modeling

Ma et al. used 2-D thermo-mechanical modeling to examine how bathymetric highs affect the topography of the overriding plate and the morphology of the subducting plate. The results show that the dramatic changes in the dip angle and the convex shape in the northern Manila Trench were caused by subduction of a large thin continental terrane, while the smooth morphology of the subducting slab in the southern segment and straight trench were associated with normal oceanic subduction with small seamounts.

Li et al. utilized 3D geodynamical numeric models to study how pre-existing transform faults interact with rifting/spreading centers. The results showed that the pre-existing transform faults affect rifting/spreading propagation, leading to the formation of ridge segments with offset distance.

Wen et al. applied two travel time correction methods to image different S-wave velocity structures the northeastern South China Sea. This study shows that sedimentary layer velocity was the main influencing factor for S-wave phase ray tracing, while the velocity of sediments had little effect on Moho S-wave reflections.

Author contributions

All authors listed have made a substantial, direct, and intellectual contribution to the work and approved it for publication.

Funding

The work throughout the conception, design and publication of this Research Topic was supported by the National Natural Science Foundation of China (42172233 and 42272250), Guangdong Province Introduced Innovative R&D Team of Geological Processes and Natural Disasters around the South China Sea (2016ZT06N331), and Guangdong Basic and Applied Basic Research Foundation (2023A1515011812).

Acknowledgments

We would like to thank all reviewers and authors for their contributions to this Research Topic. We also thank the entire

team of Frontiers in Earth Science for their dedicated effort in guiding the revision and detailed editing of the papers of the Research Topic.

Conflict of interest

The authors declare that the research was conducted in the absence of any commercial or financial relationships that could be construed as a potential conflict of interest.

Publisher's note

All claims expressed in this article are solely those of the authors and do not necessarily represent those of their affiliated organizations, or those of the publisher, the editors and the reviewers. Any product that may be evaluated in this article, or claim that may be made by its manufacturer, is not guaranteed or endorsed by the publisher.



Bathymetric Highs Control the Along-Strike Variations of the Manila Trench: 2D Numerical Modeling

Letian Ma^{1,2*}, Lin Chen³, Zihua Cheng⁴, Taras Gerya⁵ and Jiabiao Li^{1,2}

¹Key Laboratory of Submarine Geosciences and Second Institute of Oceanography, Ministry of Natural Resources, Hangzhou, China, ²Southern Marine Science and Engineering Guangdong Laboratory, Zhuhai, China, ³State Key Laboratory of Lithospheric Evolution, Institute of Geology and Geophysics, Chinese Academy of Sciences, Beijing, China, ⁴Key Laboratory of Ocean and Marginal Sea Geology, South China Sea Institute of Oceanology, Chinese Academy of Sciences, Guangzhou, China, ⁵Department of Earth Sciences, ETH Zurich, Zurich, Switzerland

OPEN ACCESS

Edited by:

Rafael Almeida,
San Diego State University,
United States

Reviewed by:

Fucheng Li,
South China Sea Institute of
Oceanology (CAS), China
Liming Dai,
OUC, China

*Correspondence:

Letian Ma
malt@sio.org.cn

Specialty section:

This article was submitted to
Structural Geology and Tectonics,
a section of the journal
Frontiers in Earth Science

Received: 13 May 2022

Accepted: 17 June 2022

Published: 11 July 2022

Citation:

Ma L, Chen L, Cheng Z, Gerya T and
Li J (2022) Bathymetric Highs Control
the Along-Strike Variations of the
Manila Trench: 2D
Numerical Modeling.
Front. Earth Sci. 10:943147.
doi: 10.3389/feart.2022.943147

The Manila Trench is located at the eastern boundary of the South China Sea (SCS). It develops through the subduction of the SCS beneath the Philippine Sea Plate (PSP) since the early Neogene, driven by the northwestern plate motion of the PSP. The northern segment of the Manila trench at around 18° N–21.5°N is characterized by an obvious eastward convex in the trench shape and abrupt changes of slab dip angle, whereas the southern segment of the Manila trench at around 15°N–18°N is featured by an almost straight NS-trending trench line and smooth subducting slab morphology. However, the cause for the along-strike variations along the Manila trench remains poorly understood. In this study, we use 2-D thermo-mechanical modeling to investigate how bathymetric highs embedded in the subducting slab affect the topography of overriding plate and the morphology of subducting plate. Three major factors of bathymetric highs are systematically examined: 1) the crustal properties, 2) the width, and 3) the thickness. Geodynamic results suggest that the most important factor controlling abrupt changes in dipping angle is the crustal properties of bathymetric highs. Also, reduction of crustal thickness and increasing the width of continental bathymetric highs favor the abrupt change of dipping angle, whereas thicker (≥ 25 km) bathymetric highs are more likely to be blocked in the subduction zone before slab break-off. According to our numerical modeling results, we suggest that dramatic changes in the dip angle in the northern Manila trench and the convex shape were caused by subduction of a large thin continental terrane, whereas the smooth morphology of subducting slab in the southern segment and straight trench were associated with normal oceanic subduction with small seamounts.

Keywords: numerical modeling, bathymetric highs, subduction, Manila trench, South China Sea

INTRODUCTION

Sharp discontinuities in trench shape and various morphologies of subducting slabs are often linked with bathymetric highs subduction (Miller et al., 2004, 2005; Mason et al., 2010). For example, the subduction of Ogasawara Plateau may have influenced the varied trench and slab morphology at the junction of the Izu-Bonin and Mariana arcs in the West Pacific (Mason et al., 2010). Similar arcuate plate boundary development is also found during the subduction of the Nazca Ridge beneath the continental South American Plate (Rosenbaum et al., 2005). These bathymetric highs include terrane

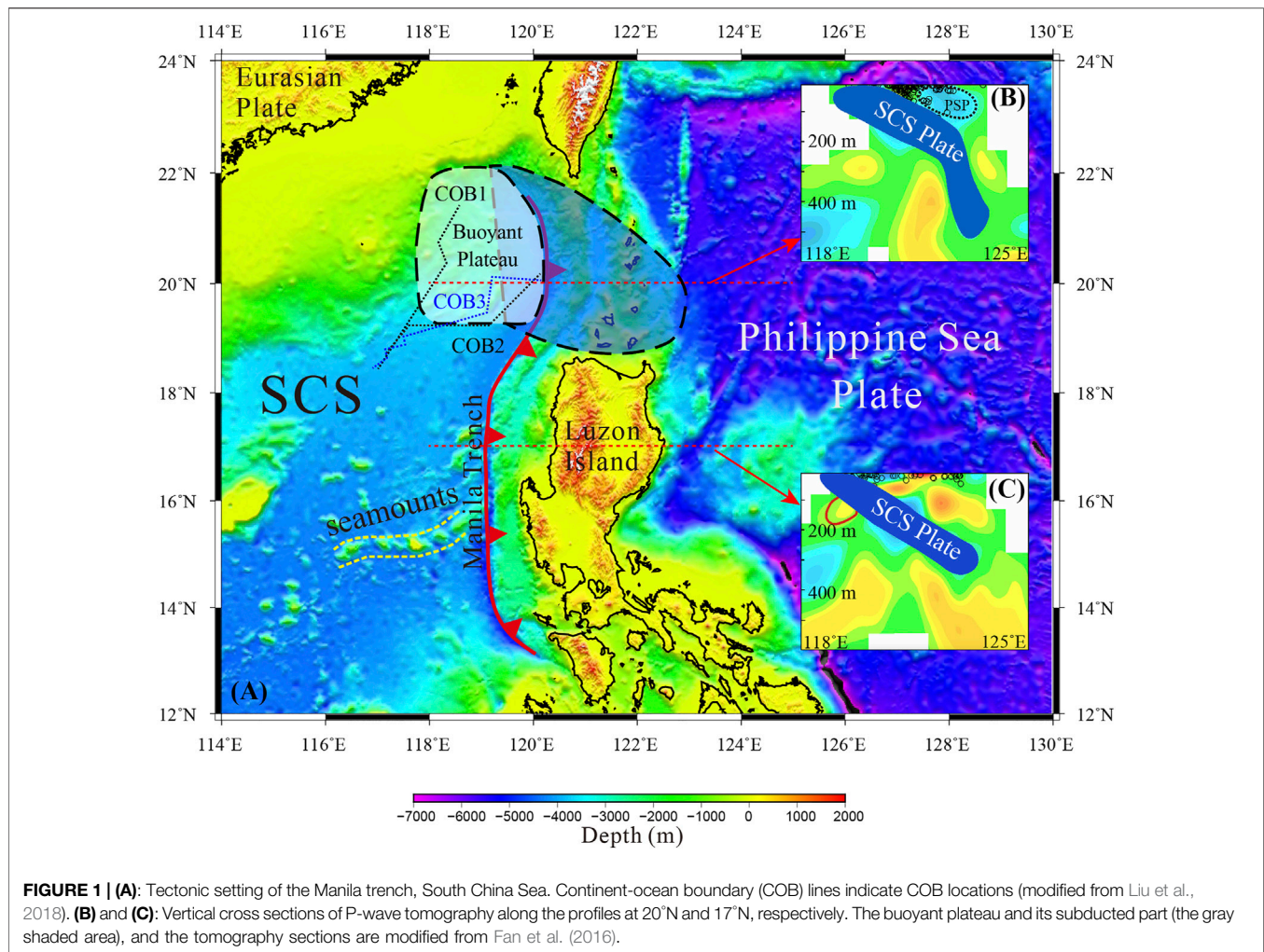


FIGURE 1 | (A): Tectonic setting of the Manila trench, South China Sea. Continent-ocean boundary (COB) lines indicate COB locations (modified from Liu et al., 2018). **(B)** and **(C):** Vertical cross sections of P-wave tomography along the profiles at 20°N and 17°N, respectively. The buoyant plateau and its subducted part (the gray shaded area), and the tomography sections are modified from Fan et al. (2016).

with oceanic crustal properties, such as oceanic plateaus, seamounts, and submarine ridges, and terrane with continent crustal properties, such as microcontinents and continental fragments. Several studies on subduction with bathymetric highs have been conducted, allowing scientists to better understand its dynamic effects: 1) the transition from flat or low angle subduction to steep-slab subduction (Van Hunen et al., 2002; Van Hunen et al., 2004; Martinod et al., 2005; Gerya et al., 2009; Huangfu et al., 2016; Manea et al., 2017; Leng and Huang, 2018; Dai et al., 2020; Yan et al., 2020, 2021), 2) indentation of the trench (Dominguez et al., 1998, 2000; Morra et al., 2006), 3) surface topography development (Li F. C. et al., 2013; Ruh, 2016) and crustal shortening (Liao et al., 2018), 4) trench migration (Li Z. H. et al., 2013; Yoshida, 2017; Tao et al., 2020), 5) continental underplating (Vogt and Gerya, 2014; Magni et al., 2017). In particular, Tetreault and Buitier (2012, 2014), Yang et al. (2018) and Liu et al. (2021) have systematically presented how various crustal properties of bathymetric highs (with continent versus oceanic crustal affinity) impact the amount of accreted/subducted crust, the distinct modes of terrane accretion/complete subduction, and the deformation type of the overriding plate. However, these recent studies have employed a fixed terrane size

and did not investigate the effects of terrane thickness and width on slab subduction processes.

The South China Sea is one of the largest marginal seas of the western Pacific (Deng et al., 2020). The Manila trench is located at the eastern boundary of the SCS. It was created by the subduction of the SCS plate beneath the Philippine Sea Plate (PSP) since the early Neogene, and it was induced by the northwestern plate motion of the PSP (Huang et al., 2006; Fan et al., 2016; Wu et al., 2016) (Figure 1A). For the northern Manila trench at around 18° N–21.5° N, where an obvious seaward convex is found, the morphology of the subducted SCS plate is characterized by dramatic changes from a horizontal subducting angle to near-vertical (Figure 1B) (Fan et al., 2016; Wu et al., 2016; Chen et al., 2021). A large buoyant plateau (≥ 300 km in width) was proposed to explain the sharp convex in the trench line, and the crustal property of the plateau was recently proposed as highly thinned continental crust (12–15 km in thickness) (Eakin et al., 2014; Lester et al., 2014; Sibuet et al., 2016; Liu et al., 2018) rather than oceanic crust as early identified (Hsu et al., 2004). For the southern Manila trench at around 15° N–18° N, the most remarkable morphological relief is an almost straight trench line and widely distributed small seamounts (≤ 100 km in

width), such as the subducting Huangyan-Zhenbei seamounts chain. Based on high-resolution P-wave tomographic images, the morphology of the subducted SCS plate beneath the southern segment of the Manila trench showed no abrupt change in dipping angle (**Figure 1C**), whereas slab break-off might occur at the depths between 60 and 190 km near 17°N (Cheng et al., 2019). The trench shape and subducting slab morphology of the northern Manila trench are distinct from the southern segment. However, there have been few comprehensive analyses to discuss the relationship between the subducting bathymetric highs and the along-strike variations of the Manila trench.

In this study, we have undertaken a series of 2-D numerical thermomechanical experiments to investigate 1) the potential crustal properties of the northeastern SCS near the Manila trench at around 20° N and 2) the key physical parameters controlling the subducting slab morphology variations between the northern and southern Manila trench. Based on our systematic numerical results, we demonstrate that dramatic changes in the dip angle in the northern Manila trench and the convex shape were caused by subduction of a large thin continental terrane, whereas the smooth morphology of subducting slab in the southern segment and straight trench were associated with normal oceanic subduction with small seamounts.

GEOLOGICAL BACKGROUND

The South China Sea is located in an important geodynamic intersection zone surrounded by Eurasian plates and the Pacific and Indian oceans. The partial subduction of the SCS along the Manila trench represents the last phase of a near-complete Wilson cycle, following continental rifting, breakup, and seafloor spreading. Based on deep-tow magnetic anomalies, multi-channel seismic data, the results of microfossils from IODP Expeditions and $^{39}\text{Ar}/^{40}\text{Ar}$ data, the SCS has undergone multiphase rifting events since the Late Cretaceous to Paleogene (Sun et al., 2009; Franke et al., 2014; Li et al., 2015; Sibuet et al., 2016; Ding et al., 2020; Zhang et al., 2020; Zhao et al., 2021), leading to the opening of the SCS basin at ~32–33 Ma, and stopped spreading at ~15 Ma in the east subbasin and ~16 Ma in the southwest subbasin, followed by eastward subduction under the Philippine Sea Plate (PSP) along the Manila trench (Li C. F. et al., 2013, 2015; Chen et al., 2017, 2021; Jian et al., 2018; Sun et al., 2018; Deng et al., 2020; Hung et al., 2020). Large amounts of magmatism persisted for nearly 10 Ma after the cessation of seafloor spreading and generated the Zhenbei-Huangyan seamount chain (Sibuet et al., 2016; Hung et al., 2020).

There is a wide discussion on the geometry of the Manila trench (Yang et al., 1996; Bautista et al., 2001; Eakin et al., 2014; Fan et al., 2015, 2016), which forms a broad bend to the east at around 21°–18° N, trends N-S almost in a straight line from 18° to 13°N, and swerves abruptly to the ESE at its southern terminus at 13°N. Several models have been proposed to explain the sharp bend in the trench line. For example, Bautista et al. (2001) interpreted these as a collision and subsequent partial subduction of a large buoyant plateau (**Figure 1**). Despite its

implications to the buoyancy effect, the crustal properties of this plateau in northeastern SCS remain controversial.

Geophysical studies on the deep lithospheric structures of the northeastern SCS near the northern Manila trench contribute to defining the continent-ocean boundary (COB) locations in the SCS. The crust located west of the Manila trench and north of the COB is thinned continental crust rather than thickened oceanic crust (Liu et al., 2018). Early studies defined COB1 (**Figure 1**) and suggested that the northeastern SCS was composed entirely of ocean crust up to 21.5°N (Hsu et al., 2004), based on E-W trending magnetic anomalies. Controversially, later evidence from refraction and multi-channel seismic (MCS) reflection data (Wang et al., 2006; Yeh et al., 2010, 2012; Lester et al., 2013, 2014; McIntosh et al., 2013, 2014; Eakin et al., 2014; Sibuet et al., 2016) defined the COB location as being more southeastward (COB2 in **Figure 1**). For example, Eakin et al. (2014) showed evidence for extended to hyper-extended continental crust subducting along the Manila trench, underplated to the accretionary prism at 21.5°N. Sibuet et al. (2016) has presented several features on MCS profiles suggesting that the crust of the northeastern part of the SCS is thinned continental crust intruded by post-rift volcanism. Most recently, an E-W oriented ocean bottom seismograph wide-angle refraction profile (21° N) is constructed in the northeastern SCS in 2015 (Liu et al., 2018) to further define the COB location (COB3 in **Figure 1**). Abundant Moho interface was shown, and a 12–15 km thick continental crust was further identified. Additionally, dramatic changes in the dipping angle of the subducted SCS plate are revealed from the northern Manila trench (20°–21.5°N). According to seismic and tomography data in this area (Fan et al., 2016), at 20°N, the SCS plate initially subducts along the Manila trench to a ~250 km depth at a low angle of ~25°. Then, it changes abruptly to a higher dip angle of ~75° to a depth of ~500 km. Further tomography studies and slab unfolding estimated the subducted portion of the SCS slab extended 400–500 km east of the present Manila trench (Wu and Suppe, 2018).

Compared to the controversial crustal properties near the northern Manila trench, the SCS plate near the southern Manila trench (at ~15–17°N) is a typical or thickened oceanic crust, subducting with numerous seamounts. As these seamounts are formed after SCS seafloor spreading cessation, the dating results of seamount ages range from 15–6.64 Ma (Tu et al., 1992; Yan et al., 2008; Wang et al., 2009; Zhang et al., 2020) based on petrological samples. Huangyan-Zhenbei seamounts chain, located in the center of the east subbasin, is an E-W trending chain of seamounts oriented obliquely to the surrounding N055° seafloor expansion trends (Zhao et al., 2018) (**Figure 1**). It consists of Zhenbei seamount in the westmost (9.1 ± 0.2 – 10.0 ± 1.8 Ma, basalts isotopic age) (Wang et al., 2009), the Huangyan seamount in the middle, and a further east one with NEE-trending that reaches the Manila trench (Cheng et al., 2019). The crustal thickness beneath the Huangyan and Zhenbei seamounts is generally between 12 and 13.2 km based on wide-angle seismic refraction data (He et al., 2016; Zhao et al., 2018). High-resolution regional tomographic studies show that the SCS slab subducts along the southern Manila trench (at

16–17°N) at an angle of ~45°–300 km depth, and the slab morphology is smooth without dramatic changes in the dipping angle (**Figure 1C**).

The 1,200 km long NS-trending Luzon island arc, stretching from 24°N to 13°N, resulted from the subduction of the SCS plate beneath the PSP along the Manila trench (Fan et al., 2016; Liu et al., 2021), which was induced by continuous NNW movement of the PSP since 25 Ma. The average plate convergence rate between the PSP and SCS was given as 7 cm/yr (Seno et al., 1993; Kreemer et al., 2003; Simons et al., 2007; Hsu et al., 2012). The Moho discontinuity is identified at a depth of 18–34 km in Luzon inferred from receiver function analysis (Besana et al., 1995). The results agree with a more recent gravity model by Manalo et al. (2015), reflecting a ~21–31 km thick crust across the Central Philippines.

NUMERICAL IMPLEMENTATION AND MODEL SETUP

Governing Equations

The momentum, continuity, and heat conservation equations for the two-dimensional creeping-flow, accounting for thermal and chemical buoyancy, were solved using modified I2VIS code (Gerya & Yuen, 2003, 2007). The incompressible continuity equation approximated conservation of mass:

$$\frac{\partial v_x}{\partial x} + \frac{\partial v_z}{\partial z} = 0$$

Two-dimensional Stokes equations:

$$\begin{aligned} \frac{\partial \sigma'_{xx}}{\partial x} + \frac{\partial \sigma'_{xz}}{\partial z} &= \frac{\partial P}{\partial x} \\ \frac{\partial \sigma'_{zz}}{\partial z} + \frac{\partial \sigma'_{xz}}{\partial x} &= \frac{\partial P}{\partial z} - g\rho(T, P, C) \end{aligned}$$

and a heat conservation equation:

$$\begin{aligned} \rho C_p \left(\frac{DT}{Dt} \right) &= -\frac{\partial q_x}{\partial x} - \frac{\partial q_z}{\partial z} + H_r + H_a + H_s \\ q_x &= -k(T, P, C) \frac{\partial T}{\partial x}, \quad q_z = -k(T, P, C) \frac{\partial T}{\partial z} \\ H_r &= \text{constant } (C), \quad H_a = T\alpha \frac{DP}{Dt}, \\ H_s &= \sigma'_{xx} \dot{\epsilon}_{xx} + \sigma'_{zz} \dot{\epsilon}_{zz} + 2\sigma'_{xz} \dot{\epsilon}_{xz} \end{aligned}$$

are used, where D/Dt is the substantive time derivative; $k(T, P, C)$ is the thermal conductivity as a function of temperature (T), pressure (P), and composition (C) (Hofmeister, 1999); C_p is the effective isobaric heat capacity, incorporating latent heat; H_r , H_a , and H_s denote radioactive heat production, the energetic effect of isothermal (de)compression (i.e., adiabatic heating/cooling), shear heating, α is the thermal expansion coefficient, σ'_{xx} , σ'_{zz} , σ'_{xz} are deviatoric stress components and $\dot{\epsilon}_{xx}$, $\dot{\epsilon}_{zz}$, $\dot{\epsilon}_{xz}$ are strain rate components.

Rock Rheology Implementation

Viscosity, dependence on strain rate, pressure, and temperature were defined in terms of deformation invariants:

$$\begin{aligned} \eta_{diffusion} &= \frac{A_D}{2\sigma_{cr}^{n-1}} \exp\left(\frac{E_a + V_a P}{RT}\right) \\ \eta_{dislocation} &= \frac{1}{2} \left(\dot{\epsilon}_{II} \right)^{\frac{1-n}{n}} (A_D)^{-\frac{1}{n}} \exp\left(\frac{E_a + V_a P}{nRT}\right) \\ \frac{1}{\eta_{ductile}} &= \frac{1}{\eta_{diffusion}} + \frac{1}{\eta_{dislocation}} \end{aligned}$$

where $\dot{\epsilon}_{II}$ is the second invariant of the strain rate; σ_{cr} denotes critical stress between dislocation creep and diffusion; A_D , E_a , V_a , and n are material constant, activation energy, activation volume, and stress exponent, respectively (Gerya, 2019; Tang et al., 2020). These material properties were determined from laboratory flow experiments and are provided in **Table 1**.

Plasticity was implemented using the Druker-Prager yield criterion (Ranalli, 1995). The calculated creep viscosity is therefore limited as follows:

$$\begin{aligned} \sigma_{yield} &= C + P \sin(\varphi_{eff}) \\ \eta_{plastic} &= \frac{\sigma_{yield}}{2\dot{\epsilon}_{II}} \end{aligned}$$

σ_{yield} is the yield stress. C is the residual rock strength. P is the dynamic pressure. φ is the internal frictional angle. φ_{eff} can be illustrated as the effective internal frictional angle.

With the $\eta_{plastic}$ and $\eta_{ductile}$, visco-plastic rheology is employed to the model where the rheology behavior depends on the minimum viscosity (Ranalli, 1995):

$$\frac{1}{\eta_{eff}} = \frac{1}{\eta_{ductile}} + \frac{1}{\eta_{plastic}}$$

Model Setup

The initial configuration of reference 2D numerical model is shown in **Figure 2**. The numerical model box with 1,361 by 351 nodal points is non-uniform and corresponded to 4,000 by 1,400 km physical dimension. The rectangular grid contain a 1,000 km wide high-resolution area of 1 by 1 km grid step size in the center of the domain. The rest of the model is at a lower resolution (up to 10 by 10 km grid step size). Over 5.7 million Lagrangian markers randomly distribute in the whole model domain.

The oceanic crust contain a thin continental terrane, fated to collide with the seaward-moving overriding continental plate. The oceanic crust is composed of 2-km-thick upper crust of hydrothermally-altered basalt, underlain by 5-km-thick lower crust of gabbroic rocks that covered 2,500 km horizontally. The continental crust is felsic and has a total thickness of 30 km, composed of 15 km upper and 15 km lower crust that extend over 1,500 km. The large 300 km wide and 15 km thick continental terrane is defined 200 km from the trench on the oceanic plate. Oceanic plateau (**Figure 2B**) paired numerical experiments with similar parameters differing only by the crustal property of the terrane are run in parallel to compare the different dynamic effects with continental terrane. Lithosphere yield stress profiles comparing the properties of continental terrane and oceanic plateau are shown in **Figures**

TABLE 1 | Material properties used in the numerical experiments.

Material	State	ρ_0 (kg m ⁻³)	k (W m ⁻¹ K ⁻¹)	H_r (μ W m ⁻³)	Plastic Sin(ϕ_{eff})	Viscous Flow law	η_0 (pa ⁿ s)	E_a (kJ mol ⁻¹)	V_a (J bar ⁻¹)	n
CUC	Solid	2,700	$0.64 + 807/(T + 77)$	1.0	0.15	Wet Quartzite	1.97×10^{17}	154	1.2	2.3
CLC	Solid	2,800	$0.64 + 807/(T + 77)$	0.25	0.15	Plagioclase_An75	4.8×10^{22}	238	0.8	3.2
OUC	Solid	3,000	$1.18 + 474/(T + 77)$	0.25	0	Wet Quartzite	1.97×10^{17}	154	0.8	2.3
OLC	Solid	3,000	$1.18 + 474/(T + 77)$	0.25	0.6	Plagioclase_An75	4.8×10^{22}	238	0.8	3.2
Mantle	Dry	3,300	$0.73 + 1293/(T + 77)$	0.022	0.6	Dry_olivine	3.98×10^{16}	532	0.8	3.5
	Wet	3,200			0	Wet_olivine	5.01×10^{20}	470	0.8	4.0
References	—	1,2	3	1	—	4	4	4	4	4

References: 1, Turcotte and Schubert, 2002; 2, Bittner and Schmeling, 1995; 3, Clauser and Huenges, 1995; 4, Ranalli, 1995. CUC, continental upper crust; CLC, continental lower crust; OUC, oceanic upper crust; OLC, oceanic lower crust.

2C,D. Both the asthenosphere and upper mantle are composed of anhydrous peridotite and are defined by the temperature profile. The rheological parameters used in the reference model are summarized in **Table 1**. We keep our model with a far-field push on the overriding plate (7 cm/yr) to be similar to the average plate convergence rates of the Manila trench (Seno et al., 1993; Kreemer et al., 2003; Simons et al., 2007; Hsu et al., 2012) while simultaneously as simple as possible to test different model parameters. It is also important to note that prescribing velocity of overlying rather than subducting plate enhances tendency of slab flattening (van Hunen et al., 2004).

All mechanical boundary conditions are free slip, and only the lower boundary was permeable, satisfying an external free slip boundary condition (Gorczyk et al., 2007; Ueda et al., 2008). In addition, on the top of the rocky portion of the model is treated as an internal free surface (Schmeling et al., 2008) by using a top layer (of 20 km thickness) with low viscosity (10^{18} Pas) and low density (1 kg/m³ for air, 1,000 kg/m³ for sea water) to allow for the surface topographic evolution.

The initial temperature field of the oceanic plate is defined by its oceanic geotherm for a specific lithospheric cooling age of 20 Ma, according to the subducting slab age of the Manila trench (Wu et al., 2016). The oceanic plateau embedded into the oceanic crust is assumed to have the same thermal structure as the oceanic lithosphere. Therefore, the initial temperature field of the continental plate is increased linearly from 0°C at the surface to 1,344°C at the lithosphere-asthenosphere boundary (140 km depth). For the asthenospheric mantle (>140 km), a thermal gradient of 0.5°C km⁻¹ is used.

SUBDUCTION OF THIN CONTINENTAL TERRANE

A series of models (Model-C100, Model-C200, Model-C300, Model-C400) are conducted to test the influence of a bathymetric high with continental affinity. We focus on the thickness and width of the terrane. Four groups of experiments with fixed terrane width (100 km, 200 km, 300 km, and 400 km for each group) are examined by changing the terrane thickness (10 km, 15 km, 20 km, 25 km,

and 30 km in thickness for each group). A representative selection of the models is shown in **Table 2** to discuss how different size terranes embedded in the subducting slab affect the subduction process.

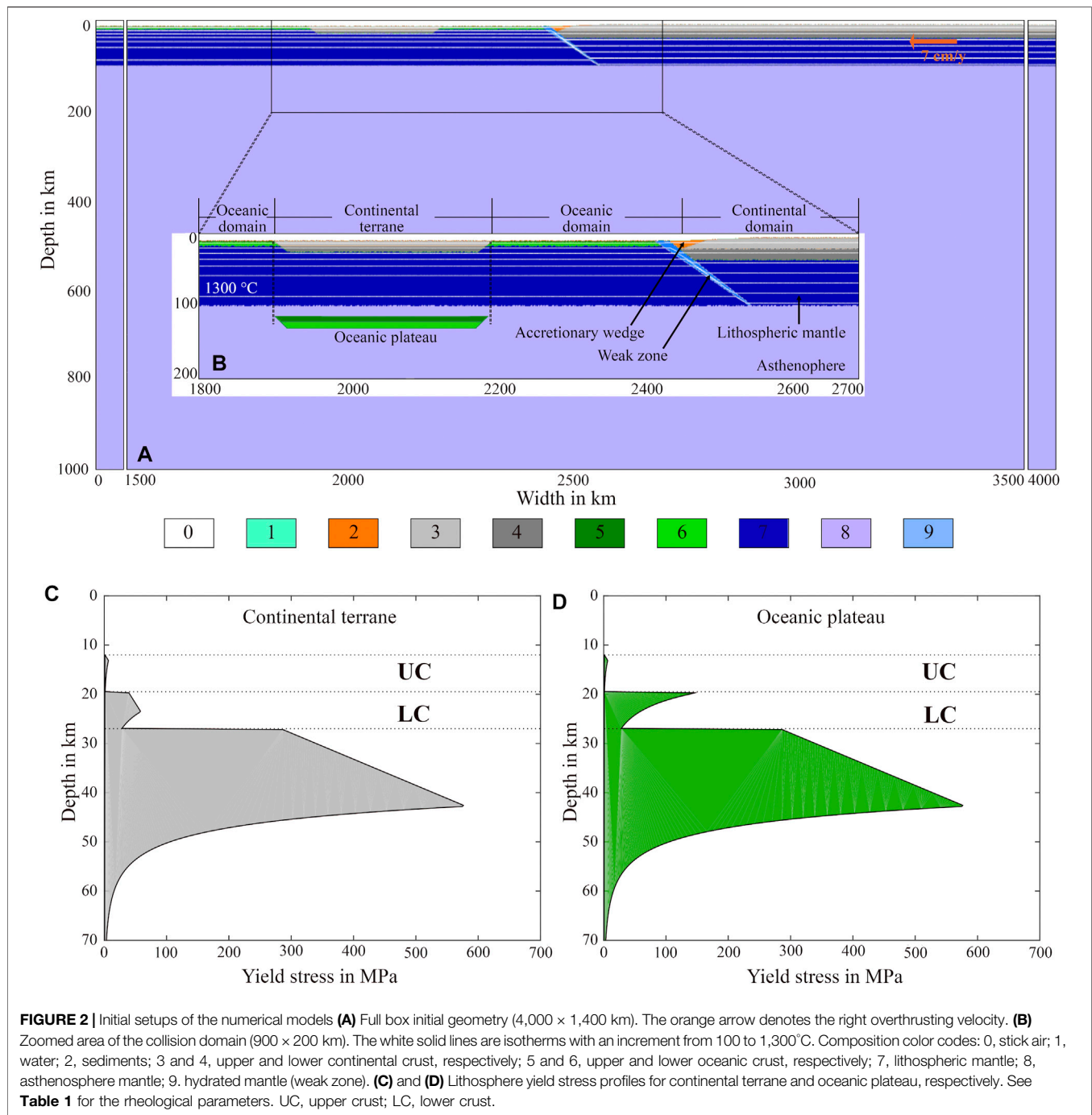
Reference Model

The numerical evolution of the reference model (Model-C300-15) is shown in **Figure 3**. In this model, a thin continental terrane (15-km thick, 300-km wide) is embedded in the oceanic plate. The slab initially subducts with a smooth morphology, and the thin continental terrane passes through the subduction channel (**Figure 3A**). A small part of the upper crust of the terrane is accreted to the overriding continent margin. This leads to an uplift in the accretionary wedge (**Figure 3B1**). Then the terrane is subducted into the deep mantle creating a shallower slab angle at a depth of ~100 km. The downgoing oceanic plate is substantially narrowed at a depth of ~250 km and shows a rheologically weak gap in the narrowed part (**Figure 3C2**), leading to an abrupt change in the dipping angle (from ~20° to ~58°) (**Figure 3C1**). Finally, the slab pull causes the occurrence of slab break-off (**Figure 3D**). This model illustrates that the subduction of a large (300-km wide) terrane with thin continental (15-km thick) affinity leads to an abrupt change in the dip angle and an uplift in the accretionary prism.

Variations in Thickness of Large-Size Terranes (≥ 300 km in Width)

Model-C400 differs from Model-C300 only because the continental terrane has a larger width (400-km wide continental terrane). The evolution of Model-C400 is similar to Model-C300. **Figure 4** shows the morphology of the subducted plate right before breaking off.

For terranes with thin continent crust (≤ 15 km in thickness) (Liu et al., 2018; Deng et al., 2020), abrupt changes in dipping angle are shown in **Figures 4A,B,F,G**, and the plates narrow at a depth of 200–300 km. **Figures 4A,B** show that the significant change in the dip angle happens after the terrane pushes into the mantle in Model-C300, whereas part of the terrane is still going through the subduction channel in Model-C400 due to a larger width.



In the case of a normal-thickness continental terrane (25–30 km in thickness), most of the terrane is blocked in the subduction zone before the slab breaks off, and only smaller parts are sheared off and dragged down into the mantle (Figures 4D,E,I,J). For both Model-C300 and Model-C400, the oceanic slab subducts at a shallow angle at an early stage and gradually steepens to nearly vertical. The morphology of the downgoing plate remained smooth and showed no abrupt change in the dipping angle before the slab broke off. Most parts of the thick continental terrane were blocked due to its buoyancy (Cloos,

1993), and terrane collision and lateral accretion occurred to accommodate the constant convergence (Figure 5). A “subduction zone jump” (Yan et al., 2021) after the collision is shown in Figure 5, which may be caused by the detachment of the buoyant crust of the terrane (Zhang et al., 2020).

Terranes with thin continent crust (20 km in thickness) act as a transition from thin terrane subduction with an abrupt morphology change to normal-thickness terrane collision. The oceanic plate is subducted at a gradually deeper angle, and there is no abrupt change in slab morphology before the slab breaks off

TABLE 2 | Parameters and results of representative experiments.

Model name	Terrane	Terrane Width (km)	Terrane Thickness (km)	Results
Model-C300-10	Continent (large)	300	10	Figure 4
Model-C300-15 (Reference model)	Continent (large)	300	15	Figure 3
Model-C300-20	Continent (large)	300	20	Figure 4
Model-C300-25	Continent (large)	300	25	Figure 4
Model-C300-30	Continent (large)	300	30	Figure 4
Model-C100-10	Continent (small)	100	10	Figure 6
Model-C100-15	Continent (small)	100	15	Figure 6
Model-C100-20	Continent (small)	100	20	Figure 6
Model-C100-25	Continent (small)	100	25	Figure 6
Model-C100-30	Continent (small)	100	30	Figure 6
Model-O300-15	Oceanic (large)	300	15	Figure 7
Model-O100-10	Oceanic (small)	100	10	Figure 8
Model-O100-15	Oceanic (small)	100	15	Figure 8
Model-O100-20	Oceanic (small)	100	20	Figure 8
Model-O100-25	Oceanic (small)	100	25	Figure 8
Model-O100-30	Oceanic (small)	100	30	Figure 8
Model-O400-10	Oceanic (large)	300	10	Figure 8
Model-O400-15	Oceanic (large)	300	15	Figure 8
Model-O400-20	Oceanic (large)	300	20	Figure 8
Model-O400-25	Oceanic (large)	300	25	Figure 8
Model-O400-30	Oceanic (large)	300	30	Figure 8

(Figures 4C,H). Most of the upper crust of the subducting thin continental terrane is accreted to the leading edge of the overriding plate. In contrast, the lower crust and minor part of the upper one bypass the accretionary prism and is lost by subduction. As a result, crustal thickening accumulate in the downgoing plate and propagate toward the accretionary wedge. The depth at which part of the terrane detached from the subducting slab is as shallow as 30 km. Thickened upper crust contributes to a vertical increase of accretionary prism (Figures 4C1,H1), which is similar to the uplift in the reference model (Figure 3B).

The Model-C300 and Model-C400 sets demonstrate that the thickness of a large continental terrane plays a vital role in slab morphology during the subduction process. A thin continental terrane causes an abrupt change in dipping angle before slab breakoff, while a normal-thickness continental terrane resists subduction and encourages “subduction zone jump” (Figure 5).

Variations in Thickness of Moderate/Small-Size Terranes (200 km/100 km in Width)

Model-C100 and Model-C200 are identical to the reference model except for the terrane width. Model-C100 has a small-size continental terrane (100-km wide) (Yan et al., 2021), and Model-C200 has a moderate-size continental terrane (200-km wide) (Gerya et al., 2009). Figure 6 shows the morphology of the subducting plate right before breaking off.

A small and thin continental terrane (100 km in width and ≤ 15 km in thickness) leads to complete terrane subduction. As the whole terrane is dragged down into the deep mantle, the downgoing plate show no change in the dipping angle (Figure 6A) or a relatively slight change from 29° to 44° (Figure 6B). The change in slab morphology is more obvious in the moderate-size continental terrane subducting process (Figures 6F,G). When the small/

moderate-size terrane has a thicker crust (20–30 km thick), the model evolution is similar to Model-C300 and Model-C400, which present the large continental terrane subduction. The subducting slab show no abrupt change in the dipping angle before breaking off (Figures 6C–F, H–J), with blocked terrane and subsequent “subduction zone jump” in normal-thickness continental terrane models (25–30 km thick), and partial terrane accretion in thin continental terrane model (20 km thick).

Model-C100 and Model-C200 illustrate that the width of the continental terrane is also a controlling factor on the subducting slab morphology. Thus, the moderate-size continental terrane or wider ones are more likely to form the abrupt change of dipping angle during the subducting process.

SUBDUCTION OF OCEANIC PLATEAU

We test the effect of oceanic plateau subduction to clarify its different influence on slab morphology from continental terrane subduction. Figure 7 show the evolution of Model-O300-15 with an oceanic plateau (15-km thick, 300-km wide) embedded in the subducting plate. The oceanic plate begin to subduct along the weak zone. Once the oceanic plateau enter the subduction zone, a large part of the upper crust of the plateau is sheared off and accreted into the accretionary prism (Figures 7A1,B1). When the oceanic plateau bypass the subduction channel, the downgoing oceanic plate show no abrupt change in dipping angle (Figures 7A1, B1, C1). Materials of the forearc region of the overriding plate do not show obvious uplift. The slab break-off occur before the whole plateau is dragged down into the subduction channel (Figure 7C1). Significant flexural stresses are generated in the subducting plate before breaking off (Figure 7B2).

A series of oceanic plateau models (Model-O100, Model-O200, Model-O300, and Model-O400) are performed to compare their influence on subducting slab morphology and

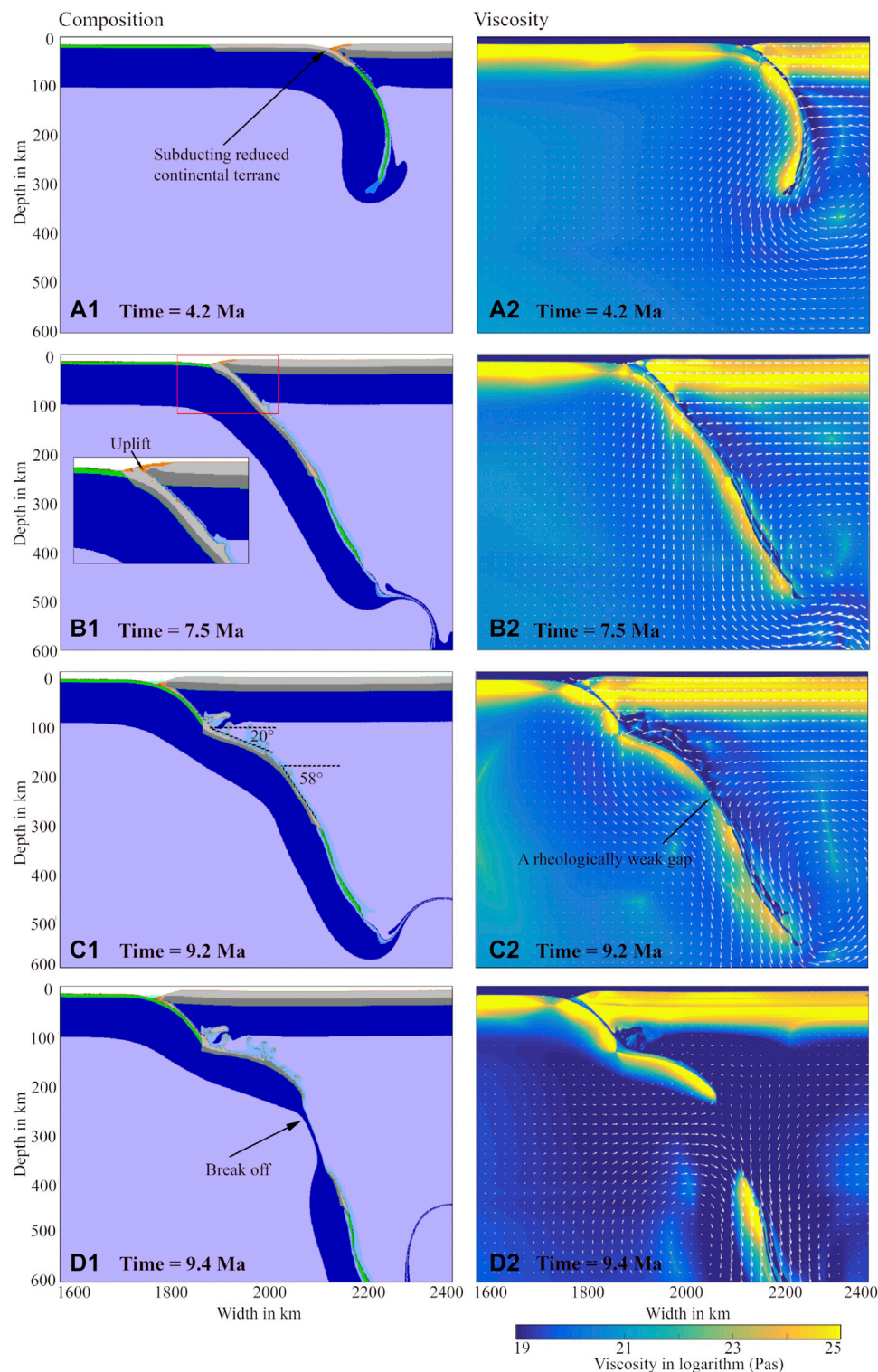


FIGURE 3 | Evolution of the reference model (Model-C300-15), with thinned continental terrane (15-km thick, 300-km wide). Left: Evolution of composition in Model-C300-15. The composition code shown here is the same as in **Figure 1**. Right: Evolution of viscosity in Model-C300-15. Black arrows in **(A1)**, **(B1)**, **(D1)** and **(C2)** indicates the partially subducted continental terrane, the uplift in the accretionary wedge, the slab break off, and the rheologically weak gap in the mantle, respectively. Red box in **(B1)** indicates the uplift in the accretionary wedge. The magnitude of angle in Figure C1 shows the abrupt change of dipping angle.

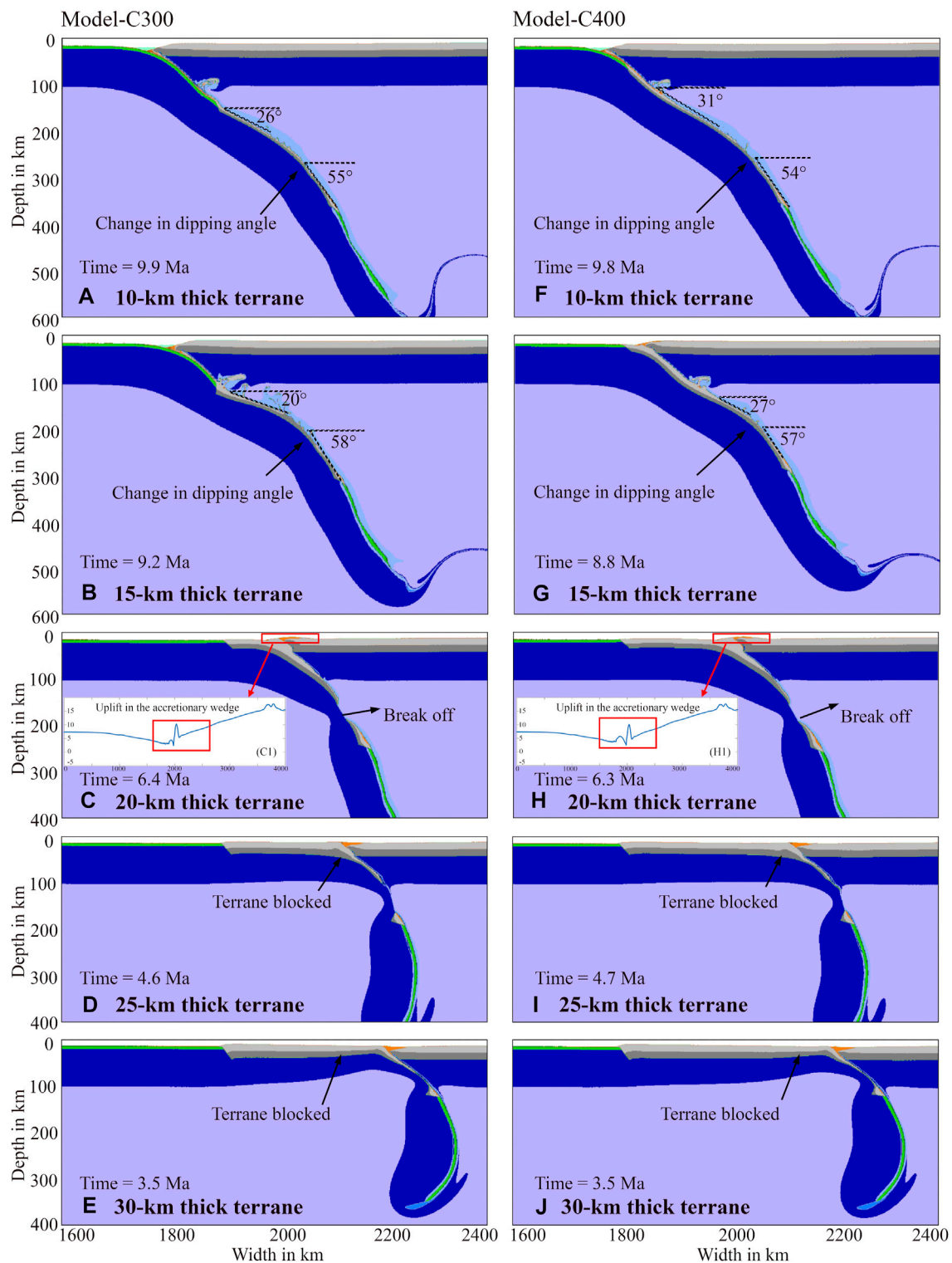
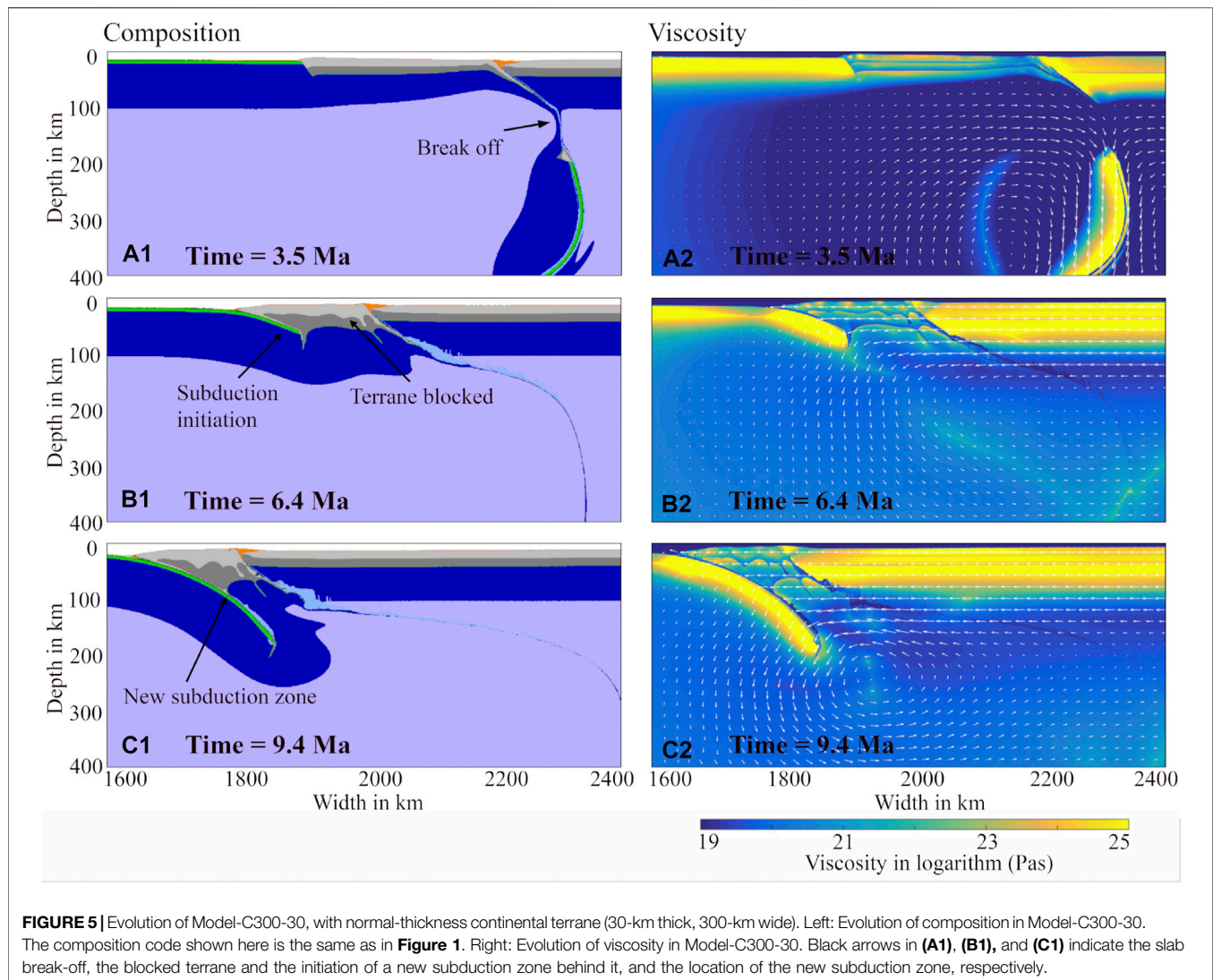


FIGURE 4 | Comparison of large-size terrane models with varied terrane thickness, showing the slab morphology right before breaking off. **(A–E)** Slab morphology of Model-C300, in which the terrane is 300 km wide. The terrane thickness is 10–30 km from A to E, respectively. **(C1)** Topography result of Figure **(C)**. **(F–J)** Slab morphology of Model-C400, in which the terrane is 400 km wide. The terrane thickness is 10–30 km from F to J, respectively. **(H1)** Topography result of Figure **(H)** and **(H1)**. The black arrows in **(A)**, **(B)**, **(F)**, and **(G)** indicate the change in dipping angle. The black arrows in **(C)** and **(H)** refer to no abrupt change in dipping angle before slab break off. The red boxes and arrows indicate the uplift in the accretionary wedge. The black arrows in **(D)**, **(E)**, **(I)**, and **(J)** show the blocked terranes.



corresponding thicknesses to continental terrane models (Model-C100, Model-C200, Model-C300, and Model-C400). Here a selection of the models performed is shown in **Figure 8** to compare models with small/large-size oceanic plateaus (100 km/400 km in width). In **Figure 8**, it is clear that neither a small oceanic plateau nor a large one favored the abrupt change in the dipping angle, irrespective of how thick the oceanic plateau is. For plateau thicknesses no more than 20 km, part of the upper crust is accreted into the accretionary wedge, and the rest of the plateaus subduct into the deep mantle (**Figures 8A–C,F–H**). For plateau with an over-thickened crust (25 km or 30 km in thickness), most part of the plateau is blocked in the subduction zone before slab break-off (**Figures 8D,E,I,J**). According to our model results, a thicker oceanic plateau on the subducting plate favor a faster break-off event.

These model results indicate that the oceanic plateau subduction is more likely to form a smooth slab morphology, differing from the abrupt change in the dipping angle in thin continental terrane subduction models.

DISCUSSION

The Role of Crustal Properties and Size of Bathymetric Highs in Subducting Slab Morphology

Figure 9 summarizes the model results from varied terrane crustal properties, width, and thickness. The reference model has a 300 km wide and 15 km thick continental terrane. It is characterized by deep continental crust subduction and by an abrupt change in subducting slab morphology ($\Delta\theta > 20^\circ$, **Figure 9**). Additional tests show that: 1) terrane width or thickness variation has no significant effect on subducting slab morphology of oceanic plateau models (Model-O100, Model-O200, Model-O300, and Model-O400). No change in the dipping angle is observed ($\Delta\theta = 0^\circ$) before slab break-off occurs (**Figures 8, 9**). 2) continental terrane models with a terrane thickness ≥ 20 km (**Figures 4C–E, H–J, Figures 6C–E, H–J** and **Figure 9**) showed no abrupt change in the dipping angle before shallow slab

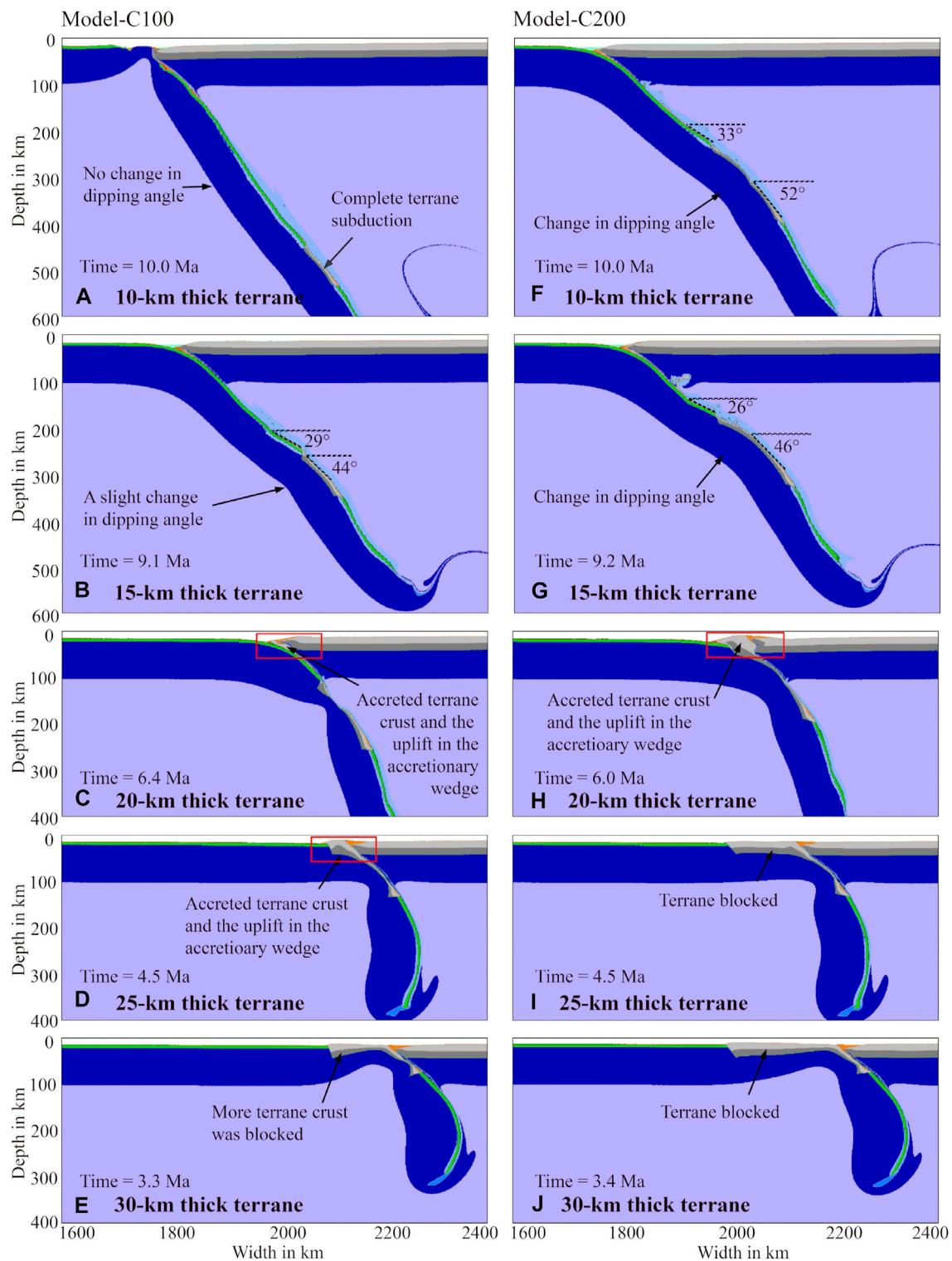


FIGURE 6 | Compared small/moderate-size continental terrane models with varied terrane thickness, showing the slab morphology right before breaking off. **(A–E)** Slab morphology of Model-C100, in which the terrane is 100 km wide. The terrane thickness is 10–30 km from A to E, respectively. **(F–J)** Slab morphology of Model-C200, in which the terrane is 200 km wide. The terrane thickness is 10–30 km from F to J, respectively. The black arrows in **(A)**, **(B)**, **(F)** and **(G)** indicate the change in dipping angle and the subducted terrane. The black arrows in **(C)**, **(D)**, and **(H)** indicate the partially accreted terrane crust. The red boxes in **(C)**, **(D)**, and **(H)** indicate the uplift in accretionary wedge. The black arrows in **(E)**, **(I)**, and **(J)** indicate the blocked terranes.

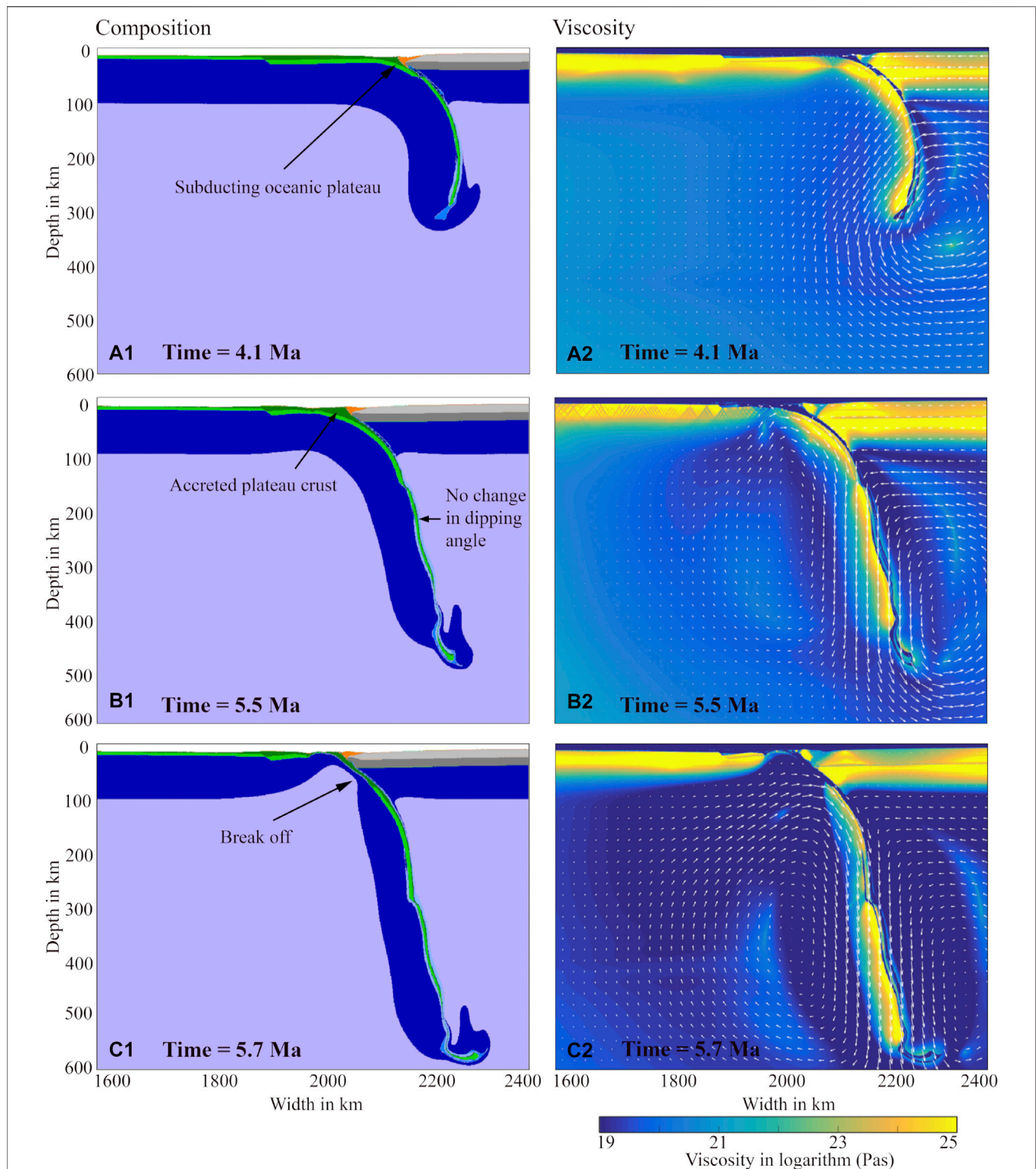


FIGURE 7 | Evolution of Model-O300-15, with oceanic plateau (15-km thick, 300-km wide). Left: Evolution of composition in Model-O300-15. The composition code shown here is the same as in **Figure 1**. Right: Evolution of viscosity in Model-O300-15. Black arrows in **(A1)**, **(B1)**, and **(C1)** indicate the subducting oceanic plateau, the partially accreted plateau crust and the smooth subducting slab morphology, and the slab break-off, respectively.

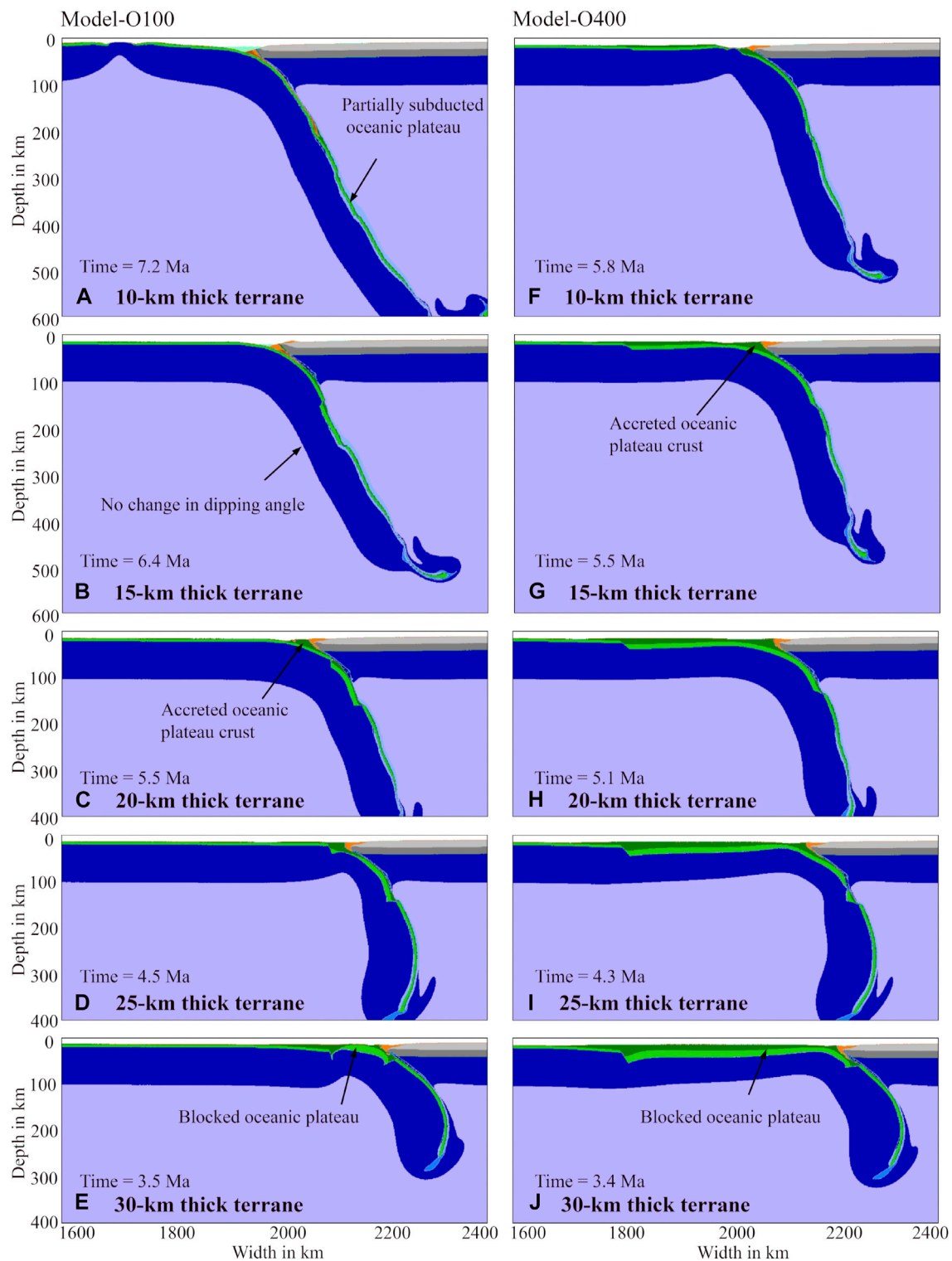
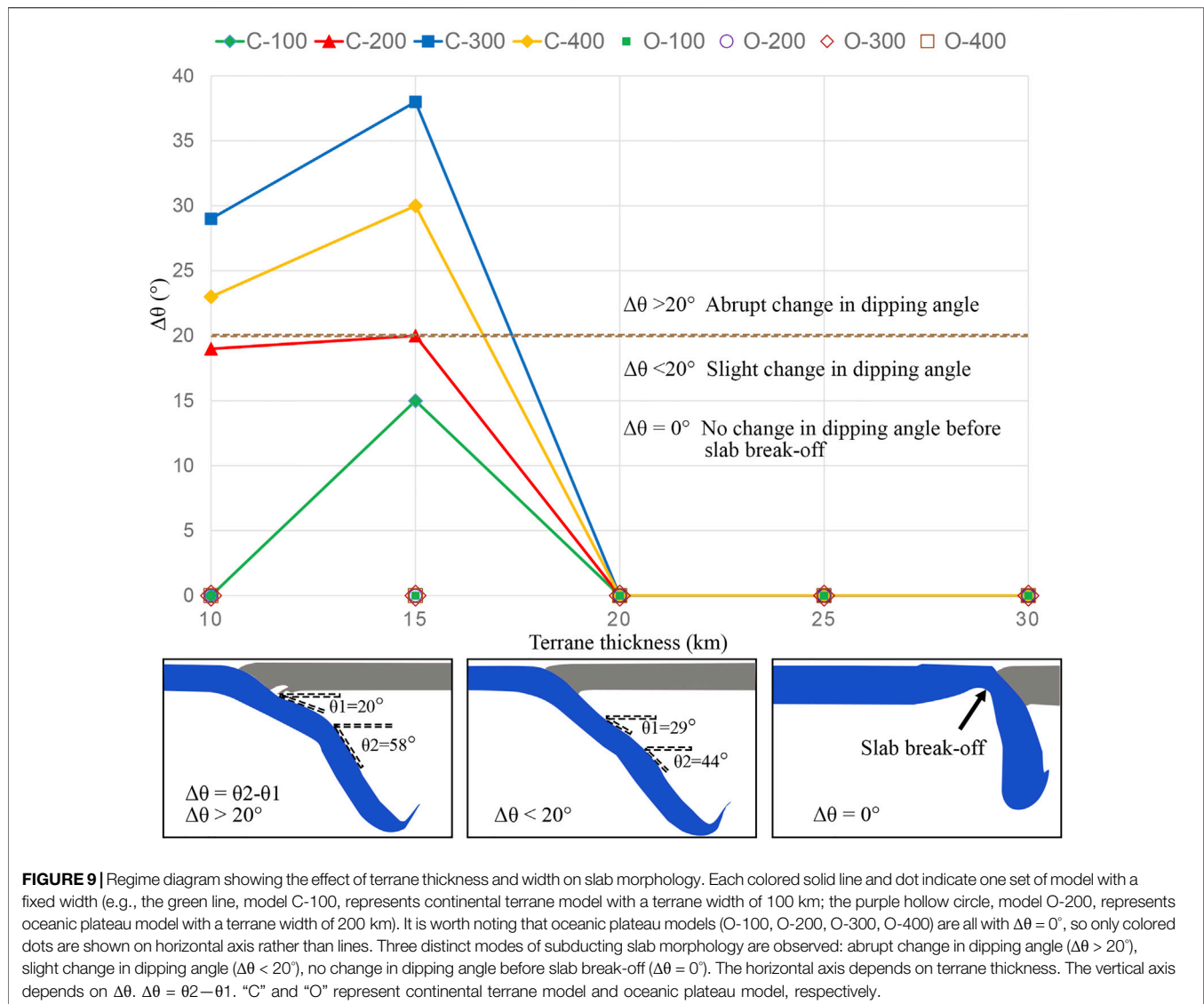


FIGURE 8 | Compared small/large-size oceanic plateau models with varied plateau thickness, showing the slab morphology right before breaking off. **(A–E)** Slab morphology of Model-O100, in which the oceanic plateau is 100 km wide. The plateau thickness is 10–30 km from A to E, respectively. **(F–J)** Slab morphology of Model-O400, in which the oceanic plateau is 400 km wide. The plateau thickness is 10–30 km from F to J, respectively. All the model results in this figure show no abrupt change in dipping angle.



break off, whatever how wide the terrane is. 3) in the context of thin continental terrane models (terrane thickness = 10 km or 15 km) (Figures 4A,B, F–G, Figure 6A,B, F–G and Figure 9), large-size terrane (Model-C300 and Model-C400) favors for the abrupt change of dipping angle ($\Delta\theta > 20^\circ$, Figure 9) during the subducting process. In contrast, small-size terrane (Model-C100) is more likely to result in a slight change in dipping angle ($\Delta\theta < 20^\circ$, Figure 9) or no change ($\Delta\theta = 0^\circ$, Figure 9) before slab break-off. Moderate-size terrane (Model-C200) is a transition type from abrupt change to slight change, and its $\Delta\theta = 20^\circ$ (Figure 9).

Our oceanic plateau models show no abrupt change in the dipping angle before slab break-off, consistent with the results of Cheng et al. (2019), who showed that seamount subduction promotes the break-off process, and Gerya et al. (2009), who showed smooth morphology of slab position lines. Other previous numerical models with bathymetric highs, including continental fragments, seamounts, oceanic plateaus, and island

arcs, focus on various types of accretion (Tetreault and Buitert, 2012, 2014; Li Z. H. et al., 2013; Vogt and Gerya, 2014; Yang et al., 2018). This partially compares well with our numerical experiments. Part of the upper crust of the subducting thin continental terrane/oceanic plateau is accreted to the leading edge of the overriding plate. The above models are 20 km thick and 100–200 km wide (small to moderate-size) bathymetric highs, consistent with the average thickness of global thin continental fragments/oceanic plateaus. Recent numerical modeling studies test small to large-size oceanic plateaus (Tao et al., 2020; Yan et al., 2021; Almeida et al., 2022; Wang et al., 2022) to investigate how buoyant plateaus contribute to dip angle change, subduction polarity reversal, and subduction zone jumping. Previous analogue models investigate the effects of seamount subduction on the structural deformation of the accretionary wedge, especially the evolution of faults in the wedge (Dominguez et al., 1998, 2000; Li F. C. et al., 2013; Wang et al., 2021). Li F. C. et al. (2013) investigates the

seamount subduction along the Manila trench by combining analog and gravity modeling, and suggests that the dip angle of subducting plate may be associated with extinct mid-ocean ridge subduction. However, as most of the analogue models focus on seamount or oceanic ridge subduction, the effects of continental terrane subduction are rarely to be compared with in analogue modeling. Our models systematically investigate the subduction process of different bathymetric highs with varied crustal properties, width, and thickness and further illustrate that the abrupt change of subducting slab morphology is not only controlled by the crustal properties of bathymetric high but also by its thickness and width.

Sharp changes in subducting slab angle imply localized slab bending, which is driven by combined effects of rheological weakness and positive buoyancy of subducted continental crust. Similar localized bending process (segmentation) of purely oceanic subducting slabs has been recently suggested by Gerya et al. (2021), which is primarily driven by strain weakening of outer-rise normal faults, and grain-size reduction (ductile damage) of the lithospheric mantle. However, our models do not consider the grain-size reduction in the slab, which prevents us from directly comparing our models with seismic tomography data beneath the Manila trench. Such comparison also requires (cf. discussion in Gerya et al., 2021) better resolution of seismic data in Manila subduction zone, which is currently unavailable.

Implications for the Subduction Along the Manila Trench

The Manila trench is characterized by distinct trench shape and subducting slab morphology between the northern and southern segment. Here, we apply our results to understand the relationship between the subducting bathymetric highs and the along-strike variations of the Manila trench. This study performed an overriding plate push at the rate of 7 cm/yr (Seno et al., 1993; Kreemer et al., 2003; Simons et al., 2007; Hsu et al., 2012), a relatively young subducting oceanic plate (20 Myrs) (Wu et al., 2016), and a thin continental terrane (15 km thick in the reference model) (Wang et al., 2006; Yeh et al., 2010, 2012; Lester et al., 2013, 2014; McIntosh et al., 2013, 2014; Eakin et al., 2014; Sibuet et al., 2016; Liu et al., 2018) to compare with the geological settings of the Manila trench.

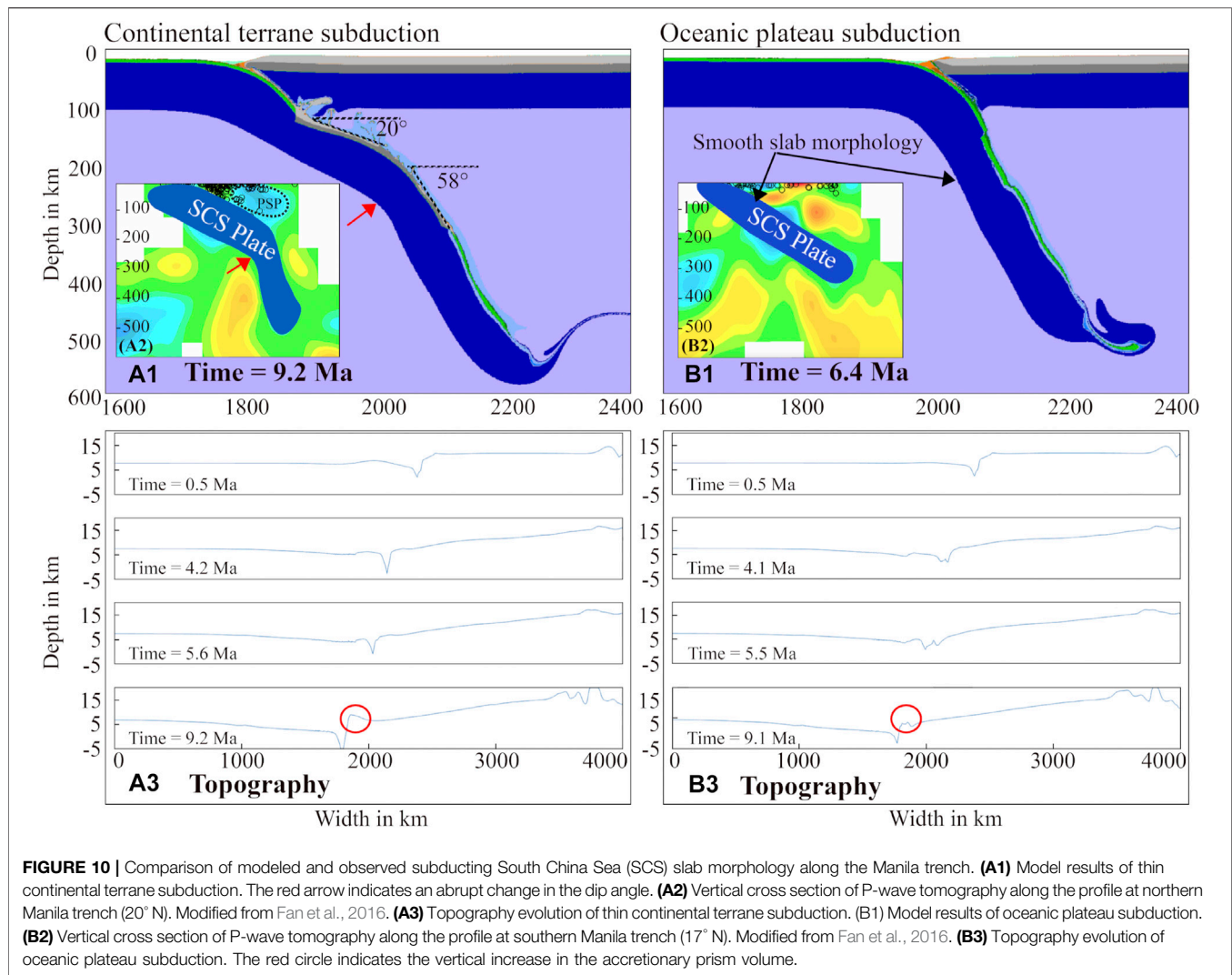
As shown in **Figure 1**, at around 20°N, where the maximum seaward convex of the Manila trench is found, the crustal property of the northeastern SCS was initially characterized as the oceanic crust (Hsu et al., 2004), whereas later studies suggested that it is thin continent crust with a thickness of ~12–15 km (Wang et al., 2006; Yeh et al., 2010, 2012; Lester et al., 2013, 2014; McIntosh et al., 2013, 2014; Eakin et al., 2014; Sibuet et al., 2016; Liu et al., 2018). Additionally, dramatic changes in the dipping angle of the subducted SCS plate are revealed from the northern Manila trench (20° N) (Fan et al., 2016; Wu et al., 2016; Chen et al., 2021). According to seismic and tomography data in this area (Fan et al., 2016), at 20° N, the SCS plate subducts initially along the Manila trench to ~250 km depth at a low angle of ~25°. Then, it abruptly changes to a higher dip angle of ~75° to a depth of ~500 km (**Figure 10A2**). In our model

results, the thin continental terrane was initially subducted along the subducting channel at a low angle. Then, it changed abruptly to a much higher dip angle (**Figure 10A1**), whereas all oceanic plateau models do not result in an abrupt change in the dipping angle. Thus, our continental terrane model result is consistent with the tomographic profile at the northern Manila trench (20°N), and further support that the crust located west of the Manila trench and around 20°N is a thin continental crust, rather than oceanic plateau.

In contrast, the southern Manila trench is characterized by widely distributed small-size seamounts (<100 km in width), e.g., Huangyan-Zhenbei seamounts chain with a crustal thickness between 13 and 14 km (He et al., 2016; Zhao et al., 2018; Cheng et al., 2019). Thus, our model with a 15 km-thick and 100 km-wide oceanic plateau is suitable for this area. This model does not result in an abrupt change in dipping angle (**Figure 10B1**), which is also compared well with the smooth slab morphology in the tomographic profile of the southern Manila trench (17° N) (**Figure 10B2**). Further investigation of lateral slab morphology variations will require application of 3D thermomechanical modelling approaches. Also, the model results indicate that the most important factor controlling the occurrence of an abrupt change in dipping angle is the crustal properties of bathymetric high along the Manila trench. Only subducting plate with continental terrane may initially subduct along the trench at a low angle and then changes abruptly to a higher dip angle, while comparable size oceanic plateau subduction favors for smooth subducting slab morphology.

Our model results exhibit that the second-order factor controlling the subducting slab morphology is the thickness of continental terrane. A thin continental terrane (10 km or 15 km thick) has a strong ability to result in an abrupt change in dipping angle before slab breakoff (**Figures 4, 6, 9**). In comparison, a thicker continental terrane (≥ 25 km thick) is more likely to be blocked in the subduction channel (**Figures 4, 6**), and favors for “subduction zone jump.” The latter point is similar to the ‘subduction zone jump’ phenomenon in Tao et al. (2020) and Yan et al. (2021), which is beyond the focus of this paper. In addition, the continental terrane width also has implications for affecting the downgoing slab morphology. According to our model results, the moderate-size continental terrane or wider ones (≥ 200 km in width) are more likely to form the abrupt change of dipping angle during the subducting process (**Figures 4, 6, 9**). These results are comparable with geological observations of the Manila trench, where large-size (≥ 300 km in width) and thin (≤ 15 km in thickness) continental terrane subduction leads to an abrupt change in the dipping angle in the northern segment, and small-size (≤ 100 km in width) seamounts subduction results in a smooth subducting slab morphology in the southern segment.

The geophysical studies of northern Manila trench indicate that the accretionary wedge shows an vertical volume increase, and it may be due to the accreted crustal material from the thin continental terrane (Eakin et al., 2014). According to our models, **Figures 10A3, B3** compare the topography evolution of large thin continental terrane subduction with small oceanic plateau



subduction. The former contributes to a relatively evident vertical increase in the accretionary wedge volume (**Figure 10A3**), which is similar with the topographic uplift in **Figures 4C1, H1**. These topographic results of continental terrane models agree with the geophysical observations from Eakin et al. (2014).

CONCLUSION

We test a series of 2-D geodynamic models to investigate subduction processes involving thin continental terrane and oceanic plateau and provide insights from numerical modeling on properties of the subducted crust of the South China Sea along the Manila trench. There are three key findings of the study.

1. The first-order factor controlling an abrupt change in the dipping angle is the crustal properties of bathymetric highs. Subducting plate with continental terrane initially subducts along the trench at a low angle and then changes abruptly to a higher dip angle. In contrast, comparable size oceanic plateau subduction does not result in the abrupt change in the dipping angle.
2. For continental terranes, the crustal thickness and terrane width affect the subducting slab morphology. The subduction of a wide continental terrane (≥ 300 km) with thin crust (≤ 15 km in thickness) favors the abrupt change in dipping angle. Overthickened terranes (≥ 25 km in thickness) are more likely to be blocked in the subduction zone.
3. The model results explain the differences in subducting slab morphology between the northern (around 20° N) and southern (around 17° N) segments of the Manila trench. For the northern Manila trench, numerical models with large thin continental terrane (≥ 300 km in width and ≤ 15 km in thickness) lead to an abrupt change in dipping angle, which corresponds to tomography profile at 20° N. On the other hand, for the southern Manila trench, models with small (≤ 100 km in width) oceanic plateaus (seamounts) are

characterized by smooth subducting slab morphology, which corresponds to the tomography profile at 17°N.

DATA AVAILABILITY STATEMENT

The original contributions presented in the study are included in the article/Supplementary Material, further inquiries can be directed to the corresponding author.

AUTHOR CONTRIBUTIONS

LM and JL conceived the study. LM and LC designed the numerical experiments. LM performed numerical experiments. LM, LC, ZC, and TG analyzed and interpreted results. TG provided the I2VIS code and guidance on improving the paper. LM, LC, ZC, TG, and JL wrote the paper.

REFERENCES

- Almeida, J., Riel, N., Rosas, F. M., Duarte, J. C., and Kaus, B. (2022). Self-replicating Subduction Zone Initiation by Polarity Reversal. *Commun. Earth Environ.* 3, 55. doi:10.1038/s43247-022-00380-2
- Bautista, B. C., Bautista, M. L. P., Oike, K., Wu, F. T., and Punongbayan, R. S. (2001). A New Insight on the Geometry of Subducting Slabs in Northern Luzon, Philippines. *Tectonophysics* 339, 279–310. doi:10.1016/S0040-1951(01)00120-2
- Besana, G. M., Shibutani, T., Hirano, N., Ando, M., Bautista, B., and Narag, I. (1995). The Shear Wave Velocity Structure of the Crust and Uppermost Mantle beneath Tagaytay, Philippines Inferred from Receiver Function Analysis. *Geophys. Res. Lett.* 22, 3143–3146. doi:10.1029/95GL03319
- Bittner, D., and Schmeling, H. (1995). Numerical Modeling of Melting Processes and Induced Diapirism in the Lower Crust. *Geophys. J. Int.* 123, 59–70. doi:10.1111/j.1365-246X.1995.tb06661.x
- Chen, L., Hu, J. W., Yang, D. H., Song, H. B., and Wang, Z. H. (2017). Kinematic Models for the Opening of the South China Sea: An Upwelling Divergent Flow Origin. *J. Geodyn.* 107, 20–33. doi:10.1016/j.jog.2017.03.002
- Chen, S. S., Gao, R., Wang, Z. W., Hou, T., Liao, J., and Yan, C. (2021). Coexistence of Hainan Plume and Stagnant Slab in the Mantle Transition Zone beneath the South China Sea Spreading Ridge: Constraints from Volcanic Glasses and Seismic Tomography. *Lithosphere* (Special 2), 1–22. doi:10.2113/2021/6619463
- Cheng, Z. H., Ding, W. W., Faccenda, M., Li, J. B., Lin, X. B., Ma, L. T., et al. (2019). Geodynamic Effects of Subducted Seamount at the Manila Trench: Insights from Numerical Modeling. *Tectonophysics* 764, 46–61. doi:10.1016/j.tecto.2019.05.011
- Clauser, C., and Huenges, E. (1995). “Thermal Conductivity of Rocks and Minerals,” in *Rock Physics and Phase Relations: A Handbook of Physical Constants*. Editor T. J. Ahrens (American Geophysical Union), 105–126.
- Cloos, M. (1993). Lithospheric Buoyancy and Collisional Orogenesis: Subduction of Oceanic Plateaus, Continental Margins, Island Arcs, Spreading Ridges, and Seamounts. *Geol. Soc. Am. Bull.* 105, 715–737. doi:10.1130/0016-7606(1993)105<0715:lbacos>2.3.co;2
- Dai, L. M., Wang, L. L., Lou, D., Li, Z. H., Dong, H., Ma, F. F., et al. (2020). Slab Rollback versus Delamination: Contrasting Fates of Flat-Slab Subduction and Implications for South China Evolution in the Mesozoic. *J. Geophys. Res. Solid Earth* 125, e2019JB019164. doi:10.1029/2019JB019164
- Deng, H. D., Ren, J. Y., Xiong, P., Rey, P. F., McClay, K. R., Watkinson, I. M., et al. (2020). South China Sea Documents the Transition from Wide Continental Rift to Continental Break up. *Nat. Commun.* 11, 4583. doi:10.1038/s41467-020-18448-y
- Ding, W. W., Sun, Z., Mohn, G., Nirrengarten, M., Tugend, J., Manatschal, G., et al. (2020). Later Evolution of the Rift-To-Drift Transition in the South China Sea: Evidence from Multi-Channel Seismic Data and IODP Expeditions 367&368 Drilling Results. *Earth Planet. Sci. Lett.* 351, 115932. doi:10.1016/j.epsl.2019.115932
- Dominguez, S., Lallemand, S. E., Malavieille, J., and von Huene, R. (1998). Upper Plate Deformations Associated with Seamount Subduction. *Tectonophysics* 293, 207–224. doi:10.1016/S0040-1951(98)00086-9
- Dominguez, S., Malavieille, J., and Lallemand, S. E. (2000). Deformation of Accretionary Wedges in Response to Seamount Subduction: Insights from Sandbox Experiments. *Tectonics* 19 (1), 182–196. doi:10.1029/1999tc900055
- Eakin, D. H., McIntosh, K. D., Van Avendonk, H. J. A., Lavie, L., Lester, R., Liu, C. S., et al. (2014). Crustal-scale Seismic Profiles across the Manila Subduction Zone: The Transition from Intraoceanic Subduction to Incipient Collision. *J. Geophys. Res. Solid Earth* 119, 1–17. doi:10.1002/2013JB010395
- Fan, J. K., Zhao, D. P., and Dong, D. D. (2016). Subduction of a Buoyant Plateau at the Manila Trench: Tomographic Evidence and Geodynamic Implications. *Geochim. Geophys. Geosyst.* 17, 571–586. doi:10.1002/2015GC006201
- Fan, J., Wu, S. G., and Spence, G. (2015). Tomographic Evidence for a Slab Tear Induced by Fossil Ridge Subduction at Manila Trench, South China Sea. *Int. Geol. Rev.* 57, 998–1013. doi:10.1080/00206814.2014.929054
- Franke, D., Savva, D., Pubellier, M., Steuer, S., Mouly, B., and Auxietre, J. L. (2014). The Final Rifting Evolution in the South China Sea. *Mar. Pet. Geol.* 58, 704–720. doi:10.1016/j.marpetgeo.2013.11.020
- Gerya, T. V., Fossati, D., Cantieni, C., and Seward, D. (2009). Dynamic Effects of Aseismic Ridge Subduction: Numerical Modelling. *Eur. J. Mineral.* 21, 649–661. doi:10.1127/0935-1221/2009/0021-1931
- Gerya, T. V. (2019). *Introduction to Numerical Geodynamic Modelling*. Second Edition. London: Cambridge Univ. Press, 73–80.
- Gerya, T. V., and Yuen, D. A. (2003). Rayleigh – Taylor Instabilities from Hydration and Melting Propel ‘Cold Plumes’ at Subduction Zone. *Earth Planet. Sci. Lett.* 212, 47–62. doi:10.1016/s0012-821x(03)00265-6
- Gerya, T. V., and Yuen, D. A. (2007). Robust Characteristics Method for Modeling Multiphase Visco- Elasto- Plastic Thermo-Mechanical Problems. *Phys. Earth Planet Inter.* 163, 83–105. doi:10.1016/j.pepi.2007.04.015
- Gorczyk, W., Willner, A. P., Gerya, T. V., Connolly, J. A. D., and Burg, J. P. (2007). Physical Controls of Magmatic Productivity at Pacific-type Convergent Margins: Numerical Modelling. *Phys. Earth Planet Inter.* 163, 209–232. doi:10.1016/j.pepi.2007.05.010
- He, E. Y., Zhao, M. H., Qiu, X. L., Sibuet, J. -C., Wang, J., and Zhang, J. Z. (2016). Crustal Structure across the Post-spreading Magmatic Ridge of the East Sub-basin in the South China Sea: Tectonic Significance. *J. Asian Earth Sci.* 121, 139–152. doi:10.1016/j.jseas.2016.03.003
- Hofmeister, A. M. (1999). Mantle Values of Thermal Conductivity and the Geotherm from Phonon Lifetimes. *Science* 283 (5408), 1699–1706. doi:10.1126/science.283.5408.1699
- Hsu, S. K., Yeh, Y. C., Doo, W. B., and Tsai, C. H. (2004). New Bathymetry and Magnetic Lineations Identifications in the Northernmost South China Sea and

FUNDING

This work is supported by Natural Science Foundation of Zhejiang, China (LQ20D060002), the Scientific Research Fund of the Second Institute of Oceanography, MNR, China (JG 1907), the Innovation Group Project of Southern Marine Science and Engineering Guangdong Laboratory (Zhuhai) (No. 311020018).

ACKNOWLEDGMENTS

The authors would like to thank Dr. Jie Liao for improving the model setup and commenting the early draft. The authors would like to thank Dr. Fucheng Li and one reviewer for their insightful and detailed reviews which substantially improved the manuscript. The authors also would like to thank Shangguo Chen for improving Figure 2.

- Their Tectonic Implications. *Mar. Geophys. Res.* 25, 29–44. doi:10.1007/s11001-005-0731-7
- Hsu, Y. J., Yu, S. B., Song, T. R. A., and Bacolcol, T. (2012). Plate Coupling along the Manila Subduction Zone between Taiwan and Northern Luzon. *J. Asian Earth Sci.* 51, 98–108. doi:10.1016/j.jseas.2012.01.005
- Huang, C. Y., Yuan, P. B., and Tsao, S. J. (2006). Temporal and Spatial Records of Active Arc-Continent Collision in Taiwan: a Synthesis. *Bull. Geol. Soc. Am.* 118 (3–4), 274–288. doi:10.1130/B25527.1
- Huangfu, P. P., Wang, Y. J., Cawood, P. A., Li, Z. H., Fan, W. M., and Gerya, T. V. (2016). Thermo-mechanical Controls of Flat Subduction: Insights from Numerical Modeling. *Gondwana Res.* 40, 170–183. doi:10.1016/j.gr.2016.08.012
- Hung, T. D., Yang, T., Le, B. M., Yu, Y. Q., Xue, M., Liu, B. H., et al. (2020). Crustal Structure across the Extinct Mid-ocean Ridge in South China Sea from OBS Receiver Functions: Insights into the Spreading Rate and Magma Supply Prior to the Ridge Cessation. *Geophys. Res. Lett.* 48, e2020GL089755. doi:10.1029/2020GL089755
- Jian, Z., Larsen, H. C., and Alvarez Zarikian, C. A. (2018). *Expedition 368 Preliminary Report: South China Sea Rifted Margin*. Texas, United States: International Ocean Discovery Program.
- Kreemer, C., Holt, W. E., and Haines, A. J. (2003). An Integrated Global Model of Present-Day Plate Motions and Plate Boundary Deformation. *Geophys. J. R. Astron. Soc.* 154 (1), 8–34. doi:10.1046/j.1365-246X.2003.01917.x
- Leng, W., and Huang, L. Z. (2018). Progress in Numerical Modeling of Subducting Plate Dynamics. *Sci. China Earth Sci.* 61, 1761–1774. doi:10.1007/s11430-017-9275-4
- Lester, R., McIntosh, K., Van Avendonk, H. J. A., Lavier, L., Liu, C. S., and Wang, T. K. (2013). Crustal Accretion in the Manila Trench Accretionary Wedge at the Transition from Subduction to Mountain-Building in Taiwan. *Earth Planet. Sci. Lett.* 375, 430–440. doi:10.1016/j.epsl.2013.06.007
- Lester, R., Van Avendonk, H. J. A., McIntosh, K., Lavier, L., Liu, C. S., Wang, T. K., et al. (2014). Rifting and Magmatism in the Northeastern South China Sea from Wide-Angle Tomography and Seismic Reflection Imaging. *J. Geophys. Res. Solid Earth* 119, 2305–2323. doi:10.1002/2013JB010639
- Li, C. F., Li, J. B., Ding, W. W., Franke, D., Yao, Y. J., Shi, H. S., et al. (2015). Seismic Stratigraphy of the Central South China Sea Basin and Implications for Neotectonics. *J. Geophys. Res. Solid Earth* 120, 1377–1399. doi:10.1002/2014JB011686
- Li, C. F., Lin, J., and Kulhanek, D. K. (2013c). *Opening of the South China Sea and its Implications for Southeast Asian Tectonics, Climates, and Deep Mantle Processes since the Late Mesozoic*. Texas, United States: International Ocean Discovery Program.
- Li, F. C., Sun, Z., Hu, D. K., and Wang, Z. W. (2013a). Crustal Structure and Deformation Associated with Seamount Subduction at the North Manila Trench Represented by Analog and Gravity Modeling. *Mar. Geophys. Res.* 34, 393–406. doi:10.1007/s11001-013-9193-5
- Li, Z. H., Xu, Z. Q., Gerya, T., and Burg, J. P. (2013b). Collision of Continental Corner from 3-d Numerical Modeling. *Earth Planet. Sci. Lett.* 380, 98–111. doi:10.1016/j.epsl.2013.08.034
- Liao, J., Gerya, T., and Malusa, M. G. (2018). 3D Modeling of Crustal Shortening Influenced by Along-Strike Lithological Changes: Implications for Continental Collision in the Western and Central Alps. *Tectonophysics* 746, 425–438. doi:10.1016/j.tecto.2018.01.031
- Liu, S. Q., Zhao, M. H., Sibuet, J. -C., Qiu, X. L., Wu, J., Zhang, J. Z., et al. (2018). Geophysical Constraints on the Lithospheric Structure in the Northeastern South China Sea and its Implication for the South China Sea Geodynamics. *Tectonophysics* 742–743, 101–119. doi:10.1016/j.tecto.2018.06.002
- Liu, Z., Dai, L. M., Li, S. Z., Wang, L. L., Xing, H. L., Liu, Y. J., et al. (2021). When Plateau Meets Subduction Zone: A Review of Numerical Models. *Earth-Science Rev.* 215, 103556. doi:10.1016/j.earscirev.2021.103556
- Magni, V., Allen, M. B., van Hunen, J., and Bouilhol, P. (2017). Continental Underplating after Slab Break-Off. *Earth Planet. Sci. Lett.* 474, 59–67. doi:10.1016/j.epsl.2017.06.017
- Manalo, P. C., Dimalanta, C. B., Faustino-Eslava, D. V., Ramos, N. T., Queaño, K. L., and Yumul, G. P., Jr. (2015). Crustal Thickness Variation from a Continental to an Island Arc Terrane: Clues from the Gravity Signatures of the Central Philippines. *J. Asian Earth Sci.* 104, 205–214. doi:10.1016/j.jseas.2014.08.031
- Manea, V. C., Manea, M., Ferrari, L., Orozco-Esquivel, T., Valenzuela, R. W., Husker, A., et al. (2017). A Review of the Geodynamic Evolution of Flat Subduction in Mexico, Peru, and Chile. *Tectonophysics* 695, 27–52. doi:10.1016/j.tecto.2016.11.037
- Martinod, J., Funicello, F., Faccenna, C., Labanieh, S., and Regard, V. (2005). Dynamical Effects of Subducting Ridges: Insights from 3-D Laboratory Models. *Geophys. J. Int.* 163, 1137–1150. doi:10.1111/j.1365-246X.2005.02797.x
- Mason, W. G., Moresi, L., Betts, P. G., and Miller, M. S. (2010). Three- Dimensional Numerical Models of the Influence of a Buoyant Oceanic Plateau on Subduction Zones. *Tectonophysics* 483, 71–79. doi:10.1016/j.tecto.2009.08.021
- McIntosh, K., Lavier, L., van Avendonk, H., Lester, R., Eakin, D., and Liu, C. S. (2014). Crustal Structure and Inferred Rifting Processes in the Northeast South China Sea. *Mar. Pet. Geol.* 58, 612–626. doi:10.1016/j.marpetgeo.2014.03.012
- McIntosh, K., van Avendonk, H., Lavier, L., Lester, R., Eakin, D., Wu, F., et al. (2013). Inversion of a Hyper-Extended Rifted Margin in the Southern Central Range of Taiwan. *Geology* 41 (8), 871–874. doi:10.1130/G34402.1
- Miller, M. S., Gorbato, A., and Kennett, B. L. N. (2005). Heterogeneity within the Subducting Pacific Slab beneath the Izu-Bonin-Mariana Arc: Evidence from Tomography Using 3D Ray Tracing Inversion Techniques. *Earth Planet. Sci. Lett.* 235, 331–342. doi:10.1016/j.epsl.2005.04.007
- Miller, M. S., Kennett, B. L. N., and Lister, G. S. (2004). Imaging Changes in Morphology, Geometry, and Physical Properties of the Subducting Pacific Plate along the Izu-Bonin-Mariana Arc. *Earth Planet. Sci. Lett.* 224, 363–370. doi:10.1016/j.epsl.2004.05.018
- Morra, G., Regenauer-Lieb, K., and Giardini, D. (2006). Curvature of Oceanic Arcs. *Geology* 34 (10), 877–880. doi:10.1130/G22462.1
- Ranalli, G. (1995). *Rheology of the Earth*. London: Chapman & Hall.
- Rosebaum, G., Giles, D., Saxon, M., Betts, P. G., Weinberg, R. F., and Duboz, C. (2005). Subduction of the Nazca Ridge and the Inca Plateau: Insights into the Formation of Ore Deposits in Peru. *Earth Planet. Sci. Lett.* 239, 18–32. doi:10.1016/j.epsl.2005.08.003
- Ruh, J. B. (2016). Submarine Landslides Caused by Seamounts Entering Accretionary Wedge Systems. *Terra Nova* 0, 1–8. doi:10.1111/ter.12204
- Schmeling, H., Babeyko, A., Enns, A., Faccenna, C., Funicello, F., Gerya, T., et al. (2008). A Benchmark Comparison of Spontaneous Subduction Models – toward a Free Surface. *Phys. Earth Planet. Inter.* 171, 198–223. doi:10.1016/j.pepi.2008.06.028
- Seno, T., Stein, S., and Gripp, A. E. (1993). A Model for the Motion of the Philippine Sea Plate Consistent with NUVEL-1 and Geological Data. *J. Geophys. Res.* 98, 17941–17948. doi:10.1029/93JB00782
- Sibuet, J. -C., Yeh, Y. C., and Lee, C. S. (2016). Geodynamics of the South China Sea. *Tectonophysics* 692, 98–119. doi:10.1016/j.tecto.2016.02.022
- Simons, W. J. F., Socquet, A., Vigny, C., Ambrosius, B. A. C., Abu, S. H., Promthong, C., et al. (2007). A Decade of GPS in Southeast Asia: Resolving Sundaland Motion and Boundaries. *J. Geophys. Res.* 112, B06420. doi:10.1029/2005JB003868
- Sun, Z., Stock, J., and Klaus, A. the Expedition 367 Scientists (2018). Expedition 367 Preliminary Report: South China Sea Rifted Margin. *Int. Ocean. Discov. Program*. doi:10.14379/iodp.pr.367.2018
- Sun, Z., Zhong, Z. H., Keep, M., Zhou, D., Cai, D. S., Li, X. S., et al. (2009). 3D Analogue Modeling of the South China Sea: A Discussion on Breakup Pattern. *J. Asian Earth Sci.* 34, 544–556. doi:10.1016/j.jseas.2008.09.002
- Tang, J., Chen, L., and Meng, Q. (2020). The Effects of the Thermal State of Overriding Continental Plate on Subduction Dynamics: Two-Dimensional Thermal-mechanical Modeling. *Sci. China Earth Sci.* 63, 1519–1539. doi:10.1007/s11430-019-9624-1
- Tao, J. L., Dai, L. M., Lou, D., Li, Z. H., Zhou, S. H., Liu, Z., et al. (2020). Accretion of Oceanic Plateaus at Continental Margins: Numerical Modeling. *Gondwana Res.* 81, 390–402. doi:10.1016/j.gr.2019.11.015
- Tetreault, J. L., and Buitert, S. J. H. (2014). Future Accreted Terranes: A Compilation of Island Arcs, Oceanic Plateaus, Submarine Ridges, Seamounts, and Continental Fragments. *Solid earth.* 5, 1243–1275. doi:10.5194/se-5-1243-2014
- Tetreault, J. L., and Buitert, S. J. H. (2012). Geodynamic Models of Terrane Accretion: Testing the Fate of Island Arcs, Oceanic Plateaus, and Continental Fragments in Subduction Zones. *J. Geophys. Res.* 117, B08403. doi:10.1029/2012JB009316

- Tu, K., Flower, M. F. J., Carlson, R. W., Xie, G. H., Chen, C. Y., and Zhang, M. (1992). Magmatism in the South China Basin: 1. Isotopic and Trace-Element Evidence for an Endogenous Dupal Mantle Component. *Chem. Geol.* 97, 47–63. doi:10.1016/0009-2541(92)90135-R
- Turcotte, D. L., and Schubert, G. (2002). *Geodynamics*. Cambridge, UK: Cambridge University Press.
- Ueda, K., Gerya, T. V., and Sobolev, S. V. (2008). Subduction Initiation by Thermal-chemical Plumes. *PhysEarth Planet Inter* 171, 296–312. doi:10.1016/j.pepi.2008.06.032
- van Hunen, J., van den Berg, A. P., and Vlaar, N. J. (2002). On the Role of Subducting Oceanic Plateaus in the Development of Shallow Flat Subduction. *Tectonophysics* 352, 317–333. doi:10.1016/S0040-1951(02)00263-9
- van Hunen, J., van den Berg, A. P., and Vlaar, N. J. (2004). Various Mechanisms to Induce Presentday Shallow Flat Subduction and Implications for the Younger Earth: a Numerical Parameter Study. *Phys. Earth Planet. Interiors* 146, 179–194. doi:10.1016/j.pepi.2003.07.027
- Vogt, K., and Gerya, T. (2014). From Oceanic Plateaus to Allochthonous Terranes: Numerical Modeling. *Gondwana Res.* 25, 494–508. doi:10.1016/j.gr.2012.11.002
- Wang, C. Y., Ding, W. W., Schellart, W. P., Li, J. B., Dong, C. Z., Fang, Y. X., et al. (2021). Effects of Multi-Seamount Subduction on Accretionary Wedge Deformation: Insights from Analogue Modelling. *J. Geodyn.* 145, 101842. doi:10.1016/j.jog.2021.101842
- Wang, L. L., Dai, L. M., Gong, W., Li, S. Z., Jiang, X. D., Foulger, G., et al. (2022). Subduction Initiation at the Solomon Back-Arc Basin: Contributions from Both Island Arc Rheological Strength and Oceanic Plateau Collision. *Geophys. Res. Lett.* 49, e2021GL097666. doi:10.1029/2021GL097666
- Wang, T. K., Chen, M. K., Lee, C. S., and Xia, K. Y. (2006). Seismic Imaging of the Transitional Crust across the Northeastern Margin of the South China Sea. *Tectonophysics* 412, 237–254. doi:10.1016/j.tecto.2005.10.039
- Wang, Y. J., Han, X. Q., Luo, Z. H., Qiu, Z. Y., Ding, W. W., Li, J. B., et al. (2009). Late Miocene Magmatism and Evolution of Zhenbei-Huangyan Seamount in the South China Sea: Evidence from Petrochemistry and Chronology. *Acta Oceanol. Sin.* 31, 93–102. (in Chinese with English abstract). doi:10.1109/CLEOE-EQEC.2009.5194697
- Wu, J., Suppe, J., Lu, R. Q., and Kanda, R. (2016). Philippine Sea and East Asian Plate Tectonics since 52 Ma Constrained by New Subducted Slab Reconstruction Methods. *J. Geophys. Res. Solid Earth* 121, 4670–4741. doi:10.1002/2016JB012923
- Wu, J., and Suppe, J. (2018). Proto-South China Sea Plate Tectonics Using Subducted Slab Constraints from Tomography. *J. Earth Sci.* 29 (6), 1304–1318. doi:10.1007/s12583-017-0813-x
- Yan, Q. S., Shi, X. F., Wang, K. S., Bu, W. R., and Xiao, L. (2008). Major Element, Trace Element, and Sr, Nd and Pb Isotope Studies of Cenozoic Basalts from the South China Sea. *Sci. China Ser. D Earth Sci.* 51, 550–566. doi:10.1007/s11430-008-0026-3
- Yan, Z. Y., Chen, L., Xiong, X., Wan, B., and Xu, H. Z. (2021). Oceanic Plateau and Subduction Zone Jump: Two-Dimensional Thermo-Mechanical Modeling. *J. Geophys. Res. Solid Earth* 126, e2021JB021855. doi:10.1029/2021JB021855
- Yan, Z. Y., Chen, L., Xiong, X., Wang, K., Xie, R. X., and Hsu, H. (2020). Observations and Modeling of Flat Subduction and its Geological Effects. *Sci. China Earth Sci.* 63, 1069–1091. (in Chinese with English abstract). doi:10.1007/s11430-019-9575-2
- Yang, S. H., Li, Z. H., Gerya, T., Xu, Z. Q., and Shi, Y. L. (2018). Dynamics of Terrane Accretion during Seaward Continental Drifting and Oceanic Subduction: Numerical Modeling and Implications for the Jurassic Crustal Growth of the Lhasa Terrane, Tibet. *Tectonophysics* 746, 212–228. doi:10.1016/j.tecto.2017.07.018
- Yang, T. F., Lee, T., Chen, C. H., Cheng, S. N., Knittel, U., Punongbayan, R. S., et al. (1996). A Double Island Arc between Taiwan and Luzon: Consequence of Ridge Subduction. *Tectonophysics* 258, 85–101. doi:10.1016/0040-1951(95)00180-8
- Yeh, Y. C., Hsu, S. K., Doo, W. B., Sibuet, J. -C., Liu, C. S., and Lee, C. S. (2012). Crustal Features of the Northeastern South China Sea: Insights from Seismic and Magnetic Interpretations. *Mar. Geophys. Res.* 33, 307–326. doi:10.1007/s11001-012-9154-4
- Yeh, Y. C., Sibuet, J. -C., Hsu, S. K., and Liu, C. S. (2010). Tectonic Evolution of the Northeastern South China Sea from Seismic Interpretation. *J. Geophys. Res. Solid Earth* 115, B06103. doi:10.1029/2009jb006354
- Yoshida, M. (2017). Trench Dynamics: Effects of Dynamically Migrating Trench on Subducting Slab Morphology and Characteristics of Subduction Zones Systems. *Phys. Earth Planet Inter.* 268, 35–53. doi:10.1016/j.pepi.2017.05.004
- Zhang, J., Li, J. B., Ruan, A. G., Ding, W. W., Niu, X. W., Wang, W., et al. (2020). Seismic Structure of a Postspreading Seamount Emplaced on the Fossil Spreading Center in Southwest Subbasin on the South China Sea. *J. Geophys. Res. Solid Earth* 125, e2020JB019827. doi:10.1029/2020JB019827
- Zhao, M. H., He, E. Y., Sibuet, J. -C., Sun, L. T., Qiu, X. L., Tan, P. C., et al. (2018). Postseafloor Spreading Volcanism in the Central East South China Sea and its Formation through an Extremely Thin Oceanic Crust. *Geochem. Geophys. Geosyst.* 19, 1–21. doi:10.1002/2017GC007034
- Zhao, Y. H., Ding, W. W., Ren, J. Y., Li, J. B., Tong, D. J., and Zhang, J. Y. (2021). Extension Discrepancy of the Hyper-Thinned Continental Crust in the Baiyun Rift, Northern Margin of the South China Sea. *Tectonics* 40, e2020TC006547. doi:10.1029/2020tc006547

Conflict of Interest: The authors declare that the research was conducted in the absence of any commercial or financial relationships that could be construed as a potential conflict of interest.

Publisher's Note: All claims expressed in this article are solely those of the authors and do not necessarily represent those of their affiliated organizations, or those of the publisher, the editors and the reviewers. Any product that may be evaluated in this article, or claim that may be made by its manufacturer, is not guaranteed or endorsed by the publisher.

Copyright © 2022 Ma, Chen, Cheng, Gerya and Li. This is an open-access article distributed under the terms of the Creative Commons Attribution License (CC BY). The use, distribution or reproduction in other forums is permitted, provided the original author(s) and the copyright owner(s) are credited and that the original publication in this journal is cited, in accordance with accepted academic practice. No use, distribution or reproduction is permitted which does not comply with these terms.



OPEN ACCESS

EDITED BY

Gang Rao,
Southwest Petroleum University, China

REVIEWED BY

Huiping Zhang,
China Earthquake Administration, China
Wen-Nan Wu,
National Central University, Taiwan

*CORRESPONDENCE

Pingchuan Tan,
tanpc@asio.org.cn

SPECIALTY SECTION

This article was submitted to Structural
Geology and Tectonics,
a section of the journal
Frontiers in Earth Science

RECEIVED 11 May 2022

ACCEPTED 12 July 2022

PUBLISHED 24 August 2022

CITATION

Tan P, Ding W and Li J (2022),
Exhumation history of the Hengchun
Ridge and its implications for Taiwan
orogenic processes.
Front. Earth Sci. 10:941040.
doi: 10.3389/feart.2022.941040

COPYRIGHT

© 2022 Tan, Ding and Li. This is an
open-access article distributed under
the terms of the [Creative Commons
Attribution License \(CC BY\)](https://creativecommons.org/licenses/by/4.0/). The use,
distribution or reproduction in other
forums is permitted, provided the
original author(s) and the copyright
owner(s) are credited and that the
original publication in this journal is
cited, in accordance with accepted
academic practice. No use, distribution
or reproduction is permitted which does
not comply with these terms.

Exhumation history of the Hengchun Ridge and its implications for Taiwan orogenic processes

Pingchuan Tan^{1,2*}, Weiwei Ding^{1,2,3} and Jiabiao Li^{1,3}

¹Key Laboratory of Submarine Geosciences, Ministry of Natural Resources & Second Institute of Oceanography, Ministry of Natural Resources, Hangzhou, China, ²Southern Marine Science and Engineering Guangdong Laboratory, Zhuhai, China, ³School of Oceanography, Shanghai Jiao Tong University, Shanghai, China

The orogenic evolution of Taiwan is thought to have occurred with a steady and southward propagating trend since the Late Miocene. Recent studies suggest a two-stage collision for the Taiwan orogen and that the collision occurred simultaneously along the entirety of the island of Taiwan. To test this hypothesis, we evaluated 270 bathymetry profiles normal to the trench to constrain variations in the width, length, and crest of the Taiwan accretionary prism from the northern Central Ridge to the southern Hengchun Ridge. South of Taiwan Island, a gradual increase in the width and elevation of the accretionary prism of the Hengchun Ridge is noted. Assuming that the uplift of Hengchun Ridge is dominated by the accretion of hyper-stretched continental crust (HSCC), we estimated the uplift rate of the ridge (ca. 0.3 km/Ma) based on a linear regression between the HSCC and the observed depth of the prism crest. Using this uplift rate, we forward modeled the prism crest depth variations from 19.7°N to 23.5°N, and compared these values to observations. The model gives a good match to observations of the Hengchun Ridge, but significantly deeper depths to the north of Hengchun Peninsula. This suggests that the Taiwan orogeny had two stages: the first stage was dominated by structurally underplated HSCC, and the second is a combination of the arrival of the continental shelf and arc–continent collision. In addition to the widely accepted arc–continent collision, our study suggests that both the location and orientation of the continent–ocean boundary play important roles in orogeny.

KEYWORDS

hengchun ridge, taiwan orogenic, manila subduction, hyper-stretched continental crust, south China sea

Introduction

The Taiwan orogeny has been described as an evolving tectonic setting resulting from active and oblique collision between the north-trending Luzon Arc and the northeast-trending Eurasian continental margin (Suppe, 1984). This tectonic setting indicates that the collision started in the north and propagated southward, as suggested by many studies (Liu et al., 2001; Willett et al., 2003; Huang et al., 2006). Both Liu et al. (2001) and Willett et al. (2003) observed a southward propagation of the collision zone (starting at 5–7 Ma) using apatite and zircon fission-track ages based on the analysis of sedimentary rocks and bedrock in the Central Ridge of Taiwan. Based on regional geological settings and records, Huang et al. (2006) proposed a scenario in which continuous southward migration of the collision zone occurred since around 6.5 Ma. Recently, based on interpretations of the detrital thermochronology record of sediment samples in Taiwan, Resentini et al. (2020) observed a southward exhumation process, and Malusa and Fitzgerald (2020) identified a migration of fast erosion rates in the accretionary wedge from the northern to southern Coastal Range since the Late Miocene. Both studies support a southward propagation of the collision zone during oblique arc–continent collision. However, several other studies have challenged the idea of a southward propagation (Mesalles et al., 2014; Lee et al., 2015). According to thermochronological constraints and the timing of rapid subsidence in the eastern Taiwan foreland basin based on recently published zircon fission-track ages, both Lee et al. (2015) and Mesalles et al. (2014) observed an onset of exhumation in both the northern and southern parts of Taiwan Island at ca. 5–7 Ma, suggesting that collision may have occurred simultaneously along the entirety of the island. In addition, slow to moderate uplift of Central Ridge rocks since 6–7 Ma, followed by a rapid uplift after 2–3 Ma (Teng, 1990; Hsu et al., 2016; Lee et al., 2006) may suggest a two-stage collision for the Taiwan orogen, rather than a single southward arc–continent collision process.

Recent geophysical studies have observed that the passive margins of the northern South China Sea (SCS) are characterized by a wide area (>200 km) of extremely thinned hyper-stretched continental crust (HSCC), rather than a narrow transition zone, which is presently subducting along the Manila Trench (Lester et al., 2013; McIntosh et al., 2013; Eakin et al., 2014; Lester et al., 2014; Liu et al., 2018) (Figure 1). In addition, the results of seismic refraction profiles across the Hengchun Ridge show that the uplift of the Hengchun Ridge is primarily caused by the accretion of HSCC (McIntosh et al., 2013). HSCC underthrusting could be the dominant process in the initial stage of mountain building in Taiwan; this is supported by a comparison between crustal structure (McIntosh et al., 2013) and geothermal gradients (Mesalles

et al., 2014) on and offshore Taiwan. Because the boundary between the oceanic crust, HSCC, and continental crust at the northern margin of the SCS have different trends than those of the Manila Trench (Figure 1), the subducted plate along the Hengchun Ridge varies from oceanic crust to HSCC to continental crust moving northward. Thus, the Hengchun Ridge can be used as an analog for studying the evolution of accretionary prisms developed from oceanic crust to HSCC subduction, providing an opportunity to study the early orogenic history of Taiwan Island. Integrating these observations with onshore geology allows us to further construct the entire tectonic evolution of the Taiwan orogeny, which developed from oceanic crust subduction to arc–continental collision.

Tectonic background

Taiwan Island features an active orogenic system resulting from the collision between SE Eurasia and the Luzon Arc west of the Philippine Sea plate (Teng, 1990). It developed by at least 10 Ma during the eastward subduction of the SCS oceanic crust (Liu et al., 2019), which is characterized by a high convergent rate (8 cm/yr) (Yu et al., 1997). The initial stages of the Taiwan collision started with the arrival of Eurasian continental crust along the Manila Trench around 5–7 Ma (Willett et al., 2003; Lee et al., 2015). Following the accretion of continental crust (McIntosh et al., 2005, 2013), the prism collided with the northernmost Luzon volcanic arc of the Philippine Sea Plate, at which time more rapid uplift occurred with the arrival of thicker continental crust intersecting the prism (Mesalles et al., 2014).

Based on present-day geological observations, the tectonic setting of the region changes from north to south along the Taiwan orogen (Figure 1). In the north, the Taiwan orogen is primarily composed of three distinct geomorphic units; from west to east, these are the subducted Eurasian continental margin, the accretionary prism, and the accreted Luzon Arc (Huang et al., 2006) (Figure 1). Morphologically, the Central Ridge of Taiwan extends continuously from Hengchun Peninsula to the offshore Hengchun Ridge (Figure 1) and has a common tectonic origin (Huang et al., 2006; McIntosh et al., 2013). The Central Ridge stretches from 22°N to 25.25°N and has a length of more than 500 km. The Hengchun Peninsula, which is located at the southernmost part of Taiwan Island, is the southern extended segment of the Central Ridge, and marks the northern most part of the accretionary prism in the Manila subduction zone (Zhang et al., 2016). Based on regional tectonostratigraphic records, Huang et al. (2006) suggested that the onset of collision in the Hengchun Peninsula could have started during the early Pliocene. To

the south, the submarine Hengchun Ridge stretches more than 350 km from 20.2°N to 22°N, representing a subduction wedge between the Manila Trench and the fore-arc basin of the Luzon Trough. This northward increase in width and elevation results in a significant change in morphology, likely in response to an earlier collision process (McIntosh et al., 2013). Two distinct structural domains (the upper and lower slope) have been observed in the Hengchun Ridge. The upper slope has imbricated thrusts and folds, while the lower slope is characterized by a sharp change in bathymetric relief (Lester et al., 2013; Eakin et al., 2014). The transition from lower to upper slope could be caused by out-of-sequence thrusts (Lin et al., 2008), or structurally underplated subducted crust (Lester et al., 2013). To the west, several seismic studies show that the northern SCS has a broad (>200 km) continental-ocean transition zone that comprises HSCC (stretching factor 3–5) with a thickness between 5 and 15 km, which is presently subducting at the Manila Trench (Wang et al., 2006; Lester et al., 2013; McIntosh et al., 2013; Eakin et al., 2014; Lester et al., 2014; Liu et al., 2018) (Figure 1). Furthermore, seismic studies reveal a high-velocity anomaly suggestive of a HSCC structurally underplated beneath the base of the accretionary prism (width 20 km, height 10 km) (Lester et al., 2013) (MGL0905-27 in Figure 1). This feature was also discovered beneath onshore Taiwan with a thicker (up to 30 km) and slightly wider spatial (ca. 30 km) extent (McIntosh et al., 2005, 2013) (OBS1995 in Figure 1). Based on regional seismic studies and magnetic anomalies, the subduction of oceanic crust at the Manila Trench probably occurs only to the south of 20.2°N (Eakin et al., 2014).

Materials and methods

Because the continental-ocean transition zone of the northern margin of the SCS trends differently than the Manila Trench, the subducted plate along the trench varies from oceanic to HSCC, and northward to continental crust subduction. To understand how the structure of prism growth is related to this process, we estimated changes in the morphology of the accretionary prism northward. The bathymetric map is derived from Tozer et al. (2019) (SRTM15+) with a resolution of 15 s. For the location of the Manila Trench between 23°N and 23.5°N, we estimated the location based on a frontal thrust fault (Laonung fault) west of the Central Range. This fault was proposed following the proto-Manila trench and acted as the deformation front of the subduction wedge during the arc-continental collision (Huang et al., 1997). Between 21.5°N and 23°N, the trench represents as a deformation front on land connecting the offshore Manila Trench (e.g., Lallemand and Tsien, 1997; Liu et al., 1997; Liu et al., 2004). Here, we estimate the sea-land

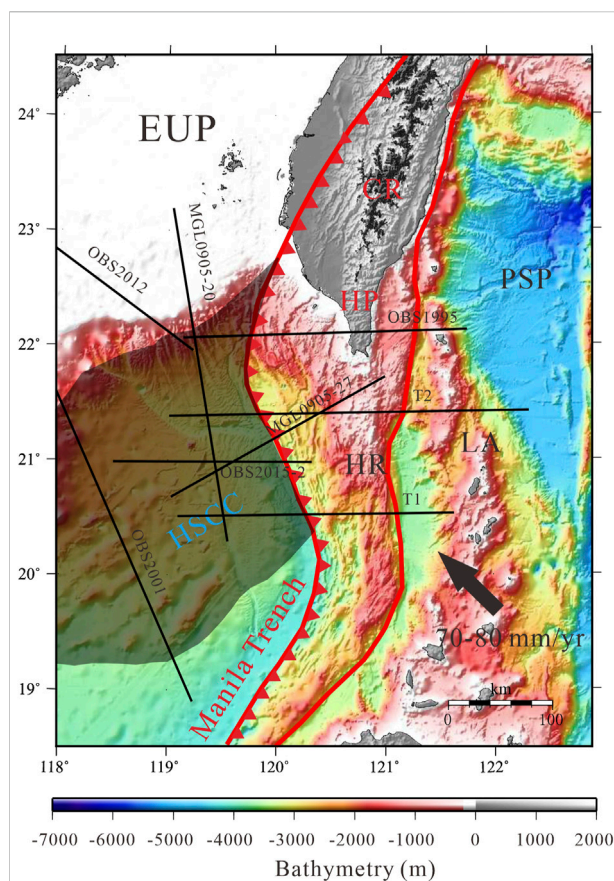
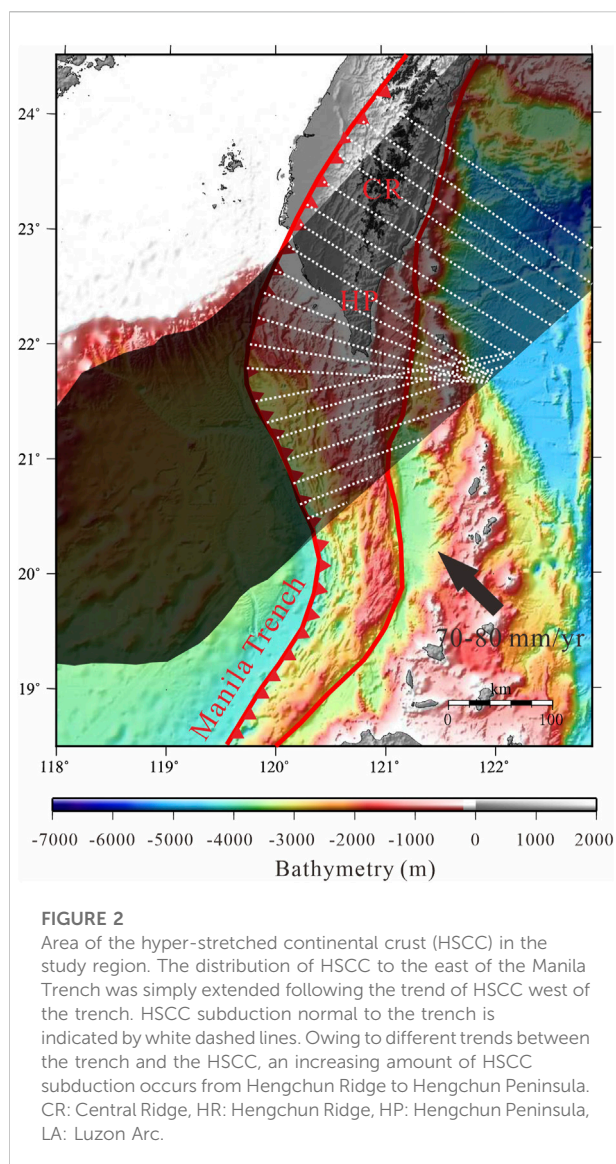


FIGURE 1

Regional features illustrated on a bathymetric map [SRTM15+; (Tozer et al., 2019)]. Solid black lines represent the locations of the regional seismic refraction profiles: OBS 2001 (Wang et al., 2006), T1 and T2 (Eakin et al., 2014), OBS 2015–2 (Liu et al., 2018), OBS 1995 (McIntosh et al., 2005), MGL0905–27 (Lester et al., 2013), MGL0905–20 (Lester et al., 2014), and OBS 2012 (Wan et al., 2017). The area of hyper-stretched continental crust (HSCC), indicated by transparent blue, is constrained by regional seismic refraction profiles and modified from Li et al. (2019). The solid red line indicates the eastern boundary of the accretionary prism. The Luzon Arc is moving northwestward towards the Eurasian continent at 70–80 mm/yr (Yu et al., 1999). CR: Central Ridge, EUP: Eurasian Plate, HR: Hengchun Ridge, HP: Hengchun Peninsula, LA: Luzon Arc, PSP: Philippine Sea Plate.

connection of the deformation front from Liu et al. (1997). Then, we extracted the bathymetry of the Taiwan accretionary prism normal to the trench every 2 km, representing a variation in width, slope, and crest of the accretionary prism from 19.7°N to 23.5°N. This resulted in the obtainment of 270 different profiles normal to the trench. Along the profile, the spacing is 1 km; this retains the main structural characteristics of the prism. The crest of the prism is calculated based on the average depth of the ten shallowest points of the prism. The width of the prism is estimated from the trench point to the western boundary of the prism (solid red line in Figure 1). The slope is estimated based on a



standard least-squares linear regression model ($y = a + b \cdot x$, where the b is the slope) for each accretionary prism using the GMT program “gmtregress” (Wessel and Smith, 1991). Although the slope could have been affected by regional processes (slumps, erosion, and mud volcanoes), a gradual process of slope change should provide a representative mechanism for the growth of the accretionary prism, where greater and lesser slopes indicate that the growth of the prism is dominated by vertical and horizontal accretion, respectively.

To analyze the exhumation history of Hengchun Ridge, it is also necessary to know its uplift rate. We first estimated the amount of subducted HSCC based on a simple geometric relationship between the Manila Trench and HSCC, where the HSCC east of the Manila Trench was simply extended following the trend of the HSCC to the west of the trench

(Figure 2). Some uncertainties related to the change of geometry of the Manila Trench were noted because the trench migrated westward during subduction; however, based on reconstructions by Seton et al. (2012), the overall configuration of the northern Manila Trench has experienced little change since the Late Miocene. Moreover, to the east of the trench, the geometry of the HSCC is generally consistent with a map of a subducted thinned continental crust slab, which is unfolded and restored to the Earth surface based on the regional tomography data provided by Wu et al. (2016) and Liu et al. (2018). Using an E–W effective convergence rate of 50 mm/yr for the northern Manila Trench (Tan, 2020), we split the E–W convergence rate normal to the trench and calculated a trench-normal subduction plate velocity along the trench. Then, the duration of the subduction of HSCC could be estimated. If the growth of the Hengchun Ridge was dominated by underplating of HSCC to the accretionary prism, a positive correlation between the duration of the subducted HSCC and the depth of the prism crest should be observed. Subsequently, the uplift rate of the Hengchun Ridge can be estimated by using linear regression to fit the data.

Results

Hyper-stretched continental crust underplating

The amount and duration of HSCC subduction between 19.7°N and 23.5°N is shown in Figure 3A. The area between 19.7°N and 21.5°N includes the Hengchun Ridge (offshore), while the Hengchun Peninsula covers an area between 21.5°N and 22.5°N. The area north of 22.5°N represents the Central Ridge. The initial stage of HSCC subduction is at 20.2°N. A gradually increasing amount of HSCC subduction is noted between 20.2°N and 21.5°N (0–230 km); this corresponds to the duration of HSCC subduction from 0 to 5 Ma. Between 21.5°N to 23.5°N, the duration and amount of subducted continental crust remain almost unchanged at 5 Ma and 240 km, respectively. The relationship between the duration of HSCC subduction and the observed depth of the prism crest over Hengchun Ridge is shown in Figure 3B. In general, a strong positive correlation is observed between the two, with a correlation coefficient (R) of 0.93. The observed prism crest increases from –2000 to 0 m and is associated with an increase in duration from 0 to 5 Ma. Linear regression determined that the uplift rate of the Hengchun Ridge is 0.296 ± 0.011 km/Ma (red circle and solid line in Figure 3B). There are some uncertainties in the uplift rate due to the uncertainties of the convergence rate. Previous studies have shown that the Philippine Sea Plate is moving toward

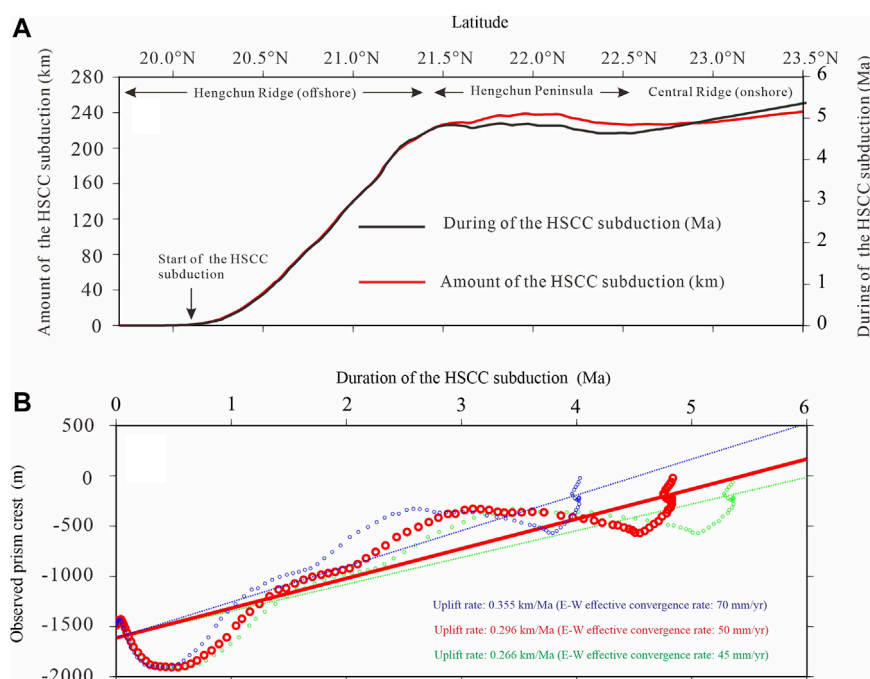


FIGURE 3

(A) Amount and duration of hyper-stretched continental crust (HSCC) subduction. The start of HSCC subduction occurs at 20.2°N. For Hengchun Ridge, the amount and duration of HSCC subduction increases from 0 to 220 km and 0 to 5 Ma, respectively. For the onshore Hengchun Peninsula and Central Ridge, the amount and duration remain constant at 240 km and 5 Ma, respectively. (B) Correlation between the duration of the HSCC subduction and observed crest of the prism over Hengchun Ridge. The red circle shows the correlation based on the E-W effective convergence rate of 50 mm/yr, and a red solid line indicates a best-fit line. The green and blue circles and dashed lines represent the correlation based on the E-W convergence rate of 45 and 70 mm/yr, respectively. The positive correlation suggests that the uplift of Hengchun Ridge is dominated by the accretion of HSCC underthrusting.

the Eurasian continent at the rate of 60–80 mm/yr in 300°–310° azimuth (Yu et al., 1997; Yu et al., 1999). This results in E–W effective convergence rate at the trench from 45 to 70 mm/yr. Here, we tested the sensitivity of the convergence rate from 45 mm/yr to 70 mm/yr to see how it changes from the uplift rate. The result shows that the changing of the convergence rate still results in a positive correlation between the duration of HSCC subduction and the prism crest, and the uplift rate changes to 0.266 km/Ma and 0.355 km/Ma at a convergence rate of 45 and 70 mm/yr, respectively, (green and blue circles and dashed lines in Figure 3B).

Morphology of the taiwan accretionary prism

The morphology of the Taiwan accretionary prism is shown in Figure 4. To the south of 20.2°N, oceanic crust subduction exhibits less variation in width (70–80 km), slope (0.04–0.05), and crest of the prism (–1,500 m to –1,200 m). Between 20.2°N and 21.3°N (the Hengchun Ridge), the crest of the prism gradually

increases (–1,500 m to –500 m); this is associated with an increase in width from 70 to 110 km. The northward increase in the size of the prism probably results from the accretion of terrigenous sediments in the SCS continental margin and Taiwan orogen to the north. The prism slope is almost the same (0.04), suggesting that the growth of the accretionary prism can be attributed to both vertical and horizontal accreted. From 21.6°N to 22.2°N, the width increases from 130 to 150 km; this is associated with a minor change in crest depth (from –500 to 0 m). A decreasing slope in this area (from 0.03 to 0.02) suggests that the growth of the accretionary prism is marked by horizontal advection. North of 22.5°N represents the Hengchun Peninsula and Central Ridge. Here the crest of the accretionary prism exhibits significant uplift from 0 to 3,500 m. The width of the accretionary prism is almost constant at 140 km, while the slope dramatically increases from 0.01 to 0.04, reflecting the rapid vertical growth of the accretionary prism. The length and slope of the accretionary prism could be affected by the uncertainties of the location of the Manila Trench just SW of Taiwan Island, as the Manila Trench gradually loses its bathymetric identity north of 21.5°N. There are several possible ways of the connection between the deformation front

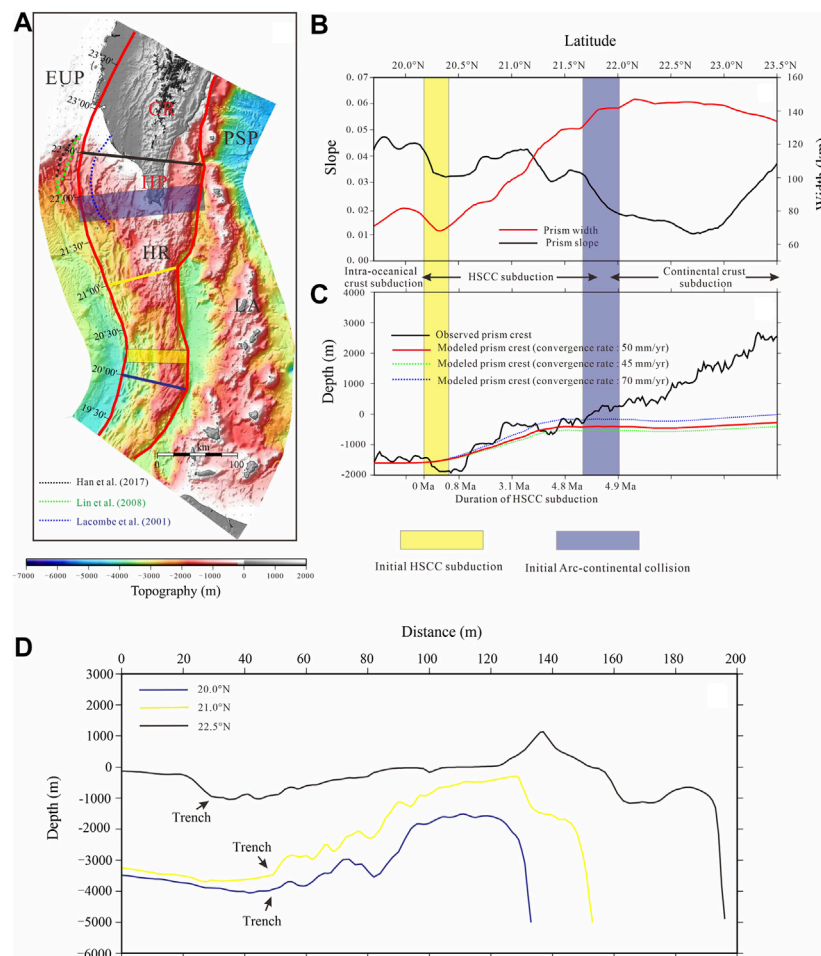


FIGURE 4

(A) Bathymetry of the Taiwan accretionary prism from 19.5°N to 24°N. Solid red lines indicate the western and eastern boundaries of the accretionary prism. Black, green, and blue dotted lines indicate possible trench locations proposed by Han et al. (2017), Lin et al. (2008), and Lacombe et al. (2001) SW of Taiwan Island. (B) Variations in prism width and slope from 19.7°N to 23.5°N. (C) Comparison between the modeled (red solid line) and observed prism crest (black solid line) from 19.7°N to 23.5°N. The modeled duration of the subducted hyperextended continental crust is shown below. The green and blue dash lines show the modeled prism crest using E-W effective convergence rate at 45 and 70 mm/yr, respectively. (D) Profiles across the accretionary prism at 20.0°N, 21.0°N, and 21.5°N, representing a typical cross section of oceanic subduction, hyper-stretched continental crust subduction, and initial arc-continent collision, respectively. CR: Central Ridge, EUP: Eurasian Plate, HR: Hengchun Ridge, HP: Hengchun Peninsula, LA: Luzon Arc, PSP: Philippine Sea Plate.

on land and the Manila Trench offshore in SW Taiwan Island (e.g., Huang et al., 2004; Yu, 2004; Han et al., 2017). Here, we test the sea-land connection proposed by Han et al. (2017), Lacombe et al. (2001), and Lin et al. (2008) (Figure 4A) to see how it changes the estimated length and slope of the accretionary prism. The test shows that the length of the accretionary prism changes of up to 40 km, while the slope to be changed by generally less than 0.01. In addition, the large amounts of mud diapirs and mud volcanos are active offshore and onshore SW Taiwan Island (e.g., Chen et al., 2014; Doo et al., 2015) could potentially change the height, accordingly the slope of the accretionary prism. Regional seismic reflection profiles show that the height of the mud

volcano is generally less than 400 m (Chen et al., 2014), which results in slope changes of up to 0.003.

Discussion

A range of interpretations have been proposed for the evolution of the Taiwan orogen. Based on regional tectonic settings, subduction of SCS crust results in an oblique arc-continent collision starting at approximately 6.5 Ma in northern Taiwan and propagating southward (Huang et al., 2006). Using stratigraphic evidence, low-temperature

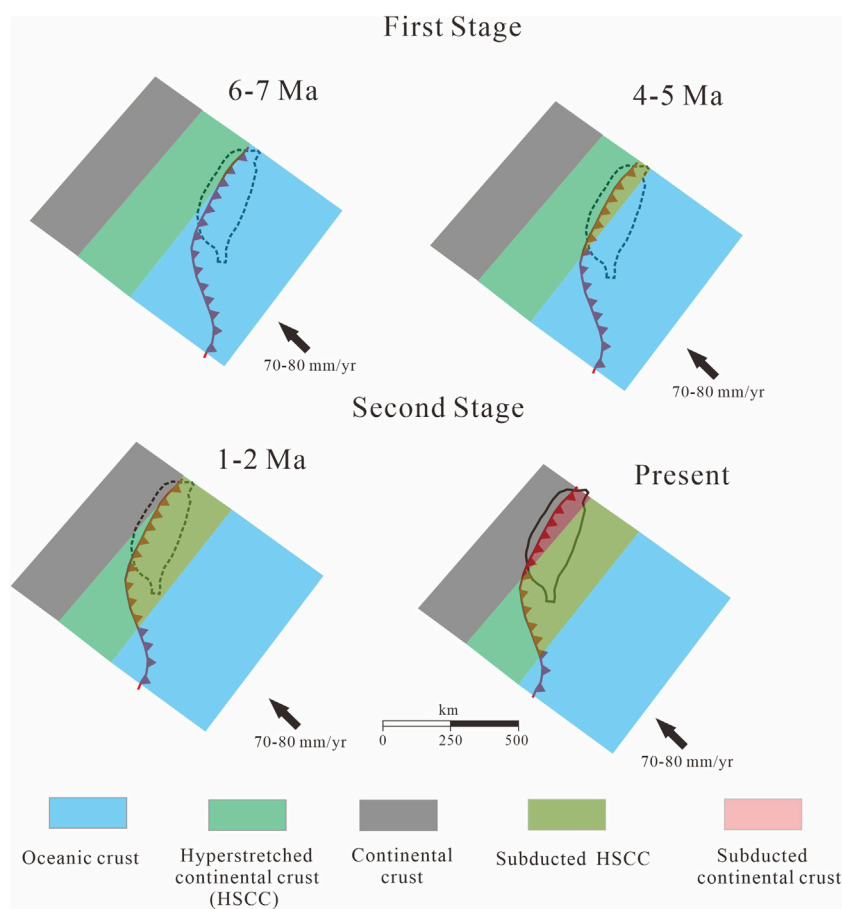


FIGURE 5

Evolution of the Taiwan accretionary prism since the Late Miocene. The location of the trench is derived from [Deng et al. \(2020\)](#) and the area of the HSCC is modified from [Li et al. \(2019\)](#). Owing to differences in orientation between the Manila Trench and the hyper-stretched continental crust (HSCC) of the northern South China Sea, the amount of HSCC subduction changes from south to north and has varied through time. The subparallel trend between the trench and the continental margin supports simultaneous mountain building along the Taiwan orogenic belt during the first stage of the Taiwan orogeny.

thermochronological analysis, and regional seismic data, several studies have proposed a two-stage collision for the Taiwan orogen ([Lee et al., 2006](#); [Mesalles et al., 2014](#); [Hsu et al., 2016](#)). The first stage started around 6–8 Ma ([Teng, 1990](#); [Liu et al., 2001](#); [Lee et al., 2006](#)) with a southward propagation of arc–continent collision ([Liu et al., 2001](#); [Willett et al., 2003](#); [Malusa and Fitzgerald, 2020](#); [Resentini et al., 2020](#)) or a simultaneous mountain building along the Taiwan orogenic belt ([Lee et al., 2006](#); [Mesalles et al., 2014](#); [Lee et al., 2015](#); [Hsu et al., 2016](#)). The simultaneous hypothesis is supported by the fact that both the Luzon Arc and continental margin exhibit subparallel northward trends during the Late Miocene ([Lee et al., 2015](#)). The uplift of the accretionary wedge can be caused by arc–continent collision ([Lee et al., 2015](#); [Resentini et al., 2020](#)), subduction of extended continental crust ([Lee et al., 2006](#); [Mesalles et al., 2014](#)), HSCC structural underplating at the base of the accretionary prism ([Lester et al., 2013](#); [McIntosh](#)

[et al., 2013](#)), and a combination of crustal accretion, subducting continental crust, and southward propagation of the arc collision ([Willett et al., 2003](#)). During this stage, the exhumation rate was slow to moderate (<0.5 km/Ma) ([Lee et al., 2006](#); [Hsu et al., 2016](#)). The second stage recorded an additional period of shortening and exhumation. The rate of exhumation significantly accelerated to 2–10 km/Ma at ca. 1–3 Ma ([Teng, 1990](#); [Willett et al., 2003](#); [Lee et al., 2006](#); [Mesalles et al., 2014](#); [Hsu et al., 2016](#)). A consistent acceleration in exhumation rate is observed along the entirety of the Taiwan orogen, but the exhumation rate at south is lower than that to the north, suggesting a longer collision history in the north ([Lee et al., 2006](#); [Hsu et al., 2016](#)). The acceleration of the exhumation rate could be caused by progressive underthrusting of thicker crust ([Lee et al., 2015](#); [Hsu et al., 2016](#)) and shortening of the prism associated with Luzon Arc collision ([Lee et al., 2006](#); [Mesalles et al., 2014](#)).

Our data show that the width and crest of the Hengchun accretionary prism gradually increase northward (Figure 4). Assuming prism growth from only the subducted HSCC, we used the duration of the HSCC and the uplift rate of the Hengchun Ridge (0.296 km/Ma) to forward model how much of the accretionary prism has been uplifted north of 19.7°N (Figure 4C). The result shows that our modeled prism crest (red solid line in Figure 4C) fits reasonably well with observations south of 22°N. Considering the uncertainties of the convergence rate, changing the E-W convergence rate to 45 mm/yr and 70 mm/yr (green and blue dashed line in Figure 4C) still result in a reasonable fit between the observed and modeled prism crest. The estimated uplift rate of the Hengchun Ridge (0.266–0.355 km/Ma) is in agreement with the exhumation rate (<0.5 km/Ma) characterizing the early stages of mountain formation in Taiwan (Lee et al., 2006; Hsu et al., 2016). In addition, our model shows that the initial age of HSCC subduction at Hengchun Peninsula (22°N) is 4–5 Ma (Figure 4C). This is comparable to the regional sedimentary record, which indicates that the onset of the submarine collision in the Hengchun Peninsula could have started during the early Pliocene (Huang et al., 2006). The slope of the Hengchun accretionary prism (21°N to 22°N) gradually decreases from 0.04 to 0.02. Considering an uncertainty of the slope by up to 0.01, it still shows a decreasing trend, suggesting that the growth of the Hengchun Ridge is dominated by horizontal advection. This is comparable to the first stages of Taiwan orogenic formation, where the horizontal transport of materials from the prism was more important than its vertical uplift (Willett et al., 2003). In conclusion, the similarity of the exhumation rate, duration, and mechanism of submarine collision both onshore and offshore Taiwan suggest a common tectonic origin between the two. It is likely that the first stage of the Taiwan orogen was dominated by HSCC subduction. The subparallel trend between the trench and the continental margin supports simultaneous mountain building along the Taiwan orogenic belt during the first stage of collision (Figure 5).

North of 22°N, the observed prism crest experienced a dramatic uplift. This region also features a significantly higher (2,000–3,000 m) prism crest than modeled values, indicating that the growth of the prism is not dominated by HSCC subduction, evidencing another stage of collision evolution. During this stage, a significant increase in prism slope (from 0.01 to 0.04) indicates the dominance of vertical uplifting over horizontal advection. This is in agreement with more rapid uplift; indeed, the exhumation rate increases to 2–10 km/Ma during the second stage of the Taiwan orogen (Lee et al., 2006; Hsu et al., 2016). In addition, considering the onset of the first stage Taiwan collision at 6–7 Ma (Lee et al., 2006) and the duration of HSCC subduction (5 Ma; Figure 4), the estimated duration of the second collision stage is 1–2 Ma. This is in agreement with several onshore studies suggesting that the second stage of the Taiwan orogen began at around 1–3 Ma (Teng, 1990; Willett et al., 2003; Lee et al., 2006; Mesalles et al., 2014). Our model shows that to the north of

the Hengchun Peninsula, thick continental crust subduction caused significant uplift the accretionary prism (Figure 5). In addition, a gradual increase in both prism crest and slope northward suggests that the north experienced rapid uplift (Figure 4C). This is consistent with lower exhumation rates recorded in the Hengchun Peninsula than the Central Ridge (Lee et al., 2006). This exhumation rate could be related to the combination of the oblique collision between the continental crust and north-trending Luzon Arc result in shortening of continental margin section, and the southward-increasing erosion rate at Taiwan Island (Malusa and Fitzgerald, 2020).

Conclusion

Based on a combination of the exhumation history of the Hengchun accretionary prism and the onshore geology of Taiwan Island, our study supports a two-stage Taiwan orogen. Owing to the difference in orientation between the Manila Trench and the HSCC of the northern SCS, the amount of HSCC subduction over the Hengchun Ridge has changed from south to north (Figure 5). We use this as an analog to analyze the first stage of the Taiwan orogeny. During this stage, the uplift rate of Hengchun Ridge is estimated based on correlations between the duration of HSCC subduction and the observed depth of the prism crest, and uses linear regression to perform the fit. The initial HSCC subduction is coeval with the start of the Taiwan orogen at 6–7 Ma. In addition, the uplift of Hengchun Ridge is dominated by an accretion of structurally underplated HSCC, which is dominated by horizontal advection rather than vertical uplift. The exhumation rate is moderate to low (ca. 0.3 km/Ma) and is comparable to the exhumation rate (<0.5 km/Ma) of the first stage of Taiwan mountain formation. The subparallel trend between the trench and continental margin supports simultaneous mountain accretion along the entire Taiwan orogen. After subduction of the entire HSCC, the second stage of the Taiwan orogeny occurred. During this stage, the exhumation rate of the prism accelerated significantly. This higher rate was most likely caused by the arrival of a thick continental shelf intersecting the prism, together with continent–arc collision. Compared to the widely accepted arc–continent collision model, our study suggests that both the location and orientation of the continental–ocean boundary can also play important roles in orogeny.

Data availability statement

The datasets presented in this study can be found in online repositories. The names of the repository/repositories and

accession number(s) can be found below: <https://figshare.com/s/dc28a50234beeb5d128d>.

Author contributions

PT and WD designed the study. PT wrote the manuscript. WD and JL helped to improve the manuscript with some suggestions. All authors contributed to the article and approved the submitted version.

Funding

This study is supported by the Natural Science Foundation of China (41890811, 42006072), Scientific Research Fund of the Second Institute of Oceanography, MNR, grant no HYGG 2001, Qianjiang talent QJD2002033, and the Innovation Group Project of Southern Marine Science and Engineering Guangdong Laboratory (Zhuhai) (No.311020018).

References

- Chen, S.-C., Hsu, S.-K., Wang, Y., Chung, S.-H., Chen, P.-C., Tsai, C.-H., et al. (2014). Distribution and characters of the mud diapirs and mud volcanoes off southwest Taiwan. *J. Asian Earth Sci.* 92, 201–214. doi:10.1016/j.jseas.2013.10.009
- Deng, H., Ren, J., Pang, X., Rey, P. F., McClay, K. R., Watkinson, I. M., et al. (2020). South China Sea documents the transition from wide continental rift to continental break up. *Nat. Commun.* 11 (1), 4583. doi:10.1038/s41467-020-18448-y
- Doo, W.-B., Hsu, S.-K., Lo, C.-L., Chen, S.-C., Tsai, C.-H., Lin, J.-Y., et al. (2015). Gravity anomalies of the active mud diapirs off southwest Taiwan. *Geophys. J. Int.* 203 (3), 2089–2098. doi:10.1093/gji/ggv430
- Eakin, D. H., McIntosh, K. D., Van Avendonk, H. J. A., Lavier, L., Lester, R., Liu, C., et al. (2014). Crustal-scale seismic profiles across the Manila subduction zone: The transition from intraoceanic subduction to incipient collision. *J. Geophys. Res. Solid Earth* 119 (1), 1–17. doi:10.1002/2013jb010395
- Han, W.-C., Liu, C.-S., Chi, W.-C., Chen, L., Lin, C.-C., Chen, S.-C., et al. (2017). Westward advance of the deformation front and evolution of submarine canyons offshore of southwestern Taiwan. *J. Asian Earth Sci.* 149, 6–19. doi:10.1016/j.jseas.2017.07.001
- Hsu, W., Byrne, T. B., Ouimet, W. B., Lee, Y., Chen, Y., Soest, M. V., et al. (2016). Pleistocene onset of rapid, punctuated exhumation in the eastern Central Range of the Taiwan orogenic belt. *Geology* 44 (9), 719–722. doi:10.1130/g37914.1
- Huang, C.-Y., Wu, W., -Y., Change, C.-P., Tsao, S., Yuan, P. B., Lin, C.-W., et al. (1997). Tectonic evolution of accretionary prism in the arc-continent collision terrane of Taiwan. *Tectonophysics* 281, 31–51. doi:10.1016/s0040-1951(97)00157-1
- Huang, C.-Y., Yuan, P. B., and Tsao, S.-J. (2006). Temporal and spatial records of active arc-continent collision in taiwan: A synthesis. *Geol. Soc. Am. Bull.* 118 (3-4), 274–288. doi:10.1130/b25527.1
- Huang, S. T., Yang, K. M., Hung, J. H., Wu, J. C., Ting, H. H., Mei, W. W., et al. (2004). Deformation front development at the northeast margin of the tainan basin, tainan-kaohsiung area, taiwan. *Mar. Geophys. Res.* 25 (1), 139–156. doi:10.1007/s11001-005-0739-z
- Lacombe, O., Mouthereau, F., Angelier, J., and Deffontaines, B. (2001). Structural, geodetic and seismological evidence for tectonic escape in SW Taiwan. *Tectonophysics* 333, 323–345. doi:10.1016/s0040-1951(00)00281-x
- Lallemand, S., and Tsien, H.-H. (1997). An introduction to active collision in Taiwan. *Tectonophysics* 274 (1), 1–4. doi:10.1016/s0040-1951(96)00294-6
- Lee, Y., Byrne, T., Wang, W., Lo, W., Rau, R., Lu, H., et al. (2015). Simultaneous mountain building in the Taiwan orogenic belt. *Geology* 43 (5), 451–454. doi:10.1130/g36373.1
- Lee, Y., Chen, C., Liu, T., Ho, H., Lu, H., Lo, W., et al. (2006). Mountain building mechanisms in the southern central range of the taiwan orogenic belt—from accretionary wedge deformation to arc-continent collision. *Earth Planet. Sci. Lett.* 252 (3-4), 413–422. doi:10.1016/j.epsl.2006.09.047
- Lester, R., McIntosh, K. D., Van Avendonk, H. J. A., Lavier, L. L., Liu, C.-S., Wang, T. K., et al. (2013). Crustal accretion in the Manila Trench accretionary wedge at the transition from subduction to mountain-building in Taiwan. *Earth Planet. Sci. Lett.* 375, 430–440. doi:10.1016/j.epsl.2013.06.007
- Lester, R., Van Avendonk, H. J. A., McIntosh, K., Lavier, L., Liu, C.-S., Wang, T. K., et al. (2014). Rifting and magmatism in the northeastern South China Sea from wide-angle tomography and seismic reflection imaging. *J. Geophys. Res. Solid Earth* 119 (3), 2305–2323. doi:10.1002/2013jb010639
- Li, F., Sun, Z., Pang, X., Liao, J., Yang, H., Xie, H., et al. (2019). Low-viscosity crustal layer controls the crustal architecture and thermal distribution at hyperextended margins: Modeling insight and application to the northern South China sea margin. *Geochim. Geophys. Res.* 20 (7), 3248–3267. doi:10.1029/2019gc008200
- Lin, A. T., Liu, C. S., Lin, C. C., Schnurle, P., Chen, G. Y., Liao, W. Z., et al. (2008). Tectonic features associated with the overriding of an accretionary wedge on top of a rifted continental margin: An example from taiwan. *Mar. Geol.* 255 (4), 186–203. doi:10.1016/j.margeo.2008.10.002
- Liu, C.-S., Deffontaines, B., Lu, C.-Y., and Lallemand, S. (2004). Deformation patterns of an accretionary wedge in the transition zone from subduction to collision offshore southwestern Taiwan. *Mar. Geophys. Res.* 25 (1-2), 123–137. doi:10.1007/s11001-005-0738-0
- Liu, C.-S., Huang, I. L., and Teng, L. S. (1997). Structural features off southwestern Taiwan. *Mar. Geol.* 137 (3), 305–319. doi:10.1016/s0025-3227(96)00093-x
- Liu, H., Yumul, P., Dimalanta, C. B., Queano, K., Xia, X. P., Peng, T. P., et al. (2019). Western northern Luzon isotopic evidence of transition from proto-south China sea to south China sea fossil ridge subduction. *Tectonics* 39, 1–21. doi:10.1029/2019tc005639
- Liu, S., Zhao, M., Sibuet, J. C., Qiu, X., Wu, J., Zhang, J., et al. (2018). Geophysical constraints on the lithospheric structure in the northeastern South China Sea and its implications for the South China Sea geodynamics. *Tectonophysics* 742–743, 101–119. doi:10.1016/j.tecto.2018.06.002
- Liu, T., Hsieh, S., Chen, Y., and Chen, W. (2001). Thermo-kinematic evolution of the Taiwan oblique-collision mountain belt as revealed by zircon fission track dating. *Earth Planet. Sci. Lett.* 186 (1), 45–56. doi:10.1016/s0012-821x(01)00232-1

Acknowledgments

We are grateful to Chuanyang Wang for his detail suggestions to improve the quality of the manuscript.

Conflict of interest

The authors declare that the research was conducted in the absence of any commercial or financial relationships that could be construed as a potential conflict of interest.

Publisher's note

All claims expressed in this article are solely those of the authors and do not necessarily represent those of their affiliated organizations, or those of the publisher, the editors and the reviewers. Any product that may be evaluated in this article, or claim that may be made by its manufacturer, is not guaranteed or endorsed by the publisher.

- Malusa, M. G., and Fitzgerald, P. G. (2020). The geologic interpretation of the detrital thermochronology record within a stratigraphic framework, with examples from the European Alps, Taiwan and the Himalayas. *Earth. Sci. Rev.* 201 (103), 103074. doi:10.1016/j.earscirev.2019.103074
- McIntosh, K. D., Nakamura, Y., Wang, T. -K., Shih, R. -C., Chen, A., Liu, C. -S., et al. (2005). Crustal-scale seismic profiles across taiwan and the Western Philippine Sea. *Tectonophysics* 401 (1-2), 23–54. doi:10.1016/j.tecto.2005.02.015
- McIntosh, K. D., Van Avendonk, H., Lavier, L. L., Lester, W. R., Eakin, D. H., Wu, F. T., et al. (2013). Inversion of a hyper-extended rifted margin in the southern Central Range of Taiwan. *Geology* 41 (8), 871–874. doi:10.1130/g34402.1
- Mesalles, L., Mouthereau, F., Bernet, M., Chang, C., Tien-Shun Lin, A., Fillon, C., et al. (2014). From submarine continental accretion to arc-continent orogenic evolution: The thermal record in southern taiwan. *Geology* 42 (10), 907–910. doi:10.1130/g35854.1
- Resentini, A., Malusa, M. G., and Garzanti, E. (2020). Ongoing exhumation of the Taiwan orogenic wedge revealed by detrital apatite thermochronology: The impact of effective mineral fertility and zero-track grains. *Earth Planet. Sci. Lett.* 544, 116374. doi:10.1016/j.epsl.2020.116374
- Seton, M., Muller, R. D., Zahirovic, S., Gaina, C., Torsvik, T., Shephard, G., et al. (2012). Global continental and ocean basin reconstructions since 200 Ma. *Earth. Sci. Rev.* 113 (3-4), 212–270. doi:10.1016/j.earscirev.2012.03.002
- Suppe, J. (1984). Kinematics of arc-continent collision, flipping of subduction, and backarc spreading near Taiwan. *Mem. Geol. Soc. China.* 6, 23–56.
- Tan, E. (2020). Subduction of transitional crust at the Manila Trench and its geophysical implications. *J. Asian Earth Sci.* 187 (104), 104100. doi:10.1016/j.jseas.2019.104100
- Teng, L. S. (1990). Geotectonic evolution of late cenozoic arc-continent collision in taiwan. *Tectonophysics* 183 (1-4), 57–76. doi:10.1016/0040-1951(90)90188-e
- Tozer, B., Sandwell, D. T., Smith, W. H. F., Olson, C., Beale, J. R., Wessel, P., et al. (2019). Global bathymetry and topography at 15 arc sec: SRTM15+. *Earth Space Sci.* 6 (10), 1847–1864. doi:10.1029/2019ea000658
- Wan, K., Xia, S., Cao, J., Sun, J., and Xu, H. (2017). Deep seismic structure of the northeastern south China sea: Origin of a high-velocity layer in the lower crust. *J. Geophys. Res. Solid Earth* 122 (4), 2831–2858. doi:10.1002/2016jb013481
- Wang, T. K., Chen, M., Lee, C., and Xia, K. (2006). Seismic imaging of the transitional crust across the northeastern margin of the South China Sea. *Tectonophysics* 412 (3-4), 237–254. doi:10.1016/j.tecto.2005.10.039
- Wessel, P., and Smith, W. H. F. (1991). Free software helps map and display data. *Eos Trans. AGU.* 72 (441), 441. doi:10.1029/90eo00319
- Willett, S. D., Fisher, D., Fuller, C., En-Chao, Y., and Chia-Yu, L. (2003). Erosion rates and orogenic-wedge kinematics in Taiwan inferred from fission-track thermochronometry. *Geol.* 31 (11), 945. doi:10.1130/g19702.1
- Wu, J., Suppe, J., Lu, R., and Kanda, R. (2016). Philippine Sea and East Asian plate tectonics since 52 Ma constrained by new subducted slab reconstruction methods. *J. Geophys. Res. Solid Earth* 121, 4670–4741. doi:10.1002/2016jb012923
- Yu, H.-S. (2004). Nature and distribution of the deformation front in the Luzon Arc-Chinese continental margin collision zone at Taiwan. *Mar. Geophys. Res.* 25 (1), 109–122. doi:10.1007/s11001-005-0737-1
- Yu, S.-B., Kuo, L.-C., Punongbayan, R. S., and Ramos, E. G. (1999). GPS observation of crustal deformation in the Taiwan-Luzon Region. *Geophys. Res. Lett.* 26 (7), 923–926. doi:10.1029/1999gl900148
- Yu, S. B., Chen, H. Y., and Kuo, L. C. (1997). Velocity field of GPS stations in the Taiwan area. *Tectonophysics* 274 (1-3), 41–59. doi:10.1016/s0040-1951(96)00297-1
- Zhang, X. C., Cawood, P. A., Huang, C. Y., Wang, Y. J., Yan, Y., Santosh, M., et al. (2016). From convergent plate margin to arc-continent collision: Formation of the kenting melange, southern taiwan. *Gondwana Res.* 38, 171–182. doi:10.1016/j.gr.2015.11.010



OPEN ACCESS

EDITED BY

Shaohong Xia,
South China Sea Institute of
Oceanology (CAS), China

REVIEWED BY

Polina Lemenkova,
Université libre de Bruxelles, Belgium
Jean Roger,
GNS Science, New Zealand

*CORRESPONDENCE

Alec Benjamin G. Ramirez,
agramirez3@up.edu.ph

SPECIALTY SECTION

This article was submitted
to Marine Geoscience,
a section of the journal
Frontiers in Earth Science

RECEIVED 11 October 2022

ACCEPTED 10 November 2022

PUBLISHED 30 November 2022

CITATION

Ramirez ABG, Ramos NT, Nawanao LP,
Mangahas-Flores RZ, Narag IC, Baba T,
Chikasada N and Satake K (2022), An
earthquake-triggered submarine mass
failure mechanism for the 1994 Mindoro
tsunami in the Philippines: Constraints
from numerical modeling and
submarine geomorphology.
Front. Earth Sci. 10:1067002.
doi: 10.3389/feart.2022.1067002

COPYRIGHT

© 2022 Ramirez, Ramos, Nawanao,
Mangahas-Flores, Narag, Baba,
Chikasada and Satake. This is an open-
access article distributed under the
terms of the [Creative Commons
Attribution License \(CC BY\)](https://creativecommons.org/licenses/by/4.0/). The use,
distribution or reproduction in other
forums is permitted, provided the
original author(s) and the copyright
owner(s) are credited and that the
original publication in this journal is
cited, in accordance with accepted
academic practice. No use, distribution
or reproduction is permitted which does
not comply with these terms.

An earthquake-triggered submarine mass failure mechanism for the 1994 Mindoro tsunami in the Philippines: Constraints from numerical modeling and submarine geomorphology

Alec Benjamin G. Ramirez^{1*}, Noelynna T. Ramos¹,
Lyndon P. Nawanao Jr¹, Robelyn Z. Mangahas-Flores²,
Ishmael C. Narag², Toshitaka Baba³, Naotaka Chikasada⁴ and
Kenji Satake⁵

¹National Institute of Geological Sciences, College of Science, University of the Philippines Diliman, Quezon City, Philippines, ²Philippine Institute of Volcanology and Seismology, Quezon City, Philippines, ³Graduate School of Science and Technology, Tokushima University, Tokushima, Japan, ⁴National Research Institute for Earth Science and Disaster Resilience, Tsukuba, Japan, ⁵Earthquake Research Institute, The University of Tokyo, Tokyo, Japan

Tsunamis have been known to result from a wide range of phenomena, such as earthquakes, volcanic eruptions, submarine mass failures, and meteorite impacts. Of earthquake-generated tsunamis, those arising from strike-slip mechanisms are less common, with the 1994 Mindoro tsunami in the Philippines among the few known examples. The 1994 Mindoro tsunami followed a M_w 7.1 earthquake along the right-lateral Aglubang River Fault. The tsunami affected the coasts surrounding the Verde Island Passage, one of the Philippines' insular seas located between the islands of Luzon and Mindoro, and east of the West Philippine Sea margin. A total of 78 lives were lost due to the earthquake and tsunami, with 41 being directly attributed to the tsunami alone. Despite the close spatial and temporal association between the 1994 Mindoro earthquake and tsunami, previous numerical modeling suggests the need for other contributing mechanisms for the 1994 tsunami. In this study, we conducted submarine geomorphological mapping of the South Pass within the Verde Island Passage, with particular focus on identifying possible submarine mass failures. Identification of submarine features were based on Red Relief Image Map (RIMM), Topographic Position Index (topographic position index)-based landform classification, and profile and plan curvatures derived from high-resolution bathymetry data. Among the important submarine features mapped include the San Andres submarine mass failure (SASMF). The San Andres submarine mass failure has an estimated volume of 0.0483 km^3 and is located within the Malaylay Submarine Canyon System in the Verde Island Passage, ~1 km offshore of San Andres in Baco, Oriental Mindoro. We also

explored two tsunami models (EQ-only and EQ+SMF) for the 1994 Mindoro tsunami using JAGURS. The source mechanisms for both models included an earthquake component based on the M_w 7.1 earthquake, while the EQ+SMF also included an additional submarine mass failure component based on the mapped San Andres submarine mass failure. Modeled wave heights from the EQ-only model drastically underestimates the observed wave heights for the 1994 Mindoro tsunami. In contrast, the EQ+SMF model tsunami wave height estimates were closer to the observed data. As such, we propose an earthquake-triggered, submarine mass failure source mechanism for the 1994 Mindoro tsunami.

KEYWORDS

1994 Mindoro earthquake and tsunami, submarine geomorphology, submarine mass failure, numerical modeling, Verde Passage, Philippines

1 Introduction

Tsunamis have been a ubiquitous phenomenon around the world, with several notable examples occurring within the past 2 decades. While most destructive tsunamis are generated by major to great megathrust earthquakes, such as the 2004 Indian Ocean and the 2011 Tohoku-oki tsunamis, more recent events arose from less common, non-seismic sources. These include the 2022 Hunga Tonga tsunami, which followed the eruption of the Hunga Tonga-Hunga Ha'apai submarine volcano, and the 2018 Sulawesi tsunami, which resulted from the combined effects of a M_w 7.5 earthquake along the Palu-Koro fault system in Indonesia (Heidarzadeh et al., 2018), associated submarine landslides (Gusman et al., 2019; Pakoksung et al., 2019), and coastal liquefaction (Sassa and Takagawa, 2018).

With exception to impact-generated tsunamis, tsunamis from strike-slip earthquakes are even much less common, as the resulting vertical seafloor displacements from such events are usually too small to initiate tsunamis (Tanioka and Satake, 1996; Heidarzadeh et al., 2017). Aside from the previously mentioned 2018 Sulawesi tsunami, the 1994 Mindoro tsunami in the Philippines is another example of a tsunami occurring after a strike-slip earthquake (Tanioka and Satake, 1996; Pakoksung et al., 2019).

The 1994 Mindoro tsunami was preceded by a M_w 7.1 earthquake along the Aglubang River Fault, within the South Pass of the Verde Island Passage in the Philippines. The tsunami produced wave heights at shore exceeding 7 m (Supplementary Table S1), despite the earthquake's dominantly right-lateral, strike-slip mechanism. Tanioka and Satake (1996) suggested that the coseismic horizontal displacement of the coastal shelf, which is intersected obliquely by the right-lateral Aglubang River Fault, played an important role in producing the observed tsunami wave amplitudes. Contrary to this, numerical modeling by the same authors has shown that a source mechanism based on M_w 7.1 earthquake alone severely underestimates the wave height

amplitudes and distribution compared to actual observations of the tsunami run-up and inundation.

The possible role of a submarine mass failure (SMF) in the generation of the 1994 Mindoro tsunami was then proposed by Tanioka and Satake (1996), and is explored in detail in this study. In general, SMF-generated tsunamis are characterized by much larger run-ups in the near-field compared to the far-field (Okal and Synolakis, 2004), which was also observed for the 1994 Mindoro tsunami (Imamura et al., 1995). Moreover, SMFs have been invoked as an important contributing mechanism for tsunamis similar to the 1994 Mindoro tsunami, wherein the estimated sea surface displacement derived from the associated earthquake is insufficient to account for the resulting run-ups. These include the 1946 Alaska (Fryer et al., 2004; von Huene et al., 2014), the 1998 Papua New Guinea (Synolakis et al., 2002; Satake and Tanioka, 2003), and the 2018 Sulawesi (Gusman et al., 2019; Pakoksung et al., 2019) tsunamis.

2 Philippine tectonics and tsunamis

The archipelagic nature of the Philippines, combined with its tectonic setting, makes it susceptible to tsunamis (Bautista et al., 2012). Most of the Philippine archipelago is within the Philippine Mobile Belt (PMB), which is bounded by oppositely-dipping subduction zones to its east and west, with the exception of the Palawan Microcontinental Block (PMCB) (Figure 1A; Gervasio, 1971; Rangin, 1991; Yumul et al., 2008; 2009; Lagmay et al., 2009; Mines and Geosciences Bureau, 2010). To the east, the Philippine Sea Plate (PSP) is subducting beneath the PMB along the Philippine Trench (Hamburger et al., 1983; Ozawa et al., 2004; Yumul et al., 2008; Mines and Geosciences Bureau, 2010). To the west, the oceanic lithospheres underlying the South China Sea, Sulu Sea, and Celebes Sea are subducting beneath the PMB along the Manila, Negros-Sulu, and Celebes trenches, respectively.

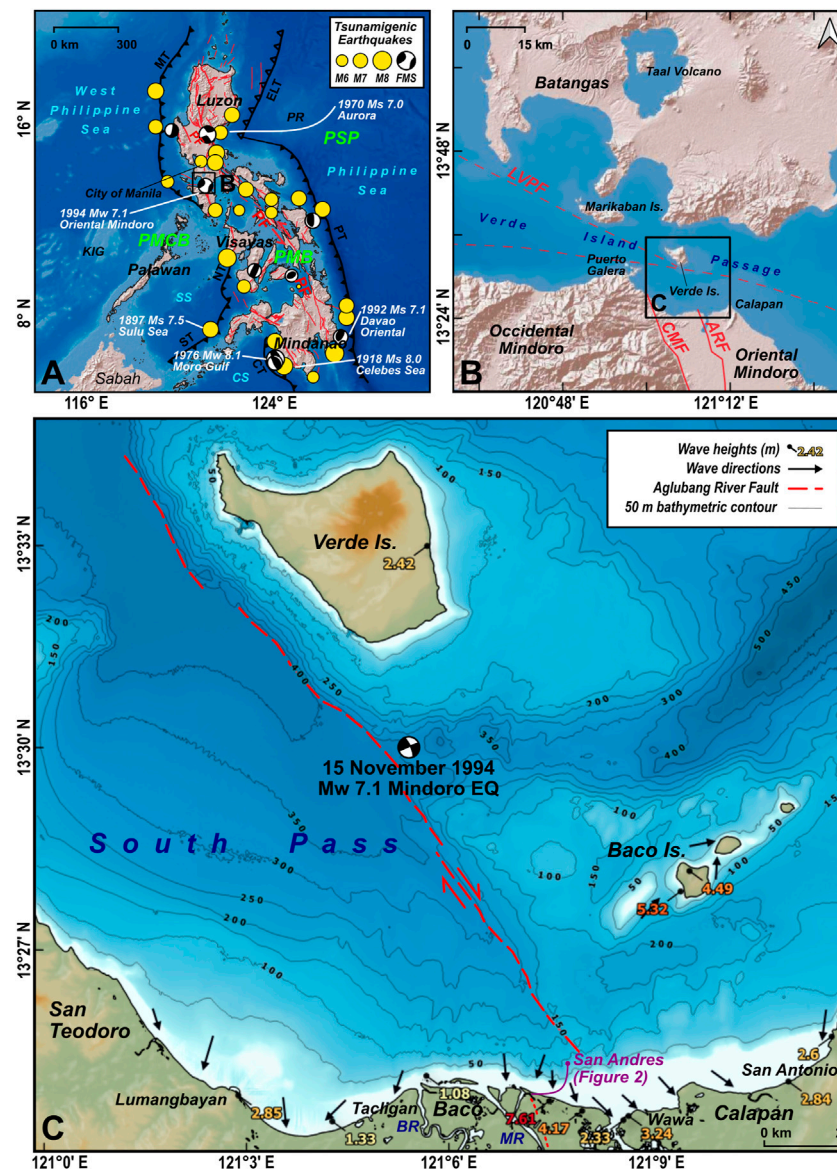


FIGURE 1

Philippine tectonic setting and notable tsunamis. (A) The 35 positive tsunamigenic earthquakes in the Philippines since 1589 AD with recorded or estimated wave heights at shore of at least 1 m (Bautista et al., 2012; NCEI/WDS, 2022) are plotted with yellow circles, or with the corresponding focal mechanism solution (FMS) diagrams. The most significant tsunamis, with maximum wave heights at shore exceeding 4 m, are also labeled. Oceanic trenches are also shown and labeled, including active faults in red (PHIVOLCS). (B) Location of the South Pass within the Verde Island Passage, where the 1994 Mindoro tsunami occurred. (C) Tsunami wave heights (modified from Imamura et al., 1995; see Supplementary Table S1) and directions of wave inundation (PHIVOLCS, 1994). The trace of the offshore extension of the Aglubang River Fault is also indicated, as mapped from the analysis of high-resolution bathymetry data in this study. FMS diagrams are from the Global Centroid Moment Tensor catalog (GCMT; Dziewonski et al., 1981; Ekstrom et al., 2012). PMB = Philippine Mobile Belt; PMCB = Palawan Microcontinental Block; PSP = Philippine Sea Plate; MT = Manila Trench; NT = Negros Trench; ST = Sulu Trench; CT = Cotabato Trench; ELT = East Luzon Trough; PT = Philippine Trench; PF = Philippine Fault; SS = Sulu Sea; CS = Celebes Sea; KIG = Kalayaan Island Group; PR = Philippine Rise; ARF = Aglubang River Fault; CMF = Central Mindoro Fault; LVPF = Lubang-Verde Passage Fault; BR = Baco River; MR = Malaylay River.

(Hayes and Lewis, 1984; Mitchell et al., 1986; Rangin et al., 1999; Yumul et al., 2008; Mines and Geosciences Bureau, 2010). Of the 35 certain tsunami events in the Philippines with wave heights of at least 1 m (Table 1; Bautista et al., 2012;

NCEI/WDS, 2022), three of the largest were generated by subduction-zone earthquakes. These are the 1897 Zamboanga tsunami, which was initiated along the Sulu Trench, and the 1918 Celebes Sea and 1976 Moro Gulf tsunamis which were

TABLE 1 The 35 tsunamigenic earthquakes in the Philippines, with recorded or estimated maximum wave heights at shore of at least 1 m.

Id	Y	M	D	Hr	Min	Long	Lat	Depth (km)	Mag ^a	Wave height ^b	Places affected
1	1828	11	9	18	30	119.5	13.7	-	6.6	1	Port of Manila
2	1840	3	22	8	30	123.85	12.95	-	6.8	2	Sorsogon Bay
3	1863	6	3	19	30	120.9	14.55	-	6.5	1–2	Manila Bay
4	1869	8	16	15	0	123.85	12.4	-	6.5	1	Masbate, Masbate
5	1880	7	18	12	40	121.55	14.9	-	7.6	2	Puerto Real, Quinanliman and Tacigan in Real, Quezon
6	1897	9	21	13	12	121.3	7.5	-	7.5	6	Sulu Sea
7	1917	1	31	12	2	125.6	5.5	-	6.4	1.5	Glan, Sarangani
8	1918	8	15	20	18	124.4	5.9	-	8	8	Celebes Sea coast; Lebak, Sultan Kudarat
9	1921	11	12	2	36	127	8	-	7.5	2	Manay, Mati, and Caraga in Davao Oriental
10	1923	7	18	10	42	125	9.3	-	5.5	1	Mambajao, Camiguin
11	1924	4	15	0	20	126.5	6.5	-	8.3	2	Pujada Bay
12	1924	5	6	0	16	119	16	-	7	1	Agno, Pangasinan
13	1925	5	5	18	7	122.7	9.3	-	6.8	1–2	Southern coast of Negros
14	1925	5	25	11	44	122.5	12.5	-	6.25	2	Tugdan, Romblon
15	1925	11	13	20	14	125	13	-	7.3	2	Batag Island, Northern Samar
16	1928	6	15	14	13	121.5	12.5	-	7	1	Mangarin Bay
17	1928	12	19	19	27	124	7	-	7.5	1	Cotabato River and Illana Bay
18	1929	6	13	17	24	127	8.5	-	7.2	2	Hinatuan Bay
19	1934	2	14	11	59	119	17.5	-	7.6	2	San Esteban and Vigan, Ilocos Sur
20	1937	8	20	19	59	121.5	14.5	-	7.5	1	Lopez and Calauag Bays
21	1948	1	25	1	46	122	10.5	-	8.2	2	San Joaquin, Miagao, Oton in Iloilo; Nueva Valencia, Guimaras
22	1968	8	2	4	19	122.2	16.5	-	7.3	3	Casiguran Bay
24	1970	4	7	13	34	121.717	15.761	-	7	4.3	Baler and San Luis, Aurora
25	1973	3	17	16	30	122.787	13.372	-	7.3	1.3	Calauag and Alabat, Quezon
26	1975	10	31	16	28	125.993	12.54	-	7.4	1–2	Taft, Eastern Samar
27	1976	8	17	0	11	124.023	6.262	33	8.1	9	Lebak, Sultan Kudarat; Moro Gulf
28	1990	2	8	15	15	124.694	9.755	16.2	6.6	1	Alijuan River, Duero, Bohol; Bohol Strait; Camiguin Island
29	1990	7	16	16	26	121.172	15.679	15	7.8	2	Brgy. Darigayos, Luna, La Union
30	1992	5	17	17	49	126.753	7.183	34	7.1	5	Manay and Caraga, Davao Oriental
31	1994	11	15	3	15	121.087	13.532	15	7.1	7	Northern Oriental Mindoro; Verde Island in Batangas
32	1995	4	21	8	34	125.58	12.059	21.7	7.3	2	San Julian and Dolores, Eastern Samar
33	1999	12	12	2	3	119.67	15.85	35.1	6.8	1.5	Iba and Palauig, Zambales
34	2002	3	6	5	15	124	6.1	28.7	7.2	2	Palimbang, Sultan Kudarat
35	2012	2	6	11	49	123.14	9.97	12	6.9	2	La Libertad, Negros Oriental

^aMoment magnitude. For earthquake magnitudes reported as surface wave (Ms) and body wave (Mb) magnitudes, empirical equations by Scordilis (2006) were used to convert the values to moment magnitude.

^bMaximum wave height at shore (meters).

The row in bold emphasizes the 1994 Mindoro tsunami, which is the focus of this study.

initiated along the Cotabato Trench. The 1976 Moro Gulf tsunami (Badillo and Astilla, 1978; Bautista et al., 2012; Claro et al., 2021) is the most destructive of the known tsunami events in the Philippines.

Earthquakes along offshore intraplate and upper-plate faults have also produced tsunamis in the Philippines—the most notable of which are the 1970 Baler, 1992 Davao Oriental, and 1994 Mindoro tsunamis (Bautista et al., 2012). The 1994 Mindoro tsunami, which is the focus of

this study, occurred within the Verde Island Passage (Figure 1B). Major tectonic structures in proximity to the Verde Island Passage include the southern terminus of the Manila Trench, and active strike-slip faults such as the WNW-trending left-lateral Lubang-Verde Passage Fault (Karig, 1983; Rangin et al., 1988), the NNW-trending Central Mindoro Fault (Karig, 1983; Rangin et al., 1988), and the NNW-trending right-lateral Aglubang River Fault (PHIVOLCS, 1994).

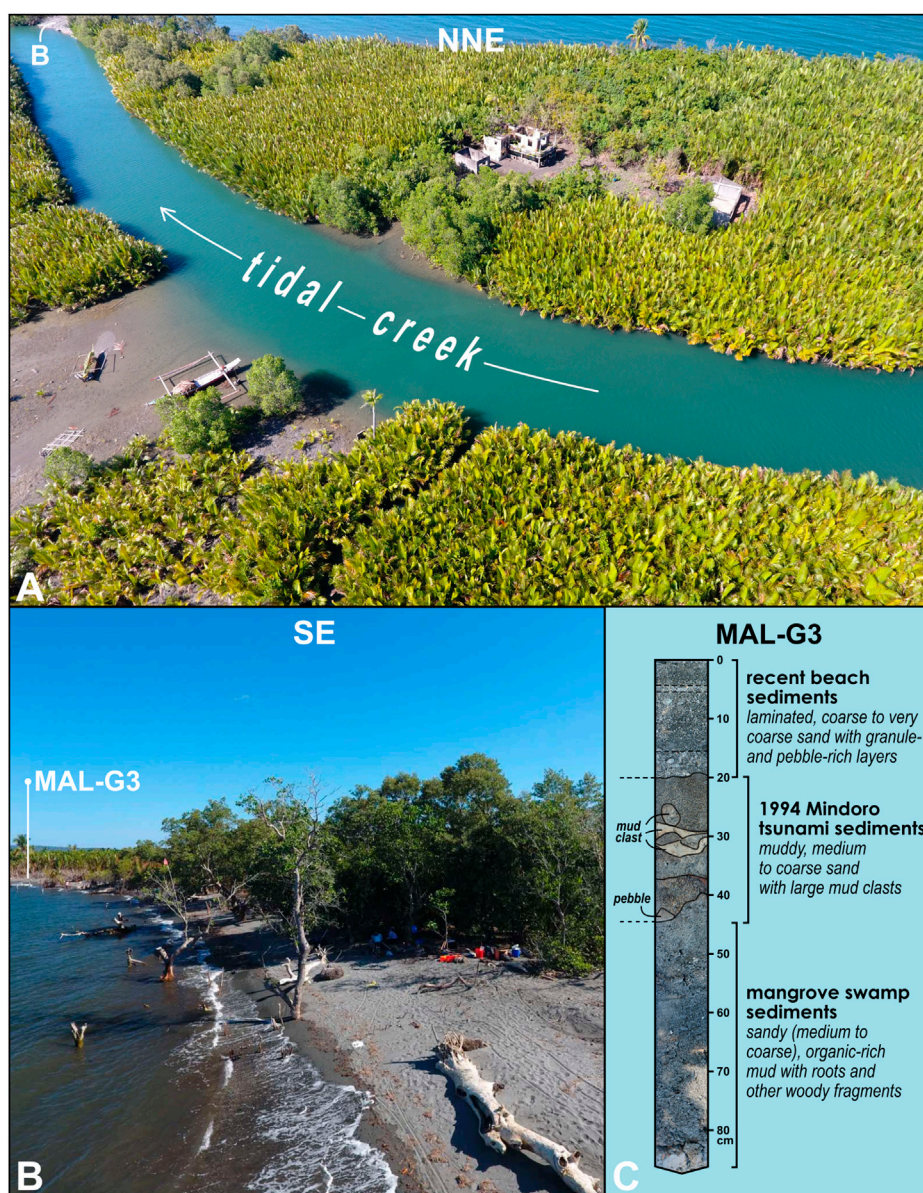


FIGURE 2

Barangay San Andres in Oriental Mindoro, 25 years after the 1994 tsunami. (A) NNE-looking image overlooking Sitio Malaylay in Barangay San Andres, taken during low tide. The area is mostly a mangrove swamp, with *Nypa fruticans* as the most common mangrove. Note the dilapidated structures which were initially damaged by the 1994 tsunami. The location of Figure 2A is shown in Figure 1C. The exposed tidal bar in the foreground of B is also labeled. (B) SE-looking, along-the-coast view of Sitio Malaylay. Note the protruding trunks of drowned mangrove trees along the foreshore and the absence of the tsunami beach ridge that was deposited by the 1994 tsunami, both of which indicate post-1994 coastal erosion. The location of a geoslicer sample, MAL-G3, is also shown. (C) Visual stratigraphic interpretation of MAL-G3. The 1994 Mindoro tsunami deposit is partially preserved, overlying the older mangrove swamp sediments.

3 The 1994 Mindoro tsunami

In the early morning of 15 November 1994, at around 3:15 a.m. local time (GMT+8), a M_w 7.1 earthquake occurred underneath the South Pass of the Verde Island Passage in the Philippines (Figures 1B–D; PHIVOLCS, 1994). The earthquake is

associated with the offshore extension of the right-lateral Aglubang River Fault, based on its epicenter (13.5 N, 121.1 E), focal mechanism solution, and surface rupture in Oriental Mindoro along the Aglubang River Fault (PHIVOLCS, 1994). Within a few minutes after the earthquake, tsunami waves hit the surrounding coastal areas of northern Oriental Mindoro, Baco

Islands, Verde Island, and Batangas in Southern Luzon (PHIVOLCS, 1994; Imamura et al., 1995). Among the hardest hit is Barangay San Andres in the town of Baco, Oriental Mindoro, and the Baco Islands, which were inundated by tsunami waves exceeding 7 m and 5 m, respectively (Supplementary Table S1). A total of 78 lives were lost, with 41 directly due to the tsunami. The cost of repairing and rehabilitating the damages to infrastructure was estimated at around PHP 5.5 million (PHIVOLCS, 1994). The 1994 tsunami also left behind a 1-m high tsunami beach ridge along the coast of Barangay San Andres (PHIVOLCS, 1994), although it was not observed during fieldwork conducted in 2019 (Figure 2). The tsunami beach ridge was most likely eroded given that the Barangay San Andres coast has been subjected to at least 120 m of coastal erosion since 1992, as observed from multiple Landsat and Sentinel-2 satellite imagery (Supplementary Figure S1). An extreme wave event deposit, most likely a preserved section of the 1994 Mindoro tsunami, was also identified in a geoslicer sample obtained in Barangay San Andres (Figure 2C). The suspected 1994 tsunami deposit is characterized by the presence of large (>5 cm) mud clasts in a muddy, medium to coarse sand matrix, with a basal erosional contact with the underlying, mangrove swamp sediments.

The 1994 Mindoro tsunami was initially assumed to be caused by the M_w 7.1 earthquake (PHIVOLCS, 1994; Bautista et al., 2012), due to the close spatial and temporal association between the two. However, as previously mentioned, results of previous numerical modeling of the 1994 tsunami based on the M_w 7.1 earthquake alone (Tanioka and Satake, 1996) are inconsistent with observed tsunami wave heights. As such, in this study, we explored the possibility of one or several submarine mass failures as a contributing mechanism for the 1994 tsunami.

4 Submarine geomorphology of the South Pass

4.1 Morphometric analysis and geomorphological interpretation of bathymetry data

The 20 m resolution digital bathymetry data for the Verde Island Passage (Supplementary Figure S2), obtained from multibeam surveys conducted by the National Mapping Resource and Information Authority (NAMRIA) in 2011, was used in the submarine geomorphological mapping. Geomorphometric analysis of the bathymetry data was performed through topographic position index (TPI)-based landform classification and derivation of land surface parameters (i.e., slope, openness, profile and plan curvature) in a GIS platform. These parameters were then used as basis in identifying submarine geomorphological features (i.e., gullies, ridges, fault line scarps, shelf breaks and scarps, seafloor bedforms, and submarine mass failures).

4.1.1 Delineation of linear features using red relief image maps

The Red Relief Image Map (RIMM; Chiba et al., 2008) is a pseudo-3D relief visualization technique that highlights both coarse- and fine-resolution surface features simultaneously across a wide variety of topographic positions, without the dependency on light directions, unlike shaded relief maps. It is generated by combining two land surface parameters: slope and differential openness. In RIMM, a red color ramp is used to visualize the slope angle, while its saturation is modified based on the differential openness. As such, convex features (e.g., ridges and crests) appear as bright areas; concave features (e.g., valleys and depressions) and steep slopes appear as red; and flat areas appear as gray.

The RRIM for the South Pass was generated in QGIS 3.22.4. The slope was calculated using the *Slope* terrain analysis module (GDAL/OGR contributors, 2020), following Horn's algorithm. The positive (PO) and negative openness (NO) were calculated using the *Topographic Openness* module from the System for Automated Geoscientific Analyses (SAGA) (Conrad et al., 2015), following the definition of openness by Yokoyama and others (2002). We then calculated the differential openness (DO) from the PO and NO, using the formula from Chiba et al. (2008):

$$DO = \frac{(PO - NO)}{2}$$

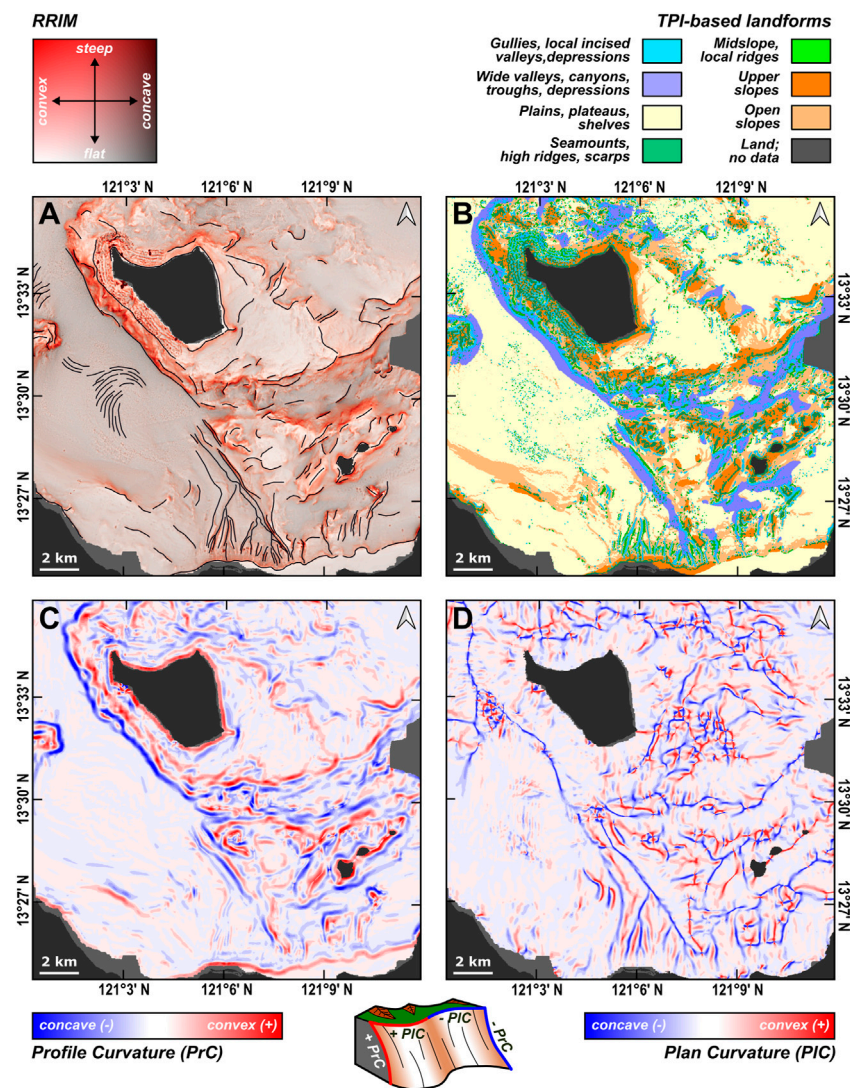
The slope was visualized using a red color ramp, while the differential openness used a black-to-white color ramp. The RRIM effect is achieved by overlaying the slope over the differential openness, using the blending mode *Multiply*. Prominent linear features were manually delineated from the RRIM (Figure 3A).

4.1.2 TPI-based landform classification

The topographic position index (TPI) is calculated by obtaining the difference between the elevation of the point of interest (Z_0) and the mean elevation (Z_C) around a neighborhood area with a predetermined size C (Guisan et al., 1999; Wilson and Gallant, 2000). By calculating the TPI using two neighborhood sizes (C_S and C_L), distinct small- and large-scale landform units can be defined based on the values of TPI and the standard deviation (SD) within C (Weiss, 2001; De Reu et al., 2013).

The TPI Based Landform Classification module in SAGA (Conrad et al., 2015) was used to derive the landform classes, using pixel (px), small (C_S), and large neighborhood (C_L) sizes of 20 m, 100 px, and 1000 px, respectively. The landform classes for submarine geomorphology were modified from those originally defined by Weiss (2001) for terrestrial landscapes (Table 2).

The modifications include the use of appropriate submarine landform terms corresponding to each landform class. For example, additional landforms such as shelves and plateaus were added to the submarine landform class 3, since both are similar to plains in terms of their low relief. Moreover, Weiss' landform classes 1, 2, and 3 were merged into a single class grouping together all narrow channel-like landforms (i.e., gullies,

**FIGURE 3**

DEM-derived layers used in the submarine geomorphological mapping of the South Pass, Verde Island Passage. (A) Red Relief Image Map (RRIM) with manually delineated linear features. (B) Landform classification based on Topographic Position Index. (C) Profile curvature. (D) Plan curvature.

upland drainages, and canyons), as well as narrow valleys and depressions. This is to simplify the distinction of negative relief landforms into narrow (class 1) and wide (class 2) morphologies. Similarly, Weiss' landform classes 8 and 9 were also merged into a single class, which includes both midslope ridges and local ridges located within valleys. This again, allows for a simpler distinction *versus* prominent ridges (high ridges, or class 7 in this study).

The TPI-based landform classification for the South Pass is shown in Figure 3B. Violet and blue were used for landform classes with negative relief (1 and 2); yellow for low relief landforms (3); orange for open and upper slopes (4 and 5); and green for positive relief landforms (6 and 7).

4.1.3 Profile and plan curvatures

Profile and plan curvatures are measures of the rate of change (radians per m) of the slope and aspect of a topographic surface, respectively. Profile curvature is measured along the vertical direction. On the other hand, plan curvature is measured along the horizontal direction, parallel to elevation contours, and hence are also referred to as contour curvature. Positive and negative values for both plan and profile curvatures correspond to convex and concave morphologies in relation to the downslope direction (Wilson and Gallant, 2001). The profile and plan curvatures in 20-m resolution for the South Pass were also calculated in 20-m resolution using SAGA, as shown in Figures 3C,D.

TABLE 2 Landform classification based on TPI values.

Small neighborhood ($C_S = 100$)	Large neighborhood ($C_L = 1,000$)	Landform classes		Id
		Weiss (2001)	This study	
$Z_0 < -SD$	$Z_0 < -SD$	Canyons, deeply incised streams	Gullies, local incised valleys and depressions	1
$Z_0 < -SD$	$0 \leq Z_0 \leq SD$	Midslope drainages, shallow valleys		
$Z_0 < -SD$	$Z_0 > SD$	Upland drainages, headwaters		
$-SD \leq Z_0 \leq SD$	$Z_0 < -SD$	U-shaped valleys	Wide valleys, canyons, troughs, and depressions	2
$-SD \leq Z_0 \leq SD$	$0 \leq Z_0 \leq SD$; slope ≤ 5	Plains	Plains, plateaus, and shelves	3
$-SD \leq Z_0 \leq SD$	$0 \leq Z_0 \leq SD$; slope > 5	Open slopes	Open slopes	4
$-SD \leq Z_0 \leq SD$	$Z_0 > SD$	Upper slopes	Upper slopes	5
$Z_0 > SD$	$Z_0 < SD$	Local ridges/hills in valleys	Midslope and local ridges	6
$Z_0 > SD$	$0 \leq Z_0 \leq SD$	Midslope ridges		
$Z_0 > SD$	$Z_0 > SD$	Mountain tops, high ridges	Seamounts, high ridges, and scarps	7

TABLE 3 Geomorphological classification of linear features.

Landform	Description ^a	TPI landform class ^b	Profile curvature	Plan curvature
Gullies	Narrow, incised channels; flanked by midslope ridges	1		concave
Ridges	Linear bathymetric highs flanked by steep slopes	6, 7	convex	convex
Fault line scarp	Linear slope breaks or steep valleys, conforms with the focal mechanism of the 15 November 1994 M_w 7.1 Mindoro earthquake ^c	1	concave	-
Shelf breaks, scarps	Linear slope breaks separating an upper, gentler slope face or shelf and a lower, steeper slope face	7; separates 3, 5 from 4	convex	-
Seafloor bedforms	Low relief, regularly-spaced crests and troughs	3	-	-
Submarine mass failures ^d				
Headwall scarps	Steep, arcuate and concave-facing downslope	7	convex	concave
Lateral margins	Scarps or ridges perpendicular to the headwall scarp	6, 7	convex	
Toe deposits	High surface roughness due to displaced blocks; occurrence of pressure ridges			

^aAs recognized from the red relief image map (RRIM).

^bSee Table 2 for the TPI, landform categories.

^cOriented subparallel to nodal plane one from GCMT, focal mechanism (Strike: N 21 W; Dip: 70; Rake: 178; Dziewonski et al., 1981; Ekstrom et al., 2012).

^dFrom morphological descriptions of submarine mass failure structures by Scarselli (2020) and morphological criteria for the identification of terrestrial landslides from high-resolution digital terrain data by Van Den Eeckhaut and others (2012) and Pawluszek (2019).

4.1.4 Geomorphological classification of linear features

The linear features delineated from the analysis of RRIM for the South Pass were manually classified based on their interpreted geomorphology. The TPI-based landform classification, profile curvature, and plan curvature were also used as guides for interpretation. A summary of the submarine geomorphological features and their expressions in the RRIM, TPI-based landform classification, and profile and plan curvatures are shown in Table 3. The resulting submarine geomorphological map and bathymetric profiles of the South Pass are also shown in Figure 4.

4.1.5 Mapping of submarine mass failures (SMFs)

Particular focus was also given on the identification of probable SMFs which were primarily based on their morphological expressions as discussed by Scarselli (2020), such as headwall scarps, lateral margins, and toe deposits. Morphological criteria for the identification of terrestrial landslides from high-resolution digital terrain data (Van Den Eeckhaut et al., 2012; Pawluszek, 2018) were also used to supplement the identification of SMFs, based on the morphological similarities between submarine and terrestrial landslides. The head scarp length, transport direction, and area of each mapped SMF was also measured in QGIS.

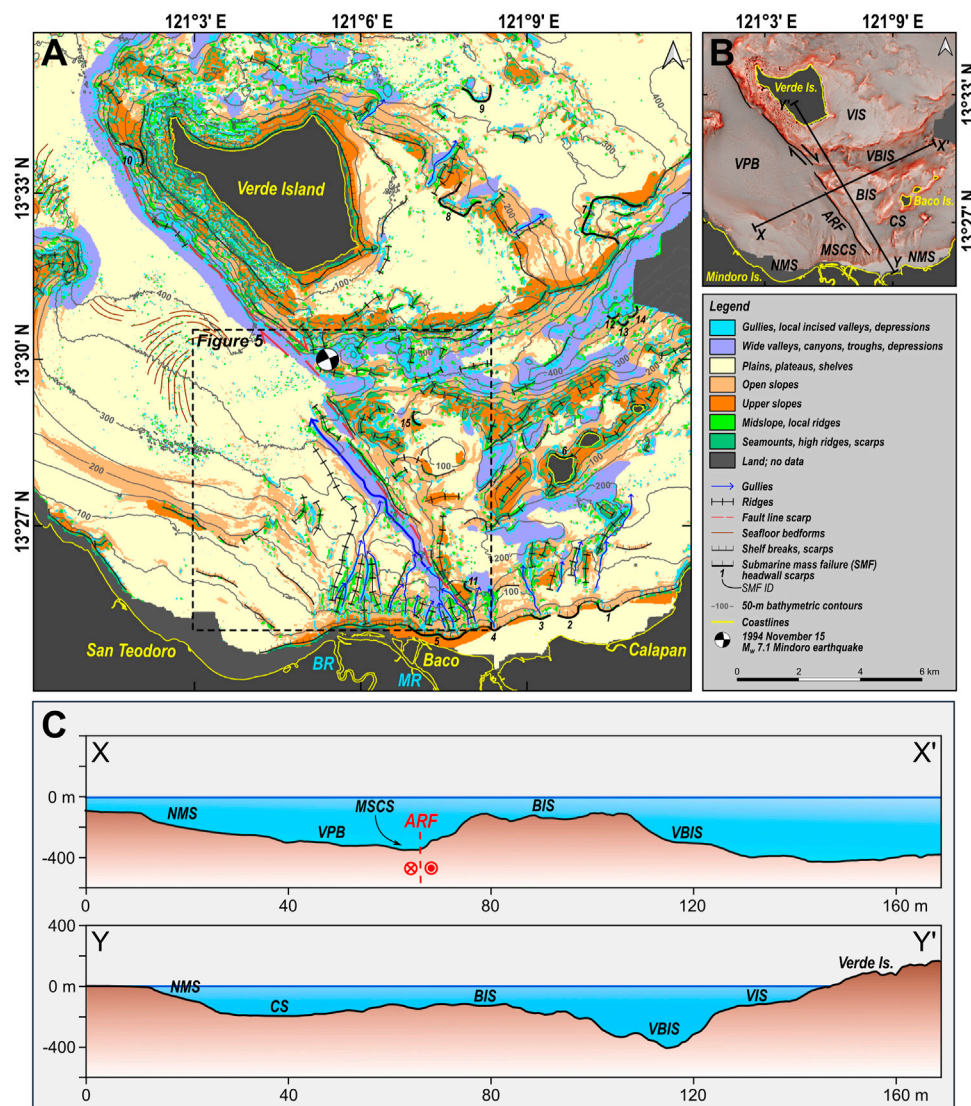


FIGURE 4

Submarine geomorphology of the South Pass, Verde Island Passage. (A) Map of submarine landforms and features. The headwall scarps of the 15 mapped probable SMFs (Table 4) are also labeled. The extent of the 3D rendering in Figure 5 is also shown. (B) Relief map of the South Pass, labeled with identified main submarine features and transects for the bathymetric profiles shown in (C). ARF = Aglubang River Fault; BIS = Baco Islands Shelf; CS = Calapan Saddle; MSCS = Malaylay Submarine Canyon System; NMS = Northern Mindoro Shelf; VBIS = Verde-Baco Islands Saddle; VIS = Verde Island Shelf; VPB = Verde Passage Basin; BR = Baco River; MR = Malaylay River.

Furthermore, we also identified the SMFs that have probably occurred after the 1950s, based on the comparison between the 2011 bathymetry with 1950s point depth sounding data. The point depth sounding data was obtained from NAMRIA topographic map of Calapan, Oriental Mindoro (3260 III), which was based on aerial photography and coastal surveys and offshore surveys from 1947 to 1953.

Both bathymetry data sets generally show minor differences with each other, with a coefficient of determination (R^2) of 0.95 (Supplementary Figure S3). As such, we can use the two bathymetry datasets to reliably estimate the net erosion from

1956 to 2011. The net erosion for each point depth location was estimated based on the difference between the two datasets. Post-1956 SMFs were identified based on the occurrence of net erosion downslope of SMF scarps.

4.2 Main undersea features

The submarine geomorphological map and bathymetric profiles of the South Pass is shown in Figure 4. The South Pass (SP) is divided into two regions of distinct bathymetric levels by a ~21 km

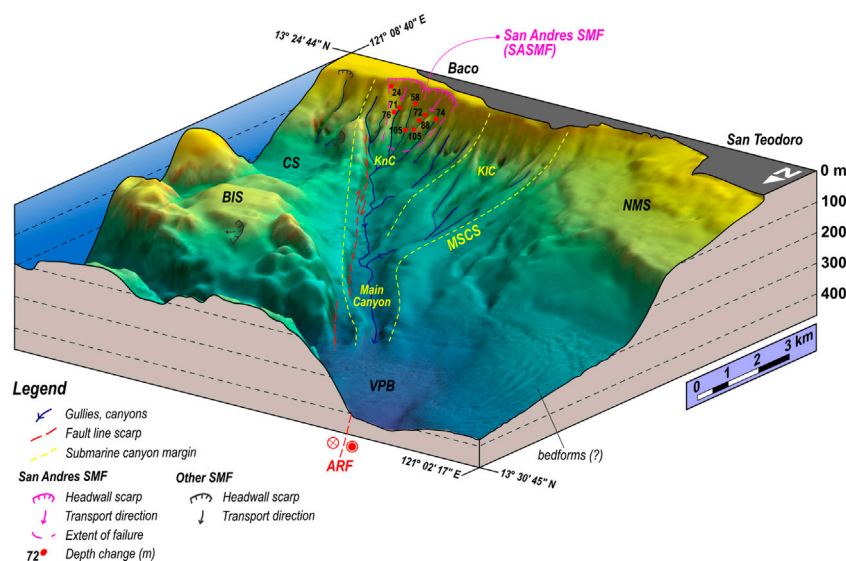


FIGURE 5

Three-dimensional view of the offshore Aglubang River Fault and the Malaylay Submarine Canyon System (MSCS). The red dots show the location of depth comparisons with the thickness of eroded material in meters. KnC = Kanan Submarine Canyon; KIC = Kaliwa Submarine Canyon.

long SW-facing slope, trending NW from the Northern Mindoro Shelf (NMS) towards Verde Island. The Verde Passage Basin (VPB) floors the SW region and further extends outside SP to the northwest, with its shallowest portions at the 300-m isobath. To its south, the VPB is bounded by the western Northern Mindoro Shelf (wNMS). The wNMS is composed of a gentle ($<5^\circ$) upper shelf with a maximum width of ~ 3 km, and a steeper ($5\text{--}10^\circ$) insular slope transitioning into the VPB.

On the other hand, the NE region of SP is much shallower than VPB, and is divided into a series of insular shelves and saddles. The eastern Northern Mindoro Shelf (eNMS) is also composed of a gentle ($<5^\circ$) upper shelf underlying the Calapan Bay, with a maximum width of ~ 1.3 km, and a steeper insular slope extending to the 150-m isobath, where it transitions to the Calapan Saddle (CS). CS is ~ 9 -km long, ~ 1.2 -km wide, and has a maximum depth of less than 250 m. To its north lies the Baco Island Shelf (BIS). Between the BIS and the Verde Island Shelf (VIS) lies the deeper Verde-Baco-Island Saddle (VBIS). The VBIS is ~ 6 -km long, ~ 1.2 -km wide, and has a maximum depth of less than 350 m. Both CS and VBIS connect the waters of Verde Island Passage and the Tayabas Bay, which lies east of the South Pass.

4.3 The offshore trace of the Aglubang River Fault (ARF)

The previously described SW-facing, steep ($10\text{--}45^\circ$) linear slope correlates with one of the nodal planes (Strike: N 21° W; Dip: 70°)

defined by the focal mechanism solution of the 15 November 1994 M_w 7.1 earthquake (Dziewonski et al., 1981; Ekstrom et al., 2012). This earthquake, associated with the Aglubang River Fault, resulted in a ~ 35 -km total onshore surface rupture in Oriental Mindoro (PHIVOLCS, 1994). As such, the NW-trending trough and scarp are interpreted as the approximate fault line scarp of the offshore extension of the Aglubang River Fault (ARF). This interpretation is in agreement with the mapped offshore extension of the ARF by Sarmiento and others (2022).

4.4 The Malaylay Submarine Canyon System (MSCS)

A prominent feature identified within the South Pass is the NW-trending, 8-km long Malaylay Submarine Canyon System (MSCS; Figure 5), eponymously named due to its proximity to Malaylay Island in Oriental Mindoro. The MSCS can be classified as a headless, shelf-incising canyon due to the absence of a shelf valley connecting it to the adjacent outlets of the Baco and Malaylay rivers. The eastern side of the MSCS is structurally controlled by the Aglubang River Fault (ARF) fault line scarp described in the previous section.

The MSCS is divided into a lower and upper course. The ~ 4.5 -km wide upper course is composed of two canyons, namely, the Kaliwa (KIC) and Kanan (KnC) canyons. These canyons are respectively equivalent to the Malaylay and Baco canyons described by Sequeiros and others (2019), with the names modified to avoid confusion with the MSCS.

TABLE 4 The 15 mapped probable SMFs in the South Pass.

SMF ID	Location ^a	Latitude	Longitude	Length (m)	Area	Transport direction	Relative age (post-1950s?) ^b
1	eNMS	13.43	121.17	880.72	0.103	N 09 E	No
2	eNMS	13.42	121.16	910.32	0.115	N 24 W	No
3	eNMS	13.42	121.15	636.40	0.053	Due N	No
4	eNMS	13.42	121.14	413.25	0.034	N 8 W	No
5	MSCS	13.42	121.12	2092.89	1.430	Due N	Yes (9; 24–105 m)
6	BIS	13.47	121.16	603.36	0.056	N 07 E	Yes (1; 31 m)
7	VIS	13.54	121.17	4,065.74	1.969	S 78 E	N/A
8	VIS	13.55	121.13	2,702.10	0.822	N 44 E	N/A
9	VIS	13.58	121.14	1,490.99	0.427	N 23 W	N/A
10	VIS	13.56	121.03	1,244.12	0.408	S 55 W	N/A
11	CS	13.43	121.13	432.05	0.041	N 63 E	N/A
12	BIS/VBIS	13.51	121.18	409.66	0.036	N 13 W	N/A
13	BIS/VBIS	13.51	121.18	415.55	0.036	Due N	N/A
14	BIS/VBIS	13.51	121.18	500.78	0.049	N 56 W	N/A
15	BIS	13.48	121.12	556.80	0.099	N 70 E	N/A

^aeNMS–eastern Northern Mindoro Shelf; MSCS–Malaylay Submarine Canyon System; BIS–Baco Islands Shelf; VIS–Verde Island Shelf; CS–Calapan Saddle; VBIS–Verde–Baco Islands Saddle.

^bBased on comparison of 2011 bathymetry and 1950s point depth sounding data. If Yes, the number of comparison points and the range of net erosion values are also indicated. No means net erosion is <10 m. N/A means no comparison points were plotted downslope of the SMF. The row in bold emphasizes the San Andres SMF, which is focused in this study.

Both the Kaliwa and Kanan canyons exit into the ~6-km long, ~1-km wide lower course dubbed as the Main Canyon by Sequeiros and others (2019). The Main Canyon eventually exits into the Verde Passage Basin at depths of ~350 m.

4.5 Submarine mass failures in the South Pass

A total of 15 probable submarine mass failures (SMFs) were identified within the South Pass, based on the occurrence of bight-shaped headwall scarps (Figure 4). Their corresponding head scarp lengths, areas, transport directions, and relative ages are also listed in Table 4. These SMFs were identified along the shelf edges of the eastern Northern Mindoro Shelf (eNMS), and within the Malaylay Submarine Canyon System (MSCS), the Verde Island Shelf (VIS), the Baco Island Shelf (BIS), the Calapan Saddle (CS), and the Verde–Baco Islands Saddle (VBIS).

The largest of the probable SMFs in terms of area are SMF 8 (0.822 km²), SMF 5 (1.430 km²), and SMF 7 (1.969 km²). Of the three, only SMF 5 can be reliably considered as having occurred after 1950s, with net erosion ranging from 24 to 105 m, based on nine measurements (Figures 5, 6). SMF 6 (0.056 km²) also shows significant net erosion of 31 m, although based only on one measurement. SMFs 1 to 4 show insignificant net erosion (<10 m), which may indicate their relatively older age. On the other hand, no comparison points were available for SMFs 7 to 15.

Aside from its size and availability of net erosion measurements, SMF 5 is particularly notable due to its

proximity to Barangay San Andres in Baco, Oriental Mindoro, which received the most damage from the tsunami. We therefore focus the following discussions on SMF 5, which we formally refer to as the San Andres SMF (SASMF).

4.6 The San Andres submarine mass failure (SASMF) and the 1994 Mindoro tsunami

The proposed occurrence of the San Andres SMF (SASMF) has been based on the net erosion derived from the comparison between two, widely spaced bathymetry datasets. The question, therefore, is whether the observed net erosion was a product of a single, catastrophic event (e.g., submarine mass failure) or a series of smaller and/or gradual processes (e.g., turbidity currents).

The occurrence of erosional events within the MSCS since 1997 has been documented and studied by Sequeiros and others (2019), in relation to the destructive effects of erosion on a gas pipeline installed in 2001. Throughout a 21-year duration (January 1997 to September 2018) with a total of 27 pipe and aerial surveys, only two significant erosional events were documented within the MSCS, both of which were attributed to typhoon-triggered turbidity currents. Of the 11 typhoons that have passed over or within the vicinity of the MSCS, only typhoons Reming (Durian) in 2006 and Nina (Nock-Ten) in 2016 caused turbidity currents, resulting in pipe displacements and damage to protective rock berms. Seabed erosion due to these turbidity currents occur within established gullies and

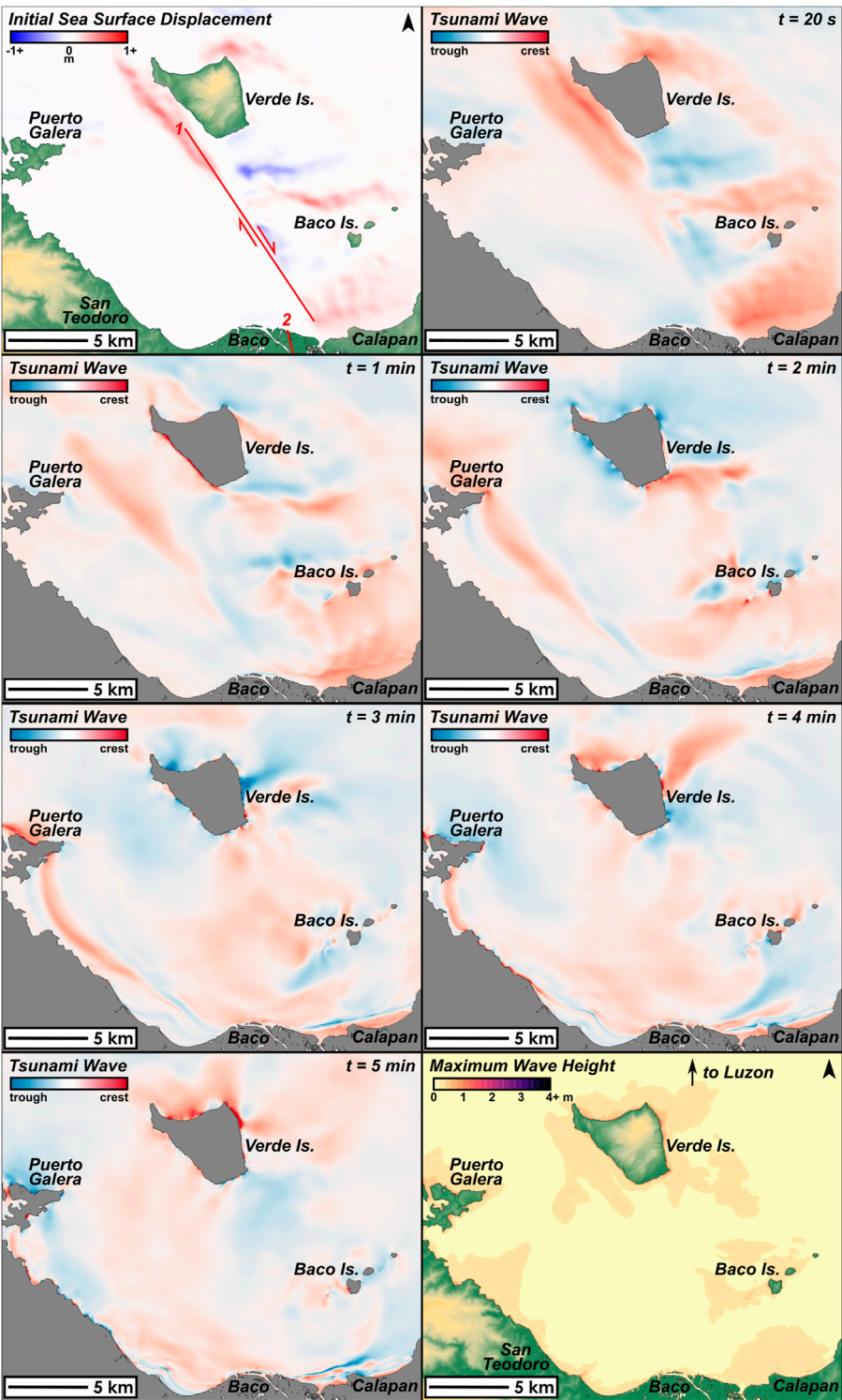


FIGURE 6
Initial sea surface displacement, tsunami propagation, and maximum wave height distribution of the EQ-only model. The Aglubang River Fault is shown in red, segmented into two sub-faults as described in [Table 5](#).

canyons of the MSCS. Erosion thickness generally does not exceed 5 m, except in some localized zones where it may reach up to 10 m. Moreover, the likelihood of turbidity currents within the MSCS due to hyperpycnal outflows from the Baco and Malaylay rivers has been ruled out, owing to insufficient sediment concentration even during annual monsoon floods.

We can then reasonably constrain the occurrence of the SASMF between the 1950s and 1997. Also, by extrapolating the frequency of typhoon-triggered turbidity currents within the MSCS as discussed above (~ 1 in 11.5 yrs), we estimate four to five erosional events between the 1950s and 1997. Assuming a 5-m average thickness of eroded material per event, the cumulative erosion thickness is roughly 20–25 m. This estimate is on the lower end of the net erosion observed for the SASMF, which ranges from 24–105 m. Note that the simple estimate presented above assumes a negligible sediment input from the Baco and Malaylay rivers, which is unlikely as sediment yields of 0.336 and 0.351 MT/yr are estimated for both rivers, respectively (Sequeiros et al., 2019). Furthermore, in contrast to the much wider extent of the SASMF (~ 1.43 km²), the extent of the turbidity currents' influence is restricted within existing gullies and canyons within the MSCS.

While further constraints on the timing of the SASMF are unavailable at present, we hypothesize that the SASMF was likely triggered by the M_w 7.1 1994 Mindoro earthquake. This idea is premised on the following: 1) the 1994 Mindoro earthquake is within the possible window of occurrence for the SASMF, as already established above; and 2) modeling the 1994 Mindoro tsunami with the SASMF as an additional source mechanism approximates the observed wave height distribution better than the model based on the 1994 earthquake alone. We further elaborate on the second point in the following sections.

5 Numerical modeling of the 1994 Mindoro tsunami

5.1 Modeling methods

The two models (EQ-only and EQ+SMF) for the 1994 Mindoro tsunami were calculated using JAGURS (Baba et al., 2015). JAGURS is a numerical code that calculates the propagation and inundation of tsunami waves over gridded terrain, based on the linear and nonlinear Shallow Water Equations (SWE), and Boussinesq Equations to account for wave dispersion (Baba et al., 2015).

5.1.1 Preparation of terrain data

The 20-m digital bathymetry and the 5-m IFSAR topography data from NAMRIA were used as terrain inputs for both models. Merging of the two datasets and interpolation for areas with

unavailable data were done in QGIS3, using the tension spline interpolation method in the SAGA raster terrain module *Close Gaps*. Final preparation of the terrain data for JAGURS was done using GDAL and GMT.

5.1.2 EQ-only model source mechanism

The source mechanism for the EQ-only model was based on the 15 November 1994 M_w 7.1 Mindoro earthquake along the right-lateral Aglubang River Fault (ARF). The initial sea surface displacement was calculated in JAGURS, based on the surface deformation due to a finite rectangular source (Okada, 1985). The effects of horizontal displacement (Tanioka and Satake, 1996) were also included in the calculations.

The fault parameters used in the calculations are shown in Table 5. We decided to segment the ARF into two sub-faults to reflect both the mapped offshore fault line scarp in this study and the mapped onshore fault rupture by PHIVOLCS (1994). As such, the strike of the sub-faults followed the general trends of the offshore fault line scarp and onshore fault rupture, while the downdip width is calculated using the scaling relationship equation based on moment magnitude by Wells and Coppersmith (1994). The dip angle (70°) is based on the GCMT focal mechanism of the M_w 7.1 earthquake (Dziewonski et al., 1981; Ekstrom et al., 2012). This dip angle generally coincides with the mapped offshore fault line scarp when projected from the hypocentral location (13.5 N, 121.1 E, 7–12 km depth) of the earthquake as reported by PHIVOLCS (1994). The slip amount was based on the maximum vertical displacement (1.9m) observed onshore at Baruyan Lake (PHIVOLCS, 1994).

5.1.3 EQ+SMF model source mechanism

A combined source mechanism is modeled based on the 1994 earthquake and SMF identified from submarine geomorphological mapping. For the earthquake component, the initial sea surface displacement from the EQ-only model was also used, as described in the previous section.

For the SMF component, we used the semi-empirical predictive equation by Sabeti and Heidarzadeh (2022), which was tested for the 1994 Skagway, Alaska and the 1998 Papua New Guinea submarine landslide-generated tsunamis. The equation relates the SMF volume (V) in km³ and the initial submergence depth (d) in m to the maximum initial wave amplitude (η_{max}) in m, as follows:

$$\eta_{max} = 50.67 \left(\frac{V}{d} \right)^{0.34}$$

The parameters used in the calculation of the SMF-generated wave are shown in Table 6. The initial sea surface displacement from the earthquake and SMF-generated wave were added to produce the EQ+SMF model initial conditions, based on the assumption that the tsunamigenic SMF was coseismic.

TABLE 5 Fault parameters for the Aglubang River Fault as used for the earthquake source mechanism. The two sub-faults are based on the geomorphological expression of the offshore extension (this study), and the mapped onshore rupture (PHIVOLCS, 1994) as labeled in Figures 6, 7.

Id	Latitude ^a	Longitude ^a	Depth ^{a,c} (km)	Strike	Dip ^d	Length (km)	Width ^e (km)	Rake ^d	Slip ^b (m)
1	13.416 ^{b,e}	121.136 ^{b,e}	0	330 ^e	70	15.6 ^e	14	-178	2
2	13.245 ^b	121.179 ^b	0	342 ^b	70	19.2 ^b	14	-178	2

^aLocation of the upper right corner of the rectangular fault plane.

^bField and instrumental data from PHIVOLCS (1994).

^cValue selected as 0 for the surface-rupturing earthquake.

^dGlobal Centroid Moment Tensor (GCMT) focal mechanism solution (Dziewonski et al., 1981; Ekstrom et al., 2012).

^eScaling relationships by Wells and Coppersmith (1994).

^fDerived from submarine geomorphological mapping (this study).

TABLE 6 SMF parameters used in this study.

SMF^a

Area (A)	1.43 sq. Km
Volume (V)	0.0483 cu. Km
Initial submergence depth (d)	10 m

SMF-generated tsunami wave

Amplitude (η_{max}) ^b	8.27 m
Radius (r) ^a	500 m
Central location (latitude, longitude) ^a	13.42176 N, 121.12342 E

^aDerived from submarine geomorphological mapping (this study).

^bCalculated using the equation by Sabeti and Heidarzadeh (2022).

5.1.4 Parameters for tsunami propagation and inundation modeling

The numerical models used a terrain grid resolution of 0.00015° (~15 m), with model bounds (NW and SE corners) of 13.65015 N, 120.9000 E and 13.4000 N, 121.19970 E. Total model duration was set at 15 min, with a calculation time step of 0.05 s. Snapshots of the model results were taken every 20 s. The effects of Coriolis motion and seawater compressibility were assumed negligible. The models used the linear shallow water equations to calculate the tsunami propagation.

5.1.5 Calculation of modeled wave height statistics and error

We obtained modeled wave height statistics (i.e., mean, median, minimum, maximum, first quartile, third quartile, standard deviation) for 22 shoreline sections (SS1—SS22) around northern Oriental Mindoro, Baco Islands, and Verde Island.

We also compared the modeled wave heights (W_m) with 11 observed wave height measurements (W_o ; see Supplementary Table S1) by calculating the root mean squared error (RMSE). The root mean squared error (RMSE) for both models was

calculated using the equation, where the number of observations (n) is 11:

$$RMSE = \sqrt{\frac{\sum (W_m - W_o)^2}{n}}$$

5.2 The EQ-only and EQ+SMF tsunami models

5.2.1 Tsunami propagation

As previously described, we modeled two scenarios (EQ-only and EQ+SMF) for the 1994 Mindoro tsunami. We used the San Andres SMF as basis for the SMF component of the EQ+SMF model. The initial sea surface displacement, snapshots of tsunami propagation, and maximum wave height distributions for the EQ-only and EQ+SMF models are shown in Figures 6, 7, respectively.

For the EQ-only model, initial sea surface displacements (Figure 6) ranged from -0.57 to 0.50 m. The sea surface displacements coincide with the locations of the insular slopes surrounding Verde Island, Baco Islands, and Calapan, which moved coseismically with the 1994 earthquake.

According to the EQ-only model, the movement of the ARF fault line scarp generated tsunami waves to the southwest, eventually reaching the coasts of Baco in 1 min; Puerto Galera in 2 min; and San Teodoro in 3 min. Meanwhile, Verde Island, Baco Islands, and Calapan were hit by tsunami waves within the first minute after the earthquake. Tsunami wave refraction around the northwestern point of Verde Island can also be observed prominently 4 min after the earthquake. At least two distinct tsunami waves hit the coasts of Oriental Mindoro (Supplementary Figure S4), consistent with anecdotes from post-tsunami field surveys (PHIVOLCS, 1994; Imamura et al., 1995).

On the other hand, the EQ+SMF model is dominated by the SMF-generated wave, which is expected given its considerably larger amplitude (± 8.27 m) compared to the earthquake-generated waves (Figure 7). The SMF produced a leading-

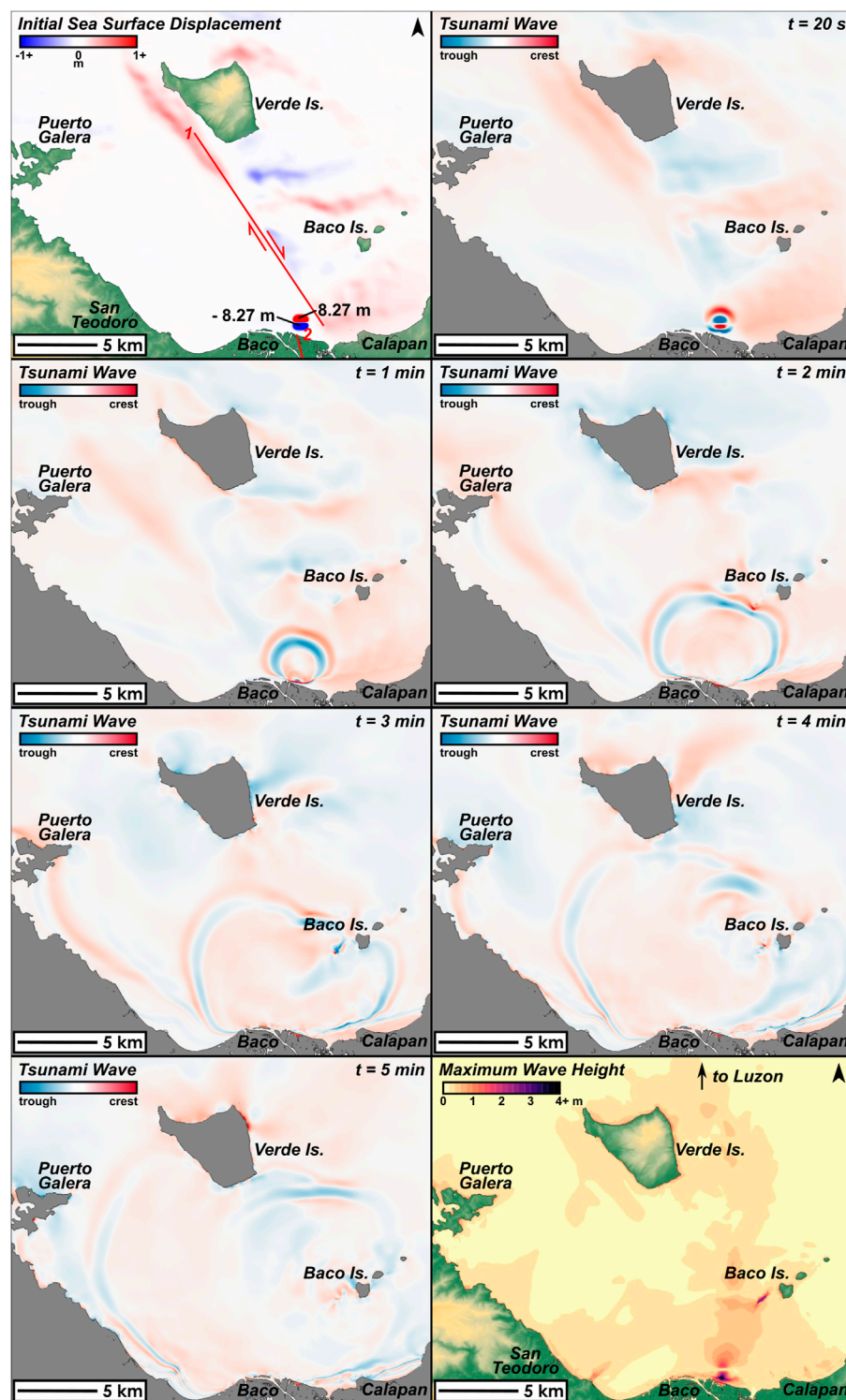


FIGURE 7

Initial sea surface displacement, tsunami propagation, and maximum wave height distribution of the EQ+SMF model. The Aglubang River Fault is shown in red, segmented into two sub-faults as described in Table 5. The amplitudes of the SMF-generated wave crests and troughs are also labeled accordingly. In the last panel, note the focused distribution of extreme wave heights (>4 m) at Baco and Baco Islands, which is consistent with observed data, and is absent in the EQ-only model.

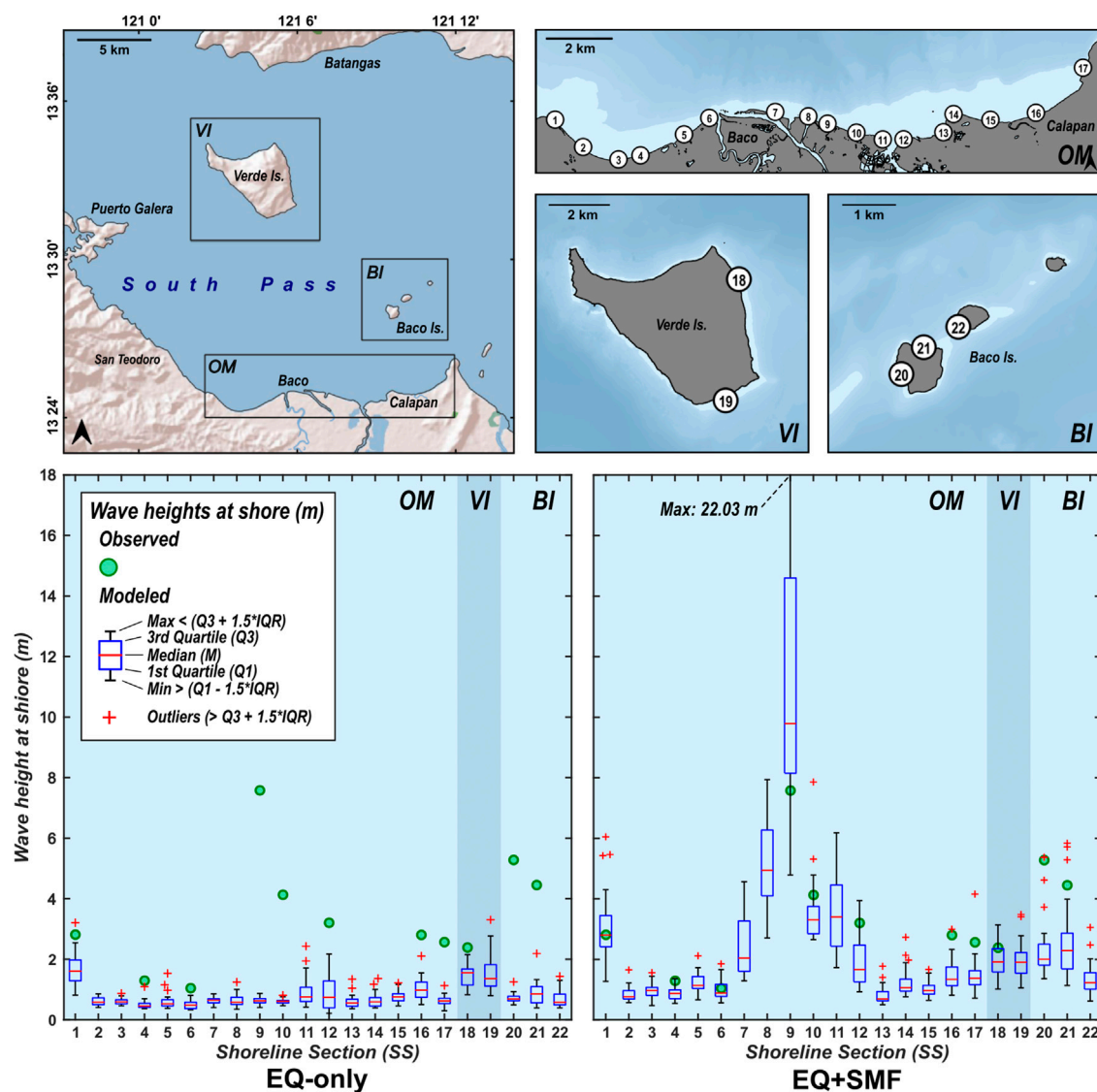


FIGURE 8

Comparison between observed and modeled (EQ-only and EQ+SMF) wave heights. The upper panels show the locations of the shoreline sections, while the lower panels show the box plots of modeled wave heights for the EQ-only and EQ+SMF tsunami models. Observed wave heights are derived from run-up measurements by Imamura and others (1995), based on the wave-height-at-shore and run-up empirical relationship equation by Smart and others (2016).

depression wave towards Baco, consistent with eyewitness accounts (PHIVOLCS, 1994; Imamura et al., 1995). The SMF-generated wave spread out in all directions, with significant refraction towards the Baco Islands as it hit the Baco Island Shelf to the northeast. Focusing of tsunami waves were also observed leeward of the largest of the Baco Islands, as was similarly inferred from post-event runup measurements (Imamura et al., 1995).

Arrival times within the South Pass for both models are very short (<1–3 min), due to the near-field nature of the tsunami

sources considered. However, the EQ+SMF model also shows farther propagation of tsunami waves north of Verde Island and towards Southern Luzon, as shown by the maximum wave height distributions (Figures 6, 7).

5.2.2 Wave heights at shore

Figure 8 shows the comparison between modeled and observed wave heights at shore for 22 selected shoreline sections. The wave height statistics from the EQ-only and EQ+SMF models for the 22 selected shoreline sections are also listed in Supplementary Table S2.

TABLE 7 Root mean squared error (RMSE) calculations for EQ-only and EQ+SMF models using mean, median, and all predicted wave heights at shore values.

	$(W_m - W_o)^2$												RMSE
	n	SS1	SS4	SS6	SS9	SS10	SS12	SS16	SS17	SS18	SS20	SS21	
EQ-only (mean)	11	1.38	0.69	0.34	48.84	12.65	5.54	3.40	3.92	0.95	21.13	12.99	3.19
EQ-only (median)	11	1.54	0.76	0.36	48.81	12.63	6.24	3.47	3.91	0.75	21.41	13.24	3.21
EQ-only (all)	341												3.20
EQ+SMF (mean)	11	0.04	0.22	0.01	13.90	0.36	1.74	1.83	1.38	0.20	9.13	3.73	1.72
EQ+SMF (median)	11	0.00	0.21	0.04	4.70	0.75	2.51	2.27	1.51	0.26	11.00	4.85	1.60
EQ+SMF (all)	341												2.34

For the EQ-only model, the predicted median wave heights for San Andres (SS9) and Baco Islands (SS20) are 0.63 m and 0.70 m, respectively. On the other hand, the predicted median wave heights from the EQ+SMF model are 9.78 m for San Andres, and 2.00 m for Baco Islands.

Furthermore, calculated RMSE values (Table 7) are consistently lower for the EQ+SMF model *versus* the EQ-only model. Using median wave heights at shore values, the RMSE for the EQ-only and EQ+SMF models are 3.21 m and 1.60 m, respectively. Using mean wave heights at shore values, the RMSE for the EQ-only and EQ+SMF models are 3.19 m and 1.72 m, respectively. Finally, using all wave heights at shore values, the RMSE for the EQ-only and EQ+SMF models are 3.20 m and 2.34 m, respectively.

5.3 The M_w 7.1 earthquake alone is not enough to produce the 1994 Mindoro tsunami

The results of our EQ-only model produced higher wave heights than those predicted by the earlier model of Tanioka and Satake (1996). Their model predicted wave heights of 0.07 m, 0.09 m, and 0.09 m for Baco, Wawa, and Calapan, respectively. Meanwhile, our EQ-only model predicted median wave heights at shore of 0.63 m (SS9), 0.74 m (SS12), and 0.98 m (SS16), respectively. These higher wave heights are likely due to the use of bathymetry data with a higher resolution. Lower resolutions smooth out bathymetric features such as insular shelves and slopes. This likely results in lower predicted wave amplitudes due to horizontal displacement of the seafloor, which is a significant contributor to initial tsunami wave heights. On the other hand, both models also predict higher wave heights for Calapan than in Baco, which is contrary to observed wave heights (2.83 m and 7.61 m, respectively).

More importantly, the EQ-only model severely underestimates the observed wave heights at shore for the 1994 Mindoro tsunami. For the EQ-only model, the predicted median wave heights for San Andres (SS9) and Baco Islands (SS20) are 0.63 m and 0.70 m, respectively. In contrast, observed wave heights at shore for San Andres and Baco Islands are 7.61 m and 5.32 m, respectively. Overall, the results of the EQ-only model clearly show that the M_w 7.1 1994 Mindoro earthquake

alone is not enough to produce the wave height magnitudes and distribution observed for the 1994 Mindoro tsunami.

5.4 The 1994 Mindoro tsunami has a combined earthquake and submarine mass failure source mechanism

The comparison between both modeled (EQ-only and EQ+SMF) and observed data wave height at shore distributions (Figure 8) shows that the EQ+SMF model approximates the observed data better than the EQ-only model. Quantitatively, this is also indicated by the lower RMSE values for the EQ+SMF model compared to the EQ-only model.

Considering the sample of the modeled wave height at shore measurements as a whole ($n=341$), the EQ-SMF model has a RMSE of 2.34 m *versus* the EQ-only model with a RMSE of 3.20 m. While this already indicates better predictions of the EQ+SMF model over the EQ-only model, the RMSE calculations for EQ+SMF are drastically affected by the large spread of predicted wave height at shore values specifically at SS9 (San Andres), with a standard deviation of 4.68 m. In contrast, the maximum spread of wave height at shore values for the EQ-only model is at SS12, with a standard deviation of 0.57 m. The larger spread observed for the EQ+SMF model is likely a function of the higher predicted wave heights compared to the EQ-only model. Moreover, constructive interference of waves would result in very high wave amplitudes at certain locations. The most extreme example is at SS9, which has predicted maximum and median wave heights at shore of 22.03 m and 9.78 m, respectively.

Furthermore, the RMSE of the EQ+SMF model improves if only the median or mean wave heights at shore values are considered in the calculation. RMSE values considering median and mean wave heights are 3.21 m and 3.19 m, and 1.60 m and 1.72 m, respectively. The two-fold increase in RMSE values between the EQ+SMF and EQ-only models clearly supports our hypothesis that the 1994 Mindoro tsunami is an earthquake-triggered, submarine mass failure tsunami.

6 Conclusion

In this study, we combined submarine geomorphological mapping and numerical modeling to constrain and describe a more probable mechanism for the 1994 Mindoro tsunami. We have identified and mapped a previously undescribed submarine mass failure within the Malaylay Submarine Canyon System (MSCS), which we refer to as the San Andres submarine mass failure (SASMF). Furthermore, we have established evidence that constrains its occurrence between the 1950s and 1997, and ruled out turbidity currents as triggering mechanisms for extensive submarine mass failure. We therefore infer that the San Andres SMF is concurrent with the M_w 7.1 1994 Mindoro earthquake, and as such, is an important contributing mechanism to the resulting 1994 Mindoro tsunami.

To test this hypothesis, we modeled two scenarios for the 1994 Mindoro tsunami; the first was based on the M_w 7.1 quake alone (EQ-only model), while the second one included a submarine mass failure component based on the San Andres SMF (EQ+SMF model). The results of the numerical modeling show that the EQ+SMF model predicted wave height at shore values closer to observed data, compared to those predicted by the EQ-only model. As such, the results of our numerical modeling support the likelihood of a combined earthquake and submarine mass failure mechanism for the 1994 Mindoro tsunami.

On the other hand, significant improvements on the EQ+SMF model can and should still be made, as evident from the RMSE values, which are still in the same order of magnitude as the wave height measurements. Such discrepancies are expected given the limitations of how we calculated the submarine mass failure (SMF) component of the source mechanism. The calculations for the SMF component, based only on the volume and initial submergence depth, do not take into account the transport mechanics (i.e., translational, slumping, debris flow, turbidity flow) and dynamic aspects (i.e., velocity, acceleration) of the submarine mass failure (Harbitz et al., 2006; Masson, et al., 2006; Løvholt et al., 2015). Constraining these parameters requires a more detailed characterization of the San Andres SMF, which is beyond the scope of this work. Moreover, because bathymetry data obtained close to the 1994 tsunami is unavailable, we have opted to use the 2011 bathymetry data in the numerical modeling. This simplification has introduced another source of error, as changes in the bathymetry due to erosional and depositional processes would have definitely occurred between 1994 and 2011.

While past research on Philippine tsunamis have been focused on earthquake-generated mechanisms, our findings highlight the importance of including SMF-generated tsunamis in assessing the country's coastal hazards. With the increasing availability of high-resolution bathymetry data not just for the inland and territorial seas of the Philippines but also globally, our methods on submarine

geomorphological mapping and numerical modeling can be replicated to map and identify past and potential SMFs and estimate the magnitude and extent of the resulting tsunamis. This is particularly important for SMFs forming along shelves proximal to populated coastal areas like the San Andres SMF, which render conventional tsunami warning systems insufficient due to very short tsunami arrival times.

Data availability statement

The original contributions presented in the study are included in the article/[Supplementary Material](#), further inquiries can be directed to the corresponding author.

Author contributions

AR conducted the submarine geomorphological mapping and numerical modeling, and wrote the paper. NR provided supervision in the conceptualization of the study, data analysis, and interpretation. KS, NR, TB, LN, RM, and IN contributed insights on the earthquake and submarine mass failure source parameters. KS, TB, and NC provided technical training and feedback on the numerical modeling of the 1994 Mindoro tsunami. NR and AR obtained funding for the study. NR, KS, TB, LN, IN, and RM were involved in the manuscript revisions.

Funding

This study was primarily funded by the Department of Science and Technology - Philippine Council for Industry, Energy and Emerging Technology Research and Development (DOST-PCIEERD) Project No. 4233, co-implemented by the University of the Philippines–National Institute of Geologic Sciences (UP-NIGS) and Philippine Institute of Volcanology and Seismology (PHIVOLCS). Additional support was also provided by UP through NIGS Research Grants 2020 and 2022.

Acknowledgments

The authors would like to thank the National Mapping Resource and Information Authority (NAMRIA) for providing the bathymetry and topography datasets; to the local government units of Oriental Mindoro, including the municipalities of Baco, Calapan, San Teodoro, and Puerto Galera, for assistance during our fieldwork in February 2019; to external reviewers ABSR and LGR; and to the Geomorphology and Active Tectonics Research (GEAR) Laboratory. Gratitude is also extended to the contributors behind JAGURS, QGIS, SAGA, GDAL, and GMT.

Conflict of interest

The authors declare that the research was conducted in the absence of any commercial or financial relationships that could be construed as a potential conflict of interest.

Publisher's note

All claims expressed in this article are solely those of the authors and do not necessarily represent those of their affiliated

organizations, or those of the publisher, the editors and the reviewers. Any product that may be evaluated in this article, or claim that may be made by its manufacturer, is not guaranteed or endorsed by the publisher.

Supplementary material

The Supplementary Material for this article can be found online at: <https://www.frontiersin.org/articles/10.3389/feart.2022.1067002/full#supplementary-material>

References

- Baba, T., Takahashi, N., Kaneda, Y., Ando, K., Matsuoka, D., and Kato, T. (2015). Parallel implementation of dispersive tsunami wave modeling with a nesting algorithm for the 2011 Tohoku Tsunami. *Pure Appl. Geophys.* 172 (12), 3455–3472. doi:10.1007/s00024-015-1049-2
- Badillo, V. L., and Astilla, Z. C. (1978). *Moro Gulf tsunami of 17 August 1976*. Quezon City: Manila Observatory.
- Bautista, M. L. P., Bautista, B. C., Salcedo, J., and Narag, I. (2012). *Philippine tsunamis and seiches (1589 – 2012): A catalogue of tsunami events in the Philippines*. Quezon City: Philippine Institute of Volcanology and Seismology (PHIVOLCS) 978-971-92395-1-2.
- Chiba, T., Kaneta, S., and Suzuki, Y. (2008). Red relief image map: New visualization method for three dimensional data. *Remote Sens. Spatial Inf. Sci.* 37.
- Claro, S. M. D., Ramos, N. T., Fernando, A. G. S., Ishimura, D., and Switzer, A. D. (2021). Sedimentological evidence of washover deposits from extreme wave events in Zamboanga del Sur, Mindanao, southern Philippines. *Mar. Geol.* 438, 106535. doi:10.1016/j.margeo.2021.106535
- Conrad, O., Bechtel, B., Bock, M., Dietrich, H., Fischer, E., Gerlitz, L., et al. (2015). System for automated geoscientific analyses (SAGA) v. 2.1.4. *Geosci. Model Dev.* 8, 1991–2007. doi:10.5194/gmd-8-1991-2015
- De Reu, J., Bourgeois, J., Bats, M., Zwervaegher, A., Gelorini, V., De Smedt, P., et al. (2013). Application of the topographic position index to heterogeneous landscapes. *Geomorphology* 186, 39–49. doi:10.1016/j.geomorph.2012.12.015
- Dziewonski, A. M., Chou, T. A., and Woodhouse, J. H. (1981). Determination of earthquake source parameters from waveform data for studies of global and regional seismicity. *J. Geophys. Res.* 86, 2825–2852. doi:10.1029/JB086iB04p02825
- Ekström, G., Nettles, M., and Dziewoński, A. M. (2012). The global CMT project 2004–2010: Centroid-moment tensors for 13, 017 earthquakes. *Phys. Earth Planet. Interiors* 200–201, 1–9. doi:10.1016/j.pepi.2012.04.002
- Fryer, G. J., Watts, P., and Pratson, L. F. (2004). Source of the great tsunami of 1 April 1946: A landslide in the upper alutian forearc. *Mar. Geol.* 203 (3–4), 201–218. doi:10.1016/s0025-3227(03)00305-0
- GDAL/OGR contributors (2020). GDAL/OGR geospatial data abstraction software library. Retrieved from: <https://gdal.org>.
- Gervasio, F. C. (1971). Geotectonic development of the Philippines. *J. Geol. Soc. Phil.* 25 (1), 18.
- Guisan, A., Weiss, S. B., and Weiss, A. D. (1999). GLM versus CCA spatial modeling of plant species distribution. *Plant Ecol.* 143, 107–122. doi:10.1023/a:1009841519580
- Gusman, A. R., Supendi, P., Nugraha, A. D., Power, W., Latief, H., Sunendar, H., et al. (2019). Source model for the tsunami inside Palu Bay following the 2018 Palu earthquake, Indonesia. *Geophys. Res. Lett.* 46, 8721–8730. doi:10.1029/2019gl082717
- Hamburger, M. W., Cardwell, R. K., and Isacks, B. L. (1983). Seismotectonics of the northern Philippine island arc. *Am. Geophys. Union Monogr.* 27, 1.
- Harbitz, C. B., Løvholt, F., Pedersen, G., and Masson, D. G. (2006). Mechanisms of tsunami generation by submarine landslides: A short review. *Nor. J. Geology/Norsk Geol. Forening* 86 (3).
- Hayes, D. E., and Lewis, S. D. (1984). A geophysical study of the Manila Trench, Luzon, Philippines I. Crustal structure, gravity and regional tectonic evolution. *J. Geophys. Res.* 89, 9171–9195. doi:10.1029/jb089ib11p09171
- Heidarzadeh, M., Muhari, A., and Wijanarto, A. B. (2018). Insights on the source of the 28 September 2018 Sulawesi Tsunami, Indonesia based on spectral analyses and numerical simulations. *Pure Appl. Geophys.* 176 (1), 25–43. doi:10.1007/s00024-018-2065-9
- Heidarzadeh, M., and Satake, K. (2017). Possible dual earthquake–landslide source of the 13 November 2016 Kaikoura, New Zealand Tsunami. *Pure Appl. Geophys.* 174 (10), 3737–3749. doi:10.1007/s00024-017-1637-4
- Imamura, F., Synolakis, C. E., Gica, E., Titov, V., Llistanco, E., and Lee, H. J. (1995). Field survey of the 1994 Mindoro island, Philippines tsunami. *Pure Appl. Geophys.* 144 (3–4), 875–890. doi:10.1007/bf00874399
- Karig, D. E. (1983). Accreted terranes in the northern part of the Philippine archipelago. *Tectonics* 2, 211–236. doi:10.1029/tc002i002p00211
- Lagmay, A. M., Tejada, M. L., Pena, R. E., Aurelio, M. A., Davy, B., David, S., et al. (2009). New definition of philippine plate boundaries and implications to the philippine mobile belt. *J. Geol. Soc. Philipp.* 64, 17.
- Løvholt, F., Pedersen, G., Harbitz, C. B., Glimsdal, S., and Kim, J. (2015). On the characteristics of landslide tsunamis. *Phil. Trans. R. Soc. A* 373 (2053), 20140376. doi:10.1098/rsta.2014.0376
- Masson, D. G., Harbitz, C. B., Wynn, R. B., Pedersen, G., and Lovholt, F. (2006). Submarine landslides: Processes, triggers and hazard prediction. *Phil. Trans. R. Soc. A* 364 (1845), 2009–2039. doi:10.1098/rsta.2006.1810
- Mines and Geosciences Bureau (2010). *Geology of the Philippines*. Quezon city: Mines and Geosciences Bureau. Editors M. A. Aurelio and R. E. Peña. 2nd Edition.
- Mitchell, A. G. H., Hernandez, F., and de la Cruz, A. P. (1986). Cenozoic evolution of the Philippine archipelago. *J. Southeast Asian Earth Sci.* 1, 3–22. doi:10.1016/0743-9547(86)90003-6
- NCEI/WDS (2022). *Global historical tsunami database*. NOAA National Centers for Environmental Information. (Accessed on November 2022). doi:10.7289/V5PN93H7
- Okada, Y. (1985). Surface deformation due to shear and tensile faults in a half-space. *Bull. Seismol. Soc. Am.* 75 (4), 1135–1154. doi:10.1785/bssa0750041135
- Okal, E. A., and Synolakis, C. E. (2004). Source discriminants for near-field tsunamis. *Geophys. J. Int.* 158 (3), 899–912. doi:10.1111/j.1365-246x.2004.02347.x
- Ozawa, A., Tagami, T., Llistanco, E. L., Arpa, C. B., and Sudo, M. (2004). Initiation and propagation of subduction along the Philippine Trench: Evidence from the temporal and spatial distribution of volcanoes. *J. Asian Earth Sci.* 23, 105–111. doi:10.1016/s1367-9120(03)00112-3
- Pakoksung, K., Suppasri, A., Imamura, F., Athanasius, C., Omang, A., and Muhari, A. (2019). Simulation of the submarine landslide tsunami on 28 september 2018 in Palu Bay, Sulawesi island, Indonesia, using a two-layer model. *Pure Appl. Geophys.* 176, 3323–3350. doi:10.1007/s00024-019-02235-y
- Pawluszek, K. (2018). Landslide features identification and morphology investigation using high-resolution DEM derivatives. *Nat. Hazards (Dordr.)* 96, 311–330. doi:10.1007/s11069-018-3543-1
- PHIVOLCS (1994). *15 november 1994 Mindoro earthquake: Preliminary report of investigation*. Quezon City, Philippines.
- QGIS (2022). *QGIS geographic information system*. QGIS Association. <http://www.qgis.org>.

- Rangin, C., Spakman, W., Pubellier, M., and Bijwaard, H. (1999). Tomographic and geological constraints on subduction along the eastern Sundaland margin (South-East Asia). *Bull. Geol. Soc. France* 170, 775.
- Rangin, C., Stephan, J. F., Blanchet, R., Baladad, D., Bouysee, P., Chen, M. P., et al. (1988). Seabeam survey at the southern end of the Manila trench. Transition between subduction and collision processes, offshore Mindoro Island, Philippines. *Tectonophysics* 146, 261–278. Issues 1–4. doi:10.1016/0040-1951(88)90095-9
- Rangin, C. (1991). The philippine mobile belt: A complex plate boundary. *J. Southeast Asian Earth Sci.* 6 (3–4), 209–220. doi:10.1016/0743-9547(91)90068-9
- Sabeti, R., and Heidarzadeh, M. (2022). A new empirical equation for predicting the maximum initial amplitude of submarine landslide-generated waves. *Landslides* 19, 491–503. doi:10.1007/s10346-021-01747-w
- Sarmiento, K. J. S., Aurelio, M. A., Flores, P. C. M., Carrillo, A. D. V., Marfito, B. J., Abigania, M. I. T., et al. (2022). Seafloor structures and static stress changes associated with two recent earthquakes in offshore southern Batangas, Philippines. *Front. Earth Sci.* 9. doi:10.3389/feart.2021.801670
- Sassa, S., and Takagawa, T. (2018). Liquefied gravity flow-induced tsunami: First evidence and comparison from the 2018 Indonesia Sulawesi earthquake and tsunami disasters. *Landslides* 16, 195–200. doi:10.1007/s10346-018-1114-x
- Satake, K., and Tanioka, Y. (2003). The July 1998 Papua New Guinea earthquake: Mechanism and quantification of unusual tsunami generation. *Pure Appl. Geophys.* 160 (10–11), 2087–2118. doi:10.1007/s00024-003-2421-1
- Scarselli, N. (2020). Submarine landslides – architecture, controlling factors and environments. A summary. *Regional Geol. Text. Princ. Geol. Analysis*, 417–439. doi:10.1016/b978-0-444-64134-2.00015-8
- Sequeiros, O. E., Bolla Pittaluga, M., Frascati, A., Pirmez, C., Masson, D. G., Weaver, P., et al. (2019). How typhoons trigger turbidity currents in submarine canyons. *Sci. Rep.* 9 (1), 9220. doi:10.1038/s41598-019-45615-z
- Smart, G. M., Crowley, K. H. M., and Lane, E. M. (2015). Estimating tsunami run-up. *Nat. Hazards (Dordr.)* 80 (3), 1933–1947. doi:10.1007/s11069-015-2052-8
- Synolakis, C. E., Bardet, J. P., Borrero, J. C., Davies, H. L., Okal, E. A., Silver, E. A., et al. (2002). The slump origin of the 1998 Papua New Guinea Tsunami. *Proc. R. Soc. Lond. A* 458 (2020), 763–789. doi:10.1098/rspa.2001.0915
- Tanioka, Y., and Satake, K. (1996). Tsunami generation by horizontal displacement of ocean bottom. *Geophys. Res. Lett.* 23 (8), 861–864. doi:10.1029/96gl00736
- Van Den Eeckhaut, M., Kerle, N., Poesen, J., and Hervás, J. (2012). Object-oriented identification of forested landslides with derivatives of single pulse LiDAR data. *Geomorphology* 173–174, 30–42. doi:10.1016/j.geomorph.2012.05.024
- Von Huene, R., Kirby, S., Miller, J., and Dartnell, P. (2014). The destructive 1946 Unimak near-field tsunami: New evidence for a submarine slide source from reprocessed marine geophysical data. *Geophys. Res. Lett.* 41 (19), 6811–6818. doi:10.1002/2014gl061759
- Weiss, A. D. (2001). *Topographic position and landforms analysis*. San Diego, CA: Poster Presentation, ESRI Users Conference.
- Wells, D., and Coppersmith, K. (1994). New empirical relationships among magnitude, rupture length, rupture width, rupture area, and surface displacement. *Bull. Seismol. Soc. Am.*, 84, 974–1002.
- Wilson, J. P., and Gallant, J. C. (2000). “Digital terrain analysis,” in *Terrain analysis - principles and applications*. New York: John Wiley & Sons, 1.
- Yokoyama, R., and Pike, R. (2002). Visualizing topography by openness: A new application of image processing to digital elevation models. *Photogrammetric Eng. Remote Sens.* 68 (3).
- Yumul, G. P., Dimalanta, C. B., Maglambayan, V. B., and Marquez, E. J. (2008). Tectonic setting of a composite terrane: A review of the philippine island arc system. *Geosci. J.* 12 (1), 7–17. doi:10.1007/s12303-008-0002-0
- Yumul, G. P., Dimalanta, C. B., Marquez, E. J., and Queaño, K. L. (2009). Onland signatures of the palawan microcontinental block and philippine mobile belt collision and crustal growth process: A review. *J. Asian Earth Sci.* 34 (5), 610–623. doi:10.1016/j.jseaes.2008.10.002



OPEN ACCESS

EDITED BY
Zhigang Li,
Sun Yat-sen University, Zhuhai Campus,
China

REVIEWED BY
Gege Hui,
Sun Yat-sen University, China
Webster Mohriak,
Rio de Janeiro State University, Brazil

*CORRESPONDENCE
Jialing Zhang,
zjl_9900@163.com
Mingju Xu,
11738013@zju.edu.cn

SPECIALTY SECTION
This article was submitted to
Marine Geoscience,
a section of the journal
Frontiers in Earth Science

RECEIVED 10 August 2022
ACCEPTED 03 October 2022
PUBLISHED 05 January 2023

CITATION
Wu Z, Zhang J, Xu M and Li H (2023),
Magnetic anomaly lineations in the
Northeastern South China Sea and their
implications for initial
seafloor spreading.
Front. Earth Sci. 10:1015856.
doi: 10.3389/feart.2022.1015856

COPYRIGHT
© 2023 Wu, Zhang, Xu and Li. This is an
open-access article distributed under
the terms of the [Creative Commons
Attribution License \(CC BY\)](https://creativecommons.org/licenses/by/4.0/). The use,
distribution or reproduction in other
forums is permitted, provided the
original author(s) and the copyright
owner(s) are credited and that the
original publication in this journal is
cited, in accordance with accepted
academic practice. No use, distribution
or reproduction is permitted which does
not comply with these terms.

Magnetic anomaly lineations in the Northeastern South China Sea and their implications for initial seafloor spreading

Zhaocai Wu¹, Jialing Zhang^{1,2*}, Mingju Xu^{1*} and Hailong Li³

¹Key Laboratory of Submarine Geoscience, Second Institute of Oceanography, Ministry of Natural Resources, Hangzhou, China, ²Ocean College, Zhejiang University, Zhoushan, China, ³The Key Laboratory of Gas Hydrate, Ministry of Natural Resources, Qingdao Institute of Marine Geology, Qingdao, China

Ridge jumps occurred during the spreading process of the South China Sea. Recent research on the lower crustal reflectors event on seismic profiles found at least two southward ridge jumps, but only one has been confirmed by geomagnetic data. Based on magnetic anomalies in the northern South China Sea and the “two ridge jumps” model, this study identified that an early ridge jump occurred at anomaly C10n (28.3 Ma), with a southward jump of 20 km. According to the magnetic lineation distribution in the northern South China Sea, initial spreading was dominated by local punctiform break-up and the oldest anomaly, C12n (~30.8 Ma), appeared at two turns of COB. In the IODP Expedition 367&368 drilling area, the continuity of magnetic anomalies from Ridge A to Ridge C was enhanced gradually, representing the transition from local magmatism before the final crustal break-up to a stable igneous oceanic crust. The earliest seafloor spreading magnetic lineation in the Northwestern Sub-basin is C12n (~30.8 Ma) and the magnetic lineation corresponding to the fossil spreading ridge is C10r (~29 Ma). The average half-spreading rate was ~27.2 mm/yr. The opening of the Northwestern Sub-basin appears to have been rotated around a fixed point at the west, with a fault at the eastern end formed by the trajectory of the conjugate point moving during seafloor spreading.

KEYWORDS

Northeastern SCS, magnetic anomaly lineations, initial seafloor spreading, two ridge jumps, 28.3 Ma

Introduction

In contrast to the stable seafloor spreading ridge in the Atlantic and the symmetric free drifts of the plates on both sides, the initial spreading of the South China Sea (SCS) was asymmetric. The north continental margin (South China Block) was relatively stable. However, the southern continental margin drifted southward (Figure 1). This implies that the spreading ridge of the SCS exhibited continuous southward movement or intermittent southward jumps during seafloor spreading (Taylor and Hayes, 1983; Briaies et al., 1993).

The magnetic lineation model of one ridge jump has been verified using recent geomagnetic data (Li et al., 2014). In previous magnetic lineation models concerning the spreading of the SCS, no reversal of magnetic lineation was present after the ridge jump. On the other hand, the one-jump model is insufficient to explain the asymmetric spreading of the SCS.

A recent study on the lower crustal reflectors based on the multi-channel seismic (MCS) profiles found that at least two southward ridge jumps occurred during the opening of the SCS. The second ridge jump event explained in this new model is consistent with the interpretation of magnetic lineation (Briaies et al., 1993; Li et al., 2014). However, the first ridge jump event has not yet been recognized in terms of magnetic anomalies.

In this study, the age of the first ridge jump event was recognized by reorganizing high-resolution magnetic anomalies in the northern SCS and combining the “two ridge jumps” model interpreted by seismic profiles. On this basis, the magnetic lineation features of initial seafloor spreading in the northern SCS were determined.

Geological background

The SCS is located at the intersection of the Eurasian Plate, Indo-Australian Plate, and the Philippine Plate. The SCS has experienced continental margin rifting, continental crust break-up, and seafloor spreading since the Cenozoic (Figure 1). Studying the spreading history and tectonic evolution of the SCS is important for understanding the Cenozoic structure in East Asia and surrounding areas (Wang et al., 2019; Li et al., 2021).

In early studies on the seafloor spreading of the SCS, a geophysical survey including the reflection seismic and geomagnetic field data was carried out towards the end of the 1960s. An approximately E-W trending magnetic anomaly lineation of unknown age was discovered, for the first time, in the Eastern sub-basin (Emery and Ben-Avraham, 1972; Ben-Avraham and Uyeda, 1973). However, this finding was uncertain due to limitations in terms of data precision. Subsequently, Briaies et al. (1993) organized all available data regarding magnetic anomalies in the SCS by 1990, and proposed the most detailed results regarding the spreading history of the SCS to date. They pointed out that the ridge jumped southward during 25–23 Ma, and the trend changed from EW to NE-SW.

Barckhausen et al. (2014) proposed that the initial spreading age of the eastern basin was 32 Ma, based on the profiling analysis results of magnetic anomalies in the SCS basin and the southward ridge jump at 25 Ma. Further, the Southwestern sub-basin began to open, and both stopped expanding simultaneously at 20.5 Ma. This phenomenon has led to significant controversy in the research community (Barckhausen et al., 2015; Chang et al., 2015). The approximately NW-trending Zhongnan Fault, between the Eastern sub-basin and Southwestern sub-basin,

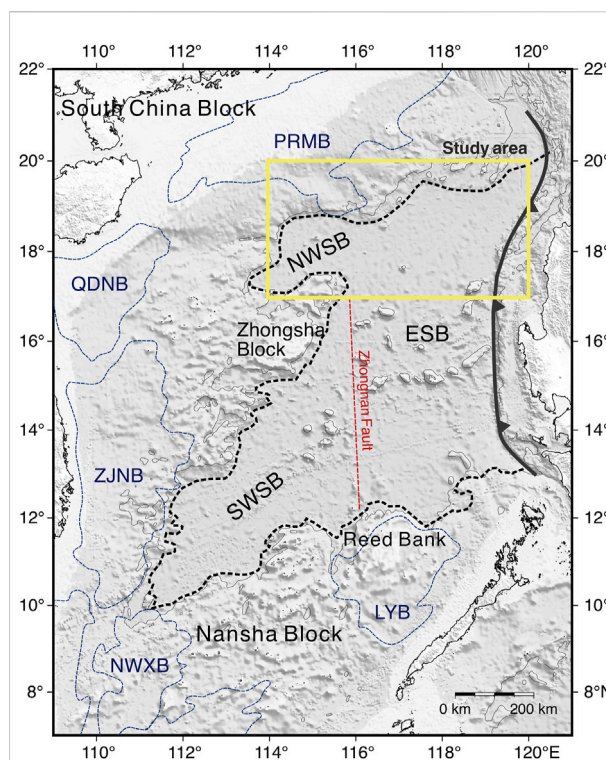


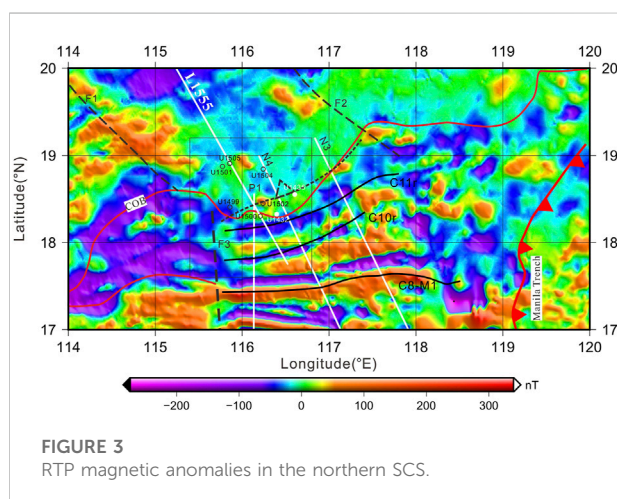
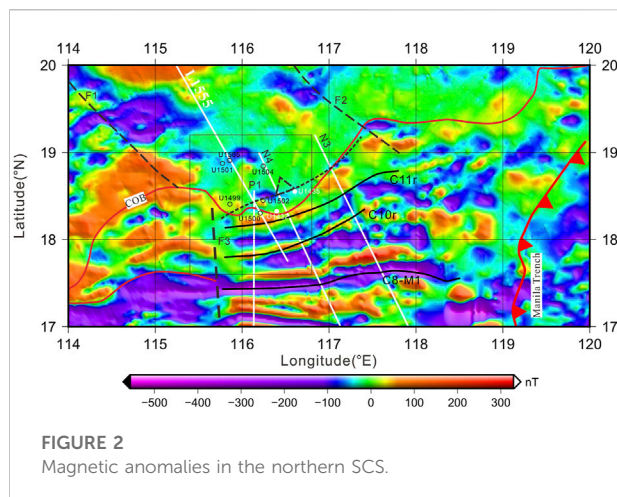
FIGURE 1

Morphological features and major tectonic of the SCS. The blue dashed lines are the boundary of the basin, and the thick black dashed line is the COB bounded by the 10 km crustal thickness (Wu et al., 2017). NWSB: Northwestern sub-basin, ESB: Eastern sub-basin, SWSB: Southwestern sub-basin, PRMB: Pearl River Mouth Basin, QDNB: Qiongdongnan Basin, ZJNB: Zhongjiannan Basin, NWXB: Nanwei Xi Basin, LYB: Liyue Basin.

has also been investigated, and the Liyue Bank is considered to be conjugated with the Zhongsha Block (Barckhausen et al., 2014).

Based on the latest deep-tow magnetic anomaly profiles and IODP349 drilling data, Li et al. (2014) determined that a southward ridge jump of 20 km occurred around 23.6 Ma in the East sub-basin. Furthermore, seafloor spreading propagated to the Southwest sub-basin during 23.6 Ma–21.6 Ma. The terminal age of seafloor spreading is 15 Ma in the Eastern sub-basin and 16 Ma in the Southwestern sub-basin. In their interpretation, an approximately NS-trending Zhongnan Fault was introduced separately into the Eastern sub-basin and Southwestern sub-basin. The extinct spreading centre before the jump was about 170 km away from the north COB and 180 km away from the current extinct spreading centre in the south.

A recent study on the lower crustal reflector (LCR) event on seismic profiles N3 and N4 of the northern SCS found two groups of conjugate LCR structures, and suggested that these conjugate events were related to episodic ridge jumps, which occurred around 27 Ma and 23.6 Ma, according to the calculations of the



asymmetric accretion offset (Ding et al., 2018). The process of the second jump, as determined based on seismic profiles, was consistent with the results of the geomagnetic interpretation model (Li et al., 2014). However, the first ridge jump has not been verified by the magnetic lineation model. Further, to the best of our knowledge, no existing magnetic lineation model has explained the age reversal of the ocean crust after the ridge jump.

Data and methods

The magnetic anomaly data used in this study was mainly shipboard magnetic data accumulated in the offshore regions of China over several years. The mean square error was smaller than 4 nT and the data grid spacing was 1 arc-minute (Wu et al., 2019). The magnetic anomalies are shown in Figure 2. Since the study area is of a low magnetic latitude, low-latitude reduction to the pole (RTP) was performed using the iterative energy-balancing method, which not only ensures the recovery of abnormalities but also

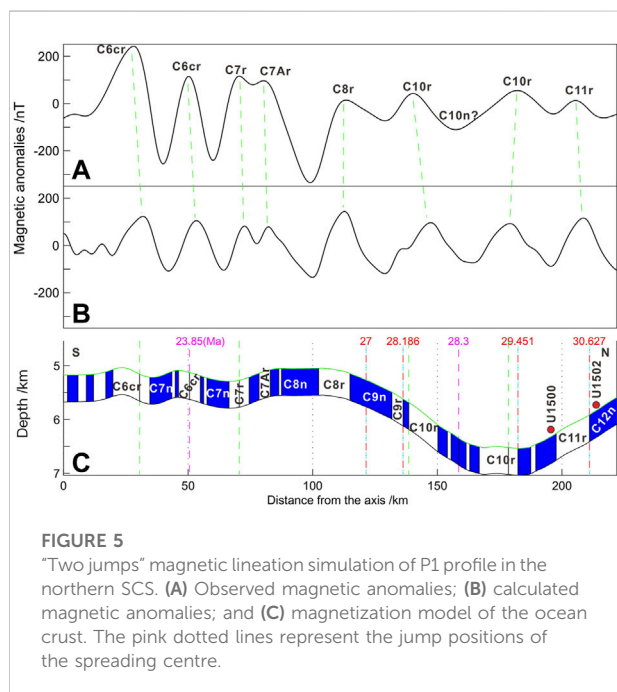
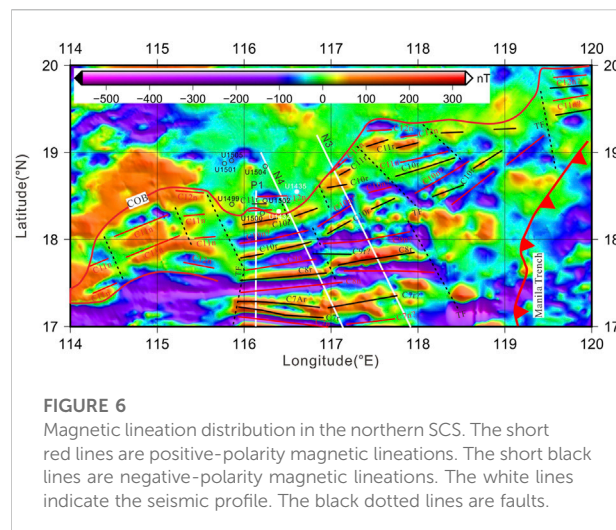
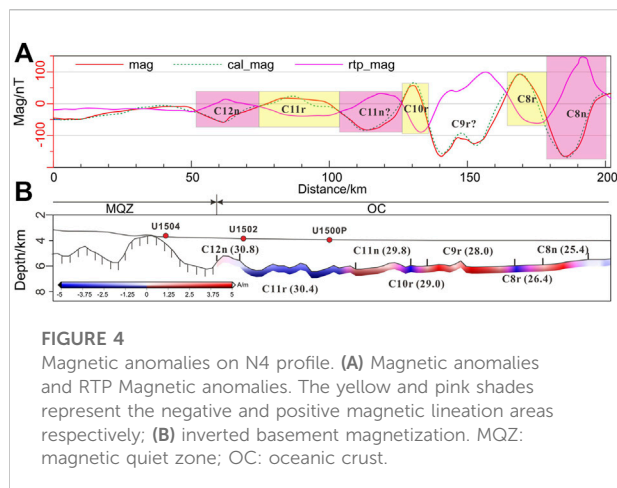
guarantees a robust anomaly amplitude (Li, 2008). The obtained RTP magnetic anomalies are shown in Figure 3. It can be seen that the previously recognised negative magnetic anomaly lineations (C11r and C10r) correspond to the positive magnetic anomaly belt before the RTP. The converse was true for the positive magnetic anomaly lineation C8, which corresponded to the negative magnetic anomaly belt before the RTP and the positive magnetic anomaly belt after the RTP. This completely agrees with the effect of magnetic anomalies under low-latitude and approximately horizontal magnetisation. Thus, the reliability of the RTP magnetic anomalies was confirmed.

The magnetic lineation fitting of profiles was conducted using MODMAG (Mendel et al., 2005), which has been extensively applied in the field of ocean magnetic lineation analysis (Li et al., 2014; Dumais et al., 2020).

Results

The magnetic anomalies and RTP magnetic anomalies in the northern SCS are shown in Figure 2 and Figure 3, respectively. The continent-ocean boundary (COB), in red, was determined according to the 10 km thickness of the crust, which was obtained by gravity inversion (Wu et al., 2017). This is consistent with the position determined by the seismic profile (Piao et al., 2022). The F1 and F2 Faults are the Yangjiang-Yitong East Fault and Huidong-Beiweitan Fault. Both were deduced to be important base faults in the Mesozoic (Chen et al., 2005) and the Mesozoic subduction accretion zone (Zhou and Yao, 2009) (black dotted lines with arrows in Figure 2 and Figure 3). F3 is the north extension of the Zhongnan Fault, which is a transform fault identified by previous researchers (Taylor and Hayes, 1980, 1983; Larsen, et al., 2018). The F1 fault connected with the F3 fault after extending southward at the border between the Eastern sub-basin and the Northwestern sub-basin. The three magnetic lineations in black solid lines originated from the data of Li et al. (2014).

The two groups of symmetric LCR structures on the seismic profile N4 were assumed to correspond to the two southward ridge jumps (Ding et al., 2018). Comparing the magnetic anomalies on N4 profile, it is clear that the previously identified magnetic lineation (Li et al., 2014) fell within the positive and negative intersection range of magnetic anomalies and RTP magnetic anomalies, which conformed to the low-latitude sub-horizontal magnetic anomaly features (Figure 4A). The inversion results of the magnetization on the N4 profile is shown in Figure 4B. The boundaries between positive and negative magnetisation are expressed as black lines. There were variations in magnetization in each interval of the positive and negative magnetizations. The negative magnetization intervals are expressed as a blue gradient, and the positive magnetization intervals are expressed as a red gradient. It is clear that these positive and negative magnetization intervals were consistent with those determined according to the magnetic anomalies in Figure 4A. However, the amplitude of C9r



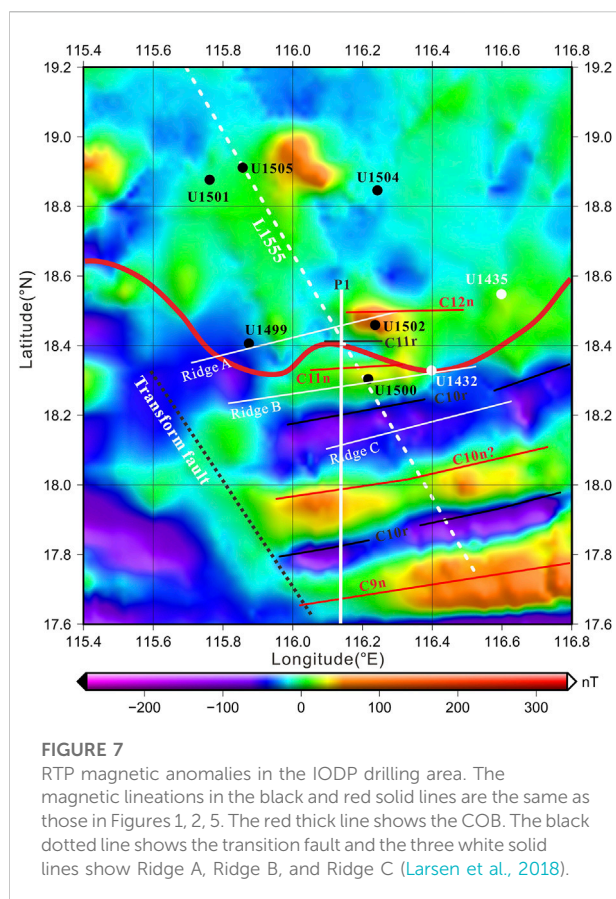
decreased significantly and the lineation features were submerged in the negative magnetic anomaly lineation produced by C10r and C8r at the two sides (Figure 4A). C9r has no negative magnetization, but a reduction in magnetization intensity in the middle. According to the magnetic lineation fitting on the deep-tow magnetic anomaly profile de12 (Li et al., 2014), the fitted positive magnetic anomaly signals corresponding to C9r were not observed. In the plane graph of magnetic anomalies (Figure 2), the weak magnetic anomalies that were approximately EW trending were among the background field of the strong negative anomalies, without signs of eastward extension. However, they were integrated with the high-amplitude magnetic anomalies toward the west. These magnetic anomalies exhibited significantly

different characteristics for the magnetic lineations at the north and south sides. A group of LCR structures exist in this region (Ding et al., 2018), indicating that this may be the location of the first ridge jump.

Therefore, one approximately NS-trending profile (P1 in Figure 2 and Figure 3) was chosen in the northern SCS for the magnetic lineation simulation according to the "two jumps" spreading model. The magnetic lineation that the profile ran through had relatively good continuity and was able to avoid the confounding effects of any breakage in the magnetic anomalies. The magnetic lineation fitting was completed using MODMAG (Mendel et al., 2005). The calculation parameters were selected in reference to the de12 deep-tow magnetic profile (Li et al., 2014). The simulation results are shown in Figure 5.

The negative magnetic anomaly region between the two magnetic lineations of C10r is the position of the first ridge jump (Figure 5). The corresponding magnetic lineation jumped 20 km southward near C10n at 28.3 Ma. The second ridge jump was near C6cr on the south side, where it jumped 20 km southward at 23.85 Ma. In the "two jumps" model, the time and position of the second jump are consistent with those in previous research. However, the positive magnetic anomalies of C9r were masked by anomalies at the two sides due to the first ridge jump at 28.3 Ma, which is in agreement with observed magnetic anomalies. In other words, C11r could move continuously toward the north, reaching the north side of U1500, and U1502 was over magnetic anomaly C12n (Figure 5).

The "two ridge jumps" model of P1 fitting conforms to the observation of magnetic anomalies and seismic profiles. On this basis, the distribution of magnetic lineations in the northern SCS was tracked (Figure 6). The results showed that, in the initial spreading stage of the SCS, the Eastern sub-basin and the Northwestern sub-basin opened almost simultaneously. The Northwestern sub-basin stopped spreading at C10r (~29.0 Ma). Subsequently, the spreading centre of the Eastern sub-basin

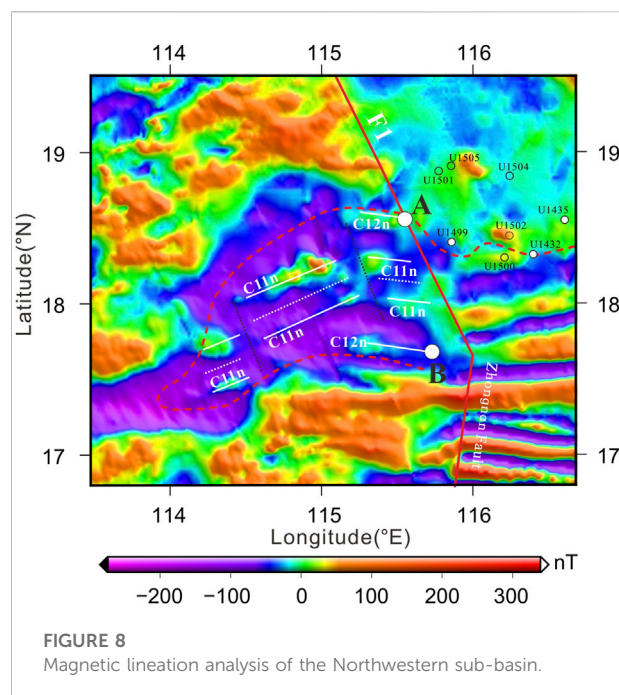


jumped southward at 28.3 Ma and then continued spreading. Specifically, the important boundary fault F1 (NW-trending Yangjiang-Yitong East Fault) in the east-west section extended towards the south during the spreading process. The north section of Zhongnan Fault was formed to regulate and separate the Eastern sub-basin and Northwestern sub-basin.

Discussion

Magnetic anomaly features of the initial spreading near the COB

During the spreading of the SCS, to its north was the relatively stable South China Block, and to its south was the southward drifting Nansha Block. Any symmetric growth of the ocean crust from the spreading centre to the two sides of each spreading position required the continuous movement of the spreading centre. The magnetic anomalies demonstrated the poor and short continuity at the position of the COB. There were two turns at 116.5°E, 18.3°N, and 117.5°E, 19.5°N along the COB, where the NW-trending Mesozoic faults F1 and F2 (shown in Figure 2) corresponded to the oldest magnetic anomaly (C12n). This



indicated that these NW-trending inherited faults influenced the continental margin rift of the SCS. Initial seafloor spreading of the SCS may be dominated by local punctiform break-up like that of the Red Sea (Bonatti, 1985). The initial spreading processes at different positions varied significantly. Finally, the differential spreading features from east to west, influenced by the COB structure, were formed (Figure 9). However, Li et al. (2014) believed that the age of the initial spreading along the COB in the northern area of the ocean basin varied by 1–2 Ma.

When the east section of COB approaching the Manila Trench, the magnetic lineation of the ocean crust was damaged by subduction. However, early seafloor spreading was generally dominated by an approximate NS-trending spreading tendency. The local, approximately NE-trending magnetic lineation, was generally adapted to spreading spaces at different positions under the regulation of the NW-trending fault, rather than the indicated changes in the spreading direction.

Magnetic anomaly characteristics in the IODP drilling area

The RTP magnetic anomalies in the IODP drilling area are shown in Figure 7. Sites U1501, U1504, and U1505 surround a small local high-magnetic anomaly and correspond to the outer margin high (OMH) on the L1555 profile (Sun et al., 2016). Ridge A, Ridge B, and Ridge C (Larsen et al., 2018) were divided according to the acoustic basement, and are shown as thin white solid lines in Figure 7.

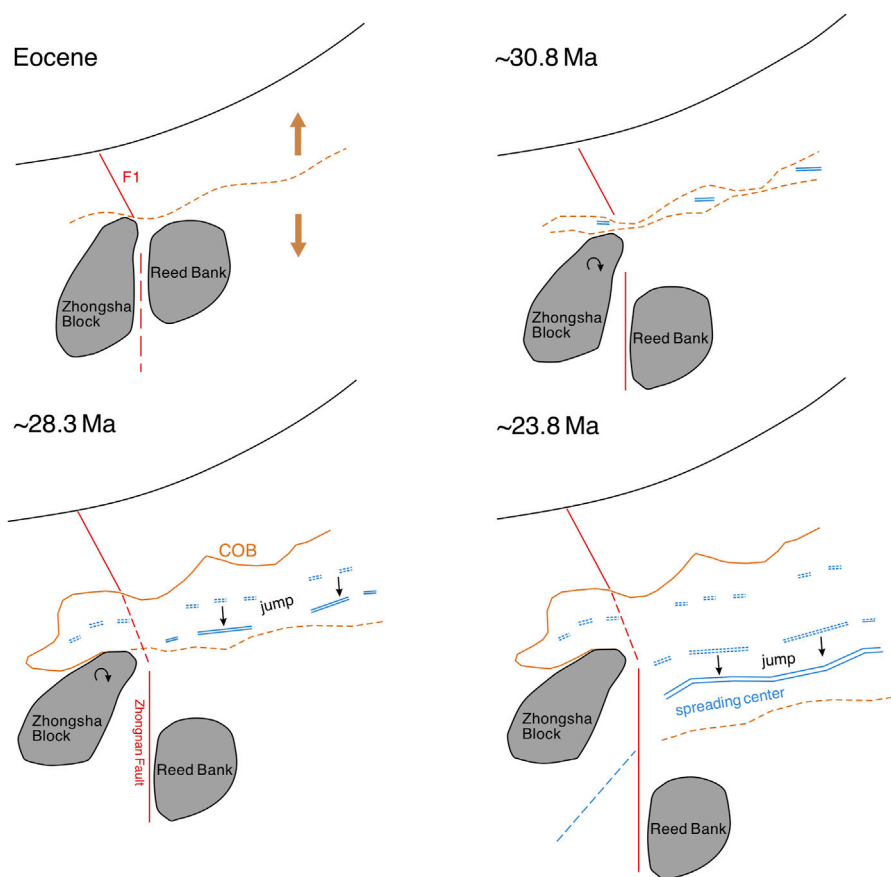


FIGURE 9
Schematic model of initial spreading and ridge jump in the northern SCS.

Ridge A, as expressed in the acoustic basement, extended from Sites U1499 to U1502 along the COB. However, the magnetic anomalies of U1499 and U1502 had significantly different characteristics. The former was a low-magnetic anomaly region, indicating the absence of any strong magnetic source. Moreover, this is consistent with the result that breccia was encountered during the drilling of the basement. Borehole U1502 was drilled on the locally high-magnetic anomalies, and the encountered basement was basalt with a strong hydrothermal alteration (Larsen et al., 2018). Hence, the locally high magnetic anomalies differed from the OMH at Sites U1501 and U1505. According to the trend of the magnetic anomalies, Ridge A could extend eastward to Site U1435 of the IODP349 expedition, and is also an OMH; therefore, they may have the same origin. The continuity of such high magnetic anomalies was unstable. For example, there were locally low-magnetic anomalies between Sites U1499 and U1502, as well as between Sites U1502 and U1435. This might be related to the local magmatic activity before the final crust break-up. According to the tracking results of the “two ridge jumps” model, the magnetic anomaly C12n was located at these positions. According to the GPTS2004 geomagnetic time scale

(Ogg and Smith, 2004), the corresponding age was between 30.627 and 31.116 Ma.

Site U1500 drilled Ridge B and penetrated pillow, which corresponded to the magnetic anomaly C11n. Ridge B had better continuity than Ridge A and could extend eastward to Site U1432. However, Ridge B is marked by local interruptions when it is extended eastward, indicating that Ridge B is closer to the location of the final crustal break-up than Ridge A.

Ridge C was in the negative lineation of the RTP magnetic anomalies. Similar to C10n, Ridge C corresponded to the first jump position in the “two ridge jumps” model. The east–west continuity of the negative magnetic lineation was extremely developed and could be found in the entire northern SCS along the COB, which was dominated by the stable accretion of igneous oceanic crust.

Spreading process of the northwestern sub-basin

The Northwestern Sub-basin has narrow spaces. On one hand, magnetic anomaly lineations are rarely sequential. On the other

hand, the morphological characteristics of these magnetic anomaly lineations have different forms than typical oceanic crust, resulting in great differences in the basin age determined according to magnetic lineations. According to the interpretation of the seismic profile, the Northwestern sub-basin has one additional set of Cenozoic sedimentary strata than the Eastern sub-basin. It is speculated that the Northwestern sub-basin is older than the Eastern sub-basin. The sedimentary sequences filling the Northwestern and Eastern sub-basins are comparable in continuity, which is attributed to simultaneous spreading. Three high-resolution seismic profiles that run through the Northwestern sub-basin all suggested that both the Northwestern and Eastern sub-basins began to open simultaneously, and that the basin opening was characterised by a spreading direction from the east to the west (Ding et al., 2009; Cameselle et al., 2015).

According to magnetic anomalies in the Northwestern sub-basin (Figure 2 and Figure 3) and the previous magnetic lineation tracking results. Combining this finding with the recognised age of the magnetic lineations in the IODP drilling area and the RTP magnetic anomaly features in the Northwestern sub-basin, it was concluded that the magnetic lineation at the initial spreading of the Northwestern sub-basin was C12n (~30.8 Ma), and the azimuth angle was about 99°. The location of the initial spreading of the Northwestern sub-basin was thus determined. The symmetric magnetic lineation near the Shuangfeng seamount was C11n (~29.8 Ma), a product of the follow-up westward spreading, with an azimuth angle of about 63°. The magnetic lineation corresponding to the fossil spreading centre was C10r (~29 Ma) (white dotted lines in Figure 8) rather than the Shuangfeng seamount. The distance between the two C12n positions was 98 km, suggesting an average half-spreading rate of about 27.2 mm/yr.

The striking changes in the recognised magnetic lineations are consistent with the boundary forms of the Northwestern sub-basin. The magnetic lineation striking (spreading direction) also changed gradually with changes in the boundary form. In other words, the boundary form controls the local spreading direction. It seems that the spreading process of the Northwestern sub-basin was formed by the rotation of the Zhongsha Block on the south side around a fixed point at the west end. In this way, the Northwestern sub-basin developed from east to west, and the north section of the Zhongnan Fault was formed along the trajectory of the initial break-up conjugation points (points A and B in Figure 8).

Based on the NW trending changes of the north section of the Zhongnan Fault and the form of the Northwestern sub-basin, it is speculated that the Northwestern sub-basin may have formed by gradual “avulsion” from east to west along the pre-existing NW trending Yangjiang-Yitong Fault (F1 in Figure 8) during the earliest spreading of the Eastern sub-basin, rather than experiencing typical spreading. In other words, the crustal break-up occurred from east to west under the extension stress of the region. This also implies that the Zhongsha Block may have experienced a clockwise rotation at about 30 Ma, rather than simply drifting southward, controlling the Northwestern sub-basin formation (Figure 9).

Conclusion

The characteristics of the magnetic anomalies and the initially spreading magnetic lineation were discussed herein based on a new survey on shipboard magnetic anomalies in the northern SCS. The calculated RTP magnetic anomalies in the lower crust reflector structures found in the seismic profiles were also analysed. Some major conclusions can be drawn, as follows.

- 1) There were two ridge jumps during the initial spreading of the SCS. The spreading centre jumped 20 km southward at 28.3 Ma. The corresponding magnetic lineation was near C10n. The second ridge jump occurred at 23.85 Ma, which was southward another 20 km. The corresponding magnetic lineation was near C6cr.
- 2) The initial spreading of the SCS was controlled by the COB in the northern SCS, which was locally dominated by punctiform break-up. The oldest magnetic anomaly (C12n) occurred at the two turns of the COB.
- 3) Ridge A, in the IODP drilling area, is a locally high-magnetic anomaly with poor continuity; it corresponds to C12n (30.8 Ma). Ridge A is related to the local magmatic activity before the final break-up. Ridge B corresponds to C11n, and its continuity is relatively good; it is located at the onset of the oceanic crust. Ridge C is close to C10n and corresponds to the first ridge jump. The magnetic lineation exhibits stable continuity from east to west, which can be seen in the entire northern SCS along the COB. In summary, Ridge C has become normal oceanic crust for stable spreading.
- 4) C12n is the oldest magnetic lineation in the Northwestern sub-basin (~30.8 Ma). C11n is the symmetric magnetic lineation near the Shuangfeng seamount (~29.8 Ma). C10r is the magnetic lineation corresponding to the fossil spreading centre (~29 Ma), with an average half-expansion rate of approximately 27.2 mm/yr. The Northwestern sub-basin seems to have opened from east to west, with rotation around a fixed point at the west end. Moreover, the north section of the Zhongnan Fault is formed along the trajectory of the conjugation break-up point during seafloor spreading.

Data availability statement

The data analyzed in this study is subject to the following licenses/restrictions: Institutions are not allowed to publish data. Requests to access these datasets should be directed to ZW, wuzc@sio.org.cn.

Author contributions

ZW: Conceived this research, Writing—original draft, Funding support, JZ: Edited this article and discussed the

results and interpretation, MX: Data Processing and Methodology, editing, HL: Funding support and review.

Funding

This research is supported by the National Natural Science Foundation of China (grant numbers 42076078 and 42006068).

Acknowledgments

We would like to thank the editor and reviewers for their critical and constructive comments. The magnetic lineation fitting was completed using MODMAG (Mendel, et al., 2005).

References

- Barckhausen, U., Engels, M., Franke, D., Ladage, S., and Pubellier, M. (2014). Evolution of the South China Sea: Revised ages for breakup and seafloor spreading. *Mar. Pet. Geol.* 58, 599–611. doi:10.1016/j.marpetgeo.2014.02.022
- Barckhausen, U., Engels, M., Franke, D., Ladage, S., and Pubellier, M. (2015). Reply to Chang et al., 2014, Evolution of the South China Sea: Revised ages for breakup and seafloor spreading. *Mar. Pet. Geol.* 59, 679–681. doi:10.1016/j.marpetgeo.2014.09.002
- Ben-Avraham, Z., and Uyeda, S. (1973). The evolution of the China Basin and the mesozoic paleogeography of Borneo. *Earth Planet. Sci. Lett.* 18, 365–376. doi:10.1016/0012-821X(73)90077-0
- Bonatti, E. (1985). Punctiform initiation of seafloor spreading in the Red Sea during transition from a continental to an oceanic rift. *Nature* 316, 33–37. doi:10.1038/316033a0
- Briais, A., Patriat, P., and Tapponnier, P. (1993). Updated interpretation of magnetic anomalies and seafloor spreading stages in the south China Sea: Implications for the tertiary tectonics of southeast Asia. *J. Geophys. Res.* 98, 6299–6328. doi:10.1029/92jb02280
- Cameselle, A. L., Ranero, C. R., Franke, D., and Barckhausen, U. (2015). The continent-ocean transition on the Northwestern South China Sea. *Basin Res.* 29, 73–95. doi:10.1111/bre.12137
- Chang, J. H., Hsu, H. H., Liu, C. S., Lee, T. Y., Chiu, S. D., Su, C. C., et al. (2015). Seismic sequence stratigraphic analysis of the carbonate platform, north offshore Taiping Island, Dangerous Grounds, South China Sea. *Tectonophysics* 702, 70–81. doi:10.1016/j.tecto.2015.12.010
- Chen, H. Z., Wu, X. J., Zhou, D., Wang, W. Y., and Hao, H. Z. (2005). Mesozoic faults in zhujiang River Mouth basin and their geodynamic background. *J. Trop. Oceanogr.* 24, 52–61.
- Ding, W., Sun, Z., Dadd, K., Fang, Y., and Li, J. (2018). Structures within the oceanic crust of the central South China Sea basin and their implications for oceanic accretionary processes. *Earth Planet. Sci. Lett.* 488, 115–125. doi:10.1016/j.epsl.2018.02.011
- Dumais, M., Gernigon, L., Olesen, O., Johansen, S. E., and Brnner, M. (2021). New interpretation of the spreading evolution of the Knipovich Ridge derived from aeromagnetic data. *Geophys. J. Int.* 224, 1422–1428. doi:10.1093/gji/ggaa527
- Emery, K. O., and Ben-Avraham, Z. (1972). Structure and stratigraphy of China basin. *Am. Assoc. Pet. Geol. Bull.* 56, 839–859. doi:10.1306/819A408E-16C5-11D7-8645000102C1865D
- Larsen, H. C., Mohn, G., Nirrengarten, M., Sun, Z., Stock, J., Jian, Z., et al. (2018). Rapid transition from continental breakup to igneous oceanic crust in the South China Sea. *Nat. Geosci.* 11, 782–789. doi:10.1038/s41561-018-0198-1
- Li, C. F., Xing, X., Jian, L., Sun, Z., Zhu, J., Yao, Y., et al. (2014). Ages and magnetic structures of the South China Sea constrained by deep tow magnetic surveys and IODP Expedition 349. *Geochem. Geophys. Geosyst.* 15, 4958–4983. doi:10.1002/2014GC005567
- Li, J., Ding, W., Lin, J., Xu, Y., Kong, F., Li, S., et al. (2021). Dynamic processes of the curved subduction system in southeast Asia: A review and future perspective. *Earth-Science Rev.* 217, 103647. doi:10.1016/j.earscirev.2021.103647
- Li, X. (2008). Magnetic reduction-to-the-pole at low latitudes: Observations and considerations. *Lead. Edge* 8, 990–1002. doi:10.1190/1.2967550
- Mendel, V., Munsch, M., and Sauter, D. (2005). MODMAG, a MATLAB program to model marine magnetic anomalies. *Comput. Geosci.* 31, 589–597. doi:10.1016/j.cageo.2004.11.007
- Ogg, J. G., and Smith, A. G. (2004). *The geomagnetic polarity time scale. A Geologic Time Scale 2004*. Editors F. M. Gradstein, J. G. Ogg, and A. G. Smith (Cambridge: Cambridge University Press), 63–86.
- Piao, Q. F., Zhang, B. J., Zhang, R. W., Geng, M. H., and Zhong, G. F. (2022). Continent-ocean transition in the northern South China Sea by high-quality deep reflection seismic data. *Chin. J. Geophys.* 65, 2546–2559. doi:10.6038/cjg2022P0663
- Sun, Z., Stock, J., Jian, Z., McIntosh, K., Alvarez-Zarikian, C. A., and Klaus, A. (2016). Expedition 367/368 scientific prospectus: South China Sea rifted margin. *Int. Ocean. Discov. Progr.* doi:10.14379/iodp.sp.367368.2016
- Taylor, B., and Hayes, D. E. (1983). "Origin and history of the south China Sea basin," in *The tectonic and geologic evolution of southeast asian seas and islands Part 2, geophysical monograph series*. Editor D. E. Hayes (Washington, DC: AGU), 23–56. doi:10.1029/gm027p0023
- Taylor, B., and Hayes, D. E. (1980). "The tectonic evolution of the south China Sea basin," in *The tectonic and geologic evolution of southeast asian seas and islands, geophysical monograph series*. Editor D. E. Hayes (Washington, DC: AGU), 89–104. doi:10.1029/gm023p0089
- Wang, P., Huang, C., Lin, J., Jian, Z., Sun, Z., and Zhao, M. (2019). The South China Sea is not a mini-atlantic: Plate-edge rifting vs intra-plate rifting. *Natl. Sci. Rev.* 6, 902–913. doi:10.1093/nsr/nwz135
- Wu, Z. C., Gao, J. Y., Ding, W. W., Shen, Z. Y., Zhang, T., and Yang, C. G. (2017). The Moho depth of the South China Sea basin from three-dimensional gravity inversion with constraint points and its characteristics. *Chin. J. Geophys.* 60, 368–383. doi:10.1002/cjg2.30053
- Wu, Z. C., Gao, J. Y., and Yang, C. G. (2019). "Magnetic anomaly map of southern China seas, 1:3,000,000," in *The marine geological series maps of China Sea*. Editors Z. Y. Wu and Z. H. Wen (Beijing: Science Press).
- Zhou, D., and Yao, B. (2009). Tectonics and sedimentary basins of the south China Sea: Challenges and progresses. *J. Earth Sci.* 20, 1–12. doi:10.1007/s12583-009-0001-8

Conflict of interest

The authors declare that the research was conducted in the absence of any commercial or financial relationships that could be construed as a potential conflict of interest.

Publisher's note

All claims expressed in this article are solely those of the authors and do not necessarily represent those of their affiliated organizations, or those of the publisher, the editors and the reviewers. Any product that may be evaluated in this article, or claim that may be made by its manufacturer, is not guaranteed or endorsed by the publisher.



OPEN ACCESS

EDITED BY

Zhigang Li,
Sun Yat-sen University, Zhuhai Campus,
China

REVIEWED BY

Hongwei Yin,
Nanjing University, China
Yi Yan,
Guangzhou Institute of Geochemistry
(CAS), China

*CORRESPONDENCE

Zhourong Cai,
caizhr@mail.sysu.edu.cn

SPECIALTY SECTION

This article was submitted to Marine
Geoscience,
a section of the journal
Frontiers in Earth Science

RECEIVED 17 July 2022

ACCEPTED 15 September 2022

PUBLISHED 06 January 2023

CITATION

Yin Z, Cai Z, Yao Y, Huang Q and Li Z
(2023), Tectonic dynamics of the
Zhongjiannan Basin in the western
South China Sea since the late Miocene.
Front. Earth Sci. 10:996267.
doi: 10.3389/feart.2022.996267

COPYRIGHT

© 2023 Yin, Cai, Yao, Huang and Li. This
is an open-access article distributed
under the terms of the [Creative
Commons Attribution License \(CC BY\)](#).
The use, distribution or reproduction in
other forums is permitted, provided the
original author(s) and the copyright
owner(s) are credited and that the
original publication in this journal is
cited, in accordance with accepted
academic practice. No use, distribution
or reproduction is permitted which does
not comply with these terms.

Tectonic dynamics of the Zhongjiannan Basin in the western South China Sea since the late Miocene

Zhengxin Yin¹, Zhourong Cai^{2,3*}, Yongjian Yao^{4,5},
Qianru Huang^{2,3} and Zhengyuan Li¹

¹Key Laboratory of Marine Environmental Survey Technology and Application, Ministry of Natural Resources, South China Sea Marine Survey and Technology Center, State Oceanic Administration, Guangzhou, China, ²School of Marine Sciences, Sun Yat-sen University, Zhuhai, China, ³Guangdong Provincial Key Laboratory of Marine Resources and Coastal Engineering, Zhuhai, China, ⁴Southern Marine Science and Engineering Guangdong Laboratory (Guangzhou), Guangzhou, China, ⁵Key Laboratory of Marine Mineral Resources, Ministry of Natural Resources, Guangzhou Marine Geological Survey, China Geological Survey, Guangzhou, China

The Zhongjiannan Basin is located west of the South China Sea (SCS) and was affected by the left-lateral strike-slip of the Red River Fault (RRF), the West Edge Fault of the South China Sea (WEFSCS) and the continental rifting of the South China Sea in the early Cenozoic. The Zhongjiannan Basin formed in a strike-pull basin with an S–N distribution. During the middle Miocene, the sea spreading of the SCS stopped, but the dynamic mechanism of the Zhongjiannan Basin, which controlled the sedimentary and the structural evolution after the late Miocene, remains unclear. In this paper, through the segment interpretation of the latest seismic section in the Zhongjiannan Basin, we conduct a comparative study of the sedimentary structure in the southern and northern Zhongjiannan Basin since the late Miocene. Combined with the regional tectonic dynamics analysis, we propose that the sedimentary and structural evolution of the Zhongjiannan Basin since the late Miocene was mainly controlled by residual magmatic activity in the Southwest Subbasin (WSB) after expansion stopped, and the compressional structure stress field weakened gradually from south to north. The compressional tectonic stress field from north to south was formed in the northern basin under the dextral strike-slip movement of the RRF. The sedimentary and structural environment was relatively stable in the middle basin. Therefore, the sedimentary-structure evolution of the Zhongjiannan Basin since the late Miocene was controlled by the two different structural stress fields. The above knowledge not only has guiding significance for oil and gas exploration in the Zhongjiannan Basin but also provides a reference for studying the initiation time of dextral strike-slip along the Red River Fault Zone, as well as the junction position between the RRF and the WEFSCS.

KEYWORDS

Zhongjiannan Basin, late Miocene, tectonic dynamics, Red River Fault (RRF), West Edge Fault of the South China Sea (WEFSCS)

1 Introduction

The Indian plate and Eurasian plate collision led to the extrusion of the Indo-china block southeast since the Cenozoic and formed the giant strike-slip structural belt of the Ailaoshan-Red River Fault Zone (Tapponnier et al., 1986; Replumaz et al., 2001; Schoenbohm et al., 2005; Schoenbohm et al., 2006). The two left-lateral strike-slip fault zones, as well as the continental rifting of the SCS, jointly controlled the sedimentary and structural evolution of the western basin in the SCS in the early Cenozoic. A series of strike-pull basins of the SCS distributed along the fault zones, such as the Yinggehai Basin, Zhongjiannan Basin and Wan'an Basin, were formed (Sun et al., 2003; Cai, 2014; Yin et al., 2015; Lei et al., 2021). To enter the Miocene, the tectonic dynamics of western basins in the SCS underwent a major change due to the seafloor spreading of the SCS ending and the sinistral strike-slip movements of RRF and WEFSCS weakening (Zhu and Lei, 2013; Cai, 2014; Sun et al., 2019a; Zhang et al., 2021). The basins transformed into a depression subsidence stage, and the tectonic activity was weak. The crustal rose and fall with sea level, causing the

basins in the western SCS conference to transition into the phase of uplift and local slow deposition. The crust of the western basins has been uplifted (denuded) and sunk (rapid subsidence) several times since the late Miocene, but the dynamic mechanism controlling the sedimentary-structure evolution of the basins during this period remains unclear. We select the Zhongjiannan Basin in the western SCS as the research object, using the latest seismic sections obtained by the Guangzhou Marine Geological Survey, and analyse the sedimentary characteristics and structural development in the northern, central and southern basins since the late Miocene. Combined with an analysis of the regional tectonic dynamic environment, the dynamic processes controlling the sedimentary-structural evolution of the Zhongjiannan Basin since the late Miocene are studied.

2 Geological setting

The Zhongjiannan Basin is located in the western SCS, with a nearly north-south lozge-shaped distribution as a whole (Chen and Zhong, 2008). It is bounded by the Qiongdongnan Basin in the north and the RRF-WEFSCS in the west and connected with the SWSB by the Xiya uplift in the southeast (Figure 1). It is a hydrocarbon basin with a complex geological structure background. The RRF (Allen et al., 1984; Liu et al., 2012) and the WEFSCS are connected in the northern part of Zhongjiannan Basin, and both are jointly control the sedimentary-structure evolution of the basin, making it a strike-slip basin (Zuchiewicz et al., 2013; Nguyen and Hoai, 2019). However, the junction position of the two faults and their relationship are still unclear. On the other hand, the Zhongjiannan Basin is influenced by several tectonic movements, such as continental margin rifting to seafloor spreading, resulting in a continental margin extension basin nature (Briais et al., 1993; Li et al., 2014). Therefore, the Zhongjiannan Basin has both strike-slip and extensional structural attributes and widely developed flower structure and extensional structure styles in the basin.

A structural pattern of alternating uplift and depression as well as faults, folds and unconformity interfaces developed in the basin. Five sets of strata were developed, namely, Holocene—Pliocene, Upper Miocene, Middle Miocene—Lower Miocene, Oligocene—Upper Eocene, and Middle Eocene—Paleocene (Gao et al., 2000; Chen and Zhong, 2008). The Cenozoic sedimentary formations are 2000–11,000 m thick. According to the seismic reflection characteristics of the unconformity interface and the regional seismic sequence division scheme, eight obvious seismic reflection interfaces, T1, T2, T3, T5, T6, T7, T8, and Tg, can be recognized in the Zhongjiannan Basin (Qiu et al., 1997; Zhong and Gao, 2005). Among them, Tg is the initial continental margin rifting and basement interface of the basin, T7 and T6 is the South China Sea breakup unconformity, T7 representing continental margin breaking and the beginning of seafloor spreading, T6

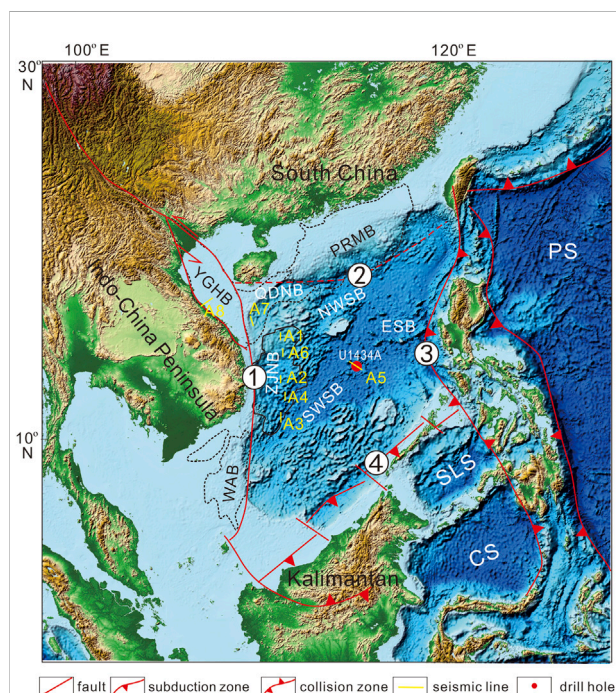


FIGURE 1

Regional tectonic background of the Zhongjiannan Basin, South China Sea YGHB- Yinggehai Basin, PRMB- Pearl River Mouth Basin, QDNB- Qiongdongnan Basin, ZJNB- Zhongjiannan Basin, WAB- Wan'an Basin, NWSB- northwest subbasin of SCS, SWSB- Southwest Subbasin of SCS, ESB- East Subbasin of SCS, SLS- Sulu Sea, CS- Celebes Sea, PS- Philippine Sea: (1)- Combined belt of Western SCS, including RRF in the north, WEFSCS in center and Wan'an Fault in the south, (2)- Combined belt of Northern SCS, namely, Qiongnan suture zone, (3)- subduction-collision zone of Eastern SCS, (4)- Subduction collision zone of SCS.

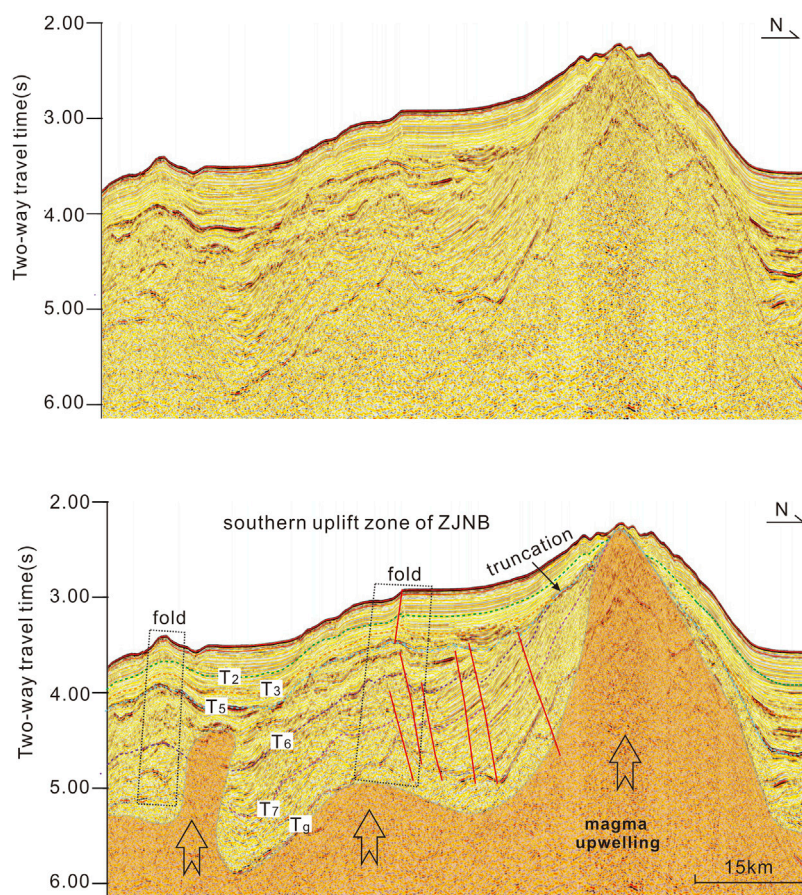


FIGURE 2

Sedimentary-structure development characteristics in the northern Zhongjiannan Basin (See line A1 in Figure 1 for profile location).

corresponds to the tectonic event of oceanic ridge jumping, and T5 is the unconformity interface formed at the end of seafloor spreading. T3 corresponds to the tectonic transition surface of important regional plate recombination events and rapid global sea level decline. Based on the comparison of drilling data and seismic data (Fyhn et al., 2009; Fyhn et al., 2013), it is determined that the age of the unconformity interface is 11.6 Ma, which is the interface between the middle Miocene and Late Miocene. This paper mainly studies the tectonic dynamics of sedimentary-structure evolution above the T3 interface (since the late Miocene) in the Zhongjiannan Basin.

3 Data and methods

The 2D seismic data used in this paper are all measured data from the marine survey conducted in Zhongjiannan Basin by the Guangzhou Marine Geological Survey. The 2D seismic data were collected in 2001, with 240 tracks and 30 coverage times, a distance of 50 m between shot points and a recording length of 9 s. The acquisition ship was the Tanbao ship, with a density of

32 km × 32 km and a distance of 4 km between velocity spectral points. The seismic data were reprocessed in 2013, with a distance of 1 km between velocity spectral points. In this way, the quality of seismic data can be improved to the maximum extent, and the sedimentary stratigraphic structure and tectonic reflection characteristics can be displayed more clearly from their recognition at shallow depths.

4 Characteristics of sedimentary structure development in the Zhongjiannan Basin since the late Miocene (T3)

In the Zhongjiannan Basin, the reflecting interface between the Middle Miocene and late Miocene (T3) is a regional unconformity interface that can be traced throughout the basin and represents a transition from slow to rapid subsidence. The sedimentary-structure features above the T3 interface can be divided into three sections: south, middle and north.

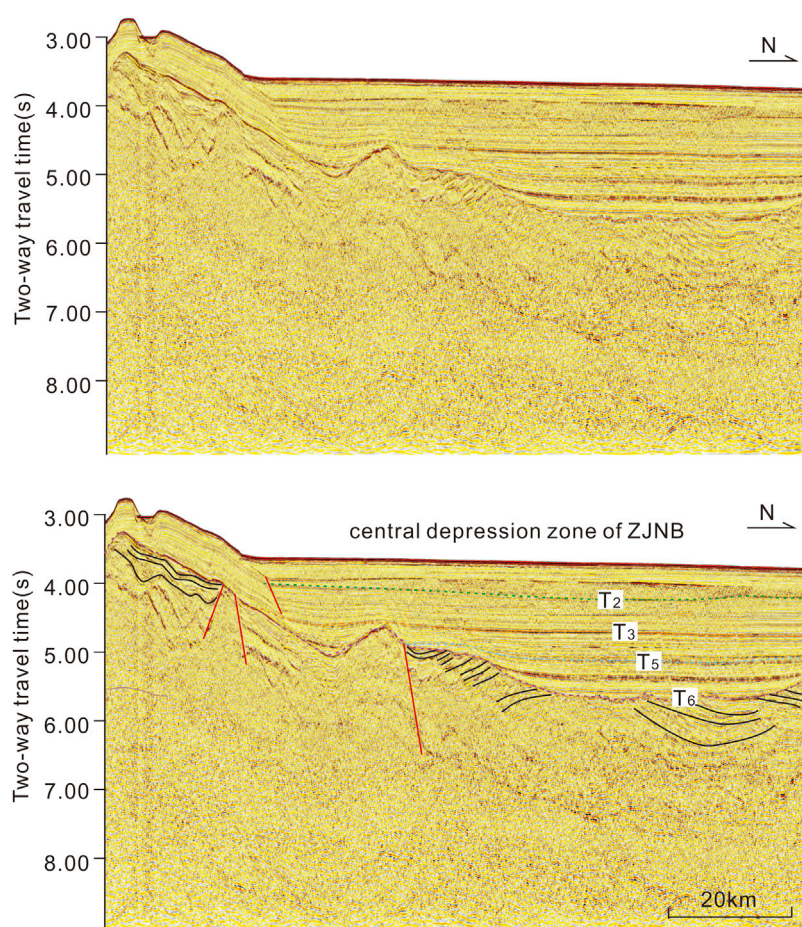


FIGURE 3

Sedimentary-structure development characteristics in the central Zhongjiannan Basin (See line A2 in Figure 1 for profile location).

The stratigraphic development of the southern section of the Zhongjiannan Basin is relatively complete. The seismic reflection characteristics are parallel or subparallel, indicating that the tectonic activity was weak, the sedimentary was stable, and the fault structure did not develop during the early deposition. However, due to the influence of magma intrusion and upwelling in the later period, the seamount emerged more, a large amount of magma formed horizontal compression on the stratum, and the stratum was arched at the seamount, showing an inclined shape and partial deflection deformation. The magmatic activity and incline and bending deformation of the strata mainly occurred in the southern uplift zone but weakened to the north (Figure 2).

In the middle Zhongjiannan Basin (middle section), the seismic reflection characteristics show parallel continuous reflection above the T3 interface, which shows that the formation retains the original sedimentary characteristics. Fault and fold structures are few, and the overall tectonic activity is weak. In addition to the northern central depression

affected by magma upwelling, the rest is characterized by stable sedimentary characteristics (Figure 3).

The sedimentary structure above the T3 interface in the northern section of the Zhongjiannan Basin is relatively complex and can be roughly divided into three layers (Figure 4). The seismic reflection of the bottom layer (T3–T32) is parallel and continuous, reflecting stable sedimentary characteristics without folding deformation and indicating that it was not affected by tectonic activity. The seismic reflection of the middle layer (T32–T2) is disorderly, and the seismic reflection interface is discontinuous and inclined or curved, indicating that the stratum is damaged and that the tectonic activity is intense. From the characteristics of the disorderly seismic reflection, tectonic activity occurred when the strata were not consolidated diagenesis, so it can be inferred that tectonic activity and deposition occurred simultaneously. The seismic reflection interface of the upper layer (above T2) is relatively continuous, but most of it is inclined and curved, reflecting that

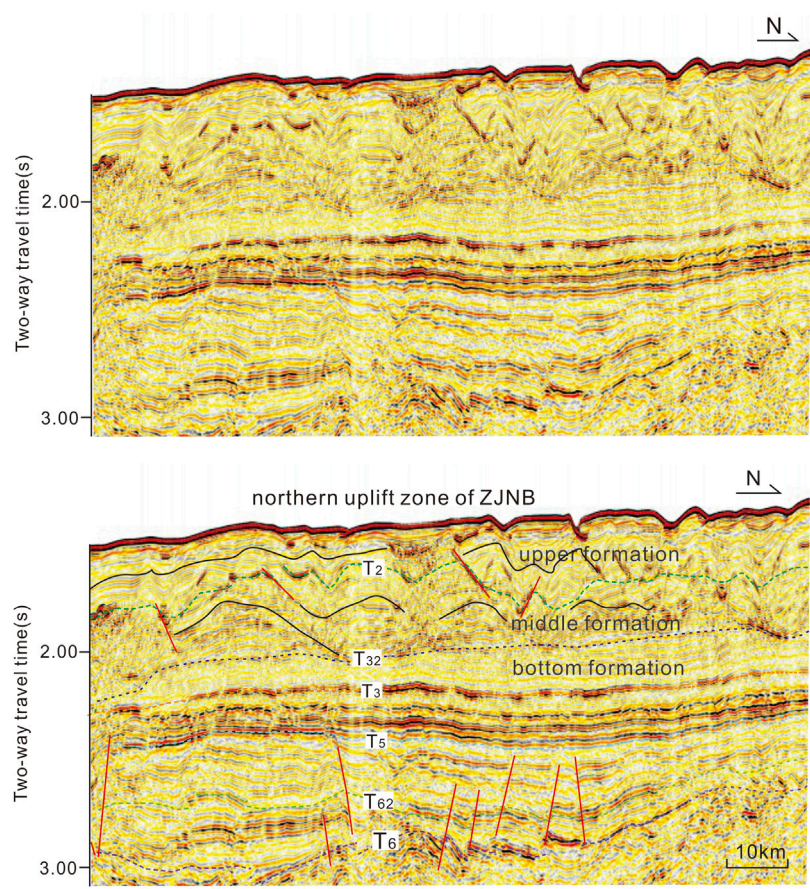


FIGURE 4
Sedimentary-structure development characteristics in the southern Zhongjiannan Basin (See line A3 in Figure 1 for profile location).

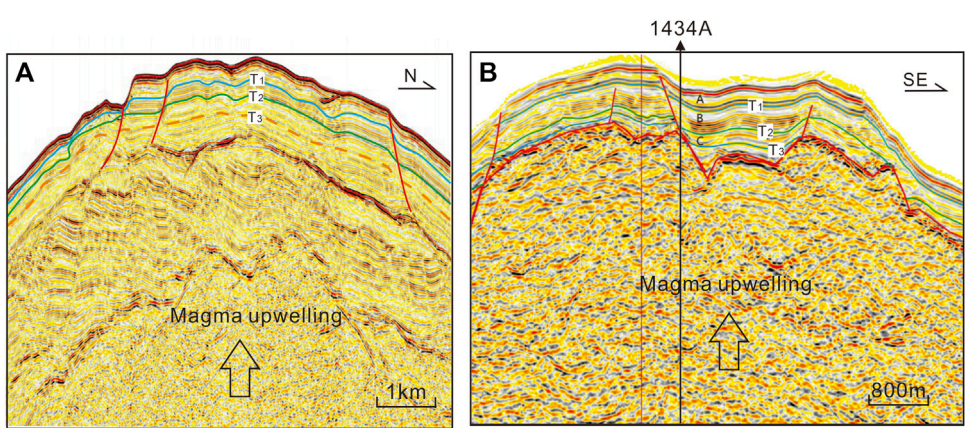


FIGURE 5
Seismic reflection characteristics between the Zhongjiannan Basin (A) and the U1434A drill of the SWSB (B). The position of profile a is shown in Box e in Figure 2A. The position of profile b can be seen along survey Line A2 in Figure 1.

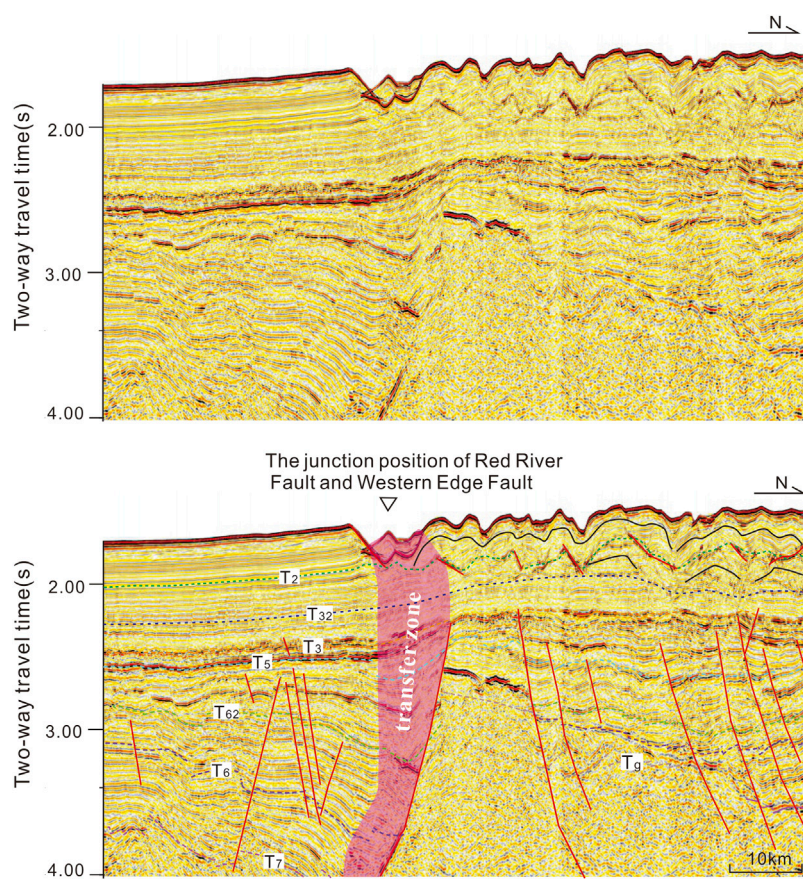


FIGURE 6

The junction position of RRF and WEFSCS in seismic section. The position of profile can be seen survey line A6 in Figure 1.

although the tectonic activity is weaker than that of the middle layer, it has continued until now, and there are still folds and faults in local areas (Figure 4).

5 Tectonic dynamics of the Zhongjiannan Basin since the late Miocene (T3)

5.1 Southern Zhongjiannan Basin

Sedimentary and structural development in the southern Zhongjiannan Basin shows that sequence stratigraphy developed stably since the late Miocene, but later influenced by magma upwelling, the stratigraphy became tilted and bent. From the formation development and structure analysis, the formation deformation caused by these magmatic activities is a long process, and the early strata (below T3) do not show obvious syndepositional folds, indicating weak magmatic activities before the late Miocene. The strata below T3 have

the characteristics of cutting (Figure 2), and the upper strata (above T3) have the phenomenon of overpassing near seamounts, indicating relatively strong magmatic activity after T3 (since Pliocene). Some magmatic rocks directly reach the seafloor to form seamounts (Figure 2), indicating that the activity has continued until now. Because the southern Zhongjiannan Basin is close to the SWSB and the magmatism in Zhongjiannan Basin weakens from south to north, we infer that these magmatic activities are from the residual magmatic activities of the SWSB after seafloor spreading (Li et al., 2014; Li et al., 2015; Sun et al., 2019b; Sun et al., 2021). By further comparing the seismic section passing through the spreading center of the SWSB (Figure 5), it is found that the development and structural characteristics of the strata above the T3 interface in the southern Zhongjiannan Basin are very similar to those of the SWSB, which were deformed by the uplift of the magma in the late stage (Figure 5). This further confirms that the tectonic dynamics in the southern Zhongjiannan Basin since the late Miocene are mainly derived from the residual magmatic activity of the SWSB. In addition, the magmatic

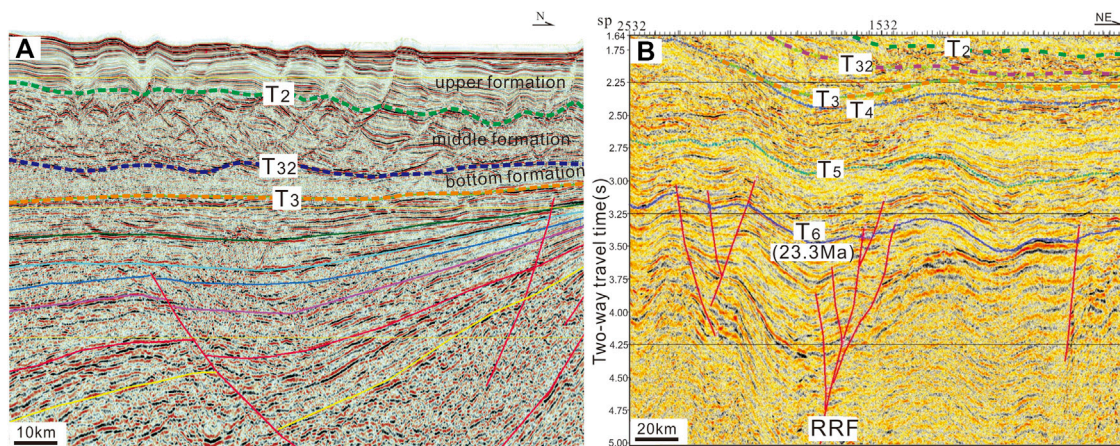


FIGURE 7

Seismic reflection sections of the Huaguang Sag of the Qiongdongnan Basin (A) and Yinggehai Basin (B), cited by Liu et al., 2015a. Note: The locations of Sections a and b are shown Lines A7 and A8 in Figure 1, respectively.

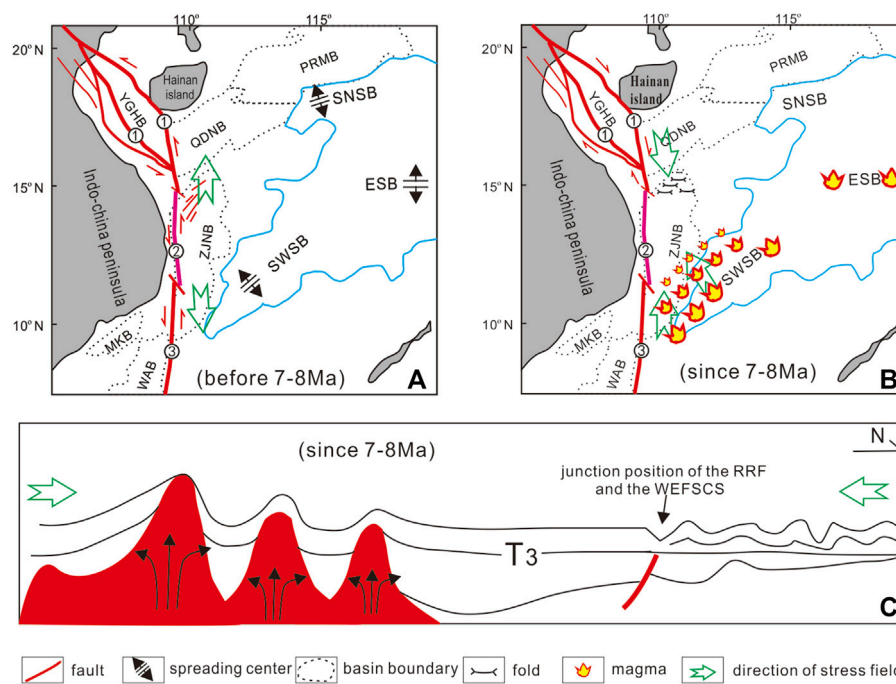


FIGURE 8

Tectonic dynamics model of the Zhongjiannan Basin before and after the late Miocene. YGHB- Yinggehai Basin, PRMB- Pearl River Mouth Basin, QDNB- Qiongdongnan Basin, ZJNB- Zhongjiannan Basin, WAB- Wan'an Basin, NWSB- northwest subbasin, SWSB- southwest subbasin, ①-RRF, ②-WEFSCS, ③-Wan'an Fault. (A) Tectonic setting and stress field orientation of Zhongjiannan Basin before the late Miocene. (B) Tectonic setting and stress field orientation of Zhongjiannan Basin after the late Miocene. (C) Structural model of the S-N profile in the western South China Sea after the late Miocene.

activity was weak in the early Miocene (before the late Miocene) and strong in the late Miocene (since the late Miocene), which may be related to the supply of deep magma. These magmatic

activities intruded into the bottom of the strata, resulting in compressional inclined or bending deformation of the strata, which was strong near the SWSB and gradually weakened to the

north, so that the central (central depression) and northern Zhongjiannan Basin were basically unaffected.

5.2 Northern Zhongjiannan Basin

The structural characteristics above the T3 interface in the northern Zhongjiannan Basin are significantly different from those in the central and southern basins, showing that the middle and upper strata (above T32) have experienced strong tectonic activity and that the strata have been severely damaged (Figure 4). Due to the stable development and weak tectonic activity of the strata above the T3 interface in the middle of the Zhongjiannan Basin, the dynamics cannot come from the south. Combined with the analysis of regional tectonic movement during this period, we speculate that it is probably related to the dextral strike-slip movement of the Red River Fault zone in the north.

At the end of the Mesozoic, the Indian plate subducted into the Eurasian plate, resulting in the formation of the Himalayan orogenic belt and Tibetan Plateau, as well as the Indochina Peninsula extruding southward along the Ailaoshan-Red River Fault Zone (Tapponnier et al., 1986; Tapponnier et al., 1990; Briaies et al., 1993; Cao et al., 2017). The Red River fault zone extends from northwest Yunnan to the SCS (Tapponnier et al., 1986; Rangin et al., 1995; Liu et al., 2015b). The fault zone has the characteristics of segmented activity in space and is characterized by early sinistral strike-slip movement and late dextral strike-slip movement over time (Trinh et al., 2012; Cai et al., 2019). At present, there are two scientific controversies concerning the RRF that have become research hotspots in earth science (Cao et al., 2011; Liu et al., 2012; Liu et al., 2015a; Cao et al., 2017). One is the starting time of dextral strike-slip movement of the RRF, which is 17 Ma (Tapponnier et al., 1990; Gilley et al., 2003), 8 Ma (Xiang et al., 2004, 2006), and 5 Ma (Leloup et al., 1993; Leloup et al., 1995; Leloup et al., 2001). The other is that the junction position and their relationship between the RRF and WEFSCS in the western SCS are still uncertain.

According to the reflection characteristics of the seismic section in the northern Zhongjiannan Basin, the formation above the T32 interface had a greater influence by the extrusion stress field, and the seismic reflection characteristics show clutter reflection, which reflects that tectonic activity occurred in unconsolidated rock and that tectonism and sedimentation occurred at the same time (Figure 4). Calculating the position of sedimentary thickness and the structural layer, we speculate that the earliest time of tectonic activity is 7–8 Ma, but the exact age is subject to subsequent drilling dating. This is the sedimentary-structure response of the dextral strike-slip of the RRF in the northern Zhongjiannan Basin. According to the location of the folds in the section (Figure 6), the junction position of the RRF and WEFSCS can be confirmed. The cut-off point is in the position between the

central seismic section and northern seismic section. At the junction position, the top seismic section shows that there is an obvious fracture trace, and there is also a deep large fault, which should be the transition zone between the RRF and WEFSCS. By measuring the junction position in this section (Figure 6) and in the western SCS (Figure 1), the junction position between the RRF and WEFSCS can be determined for the sea area of N15.5°. North of N15.5° is the influence region of the RRF, and to the south is the influence region of the WEFSCS, they are independent fault systems of each other since the late Miocene. The dextral strike-slip RRF affecting the formation only in the northern Zhongjiannan Basin is characterized by the formation of extrusion deformation and does not affect the formation in the central Zhongjiannan Basin. In other words, the WEFSCS has not experienced dextral strike-slip along with the RRF since 7–8 Ma.

We tracked the characteristics of the seismic profile in the Qiongdongnan Basin and Yinggehai Basin near the RRF (Figure 7) and discovered that the formation development and structural deformation characteristics are similar to those in the northern Zhongjiannan Basin since the late Miocene, which further confirms that the tectonic dynamics of the northern Zhongjiannan Basin came from the dextral strike-slip movement of the RRF since the late Miocene.

5.3 Tectonic dynamic model

The tectonic dynamic environments of the Zhongjiannan Basin before and since the late Miocene are completely different. Before the late Miocene, affected by Indosinian Block extrusion in the southwest direction, the RRF and WEFSCS experienced sinistral strike-slip movement together. With the seafloor spreading of the SWSB, the Zhongjiannan Basin was controlled by an extensional stress field in the N–S direction, and a strike-slip-pull-apart basin was formed with alternations between uplift and depression (Figure 8A). The Zhongjiannan Basin has been affected by two distinct tectonic dynamic environments since the late Miocene. The southern basin was mainly affected by residual magmatic activity after the expansion of the SWSB stopped. Due to magma upwelling, the Zhongjiannan Basin folds and bends, and the tectonic stress field gradually weakens from south to north, while the central Zhongjiannan Basin is basically unaffected. The northern Zhongjiannan Basin was mainly affected by dextral strike-slip movement of the RRF, and the formation above the T32 interface experienced strong folding and deformation. Sedimentary-structural features recorded that the dextral movement of the RRF occurred at 7–8 Ma and lasted until now but gradually weakened after the T2 interface (approximately 5 Ma) (Figure 8B). The WEFSCS did not follow the dextral strike-slip movement of the RRF. According to the deformation range of stratigraphic folds caused by the dextral strike-slip of the RRF, the junction position of the RRF and the WEFSCS can be determined, which is approximately N15.5° (Figure 8C).

6 Conclusion

1. There have been different sedimentary-structure characteristics in the south, middle and north of Zhongjiannan Basin since the late Miocene. Under the influence of magmatism, the formation in the southern basin was uplifted, tilted and deformed locally. The middle formation is stable, and the tectonic activity is weak. In the northern basin, a strong compressional structure occurred, and the formation was damaged or folded.
2. The Zhongjiannan Basin has been affected by two tectonic dynamics since the late Miocene. In the south, it was affected by residual magmatic activity after the expansion of the SWSB stopped, forming longitudinal uplift and a transverse compressive tectonic stress field, which gradually weakened from south to north. In the north, the tectonic activity was weak, and the deposition was stable at the early stage (T3-T32), but during the late stage (above T32), the compressional tectonic stress field was formed under the influence of the dextral strike-slip movement of the RRF, which has lasted until now.
3. The sedimentary-structure characteristics of the Zhongjiannan Basin since the late Miocene reveal that the dextral strike-slip movement of the RRF occurred at 7–8 Ma, and the junction position between the RRF and WEFSCS is approximately N15.5°.

Data availability statement

The original contributions presented in the study are included in the article, further inquiries can be directed to the corresponding author.

Author contributions

YZ, Writing, Data curation, Idea CZ, Idea, Writing, Reviewing and Editing YY, Data curation, Idea, Editing HQ, Graph drawing LZ, Graph drawing.

References

- Allen, C. R., Gillespie, A. R., Yuan, H., Sieh, K. E., Zhu, B., and Zhu, C. (1984). Red River and associated faults, Yunnan Province, China: Quaternary geology, slip rates, and seismic hazard. *Geol. Soc. Am. Bull.* 95, 686–700. doi:10.1130/0016-7606(1984)95<686:RRAAFY>2.CO;2
- Briaies, A., Patriat, P., and Tapponnier, P. (1993). Updated interpretation of magnetic anomalies and seafloor spreading stages in the south China Sea: Implications for the Tertiary tectonics of Southeast Asia. *J. Geophys. Res.* 98 (B4), 6299–6328. doi:10.1029/92JB02280
- Cai, G. F. (2014). *Cenozoic evolution of western basins in the South China Sea and its tectonic implication*. Shanghai: Tongji University. [Dissertation].
- Cai, Z. R., Lu, L. J., Huang, Qiangtai, Li, Jianfeng, Zhong, Lifeng, Xiang, Junyang, et al. (2019). Formation conditions for nanoparticles in a fault zone and their role in fault sliding. *Tectonics* 38, 159–175. doi:10.1029/2018TC005171
- Cai, Z. R., Xia, B., Lü, B. F., Yao, W. Q., and Li, J. F. (2015). Initial rifting process and dynamics mechanism of Huaguang Sag: Evidence from a numerical modeling method. *J. Earth Sci.* 25 (6), 399–406. doi:10.1007/s12583-014-0502-y
- Cao, S., Neubauer, F., Liu, J., Bernroider, M., Cheng, X., Li, J., et al. (2017). Rheological weakening of high-grade mylonites during low-temperature retrogression: The exhumed continental Ailao Shan-Red River fault zone, SE Asia. *J. Asian Earth Sci.* 139, 40–60. doi:10.1016/j.jseas.2016.10.002
- Cao, S. Y., Liu, J. L., Leiss, B., Vollbrecht, A., Genser, J., Neubauer, F., et al. (2011). Initiation of left-lateral deformation along the Ailao Shan-Red River shear zone: New microstructural, textural and geochronological constraints from the Diancang Shan metamorphic massif, SW Yunnan, China. *Int. Geol. Rev.* 54, 348–367. doi:10.1080/00206814.2010.543789
- Chen, L., and Zhong, G. J. (2008). Seismic stratigraphic analysis of Zhongjiannan Basin in south China sea. *Geophys. Prospect. Petroleum* 47 (6), 609–616. doi:10.1016/S1876-3804(08)60015-4
- Fyhn, M. B. W., Boldreel, L. O., and Nielsen, L. H. (2009). Geological development of the central and south Vietnamese margin: Implications for the establishment of The south China sea, Indochinese escape tectonics and Cenozoic volcanism. *Tectonophysics* 478, 184–214. doi:10.1016/j.tecto.2009.08.002

Funding

This research was funded by National Natural Science Foundation of China (No. U20A20100, No. 41206035, No. 42106079) and Nature Science Foundation of Guangdong Province (No. 2015A030313157, No. 2107A030312002, 2018A030313168). Special Project for Introduced Talents Team of Southern Marine Science and Engineering Guangdong Laboratory (Guangzhou) (Grant No. GML2019ZD0201). National Marine and land mineral resources map compilation and update project (No. DD20190368). The geophysical data in this paper are from Guangzhou Marine Geological Survey.

Acknowledgments

We are grateful to the reviewers and scientific editors for their very careful reviews and constructive suggestions, which greatly enhanced the scientific and technical level of the paper.

Conflict of interest

The authors declare that the research was conducted in the absence of any commercial or financial relationships that could be construed as a potential conflict of interest.

Publisher's note

All claims expressed in this article are solely those of the authors and do not necessarily represent those of their affiliated organizations, or those of the publisher, the editors and the reviewers. Any product that may be evaluated in this article, or claim that may be made by its manufacturer, is not guaranteed or endorsed by the publisher.

- Fyhn, Michael B. W., Lars, O. Boldreel, Lars, H. Nielsen, Tran, C. Giang, Le, H. Nga, Nguyen, T. M. Hong, et al. (2013). Carbonate Platform Growth and Demise offshore central Vietnam: Effects of early Miocene Transgression and subsequent Onshore uplift. *J. Asian Earth Sci.* 76 (20), 152–168. doi:10.1016/j.jseas.2013.02.023
- Gao, H. F., Bai, Z. L., and Guo, Y. Q. (2000). Cenozoic sedimentary facies and palaeogeographic evolution of Zhongjiannan basin, South China Sea. *China Offshore Oil Gas Geol.* 14 (6), 46–51.
- Gilley, L. D., Harrison, T. M., Leloup, P. H., Ryerson, F. J., Lovera, O. M., and Wang, J. H. (2003). Direct dating of left-lateral deformation along the Red River shear zone, China and Vietnam. *J. Geophys. Res.* 108 (B2), 2127. doi:10.1029/2001JB001726
- Lei, C., Ren, J. Y., Pei, J. X., Liu, B. W., Zuo, X., Liu, J. A., et al. (2021). Tectonics of the offshore Red River fault recorded in the junction of the Yinggehai and Qiongdongnan basins. *Sci. China Earth Sci.* 64 (11), 1893–1908. doi:10.1007/s11430-020-9796-2
- Leloup, P. H., Lacassin, R., Tapponnier, P., Schärer, U., Zhong, D. L., Liu, X. H., et al. (1995). The ailao Shan - Red River shear zone (Yunnan, China), Tertiary transform boundary of Indochina. *Tectonophysics* 251 (1-4), 3–84. doi:10.1016/0040-1951(95)00070-4
- Leloup, P. H., Arnaud, N., Lacassin, R., Kienast, J. R., Harrison, T. M., Phan Trong, T. T., et al. (2001). New constraints on the structure, thermochronology, and timing of the Ailao Shan-Red River shear zone, SE Asia. *J. Geophys. Res.* 106, 6683–6732. doi:10.1029/2000JB900322
- Leloup, P. H., Harrison, T. M., Ryerson, F. J., Chen, W. J., Li, Q., Tapponnier, P., et al. (1993). Structural, petrological and thermal evolution of a Tertiary ductile strike-slip shear zone, Diancang Shan, Yunnan. *J. Geophys. Res.* 98 (B4), 6715–6743. doi:10.1029/92JB02791
- Li, C. F., Li, J. B., Ding, W. W., Franke, D., Yao, Y. J., Shi, H. S., et al. (2015). Seismic stratigraphy of the central South China Sea basin and implications for neotectonics. *J. Geophys. Res. Solid Earth* 120 (3), 1377–1399. doi:10.1002/2014jb011686
- Li, C. F., Xu, X., Lin, J., Sun, Z., Zhu, J., Yao, Y. J., et al. (2014). Ages and magnetic structures of the South China Sea constrained by deep tow magnetic surveys and IODP Expedition 349. *Geochem. Geophys. Geosyst.* 15 (12), 4958–4983. doi:10.1002/2014gc005567
- Liu, H. L., Yao, Y. J., Shen, B. Y., Cai, Z. R., Zhang, Z. W., Xu, H. H., et al. (2015a). On the Linkage of the western boundary faults of The south China sea. *Eart. Sci.* 40 (4), 615–632. doi:10.3799/dqkx.2015.049
- Liu, J. L., Chen, X. Y., Wu, W. B., Tang, Y., Tran, M. D., Nguyen, Q. L., et al. (2015b). New tectono-geochronological constraints on timing of shearing along the Ailao Shan-Red River shear zone: Implications for Genesis of Ailao Shan gold mineralization. *J. Asian Earth Sci.* 103, 70–86. doi:10.1016/j.jseas.2014.11.006
- Liu, J. L., Tang, Y., Tran, M. D., Cao, S. Y., Zhao, L., Zhang, Z. C., et al. (2012). The nature of the Ailao Shan-Red River (ASRR) shear zone: Constraints from structural, microstructural and fabric analyses of metamorphic rocks from the Diancang Shan, Ailao Shan and Day Nui Con Voi massifs. *J. Asian Earth Sci.* 47, 231–251. doi:10.1016/j.jseas.2011.10.020
- Nguyen, V. V., and Hoai, L. T. T. (2019). Cenozoic paleostress evolution in south central Vietnam: Implication for changing dynamics of faulting along the eastern Indochina continental margin. *J. Asian Earth Sci.* 185, 104006. doi:10.1016/j.jseas.2019.104006
- Qiu, Y., Yao, B. C., Li, T. G., Bao, C. W., Gong, Y. H., and Zhong, H. X. (1997). Geologic and tectonic features and hydrocarbon potential of the Zhongjannan basin, South China Sea. *Geol. Res. South China Sea* 9, 37–53.
- Rangin, C., Klein, M., Roques, D., Le Pichon, X., Van Trongand Le (1995). The Red River fault system in the Tonkin Gulf, Vietnam. *Tectonophysics* 243 (3 - 4), 209–222. doi:10.1016/0040-1951(94)00207-p
- Replumaz, A., Lacassin, R., Tapponnier, P., and Leloup, P. H. (2001). Large river offsets and Plio-Quaternary dextral slip rate on the Red River fault (Yunnan, China). *J. Geophys. Res.* 106, 819–836. doi:10.1029/2000jb900135
- Schoenbohm, L. M., Burchfiel, B. C., Chen, L. Z., and Yin, J. Y. (2005). Exhumation of the Ailao Shan shear zone recorded by Cenozoic sedimentary rocks, Yunnan Province, China. *Tectonics* 24 (6), TC6015. doi:10.1029/2005tc001803
- Schoenbohm, L. M., Burchfiel, B. C., Chen, L. Z., and Yin, J. Y. (2006). Miocene to present activity along the Red River fault, China, in the context of continental extrusion, upper-crustal rotation, and lowercrustal flow. *Geol. Soc. Am. Bull.* 118, 672–688. doi:10.1130/b25816.1
- Sun, Z., Ding, W. W., Zhao, X. X., Qiu, N., Lin, J., and Li, C. F. (2019a). The latest spreading periods of The South China sea: New constraints from macrostructure analysis of IODP expedition 349 cores and geophysical data. *J. Geophys. Res. Solid Earth* 124 (10), 9980–9998. doi:10.1029/2019JB017584
- Sun, Z., Li, F. C., Lin, J., Sun, L. T., Pang, X., and Zheng, J. Y. (2021). The rifting-breakup process of the passive continental margin and its relationship with magmatism: The attribution of The south China sea. *Earth Sci.* 46 (3), 770–789. doi:10.3799/dqkx.2020.371
- Sun, Z., Lin, J., Qiu, N., Jian, Z. M., Wang, P. X., Pang, X., et al. (2019b). The role of magmatism in the thinning and breakup of the South China Sea continental margin. *Natl. Sci. Rev.* 6 (05), 871–876. doi:10.1093/nsr/nwz116
- Sun, Z., Zhou, D., Zhong, Z. H., Zeng, Z. X., and Wu, S. M. (2003). Experimental evidence for the dynamics of the formation of the Yinggehai basin, NW South China Sea. *Tectonophysics* 372, 41–58. doi:10.1016/s0040-1951(03)00230-0
- Tapponnier, P., Lacassin, R., Leloup, P. H., Schärer, U., Zhong, D. L., Wu, H. W., et al. (1990). The ailao Shan/Red River metamorphic belt: Tertiary left-lateral shear between Indochina and south China. *Nature* 343, 431–437. doi:10.1038/343431a0
- Tapponnier, P., Peltzer, G., and Armijo, R. (1986). On the mechanics of the collision between India and Asia. *Geol. Soc. Lond. Special Publ.* 19 (1), 113–157. doi:10.1144/gsl.sp.1986.019.01.07
- Trinh, P. T., Liem, N. V., Huong, N. V., Vinh, H. Q., Thom, B. V., Thao, B. T., et al. (2012). Late Quaternary tectonics and seismotectonics along the Red River Fault zone, north Vietnam. *Earth. Sci. Rev.* 114, 224–235. doi:10.1016/j.earscirev.2012.06.008
- Xiang, H. F., Wan, J. L., Han, Z. J., Guo, S. M., Zhang, W. X., Chen, L. C., et al. (2006). Geological analysis and FT dating of large dextral strike-slip movement in Red River Fault Zone. *Science in China ser. D. earth Sci.* 36 (11), 977–987.
- Xiang, H. F., Han, Z. J., Guo, S. M., Zhang, W. X., and Chen, L. C. (2004). large-scale dextral strike-slip movement and associated tectonic deformation along the Red River Fault Zone. *Seismol. Geol.* 26 (4), 598–610.
- Yin, Z. X., Cai, Z. R., Wan, Z. F., and Lv, B. F. (2015). Features and dynamic mechanisms of Cenozoic tectonic migration and its impact on the hydrocarbon accumulation in the northern South China Sea. *Acta Oceanol. Sin.* 34 (1), 100–109. doi:10.1007/s13131-015-0603-1
- Zhang, C. M., Sun, Z., Manatschal, G., Pang, X., Li, S. Z., Sauter, D., et al. (2021). Ocean-continent transition architecture and breakup mechanism at the mid-northern South China Sea. *Earth-Science Rev.* 217 (3), 103620. doi:10.1016/j.earscirev.2021.103620
- Zhong, G. J., and Gao, H. F. (2005). Sequence characteristics of Cenozoic stratigraphy in Zhongjiannan Basin, south China sea. *Geotect. Metallogenia* 29 (3), 403–409.
- Zhu, W. L., and Lei, C. (2013). Refining the model of South China Sea's tectonic evolution: Evidence from Yinggehai-Song Hong and Qiongdongnan basins. *Mar. Geophys. Res.* 34 (3-4), 325–339. doi:10.1007/s11001-013-9202-8
- Zuchiewicz, W., Cuong, N. Q., Zasadni, J., and Yem, N. T. (2013). Late Cenozoic tectonics of the Red River fault zone, Vietnam, in the light of geomorphic studies. *J. Geodyn.* 69, 11–30. doi:10.1016/j.jog.2011.10.008



OPEN ACCESS

EDITED BY

Shaohong Xia,
South China Sea Institute of
Oceanology (CAS), China

REVIEWED BY

Xiaoxiao Yu,
Guangzhou Institute of Geochemistry
(CAS), China
Luigi Jovane,
University of São Paulo, Brazil

*CORRESPONDENCE

S. Wu,
swu@idsse.ac.cn

SPECIALTY SECTION

This article was submitted to Marine
Geoscience,
a section of the journal
Frontiers in Earth Science

RECEIVED 12 September 2022

ACCEPTED 17 November 2022

PUBLISHED 09 January 2023

CITATION

Liu Y, Wu S, Li X, Chen W, Han X, Yang C,
Qin Y, Huang X, Yang Z, Sun J and Zhu L
(2023), Seismic stratigraphy and
development of a modern isolated
carbonate platform (Xuande Atoll) in the
South China Sea.
Front. Earth Sci. 10:1042371.
doi: 10.3389/feart.2022.1042371

COPYRIGHT

© 2023 Liu, Wu, Li, Chen, Han, Yang,
Qin, Huang, Yang, Sun and Zhu. This is
an open-access article distributed
under the terms of the [Creative
Commons Attribution License \(CC BY\)](#).
The use, distribution or reproduction in
other forums is permitted, provided the
original author(s) and the copyright
owner(s) are credited and that the
original publication in this journal is
cited, in accordance with accepted
academic practice. No use, distribution
or reproduction is permitted which does
not comply with these terms.

Seismic stratigraphy and development of a modern isolated carbonate platform (Xuande Atoll) in the South China Sea

Y. Liu^{1,2}, S. Wu^{1,2,3*}, X. Li^{1,4}, W. Chen^{1,2}, X. Han⁵, C. Yang⁵, Y. Qin¹,
X. Huang^{1,6}, Z. Yang⁷, J. Sun¹ and L. Zhu¹

¹Laboratory of Marine Geophysics and Georesources of Hainan Province, Institute of Deep-Sea Science and Engineering (CAS), Sanya, China, ²School of Earth Sciences, University of Chinese Academy of Sciences, Beijing, China, ³Laboratory for Marine Geology, Qingdao National Laboratory for Marine Science and Technology, Qingdao, China, ⁴Sanya Institute of South China Sea Geology, Guangzhou Marine Geological Survey, Sanya, China, ⁵Marine Geological Survey Institute of Hainan Province, Haikou, China, ⁶Institute of Earth and Environmental Science, University of Potsdam, Potsdam, Germany, ⁷Institute of Georesource, Guangzhou Marine Geology Survey, Guangzhou, China

Xuande Atoll is an isolated carbonate platform that has developed since the early Miocene. This study conducted high-resolution seismic surveys and shallow drilling to understand its internal structure and development. Five seismic sequences were observed (from bottom to top): SQ1 (early Miocene), SQ2 (middle Miocene), SQ3 (late Miocene), SQ4 (Pliocene), and SQ5 (Quaternary). The seismic data indicated that the platform formation started in the early Miocene and flourished during the early and middle Miocene. The platform shrank before the isolated platform formed in the middle Miocene. The final shrinking stage occurred in the southern and western parts of the platform at the end of the Miocene, which may reflect rapid tectonic subsidence and increased terrigenous sediment inputs owing to the formation of the semi-marginal sea. The peri-platform contains a falling sea-level sequence that was dominated by mass wasting deposits.

KEYWORDS

carbonate platform, tectonic control, monsoon, coral atoll, Xisha

Introduction

Siliciclastic sequence stratigraphy on continental margins has constrained the lateral contrasts from shelf to deep-water basin facies, which usually comprise lowstand, transgressive, and highstand sequences controlled by changes in sea level (Mitchum Jr et al., 1977; Vail et al., 1977; Van Wagoner et al., 1987; Jervy, 1988; Posamentier and Vail, 1988; Sarg, 1988; Jovane et al., 2016). However, the sequence stratigraphy of carbonate margins is not entirely understood, particularly on modern isolated platforms. The sequence and structure of the isolated carbonate platform are controlled by various factors, including tectonics, sea levels, carbonate productivity, terrigenous sediment

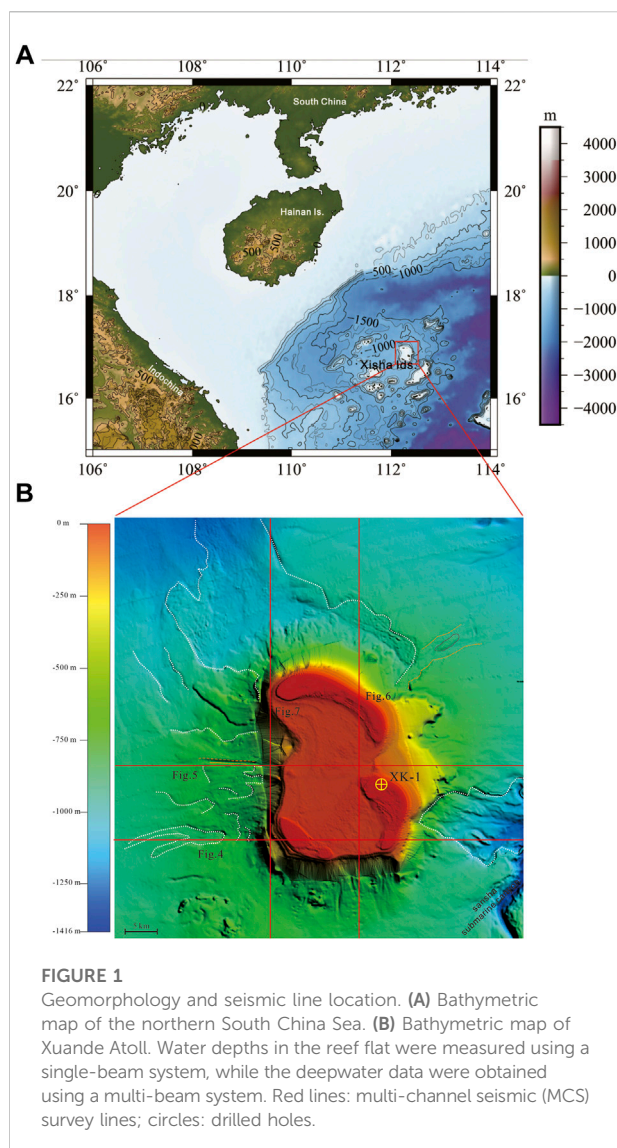


FIGURE 1
Geomorphology and seismic line location. (A) Bathymetric map of the northern South China Sea. (B) Bathymetric map of Xuande Atoll. Water depths in the reef flat were measured using a single-beam system, while the deepwater data were obtained using a multi-beam system. Red lines: multi-channel seismic (MCS) survey lines; circles: drilled holes.

inputs, and marine palaeoceanography (Eberli and Ginsburg, 1987; Wilson, 2002; Wilson, 2008; Betzler et al., 2009; Schlager and Warrlich, 2010). The structure of tropical carbonate sequences depends not only on relative decreases in sea level but also on the reef production rate, erosion rate, and accommodation space. Generally, no apparent lateral variations are observed in the reef flat but can be observed in falling sea level tracts (FSTs) on the reef slope, including strong gravity flow and bottom current deposits. Sea level, coral reef growth, and palaeoceanography also affect the structure of tropical carbonate platforms. A carbonate platform can produce debris that is then transported to the deepwater slope by gravity flow (Wilson, 2002; Fournier et al., 2004; Wilson, 2008; Schlager and Warrlich, 2010).

Although seismic imaging of drowned or buried isolated carbonate platforms has been conducted in the Gulf of Papua

New Guinea, Northeast Australia, Great Bahama Bank, and Southeast Asia (Ludmann et al., 2005; Tcherepanov et al., 2008; Wu et al., 2014), only a few high-resolution seismic surveys of the shallow lagoon and reef flat have been performed. In particular, few multi-channel seismic (MCS) surveys have been performed on most modern carbonate platforms, which are common in the Xisha archipelago in the South China Sea (SCS) (Wu et al., 2014; Shao et al., 2017).

Xuande atoll is located in the east of the Xisha archipelago. Previous studies have described the development of Xuande Atoll based on lithological observations, sedimentary facies analysis, thin section identifications, and geochemical analyses of samples from drilled wells (Shao et al., 2017). However, as all these wells were drilled on the Yongxing Island of Xuande Atoll, the results only reflect vertical facies variations; thus, the three-dimensional structure of the platform remains unclear. We conducted four seismic survey lines across Xuande Atoll in the Xisha archipelago in 2017 (Figure 1). In this study, we report on newly collected data from seismic surveys and holes drilled across Xuande Atoll. We investigated the three-dimensional growth of the platform using seismic and well data to determine the development of this modern isolated carbonate platform to improve our current understanding of modern carbonate platform development and determine the sequence stratigraphy and evolution of Cenozoic platforms (Figure 1).

Geologic setting

The Xisha archipelago is located on the continental slope of the SCS margin, which has been undergoing continental rifting, subsequent extension, and post-extensional drift since the late Cretaceous (Figure 1). The timing of the seafloor spread has recently been revised from 33 to 23.6 Ma in the northwest sub-basin and from 23.6 to 15 Ma in the east sub-basin, using data from the International Ocean Discovery Project (IODP) Site U1435 (Taylor and Hayes, 1980; Briais et al., 1993a; Cullen, 2010; Li et al., 2015). Tectonically, the Xisha archipelago is part of the Xisha uplift, which was formed by Palaeocene hyper-extended rifting bounded by high-angle faults (Tapponnier et al., 1982a; Qiu et al., 2001; Hall, 2002; Li et al., 2015). Since the late early Miocene, the regional tectonics have comprised a post-rifting setting characterised by thermal subsidence (Wu et al., 2009). In addition, the acoustic basement of the uplift is Precambrian grey granite gneiss and Mesozoic volcanic rocks, as determined from data from well XY-1 (Wang et al., 1979; Qiu et al., 2006). Recently, well XK-1 encountered metamorphic rocks and granite basement at depths of 1257.52–1268.02 m, comprising late Jurassic adamellites (152 ± 1.7 Ma) and Cretaceous granites (107.8 ± 3.6 Ma) (Zhu et al., 2017). The basement observed in well XK-1 could be volcanoclastic rocks (36.01 ± 0.59 – 37.68 ± 1.37 Ma) and Yanshanian granitic rocks (105.73 ± 1.39 – 146.10 ± 1.73 Ma), as well as scattered Precambrian crystalline basement

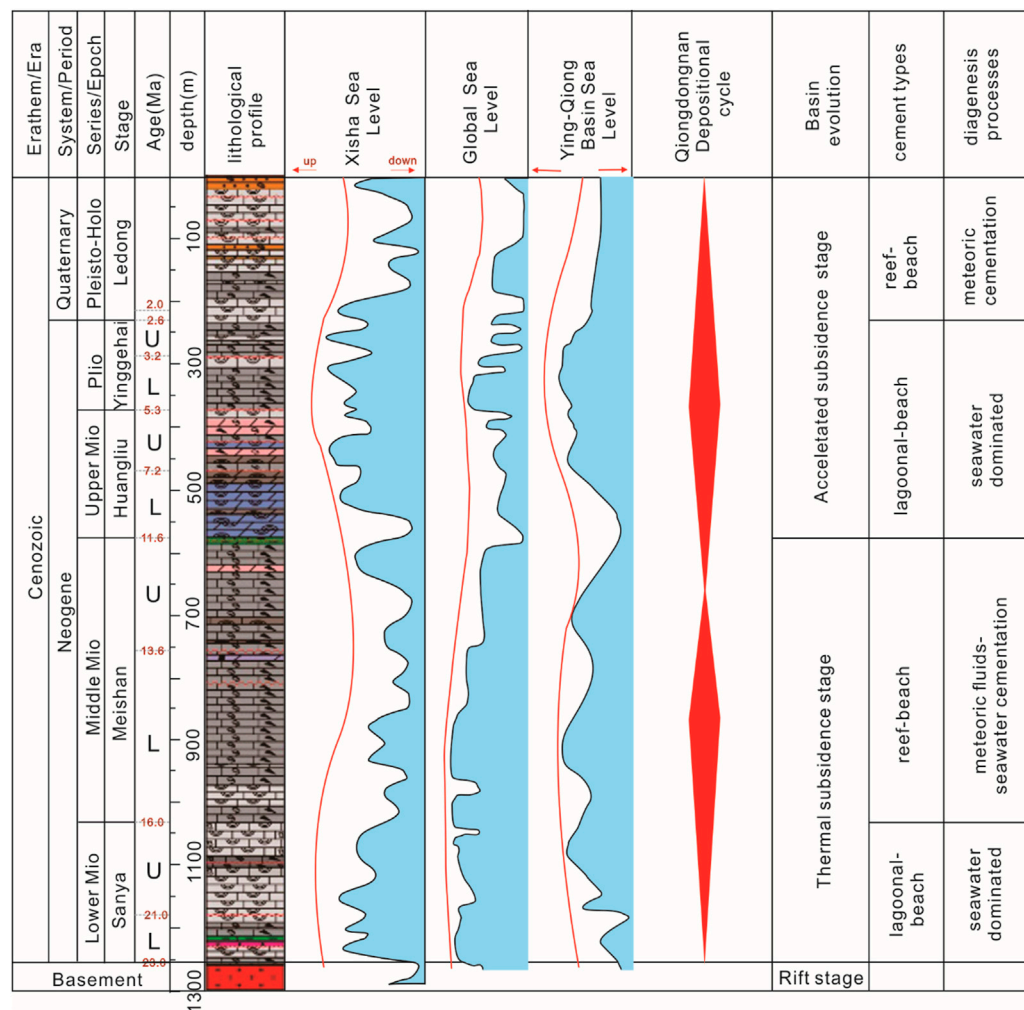


FIGURE 2

Stratigraphic contrasts in well XK-1 on Yongxing Island at Xuande Atoll (Shao et al., 2017). The drilling site is shown in Figure 1.

(623.40 ± 6.67 – 884.1 ± 7.70 Ma). Owing to the stable tectonic setting associated with the steep incline generated in the Palaeocene, the Xisha platform initiated in the early Miocene and has remained active to the present (Ma et al., 2011; Wu et al., 2014; Shao et al., 2017).

The geomorphology of Xuande Atoll has recently been investigated using dense single-beam bathymetric measurements of the reef flat and multi-beam bathymetry of the lower slope (Figure 2). Three coral reef flats are present on the huge reef platform, including Qilanyu shoal, Yongxing Island, and Southwest shoal. The water depth ranges from 0 to 65 m and rapidly increases to 800–1232 m on the platform slope. The slope reaches 30° at the reef flat front (Figure 2). The lithology and biostratigraphy of the platform have been investigated using two wells (Xiyong-1 and Xichen-1) drilled on Xuande Atoll during the 1980s and well Xike-1 drilled in

2013–2014 (Wang et al., 1979; Xu et al., 2002; Wang et al., 2015).

Four wells have been drilled on Yongxing Island. Wells XY-1, XY-2, XS-1, and XK-1 penetrated up to 1384.68, 600.02, 200.63, and 1268 m, respectively (Figures 1, 2). Based on the wells drilled on Xuande Atoll, the thicknesses of the carbonate platform determined from wells XY-1 and XK-1 are approximately 1275 m and 1251 m, respectively. The Neogene carbonate platform grew on Precambrian or Mesozoic metamorphic and volcanic basement (Zhao et al., 2011), or on Mesozoic metamorphic rocks (152.9 ± 1.7 Ma) and granites (107.8 ± 3.6 Ma) (Zhu et al., 2017). The late Cenozoic platform strata are divided into the Guangle, Xisha, Xuande, Yongle, and Yongxing formations (Figure 3). This stratigraphy was established in the 1990s; however, it has many issues related to the drilling locations and the lack of good chronology data

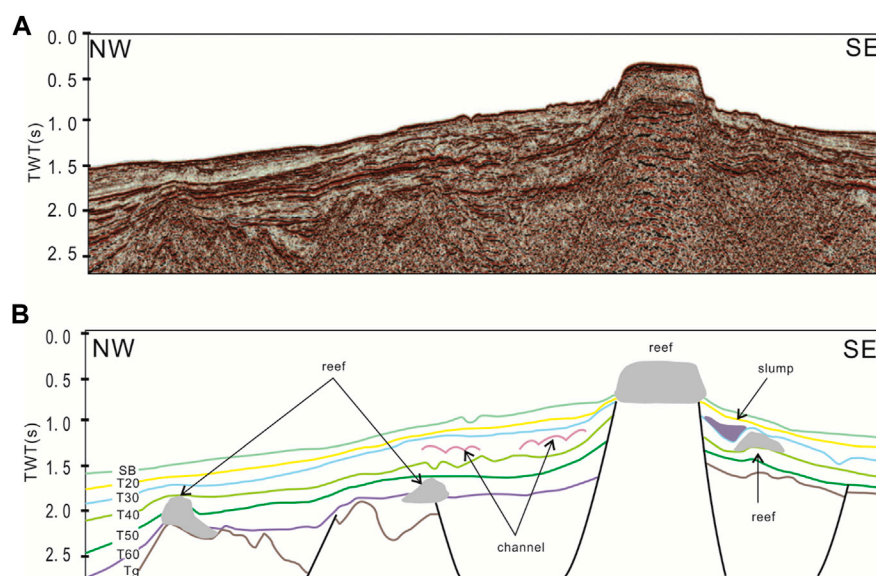


FIGURE 3

Seismic sequence stratigraphy across the Xisha Uplift in the South China Sea. **(A)** Uninterpreted and **(B)** interpreted sections. SB is the seafloor reflector, and T20, T30, T40, T50, and T60 represent the bottom of the Quaternary, Pliocene, Late Miocene, Middle Miocene, and Early Miocene, respectively. Seismic reflector Tg is the acoustic basement reflection.

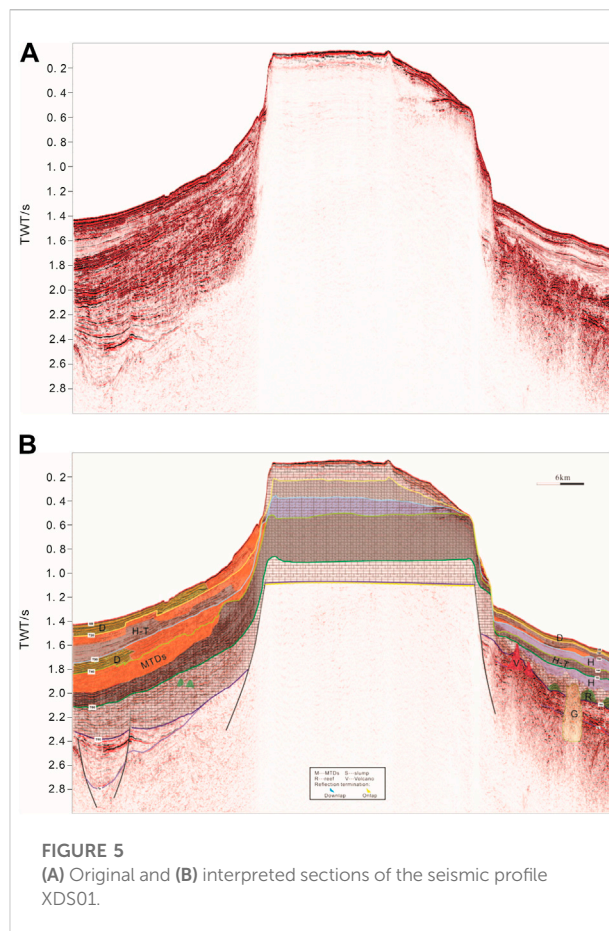
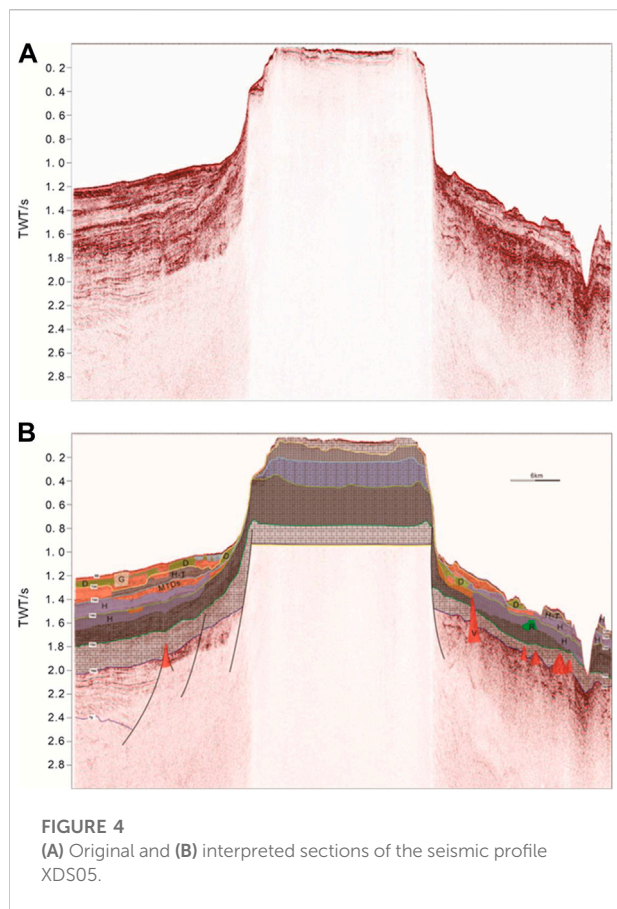
(Zhao et al., 2011; Zhu et al., 2015). Data from well XK-1 improved the stratigraphy in the region by integrating geochronological information from magnetostratigraphy and astronomical tuning as the age-depth model of well XK-1 has been calibrated (Yi et al., 2018). Based on the model, the bottom ages of the Sanya, Meishan, Huangliu, Yinggehai, and Ledong formations were determined to be 24.3, 16.6, 10.4, 5.7, and 2.2 Ma, respectively.

Data and methods

Seismic surveys were performed onboard the R/V *NH503* from 31 August to 6 September 2017. This was the first seismic experiment across a shallow carbonate platform in the SCS. The acoustic signals were generated by two clustered GI-guns with a maximum of around 210 in³ and included frequencies of 40–2000 Hz, with the dominant frequencies centred at 150–200 Hz. The seismic signals were received by a GEO-Sense 48 receiver (Netherlands) with an offset of 9.5 m. The sampling interval was 0.25 m, and the vertical resolution reached 2 m. The streamer was 600 m in length, with a 6.25 m channel distance. The source distance was 12.5 m; therefore, the seismic system had a 90 m migration distance and a 24 m overlap. Seismic data processing was performed using the GeoCluster 6100 software package. The key processing steps included: 1) muting using the frequency panel to reduce random noise, Radon transform, and

common migration offset distances; 2) suppressing multiple reflections using surface-related multiple elimination (SRME) and prediction deconvolution; 3) velocity analyses, including precision velocity analysis and migration velocity scanning; 4) remaining multiple wave suppression with spectral and static plots; 5) Kirchhoff pre-stack time migration, particularly migration offsets of the aperture and angle; and 6) pre-stack muting to obtain the true amplitude section. Data interpretation was performed using sequence stratigraphic methods. The original seismic data were interpreted using Geoframe 2012. All vertical scales used for the seismic profiles shown herein were two-way travel times. The seismic data were then used to investigate the subsurface structure and sedimentary characteristics of the platform.

Multi-beam bathymetric and single-channel seismic data collected by the Guangzhou Marine Geological Survey (GMGS) were used to image the slopes of the Xisha archipelago. A bathymetric map of the archipelago was constructed from the multi-beam depth soundings combined with satellite data. Multi-beam bathymetry data acquired with a SeaBeam 2112 system (USA) were used to analyse the geomorphology of the archipelago. The multi-beam data were processed using navigation filtering, parameter calibration, transducer draft correction, sound velocity correction, and data filtering (Chen et al., 2015). A 100 m × 100 m cell size was used for the raster grids in this study, with a vertical resolution of 3% of the water depth.



Results and interpretation

Modern carbonate platforms exhibit high-amplitude, parallel, and continuous reflections on their tops, and low-amplitude reflections in their internal regions above the basement (Figures 4–7). Six key reflectors were identified in the seismic profile across the platform. Reflector T0 is a seafloor reflector that images the morphology of the platform. T0 shows the flat on the platform and steep slopes on the margins of the platform (Figure 1). Reflector T20 represents the bottom of the Quaternary strata. Reflectors T30 (bottom of the Pliocene), T40 (bottom of the late Miocene), and T50 (bottom of the middle Miocene) represent the bases of different strata, while Tg is a reflector of the acoustic basement that varied in amplitude and frequency, occurring as an undulating interface reflector. According to the reflectors, the reef carbonate strata can be divided into six seismic sequences: SQ1 (early Miocene), SQ2 (middle Miocene), SQ3 (late Miocene), SQ4 (Pliocene), and SQ5 (Quaternary) from the basement to the seafloor (Figures 4–7).

SQ1 is located above the acoustic basement and is characterised by parallel and sub-parallel seismic reflections (Figures 4–6). The reflections onlap the basement high and have complex inner reflections in the eastern part of profile

05 (Figure 4). During the early Miocene, the Xisha uplift was drowned because of marine inundation, and reef carbonates grew on the basement high. During the beginning of the early Miocene, shallow water carbonate deposits formed on the slopes of Xuande Atoll (Figures 6–8). The reef platform was lateral and grew vertically during the early Miocene. Thus, reef carbonates are widely distributed on Xuande Atoll and in adjacent areas (Figures 6–8).

SQ2 represents middle Miocene carbonate strata and is characterised by parallel and sub-parallel seismic reflections in the western part of the profile (Figure 7). However, SQ2 has complex mound-shaped cluttered and wavy divergent reflections in the eastern part of the profile (Figure 8). During the middle Miocene, reef carbonates formed on the leeward slope of the basal uplift and started to grow on the windward slope in the eastern part. These carbonate sequences were deposited on the platform during a stable sea level period. During the late middle Miocene, the sea level increased rapidly, and the carbonate platform migrated accordingly. A pinnacle reef formed on the western slope of the atoll, whereas a wavy drift occurred on the eastern slope. The carbonate platform was only aggraded at Xuande Atoll, whereas deepwater gravity flow deposits, including mass transport deposits (MTDs), formed in the peri-platform area (Figure 8).

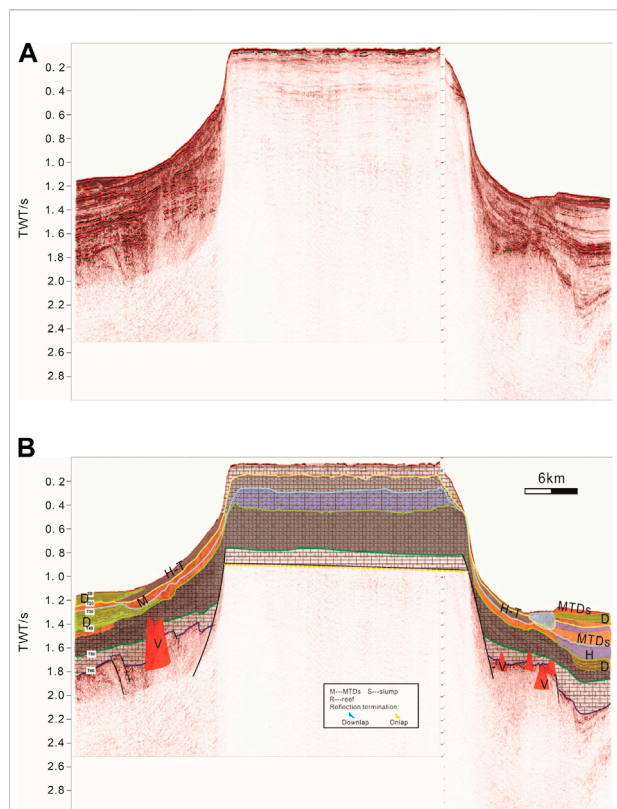


FIGURE 6
(A) Original and (B) interpreted sections of the seismic profile XDS10.

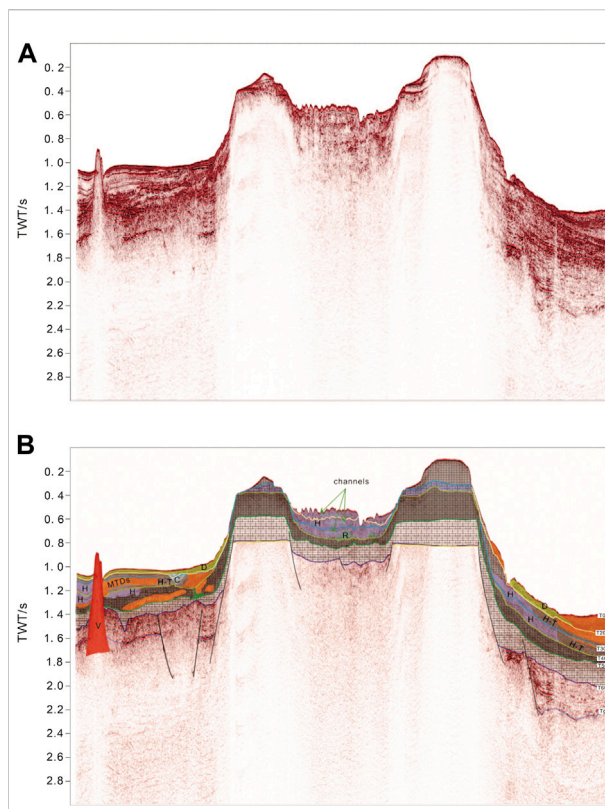


FIGURE 7
(A) Original and (B) interpreted sections of the seismic profile XDS11.

SQ3 represents late Miocene carbonate strata and is characterised by parallel and sub-parallel seismic reflections on both sides of the profile (Figure 7). SQ3 also contains S-type reflection structures in the peri-platform area. The reef carbonates grew favourably at Xuande Atoll, owing to rapid subsidence (Figures 5, 6). However, reef growth did not occur in the peri-platform area. The last apparent shrinkage of the platform occurred northward and eastward at the end of the Miocene (Figure 9).

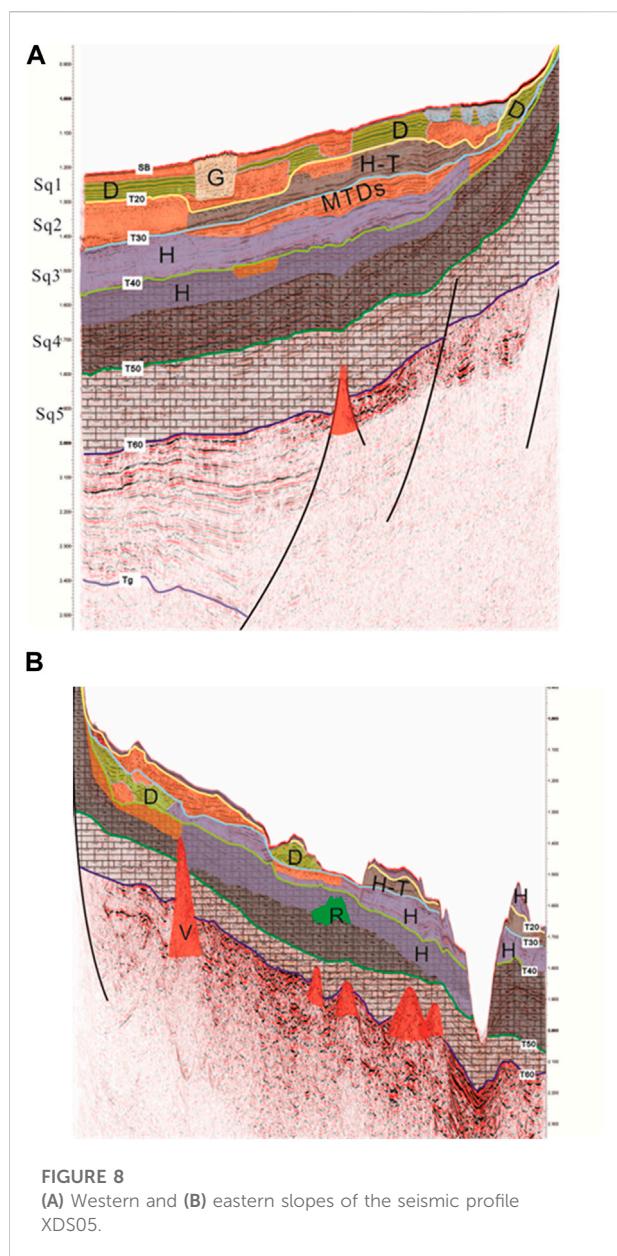
SQ4 represents Pliocene carbonate strata and is characterised by parallel and sub-parallel seismic reflections on both sides of the profile. During the Pliocene, the carbonate platform was limited at the atoll. SQ5 represents Quaternary carbonate strata and is characterised by parallel and sub-parallel seismic reflections on both sides of the profile (Figures 6, 7). High-amplitude chaotic reflections were observed on the slope of the atoll, which could represent bottom current deposits around the atoll (Figure 8). Most of the seafloor around the atoll is covered by hemipelagic sediment, and the slopes contain tidal channels or gullies (Figures 7, 8). The platform margin regressed by 8 km, and the platform decreased from the 300 m to the 60 m isoline, after which the sea level rose and lateral aggradation occurred on the eastern margin of the atoll.

Discussion

Evolution of the Xuande Atoll

The Xisha uplift was undergoing rifting and erosion during the Paleogene. During the early Miocene, coral reef carbonates covered the rapidly subsiding basement in the Xisha region, which covered most of the Xisha uplift located on the continental margin and captured little terrigenous sediment (Wu et al., 2014). Later, the bioherms of the Xisha Islands aggraded and prograded, forming the large shallow carbonate deposits observed in the seismic profiles (Figures 4–7), including the reef flat and interbedded lagoon-beach facies that were also observed in well XK-1 (Shao et al., 2017; Wu et al., 2020).

During the early and late middle Miocene, the rising sea level decelerated and then decreased (Shao et al., 2017). The carbonates in well XK-1 exhibited reef-beach facies, owing to prevailing corrosion and leaching processes in a mixed meteoric water-marine environment (Shao et al., 2017). In the early middle Miocene, shallow carbonate sequences were observed at Xuande Atoll (Figures 6, 7). The shallow carbonate deposits were distributed throughout the Xisha area (Ma et al., 2011). The



peri-platform facies then changed to deepwater facies, indicating that the carbonate platform became isolated during the late middle Miocene (Figure 10).

During the late Miocene, the isolated platform continued to aggrade. Then, when the sea level increased again from the late Miocene to the Pliocene (Shao et al., 2017), the atoll reef terraces extended more broadly and were dominated by lagoon and reef flat facies on their inner sides. However, the platform shrank on the eastern and northern margins (Figure 9). Throughout the Pleistocene, the sea level decreased from its maximum and oscillated with a few deviations. As a result, the carbonate platform on which well XK-1 is located was eroded by freshwater diagenesis. Strata with overbedded reef and beach

facies were widely produced, except for patchy carbonates preserved in relatively better conditions (Figure 10). As the upward growth rate of a carbonate platform fails to keep pace with the rates of subsidence or sea level rise, most of the pre-existing reefs and carbonate platforms will become drowned, leaving only the atoll reefs circled topographic highs to continue developing vertically (Hallock and Schlager, 1986; Belopolsky and Droxler, 2003). Such reefs grew rapidly at Xuande Atoll, and some biohermal clasts eroded by ocean waves were deposited around the reefs, partly conveyed downslope by small channels (Figure 4). Atoll reefs developed mainly around the reef islands on the Xisha uplift, represented by the Xuande and Yongle atoll reefs. The Xuande isolated platform underwent slight asymmetric development (Figure 11). The reef flats grew in the north and east, with discontinuity in the south and west (Figures 1, 4, 5, 11). Patch reefs also formed in the lagoon. Apparent platform shrinkage then occurred northward and eastward at the end of the Miocene (Figure 9).

Stratigraphic sequence

The exposed surface of an isolated carbonate platform may represent a seismic boundary at low sea levels. Six exposed surfaces were observed in the carbonate sequences of Xuande Atoll, which formed during gentle decreases in sea level (Figures 4–9). These exposed surfaces usually occurred with dissolution and highly developed porosity and caves, which generally occur in red algal limestones (Zhu et al., 2015). Falling-stage systems tracts (FSTs) could also act as markers of sequence boundaries, which formed highstand tracts (Schlager and Warrlich, 2010). The seismic profiles of Xuande Atoll showed FSTs on the northeastern margin.

The application of the FST model to the margin of the atoll has been discussed in recent years (Schlager and Purkis, 2013). Boundaries in the FST model have been proposed and indicate stratigraphic forward modelling. Comparisons with previous studies have been used to determine the controls and stability domains of two conceptual models concerning relative decreases in sea level in carbonate sequence stratigraphy. In the standard model, deposition occurs during increasing and stable relative sea level stands, whereas a continuous erosional unconformity develops during decreases in sea level. The FST model postulates that significant deposition occurs during decreases in sea level. Sedimentological principles, numerical models, and previous studies of tropical carbonate sequences indicate that the presence or absence of an FST is not simply a function of the rate of the decreasing sea level but rather depends on the balance of the erosion, decreasing sea level, and carbonate production rates. Previous studies plotted in the parameter space support the modelling results. The range of rates required for the FST is common in the geologic records. Consequently, the FST can be expected to be more common around the Xuande Atoll (Figures 7, 8).

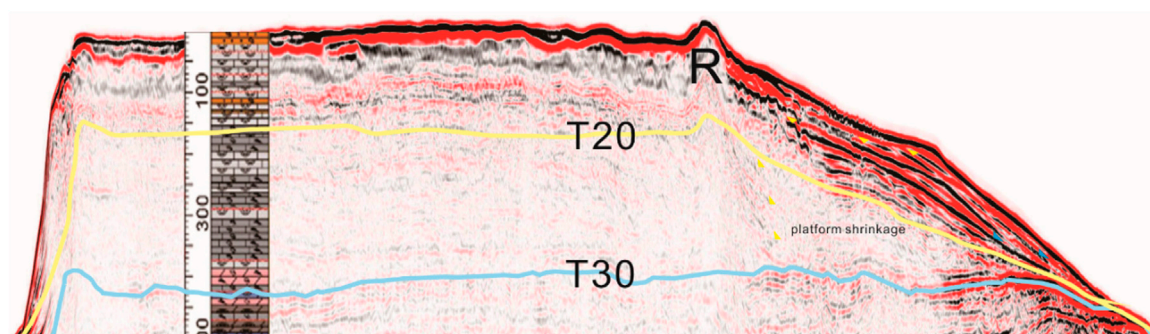


FIGURE 9
Interpreted seismic profile XDS01, showing platform shrinkage at the end of the Miocene.

Mechanisms for platform drowning

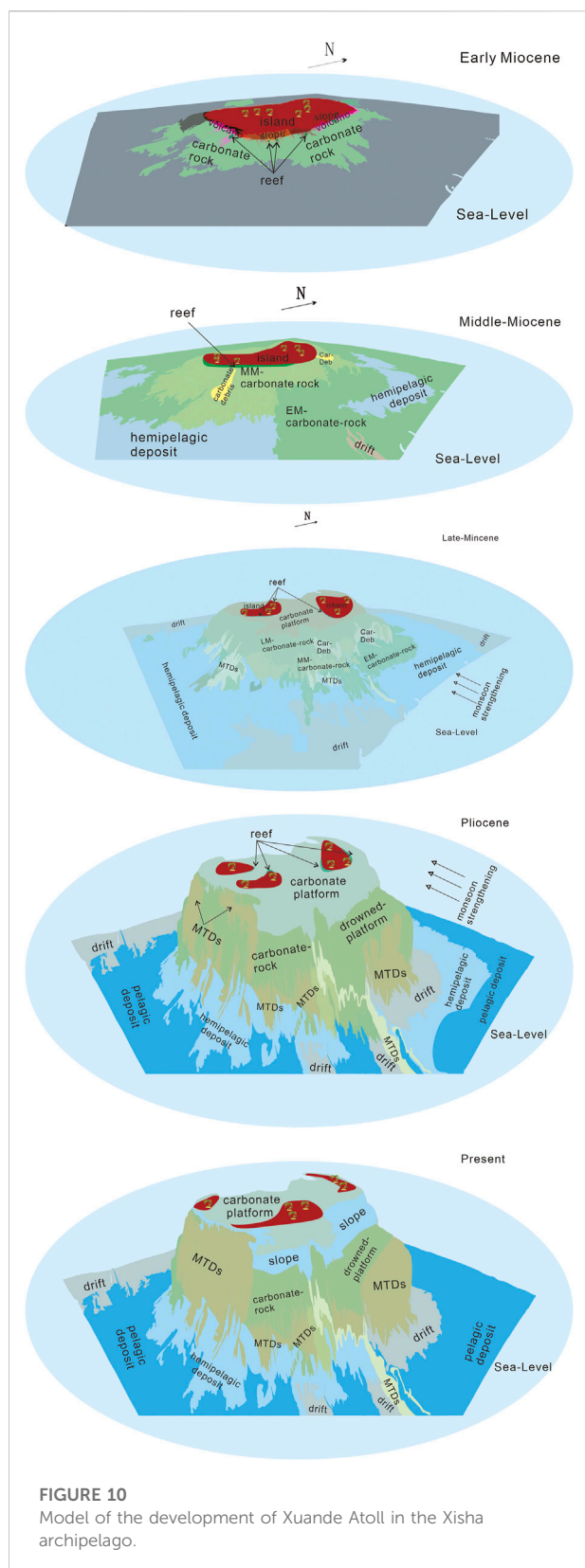
The earliest platform drowning event occurred at 15.5 Ma in the latest early Miocene, which included decreased carbonate production and increased water depth (Figure 8). The microfacies of the XY-1 and XK-1 wells at depths of 1000–1100 m included *in situ* corals and coral fragments in the low section, whereas the middle and upper sections were dominated by coralline algae and foraminifera, respectively (Ma et al., 2018). Biological studies have suggested that corals are the most successful benthic carbonate producers in oligotrophic environments but are not competitive in more nutrient-rich water (Hallock and Schlager, 1986; Mutti and Hallock, 2003; Wilson, 2008; Roger et al., 2012). Coral is symbiotic with zooxanthellae (Dubinsky and Falkowski, 2011). Increased nutrient levels stimulate plankton blooms, thereby reducing water transparency and inhibiting the photosynthesis of the zooxanthellae, which limits coral growth (Hallock and Schlager, 1986; Mutti and Hallock, 2003). Subsequently, coralline algae likely occurred in the middle section in response to variations in nutrient levels (i.e., from oligotrophic to mesotrophic conditions) (Hallock et al., 1991; Esteban, 1996; Fournier et al., 2005; Sattler et al., 2009; Lüdmann et al., 2018). In the upper section, coralline algae were gradually replaced by large benthic foraminifera (Ma et al., 2018), including *Lepidocyclina* and *Miogypsina*, which represents a eutrophic environment (Hallock et al., 1991; Sattler et al., 2009). Synchronous similar sedimentary microfacies during the drowning of carbonate platforms have been observed on the Liuhua and Malampaya carbonate platforms in the SCS (Fournier et al., 2005; Sattler et al., 2009). The vertical succession of sedimentary microfacies from *in situ* corals to coralline algae and foraminifera was not only a response to continuous increases in nutrient levels but also reflects the deepening of the depositional environment as the *Lepidocyclina*–*Miogypsina* requires a deep and low energy environment (Hallock and Schlager, 1986; Geel, 2000; Halfar and Mutti, 2005). As the water depth increased, the high

electrical resistance in this section reflected an increasingly muddy component. Carbonate platform drowning is defined by accumulation rates that fail to keep pace with long-term subsidence and sea level changes. The high production of a coral reef can easily keep up with sea level fluctuations, whereas coralline algal growth is much slower. Consequently, we concluded that increased nutrient levels caused production on the Xisha platform to fail to keep pace with subsidence (Wu et al., 2014), resulting in the drowning of the platform in the late early Miocene. While temperature changes may have also affected reef growth, temperature alone cannot change the style of reef builders (Hallock and Schlager, 1986; Sattler et al., 2009). Furthermore, the temperatures during the late early Miocene were relatively stable; thus, temperature was not likely a decisive factor. This temperature analysis was similar to that of the adjacent coeval platform demise in the Dongsha Sea region.

The most important platform drowning event occurred in the late Miocene (10.5–8.2 Ma), which corresponded to the formation of a semi-marginal sea (Li et al., 2014). The sedimentary microfacies in the two wells contained *in situ* corals in the lower section, an algal (Halimeda) dominant middle section, and a foraminiferally dominant upper section (Figure 2). Based on analyses of these sedimentary microfacies associated with slow subsidence, weak eustatic fluctuations, and slightly decreasing temperatures (Wu et al., 2014), we inferred that increased nutrient levels caused the Xisha platform to drown again in the early late Miocene.

Tectonic subsidence

The global sea level fluctuation was around 40 m in the Miocene; however, the thickness of the Miocene carbonate succession in XK-1 is nearly 1 km (Yi et al., 2018), suggesting that an accommodation space created by tectonic subsidence was the main reason for platform growth. The relative sea level is directly linked to carbonate production in carbonate depositional



systems (Tucker and Wright, 2009). Carbonate production is high when a large area of shallow water is available; however, if this area is reduced, the production decreases (Tucker and Wright, 2009). More than 1 km-thick carbonate succession since the Early Miocene indicates the higher accommodation space related to relative sea-level change caused by tectonic subsidence. The subsidence during the early Miocene was 1.0–1.5 km in the deep-water area. The total subsidence was <2 km in the northern Qiongdongnan Basin, which is similar to the results obtained from the wells in this area (Xie et al., 2008; Wu et al., 2014; Shi et al., 2017). Owing to low sediment inputs and the palaeo-water depth, the tectonic subsidence of the Xisha and Guangle uplifts cannot be accurately restored.

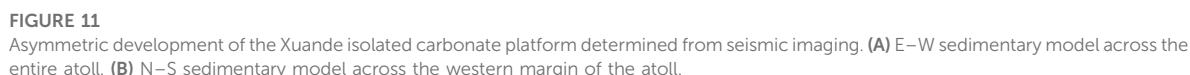
Stretching and thinning of lithospheric mantle and crust are commonly considered the primary reason for the subsidence of passive continental margin rift basins, as confirmed by the imitation of crust stretching in the north margin of the South China Sea (Cui et al., 2008; Tong et al., 2009). The mechanism driving crustal extension remains controversial between two factors: dominant extrusion of the Indochina Block and sinistral motion on the Red River Fault Zone (Tapponnier et al., 1982a; Tapponnier et al., 1982a; Briaies et al., 1993a; Briaies et al., 1993b; Leloup et al., 2001) or the subduction of a proto-SCS in the North Borneo Trench (Taylor and Hayes, 1980; Hall, 2002).

Platform development associated with East Asian monsoons

The reef builders of the Xuande platform were dominantly corals, algae, and other benthic organisms (Wu et al., 2019), which were limited by the maximum depth at which photosynthesis can occur (~100 m) (Riding, 2000a; Woodroffe and Webster, 2014).

During the Miocene, the prevailing summer wind is the East Asian summer monsoon (Clift et al., 2014). Therefore, the wind-driven surface currents and upwelling created a favourable environment for reef growth in the Xisha region. The warm summer wind satisfied the temperature requirement for the reefs. With wind-driven southwest to northeast surface currents, the intense wave action was concentrated on the windward side of the Xisha platform, which is where the reefs were centralised. As the reefs grew, reef detritus accumulated on the foreslope and formed biohermal clasts, some of which were transported by the surface currents to the leeward side of the platform and formed shoal deposits.

In addition, nutrient levels triggered by upwelling would have diffused throughout the platform by the southwestern surface current, which may have induced further reef development on



frontiersin.org

Author contributions

YL drafted the manuscript; SW and CY conceived the study; XHu, XL, XHa, and YQ contributed significantly to data analysis and manuscript preparation; WC, JS, LZ, and ZY helped perform data analysis and provided constructive discussions. All authors read and approved the final manuscript.

Funding

Financial support was received from the specific research fund of the Innovation Platform for Academicians of Hainan Province, the National Science Foundation of China (No. 91228208), the International Cooperation Project of Hainan Science and Technology Bureau (No. SQ2016KJHZ0027), and the Hainan Provincial Joint Project of Sanya Yazhou Bay Science and Technology City (420LH029).

References

- Belopolsky, A., and Droxler, A. (2003). Imaging Tertiary carbonate system-the Maldives, Indian Ocean: Insights into carbonate sequence interpretation. *Lead. Edge* 22, 646–652. doi:10.1190/1.1599690
- Betzler, C., Eberli, G. P., Lüdmann, T., Reolid, J., Kroon, D., Reijmer, J. J. G., et al. (2018). Refinement of Miocene sea level and monsoon events from the sedimentary archive of the Maldives (Indian Ocean). *Prog. Earth Planet. Sci.* 5 (1), 5–18. doi:10.1186/s40645-018-0165-x
- Betzler, C., Hubscher, C., Lindhorst, S., Reijmer, J. J. G., Romer, M., Droxler, A. W., et al. (2009). Monsoon-induced partial carbonate platform drowning (Maldives, Indian Ocean). *Geology* 37, 867–870. doi:10.1130/g25702a.1
- Briais, A., Patriat, P., and Tapponnier, P. (1993b). Updated interpretation of magnetic anomalies and seafloor spreading stages in the South China Sea: Implications for the Tertiary tectonics of Southeast Asia. *J. Geophys. Res.* 98, 6299–6328. doi:10.1029/92jb02280
- Briais, A., Patriat, P., and Tapponnier, P. (1993a). Updated interpretation of magnetic anomalies and sea-floor spreading stages in the South China sea - implications for the tertiary tectonics of southeast-asia. *J. Geophys. Res.* 98, 6299–6328. doi:10.1029/92jb02280
- Chen, J., Song, H., Guan, Y., Yang, S., Pinheiro, L. M., Bai, Y., et al. (2015). Morphologies, classification and Genesis of pockmarks, mud volcanoes and associated fluid escape features in the northern Zhongjiannan Basin, South China Sea. *Deep Sea Res. Part II Top. Stud. Oceanogr.* 122, 106–117. doi:10.1016/j.dsr2.2015.11.007
- Clift, P. D., Wan, S., and Blusztajn, J. (2014). Reconstructing chemical weathering, physical erosion and monsoon intensity since 25 Ma in the northern South China sea: A review of competing proxies. *Earth. Sci. Rev.* 130, 86–102. doi:10.1016/j.earscirev.2014.01.002
- Cui, T., Xie, X., Ren, J., and Zhang, C. (2008). Dynamic mechanism of anomalous post-rift subsidence in the Yinggehai Basin. *Eart. Scie.* 33, 349–356. doi:10.3799/dqkx.2008.046
- Cullen, A. B. (2010). Transverse segmentation of the baram-balabac basin, NW Borneo: Refining the model of borneo's tectonic evolution. *Pet. Geosci.* 16, 3–29. doi:10.1144/1354-079309-828
- Dubinsky, Z., and Falkowski, P. (2011). "Light as a source of information and energy in zooxanthellate corals," in *Coral reefs : An ecosystem in transition* (Dordrecht Netherlands: Springer), 107–118.
- Eberli, G. P., and Ginsburg, R. N. (1987). Segmentation and coalescence of cenozoic carbonate platforms, northwestern Great Bahama Bank. *Geol.* 15, 75–79. doi:10.1130/0091-7613(1987)15<75:sacoc>2.0.co;2
- Esteban, M. (1996). *An overview of Miocene reefs from mediterranean areas: General trends and facies models*. Tulsa, Oklahoma: SEPM Society for Sedimentary Geology.
- Fournier, F., Borgomano, J., and Montaggioni, L. F. (2005). Development patterns and controlling factors of Tertiary carbonate buildups: Insights from high-resolution 3D seismic and well data in the Malampaya gas field (Offshore Palawan, Philippines). *Sediment. Geol.* 175, 189–215. doi:10.1016/j.sedgeo.2005.01.009
- Fournier, F., Montaggioni, L., and Borgomano, J. (2004). Paleoenvironments and high-frequency cyclicity from cenozoic south-east Asian shallow-water carbonates: A case study from the oligo-miocene buildups of Malampaya (offshore palawan, Philippines). *Mar. Petroleum Geol.* 21, 1–21. doi:10.1016/j.marpetgeo.2003.11.012
- Geel, T. (2000). Recognition of stratigraphic sequences in carbonate platform and slope deposits: Empirical models based on microfacies analysis of palaeogene deposits in southeastern Spain. *Palaeogeogr. Palaeoclimatol. Palaeoecol.* 155, 211–238. doi:10.1016/s0031-0182(99)00117-0
- Halfar, J., and Mutti, M. (2005). Global dominance of coralline red-algal facies: A response to Miocene oceanographic events. *Geol.* 33, 481–484. doi:10.1130/g21462.1
- Hall, R. (2002). Cenozoic geological and plate tectonic evolution of SE Asia and the SW pacific: Computer-based reconstructions, model and animations. *J. Asian Earth Sci.* 20, 353–431. doi:10.1016/s1367-9120(01)00069-4
- Hallock, P., and Schlager, W. (1986). Nutrient excess and the demise of coral reefs and carbonate platforms. *Palaos* 1, 389–398. doi:10.2307/3514476
- Hallock, P., Silva, I. P., and Boersma, A. (1991). Similarities between planktonic and larger foraminiferal evolutionary trends through paleogene paleoceanographic changes. *Palaeogeogr. Palaeoclimatol. Palaeoecol.* 83, 49–64. doi:10.1016/0031-0182(91)90075-3
- Jervy, M. (1988). *Quantitative geological modeling of siliciclastic rock sequences and their seismic expression*. Tulsa, Oklahoma: SEPM Society for Sedimentary Geology.
- Jovane, L., Figueiredo, J. J. P., Alves, D. P. V., Iacopini, D., Giorgioni, M., Vannucchi, P., et al. (2016). Seismostratigraphy of the Ceará plateau: Clues to decipher the cenozoic evolution of Brazilian equatorial margin. *Front. Earth Sci. (Lausanne)*. 4, 90. doi:10.3389/feart.2016.00090
- Leloup, P. H., Arnaud, N., Lacassin, R., Kienast, J., Harrison, T., Trong, T. P., et al. (2001). New constraints on the structure, thermochronology, and timing of the Ailao Shan-Red River shear zone, SE Asia. *J. Geophys. Res.* 106, 6683–6732. doi:10.1029/2000jb900322

Acknowledgments

The authors thank the captain and crew of the R/V *NH503* for their assistance with the seismic data acquisition.

Conflict of interest

The authors declare that the research was conducted in the absence of any commercial or financial relationships that could be construed as a potential conflict of interest.

Publisher's note

All claims expressed in this article are solely those of the authors and do not necessarily represent those of their affiliated organizations, or those of the publisher, the editors, and the reviewers. Any product that may be evaluated in this article, or claim that may be made by its manufacturer, is not guaranteed or endorsed by the publisher.

- Li, C. F., Li, J. B., Ding, W. W., Franke, D., Yao, Y. J., Shi, H. S., et al. (2015). Seismic stratigraphy of the central South China Sea basin and implications for neotectonics. *J. Geophys. Res. Solid Earth* 120, 1377–1399. doi:10.1002/2014jb011686
- Li, J., Fang, X., Song, C., Pan, B., Ma, Y., and Yan, M. (2014). Late Miocene–Quaternary rapid stepwise uplift of the NE Tibetan Plateau and its effects on climatic and environmental changes. *Quat. Res.* 81, 400–423. doi:10.1016/j.yqres.2014.01.002
- Lüdmann, T., Betzler, C., Eberli, G. P., Reolid, J., Reijmer, J. J., Sloss, C. R., et al. (2018). Carbonate delta drift: A new sediment drift type. *Mar. Geol.* 401 (98), 98–111. doi:10.1016/j.margeo.2018.04.011
- Ludmann, T., Wong, H. K., and Berglar, K. (2005). Upward flow of north pacific deep water in the northern South China sea as deduced from the occurrence of drift sediments. *Geophys. Res. Lett.* 32, L05614. doi:10.1029/2004gl021967
- Ma, Y. B., Wu, S. G., Lv, F. L., Dong, D. D., Sun, Q. L., Lu, Y. T., et al. (2011). Seismic characteristics and development of the Xisha carbonate platforms, northern margin of the South China Sea. *J. Asian Earth Sci.* 40, 770–783. doi:10.1016/j.jseas.2010.11.003
- Ma, Z. L., Li, Q. Y., Liu, X. Y., Luo, W., Zhang, D. J., and Zhu, Y. H. (2018). Palaeoenvironmental significance of Miocene larger benthic foraminifera from the xisha islands, south China sea. *Palaeoworld* 27, 145–157. doi:10.1016/j.palwor.2017.05.007
- Mitchum, R. M., Jr, Vail, P. R., and Thompson, S., III (1977). Seismic stratigraphy and global changes of sea level, Part 2: The depositional sequence as a basic unit for stratigraphic analysis, Seismic stratigraphy-applications to hydrocarbon exploration. *Mem. Amer. Assoc. Petrol. Geol.* 26, 53–62.
- Mutti, M., and Hallock, P. (2003). Carbonate systems along nutrient and temperature gradients: Some sedimentological and geochemical constraints. *Int. J. Earth Sci.* 92, 465–475. doi:10.1007/s00531-003-0350-y
- Posamentier, H., and Vail, P. (1988). *Eustatic controls on clastic deposition II—sequence and systems tract models*. Tulsa, Oklahoma: SEPM Society for Sedimentary Geology.
- Qin, Y., Wu, S., and Betzler, C. (2022). Backstepping patterns of an isolated carbonate platform in the northern South China Sea and its implication for paleoceanography and paleoclimate. *Mar. Petroleum Geol.* 146, 105927. doi:10.1016/j.marpetgeo.2022.105927
- Qiu, X. L., Ye, S. Y., Wu, S. M., Shi, X. B., Zhou, D., Xia, K. Y., et al. (2001). Crustal structure across the xisha trough, northwestern South China Sea. *Tectonophysics* 341, 179–193. doi:10.1016/s0040-1951(01)00222-0
- Qiu, X. L., Zeng, G. P., Yi, X. U., Hao, T. Y., Zhi-Xiong, L. I., Priestley, K., et al. (2006). The crustal structure beneath the shidao station on xisha islands of south China sea. *Chin. J. Geophys.* 49, 1565–1575. doi:10.1002/cjg2.984
- Riding, R. (2000a). Microbial carbonates: The geological record of calcified bacterial-algal mats and biofilms. *Sedimentology* 47, 179–214. doi:10.1046/j.1365-3091.2000.00003.x
- Roger, L. M., Richardson, A. J., McKinnon, A. D., Knott, B., Matear, R., and Scadding, C. (2012). Comparison of the shell structure of two tropical thecosomata (*Creseis acicula* and *diacavolinia longirostris*) from 1963 to 2009: Potential implications of declining aragonite saturation. *ICES J. Mar. Sci.* 69, 465–474. doi:10.1093/icesjms/fsr171
- Sarg, J. (1988). *Carbonate sequence stratigraphy*. Tulsa, Oklahoma: SEPM Society for Sedimentary Geology.
- Sattler, U., Immenhauser, A., Schlager, W., and Zampetti, V. (2009). Drowning history of a Miocene carbonate platform (zhuijiang formation, south China sea). *Sediment. Geol.* 219, 318–331. doi:10.1016/j.sedgeo.2009.06.001
- Schlager, W., and Purkis, S. J. (2013). Bucket structure in carbonate accumulations of the Maldives, Chagos and Laccadive archipelagos. *Int. J. Earth Sci.* 102, 2225–2238. doi:10.1007/s00531-013-0913-5
- Schlager, W., and Warrlich, G. (2010). Record of sea-level fall in tropical carbonates. *Basin Res.* 21, 209–224. doi:10.1111/j.1365-2117.2008.00383.x
- Shao, L., Cui, Y. C., Qiao, P. J., Zhang, D. J., Liu, X. Y., and Zhang, C. L. (2017). sea-level changes and carbonate platform evolution of the xisha islands (south China sea) since the early Miocene. *Palaeogeogr. Palaeoclimatol. Palaeoecol.* 485, 504–516. doi:10.1016/j.palaeo.2017.07.006
- Shi, X., Jiang, H., Yang, J., Yang, X., and Xu, H. (2017). Models of the rapid post-rift subsidence in the eastern Qiongdongnan Basin, South China Sea: Implications for the development of the deep thermal anomaly. *Basin Res.* 29, 340–362. doi:10.1111/bre.12179
- Su, R. X., Sun, D. H., Bloemendal, J., and Zhu, Z. Y. (2006). Temporal and spatial variability of the oxygen isotopic composition of massive corals from the South China Sea: Influence of the Asian monsoon. *Palaeogeogr. Palaeoclimatol. Palaeoecol.* 240, 630–648. doi:10.1016/j.palaeo.2006.03.012
- Tapponnier, P., Peltzer, G., Dain, A. Y. L., Armijo, R., and Cobbold, P. (1982a). Propagating extrusion tectonics in Asia: New insights from simple experiments with plasticine. *Geol.* 10, 611. doi:10.1130/0091-7613(1982)10<611:petian>2.0.co;2
- Taylor, B., and Hayes, D. E. (1980). “Origin and history of the South China sea,” in *The Tectonic and geologic evolution of Southeast Asian seas and islands*. Editor D. E. Hayes (Washington, DC, USA: Geophysical monograph series), 27, 23–56.
- Tcherepanov, E. N., Droxler, A. W., Lapointe, P., and Mohn, K. (2008). Carbonate seismic stratigraphy of the Gulf of Papua mixed depositional system: Neogene stratigraphic signature and eustatic control. *Basin Res.* 20, 185–209. doi:10.1111/j.1365-2117.2008.00364.x
- Tong, D., Ren, J., Lei, C., Yang, H., and Yin, X. (2009). Lithosphere stretching model of deep water in Qiongdongnan basin, northern continental margin of South China Sea, and controlling of the post-rift subsidence. *Acta Geosci. Sin.* 34, 963–974. doi:10.1016/S1003-6326(09)60084-4
- Tucker, M. E., and Wright, V. P. (2009). *Carbonate sedimentology*. Hoboken, NJ, USA: John Wiley & Sons.
- Vail, P. R., Mitchum, R. M., and Thompson, S. (1977). *Seismic stratigraphy and global changes of sea level, part 3: Relative changes of sea level from coastal onlap*. Tulsa, Oklahoma: American Association of Petroleum Geologists.
- Van Wagoner, J., Mitchum, R., Jr, Posamentier, H., and Vail, P. (1987). *Seismic stratigraphy interpretation using sequence stratigraphy: Part 2: Key definitions of sequence stratigraphy*. Tulsa, Oklahoma: American Association of Petroleum Geologists.
- Wang, C., He, X., and Qiu, S. (1979). Preliminary study about carbonate strata and micropaleontology of well xiyong-1 in the xisha islands (paracel islands). *Petroleum Geol. Exp.* 1, 23–32.
- Wang, Z., Shi, Z., Zhang, D., Huang, K., You, L., Duan, X., et al. (2015). Microscopic features and Genesis for Miocene to Pliocene dolomite in well xike-1, xisha islands. *Earth Sci.* 40, 633–644. doi:10.3799/dqkx.2015.050
- Wilson, M. E. J. (2002). Cenozoic carbonates in Southeast Asia: Implications for equatorial carbonate development. *Sediment. Geol.* 147, 295–428. doi:10.1016/s0037-0738(01)00228-7
- Wilson, M. E. J. (2008). Global and regional influences on equatorial shallow-marine carbonates during the Cenozoic. *Palaeogeogr. Palaeoclimatol. Palaeoecol.* 265, 262–274. doi:10.1016/j.palaeo.2008.05.012
- Woodroffe, C. D., and Webster, J. M. (2014). Coral reefs and sea-level change. *Mar. Geol.* 352, 248–267. doi:10.1016/j.margeo.2013.12.006
- Wu, F., Xie, X., Li, X., Betzler, C., Shang, Z., and Cui, Y. (2019). Carbonate factory turnovers influenced by the monsoon (Xisha islands, south China sea). *J. Geol. Soc. Lond.* 176 (5), 885–897. doi:10.1144/jgs2018-086
- Wu, S., Chen, W., Huang, X., Liu, G., Li, X., and Betzler, C. (2020). Facies model on the modern isolated carbonate platform in the Xisha Archipelago, South China Sea. *Mar. Geol.* 425, 106203. doi:10.1016/j.margeo.2020.106203
- Wu, S. G., Yang, Z., Wang, D. W., Lu, F. L., Ludmann, T., Fulthorpe, C., et al. (2014). Architecture, development and geological control of the Xisha carbonate platforms, northwestern South China Sea. *Mar. Geol.* 350, 71–83. doi:10.1016/j.margeo.2013.12.016
- Wu, S., Yuan, S., Zhang, G., Ma, Y., Mi, L., and Ning, X. (2009). Seismic characteristics of a reef carbonate reservoir and implications for hydrocarbon exploration in deepwater of the Qiongdongnan Basin, northern South China Sea. *Mar. Pet. Geol.* 26, 817–823. doi:10.1016/j.marpetgeo.2008.04.008
- Xie, X. O., Muller, R. D., Ren, J. Y., Jiang, T., and Zhang, C. (2008). Stratigraphic architecture and evolution of the continental slope system in offshore Hainan, northern South China Sea. *Mar. Geol.* 247, 129–144. doi:10.1016/j.margeo.2007.08.005
- Xu, G.-q., Lu, B.-q., and Wang, H.-g. (2002). Drowning event research: Insights from Cenozoic carbonate platforms in northern South China Sea. *JOURNAL-TONGJI Univ.* 30, 35–40. doi:10.1016/j.sedgeo.2009.06.001
- Yi, L., Jian, Z., Liu, X., Zhu, Y., Zhang, D., Wang, Z., et al. (2018). Astronomical tuning and magnetostratigraphy of neogene biogenic reefs in xisha islands, south China sea. *Sci. Bull.* 63, 564–573. doi:10.1016/j.scib.2018.04.001
- Zhao, Q. A., Wu, S. G., Xu, H., Sun, Q. L., Wang, B., Sun, Y. B., et al. (2011). Sedimentary facies and evolution of aeolianites on shidao island, xisha islands. *Chin. J. Ocean. Limnol.* 29, 398–413. doi:10.1007/s00343-011-0018-6
- Zhu, W. L., Xie, X. N., Wang, Z. F., Zhang, D. J., Zhang, C. L., Cao, L. C., et al. (2017). New insights on the origin of the basement of the xisha uplift, south China sea. *Sci. China Earth Sci.* 60, 2214–2222. doi:10.1007/s11430-017-9089-9
- Zhu, W., Wang, Z., Mi, L., Du, X., Xie, X., Lu, Y., et al. (2015). Sequence stratigraphic framework and reef growth unit of well Xike-1 from Xisha Islands, South China Sea. *Earth Sci.* 40, 677–687. doi:10.3799/dqkx.2015.055



OPEN ACCESS

EDITED BY

Zhigang Li,
School of Earth Sciences and
Engineering, Sun Yat-sen University,
China

REVIEWED BY

Chuang Sun,
School of Earth Sciences and
Engineering, Sun Yat-sen University,
China
Liming Dai,
OUC, China

*CORRESPONDENCE

Zhongxian Zhao,
zxzhao@scsio.ac.cn

SPECIALTY SECTION

This article was submitted to Marine
Geoscience,
a section of the journal
Frontiers in Earth Science

RECEIVED 11 August 2022

ACCEPTED 27 September 2022

PUBLISHED 10 January 2023

CITATION

He C, Zhao Z, Lee EY and Xue Y (2023),
An approach to determine brittle upper
crustal thinning: Insights into crustal
extension discrepancy in the central
part of Qiongdongnan Basin.
Front. Earth Sci. 10:1016529.
doi: 10.3389/feart.2022.1016529

COPYRIGHT

© 2023 He, Zhao, Lee and Xue. This is an
open-access article distributed under
the terms of the [Creative Commons
Attribution License \(CC BY\)](https://creativecommons.org/licenses/by/4.0/). The use,
distribution or reproduction in other
forums is permitted, provided the
original author(s) and the copyright
owner(s) are credited and that the
original publication in this journal is
cited, in accordance with accepted
academic practice. No use, distribution
or reproduction is permitted which does
not comply with these terms.

An approach to determine brittle upper crustal thinning: Insights into crustal extension discrepancy in the central part of Qiongdongnan Basin

Chao He^{1,2}, Zhongxian Zhao^{3*}, Eun Young Lee⁴ and
Yulong Xue^{1,2}

¹Hainan Key Laboratory of Marine Geological Resources and Environment, Haikou, China, ²Marine Geological Institute of Hainan Province, Haikou, China, ³Key Laboratory of Ocean and Marginal Sea Geology, South China Sea Institute of Oceanology, Chinese Academy of Sciences, Guangzhou, China, ⁴Department of Geology, University of Vienna, Vienna, Austria

Summing fault heaves is the most commonly used method to evaluate upper crustal thinning. However, since fault deformation width (W) is often assumed as a constant in the range of 75–150 km, the stretching factor estimated from fault geometry (β_f) accompanies significant uncertainty. Here we propose a new approach to determine brittle stretching factors on the foundation of numerical analyses of W and further compare our results to previous methods, with specific reference to the central part of Qiongdongnan Basin, South China Sea (SCS). Our results suggest that the value of W is generally less than 80 km and mostly less than 50 km in the northern SCS margin. We confirm that applying an overestimated value of W can lead to an underestimated amount of fault-related extension and overstatement of extension discrepancy in the rifted margin. Results also indicate an inverse discrepancy with our new method in the southeast of the basin. The difference in syn-rift sediment thickness across the rifted margin likely drove the lower crust flow causing a transition between inverse and positive extension discrepancies.

KEYWORDS

fault deformation width, crustal extension discrepancy, stretching factor β , brittle upper crustal extension, numerical modeling, Qiongdongnan basin

1 Introduction

Rifted margins are the result of thinning and breakup processes of the continental lithosphere, leading to the formation of new oceanic lithosphere. The upper crust shows complex structural patterns inherited from brittle deformation, ductile deformation, and subsidence. Fault geometry and polyphase faulting may be impacted by interactions with lower crust and mantle melting as well as mantle exhumation. This makes it challenging to resolve the crustal extension with fault growth and further understand potential hazardous earthquakes and related mechanisms of economically important

hydrocarbon accumulations (Peron-Pinvidic and Manatschal, 2019; Sapin et al., 2021). Stretching factor (β) is a key parameter to quantify the amount of thinning. Previous studies revealed that the stretching factor measured from fault heaves (β_f , Table 1) is far less than that determined by crustal thinning and subsidence analyses in rifted continental margins (Ziegler, 1983; Driscoll and Karner, 1998; Davis and Kusznir, 2004; Kusznir and Karner, 2007). This phenomenon is defined as extension discrepancy, which has been widely reported, including around the northern South China Sea (SCS) margins (Clift et al., 2002; Tsai et al., 2004; Bai et al., 2019). However, this discrepancy has remained a matter of controversy. Some authors argue that no such discrepancy exists, i.e., recognized faults are insufficient to evaluate the total amount of upper crust extension (Walsh et al., 1991; Reston, 2007; Crosby et al., 2008). There are studies, indicating that the discrepancy might be induced by unrecognized polyphase faulting (Reston, 2005), top basement faulting (Reston, 2009), and sequential faulting (Ranero and Perez-Gussinye, 2010). Furthermore, the method to calculate the stretching factor on basis of the fault heaves are highly dependent on the fault deformation width, which is not well constrained.

The practical method proposed by Davis and Kusznir (2004) to estimated β_f in the reference frame of the extended continental lithosphere is given by

$$\beta_f(x) = 1 + \beta_0 \cos \frac{2\pi(x - x_0)}{W} \quad (1)$$

$$E = \int_0^W \left(1 - \frac{1}{\beta_f(x)} \right) dx \quad (2)$$

where x is horizontal coordinate; x_0 is fault location coordinate measured from the seismic profile; β_0 is a constant determined numerically after substituting Eq. 1 into Eq. 2; E is the amount of extension which is also measured from the profile; W is fault deformation width; which is built on basis of an assumption that W is known as a constant in the range of 75–150 km (Roberts et al., 1993; Davis and Kusznir, 2004). Whereas, the assumption ends up with same values of β_f among different faults, as long as E and W stay constant. For instance, on the condition of same amount of extension, low-angle normal fault in deep-water and

steep fault in shallow water share the same values of β_f . This error in estimating brittle extension, in turn, questions the extension discrepancy. Therefore, better constraints on upper crustal thinning are required. In this study, we propose a new approach to brittle extension on the foundation of numerical analyses of W . We verify our approach by comparing it to conventional methods. Our new methods are applied to the central part of Qiongdongnan Basin which was magma-poor during rifting with no obvious evidences of asthenospheric melting (Clift and Sun, 2006). The optimization of W is aimed at improving the estimation accuracy of the upper crustal thinning and further investigations of both positive and negative extension discrepancies.

2 Geological setting

The SCS is the largest marginal sea in the west Pacific and surrounded by the Eurasian, Pacific and Indian Plates. The tectonically complex history was due to its position, affected by the opening of SCS (Taylor and Hayes, 1983; Briaies et al., 1993), Red River strike-slip fault (Tapponnier et al., 1990; Leloup et al., 2001; Morley, 2002; Searle, 2006), oblique compression of Philippine Plate (Rangin, 1991; Hall et al., 1995), and back-arc spreading associated with the subduction of Pacific Plate to Eurasian Plate (Taylor and Hayes, 1980; Packham, 1996). Multi-stage rifting processes have taken place in the northern SCS margin, which transformed from active continental margin in the Mesozoic to passive margin in the Cenozoic (Savva et al., 2014). Due to a lack of seaward dipping reflectors (Barckhausen and Roeser, 2004; Franke et al., 2014; Brune et al., 2016), the northern SCS margin was classified into non-volcanic margin. With an advance in understanding of seismic and drilling data, the opinion about rifting-related magmatism is changing recently (Larsen et al., 2018; Sun et al., 2018; Ding et al., 2020; Li et al., 2022). However, general consensus so far is that the margin was not as magma-rich as NE Atlantic margins. The northern margin ranging from the South China Block to the oceanic crust of SCS covers a total width of over 400 km (Figure 1A). Three NE-trending extensional basins spread from east to west; Taixinan Basin, Zhujiangkou Basin and Qiongdongnan Basin.

TABLE 1 Stretching factors related to this study.

Symbol	Quantity
β	Stretching factor defined by McKenzie (1978) which is uniform in upper crust and whole crust based on pure shear model
β_{uc}	Upper crustal stretching factor
β_c	Whole crustal stretching factor
β_f	Upper crustal stretching factor based on summing fault heaves (Davis and Kusznir, 2004)
β_z	Upper crustal stretching factor based on dividing into zones (Zhao et al., 2018)
β_w	Upper crustal stretching factor based on fault deformation width

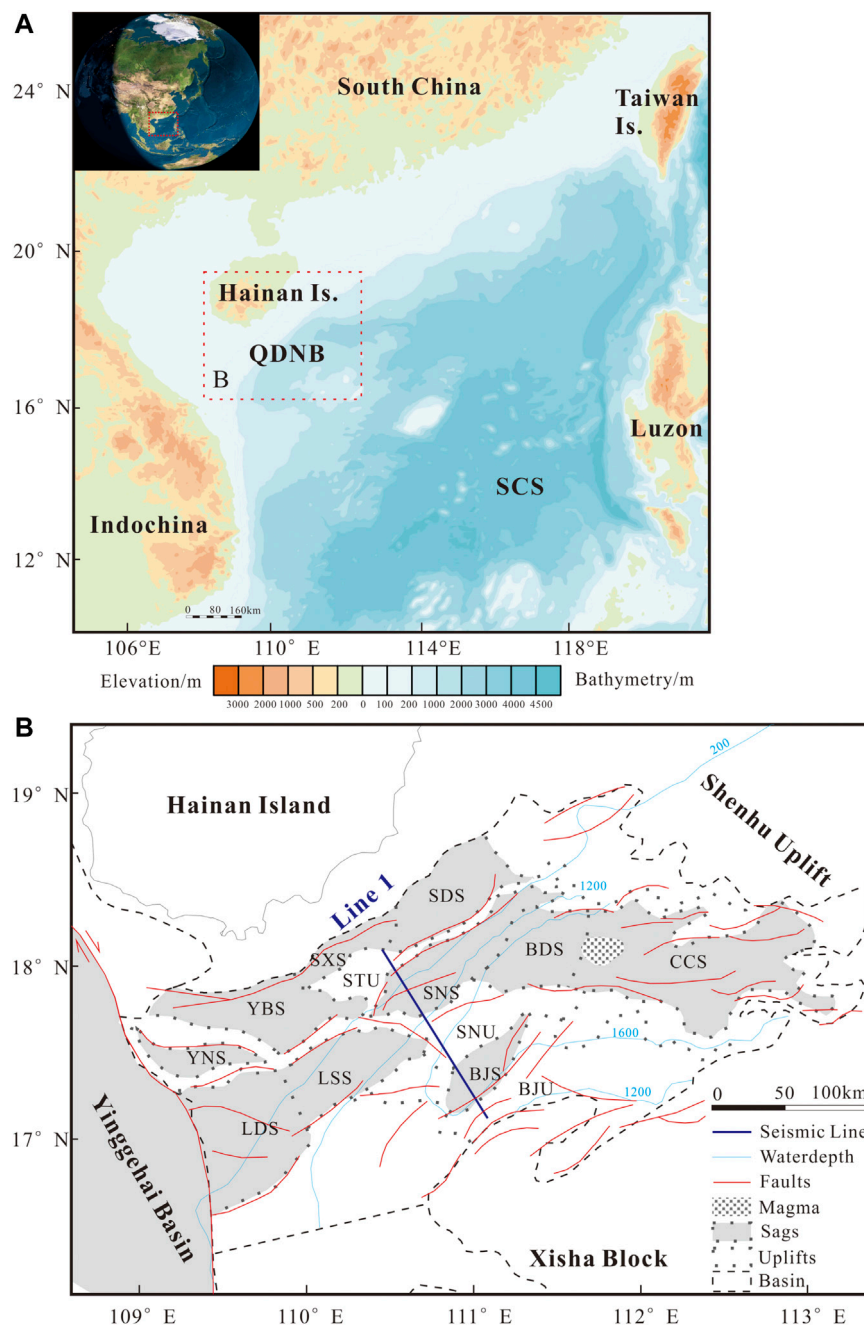


FIGURE 1

(A) Topography and bathymetry of the South China Sea (SCS) in the western Pacific. (B) Structural map of the Qiongdongnan Basin (QDNB; see location in Figure 1A). Location of a deep-reflection multichannel seismic profile (Line 1) across the central part of QDNB is shown. YNS, Yacheng Nan Sag; YBS, Yacheng Bei Sag; SXS, Songtao Xi Sag; SDS, Songtao Dong Sag; LDS, Ledong Sag; LSS, Liushui Sag; SNS, Songtao Nan Sag; BDS, Baodao Sag; CCS, Changchang Sag; BJS, Beijiao Sag.

The Qiongdongnan Basin on the northwest continental slope of SCS is located between Hainan Island in the northwest and the Xisha block in the southeast, which is featuring a narrow shelf and slope (Figure 1). The water depth deepens dramatically from 200 to 1,200 m at the Center Depression. The syn-rifting stage occurred

from ~45 Ma to ~23 Ma, followed by the post-rift period. The unconformity formed at ~23 Ma separates the basin evolution into two distinct stages: Paleocene, Eocene and Oligocene syn-rifting and Early Miocene to Quaternary post-rifting (Zhang et al., 2013). The syn-rift stage is characterized by well-developed NE-trending faults.

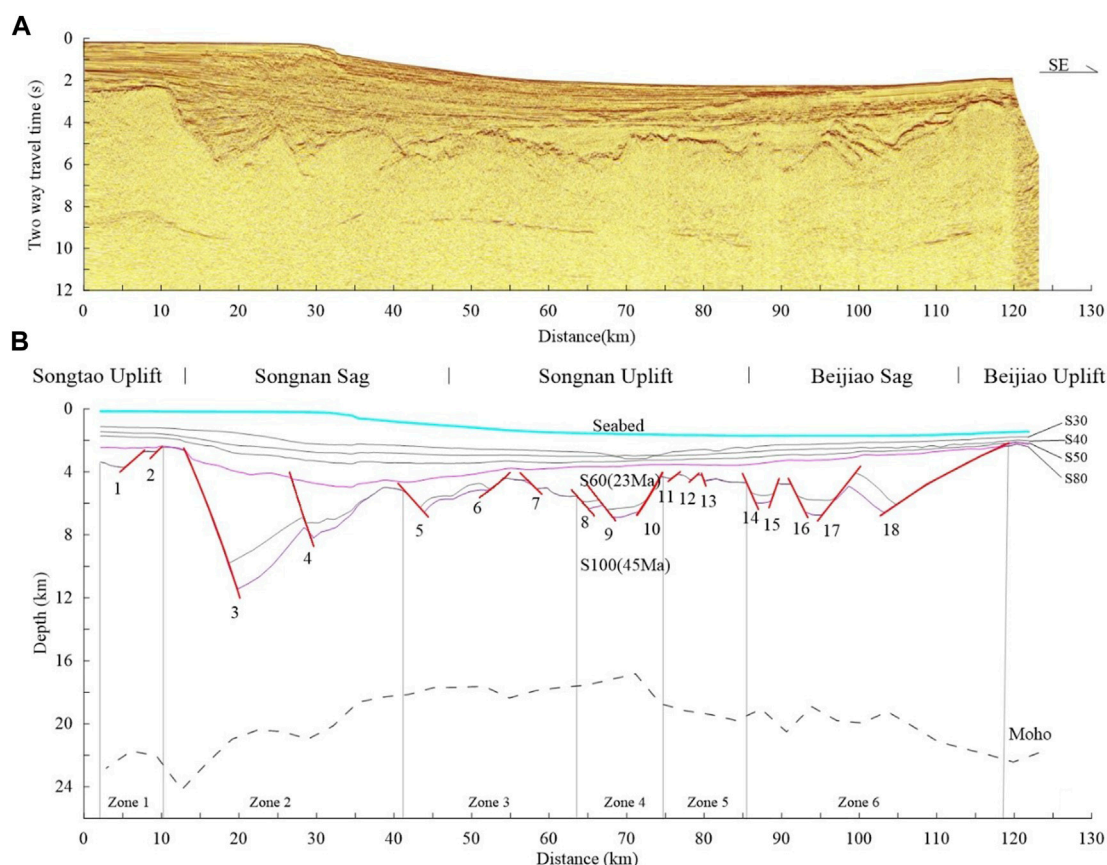


FIGURE 2

(A) Seismic profile of Line 1 (see location in Figure 1B). (B) Interpretation of Line 1 showing the Moho depth, major unconformities (S100–S30), and overall recognized 18 planar normal faults tilting SE and NW (F1 to F18). The unconformities of S100 (~45 Ma) and S60 (~23 Ma) are indicated.

In the eastern part, however, nearly EW-trending faults are present and rift-related magmatism was reported in the Changchang Sag (Figure 1B). In the western part, a large scale detachment fault cutting the Moho was identified, which is connected to the adjacent Red River Fault Zone (Zhao et al., 2018). Previous studies have focused on the distinct differences between the eastern and western Qiongdongnan Basin, including but not limited to structure (Zhang et al., 2013), sedimentation, subsidence (Zhao et al., 2013) and mechanism (Zhao et al., 2015).

3 Materials and methods

3.1 Seismic data

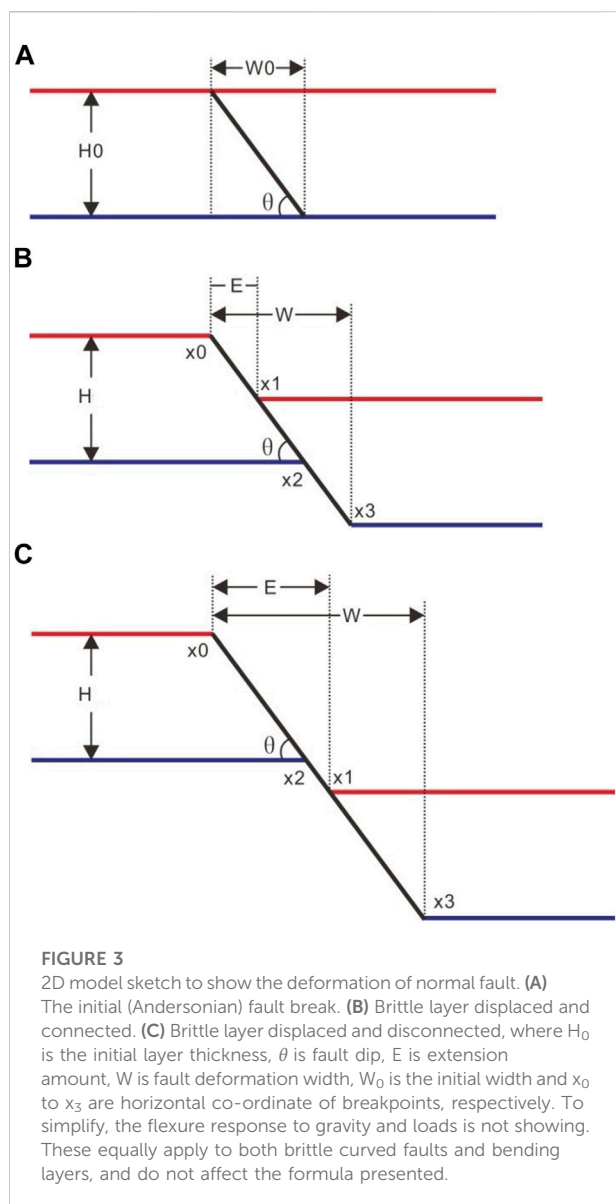
The deep-reflection multichannel seismic Line 1, provided by China National Offshore Oil Corporation, was chosen for this study (see location in Figure 1B). The profile is perpendicular to the structural strike and well-developed faults in the central part of Qiongdongnan Basin. Eighteen planar normal faults (F1 to F18;

Figure 2) developed during the rifting were identified, which show variability in dips and sizes. F18 at the southeast end is the largest fault with greatest offset and low-angle dip. F3, F13, and F15 have steeper dip angles with $\theta > 50^\circ$. These faults, tilting SE and NW, compose a graben and half-grabens which exhibit features of both symmetric and asymmetric geometry. The profile recorded reflectors of the stratigraphic unconformities and Moho depth with discontinuity. The unconformities at S100 (~45 Ma) and S60 (~23 Ma) correspond to the start and end of the syn-rifting, respectively.

3.2 Stretching factor evaluation with new method

3.2.1 Initial model setup

In the 2D model of brittle upper crust (Figure 3A), the instantaneous stretching is supposed as two results: brittle layer connected (Figure 3B) and disconnected (Figure 3C). The rotation of faults or beds (i.e., the dip maintains during



thinning) was not counted for this model, as the brittle faults in deformation response incline to vertical shear, rather than the domino-style (Anderson, 1951; Westaway and Kusznir, 1993; Davis and Kusznir, 2004).

The stretching factor β is defined as the ratio of the final length to the initial length by Mckenzie (1978), which is shown in Figure 3:

$$\beta = \frac{W}{W_0} \quad (3)$$

Figure 3A shows the simple trigonometry:

$$W_0 = \frac{H_0}{\tan \theta} \quad (4)$$

From the geometry illustrated in Figures 3B,C, if taken $x_0 = 0$:

$$W = x_3 = \frac{H_0}{\tan \theta} + E \quad (5)$$

Thus, substituting Eqs 4, 5 into Eq. 3 yields the average β :

$$\beta = 1 + E \times \tan \frac{\theta}{H_0} \quad (6)$$

Hence, both values of deformation width (W) and stretching factor (β) are highly dependent on the initial brittle crustal thickness and fault attitude. W is positively proportional to initial layer thickness (H_0) and extension amount (E), and inversely proportional to dip (θ). β is the opposite of W .

Given that H is the layer thickness after stretching, $x_0 = 0$, $x_1 = E$, $x_2 = H_0/\tan \theta$ and $x_3 = x_2 + E$, H in case of fault displaced and connected (Figure 3B), is determined:

$$H = \begin{cases} H_0 - x \times \tan \theta & (0 \leq x < x_1) \\ (x_2 - x_1) \times \tan \theta & (x_1 \leq x < x_2) \\ H_0 - (x_3 - x) \times \tan \theta & (x_2 \leq x \leq x_3) \end{cases} \quad (7)$$

H where fault displaced and disconnected (Figure 3C) is as follows:

$$H = \begin{cases} H_0 - x \times \tan \theta & (0 \leq x < x_1) \\ 0 & (x_1 \leq x < x_2) \\ H_0 - (x_3 - x) \times \tan \theta & (x_2 \leq x \leq x_3) \end{cases} \quad (8)$$

Combined with Eqs 7, 8, any horizontal coordinate (x) is given on account of the fact that measured vertical lengths are more reliable than horizontal lengths (Davis and Kusznir, 2004):

$$\beta(x) = \frac{H(x)}{H_0} \quad (9)$$

3.2.2 Parametric analysis

Quantitative analysis of W and β in different faulting geometries was conducted by applying Eqs 5–9, respectively. Sensitivity analysis of each individual parameter (H_0 , θ , E) based on Eqs 6–9 is given in Supplementary Figures S1–S3. H_0 was examined from 5 km to 50 km with an increment of 5 km at each step in Figures 4, 5. At thicknesses over 50 km, a change of H_0 had little impact on the outcome (Supplementary Figure S1).

Figure 4 presents plots of varying W values in the parameter domain space (dip–offset) with a set of initial thickness values ($H_0 = 5, 10, \dots, 50$ km). The contour-plots show that the deformation width increases with the initial thickness in general. But it highlights that H_0 has limited effect on W after $H_0 = 30$ km. When $H_0 = 5$ km–20 km, W changes exponentially at the central of the domain and linearly at the upper left and bottom of the domain. Specifically, in the case of $H_0 = 5$ km, W is a single variable with dip when ($\theta < 5^\circ$). As the dip goes steeper ($5^\circ < \theta < 12^\circ$), W is linear increasing with offsets at beginning ($E < 10$ km), then this trend changes to exponential growth. As long as $\theta > 45^\circ$, the trend converts back into linear growth. Overall, the exponential changes gradually

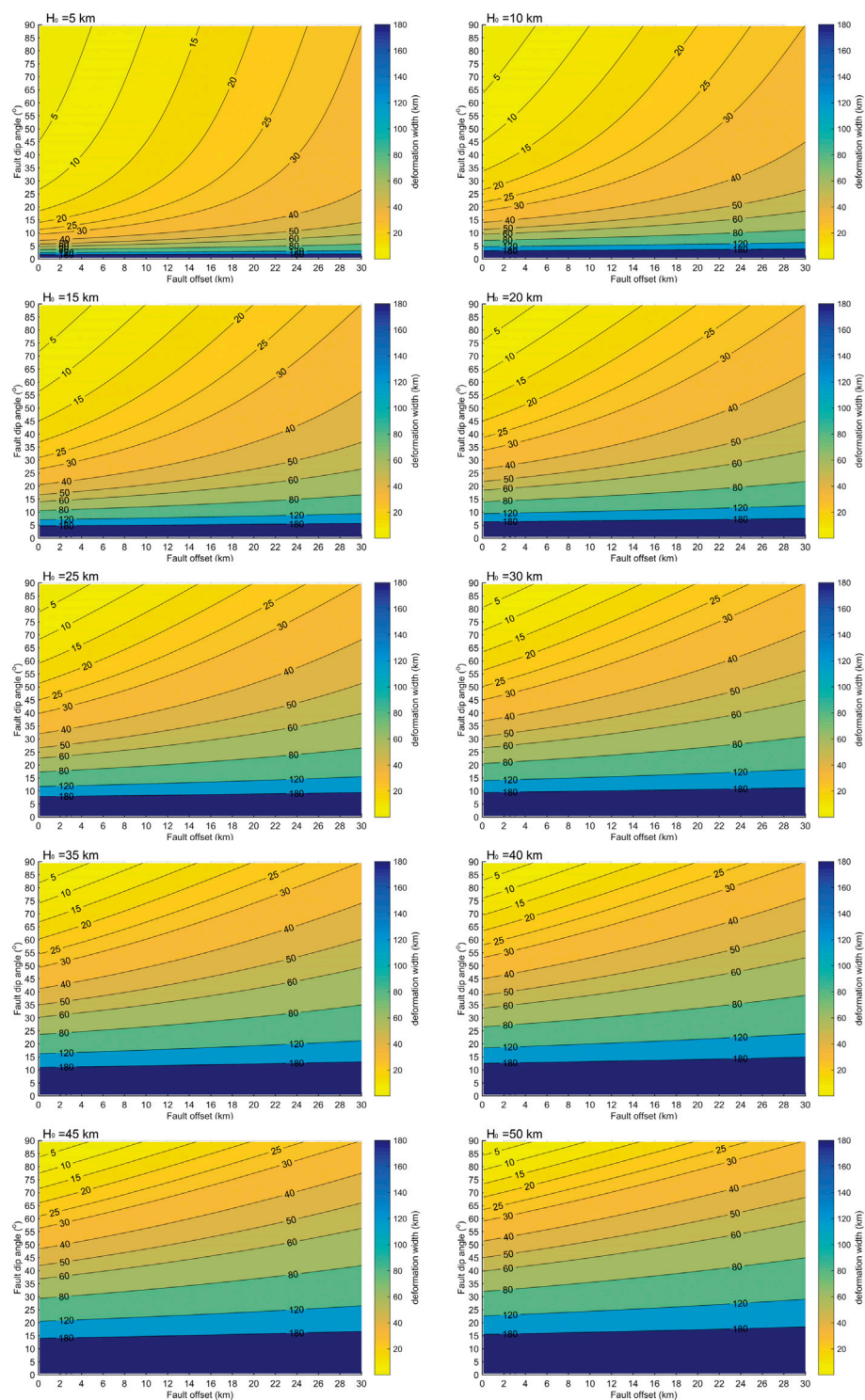


FIGURE 4
Comparison of deformation width (W) contour-plots in the parameter domain space (dip-offset) are shown at $H_0 = 5$ km, 10 km, 15 km, 20 km, 25 km, 30 km, 35 km, 40 km, 45 km, and 50 km.

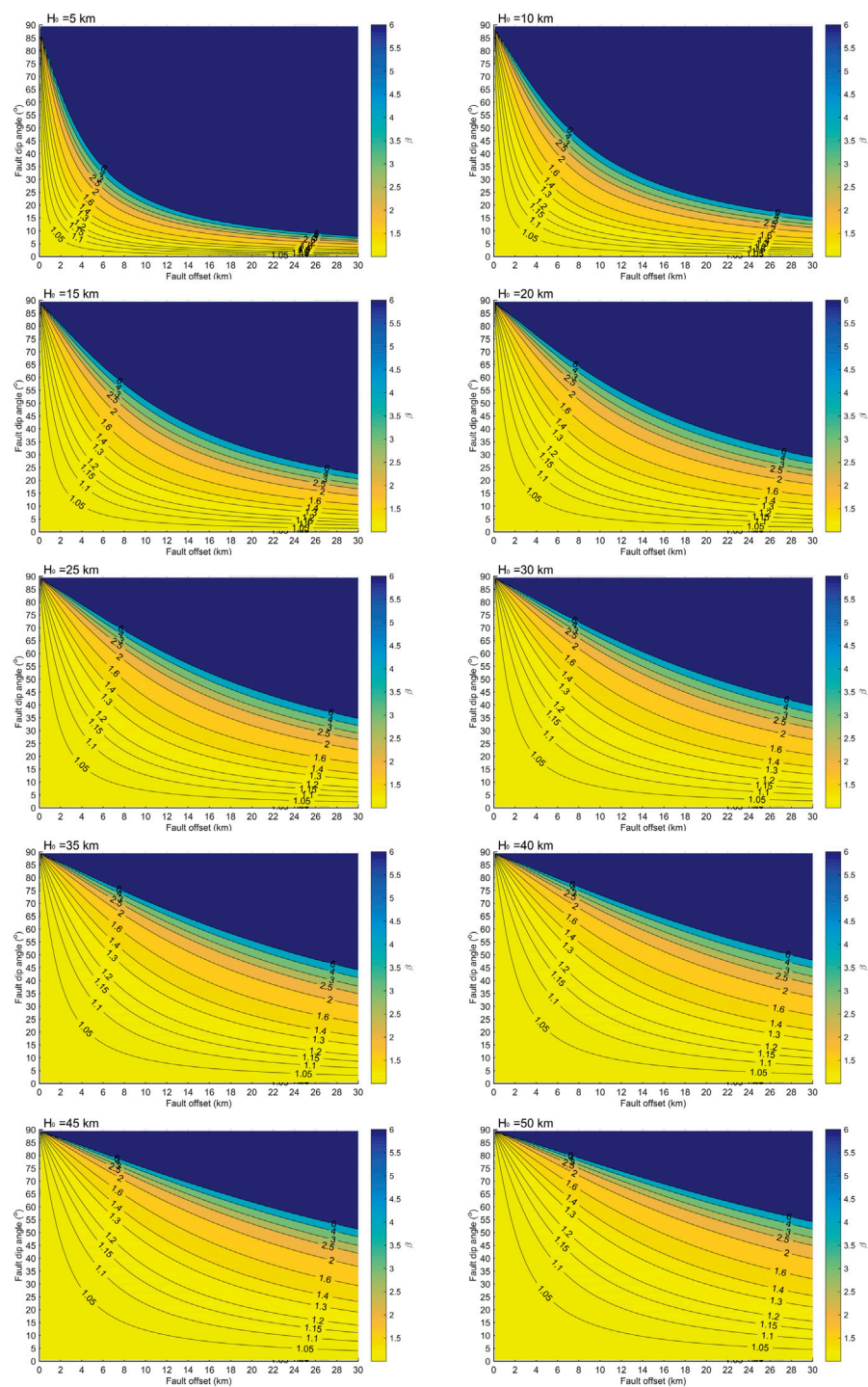


FIGURE 5 Comparison of β contour-plots in the parameter domain space (dip-offset) are shown at $H_0 = 5$ km, 10 km, 15 km, 20 km, 25 km, 30 km, 35 km, 40 km, 45 km, and 50 km.

to linear as H_0 increases. After H_0 reaches 40 km, the contours of W are characterized by linearly distribution. In practice, the value of W of subhorizontal listric fault should be larger than 120 km whether large or small scale (Figure 4 $H_0 = 10$ km).

Figure 5 depicts β values in the parameter domain space (dip-offset) with the same set of initial thickness values ($H_0 = 5, 10, \dots, 50$ km). The contour-plots show that β decreases rapidly with increasing $H_0 = 5\text{--}30$ km, then decreases slowly. With an increasing H_0 , β shows a transition from exponential decline to linear decline curves, particularly in the upper right part of the domain. In practice, high angle normal faults with small scale and low angle faults of large offsets achieve the same degree of thinning.

3.2.3 β function

White and McKenzie (1988) expressed β with a Gaussian function. On the basis of E measured from fault heaves, $\beta(x)$ is mapped to a profile of β applying the continuous cosine function Eq. 1 (Davis and Kuszniir, 2004). The form and width of the function, which does not alter the total extensions, are arbitrary and not critical (Davis and Kuszniir, 2004). Based on these previous studies and line-types of β curves shown in Supplementary Figures. S1–S3, we choose a sine function after comparing with Eq. 1, which is defined as:

$$\beta_w(x) = 1 + \beta_0 \left[\sin\left(\frac{\pi x}{2W} + \frac{\pi}{4}\right) - \sin\frac{\pi}{4} \right] \quad (10)$$

Replacing W in Eq. 10 by Eq. 5 gives the β_w as follows:

$$\beta_w(x) = 1 + \beta_0 \left[\sin\left(\frac{\pi \tan \theta x}{2H_0 + 2E \tan \theta} + \frac{\pi}{4}\right) - \sin\frac{\pi}{4} \right] \quad (11)$$

As it is shown in Figure 6, the calculated curves using Eq. 11 are generally consistent with corresponding curves estimated from Eq. 9, slightly higher in the middle and lower in both flanks. This numerical approach incorporates the role of fault deformation width (W), which is neglected in the early model and leads to an underestimation of upper crustal stretching factor. This difference has implication on the evolution and development of rifted basins and margins. Moreover, faults are assumed to be planar in the model of Davis and Kuszniir (2004). Since listric faults are common in the Qiongdongnan Basin as shown in Line 1 (Figure 2), this sine function is adequate to approximate faulting patterns in the study area.

3.3 Stretching factors of upper and whole crust in the central part of Qiongdongnan Basin

The stretching factors of the upper crust (β_{uc}) along Line 1 are estimated using three methods: the aforementioned method (β_w), as well as methods based on fault geometry (β_f) (Davis and

Kuszniir, 2004) and zone division (β_z) (Zhao et al., 2018). Parameters for each fault and zone (Figure 2B) are given in Table 2.

In Eqs 5–9, the initial thickness of the brittle layer (H_0) is unknown. It is usually infeasible to estimate, because the transition of brittle and ductile crust is difficult to identify on the seismic profile. To assess the range of reasonable values, we propose 10 km as the H_0 minimum, which corresponds to ~33% of the initial whole crust thickness in the west of Qiongdongnan Basin (~22–40 km; Zhao et al., 2018) as the case of the northern SCS at the Early Cenozoic suggested by Dong (2020). It also conforms to the 10–15 km range suggested for the transition depth of brittle and ductile crust in the present South China Block (Zuber et al., 1986; Clift et al., 2001). Furthermore, since faults do not cut through the Moho as shown in Figure 2A, thus we propose the present crust thickness (CT) at the breaking point (x_2 in Figures 4B,C) on the footwall as the H_0 -maxima (Table 1; for $H_0 = CT$ in Figure 7A). In Eqs 1, 2, since W has been assumed ranging of 75–150 km, we also evaluate W at 150 km and 75 km. To account for the unrecognized or small-scale faults below the seismic resolution, the amount of fault heaves (β_f) is increased by 40% (Walsh et al., 1991).

The whole crust stretching factor (β_c) is defined as the ratio of the initial crust thickness to the final crust thickness. The pre-rifted crustal thickness of the northern SCS margin is assumed to be 32 km in this study (Zhao et al., 2018). The thicknesses of syn-rift (45–23 Ma), and post-rift (23–0 Ma) sediments are estimated using two-way travel time (TWT) of the seismic data (Figure 2A). The time-depth conversion of the stratigraphic sequences is based on VSP data (Zhao et al., 2015). The crustal thickness is derived by assuming an average crustal P-wave velocity of ~6.5 km/s as previous studies (Zhao et al., 2015).

4 Results

4.1 Upper crust thinning

In the upper crust, β_w is 1–2.4 by assuming $H_0 = CT$, while β_w varies from 1 to 3.3 by applying $H_0 = 10$ km to all faults (Figure 7A). The curve of β_w ($H_0 = 10$) exhibits β -maxima at a distance of ~95 km with the highest frequency variation among all the three methods on upper crust.

β_f shows a smooth function curve between 1.6 and 2.0 with $W = 150$ km for each fault set and between 1.7 and 2.3 with $W = 75$ km, while it expands to 1.4–2.9 with $W = 20$ km (Figure 7A). When applying lower values of W from 150 km to 20 km, the variation of β_f is gradually amplifying; e.g., when $W = 20$ km, a peak of $\beta_f = \sim 2.9$ is indicated at the distance of ~100 km. The curve of β_f ($W = 150$ km) exhibits near-symmetry, while that of β_f ($W = 20$ km) is characterized by asymmetry. All three β_f -minima exceed those of β_w and β_z as the result of correction.

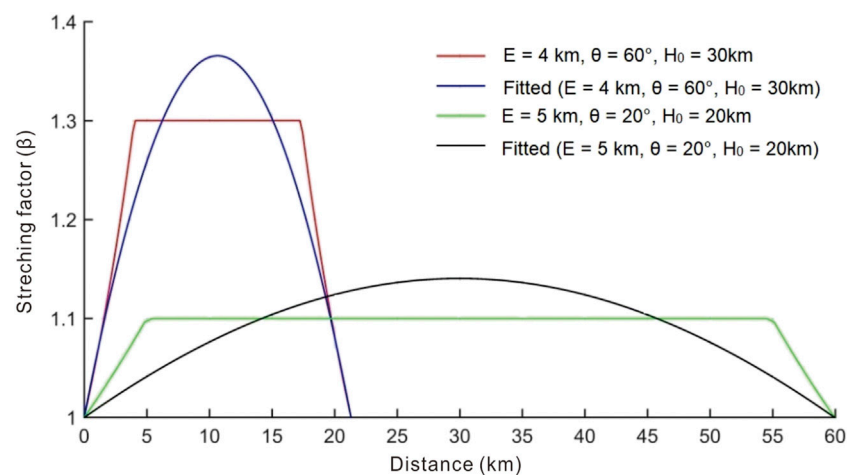


FIGURE 6

Two β profiles generated by Eq. 9 under the given of two parameter sets are shown in red and green, respectively. The best fit β curves by Eq. 11 with the corresponding parameter sets are presented in blue and black.

TABLE 2 Parameters of faults (F1 to F18 in Line 1; see location in Figure 2). Zone length, zone offset and β_z of six zones (Figure 2B) are provided.

Fault num	Loc. (km)	Dip dir	Dip (°)	Offset (km)	H ₀ (km)	Zone	Zone length (km)	Zone offset (km)	β_z
1	7.6	left	23.2	2.4	17.4	1	10.6	3.0	1.4
2	9.9	left	26.8	0.6	16.6				
3	12.9	right	52.9	6.7	15.6	2	28.5	9.9	1.5
4	26.5	right	50.6	3.2	13.2				
5	41.3	right	26.6	2.5	10.3	3	22.2	5.4	1.3
6	54.2	left	23.2	1.8	12.0				
7	57.5	right	27.7	1.0	11.7				
8	63.8	right	31.7	1.3	12.3	4	10.8	5.3	2.0
9	66.7	right	33.5	1.6	13.0				
10	74.4	left	41.7	2.5	13.8				
11	76.6	left	21.1	0.9	13.6	5	11.1	2.1	1.2
12	79.1	left	20.9	0.9	13.3				
13	79.8	right	54.4	0.3	13.3				
14	85.5	right	48.3	1.1	13.3	6	33.4	22.7	3.1
15	89.3	left	55.6	0.7	13.7				
16	91.3	right	45.0	1.8	14.1				
17	99.6	left	31.9	4.4	16.2				
18	117.9	left	15.9	14.7	19.2				

β_z values of six zones (1.2–3.1; Table 1) are presented in Figure 7A. Compared to the other curves, β_z is shown as a stepwise line with large $\Delta\beta_z$, since values are estimated on the basis of averaging the exaggerated geometry of trough and crest in each zone.

4.2 Crustal thickness and thinning

Along Line 1, the crust thickness shows a large variation ranging from maxima of >20 km at the basin margins to a minimum of <10 km at a distance of ~20 km (Figure 7B).

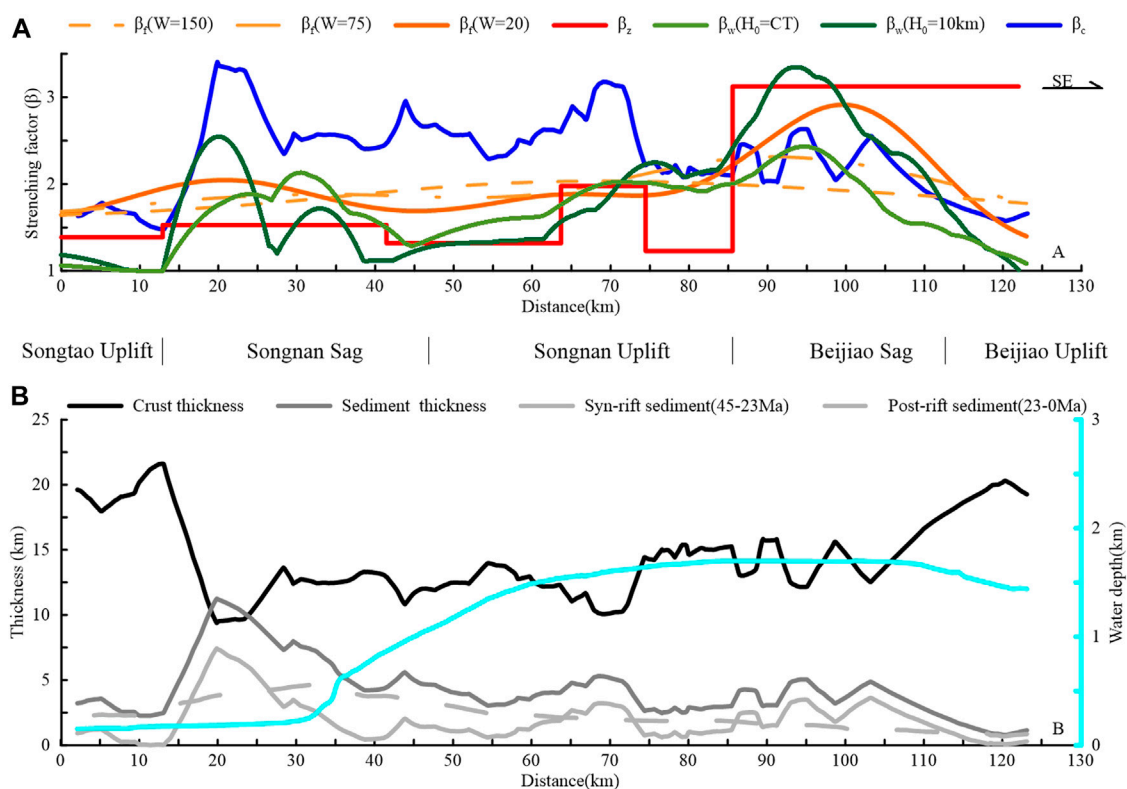


FIGURE 7

(A) β -Profiles along Line 1, evaluated by different methods and parameters. (B) Crust thickness, sediments thickness and water depth along Line 1. Sediment thicknesses of the total, syn-rift and post-rift are shown. The crust thinned sharply from 21.6 to 9.4 km over a ~7 km distance at the north of Songnan Sag, which corresponds to the transition of thickest to thinnest crust.

The thinner crusts of ~10 km at the two flanks of Songnan Sag and Songnan Uplift correspond to the maxima of β_c . Between the distance of 20 and 110 km, the thickness varies around ~12.5 km with a slight increase from ~10 km to ~15 km.

In Figure 7A, the extension discrepancy is indicated at a distance of c. 20–70 km, which is significant in the center of Songnan Sag and Songnan Uplift. However, it appears to be ambiguous in the Beijiao Sag and Southern Uplift where the water depth stabilizes at ~1.6 km.

5 Discussion

5.1 Role of fault deformation width in estimating brittle crustal stretching factor

Fault deformation width (W) has been an unknown parameter and cannot be calculated (Roberts, 1993; Davis, 2004; Zhao, 2018), which is fundamentally important in determining the stretching factor of brittle crustal extension. Roberts (1993) set up W as constant of

75–150 km for contrastive analysis of backstripping and forward modelling in the North Sea, and it has since been adopted as default by subsequent works. However, the assumption contains potential uncertainties, because it is disregarding differences in faults heaves, dips and initial brittle crustal thicknesses. To capture the uncertainty derived from using the constant W range, we revisit the conventional method (Davis and Kusznir, 2004) and evaluate the role of W (Figure 8). Theoretically, applying the most favorable W value in the suggested range (75–150 km) to one single fault leads to $\Delta\beta_f = 0.14$ at most. W , therefore, seems to have negligible impact on β_f . However, its importance becomes more apparent as it decreases, e.g., $\Delta\beta_f = 0.8$ if a maximum of 150 km and a minimum of 20 km are assigned to W . Even a proposed value of W ($W = 75$ km) results in a substantial underestimation (i.e., $\Delta\beta_f = 0.7$).

Our results indicate that W is generally less than 80 km and narrow it down to the range of 10–60 km even in the marginal case of $H_0 = 50$ km with dip in the range of 30°–75° (Figure 4). Since the ductile-brittle transition is suggested between 10 and 15 km in the modern South China Block (Zuber et al., 1986; Clift et al., 2001), the W value in the

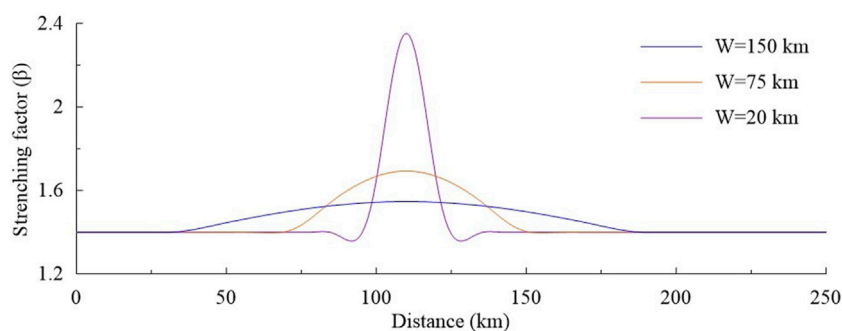


FIGURE 8
 β -Profiles generated from different values of W and the same single fault based on Eqs 1, 2, all with 40% correction.

northern SCS is proposed as less than 50 km (extreme case is $H_0 = 15$ km in Figure 4). As we decrease $W = 150$ km to $W = 20$ km, the trend of β_f curves changes to multi-wave converging towards the functions of β_z and β_w as shown in Figure 7A. Our findings demonstrate that W is an important control on the brittle extensional estimation, but has been overestimated in previous studies. A lower W value than the conventionally used range may lead to more accurate model outcomes. The discord is likely a critical cause for underestimation of the upper crustal stretching factor.

Stretching estimation based on current fault geometry shown in seismic image is insufficient to evaluate the brittle upper crust thinning due to undetected faulting. According to Reston (2005; 2007), polyphase faulting incurs geometric changes such as shallower-dipping, which could be crosscut by steeper normal faults developed in later stages. The extension by unrecognized faulting is generally corrected by increasing its value by a factor of 40% (Walsh et al., 1991). However, since more complex fault geometries have experienced larger heaves and stronger deformation, a different degree of correction is required in consideration of geometric complexity (Clift et al., 2001), and *vice versa*. Our method improves this accuracy by numerical analyses of W (Figure 7A). Our results show that β_f at $W = 150$ stays mostly uniform over the entire profile with a slight maximum in the Songnan Sag, but peaks of β_f curves at lower W values were recorded in the Beijiao Sag, with 2.3 for $W = 75$ and 2.9 for $W = 20$, respectively (Figure 7A). The peaks correspond to the β_z trend, which shows the highest value in the Beijiao Sag and the second highest value in the Songnan Sag (Figure 7A). Although β_z is less accurate by exaggerating both maxima and minima, it is advantageous to see the overall variation trend with limits.

5.2 Limitations

Our methodology underlines the importance of W , which is beneficial to estimate the upper crustal extension and can be applied

to other studies on brittle extension. However, if the estimation requires sophisticated controls for the extension over time and depth, some improvements are required. Above all, the rotation of faults or beds has to be considered as the stretching factor β_d is based on a domino-style fault block model, which can contribute critically to avoid underestimation of β_f as well as the uncertainty of extension discrepancy. Several studies have indicated that initial dips of normal faults may subsequently rotate to shallower ones due to isostatic response (Spencer, 1984; Wernicke and Axen, 1988), particularly faults with large offsets (Buck, 1988), i.e., their initial dips are larger than the current dips identified from profiles. A numerical simulation model by Lavier and Manatschal (2006) confirmed that steep normal faults rotate to conjugate concave downward faults, which lead to crust thinning at magma-poor margins. A balanced kinematic model proved that sequential faulting turns high-angle normal faults into low-angle ones as accommodation of thinning, which is limited by lower crust, deforming in response to upper crust in the cold basin or lithosphere (Ranero and Perez-Gussinye, 2010). For instance, we infer that the original dip of F18 with offset up to ~ 14.7 km could be much higher than 15.9° . It is supported by the cases that normal faults in the brittle upper crust develop at dips $\theta > 45^\circ$ and stay active at dips $\theta \geq 30^\circ$ with offset < 10 km (Anderson, 1951; Byerlee, 1978; Sibson, 1985; Buck, 2007; Reston, 2007). This is one potential cause for the drastic drop of β_w in the Beijiao Sag and Beijiao Uplift. Another aspect to consider is the inapplicability of heat flow on older basins and underestimation of crustal thinning affected by asthenospheric melting. During the rifting, heat flow increases due to lithosphere thinning and rising of the asthenospheric mantle, which is closely associated with the crustal stretching, flexural uplift, and subsidence. The thermal effect of depositing cold sediments on top of the lithosphere leads to a depression in the thermal gradient, extending down into the lithosphere (the thermal blanketing effect) (Karner, 1991; Kim et al., 2020). Such lithospheric and asthenospheric-scale mechanisms during rifting require comprehensive considerations of the thermal evolution in our numerical methods.

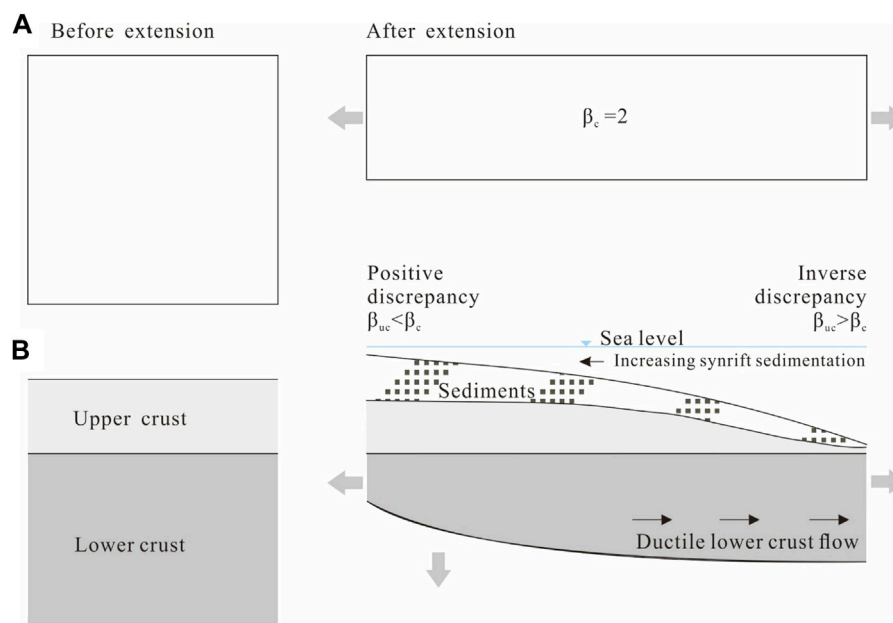


FIGURE 9

(A) Cross sectional area remains constant before and after extension; (B) Schematic illustrations showing that the pressure by variation of sediment thickness drives the ductile lower crust flowing.

5.3 Insights into extension discrepancy

The extension discrepancy has been widely reported in the northern SCS (Clift et al., 2002; Tsai et al., 2004; Bai et al., 2019). In this study, significant extension discrepancy was also indicated at the distance of c. 20–70 km of Line 1 (Figure 7A), which corresponds to the Songnan Sag and Uplift characterized by asymmetrical half-grabens. In the Beijiao Sag which is dominated by grabens, positive extension discrepancy is indicated by β_f when applying $W = 150$, while inverse discrepancy is widely discovered when evaluating β_f with $W = 20$. We infer that the extension discrepancy in previous studies is over-predicted by an overestimated W . The inverse discrepancy has so far been overlooked in the northern SCS. A balancing of positive discrepancy and inverse discrepancy along the extension direction supports the presence of crustal extension discrepancy, as the same amount of thinning is expected across the entire profile at crustal scale (Reston, 2007), i.e. cross sectional area of crust along the extension direction maintains the uniform β during syn-rifting and post-rifting (Figure 9A).

Depth Dependent Stretching (DDS) or Depth Dependent Thinning (DDT) (Royden and Keen, 1980; Rowley and Sahagian, 1986; Roberts et al., 1993; Kusznir and Karner, 2007) seems to be the convincing model to explain the mechanism of extension discrepancy. However, the depth dependence at lithospheric level is unsuitable to explain the estimation in the central part of

Qiongdongnan Basin where a local positive discrepancy is located next to a local inverse discrepancy. The potential explanations for inverse discrepancy include: 1) upper plate (hanging wall) of detachment fault of simple shear (Wernicke, 1985) which is in conflict with the observation showing symmetric grabens and asymmetric half-grabens, being firstly excluded. 2) top-down break up (Anderson, 2001). i.e., the first degree break-up of upper crust precedes that of lower crust as tensile stress instead of magmatism upwelling from asthenosphere takes charge. This is an attractive interpretation since the magmatism upwelling did not occur in the central part of Qiongdongnan Basin during rifting. However, this model suggests that the upper crust thinning is greater than that of lower crust, which results in an inverse discrepancy at the thinnest whole crust location (Reston and McDermott, 2014). It does not fit in the study area that a positive discrepancy is described at the thinnest crust. Moreover, previous studies (Davis and Kusznir, 2004) suggested that the breakup of lithosphere inclines to bottom up in the deep-water area, like the Beijiao Sag. 3) lower crust flow in hot lithosphere like northern SCS (Figure 9B). During rifting, the syn-rift sediments were deposited up to ~8 km in the northwest (Figure 7B), which is closer to Hainan Island and exhibits positive discrepancy. The inverse discrepancy is predominant in the southeast where it shows relatively thin thickness of syn-rift sediments (up to 4 km; Figure 7B). Compared to the northwest, the southeast area was far away from provenance. Such variation in sediment thickness

could contribute to a laterally differential pressure, which might drive the lower crust flow causing transitions between inverse and positive discrepancies. The ductile lower crust is generally inclined to flow along the rifting direction (McKenzie and Jackson, 2002). This is an elementary impact since sediment thickness is also dependent on subsidence associated with tectonic processes and thermal effects, which we will investigate further to understand the mechanism in the future studies.

6 Conclusion

We evaluate the role of fault deformation width in estimating upper crust extension. This parameter plays an important role in the determination of upper crustal stretching factor. Our results suggest that the value of W has often been overestimated in previous studies, and should be less than 80 km in general and less than 50 km in the northern SCS. The overestimated value of W causes a considerable underestimation of upper crustal stretching and over-reported extension discrepancy. When our new approach and/or a lower value of W ($W = 20$ km) are applied to estimation of the upper crustal extension in the central part of Qiongdongnan Basin, an inverse discrepancy is indicated in the deep-water area featured by symmetrical grabens. We suggest that the significant difference in syn-rift sediment thickness probably drives the lower crust flow causing a transition between inverse discrepancy and positive discrepancy in the central part of Qiongdongnan Basin.

Data availability statement

The original contributions presented in the study are included in the article/Supplementary Material, further inquiries can be directed to the corresponding author.

Author contributions

CH and ZZ designed the concept of the study. ZZ provided the new method and dataset. CH performed the statistical analysis. YX provided the base map of Figure 1A. ZZ and

CH drafted the first version of the manuscript. CH and EL further developed the manuscript. CH, ZZ, and EL contributed to manuscript revision, read, and approved the submitted version.

Funding

This research was supported by CAS Youth Innovation Promotion Association, by National Key Research and Development Program of China (2021YFC3100604), by National Natural Science Foundation of China (NO. 42076077), by Guangzhou Municipal Science and technology program (NO. 201904010285).

Acknowledgments

We are grateful to handling editor and the two reviewers for their helpful and constructive reviews.

Conflict of interest

The authors declare that the research was conducted in the absence of any commercial or financial relationships that could be construed as a potential conflict of interest.

Publisher's note

All claims expressed in this article are solely those of the authors and do not necessarily represent those of their affiliated organizations, or those of the publisher, the editors and the reviewers. Any product that may be evaluated in this article, or claim that may be made by its manufacturer, is not guaranteed or endorsed by the publisher.

Supplementary material

The Supplementary Material for this article can be found online at: <https://www.frontiersin.org/articles/10.3389/feart.2022.1016529/full#supplementary-material>

References

- Anderson, D. (2001). Top-down tectonics? *Science* 293, 2016–2018. doi:10.1126/science.1065448
- Anderson, E. M. (1951). *The dynamics of faulting*. Edinburgh: Oliver & Boyd.
- Bai, Y. L., Dong, D. D., Brune, S., Wu, S. G., and Wang, Z. J. (2019). Crustal stretching style variations in the northern margin of the South China Sea. *Tectonophysics* 751, 1–12. doi:10.1016/j.tecto.2018.12.012
- Barckhausen, U., and Roeser, H. A. (2004). Seafloor spreading anomalies in the South China Sea revisited. *Continent-Ocean Interact. within East Asian Marg. Seas.* 149, 121–125. doi:10.1029/149gm07
- Briais, A., Patriat, P., and Tapponnier, P. (1993). Updated interpretation of magnetic anomalies and sea-floor spreading stages in the south China sea - implications for the tertiary tectonics of southeast-asia. *J. Geophys. Res.* 98, 6299–6328. doi:10.1029/92jb02280

- Brune, S., Williams, S. E., Butterworth, N. P., and Muller, R. D. (2016). Abrupt plate accelerations shape rifted continental margins. *Nature* 536 201, doi:10.1038/nature18319
- Buck, W. R. (1988). Flexural rotation of normal faults. *Tectonics* 7 959–973. doi:10.1029/Tc007i005p00959
- Buck, W. R. (2007). *The dynamics of continental breakup and extension*. New York: Columbia University.
- Byerlee, J. (1978). Friction of rocks. *Pure Appl. Geophys.* 116, 615–626. doi:10.1007/bf00876528
- Clift, P. D., and Sun, Z. (2006). The sedimentary and tectonic evolution of the Yinggehai-Song Hong basin and the southern Hainan margin, South China Sea: Implications for Tibetan uplift and monsoon intensification. *J. Geophys. Res.* 111, 1–28. doi:10.1029/2005jb004048
- Clift, P., Lin, J., and Barckhausen, U. (2002). Evidence of low flexural rigidity and low viscosity lower continental crust during continental break-up in the South China Sea. *Mar. petroleum Geol.* 19, 951–970. doi:10.1016/s0264-8172(02)00108-3
- Clift, P., Lin, J., and Party, O. L. S. (2001). *Patterns of extension and magmatism along the continent-ocean boundary, South China margin*, 187. London, England: Geological Society, London, Special Publication, 489.
- Crosby, A., White, N., Edwards, G., and Shillington, D. J. (2008). Evolution of the Newfoundland-Iberia conjugate rifted margins. *Earth Planet. Sci. Lett.* 273 (1-2), 214–226. doi:10.1016/j.epsl.2008.06.039
- Davis, M., and Kusznir, N. (2004). Depth-dependent lithospheric stretching at rifted continental margins.” in *Proceedings of national science foundation rifted margins theoretical institute*. New York: Columbia University Press, 92
- Ding, W. W., Sun, Z., Mohn, G., Nirrengarten, M., Tugend, J., Manatschal, G., et al. (2020). Lateral evolution of the rift-to-drift transition in the south china sea: Evidence from multi-channel seismic data and IODP Expeditions 367&368 drilling results. *Earth Planet. Sci. Lett.* 531, 115932. doi:10.1016/j.epsl.2019.115932
- Dong, M., Zhang, J., Brune, S., Wu, S. G., Fang, G., and Yu, L. (2020). Quantifying postrift lower crustal flow in the northern margin of the south China sea. *J. Geophys. Res. Solid Earth* 125, 18910. doi:10.1029/2019JB018910
- Driscoll, N. W., and Karner, G. D. (1998). Lower crustal extension across the northern Carnarvon basin, australia: Evidence for an eastward dipping detachment. *J. Geophys. Res.* 103 (B3), 4975–4991. doi:10.1029/97jb03295
- Franke, D., Savva, D., Pubellier, M., Steuer, S., Mouly, B., Auxietre, J. L., et al. (2014). The final rifting evolution in the South China Sea. *Mar. Petroleum Geol.* 58, 704–720. doi:10.1016/j.marpetgeo.2013.11.020
- Hall, R., Ali, J. R., Anderson, C. D., and Baker, S. J. (1995). Origin and motion history of the philippine sea plate. *Tectonophysics* 251 (1-4), 229–250. doi:10.1016/0040-1951(95)00038-0
- Karner, G. D. (1991). Sediment blanketing and the flexural strength of extended continental lithosphere. *Basin Res.* 3 (4), 177–185. doi:10.1111/j.1365-2117.1991.tb00127.x
- Kim, Y., Huh, M., and Lee, E. Y. (2020). Numerical modelling to evaluate sedimentation effects on heat flow and subsidence during continental rifting. *Geosciences* 10 (11), 451. doi:10.3390/geosciences10110451
- Kusznir, N. J., and Karner, G. D. (2007). *Continental lithospheric thinning and breakup in response to upwelling divergent mantle flow: application to the Woodlark, Newfoundland and Iberia margins*, London, England: Geological Society, London, Special Publication, 389
- Larsen, H. C., Mohn, G., Nirrengarten, M., Sun, Z., Stock, J., Jian, Z., et al. (2018). Rapid transition from continental breakup to igneous oceanic crust in the South China Sea. *Nat. Geosci.* 11(10), 782, doi:10.1038/s41561-018-0198-1
- Leloup, P. H., Arnaud, N., Lacassin, R., Kienast, J. R., Harrison, T. M., Trong, T. T. P., et al. (2001). New constraints on the structure, thermochronology, and timing of the Ailao Shan-Red River shear zone, SE Asia. *J. Geophys. Res.* 106, 6683–6732. doi:10.1029/2000jb900322
- Li, G., Mei, L., Pang, X., Zheng, J., Ye, Q., and Hao, S. (2022). Magmatism within the northern margin of the South China Sea during the post-rift stage: An overview, and new insights into the geodynamics. *Earth-Science Rev.* 225, 103917. doi:10.1016/j.earscirev.2022.103917
- McKenzie, D., and Jackson, J. (2002). Conditions for flow in the continental crust. *Tectonics* 21 (6), 5-1–5-7. doi:10.1029/2002tc001394
- Morley, C. K. (2002). A tectonic model for the tertiary evolution of strike-slip faults and rift basins in SE Asia. *Tectonophysics* 347, 189–215. doi:10.1016/s0040-1951(02)00061-6
- Packham, G. (1996). Cenozoic SE asia: Reconstructing its aggregation and reorganization. *Geol. Soc. Lond. Spec. Publ.* 106 (1), 123–152. doi:10.1144/gsl.sp.1996.106.01.10
- Peron-Pinvidic, G., and Manatschal, G. (2019). Mini review rifted margins: State of the art and future challenges. *Earth Sci. Front.* 7, 218. doi:10.3389/feart.2019.00218
- Ranero, C. R., and Perez-Gussinye, M. (2010). Sequential faulting explains the asymmetry and extension discrepancy of conjugate margins. *Nature* 468 (7321), 294–299. doi:10.1038/nature09520
- Rangin, C. (1991). The philippine mobile belt: A complex plate boundary. *J. Southeast Asian Earth Sci.* 6 (3-4), 209–220. doi:10.1016/0743-9547(91)90068-9
- Reston, T. J. (2007). Extension discrepancy at North Atlantic nonvolcanic rifted margins: Depth-dependent stretching or unrecognized faulting? *Geol.* 35 (4), 367–370. doi:10.1130/G23213a.1
- Reston, T. J. (2005). Polyphase faulting during the development of the west Galicia rifted margin. *Earth Planet. Sci. Lett.* 237, 561–576. doi:10.1016/j.epsl.2005.06.019
- Reston, T. J. (2009). The extension discrepancy and syn-rift subsidence deficit at rifted margins. *Pet. Geosci.* 15 (3), 217–237. doi:10.1144/1354-079309-845
- Reston, T., and McDermott, K. (2014). An assessment of the cause of the extension discrepancy with reference to the west Galicia margin. *Basin Res.* 26 (1), 135–153. doi:10.1111/bre.12042
- Roberts, A. M., Yielding, G., Kusznir, N. J., Walker, I. M., and Dorn-Lopez, D. (1993). *Mesozoic extension in the north sea: Constraints from flexural backstripping, forward modelling and fault populations*. London: Geological Society of London.
- Rowley, D. B., and Sahagian, D. (1986). Depth-dependent stretching: A different approach. *Geol.* 14, 32–35. doi:10.1130/0091-7613(1986)14<32:dsada>2.0.co;2
- Royden, L., and Keen, C. E. (1980). Rifting process and thermal evolution of the continental margin of Eastern Canada determined from subsidence curves. *Earth Planet. Sci. Lett.* 51 (2), 343–361. doi:10.1016/0012-821x(80)90216-2
- Sapin, F., Ringenbach, J. C., and Clerc, C. (2021). Rifted margins classification and forcing parameters. *Sci. Rep.* 11 (1), 8199. doi:10.1038/s41598-021-87648-3
- Savva, D., Pubellier, M., Franke, D., Chamot-Rooke, N., Meresse, F., Steuer, S., et al. (2014). Different expressions of rifting on the South China Sea margins. *Mar. Petroleum Geol.* 58, 579–598. doi:10.1016/j.marpetgeo.2014.05.023
- Searle, M. P. (2006). Role of the Red River shear zone, yunnan and vietnam, in the continental extrusion of SE asia. *J. Geol. Soc. Lond.* 163, 1025–1036. doi:10.1144/0016-76492005-144
- Sibson, R. H. (1985). A note on fault reactivation. *J. Struct. Geol.* 7 (6), 751–754. doi:10.1016/0191-8141(85)90150-6
- Spencer, J. E. (1984). Role of tectonic denudation in warping and uplift of low-angle normal faults. *Geol.* 12 (2), 95–98. doi:10.1130/0091-7613(1984)12<95:rotidw>2.0.co;2
- Sun, Z., Jian, Z., Stock, J. M., Larsen, H. C., Klaus, A., Zarikian, A., et al. (2018). South China sea rifted margin” in. *Proceedings of the International Ocean Discovery Program*. College Station, TX: International Ocean Discovery Program. doi:10.14379/iodp.proc.367368.101.2018
- Tapponnier, P., Lacassin, R., Leloup, P. H., Scharer, U., Zhong, D. L., Wu, H. W., et al. (1990). The ailaoshan Red River metamorphic belt - tertiary left-lateral shear between indochina and South China. *Nature* 343, 431–437. doi:10.1038/343431a0
- Taylor, B., and Hayes, D. E. (1983). “Origin and history of the south China sea basin,” in *The tectonic and geologic evolution of SouthEastern asia seas and islands*, Part 2. Editor D. E. Hayes (Washington, DC: American Geophysics Union), 23
- Taylor, B., and Hayes, D. E. (1980). “The tectonic evolution of the south China sea basin,” in *The tectonic and geologic evolution of SouthEastern asia seas and islands*, Part 1. Editor D. E. Hayes (Washington, DC: American Geophysics Union), 89.
- Tsai, C. H., Hsu, S. K., Yeh, Y. C., Lee, C. S., and Xia, K. Y. (2004). Crustal thinning of the northern continental margin of the South China Sea. *Mar. Geophys. Res. (Dordr.)* 25 (1-2), 63–78. doi:10.1007/s11001-005-0733-5
- Walsh, W., and Yielding, G. (1991). The importance of small-scale faulting in regional extension. *Nature* 351, 391–393. doi:10.1038/351391a0

- Wernicke, B., and Axen, G. J. (1988). On the role of isostasy in the evolution of normal-fault systems. *Geol.* 16, 848–851. doi:10.1130/0091-7613(1988)016<0848:Otroii>2.3.Co;2
- Wernicke, B. (1985). Uniform-sense normal simple shear of the continental lithosphere. *Can. J. Earth Sci.* 22 (1), 108–125. doi:10.1139/e85-009
- Westaway, R., and Kusznir, N. J. (1993). Fault and bed 'rotation' during continental extension: Block rotation or vertical shear? *J. Struct. Geol.* 15, 753–770. doi:10.1016/0191-8141(93)90060-n
- Zhang, C. M., Wang, Z. F., Sun, Z. P., Sun, Z., Liu, J. B., and Wang, Z. W. (2013). Structural differences between the Western and eastern Qiongdongnan Basin: Evidence of indochina block extrusion and South China sea seafloor spreading. *Mar. Geophys. Res.* 34, 309–323. doi:10.1007/s11001-013-9187-3
- Zhao, Z., Sun, Z., Liu, J., Pérez-Gussinyé, M., and Zhuo, H. (2018). The continental extension discrepancy and anomalous subsidence pattern in the western Qiongdongnan basin, south China Sea. *Earth Planet. Sci. Lett.* 501, 180–191. doi:10.1016/j.epsl.2018.08.048
- Zhao, Z. X., Sun, Z., Wang, Z. F., Sun, Z. P., Liu, J. B., Wang, Z. W., et al. (2013). The dynamic mechanism of post-rift accelerated subsidence in Qiongdongnan Basin, northern South China Sea. *Mar. Geophys. Res.* 34 (3–4), 295–308. doi:10.1007/s11001-013-9188-2
- Zhao, Z. X., Sun, Z., Wang, Z. F., and Sun, Z. P. (2015). The mechanics of continental extension in Qiongdongnan Basin, northern South China Sea. *Mar. Geophys. Res.* 36 (2–3), 197–210. doi:10.1007/s11001-014-9238-4
- Ziegler, P. A. (1983). Crustal thinning and subsidence in the north-sea. *Nature* 304, 561–561. doi:10.1038/304561a0
- Zuber, M. T., Parmentier, E. M., and Fletcher, R. C. (1986). Extension of continental lithosphere: A model for two scales of Basin and range deformation. *J. Geophys. Res.* 91, 4826–4838. doi:10.1029/Jb091ib05p04826



OPEN ACCESS

EDITED BY
Weiwei Ding,
Ministry of Natural Resources, China

REVIEWED BY
Nosir Shukurov,
Institute of Geology and Geophysics,
Uzbekistan
Xinggong Kong,
Nanjing Normal University, China

*CORRESPONDENCE
Xiaoqiang Yang,
eesyxq@mail.sysu.edu.cn

SPECIALTY SECTION
This article was submitted to Marine
Geoscience,
a section of the journal
Frontiers in Earth Science

RECEIVED 10 August 2022
ACCEPTED 14 November 2022
PUBLISHED 12 January 2023

CITATION
Yang X, Wu S, Shang S and Chen Y
(2023), Hydrodynamic variations and
human activities have influenced
sediment fluxes in the pearl river delta
since the late holocene.
Front. Earth Sci. 10:1015697.
doi: 10.3389/feart.2022.1015697

COPYRIGHT
© 2023 Yang, Wu, Shang and Chen. This
is an open-access article distributed
under the terms of the [Creative
Commons Attribution License \(CC BY\)](#).
The use, distribution or reproduction in
other forums is permitted, provided the
original author(s) and the copyright
owner(s) are credited and that the
original publication in this journal is
cited, in accordance with accepted
academic practice. No use, distribution
or reproduction is permitted which does
not comply with these terms.

Hydrodynamic variations and human activities have influenced sediment fluxes in the pearl river delta since the late holocene

Xiaoqiang Yang^{1*}, Shuang Wu¹, Shentang Shang¹ and Yan Chen²

¹School of Earth Sciences and Engineering/Guangdong Provincial Key Laboratory of Geodynamics and Geohazards/Southern Marine Science and Engineering Guangdong Laboratory (Zhuhai), Sun Yat-Sen University, Zhuhai, China, ²Key Laboratory of Oil and Gas Resources, CAS Institute of Geology and Geophysics, Chinese Academy of Sciences, Beijing, China

Climate change and human activity can both exert a role in the river discharge and sediment load in river deltas when the sea level remains relatively stable. The Pearl River Delta constitutes the metropolitan region of the Guangdong–Hong Kong–Macau Greater Bay Area, and its evolution in the past and future impacts the sustainable development of this region. In this manuscript, a core situated in the northern South China Sea, adjacent to Qiao Island of Zhuhai city in the Pearl River Delta, was selected to investigate the hydrodynamic variation influenced by tropical processes and the sediment flux imposed by human activities. Using paleosecular variations (PSVs) in geomagnetic field correlations constrained by seven radiocarbon ages, an ~2.5 kyr chronology was provided for core sediments ~2.8 m in length. The magnetic fabric results suggest that deposition was influenced by the two types of hydrodynamic-weak energy modulated by El Niño–Southern Oscillation (ENSO) activity and higher energy regulated by high-frequency tropical storms. The cyclic variations in the degree of anisotropy of magnetic susceptibility (P) indicate two periodic changes at approximately 300 and 100 years, which were forced by ENSO activity, while the ratio of lineation with foliation (q value) implies a higher energy flow period of 1.3–1.9 kyr, arising from strong tropical storms. Moreover, the high saturation remanence (SIRM) introduces more sediment flux, which is impacted by growing human activity during the period of 1.0–1.6 kyr.

KEYWORDS

pearl river delta, magnetic fabric, ENSO activity, tropical storm, human activity

Introduction

River deltas occupy the most economically dynamic land area in the world and contain more than 322 million people (Macklin and Lewin, 2015). The formation and evolution of deltas have been dominantly controlled by natural processes, such as climate change, sea-level fluctuations and tectonic activities, on a geological time scale (Goodbred

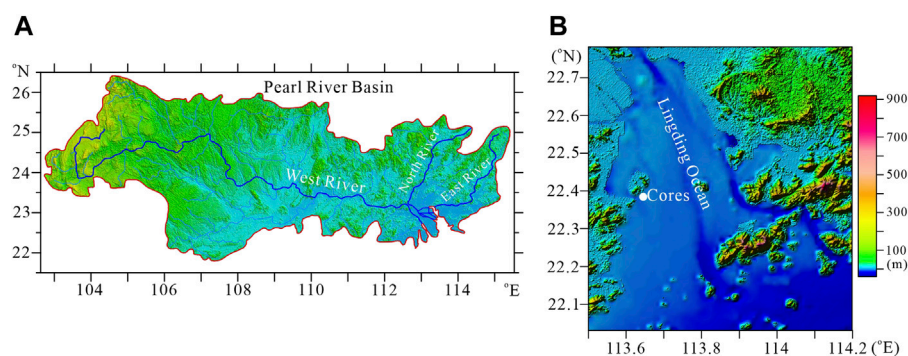


FIGURE 1

The Pearl River drainage basin (redrawn from Wei et al., 2020) (A) and core locations (B).

and Kuehl, 2000; Zong et al., 2009). However, the terrigenous debris flux accompanied by river discharge may exert a crucial impact on the morphology of the delta when the sea level and tectonic activity remain relatively stable (McManus, 2002). The enhanced river flow is linked to the patterns and processes of sediment erosion and accumulation that modulate delta progradation and distributary channel extension laterally (Shaw et al., 2016). Sediment retention, which is influenced by natural processes or human activities, may cause delta degradation, while marine processes intensify in the context of global warming (Wu et al., 2016; Hoitink et al., 2017; Ranasinghe et al., 2019; Xie et al., 2022). Especially in the Anthropocene, the double impacts of human activity and climate change on river discharge and sediment inputs are responsible for the rapid transition of the delta shape (Hassan, 1997; Macklin & Lewin, 2015; Hoitink et al., 2017; Liu et al., 2019; Zhou et al., 2019). Enhanced weathering processes, intensified precipitation and developing agricultural industrialization can cause delta progradation and channel migration, while the embankment of channels and the construction of dams may result in delta retrogradation (Hassan, 1977; Macklin and Lewin, 2015; Nian et al., 2022).

The Pearl River Delta, a metropolitan region of the Guangdong-Hong Kong-Macau Greater Bay Area, is one of the most densely urbanized regions in the world, with a population of more than 67 million (Yang et al., 2019). Heavy rainfall arising from tropical storms and ENSO activity enhances river discharge and causes a large amount of sediments to enter the lower reaches of the delta region (Liu et al., 2017; Deng et al., 2018; Chen et al., 2020; Yan et al., 2022). In contrast, urbanization prevents the production of terrigenous debris and channel reformation (Zhou et al., 2019; He et al., 2022). This delta is a typical zone in which to research the evolution of river discharge and sediment input under the interaction of natural processes and human activity. In this manuscript, we select a sediment core to investigate the hydrodynamic variability and terrigenous flux

since approximately 2.5 kyr BP, which would be beneficial for understanding the morphological evolution of the delta during the period of strong human activity. Radiocarbon dating and paleomagnetic secular variations are employed to determine the sediment chronology, and the anisotropy of magnetic susceptibility and the fraction of fine sand are used to analyze the hydrodynamic conditions. The saturation remanence (SIRM) and high coercivity remanence (HIRM) are employed as proxies for terrigenous debris inputs.

Geographical context and methods

The Pearl River Delta covers a region of $\sim 5.5 \times 10^4 \text{ km}^2$, which is formed by three major rivers (West River, North River and East River) flowing into the northern South China Sea (Figure 1). Lingdingyang is one of the largest estuary bays that formed after the deglaciation period (Zong et al., 2009). The drainage system of the three rivers extends to the southeastern margin of Tibet across Guangdong, Guangxi and Guizhou Provinces, constituting diverse geomorphic conditions, such as karst landforms, hills, basins in the upper and middle streams and the highly urbanized delta plain downstream (Wei et al., 2020). The area of soil erosion, which provides abundant terrigenous debris for river loading, is approximately $58,900 \text{ km}^2$ and remained almost unchanged from 1995 to 2004 (Zhou et al., 2019; Wei et al., 2020). The annual water discharge varied around a mean value of $\sim 2.8 \times 10^{10} \text{ m}^3$, while the sediment load exhibited a decreasing trend at a rate of $-2.24 \times 10^4 \text{ t/year}$ between 1955 and 2018 (Wei et al., 2020). The average annual precipitation (1954–2018) varied from 1120 to 1981 mm, with a mean value of 1559 mm. ENSO activity and tropical storms exert a crucial impact on the precipitation in this region. Large precipitation variations ($>5\%$) and most of the years with low precipitation are associated with ENSO events (El Niño years) (Wei et al., 2020).

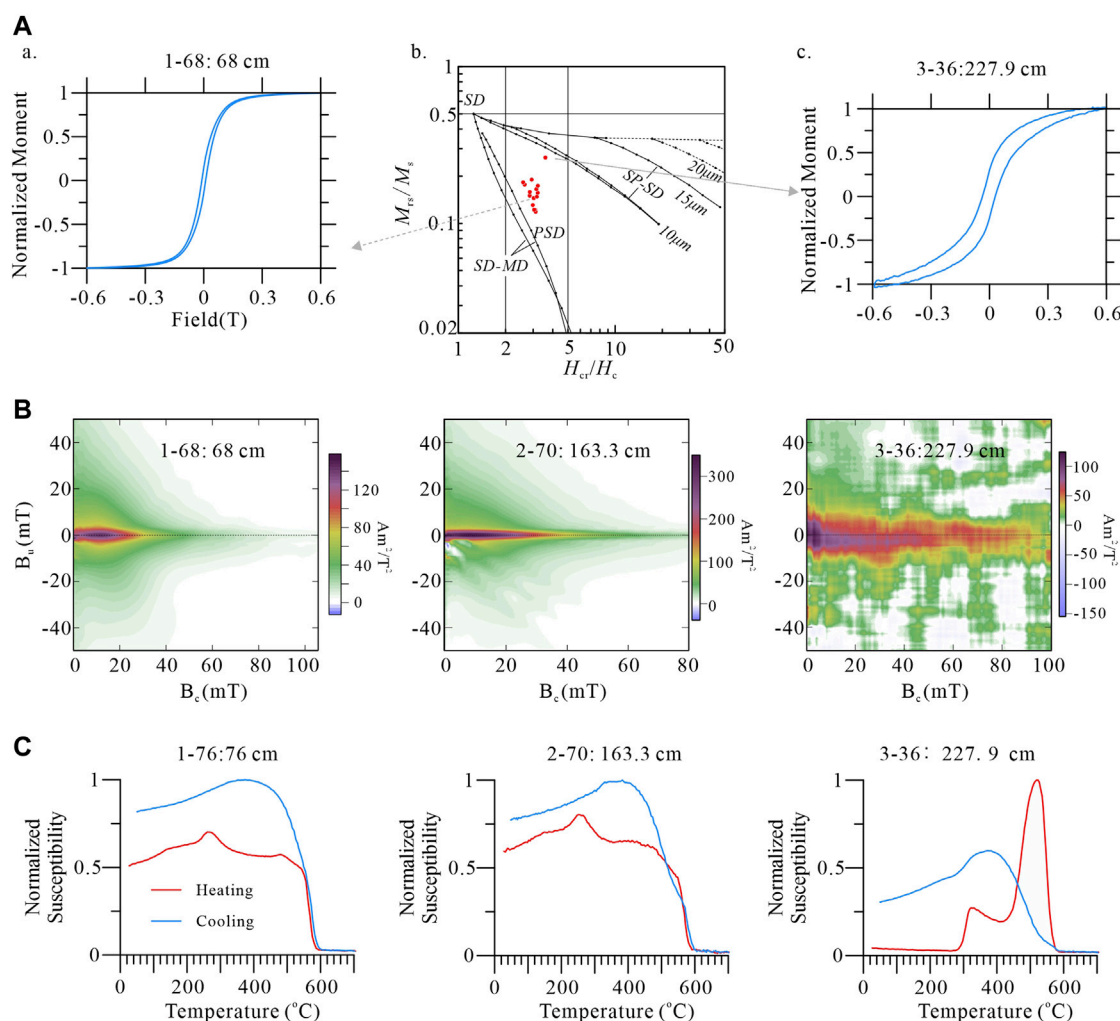


FIGURE 2

Hysteresis loops and Day-plot project following Dunlop (2002) for the representative samples (A); FORC diagram processed using FORCinel software (Egli, 2013) and temperature dependence of magnetic susceptibility variation are displayed in (B) and (C), respectively. In (A), SD = single domain; PSD = pseudosingle domain and MD = multidomain. (C) FORC diagrams of several typical samples.

Two piston cores, ZH06 (2.81 m in length) and ZH05 (1.82 m in length) (22.39°N, 113.64°E), in the Lingdingyang Sea area adjacent to Qiao Island of Zhuhai city were selected in 2008 (Figure 1). The sediments in the two cores were homogenous silt and clay and were gray in color. Two cores were split, and one-half was continuously sampled by pushing ceramic boxes (1*1*1 cm) into the core sections. A total of 278 and 179 samples were collected in cores ZH06 and ZH05, respectively, for paleomagnetic measurements. Moreover, the paired powder samples were selected for grain size analysis. The volume magnetic susceptibility of the sediments from the two cores displays a similar pattern (Supplementary Figure S1), exhibiting the same stratigraphy and consistent deposition processes. Here, the experimental works were mainly focused on the ZH06 core samples.

All box samples were measured for natural remanent magnetization (NRM) and then stepwise demagnetized with a fully automated 2G-Rapid system using peak fields of 0–80 mT (total of 10 steps) after the volume magnetic susceptibility and magnetic fabric (MF) were initially measured using a Bartington MS2 system and an MFK1 Kappabridge, respectively. The parameters of MF, such as the degree of anisotropy susceptibility (p), foliation (F), lineation (L), shape factors (q and T) and imbrication angle (β), were calculated from the statistical methods of Constable & Tauxe (1990) and (Taira, 1989). Anhysteretic remanence (ARM) was then imparted with a 0.05 mT steady field and an 80 mT alternating field, and saturation isothermal remanence (SIRM) was imposed using a DC field

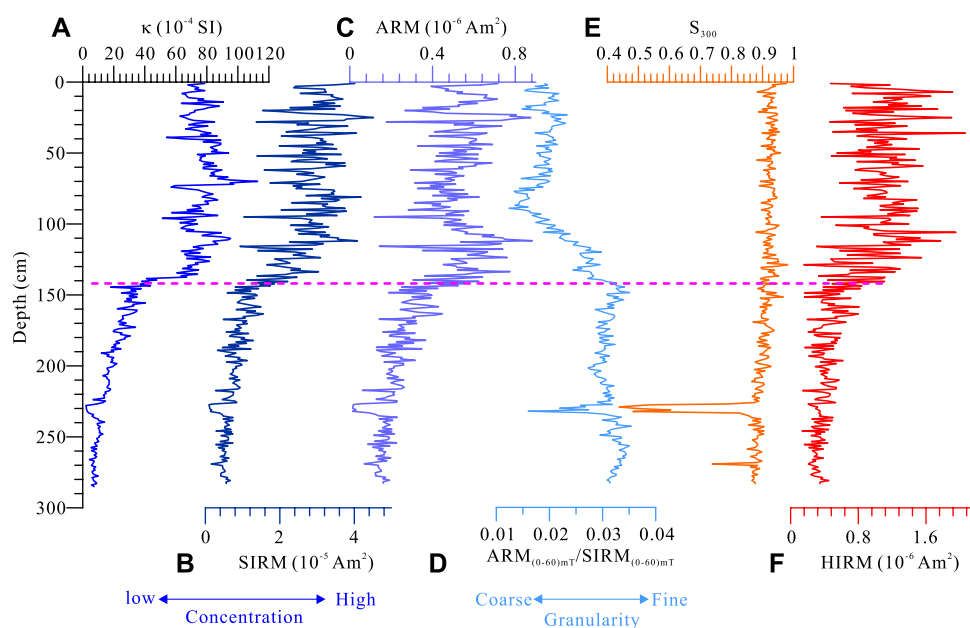


FIGURE 3

Downcore variations in environmental magnetism proxies of volume magnetic susceptibility (κ) (A), saturation isothermal remanence (SIRM) (B), anhyseretic remanence (ARM) (C) and the ratio of $ARM_{(0-60)mT}/SIRM_{(0-60)mT}$ (D), S_{300} (E) and HIRM (F).

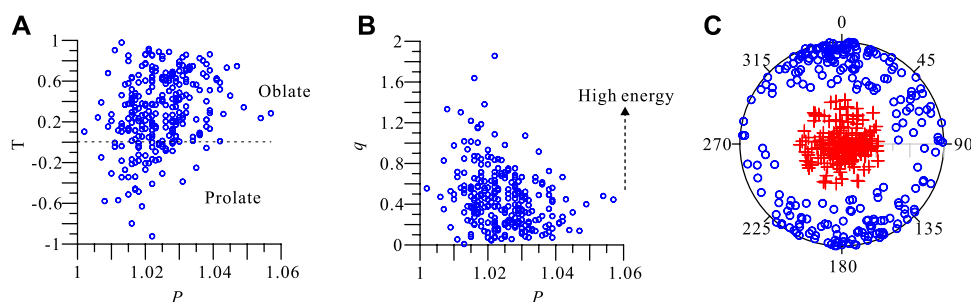


FIGURE 4

Projection of the magnetic fabric parameters of the shape factor (T)-degree of anisotropy (P) (A) and shape factor (q)-P (B).

of 1 T. IRM-300 mT was then measured, giving a reverse 300 mT field. High coercivity remanence HIRM and S_{300} ratios were determined by $(SIRM-IRM_{300})/2$ and $IRM_{300}/SIRM$, respectively. Both ARM and SIRM were also demagnetized and measured at 20, 40, 60 and 80 mT fields. The magnetic susceptibility variations independent of temperature (κ -T) were measured in argon conditions within a cycle from room temperature to $\sim 700^\circ\text{C}$ for four freeze-dried powder samples in an MFK1 Kappabridge. The hysteresis properties of the samples were determined using a Princeton Measurements Corporation vibrating sample magnetometer (MicroMag 3900) with a maximum applied

field of 1 T. The saturation magnetization (M_s) (at 1.0 T), saturation remanence (M_{rs}), and coercivity (B_c) were obtained after correcting for the paramagnetic contribution identified from the slope of the high field sections of the curve. Subsequently, the coercivity of the remanence (B_{cr}) was determined using the demagnetized curve of M_{rs} . FORC diagram measurements were performed on for four samples following the methods of Harrison and Feinberg (2008). The maximum saturation field was 1.0 T, and the regular grid comprised 150 hysteresis loop curves with a 500 ms averaging time. The FORC data were processed using FORCinel software with a VARIFORC smoothing algorithm (Egli, 2013).

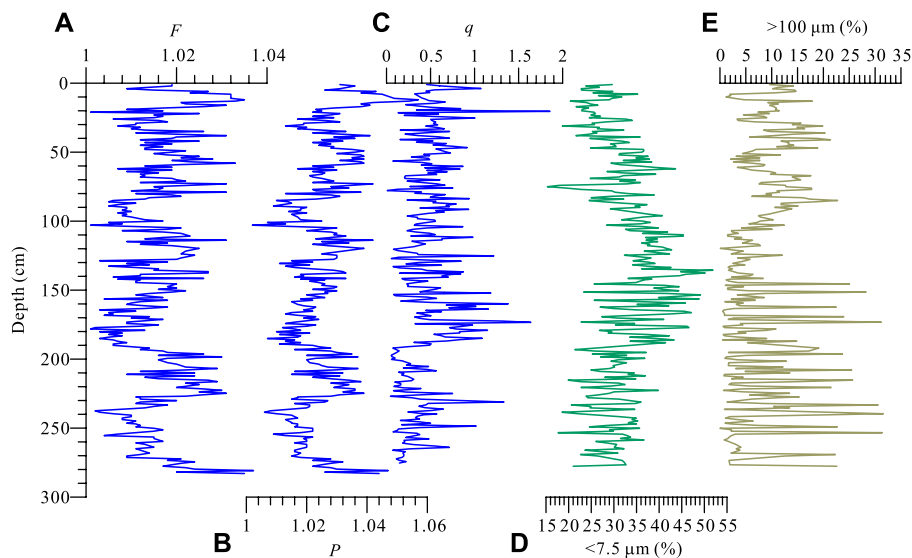


FIGURE 5
Variations in foliation (F) (A), degree of anisotropy (P) (B), and shape factor (q) (C) coeval with the particle size fractions of <7.5 (D) and >100 μm (E).

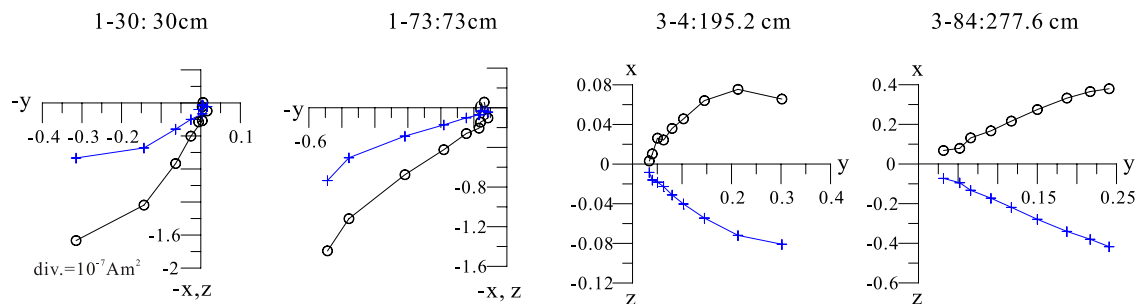


FIGURE 6
Principal component plots (top) (Kirschvink, 1980) of representative specimens. Open circles (cross) display projections onto the vertical (horizontal) plane.

The samples for grain size analysis were pretreated with HCl (10%) hydrogen peroxide (H_2O_2) (30%) to remove the carbonate and organic matter, and then $(\text{NaPO}_3)_6$ was added to prohibit the fine particles from aggregating. Experiments were performed with a MasterSizer 2000 laser particle analyzer, achieving a distribution from 0.2 to 1000 μm. These magnetic and grain size experiments were performed at the Institute of Geology and Geophysics, Chinese Academy of Sciences (CAS) and Sun Yat-Sen University, respectively.

Intact shells, conches and terrigenous plant debris were selected for radiocarbon dating. Five samples were prepared into graphite at the Guangzhou Institute of Geochemistry, Chinese Academy of Sciences and then determined at the Key

Laboratory of Heavy Ion Physics, Beijing University, and two samples were measured at the Beta Laboratory.

Results

Magnetic mineral assemblage

The hysteresis loops of four representative samples displayed a narrow shape and reached saturation magnetization below a 300 mT field. The coercivity of remanence (B_{cr}) varied from 20 to 35 mT. The Day-plot projection describes the PSD state of magnetic mineral

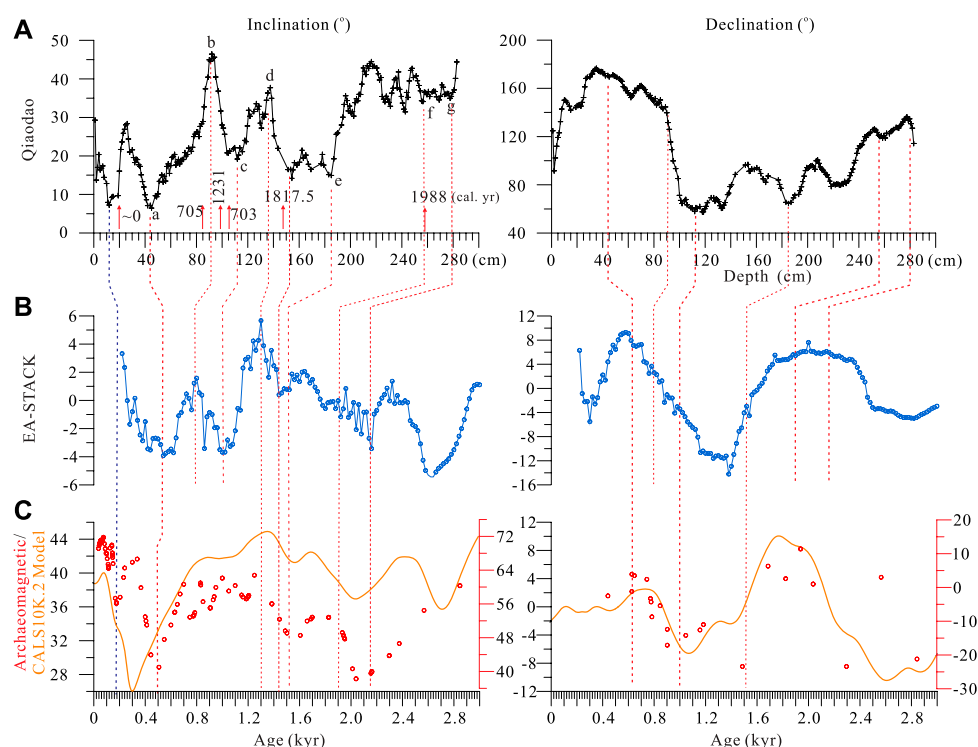


FIGURE 7

Correlation of the ChRM directions of core ZH06 (A) with eastern Asian stack curves (EA-STACK) (Zheng J et al., 2014) (B) and archaeomagnetic/CALS10k.2 model results of eastern China (Brown et al., 2015) (C). The radiocarbon ages are displayed in (A). The dotted lines show the favorite tied points between the different curves.

grains (Dunlop, 2002) (Figure 2). The κ -T profiles have the most magnetic susceptibility loss at approximately 580°C, although a prominent increase at approximately 260°C existed. One sample at a depth of ~227.9 cm displayed a “waist-shaped” loop with relatively high B_{cr} (~118 mT) and B_c (~32.9 mT) values. The susceptibility of the heating curve showed two stages, rising at temperatures of approximately 320°C and 500°C (Figure 2), which may arise from the contributions of pyrrhotite and pyrite (Yang et al., 2008). The S_{300} ratio value preserved a relatively stable mean value of approximately 0.93 except in the interval of 2.26–2.38 m (decreased to 0.43). The remanence ratio of ARM and SIRM from 0 to 60 mT with their primary values are generally greater than 0.8 ($ARM_{(0-60)mT}/ARM$ and $SIRM_{(0-60)mT}/SIRM$), and the $SIRM/\kappa$ ratio does not show very high values. The magnetic hysteresis data of M_{rs}/M_r were less than <0.5, and B_{cr}/B_c exceeded 2, indicating little influence of iron sulfides (Roberts et al., 2011). These results demonstrate that the magnetic minerals of sediments were mainly dominated by soft magnetite, while the contribution of a few iron sulfides to the remanence is minor (Deng et al., 2001; Roberts et al., 2011). The high-

coercivity minerals are preserved only in the sediments within 2.26–2.38 m.

Generally, the ratios of ARM/SIRM can serve as a proxy of the magnetic grain size variations when the remanence of sediments is mainly dominated by magnetite. To remove the influence of a few iron sulfides on the remanence, we employ the remanence difference ratios in the 0–60 mT demagnetization field ($ARM_{(0-60)mT}/SIRM_{(0-60)mT}$) to estimate the relative variations in the magnetic grain size. The variations in the volume magnetic susceptibility (κ), SIRM and ARM display a clear two-stage pattern (Figure 3). Below ~140 cm, low values associated with a weak increasing trend denote low concentrations of magnetic minerals, while high values above 140 cm represent high concentrations. Low and high concentration values are linked to fine and coarse magnetic mineral granularity, respectively (ARM/SIRM). This stage shift should arise from the magnetic mineral inputs while the mineral assemblages are consistent (the relatively stable S_{300} ratio). The HIRM values also increased following the SIRM and ARM, exhibiting that the high-coercivity components in the sediments, such as hematite (Roberts

TABLE 1 The age-depth relation of Core Zh06.

a. Radio-carbon ages

Sample	Materials	Depth (cm)	Lab. No.	Measuring results (yr BP)	Calibration results (1 sigma, yr BP)
ZH06-1-2	Shell	20	GZ4472	Present	
ZH06-1-4	Shell	85	GZ4473	805 ± 25	689–713
ZH06-2-1	Plant debris	99.5	BETA	1280 ± 30	1243–1273
ZH06-2-2	Shell	106	GZ4474	795 ± 25	702–723
ZH06-2	conchs	106	GZ4749	710 ± 30	652–676
ZH06-2-3	Plant debris	145.5	BETA	1920 ± 30	1819–1885
ZH06-3-5	conch	258	GZ4475	2045 ± 25	1972–2003

b. Determining ages using PSV correlation

Depth (cm)	Correlation age (kyr)	Error (kyr)
12	0.17	0.01
44	0.5	0.05
91	0.8	0.02
112	1.0	0.05
136	1.3	0.02
152	1.44	0.04
185	1.55	0.04
258	1.9	0.02
280	2.16	0.05

et al., 2021; Jiang et al., 2022), which formed during pedogenic processes in the catchment areas, were transported to the Pearl River Delta region.

Magnetic fabric and particle size variations

The stereographic projection of the anisotropy principal axes displays a normal depositional fabric (Supplementary Figure S2A). The maximum axes are scattered around the horizontal plane, and the minimum axes cluster tightly around the vertical plane. The principal directions of the long axes are aligned along the northeast direction after correction based on the natural remanence declination of the uppermost sediments (Supplementary Figure S2B). The T-P projection of magnetic fabric indicates that most specimens had oblate shapes, whereas a few prolate samples had small p values (<1.04) (Tarling & Hrouda, 1993) (Figure 4). The q -P plot shows that the deposition was dominated by normal currents, slope gravity and viscous suspension (Taira, A., 1989; Bradák-Hayashia et al., 2017). However, some large q values (>0.6) present

increasing tangential stress and higher energy. A weak negative correlation between p and q suggests that increasing q is accompanied by decreasing anisotropy, possibly due to rearrangement and the relatively chaotic behavior of grains in higher-energy dynamics conditions.

The higher anisotropy (larger p -value) with low L in the foliation plane may correspond to the relatively lower-energy currents and the strengthening of the gravitational force during grain transport (Figure 5). The foliation (F) and the degree of anisotropy (p) varied in cycles. Increasing p indicates relatively enhanced hydroenergy at the boundary of the water and sediment surfaces. However, the terrigenous particle size did not mimic the cyclic variations in the magnetic fabric parameters. The fine silt and clay fraction ($<7.5\ \mu\text{m}$) appeared high in the middle part and low in the upper and lower parts. The coarse size fraction exhibited high frequency fluctuation below ~ 140 cm and a relatively high value above 100 cm. The different changing patterns of p and particle size present two types of hydrodynamic conditions. The magnetic fabric is related to the bottom hydroconditions, while the coarse particle size is responsible for higher-energy currents.

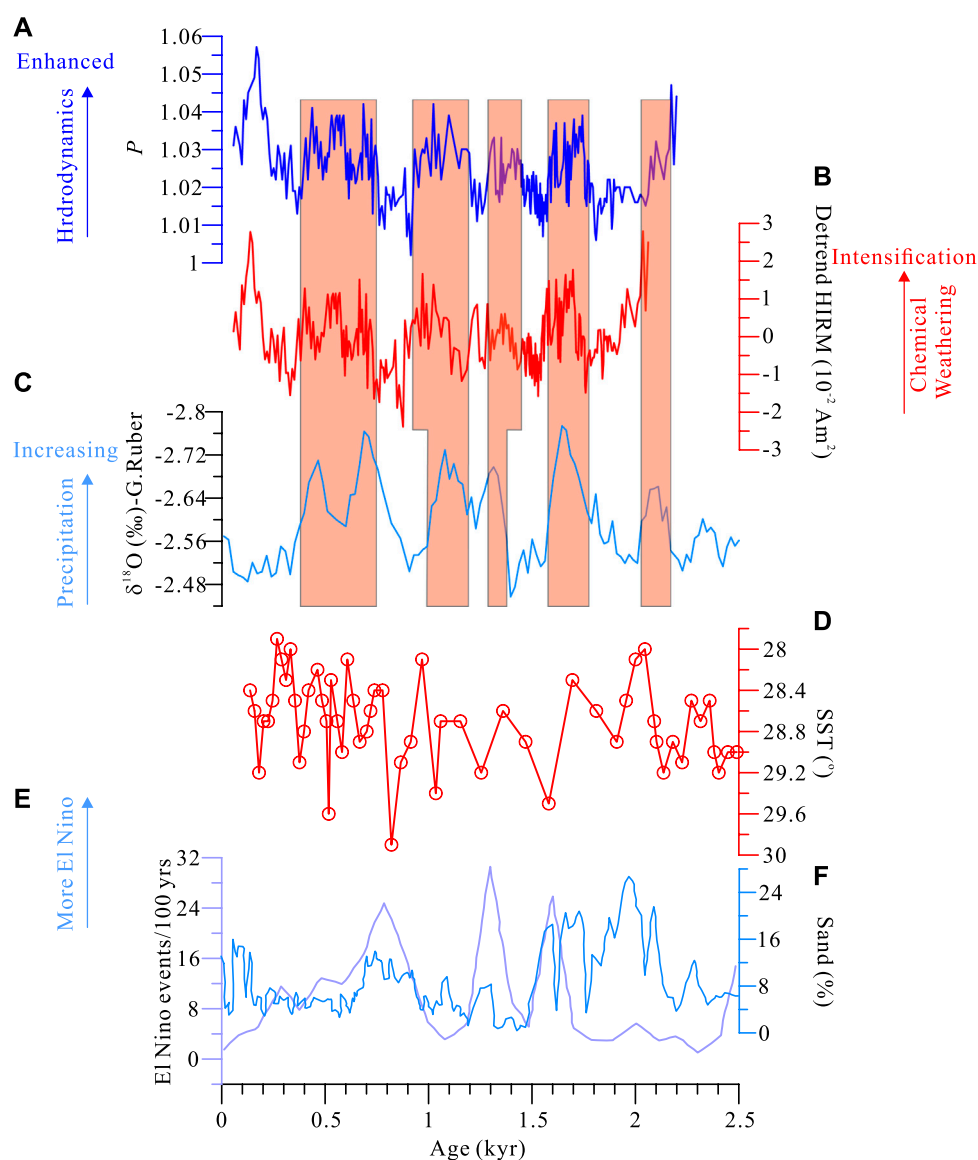


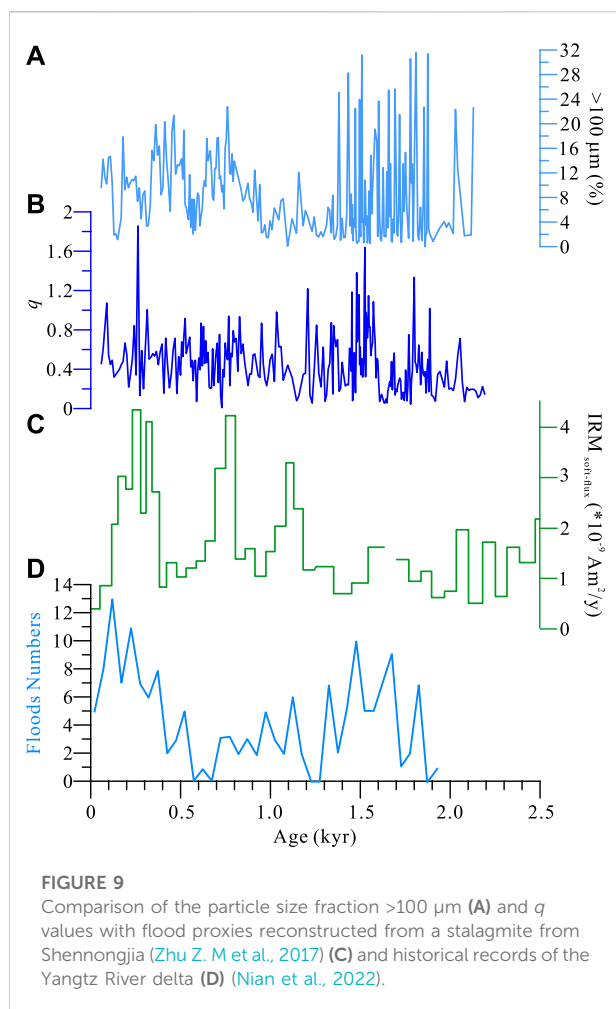
FIGURE 8

Comparison of p (A), HIRM (B) with $\delta^{18}\text{O}$ of core 17,940 (C) (Wang et al., 1999), the sea surface temperature (SST) of the western Pacific (E) (Stott et al., 2004) and ENSO proxies (F,G) (Moy et al., 2002; Conroy et al., 2008)

Natural remanence (NRM)

The NRM of all samples can be demagnetized using alternative fields (AFs) of 0–80 mT. A weak second NRM component can be removed in a few samples at AFs of 10–20 mT (Figure 6). The characteristic remanent magnetization (ChRM) and maximum angle deviation (MAD) can be evaluated between 20 and 80 mT. The remanence of only 47 samples displayed a relatively scattered distribution, and these samples were rejected when analyzing the directional changes in core sediments.

Downcore variations in ChRM inclinations and declinations are shown in Figure 7 (the declination represents only the relative change). The MAD values are generally $<5^{\circ}$, confirming that the magnetization components are well defined. The directions of both inclination and declination are characterized by several prominent lows and peaks, which represent the paleosecular variations in the geomagnetic field. The large variability in the directions in the upper layer (from 100 to 10 cm) exceeds the results of the archaeomagnetic and CALS 10 K.2 models (Brown et al., 2015; Cai et al., 2017), which may result in debate about the reliability of the



paleomagnetic directions. However, we do not have enough reason to reject these results because the well-preserved natural remanence, the minimal sediment disturbance, and the relatively low p values (<1.06) associated with fine sediments (the fraction of the grain size $<60 \mu\text{m}$ varied around 80%) are conducive to record the geomagnetic field.

Radiocarbon dating results

The radiocarbon ages are given in Table 1a. The ages from the different labs may have a little discrepancy for the same layer sediments, which can arise from the dating materials and lab error. The calibrated ages suggest that the core sediments are younger than 2.5 kyr despite the nonlinear distribution of seven ages. Although the dating materials are intact shells, conches and terrigenous debris, the complex deposition process and possible reworking under delta conditions may prevent the construction of a reliable chronology of sediments. Almost the same age at the different depths of

85 cm and 106 cm may originate from the downward activity of benthic shells or conches. The reverse age at a depth of 99.5 cm with the adjacent layers may reflect old plant debris pollution from the drainage system.

Discussion

Constructing the chronology based on the PSV correlation

The paleomagnetic field variations (PSVs) were determined as the long-term temporal changes in the Earth's magnetic field longer than several hundreds of years, which resulted from the effect of magnetic diffusion in the core-mantle boundary zone (Korte & Holme, 2010; Korte et al., 2011; Laj & Channell, 2015). A series of studies have suggested that the PSV can serve as an effective dating tool within a region of thousands of kilometers (Yang et al., 2009; Shanahan et al., 2013). In eastern China, the nondipole field has a common influence on the geomagnetic field, and the PSV has had a similar pattern since the Holocene (Korte & Holme, 2010). This feature meets the criteria of PSV dating of the sediments. Zheng Y et al. (2014) reconstructed a PSV stack of East Asia (EA-Stack) by synthesizing sedimentary and archeological results, which provides an important reference curve for a large region.

During the river delta deposition process, ocean currents and bottom fauna often disturb the materials; however, the reworked sediments mostly occur near the water-sediment interface. The magnetic minerals are realigned along the Earth's magnetic field after these disturbances. The natural remanence preserved in such sediments can record the features of the Earth's magnetic field. We link our inclination and declination records to the EA-Stack constrained by the radiocarbon ages, and six tied points can be recognized in the inclination correlation (Figure 7). For the upper 20 cm sediments, we correlate them to the archaeomagnetic records of East Asia and the CALS10k.2 model results (Brown et al., 2015; Cai et al., 2017) to achieve a tied point at ~ 12 cm. Hence, a correlation depth-age model can be reconstructed based on these tied points (Table 1b). A possible error may occur within 180–280 cm. Our inclination displayed a relatively stable plateau with some fluctuations, while the EA-Stack exhibited a decreasing trend. However, the radiocarbon ages of 1852 and 1988 at depths of 145.5 cm and 258 cm provide two constrained points. The chronology of core sediments can be established by the deposition rate and correlation age. The results attest that the core sediments approximately 283 cm in length document a deposition of approximately 2.1 kyr.

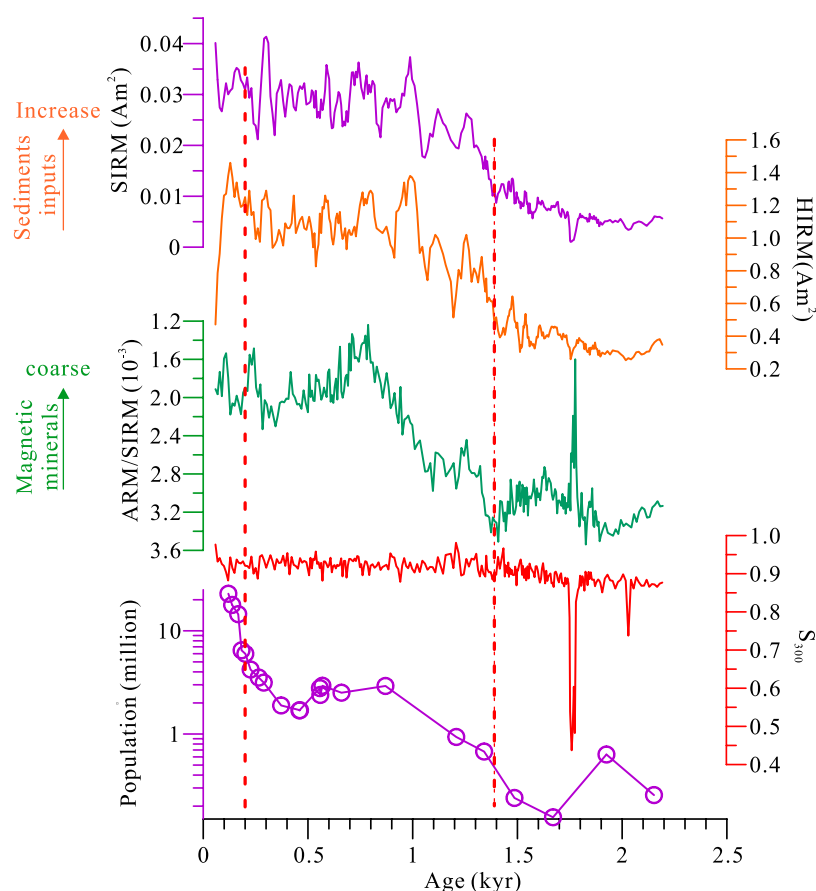


FIGURE 10

The relation of sediment inputs expressed by magnetic proxies with population growth in Guangdong Province (Zhu et al., 1988).

Hydrodynamic change and tropical precipitation

Anisotropic magnetic susceptibility reflects the fabric acquired by the sediments during deposition (Wassmer et al., 2015), which is often used to determine the paleocurrent direction, tsunami events and deposition process (Schneider et al., 2014; Bradak-Hayashi et al., 2017). The different flow stresses in the bottom layer can induce the varying p and the orientation of the long axis (K_{\max}). When the currents have weak or laminar flow, K_{\max} is parallel to the flow direction (Tarling & Hrouda, 1993). The p values of our core were less than 1.04 for most sediments, which are mainly dominated by foliation (F). Low and high p values indicate weak and increased flow stress during the deposition period, respectively. The flow strength at the core site may be a mixture of river currents with waves and tides; however, the latter two should have a relatively mean stable strength with daily and monthly fluctuations. The change in the flow stress should mainly arise from the river discharge influence, which is heavily controlled by precipitation. Comparing the variations in p with the detrended HIRM values, a consistent pattern appeared (Figure 8). A high

HIRM represents a greater flux of terrigenous debris under the intensification of pedogenic processes in subtropical regions with warm and wet climate conditions (producing more high-coercivity minerals) (Long et al., 2011; Jiang et al., 2018; Jiang et al., 2022). Enhanced rainfall strengthens the river discharge and sediment load (Liu et al., 2017), which increases p values. Hence, cyclic p and HIRM indicate the periodicity of tropical precipitation. Performing the spectral analysis for p values (Li et al., 2019), two periods of approximately 300 years and 100 years are significant (Supplementary Figure S3). High p values remain consistent with the sea surface temperature of the western tropics (Stott et al., 2004), which would induce an ENSO boom (Moy et al., 2002; Conroy et al., 2008; Karamperidou et al., 2015; Barr et al., 2019). Simulation studies and modern observation records also confirm that in contrast to the monsoon change recorded in stalagmites, ENSO activities and tropical storms play an important role in tropical precipitation, although an ambiguous relationship exists at interannual time scales (Liu et al., 2017; Deng et al., 2018; Yan et al., 2022). Strong ENSO activities (La Niña years) induce more rainfall in river basins (Barr et al., 2019), which influences land and ocean areas. The $\delta^{18}\text{O}_{\text{G. Ruber}}$ of core

17,940 selected from the northern South China Sea (Wang et al., 1999) agrees well with the p and HIRM curves, suggesting a common forcing process arising from precipitation.

Strong tropical storms, especially typhoons, can induce heavy rainfall in a short time (Yan et al., 2022). This process causes higher energy transport, high-density water and grain-to-grain interactions, and the sediments in the bottom layer are “slurry-like”. The q values of the magnetic fabric increase with low p values and coarse particle sizes. That is, the large q values can hint at floods and a high-energy flow. During the period of 1.4–1.9 kyr BP (Figure 9), coarse particle grains fluctuate with high frequency and amplitude, and the q values have a corresponding pattern. They present high-frequency tropical storms, agreeing well with the flood events that occurred in the Yangtze River Delta (Zheng J et al., 2014; Nian et al., 2022) and central China, which were reconstructed from the historical reference and IRM flux in the stalagmite (Zhu Y. N et al., 2017), respectively. The high-frequency typhoon events correspond to the low temperature in eastern China (Ge et al., 2003). When the temperature increased, the typhoon frequency decreased. The consistent high-frequency tropical storms forced flood events, which affected not only the eastern coastal area of China but also the central part of China.

Human activity-induced sediment flux

The remanence of sediments was mainly dominated by soft magnetite, and SIRM variations arose from the concentration of magnetite, which depends on terrigenous inputs. The sediment load increase should have responded to an increasing SIRM trend from approximately 1.6–1.0 kyr BP (Figure 10). Neither high-energy tropical storms nor relatively weak ENSO activity display this long-term trend (Conroy et al., 2008; Nan et al., 2014) (Figures 8, 9), and the increase in the sediment load may arise from other factors. Some investigations show that the sediment supply from the Pearl River over the last ~150 years was dominated by human activities (Ranasinghe et al., 2019). The population of Guangdong Province grew from 240,000 to 2,920,000, and most of them lived in the Pearl River Basin (Zhu et al., 1988). Increasing cultivation activities destroyed vegetation and produced a large amount of debris, which was transported to the lower reaches of the delta. Since approximately 500 years ago, the population has also increased rapidly, but the central region has migrated to the lower reaches of the delta region, and dam construction and reclamation have limited the debris into the river system. Therefore, the relationship between population growth and sediment flux at approximately 2.5 kyr BP indicates that different human activities have an important impact on sediment inputs. In an agricultural society, planting activities in river basins increase sediment inputs, but modern human activities in the lower reaches of the delta may reduce the inflow of debris despite natural processes.

Conclusion

The sediments of core ZH06, which is from the Pearl River subaqueous delta and is ~2.8 m in length, provide the hydrodynamic evolution process and sediment input history impacted by human activity. The paleomagnetism and magnetic fabric analysis provide the chronology of sediments and the proxies indicating the water energy and sediment flux. Based on the environmental and magnetism investigations, we can infer some insights about the deposition process in the Pearl River Delta region.

- 1) The deposition may be disturbed by various factors, and the radiocarbon ages have difficulty constraining the age of sediments. The paleosecular variations, which rely on geomagnetic field variations over hundreds to thousands of years, have provided a reliable chronology since approximately 2.5 kyr.
- 2) Cyclic variations in the degree of anisotropy of magnetic susceptibility (P) at 100 and 300 years imply relatively weak energy arising from ENSO activities, which dominate the precipitation in this region.
- 3) The large shape factor (q) values coeval with the coarser particle size fraction denote the higher-energy current, which can induce the “slurry-like” transport of sediments during the period of 1.3–1.9 kyr, in which the strong tropical storms occurred at high frequencies and intensities.
- 4) The increasing trend of the SIRM from 1.3 to 10 kyr BP indicates increasing human activity after the Sui Dynasty. The agricultural planting in the river basin destroyed the vegetation and produced large amounts of debris, which flowed into the river and were transported to the lower reaches of the delta.

Data availability statement

The raw data supporting the conclusions of this article will be made available by the authors, without undue reservation.

Author contributions

XQ, Responsible for the article SW, ST, and YC, Sampling and Experiments.

Funding

This study was supported by the Guangdong Province Introduced Innovative R&D Team of Geological Processes and Natural Disasters around the South China Sea (Grant No. 2016ZT06N331) and the National Natural Science Foundation

of China (Grant No. 41872217). All new raw data collected in this manuscript are accessible through the corresponding author.

Acknowledgments

We wish to thank Yonggang Yan for assistance with sample processing.

Conflict of interest

The authors declare that the research was conducted in the absence of any commercial or financial relationships that could be construed as a potential conflict of interest.

References

- Barr, C., Tibby, J., Leng, M. J., Tyler, J. J., Henderson, A. C. G., Overpeck, J. T., et al. (2019). Holocene El Niño–southern oscillation variability reflected in subtropical Australian precipitation. *Sci. Rep.* 9, 1627. doi:10.1038/s41598-019-38626-3
- Bradák-Hayashia, B., Tanigawa, K., Hyodo, M., and Seto, Y. (2017). Magnetic fabric evidence for rapid, characteristic changes in the dynamics of the 2011 Tohoku-oki tsunami. *Mar. Geol.* 387, 85–96. doi:10.1016/j.margeo.2017.04.003
- Brown, M. C., Donadini, F., Nilsson, A., Panovska, S., Frank, U., Korhonen, K., et al. (2015). GEOMAGIA50.v3: 2. A new paleomagnetic database for lake and marine sediments. *Earth Planets Space* 67, 70. doi:10.1186/s40623-015-0233-z
- Cai, S. H., Jin, G. Y., Tauxe, L., Deng, C. L., Qin, H. F., Pan, Y. X., et al. (2017). Archaeointensity results spanning the past 6 kiloyears from eastern China and implications for extreme behaviors of the geomagnetic field. *Proc. Natl. Acad. Sci. U. S. A.* 114 (1), 39–44. doi:10.1073/pnas.1616976114
- Chen, J. L., Wang, Z. Q., Tam, C. Y., Lau, N. C., Dickson, L. D. S., and Mok, H. Y. (2020). Impacts of climate change on tropical cyclones and induced storm surges in the Pearl River Delta region using pseudo-global-warming method. *Sci. Rep.* 10, 1965. doi:10.1038/s41598-020-58824-8
- Conroy, J. L., Overpeck, J. T., Cole, J. E., Shanahan, T. M., and Steinitz-Kannan, M. (2008). Holocene changes in eastern tropical Pacific climate inferred from a Galápagos lake sediment record. *Quat. Sci. Rev.* 27, 1166–1180. doi:10.1016/j.quascirev.2008.02.015
- Constable, C., and Tauxe, L. (1990). The Bootstrap for magnetic susceptibility tensors. *J. Geophys. Res.* 95 (B6), 8383–8395. doi:10.1029/JB095iB06p08383
- Deng, C. L., Zhu, R. X., Jackson, M. J., Verosub, K. L., and Singer, M. J. (2001). Variability of the temperature-dependent susceptibility of the Holocene eolian deposits in the Chinese loess plateau: A pedogenesis indicator. *Phys. Chem. Earth, Part A Solid Earth Geodesy* 26 (11–12), 873–878. doi:10.1016/S1464-1895(01)00135-1
- Deng, S. L., Chen, T., Yang, N., Qu, L., Li, M. H., and Chen, D. (2018). Spatial and temporal distribution of rainfall and drought characteristics across the Pearl River basin. *Sci. Total Environ.* 619–620, 28–41. doi:10.1016/j.scitotenv.2017.10.339
- Egli, R. (2013). Variforc: An optimized protocol for calculating non-regular first-order reversal curve (FORC) diagrams. *Glob. Planet. Change* 110, 302–320. doi:10.1016/j.gloplacha.2013.08.003
- Ge, Q. S., Zheng, J. Y., Fang, X. Q., Man, Z. M., Zhang, X. Q., Zhang, P. Y., et al. (2003). Winter half-year temperature reconstruction for the middle and lower reaches of the Yellow River and Yangtze River, China, during the past 2000 years. *Holocene* 13 (6), 933–940. doi:10.1191/0959683603hl680rr
- Goodbred, S. L., and Kuehl, S. A. (2000). The significance of large sediment supply, active tectonism, and eustasy on margin sequence development: Late Quaternary stratigraphy and evolution of the Ganges-Brahmaputra delta. *Sediment. Geol.* 133 (3–4), 227–248. doi:10.1016/S0037-0738(00)00041-5
- Harrison, R. J., and Feinberg, J. M. (2008). FORCinel: An improved algorithm for calculating first-order reversal curve distributions using locally weighted regression smoothing. *Geochem. Geophys. Geosyst.* 9, Q05016. doi:10.1029/2008GC001987
- Hassan, F. A. (1997). The dynamics of a riverine civilization: A geoarchaeological perspective on the Nile valley, Egypt. *World Archaeol.* 29, 51–74. doi:10.1080/00438243.1997.9980363
- He, Y., Liu, X. J., Duan, Z. H., Liu, C., Hou, P., Lu, C., et al. (2022). Long-term morphodynamic evolution in the modern estuary of the Pearl River Delta, South China. *Geomorphology* 398, 108057. doi:10.1016/j.geomorph.2021.108057
- Hoitink, A. J. F., Wang, Z. B., Vermeulen, B., Huismans, Y., and Kastner, K. (2017). Tidal controls on river delta morphology. *Nat. Geosci.* 10, 637–645. doi:10.1038/ngeo3000
- Jiang, Z. X., Liu, Q. S., Roberts, A. P., Barrón, V., Torrent, J., and Zhang, Q. (2018). A new model for transformation of ferrihydrite to hematite in soils and sediments. *Geology* 46 (11), 987–990. doi:10.1130/G45386.1
- Jiang, Z. X., Liu, Q. S., Roberts, A. P., Dekkers, M. J., Barrón, V., Torrent, J., et al. (2022). The magnetic and color reflectance properties of hematite: From Earth to mars. *Rev. Geophys.* 60 (1), e2020RG000698. doi:10.1029/2020RG000698
- Karamperidou, C., Nezio, P. N. D., Timmermann, A., Jin, F.-F., and Cobb, K. M. (2015). The response of ENSO flavors to mid-Holocene climate: Implications for proxy interpretation. *Paleoceanography* 30, 527–547. doi:10.1002/2014PA002742
- Korte, M., Constable, C., Donadini, F., and Holme, R. (2011). On the persistence of geomagnetic flux lobes in global Holocene field models. *Phys. Earth Planet. Interiors* 312 (3–4), 179–186. doi:10.1016/j.pepi.2010.08.006
- Korte, M., and Holme, R. (2010). On the persistence of geomagnetic flux lobes in global Holocene field models. *Phys. Earth Planet. Interiors* 182, 179–186. doi:10.1016/j.pepi.2010.08.006
- Laj, C., and Channell, J. E. T. (2015). *Geomagnetic excursions in treatise on Geophysics*. 2nd Edition. Netherlands: Elsevier B.V., 5343–5363. Editor-in-Chief Schubert G.
- Li, M. S., Hinnov, L., and Kump, L. (2019). Acycle: Time-series analysis software for paleoclimate research and education. *Comput. Geosci.* 127, 12–22. doi:10.1016/j.cageo.2019.02.011
- Liu, F., Chen, H., Cai, H. Y., Luo, X. X., Ou, S. Y., and Yang, Q. S. (2017). Impacts of ENSO on multi-scale variations in sediment discharge from the Pearl River to the South China sea. *Geomorphology* 293, 24–36. doi:10.1016/j.geomorph.2017.05.007
- Liu, F., Xie, R. Y., Luo, X. L., Yang, L. Z., Cai, H. Y., and Yang, Q. S. (2019). Stepwise adjustment of deltaic channels in response to human interventions and its hydrological implications for sustainable water managements in the Pearl River Delta, China. *J. Hydrology* 573, 194–206. doi:10.1016/j.jhydrol.2019.03.063
- Long, X., Ji, J., and Balsam, W. (2011). Rainfall-dependent transformations of iron oxides in a tropical saprolite transect of Hainan Island, South China: Spectral and magnetic measurements. *J. Geophys. Res.* 116, F03015. doi:10.1029/2010JF001712
- Macklin, M. G., and Lewin, J. (2015). The rivers of civilization. *Quat. Sci. Rev.* 114, 228–244. doi:10.1016/j.quascirev.2015.02.004
- McManus, J. (2002). Deltaic responses to changes in river regimes. *Mar. Chem.* 79, 155–170. doi:10.1016/S0304-4203(02)00061-0

Publisher's note

All claims expressed in this article are solely those of the authors and do not necessarily represent those of their affiliated organizations, or those of the publisher, the editors and the reviewers. Any product that may be evaluated in this article, or claim that may be made by its manufacturer, is not guaranteed or endorsed by the publisher.

Supplementary material

The Supplementary Material for this article can be found online at: <https://www.frontiersin.org/articles/10.3389/feart.2022.1015697/full#supplementary-material>

- Moy, C. M., Seltzer, G. O., Rodbell, D. T., and Anderson, D. M. (2002). Variability of El nino/southern oscillation activity at millennial timescales during the Holocene epoch. *Nature* 420, 162–165. doi:10.1038/nature01194
- Nan, Q. Y., Li, T. G., Chen, J. X., Nigma, R., Yu, X. K., Xu, Z. K., et al. (2014). Late Holocene (~2 ka) East asian monsoon variations inferred from river discharge and climate interrelationships in the Pearl River estuary. *Quat. Res.* 81, 240–250. doi:10.1016/j.yqres.2013.12.004
- Nian, X. M., Zhang, W. G., Wang, X. T., Hutchinson, S. M., Zhao, X. Q., and Liu, K.-B. (2022). Multi-centennial variability of Yangtze delta growth over the last 2000 Years: Interplay of climate and people. *Earth's Future* 10 (8), e2021EF002461. doi:10.1029/2021EF002461
- Ranasinghe, R., Wu, C. S., Conallin, J., Duong, T. M., and Anthony, E. J. (2019). Disentangling the relative impacts of climate change and human activities on fluvial sediment supply to the coast by the world's large rivers: Pearl River Basin, China. *Sci. Rep.* 9, 9236. doi:10.1038/s41598-019-45442-2
- Roberts, A. P., Chang, L., Rowan, C. J., Horng, C.-S., and Florindo, F. (2011). Magnetic properties of sedimentary greigite (Fe₃S₄): An update. *Rev. Geophys.* 49, RG1002. doi:10.1029/2010RG000336
- Roberts, A. P., Zhao, X., Hu, P., Abrajewitch, A., Chen, Y.-H., Harrison, R. J., et al. (2021). Magnetic domain state and anisotropy in hematite (α-Fe₂O₃) from first-order reversal curve diagrams. *JGR. Solid Earth* 126, e2021JB023027. doi:10.1029/2021jb023027
- Schneider, J.-L., Catherine, C.-G., Jean-Luc, B., James, G., Daisuke, S., Kazuhisa, G., et al. (2014). Using magnetic fabric to reconstruct the dynamics of tsunami deposition on the Sendai Plain, Japan - the 2011 Tohoku-oki tsunami. *Mar. Geol.* 358, 89–106. doi:10.1016/j.margeo.2014.06.010
- Shanahan, T. M., Peck, J. A., McKay, N., Heil, C. W., King, J., Forman, S., et al. (2013). Age models for long lacustrine sediment records using multiple dating approaches—An example from Lake Bosumtwi, Ghana. *Quat. Geochronol.* 15, 47–60. doi:10.1016/j.quageo.2012.12.001
- Shaw, J. B., David, M., and Wayne and, W. R. (2016). Flow patterns and morphology of a prograding river delta. *J. Geophys. Res. Earth Surf.* 121 (2), 372–391. doi:10.1002/2015JF003570
- Stott, L., Cannariato, K., Thunell, R., Huag, G. H., Koutavas, A., and Lund, S. (2004). Decline of surface temperature and salinity in the Western tropical Pacific Ocean in the Holocene epoch. *Nature* 431, 56–59. doi:10.1038/nature02903
- Taira, A. (1989). "Magnetic fabrics and depositional processes," in *Sedimentary facies in the active plate margin*. Editors A. Taira and F. Masuda (Tokyo: Terra Scientific Publishing Company), 43–77.
- Tarling, D. H., and Hrouda, F. (1993). *The magnetic anisotropy of rocks*. London: Chapman & Hall.
- Wang, L. J., Sarnthein, M., Erlenkeuser, H., Grootes, P. M., Grimalt, J. O., Pelejero, C., et al. (1999). Holocene variations in asian monsoon moisture: A bidecadal sediment record from the South China sea. *Geophys. Res. Lett.* 26 (18), 2889–2892. doi:10.1029/1999GL900443
- Wassmer, P. C., Gomez, C. A., Iskandaryah, T. Y. W. M., Lavigne, F., and Sartohadi, J. (2015). Contribution of anisotropy of magneticsusceptibility (AMS) to reconstruct flooding characteristics of a 4220 BP tsunami from a thick unconsolidated structureless deposit (Banda Aceh, Sumatra). *Front. Earth Sci. (Lausanne)*. 3, 40. doi:10.3389/feart.2015.00040
- Wei, X., Cai, S. Q., Ni, P. T., and Zhan, W. K. (2020). Impacts of climate change and human activities on the water discharge and sediment load of the Pearl River, southern China. *Sci. Rep.* 10, 16743. doi:10.1038/s41598-020-73939-8
- Wu, Z. Y., Saito, Y., Zhao, D. N., Zhou, J. Q., Cao, Z. Y., Li, S. J., et al. (2016). Impact of human activities on subaqueous topographic change in Lingding Bay of the Pearl River estuary, China, during 1955–2013. *Sci. Rep.* 6, 37742. doi:10.1038/srep37742
- Xie, C. J., Cui, B. S., Ning, Z. H., Yu, S. L., and Xie, T. (2022). Longitudinal dynamics of hydrological connectivity in the yellow River Delta, China. *Front. Mar. Sci.* 9, 899671. doi:10.3389/fmars.2022.899671
- Yan, Y., Wang, G. H., Wu, H., Gu, G. J., and Nanding, N. (2022). Characteristics of precipitation and floods during typhoons in Guangdong Province. *Remote Sens.* 14, 1945. doi:10.3390/rs14081945
- Yang, C., Li, Q. Q., Zhao, T. H., Liu, H. Z., Gao, W. X., Shi, T. Z., et al. (2019). Detecting spatiotemporal features and rationalities of urban expansions within the Guangdong–Hong Kong–Macau greater bay area of China from 1987 to 2017 using time-series landsat images and socioeconomic data. *Remote Sens.* 11, 2215. doi:10.3390/rs11192215
- Yang, X. Q., Graphes, R., Zhou, H. Y., and Yang, J. (2008). Magnetic properties of sediments from the Pearl River Delta, South China: Paleoenvironmental implications. *Sci. China Ser. D-Earth. Sci.* 51 (1), 56–66. doi:10.1007/s11430-007-0151-4
- Yang, X. Q., Heller, F., Yang, J., and Su, Z. H. (2009). Paleosecular variations since ~9000 yr BP as recorded by sediments from maar lake Shuangchiling, Hainan, South China. *Earth Planet. Sci. Lett.* 288 (1–2), 1–9. doi:10.1016/j.epsl.2009.07.023
- Zheng, J., Hao, Z., Fang, X., and Ge, Q. (2014). Changing characteristics of extreme climate events during past 2000 years in China. (In Chinese). *Prog. Geogr.* 33, 3–12. doi:10.11820/dlkxjz.2014.01.001
- Zheng, Y., Zheng, H. B., Deng, C. L., and Liu, Q. S. (2014). Holocene paleomagnetic secular variation from East China sea and a PSV stack of East Asia. *Phys. Earth Planet. Interiors* 236, 69–78. doi:10.1016/j.pepi.2014.07.001
- Zhou, H. Y., Wang, Z. L., Wu, X. S., Chen, Y. H., Zhong, Y. X., Li, Z. Y., et al. (2019). Spatiotemporal variation of annual runoff and sediment load in the Pearl River during 1953–2017. *Sustainability* 11, 5007. doi:10.3390/su11185007
- Zhu, Y. C., Chen, H. G., and Lu, D. T. (1988). *Population of China (Guangdong branch)*. Beijing: China Financial & Economic Publishing House, 40–57. In Chinese7-5005-0022-X/F.0022.
- Zhu, Y. N., Liu, Z. H., Zhao, Y., Li, H. H., He, F., Zhao, J. Q., et al. (2017). Flood simulations and uncertainty analysis for the Pearl River Basin using the coupled land surface and hydrological model system. *Water* 9 (6), 391. doi:10.3390/w9060391
- Zhu, Z. M., Feinberg, J. M., Xie, S. C., Bourne, M. D., Huang, C. J., Hu, C. Y., et al. (2017). Holocene ENSO-related cyclic storms recorded by magnetic minerals in speleothems of central China. *Proc. Natl. Acad. Sci. U. S. A.* 114 (5), 852–857. doi:10.1073/pnas.1610930114
- Zong, Y., Yim, W. W.-S., Yu, F., and Huang, G. (2009). Late Quaternary environmental changes in the Pearl River mouth region, China. *Quat. Int.* 206, 35–45. doi:10.1016/j.quaint.2008.10.012



OPEN ACCESS

EDITED BY

Shiming Wan,
Institute of Oceanology (CAS), China

REVIEWED BY

Kai Deng,
ETH Zürich, Switzerland
Yongjian Yao,
Guangzhou Marine Geological Survey,
China

*CORRESPONDENCE

Hao Liang,
liangh27@mail2.sysu.edu.cn

SPECIALTY SECTION

This article was submitted to Quaternary Science, Geomorphology and Paleoenvironment, a section of the journal Frontiers in Earth Science

RECEIVED 23 August 2022

ACCEPTED 07 November 2022

PUBLISHED 13 January 2023

CITATION

Liang H, Zhang K, Li Z, Chen Z, Hui G, Huang P, Tian Q, Tang Y, Chen C, Zhang Y, He X, Yan Y, Dai X, Li Z, Wang W and Zhang P (2023), Temporally varied coastal uplift rates north of the Littoral Fault Zone since the late Quaternary in the northern South China Sea: Insights from the wave-cut platform and cosmogenic exposure dating. *Front. Earth Sci.* 10:1026181. doi: 10.3389/feart.2022.1026181

COPYRIGHT

© 2023 Liang, Zhang, Li, Chen, Hui, Huang, Tian, Tang, Chen, Zhang, He, Yan, Dai, Li, Wang and Zhang. This is an open-access article distributed under the terms of the [Creative Commons Attribution License \(CC BY\)](https://creativecommons.org/licenses/by/4.0/). The use, distribution or reproduction in other forums is permitted, provided the original author(s) and the copyright owner(s) are credited and that the original publication in this journal is cited, in accordance with accepted academic practice. No use, distribution or reproduction is permitted which does not comply with these terms.

Temporally varied coastal uplift rates north of the Littoral Fault Zone since the late Quaternary in the northern South China Sea: Insights from the wave-cut platform and cosmogenic exposure dating

Hao Liang^{1,2*}, Ke Zhang^{1,2}, Zhigang Li^{1,2}, Zhen Chen¹, Gege Hui^{1,2}, Ping Huang³, Qingying Tian⁴, Yongjie Tang^{1,2}, Cong Chen^{1,2}, Yipeng Zhang^{1,2}, Xiaohui He^{1,2}, Yonggang Yan^{1,2}, Xiangming Dai^{1,2}, Zhongyun Li⁵, Weitao Wang^{1,2} and Peizhen Zhang^{1,2}

¹Guangdong Provincial Key Laboratory of Geodynamics and Geohazards, School of Earth Sciences and Engineering, Sun Yat-sen University, Zhuhai, China, ²Southern Marine Science and Engineering Guangdong Laboratory, Zhuhai, China, ³GDZD Institute on Deep-Earth Sciences, Guangzhou, China, ⁴Guangdong Provincial Seismological Bureau, Guangzhou, China, ⁵School of Tourism and Geography, Shaoguan University, Shaoguan, China

While understanding the long-term slip rate of active normal faults is essential for the comprehensive assessment of seismic activity, it is difficult due to the absence of age control in the erosional bedrock region. The preserved sequence of wave-cut platforms in granite allows exploration of the long-term slip rate in the footwall of some normal faults. We investigated wave-cut platforms in the southern Pearl River Delta (PRD), a coastal delta transected by the seismically active Littoral Fault Zone (LFZ) in the northern South China Sea, to derive slip rates and their impacts on the seismic hazard potential. We mapped a flight of four wave-cut platforms (T_1 – T_4), dated the T_2 and T_4 platforms by ^{10}Be cosmogenic nuclide dating, and used the absolute age to correlate the un-dated platform to global sea-level highstands. Our results allocate the ages of 128 ka, 197 ka, and 239 ka to the upper three wave-cut platforms and yield temporally varied uplift rates ranging from 0.30 to 0.38 mm/a during 239–128 ka to 0.09 mm/a since 128 ka. A decrease in the uplift rate, which coincided with a decreased subsidence rate within the PRD in previous work, implied a weakened differential uplift onshore of the LFZ system. Our findings infer that the transgression event occurred as early as marine isotope stage (MIS) 7 in the PRD, consistent with the view that Pleistocene sedimentation began in MIS 5 or earlier in the PRD.

KEYWORDS

coastal uplift, Littoral Fault Zone, wave-cut platform, cosmogenic dating, Pearl River Delta

Introduction

The slip rate at the coastline from the area of distributed normal faulting in the continental margin is commonly used to gain insights into the processes of intraplate deformation (Merritts and Bull, 1989; Monaco et al., 1997; Palyvos et al., 2005). Because the inner edge between a subhorizontal wave-cut platform and a steep coastal cliff represents an approximation of zero height above sea level at the time of platform formation, their current altitudes can be used to correlate with oscillating sea-level highstands and to further quantify the slip rate of faults for long-term seismic hazard analysis (Roberts et al., 2013; Jara-Muñoz et al., 2015; Meschis et al., 2018; Pedoja et al., 2018).

However, obtaining precise dating results on erosional or thin depositional wave-cut platforms is challenging and, thus, less studied. Fortunately, cosmogenic nuclide dating provides the exposure age of the wave-cut platforms, and further permits slip rate calculations when the initial and modern altitudes of platforms are determined (Marquardt et al., 2004; Saillard et al., 2011; Rodríguez et al., 2013). This approach accurately evaluates Quaternary tectonic activity in erosional bedrock regions, which helps to quantitatively understand long-term seismic hazard assessment along faults.

The Pearl River Delta (PRD), where major drainages converge into the South China Sea from several estuaries, is one of the largest coastal deltas in China (Figure 1). The bedrock

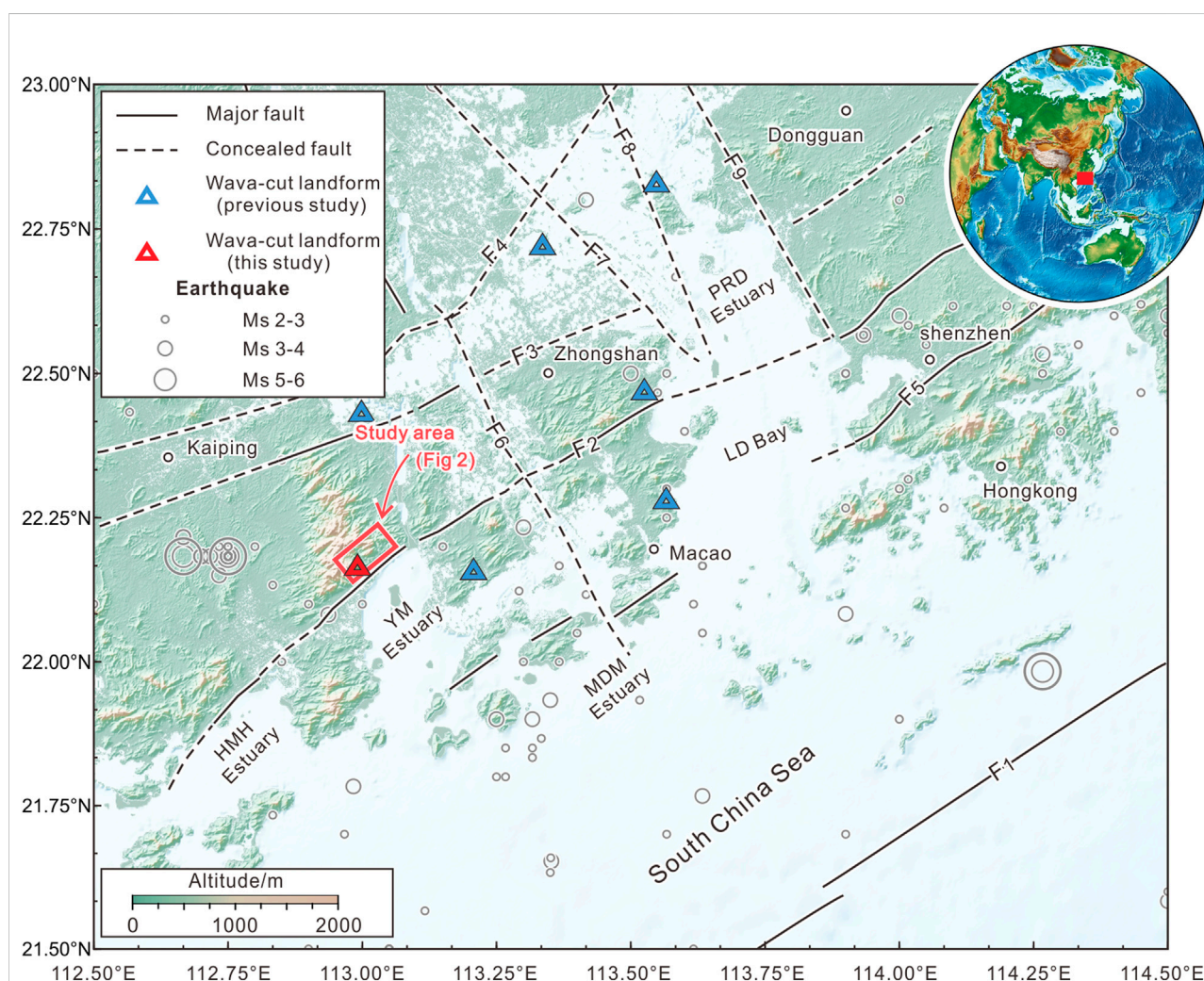


FIGURE 1

Tectonic setting of the northern margin of the South China Sea, southern China. The earthquake locations are constrained to a depth of <30 km between 1976 and 2022 from data from the China Earthquake Network Center and Guangdong Provincial Seismological Bureau. The faults are adapted from Huang et al. (1982), Yu et al. (2016), and Huang et al. (2021). The locations of the wave-cut platforms in previous studies are from Huang et al. (1982), Jiang and Hu (1994), Wang et al. (2011), and Zhao (2017). F1: Littoral Fault Zone; F2: South Wuguishan Fault; F3: North Wuguishan Fault; F4: Xinhui–Shiqiao Fault; F5: Wuhua–Shenzhen Fault; F6: Xijiang Fault; F7: Baini–Shawan Fault; F8: Hualong–Huangge Fault; F9: Nangang–Taiping Fault. The topography is from the Shuttle Radar Topography Mission (SRTM) digital elevation model at 90-m resolution.

of the PRD is predominately composed of Mesozoic granite and is cut through by a set of conjugate ENE-striking and NNW-striking faults (Huang et al., 1982; Chen et al., 2002; Yao et al., 2008). The ENE-striking Littoral Fault Zone (LFZ) system is a major intraplate extensional zone in the northern South China Sea that could present potentially intense seismic activity (Liu, 1985; Zhao et al., 2004; Cao et al., 2018; Hui et al., 2021; Dai et al., 2022a; Hui et al., 2022; Li et al., 2022) and has caused several strong earthquakes historically [e.g., the 1918 Ms 7.5 Nan'ao earthquake, Xia et al. (2020)]. To elucidate the slip rates of this active normal-fault system, numerous samples from the subsiding hanging wall of the ENE-striking faults where Quaternary deposits were preserved have been dated (Huang et al., 1983, 1985; Chen et al., 1994; Yao et al., 2008). However, few dating results exist from the uplifting footwall due to poor preservation for sediment dating. Thus, understanding the longer-term activity of these normal faults through the Quaternary, which requires robust dating on both fault walls, is lacking. Fortunately, Pleistocene differential uplift is visible in sequences of preserved wave-cut platforms throughout the coast in the PRD. In this study, we present sequential wave-cut platforms in the footwall of a coastal ENE-striking fault in the southern PRD. We dated the granite-composed wave-cut platform according to the ^{10}Be cosmogenic depth profile, calculated the uplift rates, and correlated the un-dated platforms to past eustatic sea-level highstands based on the best-fit predictions. As a result, we identified marine isotope stages (MISs) 5e, 7a, and 7e platforms in the study site. Moreover, we observed temporally varied slip rates before and after approximately 128 ka, which may be relevant to a weakened differential uplift onshore in the LFZ system.

Background

Brief genetic process of wave-cut platforms

A new wave-cut platform is created by continuous wave abrasion and consists of two distinct features: a gently seaward dipping erosional platform and a seaward dipping sea cliff (Armijo et al., 1996). The junction of the platform and sea cliff is the inner edge of the platform and often preserves the wave-cut notch. The inner edge of the platform occurs at the shoreline and represents the peak of local sea level at a short time of its formation (<1 ka). Hence, the wave-cut platform can correspond to the fixed dates of highstands (e.g., 128, 197, 239, 290, or 338 ka). Platforms or notches that are formed below the highstand are destroyed or overprinted by wave erosion during subsequent sea-level highstands. With tectonic uplift, the platform rises above sea level and becomes a paleo-horizontal indicator.

Littoral Fault Zone

The LFZ is an ENE-striking intraplate deformation zone along the northern margin of the South China Sea. The entire fault zone extends approximately 1,000 km along the South China coastline with an approximate width of 20 km (Liu, 1985; Zhao et al., 2004; Cao et al., 2018; Hui et al., 2021, 2022). Offshore of the PRD estuary at water depths of 30–50 m, the LFZ (F1) presents right-step dextral features on the horizontal view, and southeast-dipping normal faulting in the vertical view (Liu, 1985; Zhao et al., 2004; Cao et al., 2018; Hui et al., 2021, 2022). Seismic profiles reveal that the LFZ acted as a northern boundary fault of the South China Sea with a width of 6–10 km (Li et al., 2022). The Cenozoic history of the LFZ is complex, containing initial fault activity of low-angle basement decollement, then inherited high-angle SE-dipping normal faulting, and finally strike-slip faulting. The active LFZ had potentially produced 18 large earthquakes (>Ms 6.0), including the Ms 7.0 Nan'ao earthquake in 1600, Ms 7.5 Qionghai earthquake in 1605, and Ms 7.5 Nan'ao earthquake in 1918 (Xia et al., 2020; Dai et al., 2022; Hui et al., 2022). Onshore, the granitic basement of the PRD is transected by three NE- to ENE-striking faults (South Wuguishan Fault, F2; North Wuguishan Fault, F3; and Xinhui-Shiqiao Fault, F4, Figure 1) and several NNW-striking faults (Chen et al., 2002; Yu et al., 2016). The NE- to ENE-striking faults exhibit normal faulting with high dipping angles (Huang et al., 1985; Chen et al., 1994), showing uplifts in their footwalls. The NNW-striking faults bound the river course and segmented the NE- to ENE-striking faults in places, but their activities are less well known. We are interested in the onshore ENE-striking F2 in the southern PRD because it appears to control the opening of estuaries and dominate the differential uplift that can be explored through the mapping and dating of wave-cut platforms.

Sediment dating in the PRD

Following long-term peneplanation since the Oligocene (Huang et al., 1982), sedimentation in the PRD only produced two Quaternary terrestrial-marine units: T1–M1 (Terrestrial–Marine units 1, upper) and T2–M2 (Terrestrial–Marine units 2, lower) that correspond to sea-level fluctuations (Huang et al., 1982; Zong et al., 2009b; Xu et al., 2022). The T1–M1 unit has a consensus age of Holocene (Zong et al., 2009a; Xu et al., 2020), whereas the deposition age of the T2–M2 unit remains controversial. Early works dated the M2 unit to MIS 3 (approximately 32–64 ka) by the ^{14}C approach (Huang et al., 1982; Chen et al., 1994; Wang et al., 2009). However, subsequent studies suggested that contamination with younger carbon and the upper limit of radiocarbon dating (<50 ka) would lead to significant age underestimation (Yim et al., 1990, 2008; Zong et al., 2009b; Yu et al., 2016) and

suggested MIS 5 (approximately 82–128 ka) for M2 deposition. The wide disparity in the time results in various interpretations of the tectonic context of the PRD in the Late Quaternary. In the MIS 3 view, M2 formed during the highstand of MIS 3 (approximately –60 m to –80 m) and was tectonically raised to the modern average depths (approximately –15 m to –30 m), for which the dates are obtained from quartz optically stimulated luminescence (OSL) of sandy sediments in the T2 unit (Tang et al., 2011; Wang et al., 2015). In contrast, in the MIS 5 view, M2 formed during the highstand of MIS 5 (approximately –20 m to 5 m) and tectonically subsided to the modern average depth, a view that is supported by feldspar OSL dating (Yim et al., 2008; Zong et al., 2009b; Yu et al., 2016; Xu et al., 2022). One way to address the dipolar age issue is to determine a regional uplift rate and examine whether deposits related to the MIS 3 highstand could rise to the modern depth based on the resultant rate. This challenge motivated us to examine landforms related to highstands in the erosional area. Wave-cut platforms, which occur where uplift outpaces sea-level highstands, commonly document long-term tectonic activity (Armijo et al., 1996; Roberts et al., 2013, 2013; Jara-Muñoz et al., 2015; Meschis et al., 2018; Padoja et al., 2018; Robertson et al., 2019; Racano et al., 2020) and are ideal for addressing the dipolar age issue. A previous study indicated that at least 67 sites of wave-cut platforms (or notches) are preserved in the PRD (Wang et al., 2011). Because most sites preserved few sediments and lacked age control, previous studies provided only a rough understanding of tectonics (Wang et al., 2011; Zhao, 2017). In our recent investigation, wave-cut platforms preserved in granite were observed along the footwall of the coastal F2 (Figure 1), which is suitable for ^{10}Be cosmogenic exposure dating. We conducted field investigations, digital elevation model (DEM) measurements, and dating to allocate the highstands to wave-cut platforms and then discussed differential uplift in the PRD region.

Methods

Investigation of the wave-cut platforms

Because the inner edges of the wave-cut platforms represent paleo-sea-level highstands, we mapped the platform extent through topographic profiles from a 12.5-m DEM (from Advanced Land Observing Satellite-1, ALOS 12.5-m resolution DEM, <https://search.asf.alaska.edu>) and field-based measurements. Because of thick vegetation and their relatively small size, it was difficult to recognize the apparent extents of the wave-cut platforms along their strike solely from the DEM data. Therefore, we selected 13 serial topographic profiles perpendicular to the strike of the coast (Figure 2) and recorded the positions and altitudes of the landward up-dip slope breaks as indicators of the inner edges

of the wave-cut platforms. Areas with apparent fluvial incisions were skipped to ensure wave-cut-induced geomorphic features. We defined each inner edge of the wave-cut platform based on three or more slope breaks with similar altitudes in the topographic profiles. The DEM-based inner edges were verified through field observations with indicators including slightly seaward-sloping surfaces that were up-dip bounded by abrupt paleoclip-like features or marked wave-cut notches and stacks. Field measurements were recorded using a differential global positioning system (DGPS; vertical error up to 0.1 m) and laser distance measuring equipment (0.1 m resolution within 300 m). The verified inner edges were correlated with DEM elevation to obtain a robust regional cross-section of the uplifted wave-cut platform. Each platform was ordered from low to high and specified with subscripts.

Chronological sampling, preparation, and modeling approach

We applied cosmogenic ^{10}Be exposure dating to the granite platform trends to constrain the potential formation ages of the wave-cut platforms. For the surface sample, we collected one sample on a wave-cut platform without apparent weathering. For the depth profile, we collected four samples from a ~1-m man-made quarried wall downward at intervals of 25–35 cm/site. Because of rainfall and intermittent runoff, part of the platform surface was eroded at the top of the quarried wall. The erosional thickness between the platform extent to the edge of the quarried wall was estimated for correction in the depth profile modeling. Approximately 1,500 g of rock was collected for each sample. The samples were pretreated at the Guangdong Provincial Key Laboratory of Geodynamics and Geohazards and the State Key Laboratory of Environmental Geochemistry, Institute of Geochemistry, Chinese Academy of Sciences, as described by Kohl and Nishiizumi (1992).

The cosmogenic nuclide concentration of surface ($N_{z(t)}$, atoms/g) exposed at time t (a) at constant production and erosion rates can be expressed as:

$$N_{z(t)} = P_{n,0} e^{-\frac{\rho z}{\Lambda_n}} \left(\frac{1 - e^{-\left(\frac{\rho r}{\Lambda_n} + \lambda\right)t}}{\frac{\rho r}{\Lambda_n} + \lambda} \right) + P_{m1,0} e^{-\frac{\rho z}{\Lambda_{m1}}} \left(\frac{1 - e^{-\left(\frac{\rho r}{\Lambda_{m1}} + \lambda\right)t}}{\frac{\rho r}{\Lambda_{m1}} + \lambda} \right) + P_{m2,0} e^{-\frac{\rho z}{\Lambda_{m2}}} \left(\frac{1 - e^{-\left(\frac{\rho r}{\Lambda_{m2}} + \lambda\right)t}}{\frac{\rho r}{\Lambda_{m2}} + \lambda} \right) \quad (1)$$

where $P_{n,0}$, $P_{m1,0}$, and $P_{m2,0}$ are the surface production rates (atoms/(g*a)) induced by nucleons, negative muons, and fast muons; Λ_n , Λ_{m1} , and Λ_{m2} are the attenuation lengths (g/cm²) of the nucleons and muons (negative and fast), respectively; z is the surface depth (cm); λ is the decay constant; ρ is the density (g/cm³); and r is a constant erosion rate (cm/ka).

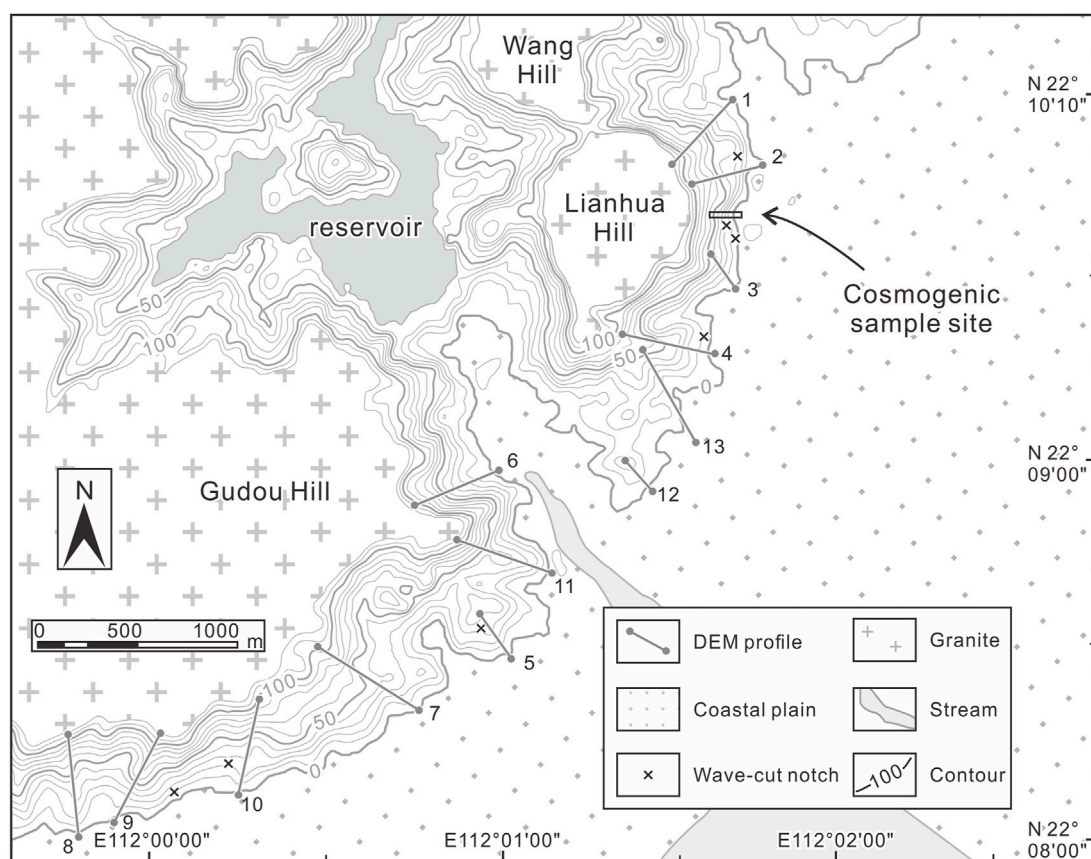


FIGURE 2

Simplified topographic and geological map of the study area. Locations of topographic profiles 1 to 13 and the ^{10}Be cosmogenic sampling site are shown with a 10-m topographic contour spacing interval ranging from 0-m to 120-m at altitude.

For the depth profile samples, the measured ^{10}Be concentration (C , atoms/g) included the *in situ*-produced (N_z , atoms/g), and the inherited (C_{inh} , atoms/g) concentrations:

$$C = N_z(t) + C_{inh} = \sum P_{zi}T_{ei} + C_{inh} \quad (2)$$

where $N_z(t) = \sum P_{zi}T_{ei}$, $P_{zi} = P_{i,0}e^{-\frac{\rho z}{\Lambda_i}}$, $T_{ei} = \left(\frac{1 - e^{-\frac{\rho z}{\Lambda_i}}}{\frac{\rho z}{\Lambda_i} + \lambda}\right)$, $i = n, m_1, m_2$

T_e is the effective exposure age (ka), which is the time required to accumulate a concentration N_z at production rate P_z without erosion and radioactive decay (Wang and Oskin, 2021).

In realistic cases, the estimated total eroded thickness (D , cm) from field evidence can be more straightforward than obtaining an erosion rate r . With eroded thickness, the effective exposure age can be rewritten as:

$$T_{ei} = \left(\frac{1 - e^{-\left(\frac{\rho D}{\Lambda_i} + \lambda t\right)}}{\frac{\rho D}{\Lambda_i} + \lambda}\right) i = n, m_1, m_2 \quad (3)$$

Taking account of Eq. 3, one would expect to use linear regression to obtain the inheritance. To rewrite Eq. 3 into a linear

form, the natural logarithm of the T_{em} over T_{en} ratio can be expressed by Maclaurin expansion as an approximation (Wang and Oskin, 2021):

$$g_i = \frac{T_{emi}}{T_{en}} \approx e^{-\frac{1}{2} \left(\frac{\rho D}{\Lambda_{mi}} - \frac{\rho D}{\Lambda_n} \right) + 1/24 \left[\left(\left(\frac{\rho D}{\Lambda_{mi}} \right)^2 - \left(\frac{\rho D}{\Lambda_n} \right)^2 \right) \right]}, i = 1, 2 \quad (4)$$

Bringing Eq. 4 into Eqs 1, 2 results in the following,

$$\begin{aligned} C(z) &= P_{zn}T_{en} + P_{zm1}g_1T_{em1} + P_{zm2}g_2T_{em2} + C_{inh} \\ &= P_{ze}T_{en} + C_{inh} \end{aligned} \quad (5a)$$

where

$$P_{ze} = P_{zn} + P_{zm1}g_1 + P_{zm2}g_2 \quad (5b)$$

In which Eq. 5 satisfies the linear form and linear least squares can be applied. By applying linear least squares inversion with known production rates, eroded thickness, and sample concentrations, the fitted T_{en} and C_{inh} can be determined.

To compute the exposure age, inheritance of cosmogenic production, and estimated erosion rate of the depth profile, we applied the Monte Carlo approach described by Wang and Oskin (2021) to find the best-fit results according to the distributions of the predicted iterations. To compute the exposure age of the surface sample, we applied a web-based calculator (<https://crep.otelo.univ-lorraine.fr/#/samples>) to obtain a reference age, assuming that the erosion rate and inheritance from the depth profile are constant over time. The detailed methods for sample pretreatment and calculation of cosmogenic nuclide concentrations are shown in the [Supplementary Material](#).

Allocating the wave-cut platforms to sea-level highstands

The predicted elevation of the highstands (E_p) can be calculated from the relationship between the highstand age related to the wave-cut platform formation age (T) and the sea-level elevation of the highstand (SL) under a given uplift rate (u):

$$E_p = (T \times u) + SL \quad (6)$$

If the highstand age (T) is independently known, an average uplift rate (u) over the duration (T) is easily obtained by Eq. 6. In a realistic case, a constant uplift rate over time is questionable, which could significantly affect the allocation between Quaternary sea-level highstands and individual wave-cut platforms. We applied the following process to test the uplift-rate scenarios: (a) obtain an initial uplift rate (u_0) by correlating the elevation (E_m) of a dated wave-cut platform (in an age of T_0) with sea-level data, assuming a constant uplift rate through T_0 ; (b) apply u_0 to examine whether E_p matches all E_m in the study area; (c) if not, iterate a new uplift rate (u_i) to find the best fit for the elevations of the older wave-cut platforms (E_{pi}) at T_i (greater than T_0), which can be expressed as:

$$E_{pi} = (T_i - T_0) \times u_i + (T_0 \times u_0) + SL \quad (7)$$

The fit between E_p and E_m is evaluated by their absolute difference (ΔE) for a given highstand age (T_i) and uplift rate (u_i). The elevations (SL) and ages (T_i) of each highstand are up to 500 ka, from Grant et al. (2014). The calculations are facilitated by the uplift rate (u_i) in an interval of 0.01 mm/a. We defined the best-fit uplift rate (u_i) of each undated platform by $\Delta E < 5$; lower platforms with fitted uplift rates should correlate with younger highstands and a uniform uplift rate in individual glacial-interglacial cycles.

Uncertainties and errors

The average elevation measurement errors from DEM were ± 10 m. The uncertainties in ^{10}Be concentrations, as

shown in Table 1, depend on the combined uncertainties by sampling ($< 5\%$), propagating the production rate and analytical uncertainty in the laboratory. Sea-level curve uncertainties vary with the data used. The reported uncertainty of the Grant et al. (2014) curve is 12 m.

We applied the standard error (SE) described by Robertson et al. (2019) to propagate the uplift value error equation:

$$SE(u)^2 = u^2 \times ((\sigma_H^2 / (H_T - H_{SL})^2) + (\sigma_T^2 / T^2)) \quad (8)$$

where u is the uplift rate, σ_H is the combined uncertainty for the measured wave-cut platform elevation and sea-level curve, H_T is the measured inner-edge elevation of the wave-cut platform, H_{SL} is the predicted sea level of the highstand, and σ_T is the dating error.

Results

Elevation of the wave-cut platforms

From the 13 DEM-based topographic profiles and approximately 40% field-based verifications excluding areas with thick vegetation or limited access to platforms, we identified the inner edges of the wave-cut platforms in the study area (Figures 3A,B). The cross-plots of DEM-based inner-edge elevations against the field-based inner-edge elevations provided confidence in the verification of the wave-cut platforms ($R^2 = 0.989$; Figure 3C). According to the inner-edge elevations, a flight of four wave-cut platforms was defined in the study area (Figure 3D).

The T_4 platform, bounded landward by inner edges reaching an altitude of 33–38 m above sea level (a.s.l.; Figures 3A, 4A), is characterized by remnants of narrow platforms that are carved in Mesozoic granite. Notches can be observed close to the inner edge of the platform, without apparent weathering. We collected one sample (XC) on the wave-cut platform surface (Table 1). Downslope, the T_3 platform outcrops with the altitude of the inner edge ranging from 23 to 25 m a.s.l. (Figures 3A, 4B). Because of thick vegetation, the narrow T_3 platforms are visible only in a few places.

The T_2 platform is extensive, with the inner edge ranging from 14 to 18 m a.s.l. (Figure 3B). Because of rainfall and intermittent runoff, approximately 40 cm of bedrock was eroded at the seaward edge of the platform. Quarrying was conducted on the platform to expose a freshly quarried wall for ^{10}Be depth profile dating (Figure 4C). We collected four samples (GDS-P1 to GDS-P4) downward the platform tread at 25–35-cm intervals. The T_1 platform is the lowest order of the terrace sequence, with an altitude of 1–3 m a.s.l. This platform shows a wide, flat surface with remnant sea stacks and merges with the coastal plain (Figures 3B, 4D,E).

TABLE 1 ^{10}Be sample locations and analysis.

Coordinates and altitude	Sample ID	Depth (cm)	Thickness (cm)	Surface production rate (atoms/(g*a)) ^a	^{10}Be (10^4 atoms/g)	^{10}Be error (10^4 atoms/g)
22.1597°N 113.0279°E 17 m a.s.l	GDS-P1	5	5	3.0171	21.3	0.57
	GDS-P2	35	5		10.2	0.41
	GDS-P3	55	5		7.6	0.31
	GDS-P4	80	5		6.1	0.28
22.1597°N 113.0279°E 35 m a.s.l	XC	0	5	3.0171	34.1	1.09

^aSurface production rates of ^{10}Be are calculated based on MATLAB scripts (Hidy et al., 2010; Lifton et al., 2014).

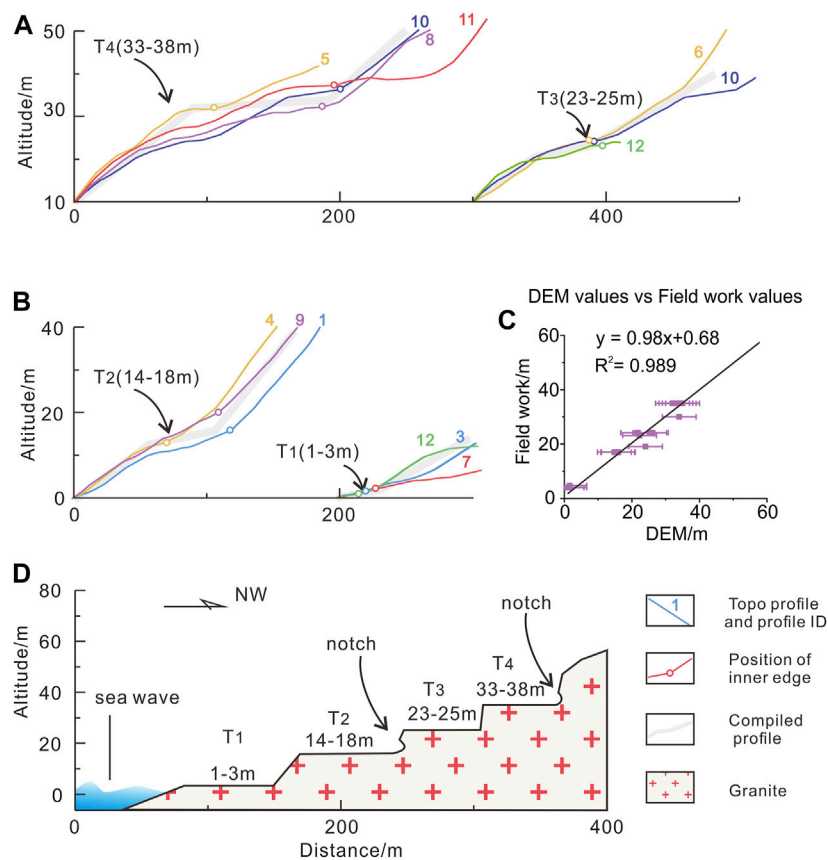


FIGURE 3

Compiled profiles of wave-cut platforms reproduced by digital elevation model (DEM)-based topographic profiles. The elevations of the slope breaks are at altitudes of 33–38 m and 23–25 m in (A), and at 14–18 m and 1–3 m in (B). The profile IDs are labeled. (C) Cross-plots of DEM-based inner-edge elevations against the field-based inner-edge elevations. (D) Cross-section of wave-cut platforms in the study area.

Results of ^{10}Be exposure dating

The measured ^{10}Be concentrations of the one surface sample and four depth profile samples, ranging between $6.15 \pm 0.28 \times 10^4$ atoms/g and $34.10 \pm 1.09 \times 10^4$ atoms/g, are listed in Table 1 along with the 1σ errors. We use the eroded-thickness approach to invert the inherited

concentration, erosion rate, and exposure age of the depth profile for a uniformly distributed, field-measured 0–40 cm eroded-thickness (Figure 4C).

By applying least-squares linear inversion, the fitted lines of the model data and depth profile curves are shown in Figure 5A,B. The distribution of T_e (95% confidence) yields ranged from 66.5 to 119.0 ka, with a peak at 86.0–88.0 ka



FIGURE 4

(A) View of the T₄ platform with a notch close to the inner edge. (B) View of the T₃ (red shading) platform. (C) The T₂ platform and the locations of ¹⁰Be cosmogenic dating depth profile samples; note that approximately 40 cm of bedrock was eroded. (D) View of T₂ (yellow shading), and T₁ (blue shading) platforms. (E) The sea stack is preserved on the T₁ platform close to the coastal plain.

(Figure 5C). The inheritance was very low, with most modeling results in the range of -9.00 to -1.20×10^4 atoms/g (95% confidence). Although inheritance should be greater than zero, removing negative inheritance would bias the best-fit distribution toward a younger age (Wang and Oskin, 2021). Thus, for samples with very low inheritance, truncating negative inheritance results would shift the realistic age to the extreme older tail of the age distribution. As all predictions are required to estimate the full distribution of the exposure age within errors, those negative values were permitted statistically and subsequently excluded. Excluding the negative results, the possible range of inheritance was 0 – 0.74×10^4 atoms/g (Figure 5D). The corresponding exposure age and erosion rate of the T₂ platform ranged from 101.38 ka to 132.16 ka (Figure 5E, 95% confidence) and 0.36–0.40 cm/ka, respectively (Figure 5F, 95% confidence). The predicted erosional thickness was 45 cm, consistent with the erosional thickness measured in the field (Figure 5G).

Assuming a constant erosion rate and very low inheritance (0.36–0.40 cm/ka and nearly zero from resultant data of the T₂ platform), we obtained an age of 239.87 ± 14.18 ka for the T₄ platform based on the ¹⁰Be concentration of the surface sample.

Discussion

Allocation of highstand ages for the wave-cut platforms

The estimated exposure age suggests that the T₂ platform could be allocated to a highstand at approximately 128 ka, which is equivalent to MIS 5e. Given this age and the elevation of sea level described by Grant et al. (2014), we obtain an initial uplift rate (u_0) of 0.09 ± 0.030 mm/a since 128 ka. Although the surface sample of T₄ suggests a reference age of approximately 239 ka, which is equivalent to MIS 7e, whether the platform would be overprinted independently in such time requires further examination.

When applying u_0 to examine whether the E_p values of the T₃ and T₄ platforms matched the E_m values in the study area, the resultant fit failed to reach the range of $\Delta E < 5$, suggesting that the uplift rate was not constant during the formation of the T₃ and T₄ platforms. Following the iterations of best fit with a fixed uplift rate since 128 ka (0.09 mm/a) and a given uplift rate ranging from 0 mm/a to 0.5 mm/a with an interval of 0.01 mm/a during 128–500 ka revealed three predicted scenarios that satisfied our defined fit condition: 1) T₃ and T₄

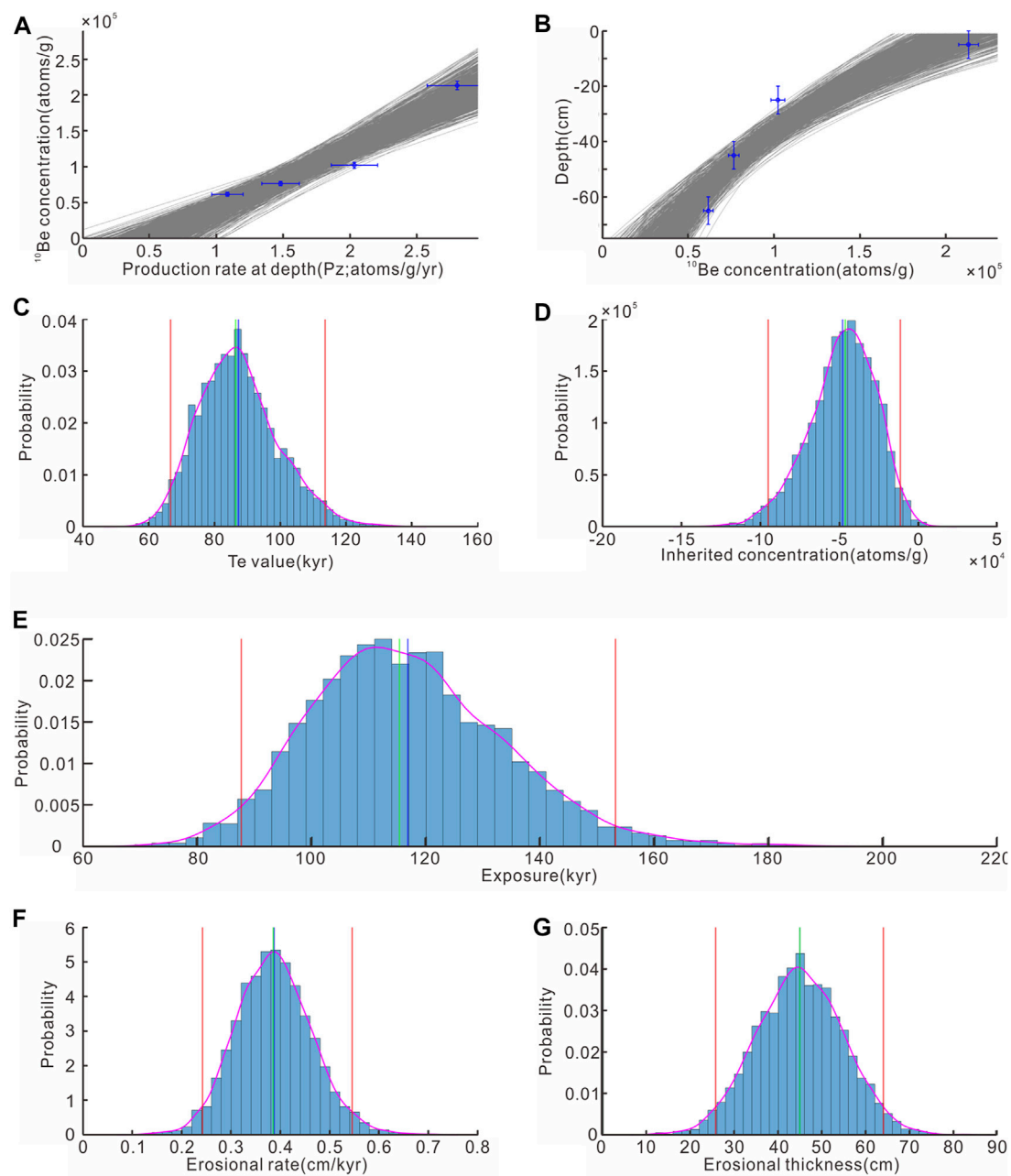
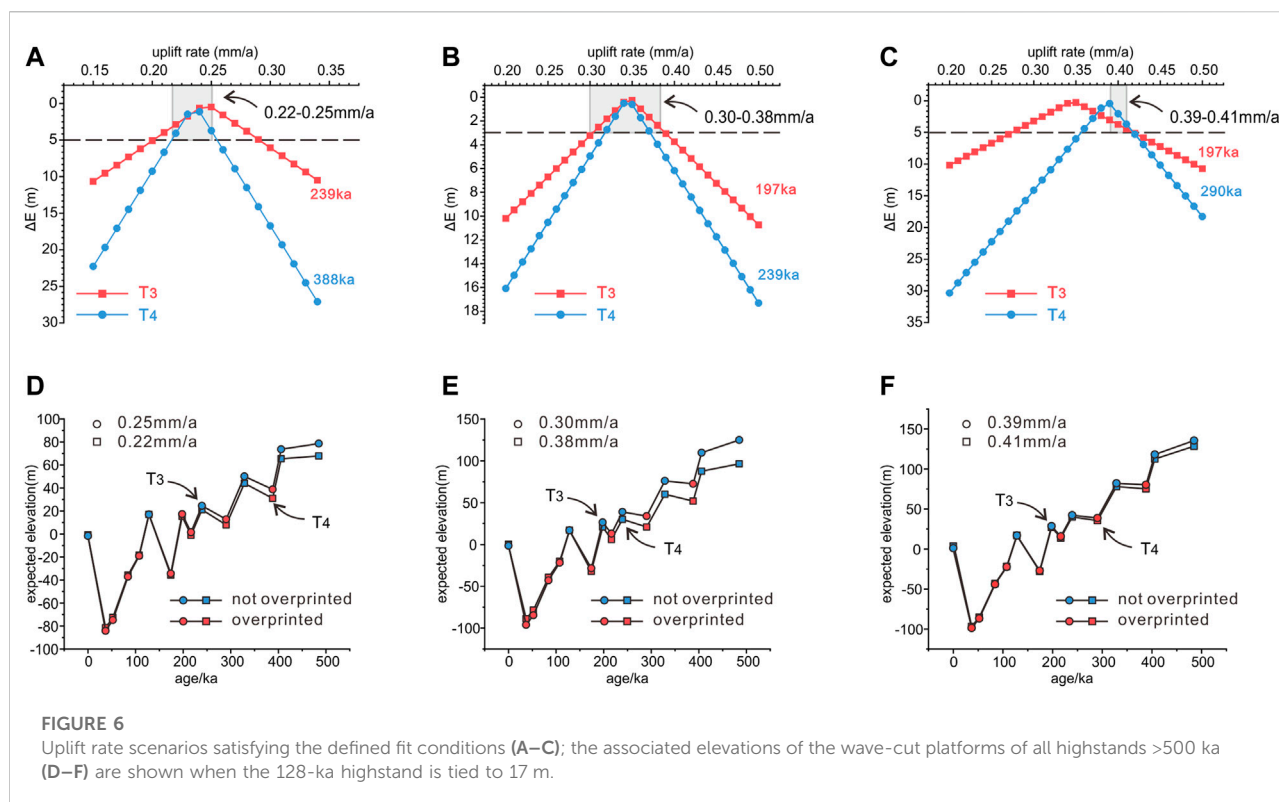


FIGURE 5

Linear regression results for the GDS data set with the eroded-thickness approach after 100,000 iterations. (A) Relationship of sample concentration to production rate at depth. (B) Distribution of the depth profile models with best-fit curves. (C) Distribution of the effective exposure age (T_e). (D) Modeling-inherited concentration. (E) Estimated exposure age based on a preset erosional thickness. (F) Distribution of erosion rates. (G) Distribution of predicted erosional thicknesses.

platforms with highstand ages of 239 ka and 388 ka and uplift rates in the range of 0.22–0.25 mm/a; 2) T_3 and T_4 platforms with highstand ages of 197 ka and 239 ka and uplift rates in the range of 0.30–0.38 mm/a; and 3) T_3 and T_4 platforms with highstand ages of 197 ka and 290 ka and uplift rates in the range of 0.39–0.41 mm/a (Figures 6A–C).

We plotted highstand elevations with the fit rates for each scenario to examine whether the predicted wave-cut platform would be overprinted in a subsequent highstand. In the scenario of 0.22–0.25 mm/a, the elevations of the T_3 and T_4 platforms were 21.1–24.5 m and 30.9–38.7 m. However, the predicted elevations of the platforms for 328 ka (44.0–50.1 m) would



overprint the T_4 platform (Figure 6D), suggesting that this scenario was unlikely to occur. In the scenario of 0.30–0.38 mm/a, the elevations of the T_3 and T_4 platforms were 20.7–26.4 m and 30.0–38.9 m and were preserved without significant overprinting (Figure 6E). In the scenario of 0.39–0.41 mm/a, the elevations of the T_3 and T_4 platforms were 27.1–28.5 m and 35.4–38.7 m. Analogous to the scenario of 0.22–0.25 mm/a, the predicted elevations of the platform relating to 239 ka (40.1–42.3 m) would overprint the T_4 platform (Figure 6F), suggesting that this scenario was unlikely to occur. The best-fit uplift rate and results of our examination of highstand overprinting suggested that the T_3 and T_4 platforms could be allocated to highstands at 197 ka (MIS 7a) and 239 ka (MIS 7e), respectively. These results well matched the reference ^{10}Be exposure age of the T_4 platform. Considering the errors in field measurements, the uncertainty of the uplift rate would range from 0.017 mm/a to 0.034 mm/a. Overall, the T_2 , T_3 , and T_4 wave-cut platforms were assigned to 128 ka (MIS 5e), 197 ka (MIS 7a), and 239 ka (MIS 7e), with a decreasing uplift rate ranging from 0.30 ± 0.034 mm/a to 0.38 ± 0.017 mm/a before 128 ka and to 0.09 ± 0.030 mm/a since 128 ka.

Implications

Considering the controversial context of the T_2 – M_2 unit, our preferred allocations of highstand ages for the wave-cut

platforms have several implications. First, transgression events likely occurred as early as MIS 7 (190–239 ka) in the southern PRD, as indicated by the allocated highstand age of the highest T_4 platform (Figure 7). Recent OSL dating has revealed pre-MIS-5 deposits in the southern PRD, suggesting that Quaternary sedimentation was likely initiated before 128 ka (Xu et al., 2022). If correct, our finding would be consistent with the suggestion that M_2 is at least correlated with MIS 5 and perhaps even older. Moreover, the elevation of the predicted wave-cut platforms in MIS 3 were allocated at –78 m to –97 m in our best-fit model. These elevations are much lower than the average depth of M_2 in the PRD (approximately –15 m to –30 m), suggesting that is unlikely to preserve MIS 3 wave-cut platforms or sediments in the uplifted wall areas.

Second, our preferred uplift rates provide significant benchmarks for elucidating the differential uplift in the PRD. Considering M_2 as deposits of MIS 5e (Xu et al., 2022), the estimated offset between the top of M_2 (approximately –23 m) and the elevation of the T_2 wave-cut platform (17 m) is approximately 40 m along F2. Given this offset, the average slip rate along the F2 could reach 0.31 mm/a since 128 ka. As the ENE-striking faults are segmented by the NNW-striking ones, this estimated rate could vary spatially. However, the uplift rate decrease derived from our results coincides with decreasing slip rates in the inland PRD (0.34 mm/a before 128 ka and 0.16 mm/a since 128 ka, Huang et al., 2021),

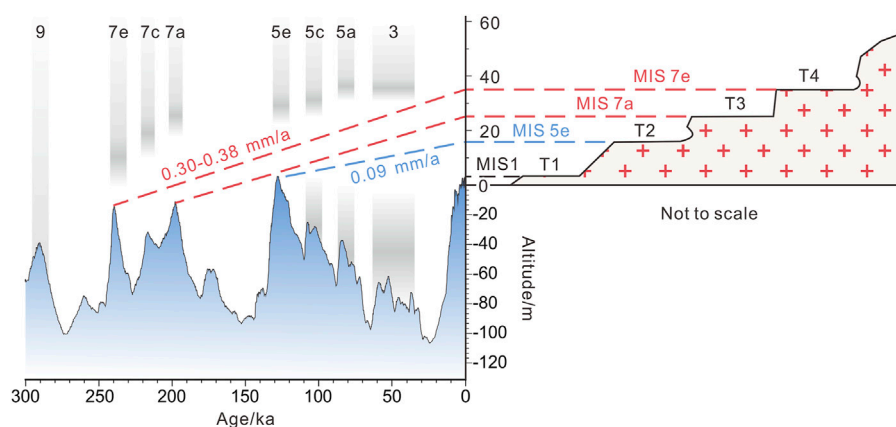


FIGURE 7

Calculated uplift rates from allocations between the altitudes of wave-cut platforms and the ages of sea-level highstands. The sea-level data are from Grant et al. (2014). Light gray bands: marine isotope stages (MISs).

implying that the differential uplift is uniform across the NNW faults. Although the cause for temporally various rates remains unclear, our finding likely implies a weakened differential uplift since 128 ka onshore of the LFZ. Notably, compared to the coastal faults in the Andes or Sicily (ranging from 0.4–0.8 mm/a, Saillard et al., 2011; Meschis et al., 2018), this slip rate is relatively slow. However, this does not mean a lower geohazard risk. As several large earthquakes have occurred around the PRD, the risk defense of geohazards should be explicitly considered in engineering and city construction.

Third, the granitic wave-cut platforms can be used to provide cosmogenic dating ages that correlate with the highstands and, hence, would be an effective way to constrain the uplift rate in the area without fault-related sediments. This may have wider significance because wave-cut platforms suitable for ^{10}Be cosmogenic exposure dating are more common than sites containing corals suitable for U-series dating. The application of the ^{10}Be cosmogenic approach allows many more sites to be dated across a wider region, as granitic wave-cut platforms are widely developed along the coast of southern China. Moreover, this approach provides an independent correlation with sediments in the subsiding wall where the Quaternary sediments were deposited. With clear benchmarks of both uplifting and subsiding walls, a more comprehensive and precise slip rate, and ultimately the tectonic pattern of the PRD could be determined.

Conclusion

- (1) The measured uplift wave-cut platforms, constrained by ^{10}Be cosmogenic dating and the best-fit allocation of undated wave-

cut platforms, were correlated with sea-level highstands at 128 ka and 239 ka, suggesting uplift rates of 0.30–0.38 mm/a during 239–128 ka and 0.09 mm/a from 128 ka in the footwall of coastal F2.

- (2) The observed oldest wave-cut platforms implied a transgression event as early as MIS 7 (239–190 ka) in the southern PRD, implying that Pleistocene deposition likely started at 239 ka, coeval with the recently inferred OSL dating age.
- (3) ^{10}Be cosmogenic exposure dating of wave-cut platforms, in combination with sea-level highstand correlation, is an acceptable method to derive the long-term slip rate of the LFZ and its paralleled offshore faults in the granitic coastline in the northern margin of the South China Sea.

Data availability statement

The original contributions presented in the study are included in the article/Supplementary Material. Further inquiries can be directed to the corresponding author.

Author contributions

HL and KZ: study conception, writing—original draft, funding support; KZ, ZGL, ZC, GH, PH, YZ, YY, XD, and ZYL: manuscript editing, results discussion and interpretation; GH, QT, YT, and CC: data processing and methodology, editing; KZ, ZC, WW, and PZ: funding support and review.

Funding

This work was funded by the National Natural Science Foundation of China (Grant nos. 41572178, 41802225, and 42272250), the Guangdong Province Introduced Innovative R&D Team of Geological Processes and Natural Disasters around the South China Sea (Grant no. 2016ZT06N331), the National Key Research and Development Program of China (Grant no. 2017YFC1500101), the Special Fund for Special Project of Geological Hazard Control, Guangdong Province, China (Grant no. 2017201), the Fundamental Research Funds for the Central Universities, Sun Yat-sen University (Grant no. 22qntd2101), and the Scientific Research Startup Funds of Shaoguan University (Grant no. 9900064604), Guangdong Special Fund for National Park Construction (Grant no. 2021GJGY026).

Acknowledgments

We are grateful to the two reviewers for their thorough comments, which considerably improved the manuscript. We are also grateful to Zihao Chen and Dehui Zhang for their assistance in the laboratory and the field.

References

- Armijo, R., Meyer, B., King, G. C. P., Rigo, A., and Papanastassiou, D. (1996). Quaternary evolution of the corinth rift and its implications for the late cenozoic evolution of the aegian. *Geophys. J. Int.* 126, 11–53. doi:10.1111/j.1365-246X.1996.tb05264.x
- Cao, J., Xia, S., Sun, J., Zhao, F., Wan, K., and Xu, H. (2018). offshore fault geometries in the Pearl River estuary, southeastern China: Evidence from seismic reflection data. *J. Ocean. Univ. China* 17, 799–810. doi:10.1007/s11802-018-3499-5
- Chen, G., Zhang, K., He, X., Chen, F., and Nian, H. (1994). Paleo-geographic evolution of the Pearl River delta since the late Pleistocene. *Quat. Sci.*, 67–74.
- Chen, G., Zhang, K., Li, L., Shao, R., Zhuang, W., and Lin, X. (2002). Development of the Pearl River Delta in SE China and its relations to reactivation of basement faults. *J. Geosciences China* 14, 17–24.
- Dai, X., Li, Z., Sun, C., Li, L., Wang, W., Hui, G., et al. (2022a). 3D structural growth and lateral linkage of the normal fault system: A case study from lufeng sag in the northern South China sea. *ACTA Geol. SIN.* 96, 1922–1936.
- Dai, X., Li, Z., Wang, W., Sun, C., Yan, Y., Hui, G., et al. (2022b). The tectonic deformation characteristics of the Pearl River Mouth Basin and tectonic-sedimentary forward modeling of the Baiyun Sag. *Geotect. Metallogenia* 46, 517–529.
- Grant, K. M., Rohling, E. J., Ramsey, C. B., Cheng, H., Edwards, R. L., Florindo, F., et al. (2014). Sea-level variability over five glacial cycles. *Nat. Commun.* 5, 5076. doi:10.1038/ncomms6076
- Hidy, A. J., Gosse, J. C., Pederson, J. L., Mattern, J. P., and Finkel, R. C. (2010). A geologically constrained Monte Carlo approach to modeling exposure ages from profiles of cosmogenic nuclides: An example from Lees Ferry, Arizona. *Geochim. Geophys. Geosyst.* 11, Q0AA10. doi:10.1029/2010GC003084
- Huang, P., Zhang, K., Yu, Z., Liang, H., Li, Z., Chen, Z., et al. (2021). Reanalysis of the stratigraphic sequence and new understanding of Neotectonic movement of the Pearl River Delta since the late Pleistocene. *South China J. Seismol.* 41, 10–20.
- Huang, Y., Xia, F., and Chen, G. (1983). The formation and evolution of the Pearl River Delta in response to faulting activities. *ACTA Oceanol. SIN.* 5, 316–327.
- Huang, Y., Xia, F., and Chen, G. (1985). The characteristics of the faults in Wugui Mountain area and the formation and development of the fault-block uplifted area. *ACTA Sci. Nat. Univ. SUNYATSENI* 1, 52–62.
- Huang, Z., Li, P., Zhang, Z., Li, K., and Qiao, P. (1982). *Zhujiang (Pearl River) delta*. Guangzhou, China: General Scientific Press.
- Hui, G., Li, S., Guo, L., Wang, P., Liu, B., Wang, G., et al. (2021). A review of geohazards on the northern continental margin of the South China Sea. *Earth-Science Rev.* 220, 103733. doi:10.1016/j.earscirev.2021.103733
- Hui, G., Li, Z., Wang, W., Hu, L., Liang, H., Zhang, Y., et al. (2022). The fault assembly characteristics on the northern South China Sea continental margin and its implications on the South China Sea spreading. *Geotect. Metallogenia* 46, 501–516.
- Jara-Muñoz, J., Melnick, D., Brill, D., and Strecker, M. R. (2015). Segmentation of the 2010 Maule Chile earthquake rupture from a joint analysis of uplifted marine terraces and seismic-cycle deformation patterns. *Quat. Sci. Rev.* 113, 171–192. doi:10.1016/j.quascirev.2015.01.005
- Jiang, J., and Hu, S. (1994). Discover of paleo marine notch in maoer hill, xiaogang town, Xinhui city, China. *Trop. Geogr.* 4, 304.
- Kohl, C. P., and Nishiizumi, K. (1992). Chemical isolation of quartz for measurement of *in-situ* -produced cosmogenic nuclides. *Geochimica Cosmochimica Acta* 56, 3583–3587. doi:10.1016/0016-7037(92)90401-4
- Li, Z., Zhang, P., Hui, G., Hu, L., Li, G., Zhang, Y., et al. (2022). Current status and prospect of the deep structure exploration of the littoral fault zone in the northern South China Sea. *ACTA Sci. Nat. Univ. SUNYATSENI* 61, 55–62.
- Lifton, N., Sato, T., and Dunai, T. J. (2014). Scaling *in situ* cosmogenic nuclide production rates using analytical approximations to atmospheric cosmic-ray fluxes. *Earth Planet. Sci. Lett.* 386, 149–160. doi:10.1016/j.epsl.2013.10.052
- Liu, Y. (1985). The active fractures in South China coast. *Mar. Geol. Quat. Geol.* 5, 11–21.
- Marquardt, C., Lavenue, A., Ortlieb, L., Godoy, E., and Comte, D. (2004). Coastal neotectonics in southern central andes: Uplift and deformation of marine terraces in northern Chile (27°S). *Tectonophysics* 394, 193–219. doi:10.1016/j.tecto.2004.07.059
- Merritts, D., and Bull, W. B. (1989). 17. CO, 10202. doi:10.1130/0091-7613(1989)017<Interpreting Quaternary uplift rates at the Mendocino triple junction, northern California, from uplifted marine terraces>2.0.CO;2
- Meschis, M., Roberts, G. P., Robertson, J., and Briant, R. M. (2018). The relationships between regional quaternary uplift, deformation across active normal faults, and historical seismicity in the upper plate of Subduction zones:

Conflict of interest

The authors declare that the research was conducted in the absence of any commercial or financial relationships that could be construed as a potential conflict of interest.

Publisher's note

All claims expressed in this article are solely those of the authors and do not necessarily represent those of their affiliated organizations, or those of the publisher, the editors, and the reviewers. Any product that may be evaluated in this article, or claim that may be made by its manufacturer, is not guaranteed or endorsed by the publisher.

Supplementary material

The Supplementary Material for this article can be found online at: <https://www.frontiersin.org/articles/10.3389/feart.2022.1026181/full#supplementary-material>

The Capo D'Orlando fault, NE Sicily. *Tectonics* 37, 1231–1255. doi:10.1029/2017tc004705

Monaco, C., Tapponnier, P., Tortorici, L., and Gillot, P. Y. (1997). Late Quaternary slip rates on the Acireale-Piedimonte normal faults and tectonic origin of Mt. Etna (Sicily). *Earth Planet. Sci. Lett.* 147, 125–139. doi:10.1016/S0012-821X(97)00005-8

Palyvos, N., Pantosti, D., De Martini, P. M., Lemeille, F., Sorel, D., and Pavlopoulos, K. (2005). The Aigion–Neos Erineos coastal normal fault system (Western Corinth Gulf Rift, Greece): Geomorphological signature, recent earthquake history, and evolution. *J. Geophys. Res.* 110. doi:10.1029/2004JB003165

Pedroja, K., Jara-Muñoz, J., De Gelder, G., Robertson, J., Meschis, M., Fernandez-Blanco, D., et al. (2018). Neogene–Quaternary slow coastal uplift of Western Europe through the perspective of sequences of strandlines from the Cotentin Peninsula (Normandy, France). *Geomorphology* 303, 338–356. doi:10.1016/j.geomorph.2017.11.021

Racano, S., Jara-Muñoz, J., Cosentino, D., and Melnick, D. (2020). Variable quaternary uplift along the southern margin of the central Anatolian plateau inferred from modeling marine terrace sequences. *Tectonics* 39, e2019TC005921. doi:10.1029/2019tc005921

Roberts, G. P., Meschis, M., Houghton, S., Underwood, C., and Briant, R. M. (2013). The implications of revised Quaternary palaeoshoreline chronologies for the rates of active extension and uplift in the upper plate of subduction zones. *Quat. Sci. Rev.* 78, 169–187. doi:10.1016/j.quascirev.2013.08.006

Robertson, J., Meschis, M., Roberts, G. P., Ganas, A., and Gheorghiu, D. M. (2019). Temporally constant Quaternary uplift rates and their relationship with extensional upper-plate faults in south Crete (Greece), constrained with ³⁶Cl cosmogenic exposure dating. *Tectonics* 38, 1189–1222. doi:10.1029/2018tc005410

Rodríguez, M. P., Carretier, S., Charrier, R., Saillard, M., Regard, V., Hérail, G., et al. (2013). Geochronology of pediments and marine terraces in north-central Chile and their implications for Quaternary uplift in the Western Andes. *Geomorphology* 180–181, 33–46. doi:10.1016/j.geomorph.2012.09.003

Saillard, M., Hall, S. R., Audin, L., Farber, D. L., Regard, V., and Hérail, G. (2011). Andean coastal uplift and active tectonics in southern Peru: 10Be surface exposure dating of differentially uplifted marine terrace sequences (san juan de Marcona, ~15.4°S). *Geomorphology* 128, 178–190. doi:10.1016/j.geomorph.2011.01.004

Tang, Y., Chen, G., Peng, Z., and Zhang, K. (2011). Late quaternary tectonics of the Pearl River delta, SE China: Evidence from xilingang. *Geodin. Acta* 24, 133–139. doi:10.3166/ga.24.133-139

Wang, J., Cao, L., Wang, X., Yang, X., Yang, J., and Su, Z. (2009). Evolution of sedimentary facies and paleoenvironment during the late quaternary in wanqingsha area of the Pearl River delta. *Mar. Geol. Quat. Geol.* 29, 35–42. doi:10.3724/sp.j.1140.2009.06035

Wang, J., Chen, G., Peng, Z., and Grapes, R. (2015). Loess-like deposits in the Pearl River delta area, southeast China. *Aeolian Res.* 19, 113–122. doi:10.1016/j.aeolia.2015.09.005

Wang, W., Wu, C., Xu, L., Wei, X., and Huang, S. (2011). Factors affecting the heights of ancient and present wave-cut benches in the Pearl River Delta area. *Chin. Sci. Bull.* 56, 342–353. doi:10.1360/972010-1035

Wang, Y., and Oskin, M. E. (2021). Combined linear regression and Monte Carlo approach to modelling exposure age depth profiles. *Geochronol. Discuss.*, 1–25.

Xia, S., Zhou, P., Zhao, D., and Cao, J. (2020). Seismogenic structure in the source zone of the 1918 M7.5 NanAo earthquake in the northern South China Sea. *Phys. Earth Planet. Interiors* 302, 106472. doi:10.1016/j.pepi.2020.106472

Xu, X., Li, H., Tang, L., Lai, Z., Xu, G., Zhang, X., et al. (2020). Chronology of a Holocene core from the Pearl River delta in southern China. *Front. Earth Sci. (Lausanne)*. 8. [Accessed August 22, 2022]. doi:10.3389/feart.2020.00262

Xu, X., Zhong, J., Huang, X., Li, H., Ding, Z., and Lai, Z. (2022). Age comparison by luminescence using quartz and feldspar on core HPQK01 from the Pearl River delta in China. *Quat. Geochronol.* 71, 101320. doi:10.1016/j.quageo.2022.101320

Yao, Y., Zhan, W. H., and Liu, Z. (2008). Neotectonics of the Pearl River delta and its relationship with the deltaic evolution. *South China J. Seismol.* 28, 29–40.

Yim, W. W.-S., Hilgers, A., Huang, G., and Radtke, U. (2008). Stratigraphy and optically stimulated luminescence dating of subaerially exposed Quaternary deposits from two shallow bays in Hong Kong, China. *Quat. Int.* 183, 23–39. doi:10.1016/j.quaint.2007.07.004

Yim, W. W.-S., Ivanovich, M., and Yu, K.-F. (1990). Young age bias of radiocarbon dates in pre-Holocene marine deposits of Hong Kong and implications for Pleistocene stratigraphy. *Geo-Marine Lett.* 10, 165–172. doi:10.1007/BF02085932

Yu, Z., Zhang, K., Liang, H., and Li, Z. (2016). Late Quaternary tectonic movements in the Pearl River Delta, China, revealed from stratigraphic profiles. *Trop. Geogr.* 36, 334–342.

Zhao, H. (2017). Discovery and scientific significance of qixinggang relics of ancient coast, Guangzhou. *Trop. Geogr.* 37, 610–619.

Zhao, M., Qiu, X., Ye, C., Xia, K., Huang, C., Xie, J., et al. (2004). An analysis on deep crustal structure along the onshore-offshore seismic profile Across the binghai (littoral) fault zone in Ne south China sea. *Chin. J. Geophys.* 47, 954–961. doi:10.1002/cjg2.573

Zong, Y., Huang, G., Switzer, A. D., Yu, F., and Yim, W. W.-S. (2009a). An evolutionary model for the Holocene formation of the Pearl River delta, China. *Holocene* 19, 129–142. doi:10.1177/0959683608098957

Zong, Y., Yim, W. W.-S., Yu, F., and Huang, G. (2009b). Late Quaternary environmental changes in the Pearl River mouth region, China. *Quat. Int.* 206, 35–45. doi:10.1016/j.quaint.2008.10.012



OPEN ACCESS

EDITED BY

Shaohong Xia,
South China Sea Institute of
Oceanology (CAS), China

REVIEWED BY

Jiangyang Zhang,
South China Sea Institute of
Oceanology (CAS), China
Chao Lei,
China University of Geosciences
Wuhan, China

*CORRESPONDENCE

Jie Liao,
liaojie5@mail.sysu.edu.cn

SPECIALTY SECTION

This article was submitted to Solid Earth
Geophysics,
a section of the journal
Frontiers in Earth Science

RECEIVED 27 September 2022

ACCEPTED 14 November 2022

PUBLISHED 20 January 2023

CITATION

Li H, Liao J, Shen Y, Qing J, Wu Y, Zhao Z
and Shi X (2023), Rifting/spreading
propagation interacts with preexisting
transform faults: 3D
geodynamic modeling.
Front. Earth Sci. 10:1054747.
doi: 10.3389/feart.2022.1054747

COPYRIGHT

© 2023 Li, Liao, Shen, Qing, Wu, Zhao
and Shi. This is an open-access article
distributed under the terms of the
[Creative Commons Attribution License
\(CC BY\)](https://creativecommons.org/licenses/by/4.0/). The use, distribution or
reproduction in other forums is
permitted, provided the original
author(s) and the copyright owner(s) are
credited and that the original
publication in this journal is cited, in
accordance with accepted academic
practice. No use, distribution or
reproduction is permitted which does
not comply with these terms.

Rifting/spreading propagation interacts with preexisting transform faults: 3D geodynamic modeling

Hao Li¹, Jie Liao^{1,2,3*}, Yongqiang Shen¹, Jiarong Qing¹,
Yangming Wu¹, Zhongxian Zhao⁴ and Xiaobin Shi⁴

¹School of Earth Sciences and Engineering, Sun Yat-Sen University, Guangzhou, China, ²Southern Marine Science and Engineering Guangdong Laboratory (Zhuhai), Zhuhai, China, ³Guangdong Provincial Key Lab of Geodynamics and Geohazards, Guangzhou, China, ⁴Key Laboratory of Ocean and Marginal Sea Geology, South China Sea Institute of Oceanology, Chinese Academy of Sciences, Guangzhou, China

The divergent rifting/spreading centers and the strike-slip transform faults are the essential tectonic units on Earth, the dynamic evolution of which regulates the development of rifting/spreading basins. The propagation of rifting/spreading centers may interact with pre-existing transform faults, but how they interact with each other remains enigmatic. Here we use three-dimensional geodynamical numeric models to systematically simulate the interaction between rifting/spreading propagation and the pre-existing transform faults. Our model results provide the following findings. 1) The pre-existing transform faults affect rifting/spreading propagation promoting the formation of ridge segments with an offset distance, facilitating the process of spreading of the western sea basin and restraining the propagation of the east sea basin. Yet, the evolution of the transform faults is regulated by rifting/spreading propagation, featured by the increase of its length, the change in its width along strike and the presence of lineated magmatism. 2) The initial length and orientation of the pre-existing transform faults largely affect rifting/spreading propagation, i.e., large transform fault length favors the formation of large offset between ridge segments, and oblique transform faults facilitate the formation of overlapped spreading centers. 3) Model results shed new light on the evolution of the South China Sea basin, implying that the observed ridge segments in the east and southwest sub-basins, the difference of the Zhongnan Fault Zone width along strike and the lineated volcanos along the Zhongnan Fault Zone are the results of the interaction between the rifting/spreading propagation and the pre-existing transform fault.

KEYWORDS

rifting/spreading propagation, pre-existing transform faults, geodynamic modeling, South China Sea, Zhongnan Fault Zone

Introduction

Rifting/spreading centers and (continental/oceanic) transform faults are essential tectonic units affecting lithosphere dynamics. These two tectonic units are not isolated in nature but often show intensive interactions. A possible interaction between the two units is how the pre-existing transform faults interact with rifting/spreading propagation, as observed in many natural examples (e.g., the

South China Sea basin). Individual process of either transform fault evolution or rifting/spreading propagation is largely investigated in previous studies (e.g., Hey et al., 1980; Courtillot, 1982; Vink, 1982; Gerya, 2013; Le Pourhiet et al., 2017; Illsley-Kemp et al., 2018; Le Pourhiet et al., 2018), but the interaction between rifting/spreading propagation and pre-existing transform faults remains poorly understood.

The South China Sea basin is a possible example showing rifting/spreading propagation interacted by the pre-existing

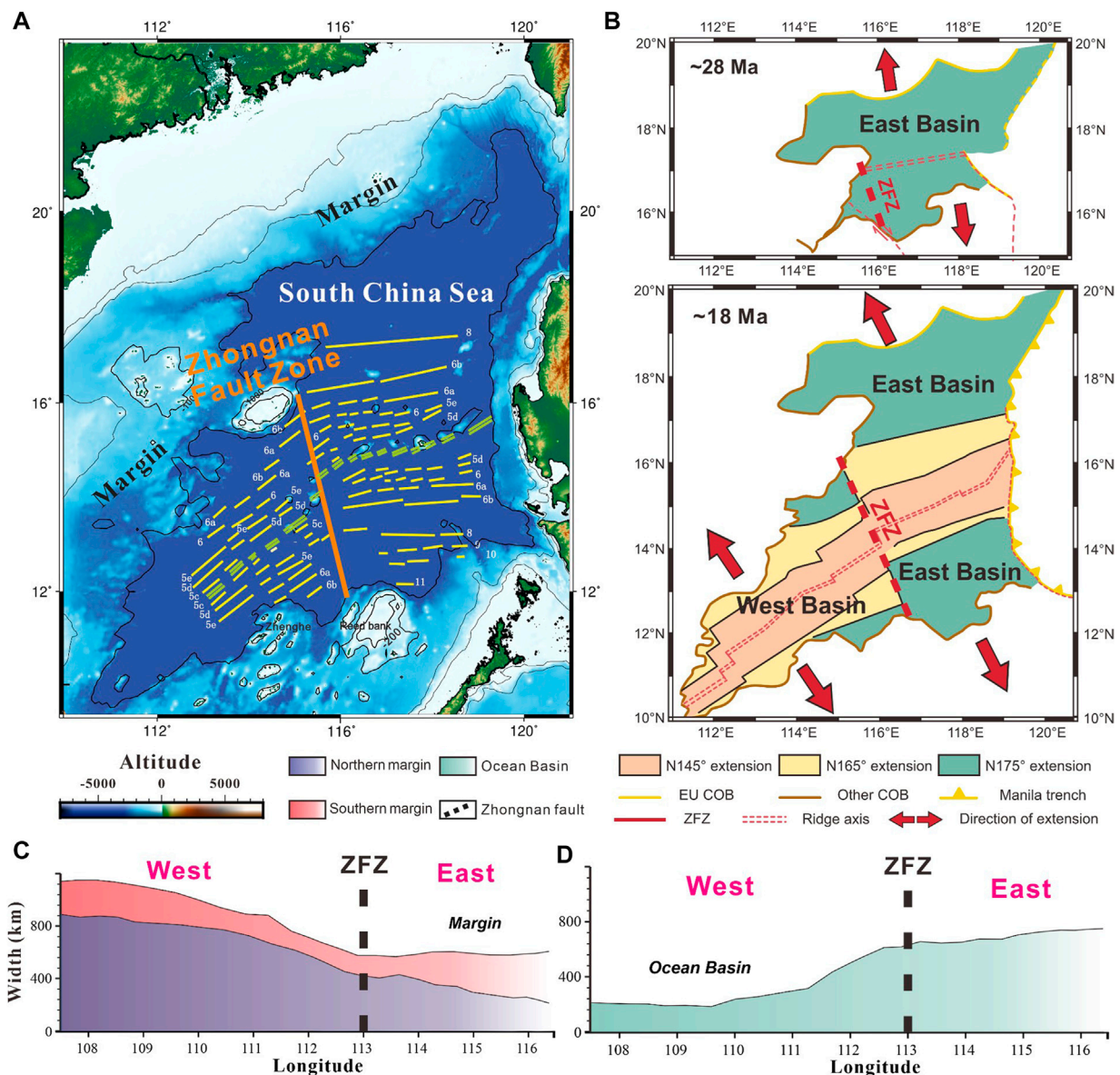
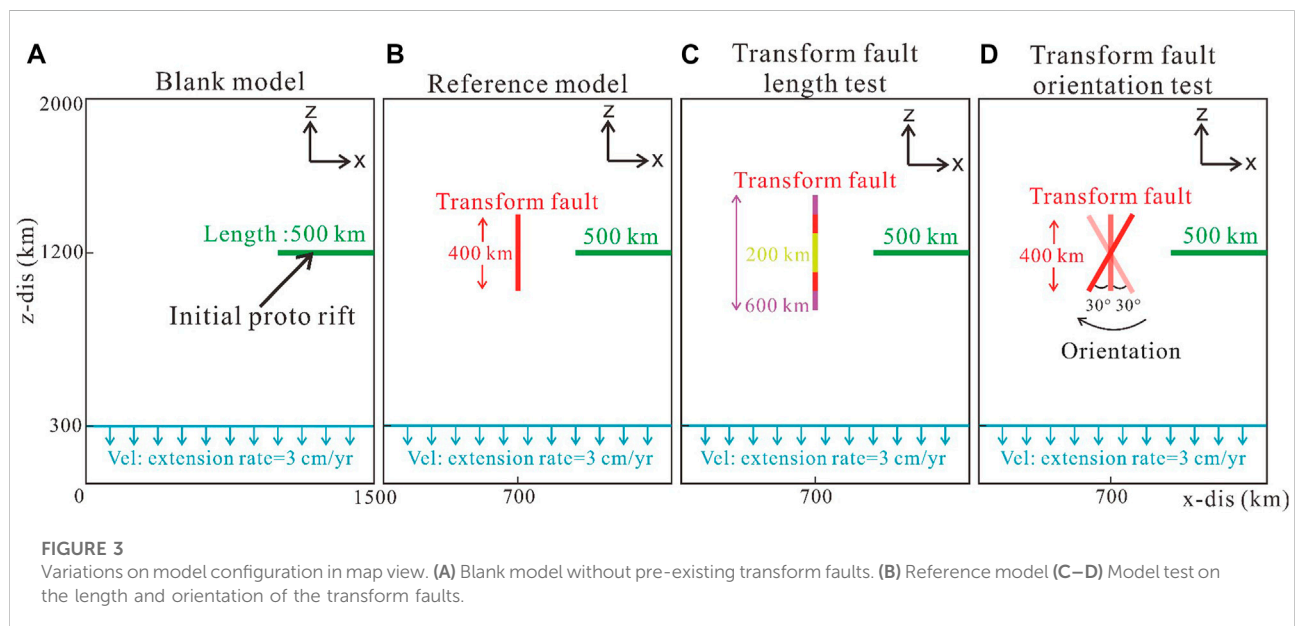
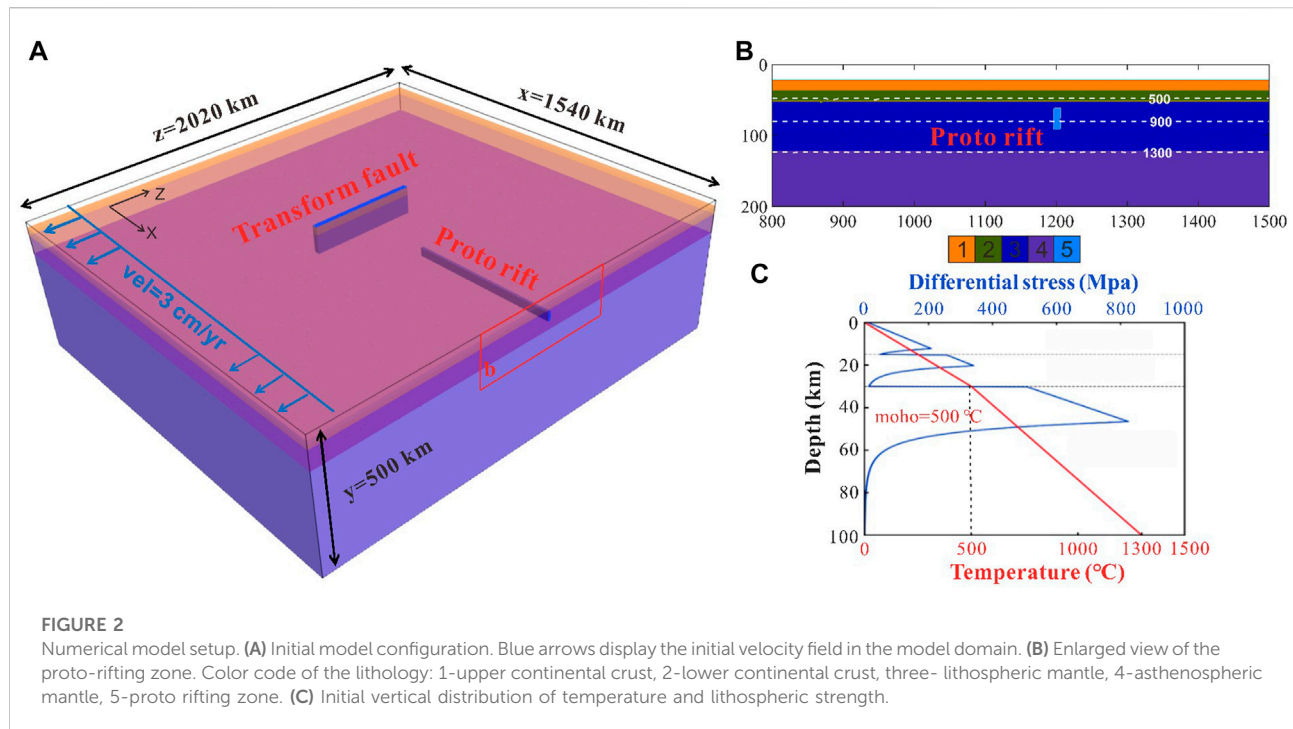


FIGURE 1

Natural example of the South China Sea basin showing rifting/spreading propagation and the pre-existing transform fault. (A) Simplified tectonic background of the South China Sea basin. Yellow line represents the magnetic anomalies (from Sibuet et al., 2016). Orange line is the Zhongnan Fault Zone (ZFZ). (B) Plate kinematic reconstruction sketches at different times (C–D) Variations in margin width and ocean basin width along the strike of the spreading ridge. We used the movement track of the South China Sea margin reconstructed by Bai et al. (2015) and the COB track reconstructed by Muller et al. (2016) to compute the basin and margin width along longitude.



Zhongnan Fault Zone (Figure 1A), which evolved from a continental transform fault in the rifting stage to an oceanic transform fault in the spreading stage since. The South China Sea basin spreading started at ~ 32 Ma and terminated at ~ 15 Ma (Briais et al., 1993; Li et al., 2012; Sibuet et al., 2016), and the spreading process is largely three-dimensional with strong lateral variations. The spreading ridge of the South China Sea basin

propagated from east to west (Figure 1B), with decreasing oceanic basin width from east to west (Figures 1C, D). The Zhongnan Fault Zone is a boundary separating the east ocean basin from the west (Barckhausen et al., 2004; Li et al., 2008; Li et al., 2012, 2014; Barckhausen and Roeser, 2014). Although the age of the Zhongnan Fault Zone is debated (Tongkul et al., 1993; Li et al., 2008; Yan, 2008; Li et al., 2012; Li et al., 2014; Ruan et al.,

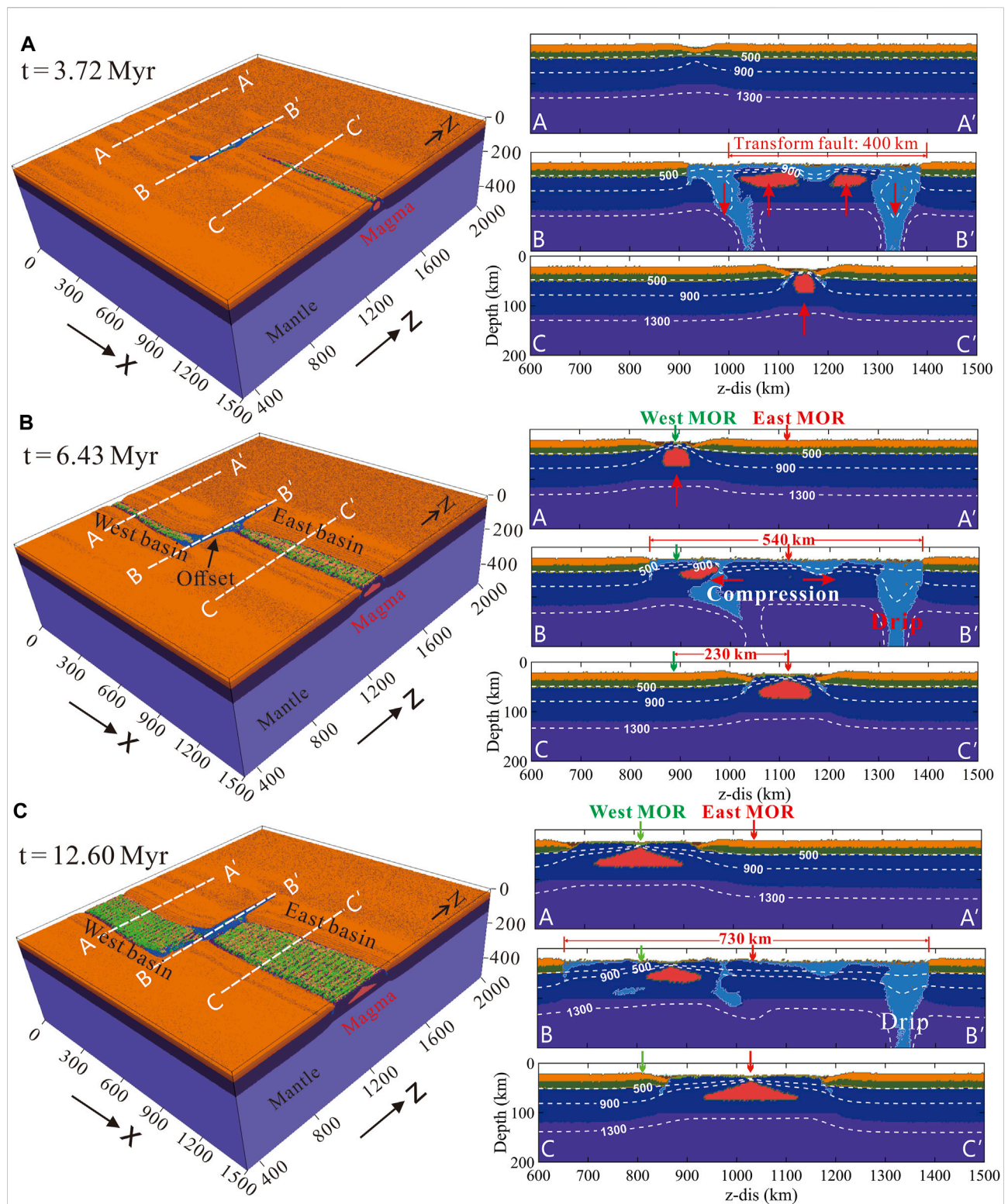
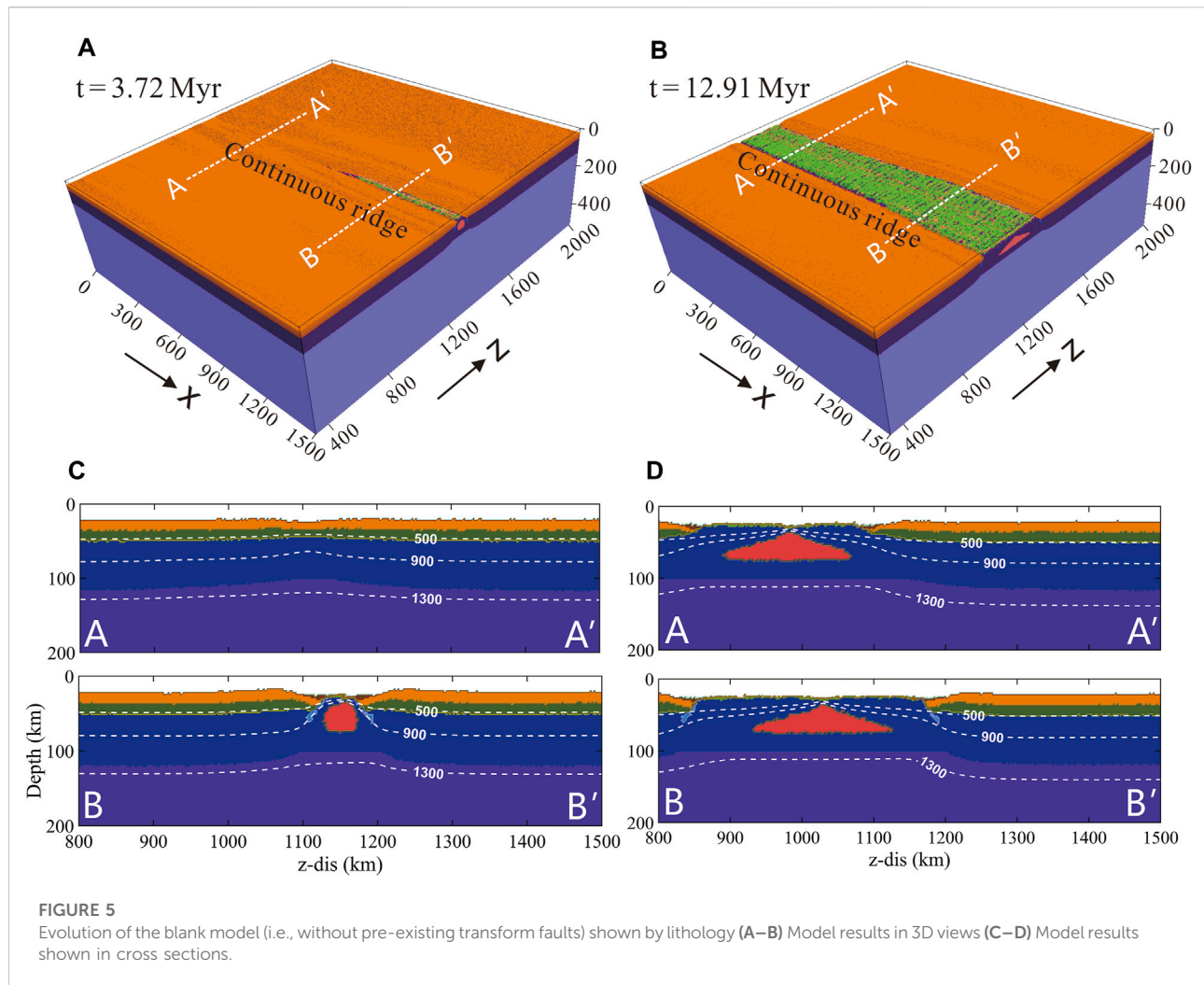


FIGURE 4

Evolution of the reference model shown by lithology snapshots (A–C) Model results at 3.72 Myr, 6.43 Myr, and 12.60 Myr, respectively. Left panels: 3D visualization. White dashed lines show the locations of the cross sections displayed in the right panels. Right panels: Cross sections. White dashed lines represent the isotherms.



2016; Sibuet et al., 2016), increasing studies proposed that the Zhongnan Fault Zone was formed before the South China Sea basin spreading (Briais et al., 1993; Yan, 2008; Sibuet et al., 2016; Li et al., 2017). The recent studies using seismic reflection data demonstrated that the Zhongnan Fault Zone developed before the opening of the South China Sea basin (Li et al., 2017; Xu et al., 2019; Xu et al., 2021).

This study investigates systematically how pre-existing transform faults interact with rifting/spreading propagation using a three-dimensional thermomechanical coupled numeric model. The model results suggest that the pre-existing transform faults strongly interact with rifting/spreading propagation, forming discontinuous ridge segments and promoting the growth of transform faults. Our results shed new light on the dynamic evolution of rifting/spreading propagation and transform fault growth in the South China Sea basin.

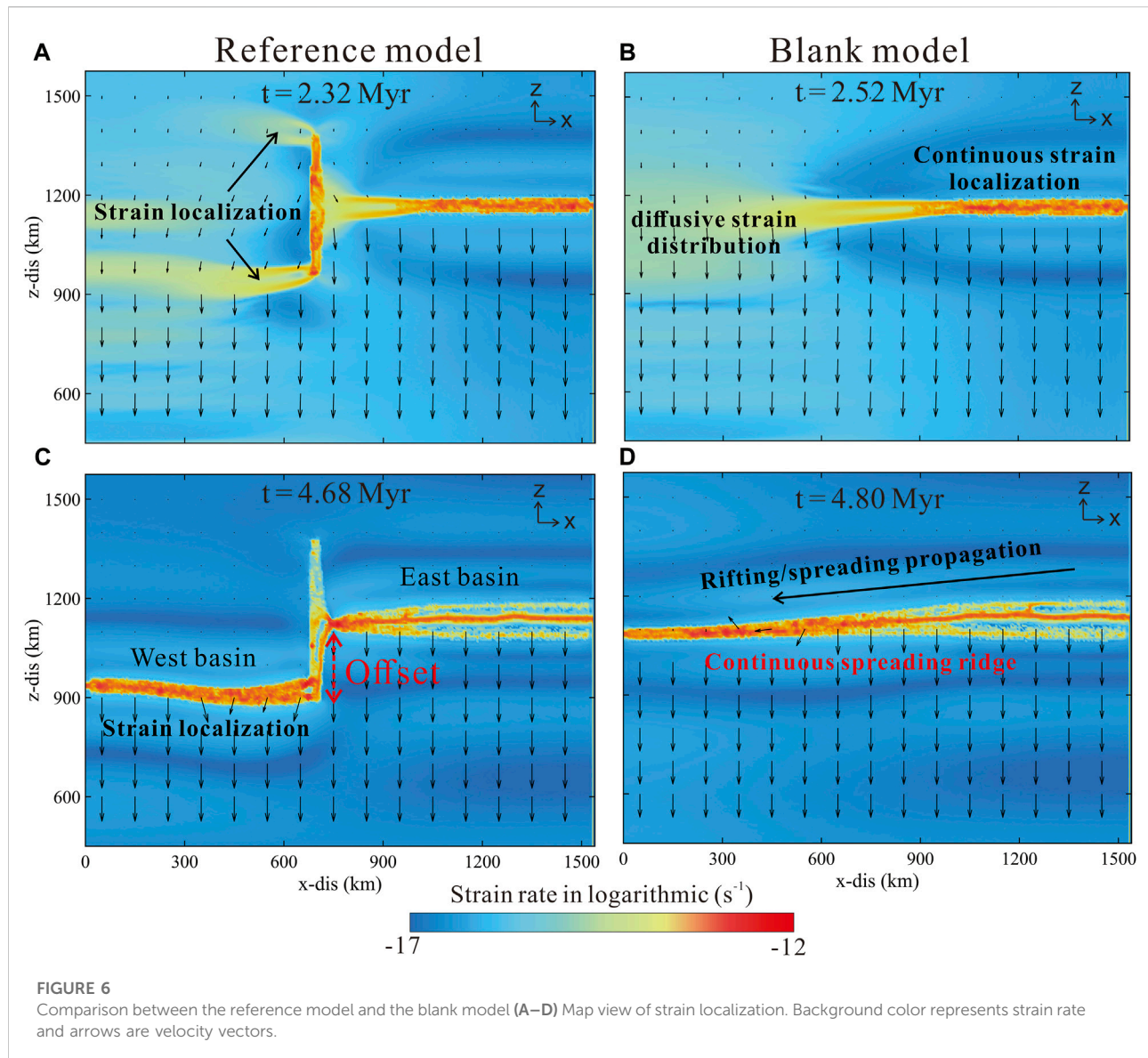
Methods

Numerical methods

We use the 3D thermomechanical code I3ELVIS (Gerya and Yuen, 2003; Gerya, 2013) to conduct numerical simulations. The code solves the three-dimensional mass conservation equation (incompressible medium), momentum conservation equation, and energy conservation equation using the finite difference algorithm. The Stokes flow is coupled with the time-dependent heat conservation equation. The following three governing equations (i.e., the mass, momentum and energy conservation equations) are solved in the numerical code:

$$\text{div}(v_i) = \frac{\partial v_i}{\partial x_i} = 0$$

$$\frac{\partial \sigma'_{ij}}{\partial x_j} = \frac{\partial P}{\partial x_i} - g\rho(C, M, P, T)$$



$$\rho C_p \left(\frac{dT}{dt} \right) = \frac{\partial}{\partial x_i} \left(k \frac{\partial T}{\partial x_i} \right) + H$$

where v_i is the velocity vector, ρ is the density of rock, which changes with rock parameters, g is gravitational acceleration, σ'_{ij} is the deviatoric stress tensor, σ_{xi} is the shear stress tensor, C_p is isobaric heat capacity, dT/dt is the partial derivative of temperature T with respect to time T , k is the thermal conductivity, which is affected by temperature T , pressure P and rock type C , H represents internal heat source, including radioactive heat source, shear heat source, adiabatic pressure heat source and phase change heat source (Burg and Gerya, 2005).

The numerical simulation program in this study integrates the rheological relationship of the strain rate with the viscoplastic constitutive relationship to calculate the deviatoric stress

tensor. Plastic rheology is described by the Drucker–Prager yield criterion, where the yield stress (σ_{yield}) is pressure-dependent (C is rock cohesion, φ is internal friction angle and λ is the pore fluid coefficient). Viscosity due to plastic deformation ($\eta_{plastic}$) is computed based on the square root of the second invariant of strain rate ($\dot{\epsilon}_{II}$). Eventually, the effective viscosity of rocks (η_{eff}) is constrained by both viscous and plastic deformation.

$$\eta_{ductile} = \dot{\epsilon}_{II}^{\frac{1-n}{n}} A^{\frac{1}{n}} \exp \left(\frac{E_a + PV_a}{nRT} \right)$$

$$\sigma_{yield} = C_0 + P \sin(\varphi) (1 - \lambda)$$

$$\eta_{plastic} = \frac{\sigma_{yield}}{2\dot{\epsilon}_{II}}$$

$$\eta_{eff} = \min(\eta_{ductile}, \eta_{plastic})$$

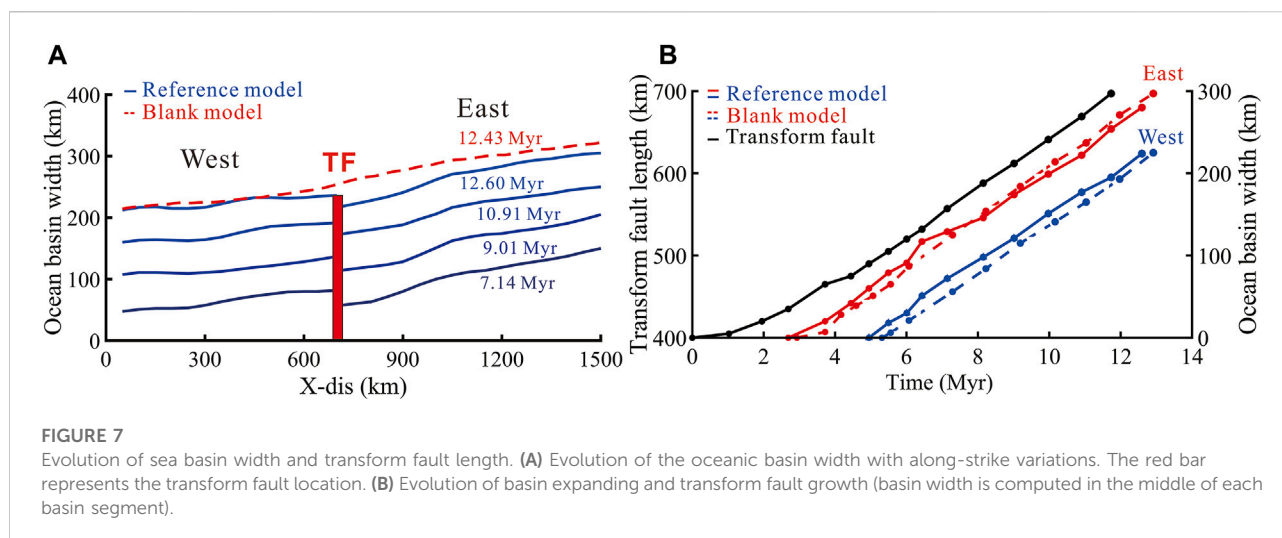


FIGURE 7

Evolution of sea basin width and transform fault length. (A) Evolution of the oceanic basin width with along-strike variations. The red bar represents the transform fault location. (B) Evolution of basin expanding and transform fault growth (basin width is computed in the middle of each basin segment).

In the simulation, rock deformation and material migration are solved by marker-in-cell method. The rock deformation (nonlinear visco-plastic deformation) of each layer is controlled by the rheological properties of different lithology. In addition, partial melting, plate dehydration, water migration and mineral phase transformation are introduced into the calculation program to simulate the various processes of natural tectonic movement.

Model setup

The physical dimension of our models is $2,020 \text{ km} \times 1,540 \text{ km} \times 500 \text{ km}$ (in the order of x , y and z directions), with a uniform grid consisting of $308 \times 404 \times 100$ Eulerian nodes. The thickness of the lithosphere in our model is 120 km, with a 15 km thick upper crust and a 15 km thick lower crust. A transform fault with the length of 300 km and the width of 20 km is imposed in the middle of the model domain, parallel to the direction of boundary extension. A proto rifting zone with the length of 500 km and the width of 20 km is employed on the right edge of the model domain, which evolves to a mature rifting and spreading center. Different lithological compositions are employed to control the initial physical and chemical properties in the model. Wet quartzite and felsic granulite are applied for the continental upper and lower crust, respectively. Dry olivine is used for the lithospheric and asthenospheric mantle. Wet Olivine that has weak rheological properties is employed to the transform fault zone and the proto rifting zone. In addition, a layer of 'sticky' air (viscosity of 10^{18} Pa s) is applied above the crust which allows the surface of the crust to deform freely and spontaneously (Crameri et al., 2012).

A linear temperature structure is employed for the lithosphere. The temperature increases linearly from 273 K at the surface (20 km) to 773 K at the moho surface (50 km) and increases

linearly from the moho to 1573 K at the lithosphere and asthenosphere boundary (120 km). The asthenospheric mantle is adiabatic with thermal gradient of $0.5^\circ\text{C}/\text{km}$. Constant temperature is applied at the top and bottom boundaries. The left and right boundaries are thermal isolated with no heat flux across.

Velocity boundary conditions are free slip on all boundaries. Additional internal boundary velocities (e.g., 3 cm/yr in the blank model as well as in the reference model, Figures 2A, 3) are set at the southern boundary at $z = 300 \text{ km}$.

Due to the imposed "sticky air" layer, the crustal surface is roughly described as a free surface and can therefore deform spontaneously. We use simplified erosion and sedimentation method that are independent of topographic slope and local elevation (Burov and Cloetingh, 1997). Constant and moderate erosion and deposition rates (0.315 mm/year) that within the range of natural data are employed. The surface erosion and sedimentation are simulated by resolving the transport equation at the Eulerian node for each time step (Gerya and Yuen, 2003):

$$\frac{\partial y_s}{\partial T} = v_y - v_x \frac{\partial y_s}{\partial x} - v_s + v_e$$

where y_s is the vertical position of the crustal surface, v_y and v_x are the vertical and horizontal velocity components on the crustal surface, v_s and v_e are the rates of sedimentation and erosion, respectively, which correspond to the following relations: $v_s = 0$ and $v_e = 0.315 \text{ mm/yr}$ for $y_s < 20 \text{ km}$, $v_s = 0.315 \text{ mm/yr}$ and $v_e = 0$ for $y_s \geq 20 \text{ km}$ (the initial depth of the crustal surface is 20 km).

We set up a series of geodynamic numerical models to explore the interaction between the pre-existing transform faults and the rifting/spreading propagation (map view of the initial model configuration in terms of the location of the rifting/spreading center and the transform fault; Figure 3). We further run a blank model without pre-existing transform faults to compare rifting/spreading propagation (Figure 3A). Based on

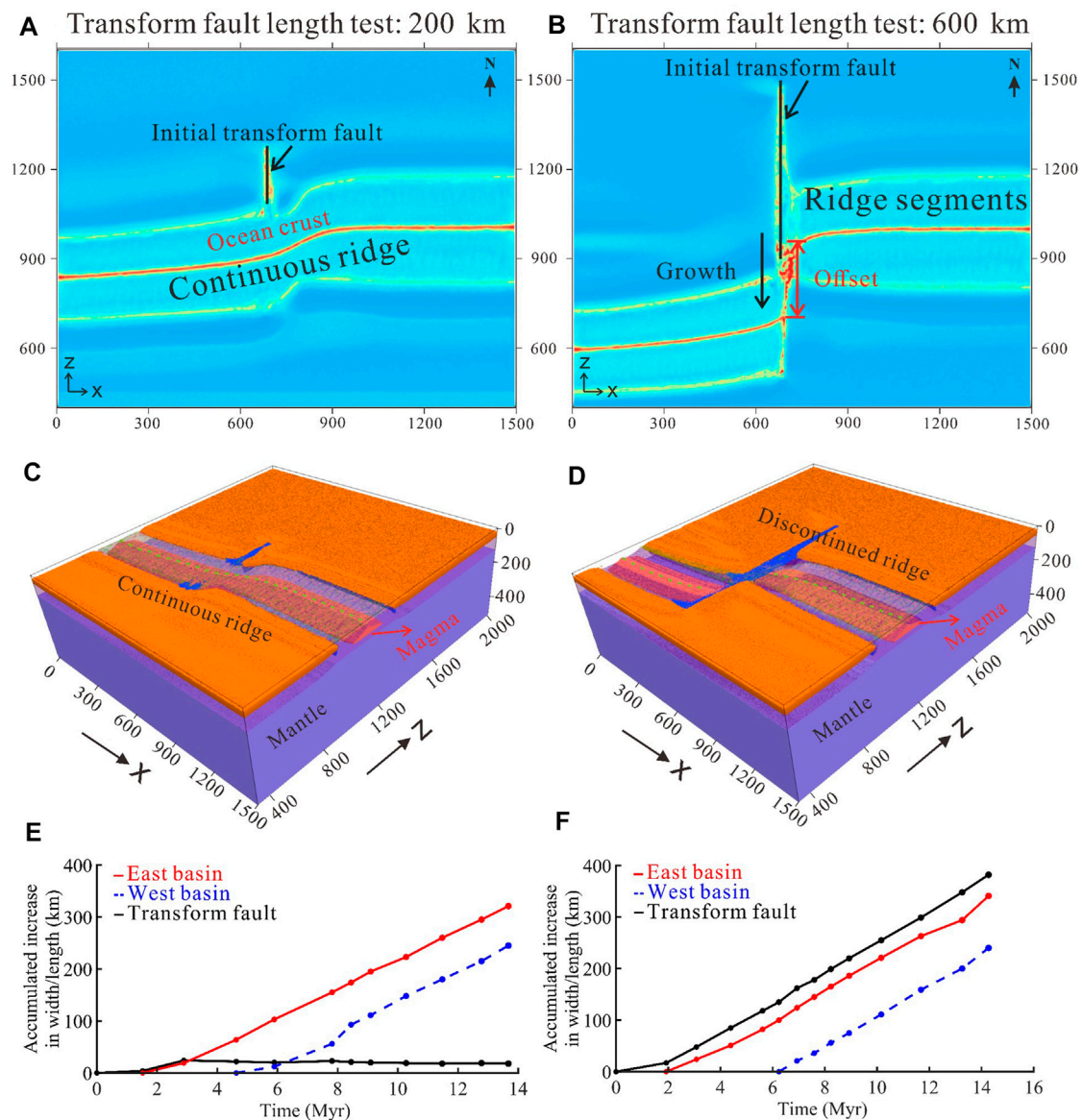


FIGURE 8

Effect of transform fault length (A–B) Map view of viscosity fields (C–D) Lithology field in 3D view. Mid-ocean ridges are indicated by the green dashed lines (E–F) Growth of transform faults and oceanic basins (Data are taken from the middle of the ocean basin and transform fault).

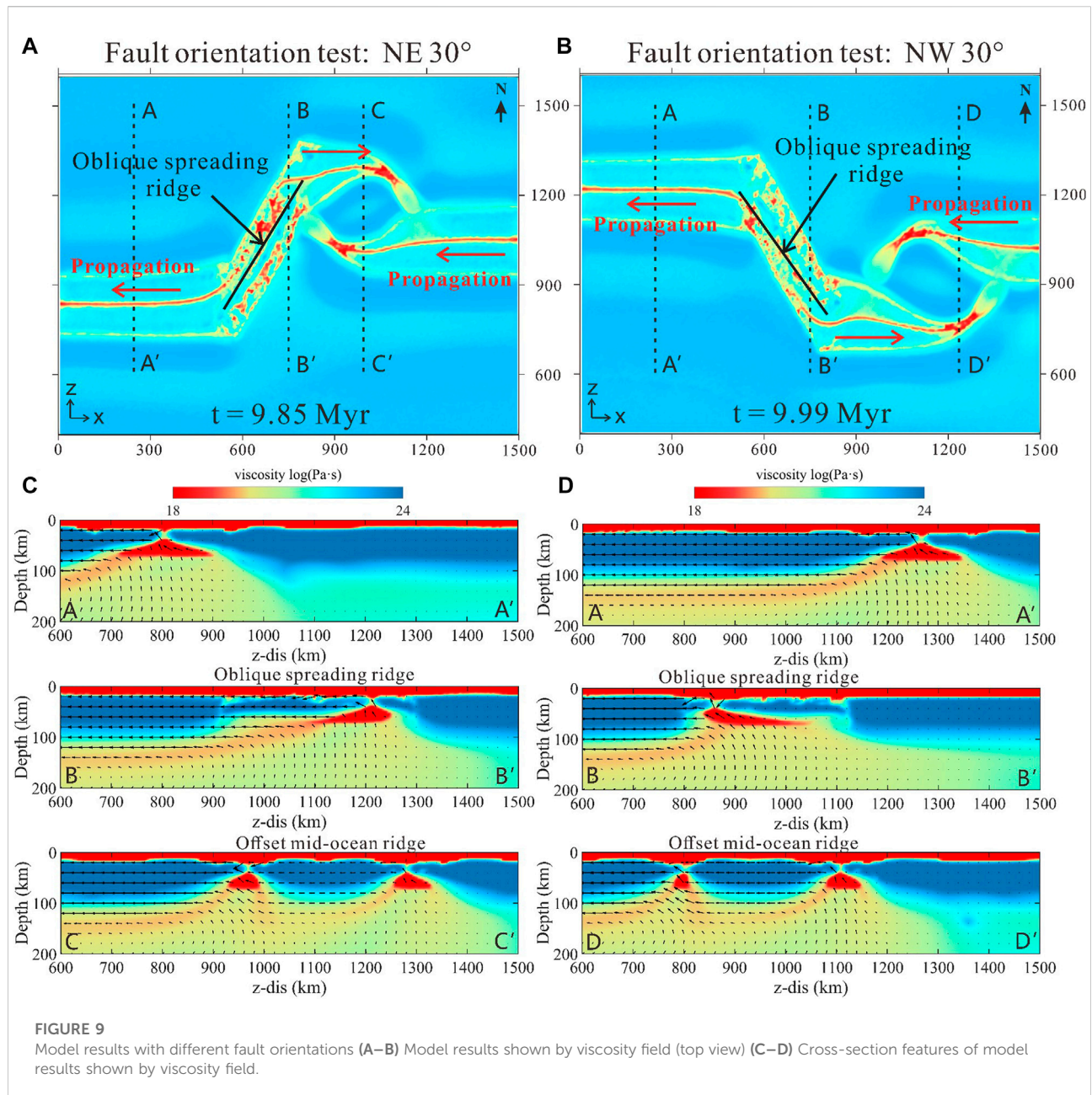
the reference model (Figure 3B), we further investigate parameter effects in terms of the length and orientation of the pre-existing transform fault (Figures 3C,D).

Results

Reference model evolution

We conducted a series of numerical models to investigate the influence of pre-existing transform faults on rifting/

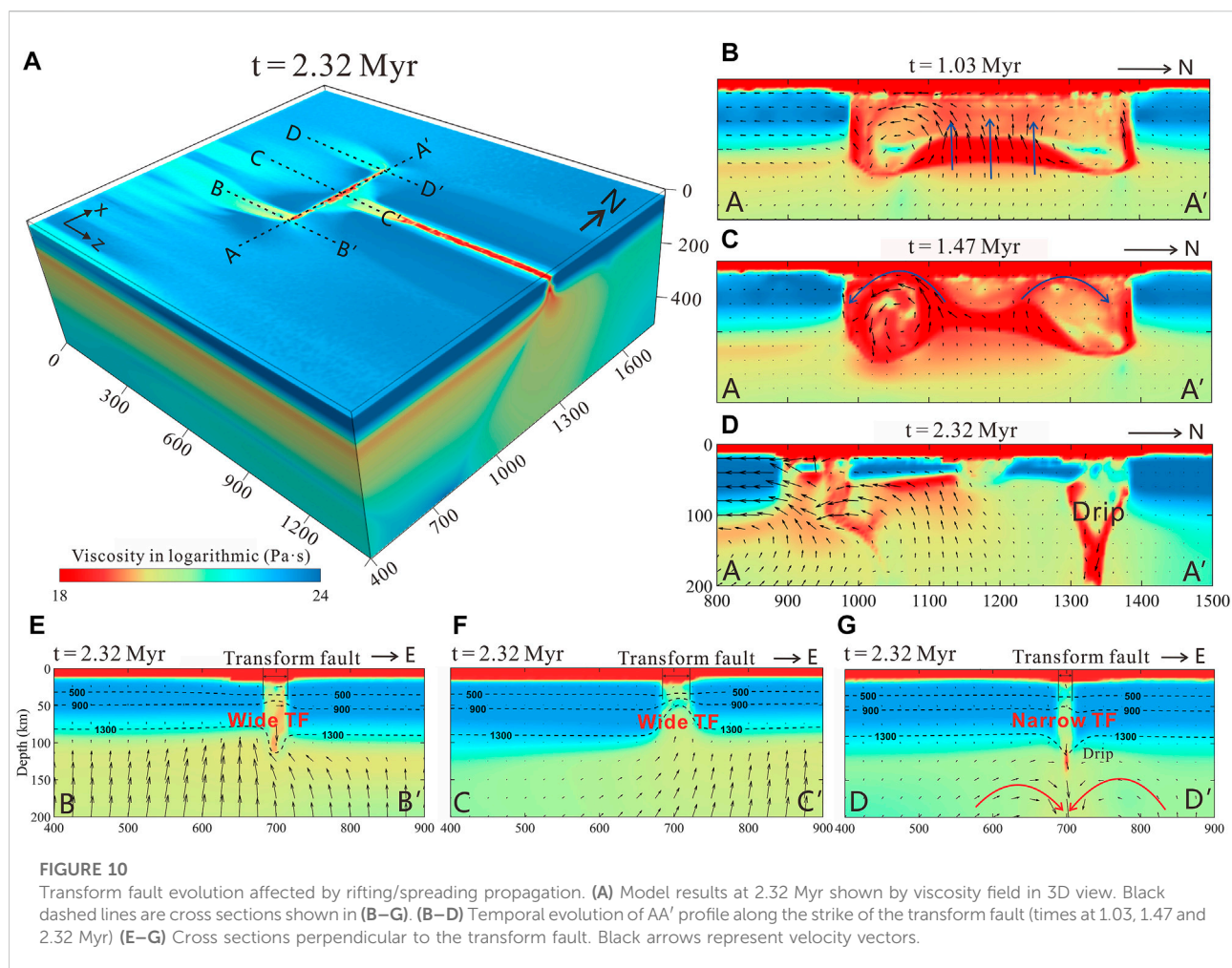
spreading propagation. Typical evolution stages of the reference model are documented (Figure 4 and Supplementary Figure S1). 1) In the early stage, rifting propagation dominates model evolution (Figure 4A). The rifting center is formed along the prescribed proto rifting zone, and propagates laterally. In front of the propagated rifting center, the evolution of the pre-existing transform fault is featured by transtensional deformation in the middle and transpressional deformation at the ends. As a consequence of the transtensional and transpressional deformation, material upwelling and downwelling in the



fault zone is observed, respectively (BB' profile, Figure 4A). 2) With further model evolution, propagation of the rifting/spreading center is affected by the presence of the transform fault, and the remarkable feature is the formation of the two ridge segments with an offset distance (Figure 4B). The younger ridge segment connects the tip of the transform fault, and the offset distance between the two ridge segments is half of the transform fault length. The ridge-transform fault-ridge system is established. 3) In the late stage, steady spreading forms leading to the widening of sea basins. The transform fault grows dramatically with the increase in its

length, from the original length of 400 km to ~730 km at this moment (BB' profile, Figure 4C).

We further run a blank model to investigate the propagation of rifting/spreading centers without the influence of pre-existing transform faults (Figure 5). Similar to the reference model, the rifting/spreading centers first develop along the proto rifting zone, and propagate laterally to the other side of the model domain. The main difference is that a relatively straight and continuous spreading ridge is formed in the blank model, in contrast to the formation of two ridge segments affected by the pre-existing transform fault in the reference model.



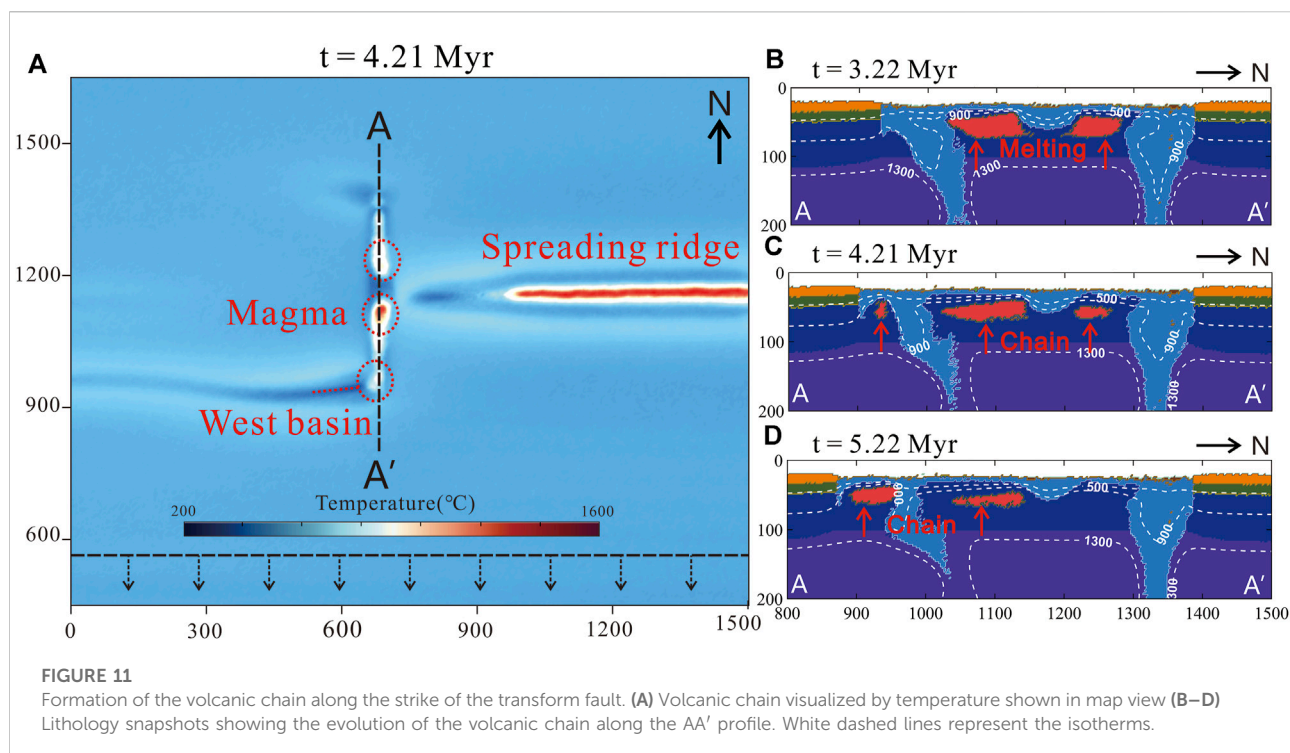
The difference between the two models is further compared in terms of strain rate evolution (Figure 6). In the reference model, the transform fault interacts rifting/spreading propagation, inhibiting the continuous strain localization ahead of the propagated spreading center. Two strain localization zones connecting to the ends of the transform fault are formed (Figure 6A), and the one locates closer to the extensional boundary evolves to a spreading center finally, while the other one becomes abandoned (Figure 6C). In the blank model, strain localization continuously formed ahead of the propagated rifting/spreading center, although diffusive strain distribution is seen in the early stage (Figures 6B,D).

In addition, the extending of the sea basins is computed in the reference model and compared to that in the blank model (Figure 7). The eastern sea basin (separated by the transform fault) is wider than that of the western sea basin since it develops earlier (Figure 7). Gradual decrease in the width of the eastern sea basin is observed (Figure 7A), as a consequence to spreading propagation. The width of the western basin, however, is relatively constant with negligible variation along strike

(Figure 7A). The main reason is the fast strain localization in the western basin facilitated by the southern end of the transform fault. The blank model without the pre-existing transform fault shows a gradual decrease in the width of the sea basin from east to west in the entire model. Besides, the width of the western basin in the reference model is slightly larger than that in the blank model (Figure 7B), suggesting the promotion of the pre-existing transform fault on the development of the western basin.

Influence of transform fault length

We further conduct a series of numerical experiments to study the influence of transform fault length. Based on the reference model (i.e., 400 km of the transform fault length), we test the models with a shorter (i.e., 200 km) and a longer (i.e., 600 km) pre-existing transform fault (Figure 8). In the model with a shorter pre-existing transform fault (i.e., 200 km; Figure 8A), a continuous spreading ridge with slight curvature around the transform fault is formed (Figure 8A). The growth of



the transform fault terminates after the spreading ridge propagating to the fault and breaking the preexisting transform fault (Figure 8E). In the model with a longer transform fault (i.e., 600 km; Figure 8B), however, two ridge segments are formed with a larger offset distance compared to that in the reference model. The transform fault continues to grow with the spreading of the ridge centers (Figure 8F). These differences suggest that long transform faults promote the formation of two separated ridge segments during spreading propagation.

Influence of transform fault orientation

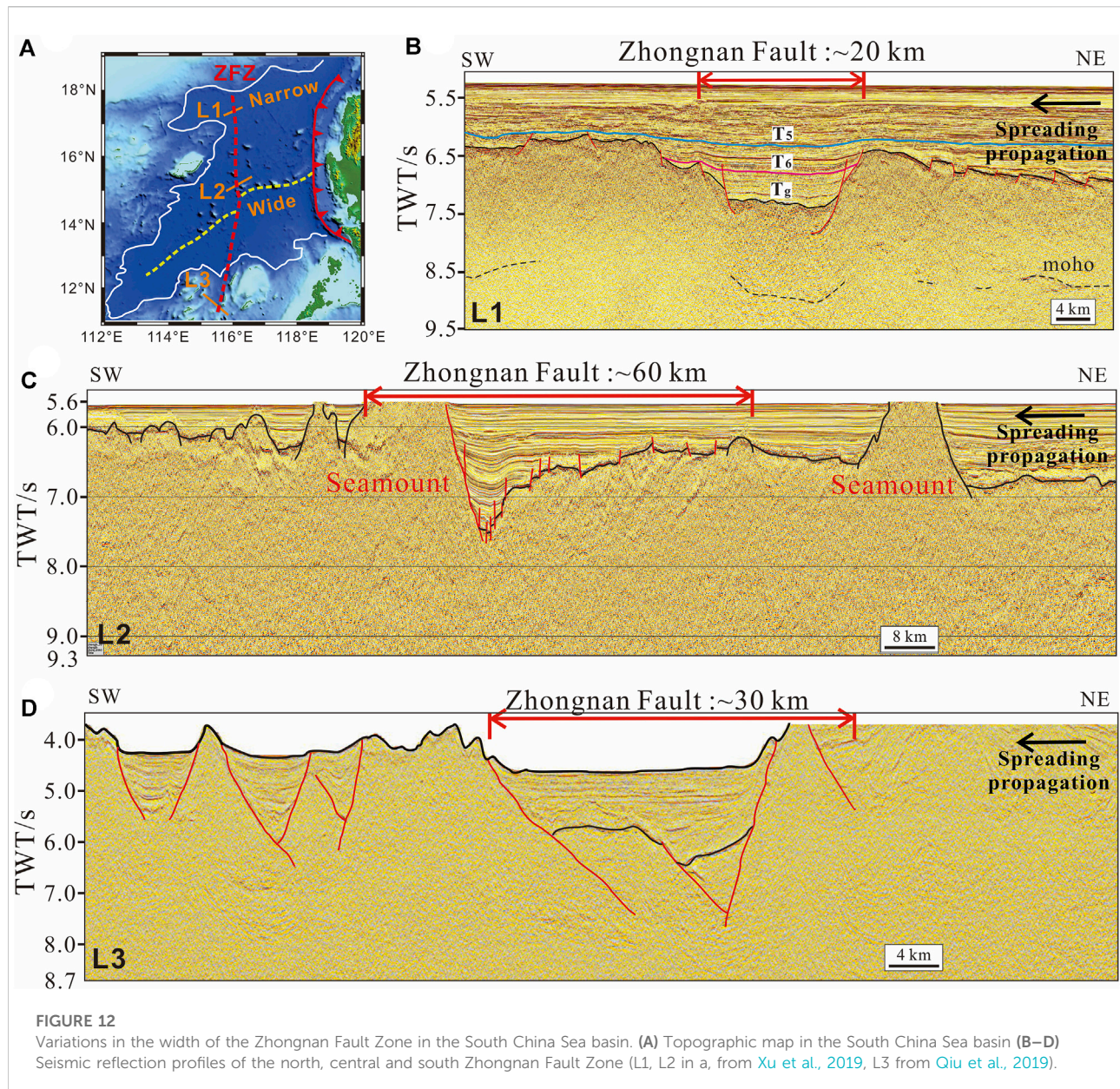
The initial orientation of the transform faults may influence rifting/spreading propagation. Based on the reference model with a pre-existing orthogonal transform fault, the models with obliquely distributed transform faults (i.e., rotated leftwards/rightwards by 30°) are further tested (Figure 9). Results show that model evolution differs largely from the reference model. 1) Firstly, the initially obliquely orientated transform faults fail to evolve to mature oceanic transform faults. Instead, the oblique transform faults experience intensive extension, forming inclined spreading ridges (Figures 9A, B). 2) Secondly, two ridge segments are formed in these models. However, unlike the reference model that ridge segments are connected to the transform fault, overlapping ridge segments are established in these models with the rotation of the

microplate in between (Figures 7C, D). The resulted overlapping ridge segments reflect strong interaction of the oblique transform faults on rifting/spreading propagation.

Discussion

Transform fault evolution affected by rifting/spreading propagation

The evolution of the pre-existing transform fault is also affected by rifting/spreading propagation. 1) Along the strike of the transform fault, two small-scale mantle convection cells are developed beneath the transform fault, with upwelling in the middle and downwelling at the ends (Figure 10C). These two convection cells are asymmetric and the one locates closer to the extensional boundary is more intense (Figure 10D). As a consequence to the upwelling/downwelling, decompressional melting and material dripping are formed in the middle and at the ends of the transform fault, respectively. Thus, the growth of the transform fault (i.e., increase of its length) is mainly due to the extension in the middle. The two ends of the transform fault are mainly under compression. 2) Perpendicular to the strike of the transform fault, cross sections reveal the variation of transform fault width. Ahead of the propagating ridge, the middle part of the transform fault becomes much wider, due to asthenospheric mantle upwelling triggered by ridge propagation. The southern end of the transform fault becomes



wider than the northern end, mainly because the transform fault grows to the south affected by the prescribed boundary extension (Figures 10E, F). Fault growth at the northern end is negligible, with very minor influence from the two ridge segments.

Besides, evolution of the transform fault is characterized by the formation of a volcanic chain (Figure 11A) due to the punctuated distribution of decompressional melting along the strike of the transform fault (Figure 11B). The volcanic chain is thus the surface expression of the deep discontinuous melting centers (Figure 10A). The deep discontinuous melting centers appear first in the middle of the transform fault (Figure 11B), and then establish at the southern end of the fault (Figure 11C), and finally migrate southward with the growth of the transform fault

(Figure 11D). The discontinuous randomly distributed melting centers along the transform fault are caused by the small-scale mantle convection cells due to transtensional and tranpressional deformation as described above.

Implications for the spreading of the south China sea basin

Our model results are comparable to the observations of the South China Sea basin, in terms of the growth of transform faults, the formation of ridge segments and the establishment of a volcanic chain. According to the fine interpretation of the seismic reflection

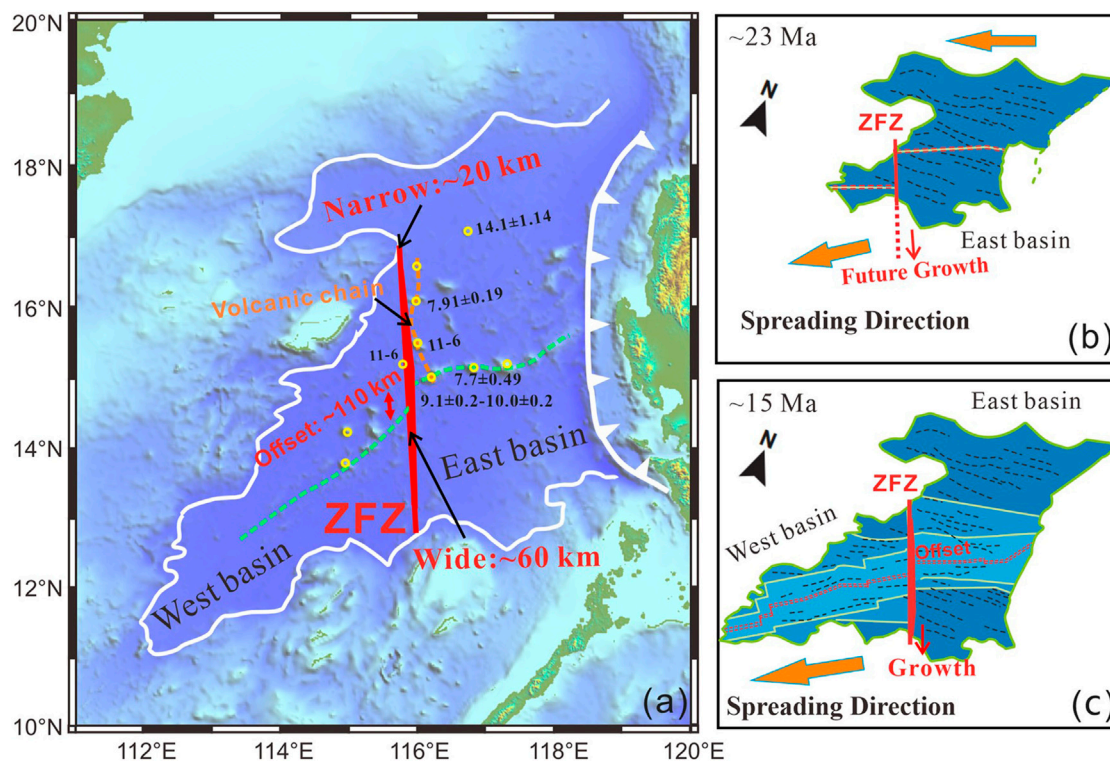


FIGURE 13

Plate reconstructions of the South China Sea basin at 23 and 15 Ma and post-spreading Seamounts distribution. (A) Schematic diagram of the South China Sea basin tectonics, the red line is the Zhongnan Fault Zone, the yellow dots represent sea seamounts. The seamount ages are from Pautot et al., 1990; Tongkul 1993; Wang et al., 1985, Wang et al., 2009; Yan et al., 2008; Yan et al., 2008; Yan et al., 2014 (B–C) Plate reconstructions of the South China Sea basin (~23, 15 Ma, from Sibuet et al., 2016), the red dashed line is the mid-ocean ridge, and the red solid line is the Zhongnan Fault Zone.

profiles in the South China Sea basin (Figure 12B), the Zhongnan Fault Zone cuts through the T6 horizon as well as the Tg horizon, but does not cut through the T5 horizon (where T5, T6 and Tg represents the early Miocene interface, the late Oligocene interface, and the early Oligocene basement, respectively), indicating that the Zhongnan Fault Zone was active before the early Oligocene-prior to the spreading of the South China Sea basin (~32 Ma; e.g., Li, 2012; Xu et al., 2019). This supports that the Zhongnan Fault Zone was a continental transform fault which evolved to an oceanic transform fault before and after the South China Sea basin spreading.

Firstly, the dynamic growth of the transform fault modeled in our study is comparable to the Zhongnan Fault Zone in the South China Sea basin (Figure 12; Xu et al., 2019; Barckhausen and Roeser, 2004, Barckhausen et al., 2014; Frank, 2013; Frank et al., 2004; Ruan et al., 2016; Sibuet et al., 2016). 1) The Zhongnan Fault Zone is 15–25 km wide at its northern end (Figure 12B), 60 km wide in the middle (Figure 12C) and ~35 km wide in the southern end (Figure 12D) revealed by seismic reflection data (Ruan et al., 2016; Qiu et al., 2019; Xu et al., 2021). Our model results are consistent with this phenomenon (Figure 10), and the increased width of the Zhongnan Fault in its middle, as suggested by our model results,

is likely caused by asthenospheric mantle upwelling ahead of the propagated spreading ridge. 2) The length of the Zhongnan Fault increased with the extension of the South China Sea basin. According to the plate reconstruction of the South China Sea basin (Briais et al., 1993) and the relative positions of the Zhongsha block and the Liyue-North Palawan micro-continent (Li, 2011), the Zhongnan Fault has been continuously growing southward with the significant increase in its length (Yan et al., 2014; Li et al., 2017). Our model results of transform fault growth are thus consistent with this observation.

Secondly, the formation of ridge segments with an offset distance is a remarkable feature of the South China Sea basin. Seafloor spreading in the southwest sub-basin of the South China Sea initiated at the south end of the Zhongnan Fault Zone, and propagated from east to west since 23.8 Ma (Figure 13B). An offset distance of ~110 km is formed between the two ridge segments in the east and southwest sub-basins (Figure 13A). Our model results are consistent with this phenomenon and indicate that the Zhongnan Fault Zone facilitated strain localization and promoted the formation of the ridge segment in the southwest sub-basin.

Thirdly, the lineated volcanic chain is observed along the Zhongnan Fault Zone in the South China Sea basin (Figure 13A).

According to our model results, formation of the lineated volcanic chain is likely related to the extensional deformation along the transform fault (Figure 11A). The reported ages of the volcanos from the volcanic chain along the Zhongnan Fault Zone were younger than the termination of the South China Sea basin spreading (Wang et al., 1985; Wang et al., 2009; Pautot et al., 1990; Tongkul 1993; Yan et al., 2008; Yan et al., 2008; Yan et al., 2014), indicating post-spreading magmatism. Whether there were older magmatic events along the Zhongnan Fault Zone remains enigmatic and need to be explored in the future.

The uplifting elevated topography and Moho surface of the transform fault suggested revealed by our models are observed at the Zhongnan Fault Zone, where there is only 8–10 km crust left and high values of gravity anomaly features (Ruan et al., 2016; Jourdon et al., 2020). In addition, a linear post-spreading seamount chain developed along the Zhongnan Fault Zone (Li et al., 2017; Xu et al., 2021), which indicates thin lithosphere and upwelling of hot asthenospheric underneath the fault zone. These observations suggest that the Zhongnan Fault Zone may have interacted with the spreading ridge of the east subbasin and experienced stages of extension. However, the Zhongnan Fault Zone/transform fault has only been discussed in earlier studies for its morphology, dynamic evolution and deep structure, its influence on sea floor spreading is not fully investigated (Barckhausen et al., 2004; Frank et al., 2004; Frank, 2013; Barckhausen et al., 2014; Ruan et al., 2016; Sibuet et al., 2016). Our results suggest that transform faults perpendicular to mid-ocean ridges have a significant influence on the spreading processes and evolution of ocean basins (e.g., North Iceland, Karson et al., 2019). The interaction with the oceanic spreading meanwhile leads to faults growth in its width and length. Brune et al., 2014, Clauser and Huenges, 1995, Gerya, 2010, Glerum et al., 2020, Gudmundsson et al., 2007, Guo et al., 2019, Huang et al., 2014, Lei et al., 2020, Li et al., 2011, Li et al., 2018, Li et al., 2019, Liao and Gerya, 2015, Karson et al., 1984, Ranalli, 1995, Ros et al., 2017, Taylor and Hayes, 1980, Wang et al., 2022.

Conclusion

We conducted a systematic study to investigate the interaction between pre-existing transform faults and rifting/spreading propagation using 3D dynamical numerical simulations. The main conclusions are given below:

- 1) The pre-existing transform faults affect rifting/spreading propagation promoting the formation of ridge segments with offset distances. The formation and development of the younger ridge segment is promoted by the pre-existing transform faults. Evolution of the pre-existing transform faults is also affected by spreading propagation featured by fault widening with melting and fault growth with increased length.
- 2) The initial length and orientation of the pre-existing transform faults affect rifting/spreading propagation, controlling the offset distance between the ridge segments and the formation of overlapping ridge segments.
- 3) Our model results are comparable with natural observations in the South China Sea basin, in terms of the formation of offset ridge segments and transform fault evolution. We suggest that the pre-existing Zhongnan fault zone interacted rifting/spreading propagation and regulated seafloor spreading of the South China Sea basin.

Data availability statement

The raw data supporting the conclusions of this article will be made available by the authors, without undue reservation.

Author contributions

HL and JL designed the study. HL wrote the manuscript. YS, JQ and YW improve the manuscript. ZZ and XS helped to improve the manuscript with some suggestions. All authors contributed to the article and approved the submitted version.

Funding

This research is financially supported by NSFC projects (U1901214, 41974104, 91855208, 42109043) and the Guangdong project 2017ZT07Z006.

Acknowledgments

We thank Taras Gerya for his long-lasting guidance on our geodynamical modeling. We thank Linfeng Liao and Hao Su for their constructive suggestions. Numerical simulations were run with the clusters of National Supercomputer Center in Guangzhou (Tianhe-II). We would like to thank Ziyang Xu and Ning Qiu for their fine seismic profile results.

Conflict of interest

The authors declare that the research was conducted in the absence of any commercial or financial relationships that could be construed as a potential conflict of interest.

Publisher's note

All claims expressed in this article are solely those of the authors and do not necessarily represent those of their

affiliated organizations, or those of the publisher, the editors and the reviewers. Any product that may be evaluated in this article, or claim that may be made by its manufacturer, is not guaranteed or endorsed by the publisher.

References

- Bai, Y., Wu, S., Liu, Z., Müller, R., Williams, S., Zahirovic, S., et al. (2015). Full fit reconstruction of the South China Sea conjugate margins. *Tectonophysics* 661, 121–135. doi:10.1016/j.tecto.2015.08.028
- Barckhausen, U., Engels, M., Franke, D., Ladage, S., and Pubellier, M. (2014). Evolution of the South China Sea: Revised ages for breakup and seafloor spreading. *Mar. Petroleum Geol.* 58, 599–611. doi:10.1016/j.marpetgeo.2014.02.022
- Barckhausen, U., and Roeser, H. (2004). "Seafloor spreading anomalies in the South China sea revisited," in *Continent-Ocean interactions within east asian marginal seas*. Editors P. Clift, W. Kuhnt, P. Wang, and D. Hayes (Washington, DC: AGU), 121–125. doi:10.1029/92jagm07
- Briaies, A., Patriat, P., and Tapponnier, P. (1993). Updated interpretation of magnetic anomalies and seafloor spreading stages in the south China Sea: Implications for the Tertiary tectonics of Southeast Asia. *J. Geophys. Res.* 98 (B4), 6299–6328. doi:10.1029/92jb02280
- Brune, S., Heine, C., Pérez-Gussinyé, M., and Sobolev, S. (2014). Rift migration explains continental margin asymmetry and crustal hyper-extension. *Nat. Commun.* 5, 4014. doi:10.1038/ncomms5014
- Burg, J., and Gerya, T. (2005). The role of viscous heating in Barrovian metamorphism of collisional orogens; thermomechanical models and application to the Lepontine Dome in the Central Alps. *J. Metamorph. Geol.* 23 (2), 75–95. doi:10.1111/j.1525-1314.2005.00563.x
- Burov, E., and Cloetingh, S. (1997). Erosion and rift dynamics: New thermomechanical aspects of post-rift evolution of extensional basins. *Earth Planet. Sci. Lett.* 150 (1–2), 7–26. doi:10.1016/s0012-821x(97)00069-1
- Clauser, C., and Huenges, E. (1995). Thermal conductivity of rocks and minerals. *Rock Phys. Phase Relat. A Handb. Phys. Constants* 3, 105–126.
- Courtillot, V. (1982). Propagating rifts and continental breakup. *Tectonics* 1 (3), 239–250. doi:10.1029/TC001i003p0239
- Cramer, F., Schmeling, H., Golabek, G., Duretz, T., Orendt, R., Buitert, S., et al. (2012). A comparison of numerical surface topography calculations in geodynamic modelling: An evaluation of the 'sticky air' method. *Geophys. J. Int.* 189 (1), 38–54. doi:10.1111/j.1365-246X.2012.05388.x
- Franke, D., Dimitri, S., Manuel, P., Stephan, S., Benoit, M., Jean-Luc, A., et al. (2004). The final rifting evolution in the South China Sea. *Mar. Petroleum Geol.* 58, 704–720. ISSN 0264-8172. doi:10.1016/j.marpetgeo.2013.11.020
- Franke, D. (2013). Rifting, lithosphere breakup and volcanism: Comparison of magma-poor and volcanic rifted margins. *Mar. Petroleum Geol.* 43, 63–87. 0264-8172. doi:10.1016/j.marpetgeo.2012.11.003
- Gerya, T. V. (2010). *Introduction to numerical geodynamic modeling*. Cambridge University Press. doi:10.1017/CBO9780511809101
- Gerya, T. V. (2013). Three-dimensional thermomechanical modeling of oceanic spreading initiation and evolution. *Phys. earth Planet. interiors* 214, 35–52. doi:10.1016/j.pepi.2012.10.007
- Gerya, T. V., and Yuen, D. A. (2003). Rayleigh-Taylor instabilities from hydration and melting propel "cold plumes" at subduction zones. *Earth Planet. Sci. Lett.* 212 (1–2), 47–62. doi:10.1016/s0012-821x(03)00265-6
- Glerum, A., Brune, S., Stamps, D., and Strecker, M. (2020). Victoria continental microplate dynamics controlled by the lithospheric strength distribution of the East African Rift. *Nat. Commun.* 11 (1), 2881. doi:10.1038/s41467-020-16176-x
- Gudmundsson, A., Jacoby, W. R., and Gudmundsson, M. T. (2007). Infrastructure and evolution of ocean-ridge discontinuities in Iceland. *J. Geodyn.* 43 (1), 6–29. doi:10.1016/j.jog.2006.09.002
- Guo, L., Gao, R., Shi, L., Huang, Z., and Ma, Y. (2019). Crustal thickness and Poisson's ratios of South China revealed from joint inversion of receiver function and gravity data. *Earth Planet. Sci. Lett.* 510, 142–152. doi:10.1016/j.epsl.2018.12.039
- Hey, R., Duennebie, F. K., and Morgan, W. J. (1980). Propagating rifts on midocean ridges. *J. Geophys. Res.* 85 (B7), 3647–3658. doi:10.1029/JB085iB07p03647
- Huang, H., Guo, X., Xia, S., and Qiu, X. (2014). Crustal thickness and Poisson's ratio in the coastal areas of South China[J]. *Chin. J. Geophys.* 57(12): 3896–3906. (in Chinese). doi:10.6038/cjg20141204
- Illsley-Kemp, F., Bull, J. M., Keir, D., Gerya, T., Pagli, C., Gernon, T., et al. (2018). Initiation of a proto-transform fault prior to seafloor spreading. *Geochim. Geophys. Geosyst.* 19 (12), 2018GC007947–4756. doi:10.1029/2018GC007947
- Jourdon, A., Le Pourhiet, L., Mouthereau, F., and May, D. (2020). Modes of propagation of continental breakup and associated oblique rift structures. *J. Geophys. Res. Solid Earth* 125, e2020JB019906. doi:10.1029/2020JB019906
- Karson, J. A., Fox, P. J., Crane, K. T., Kidd, W. S. F., Bonatti, E., et al. (1984). The geology of the Oceanographer Transform: The ridge-transform intersection. *Mar. Geophys. Res. (Dordr.)* 6, 109–141. doi:10.1007/BF00285956
- Karson, J., Brandsdóttir, B., Einarsson, P., Sæmundsson, K., Farrell, J., and Horst, A. (2019). Evolution of migrating transform faults in anisotropic oceanic crust; examples from Iceland. *Can. J. Earth Sci.* 56 (12), 1297–1308. doi:10.1139/cjes-2018-0260
- Le Pourhiet, L., Chamot-Rooke, N., Delescluse, M., May, D. A., Watremez, L., and Pubellier, M. (2018). Continental break-up of the South China Sea stalled by far-field compression. *Nat. Geosci.* 11 (8), 605–609. doi:10.1038/s41561-018-0178-5
- Le Pourhiet, L., May, D., Huille, L., Watremez, L., and Leroy, S. (2017). A genetic link between transform and hyper-extended margins. *Earth Planet. Sci. Lett.* 465, 184–192. doi:10.1016/j.epsl.2017.02.043
- Lei, C., Alves, T., Ren, J., and Tong, C. (2020). Rift structure and sediment infill of hyperextended continental crust: Insights from 3D seismic and well data (xisha trough, south China sea). *J. Geophys. Res. Solid Earth* 125, e2019j-e18610J. doi:10.1029/2019jb018610
- Li, C., and Song, T. (2012). Magnetic recording of the Cenozoic oceanic crustal accretion and evolution of the South China Sea basin. *Chin. Sci. Bull.* 57, 3165–3181. doi:10.1007/s11434-012-5063-9
- Li, C., Xu, X., Lin, J., Sun, Z., Zhu, J., Yao, Y., et al. (2014). Ages and magnetic structures of the South China Sea constrained by deep tow magnetic surveys and IODP Expedition 349. *Geochim. Geophys. Geosyst.* 15, 4958–4983. doi:10.1002/2014GC005567
- Li, C., Zhou, Z., Li, J., Chen, B., and Geng, J. (2008). Magnetic zoning and seismic structure of the South China Sea ocean basin. *Mar. Geophys. Res. (Dordr.)* 29, 223–238. doi:10.1007/s11001-008-9059-4
- Li, F., Sun, Z., Pang, X., Liao, J., Yang, H., Xie, H., et al. (2019). Low-viscosity crustal layer controls the crustal architecture and thermal distribution at hyperextended margins; modeling insight and application to the northern South China Sea margin. *Geochim. Geophys. Geosyst.* 20 (7), 3248–3267. doi:10.1029/2019gc008200
- Li, F., Sun, Z., and Yang, H. (2018). Possible spatial distribution of the Mesozoic volcanic arc in the present-day South China Sea continental margin and its tectonic implications. *J. Geophys. Res. Solid Earth* 123 (8), 6215–6235. doi:10.1029/2017jb014861
- Li, J., Ding, W., Gao, J., Wu, Z. Y., and Zhang, J. (2011). Cenozoic evolution model of the sea-floor spreading in south China sea: New constraints from high resolution geophysical data[J]. *Chin. J. Geophys.* 54(12): 894–906. doi:10.1002/cjg2.1672in Chinese with English abstract
- Li, J. (2011). Dynamics of the continental margins in south China sea: Scientific experiments and research progresses. *Chin. J. Geophys.* 54 (12), 883–893. doi:10.1002/cjg2.1671
- Li, Y., Liu, H., Zhu, R., Wang, Y., Zhou, Y., and Xu, Z. (2017). Extension of the zhongnan-siling Fault Zone in south China sea and its bearing on seafloor spreading [J]. *Mar. Geol. Quat. Geol.*, 37(2): 82–98. In Chinese. doi:10.16562/j.cnki.0256-1492.2017.02.009
- Liao, J., and Gerya, T. (2015). From continental rifting to seafloor spreading: Insight from 3D thermo-mechanical modeling. *Gondwana Res.* 28 (4), 1329–1343. doi:10.1016/j.gr.2014.11.004

Supplementary material

The Supplementary Material for this article can be found online at: <https://www.frontiersin.org/articles/10.3389/feart.2022.1054747/full#supplementary-material>

- Müller, R. D., Seton, M., Zahirovic, S., Williams, S. E., Matthews, K. J., Wright, N. M., et al. (2016). Ocean basin evolution and global-scale plate reorganization events since Pangea breakup. *Annu. Rev. Earth Planet. Sci.* 44, 107–138. doi:10.1146/annurev-earth-060115-012211
- Pautot, G., Rangin, C., Briais, A., Wu, J. L., Han, S. Q., Li, H. X., et al. (1990). The axial ridge of the South China sea: A seabeam and geophysical survey. *Oceanol. Acta* 13 (2), 129–143.
- Qiu, N., Yao, Y., Zhang, Y., et al. (2019). Characteristics of the crustal and its tectonic significance of the continental margin of SE South China Sea. *Chin. J. Geophys.* 62 (7), 2607–2621. in Chinese.
- Ranalli, G. (1995). *Rheology of the Earth*. Springer Science & Business Media.
- Ros, E., Perez-Gussinye, M., Araujo, M., Thoaldo Romeiro, M., Andres-Martinez, M., and Morgan, J. P. (2017). Lower crustal strength controls on melting and serpentinization at magma-poor margins: Potential implications for the South atlantic. *Geochem. Geophys. Geosyst.* 18, 4538–4557. doi:10.1002/2017GC007212
- Ruan, A., Wei, X., Niu, X., Zhang, J., Dong, C., Wu, Z., et al. (2016). Crustal structure and fracture zone in the Central Basin of the South China Sea from wide angle seismic experiments using OBS. *Tectonophysics* 688, 1–10. ISSN 0040-1951. doi:10.1016/j.tecto.2016.09.022
- Sibuet, J. C., Yeh, Y. C., Lee, C. S., et al. (2016). Geodynamics of the South China sea. *Tectonophysics* 692, 98–119. doi:10.1016/j.tecto.2016.02.022
- Taylor, B., and Hayes, D. E. (1980). “The tectonic evolution of the South China Sea Basin” in *The tectonic and geologic evolution of South East Asian Seas and Islands*. Editor D. E. Hayes. *Geophys. Monogr. Ser.* 27 (Washington, DC: AGU), 23–56. doi:10.1029/GM023p0089
- Tongkul, F. (1993). Tectonic control on the development of the neogene basins in sabah, east Malaysia[C]. Proceedings Symposium on the Tectonic Framework and Energy Resources of the Western Margin of the Pacific Basin. Kuala Lumpur, Malaysia. Geological Society of Malaysia. 95–103. November 1993. doi:10.7186/bgsm33199307
- Vink, G. E. (1982). Continental rifting and the implications for plate tectonic reconstructions. *J. Geophys. Res.* 87 (13), 10677–10688. doi:10.1029/JB087iB13p10677
- Wang, X., Wu, M., Liang, D., and Yin, A. (1985). Some geochemical characteristics of basalts in the South China Sea. *Chin. J. Geochem.* 4 (4), 380–390. doi:10.1007/bf02843275
- Wang, Y., Han, X., Luo, Z., Qiu, Z., Ding, W., Li, J., et al. (2009). Late Miocene magmatism and evolution of zhenbei-huangyan seamount in the South China sea: Evidence from petrochemistry and chronology. *Acta Oceanol. Sin.* 283 (5747), 532–537. in Chinese with English abstract. doi:10.1038/283532a0
- Wang, Z., Singh, S. C., Prigent, C., Gregory, E. P. M., and Marjanovic, M. (2022). Deep hydration and lithospheric thinning at oceanic transform plate boundaries. *Nat. Geosci.* 15, 741–746. doi:10.1038/s41561-022-01003-3
- Xu, Z., Wang, J., Gao, H., Sun, G., Sun, M., Nie, X., et al. (2019). Research progress on the zhongnan-liyue Fault Zone in the South China Sea Basin*[J]. *J. Trop. Oceanogr.* 38(2): 86–94. In Chinese with English Abstract.
- Xu, Z., Wang, J., Yao, Y., Tang, J., Gao, H., and Li, X. (2021). The temporal-spatial distribution and deep structure of the zhongnan- liyue Fault Zone in the north of the South China Sea Basin. *Earth Sci.* 46 (3), 942–955. In Chinese with English Abstract. doi:10.3799/dqkx.2020.400
- Yan, Q., Shi, X., and Castillo, P. R. (2014). The late mesozoic–cenozoic tectonic evolution of the South China sea: A petrologic perspective. *J. Asian Earth Sci.* 85 (2), 178–201. doi:10.1016/j.jseaes.2014.02.005
- Yan, Q., Shi, X., Wang, K., Bu, W., and Xiao, L. (2008). Major element, trace element, and Sr, Nd and Pb isotope studies of Cenozoic basalts from the South China Sea. *Sci. China Ser. D-Earth. Sci.* 51 (4), 550–566. doi:10.1007/s11430-008-0026-3
- Yan, Q., Shi, X., Yang, Y., and Wang, K. (2008). Potassium-argon/argon-40-argon-39 geochronology of Cenozoic alkali basalts from the South China Sea. *Acta Oceanol. Sin.* 27 (6), 115–123.



OPEN ACCESS

EDITED BY

Hao Liang,
Sun Yat-sen University, China

REVIEWED BY

Pengcheng Wang,
Ocean University of China, China
Linlin Li,
School of Earth Sciences and
Engineering, Sun Yat-sen University,
China

*CORRESPONDENCE

Jiao Zhou,
✉ 464946523@qq.com

SPECIALTY SECTION

This article was submitted to
Geohazards and Georisks,
a section of the journal
Frontiers in Earth Science

RECEIVED 08 August 2022

ACCEPTED 02 December 2022

PUBLISHED 23 January 2023

CITATION

Zhou J, Chen H, Chen J, Yi S, Guo L,
Hu X, Du W and Sun M (2023),
Characteristics and distribution of
geohazards since the middle miocene
of the Xisha sea area, South China Sea.
Front. Earth Sci. 10:1012144.
doi: 10.3389/feart.2022.1012144

COPYRIGHT

© 2023 Zhou, Chen, Chen, Yi, Guo, Hu,
Du and Sun. This is an open-access
article distributed under the terms of the
[Creative Commons Attribution License
\(CC BY\)](https://creativecommons.org/licenses/by/4.0/). The use, distribution or
reproduction in other forums is
permitted, provided the original
author(s) and the copyright owner(s) are
credited and that the original
publication in this journal is cited, in
accordance with accepted academic
practice. No use, distribution or
reproduction is permitted which does
not comply with these terms.

Characteristics and distribution of geohazards since the middle miocene of the Xisha sea area, South China Sea

Jiao Zhou^{1,2,3*}, Hongjun Chen^{1,2,3}, Jiale Chen^{1,3}, Shantang Yi^{1,3},
Lihua Guo^{1,3}, Xiaosan Hu^{1,2,3}, Wenbo Du^{1,2,3} and Meijing Sun^{1,2,3}

¹Key Laboratory of Marine Mineral Resources, Ministry of Natural Resources, Guangzhou Marine Geological Survey, China Geological Survey, Guangzhou, China, ²Key Special Project for Introduced Talents Team of Southern Marine Science and Engineering Guangdong Laboratory, Guangzhou, China, ³National Engineering Research Center for Gas Hydrate Exploration and Development, Guangzhou, China

Geological hazards can cause significant harm to the construction and maintenance of reef infrastructure projects in the Xisha Sea area. This study uses high-resolution multichannel earthquake data, single-channel seismic profiles, and multi-beam survey data to identify and analyze the geological hazards in the Xisha Sea area since the Miocene. Based on the geophysical data interpretation, the destructive geological disaster factors that are active, such as active faults, shallow gas, diapers, landslides, multistage scarps (steps), scouring troughs, and canyons, as well as the restrictive geological disaster factors without activity ability, such as buried paleochannels, pockmarks, reefs, and undersea volcanoes, are identified and analyzed. This paper discusses the causes and hazards of geological hazards and, for the first time, draws a comprehensive plane layout of the geological hazards. The above analysis demonstrates that the scarps are mainly located around the atolls or platforms, and the slope of the southeast seabed topography is significantly higher than that of the northwest. There are seven medium and large landslides, mainly located around Yongxing Plateau and Yongle Plateau, caused by gravity and faulting. Shallow gas is mainly developed in the southern part of the North Reef and is indicated by diaper structures, faults, and gas chimneys. A series of shallow faults are developed in the study area, mainly steep normal faults. The scouring troughs are primarily distributed near the Yongxing Platform, Zhongjian North Platform, and Huaguang Platform. Submarine canyons are primarily located in the northern and southern parts of the Shidao Platform. Affected by multiple factors such as hydrodynamic conditions, the stability of sedimentary layers, and sediment supply, the scour degree varies, with the general depth ranging from several meters to several hundred meters. Underwater infrastructure in the study area should not be constructed in areas with active and destructive geological hazards. The results of this study can serve as a guide for further exploration in the Xisha area and disaster prevention and mitigation during construction activity in the area.

KEYWORDS

Xisha sea area, high-resolution seismic, geological hazards, seabed scarps, submarine landslides, scour trough, spatial distribution

1 Introduction

Hazardous geology refers to naturally occurring or man-made geological conditions/phenomena that cause or can cause harm to human life or property. The research objectives of hazardous geological studies are the factors causing geological disasters, including geological bodies and geological phenomena and their occurrence, development mechanisms, and distribution (Liu et al., 2002). With the vigorous development of resource surveys in marine environments, such as for oil and gas, natural gas hydrate, and other marine engineering operations, the demand for a census of marine geological hazards has also been increasing. Marine disaster geology has also been continuously applied in practice, becoming a powerful means for achieving disaster prevention and mitigation in marine development activities (Bao and Jiang, 1993). In recent years, the instability of seabed geological conditions and the frequent occurrence of various marine disasters have increasingly affected human activities and economies (Ni, 2009; Li, 2013; Ma et al., 2014).

The South China Sea is located at the intersection of the Eurasian, Pacific, and Indo-Australian tectonic plates. The Xisha Islands are located northwest of the South China Sea (Figure 1). More than 40 islands, sandbars, reefs, and beaches are distributed in this sea. With a total island area of 8 km², the Xisha Islands are the archipelago with the largest total land area among the four major archipelagos in the South China Sea. The development of infrastructure in the Paracel Islands and the development of industries such as the fishery and tourism industries have been essential to safeguarding national sovereignty. In recent years, the construction of Sansha City has been carried out rapidly.

Determining geological engineering conditions is crucial to ensure proper site selection and the safe construction of various projects. With the development, management, and promotion of tourism, fisheries, and seabed resources in the Xisha Islands, close attention must be paid to the possible risks of marine geological disasters affecting marine engineering facilities and the marine environment.

From the perspective of disaster-causing factors and disaster-laden environments, China's sea area is divided into four levels of geological disaster risk (Ye et al., 2011). Among them, the Xisha waters in the South China Sea belong to the land slope (island slope) disaster geological area (III₃), a high-risk designation. There are few studies on the disaster geology of the Xisha sea area. Chen et al. (2021) studied the types and distribution characteristics of the disaster geology in the southeast of the Xuande Atoll in the Xisha Sea area. However, the research scope was small and with limitations. Using geophysical data collected since 2015, this paper comprehensively studied the types of geological disasters in the Xisha sea area and explored the causes of geological hazards. It is critical to fill the research gap, provide a basis for further exploration and disaster prevention and reduction to avoid the hazards in engineering construction, and provide a guarantee for particular navigation.

2 Geological setting

The South China Sea is located at the Indo-Australian Plate, the Eurasian Plate, and the Pacific Plate. It is the largest marginal sea basin in the Western Pacific and is part of the Western Pacific marginal trench-arc-basin system. The formation of continental

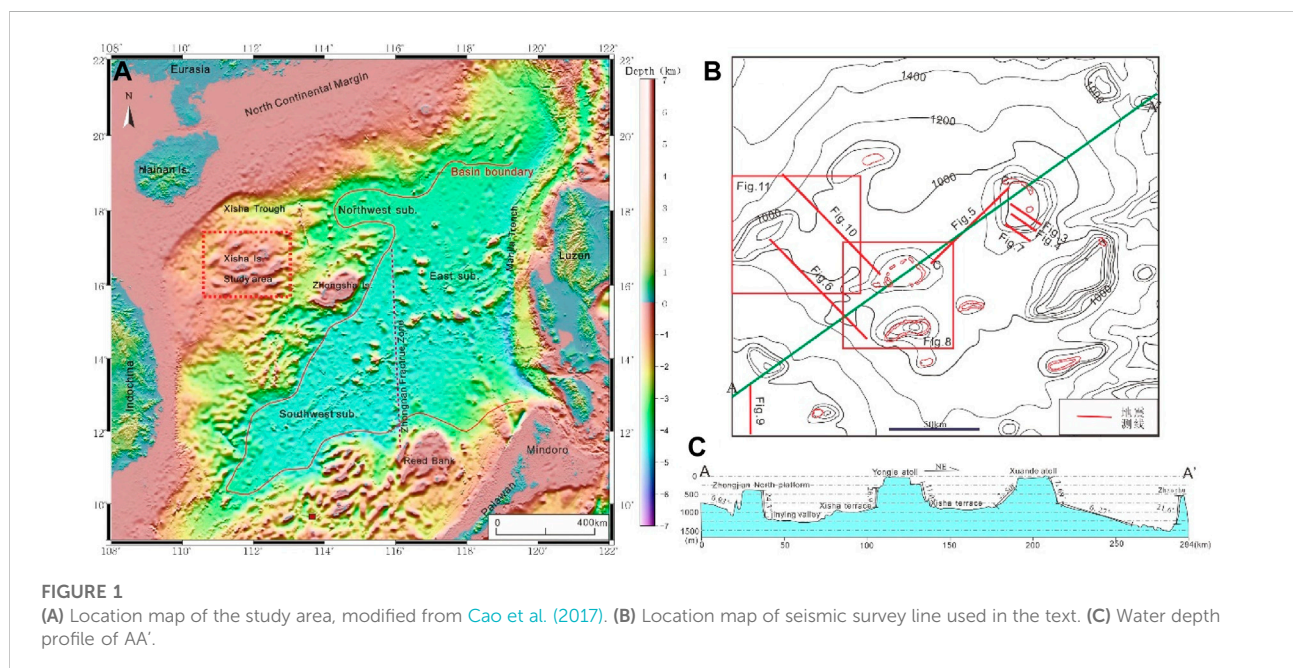


FIGURE 1
(A) Location map of the study area, modified from Cao et al. (2017). (B) Location map of seismic survey line used in the text. (C) Water depth profile of AA'.

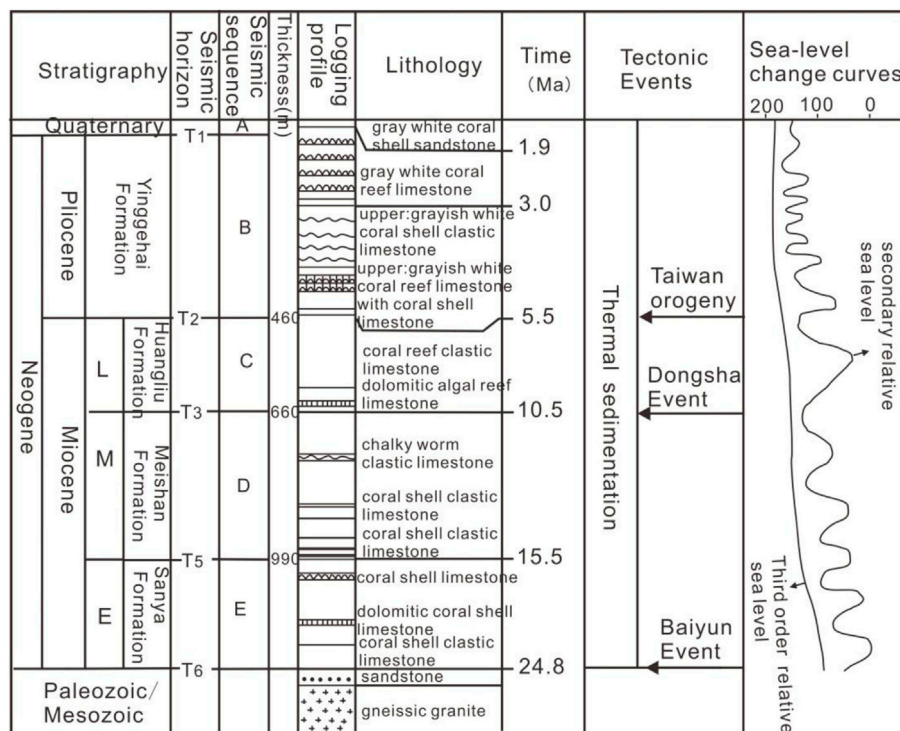


FIGURE 2

The stratigraphic column of XY1 well in the Xisha Sea area (Modified from Ma et al. (2010)).

margin basins in the northern part of the South China Sea is mainly related to the South China Sea movement and the Dongsha movement. It has undergone three stages: rifting, rifting with thermal subsidence, and the Cenozoic tectonic activity period (Kuang et al., 2014; Yang et al., 2016). The study area is located in the western part of the continental shelf and slope transition zone of the passive continental margin in the north of the South China Sea (Figure 1). It is adjacent to the continental shelf of Hainan Island in the west, the Xisha Trough in the north, and the Zhongsha Trough and South China Sea Basin in the East and south, respectively. The terrain is complex and changeable, mainly composed of islands, reefs, platforms, and valleys with a water depth of 0–2600 m.

The Xisha Sea area has experienced two tectonic evolution stages, the Paleogene fault depression, and the Neogene depression. It has a double-layer structure of a lower fault and upper depression, correspondingly forming two tectonic layers. The Xisha uplift area was in a state of uplift and denudation before the Miocene. Since the Miocene and the thermal subsidence of the South China Sea, the Xisha Sea area has sunk underwater and entered a period of large-scale reef formation. Reef formation has occurred in the area for more than 20 million years, and at present, reef facies sediments with a thickness of more than 1,200 m are present (He and Zhang, 1986; Lv et al., 2002; Lv et al., 2011; Yang et al., 2016). In the Xisha Sea

area, the drilling data of Well XY1 shows that since the Miocene, a vast reef formation developed on the Precambrian granite basement, reaching 1,251 m in thickness (Gong and Li, 1997; Zhao, 2010). Drilling data show that the entire area of the Xisha Islands subsided underwater since the Miocene, making the area have a suitable temperature, salinity, and water depth for the widespread development of reef carbonate formations.

The sequence stratigraphic framework since the Miocene in the study area has been established based on geophysical and drilling data (He and Zhang, 1986; Ma et al., 2010). Five third-order sequence interfaces (T₁, T₂, T₃, T₅, and T₆ (Figure 2)) are identified, which correspond to the bottom boundaries of the Quaternary, Pliocene, Late Miocene, Middle Miocene, and Early Miocene, respectively.

3 Materials and methods

Since 2015, the Guangzhou Marine Geological Survey has carried out 3,988 km of high-resolution single-channel seismic surveys, 1,205.7 km of multichannel seismic surveys, and 15,467 km of multi-beam bathymetry surveys in the Xisha Sea area (16°N–17°N, 111°E–112°30'E). The survey work has led to identifying the types and distributions of the geological hazards in the Xisha Sea area.

The single-channel seismic measurement used the IXSEA DELPH SEISMIC single-channel data acquisition and processing system. The seismic source adopted a GI gun source system, with a working pressure of 2000 psi and a capacity of 210. The SURESHOT source gun control system was used; the cable sinking depth was 0.5–1.5 m, and the subsidence depth of the source was 3 m. The offset distance between the GI air gun source and the receiving cable was 8–10 m. The length of the collected data record was 1000 m, and the width of the printed simulation profile was 400 m. In the muddy sedimentary area with a water depth of more than 30 m, the detection depth can reach (vertically) >100 m, and the vertical resolution was better than 3 m; under normal circumstances, the continuous missed test was less than 250 m, and the cumulative missed test was less than 6% of the entire survey line.

The shallow formation profile measurement used the EdgeTech3200XS CHIRP type shallow formation profiler. The recorded formation reflection signal was coherent and clear, and the formation reflection interface layer was clear and easy to trace continuously. The penetration depth in the work area reached ~30 m. The penetration depth could exceed 80 m.

The multichannel seismic measurement source system was composed of three rows of sub-arrays with a capacity of 1270 cu. in. and a total capacity of 3810 cu. in. The air gun controller was the Bigshot air gun synchronization controller produced by the Real Time System Company in the United States. The air compressor was the JOY4 air compressor. The working pressure was 2000PSI. The receiving cable of the receiving system adopted a Sentinel 24-bit digital solid cable of the France Sercel company, and 360 solid cables were used during the operation. The SYS3 water bird control system and the 5011E export compass controlled the cable depth control system. It consisted of a depth gauge and a 5010-type depth gauge; the water depth in the survey area was shallow, and the maximum water depth was less than 1200 m. Therefore, the multichannel seismic measurement adopted a parameter system with a focal depth of 7 m, a capacity of 3810 in^3 , and a cable depth of 9 m. Most of the measuring lines have an accuracy of less than 0.5 m. The first-grade rate was 92.28%, the second-grade rate was 7.72%, and the self-assessment pass rate was 100%.

The SIMRAD EM710S multi-beam bathymetry system was used according to the requirements for tolerance in the “Ocean Multi-beam Measurement Regulations” (DZ/T 0292–2016); the time limit difference was 0.6 m when the water depth was less than 30 m. When the water depth was greater than 30 m, the limit difference was 2% of the water depth.

4 Types of hazardous geology

At present, the classification of geological disasters in China is not consistent. Based on the disaster location, they are classified into surface and underground types. They are then subdivided into

direct, potential, and direct obstacles (Li, 1990). They are also classified into lithospheric, atmospheric, hydrosphere, and biosphere, according to the different spheres that cause disasters (Liu et al., 1992). Some scholars have proposed the types of hydrodynamics, aerodynamics, soil mechanics, gravity, and tectonic stress according to the dynamics that cause geological disasters (Chen and Li, 1993). In addition, according to the activity of the disaster geological factors, scholars have divided geological disasters into two types: those with destructive capabilities and those without destructive capabilities (Feng et al., 1996; Liu, 1996).

Further, based on the location of the internal and external dynamic systems and geological disaster factors, some scholars have divided geological disasters into four types: structural, coastal, submarine, and shallow (Liu et al., 2000). The authors of this paper believe that the purpose of geological disaster classification is to directly classify the geological disasters and their degree of harm and to clarify which geological disasters can be prevented and which cannot be prevented and only avoided. Therefore, based on the interpretation results of geophysical survey data in this study, the geological disasters are divided into two categories (Table 1): active and destructive geological disasters, such as active faults, shallow gas, diapirs, landslides, steep ridges, scour troughs, etc. The second comprises inactive geological hazards, such as buried ancient river channels, pockmarks, volcanic structures, etc.

5 Characteristics, distribution, and causes of major geological hazards

According to previous investigations and research results, numerous volcanoes (Zhang BK. et al., 2014; Zhang et al., 2014b; Feng et al., 2017), normal faults (Lin et al., 2009; Yang et al., 2015; Du et al., 2021), reefs (Wei et al., 2008; Yang et al., 2011), etc. Have been developed in the Xisha Sea area since Pliocene, and scarps, landslides, faults, etc. (Chen et al., 2021) are developed in the southeast of Xuande Atoll, A large number of pits are developed near the Xisha Uplift area (Chen, 2011; Sun et al., 2012; Guan et al., 2014; Chen et al., 2015; Ye et al., 2019; Yang et al., 2020; Wang et al., 2021). Based on a large amount of new measured data, a large number of steep slopes, shallow gas, buried ancient river channels, large landslides, shallow faults, and scour channels have been newly discovered in this paper. The geological disasters in Xisha Islands have been systematically summarized for the first time. Landslides, steep slopes, shallow gas, mud diapirs, buried ancient river channels, shallow active faults, pits, scour channels, and other geological hazard phenomena are primarily located throughout the study area (Figure 3), which are potentially harmful to marine engineering. The following describes the main geological characteristics and the distribution of the geological hazards.



FIGURE 3
Geological distribution map of environmental hazards in Xisha Sea area.

5.1 Destructive and active geological hazards

5.1.1 Multistage scarps (steps)

The seabed topography is mainly controlled by the Xisha platform and is closely related to the distribution of islands in the study area. The overall topography is characterized by islands at the center, declining altitude towards the surrounding area, with the upper slope being steep and the lower slope being gentler. The water depth ranges from 0 m to 800 m, and coral islands, reefs, and their subordinate platforms are developed throughout. The topographic variations of each island and reef are similar, characterized by a steep slope in the southeast and a gentle slope in the northwest. The average slope value of the periphery ranges between 5.0° and 22.0° . The distribution of landslide masses from north to south can reach 30 km, which is considerable. The water depth is less than 300 m, and the steep slope of the plateau changes violently, with a slope of about 21° . The plateau slope reduces within a water depth of 300–950 m with a slope value of about 1.5° .

The study area includes Yongle Atoll and Xuande Atoll, where many reefs and reef platform uplifts are developed. In many platform edges or steep areas, the coral reef strata grow in a cliff-like manner and go down the platform with a multi-level steep ridge (more than 5.6° – 10° , Figure 4). The height difference ranges from hundreds of meters to kilometers, and there is a gradual downward slope reduction in the multi-level scarps. The scarps in the study area are primarily located at the edges of the Ganquan Platform, the China Construction Beihai Platform, the Yongxing Atoll, the Yongle Atoll, the Dongdao Platform, etc. The submarine topographic slope of the southeast side is significantly higher than that of the northwest side. The average submarine slope of the scarps on the northwest side of the island reef area is about 4.6° , and the average submarine slope of the scarps on the southeast side is about 22° . For example, the scarp in the southeast of Xuande Atoll (Figure 4) is a two-level scarp, of which the primary scarp has a gradient of 7.8° and an elevation of 416 m. The secondary scarp has a gradient of 14.8° and an elevation of 460 m.

The scarps in the study area are closely related to the development of the carbonate platform in the Xisha area.

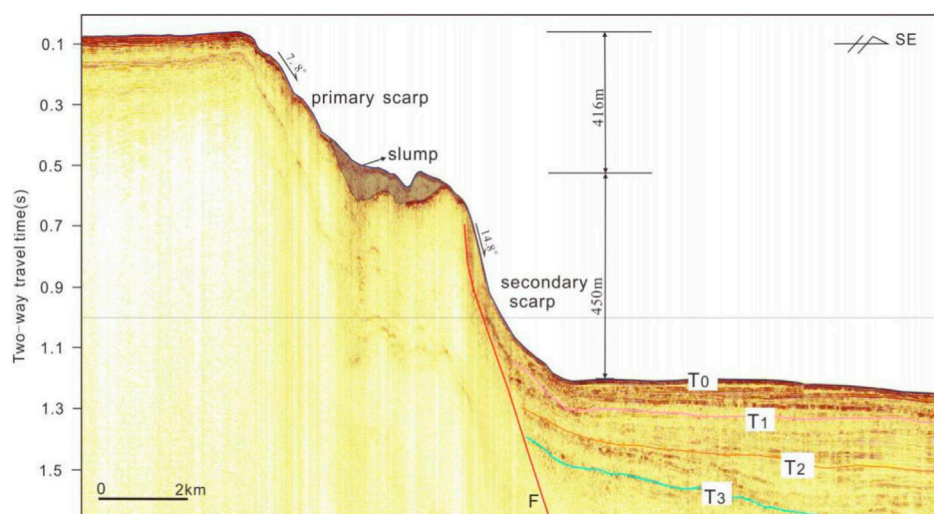


FIGURE 4

The reflection characteristics of stepped scarps and slumping deposits are shown on a single earthquake.

During the Middle Miocene, the sea level was relatively high, and the carbonate platform expanded vertically and horizontally. The slope basin around the platform gradually entered the semi-deep sea environment and began receiving numerous gravity flow sediments transported in turbidity currents. During the late Miocene, the relative sea level rose rapidly again, and the platform mainly grew longitudinally (Yang et al., 2014; 2016; Li et al., 2020). The platform as a whole deposited a thicker layer of carbonate rock strata, forming a large atoll reef several kilometers above the sea floor (Ma et al., 2011). This has resulted in the formation of many scarps and landslides. These scarps can cause erosion, fracture activity, landslides, and other effects and should be regarded as active, destructive geological hazards (Ma et al., 2017). Generally, the degree of soil consolidation in these scarps is poor, which makes them an adverse topographic factor when laying and maintaining submarine pipelines. They can also easily cause platform tilt and pipeline sliding (Liu et al., 2014).

5.1.2 Submarine collapse/landslide

A submarine landslide is a phenomenon in which unconsolidated soft sediments or rocks with weak structural planes on the sea floor move downward along a weak structural plane under gravity. It includes geological processes such as sliding, collapse, and debris flow (Hampton et al., 1996; Locat and Li, 2002; Moscardelli et al., 2006; Moscardelli and Wood, 2008; Wang Dawei et al., 2009, 2011; Wu et al., 2011). They also include mass transport deposits (MTDS).

Submarine collapses/landslides in the study area are related to local magmatic activities, faults, scarps, or steep slopes. Generally, they occur in areas with a particular drop in the

terrain, such as slope areas around a platform and the edges of seamounts (mounds). Due to their gravity, faults, and other factors, local sediments lose stability, slide down, and collapse along the slope or fault. They then pile up disorderly at places with flat terrain and open accommodation spaces on the platform slope, forming collapsed sedimentary bodies. This collapsing phenomenon in the study area is mainly distributed on the slopes around the platform, with irregular shapes or multiple mound-shaped reflections, internal chaotic reflections (Figure 5 and Figure 6), no stratification, and mainly reef debris accumulations. There are seven medium and large landslides identified in the study area, including two in the west and one in the southeast of Yongxing Plateau, two in the west and two in the south of Yongle Plateau, with an area of 323 km², 100 km², 176 km², 116 km², 96 km², 173 km², and 99 km². Here, we take the large landslide with an area of 323 km² found on the west side of the Yongxing Plateau as an example (Figure 6), distributed within 500–950 m of water depth. The length of the landslide mass from north to south can reach 30 km, the maximum width is 13 km, and the cliff on the side wall of the landslide can reach 345 m. The seismic profile shows that the landslide comprises two parts: the slow accumulation landslide at the back end and the fast accumulation landslide at the front end, which was formed during the late Miocene. Multiple landslide surfaces are developed inside, indicating that the landslide is characterized by multistage and multistage development. There are many waterways and buried ancient rivers in the landslide body. The waterways are generally 700 m wide and 30 m deep, with an average gradient of 5.5°. Multistage secondary small landslides are widely developed on both sides of the waterways. The front rapid landslide body has chaotic

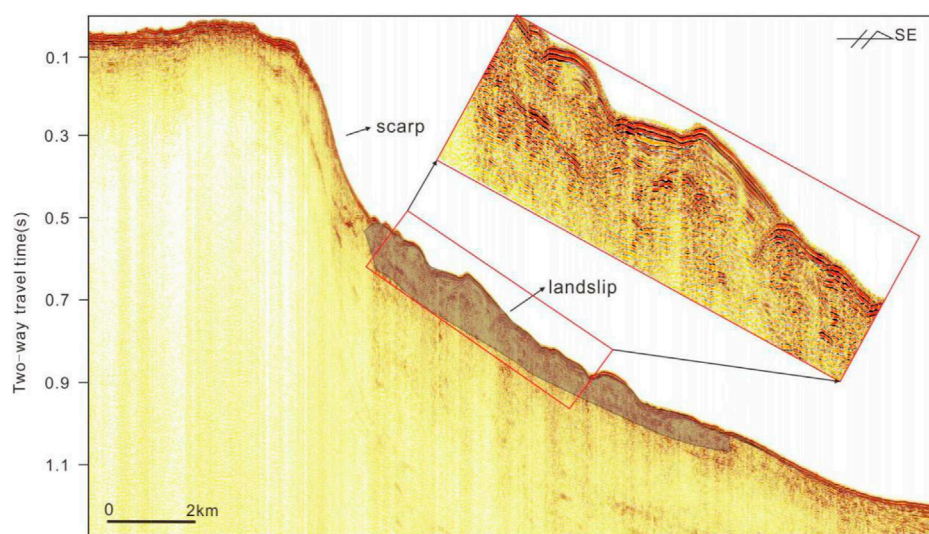


FIGURE 5

The reflection characteristics of landslides on the platform slope are displayed on a single earthquake.

reflection seismic facies, reflecting the rapid accumulation of sediments. It is a typical submarine landslide fan. In addition, some submarine landslide valleys have not been filled by sediments, indicating that there was still activity during the Quaternary.

A landslide is very harmful to offshore engineering facilities. Due to its instability, it often leads to the collapse of offshore structures installed on it. This causes damage to offshore engineering facilities, such as deep-sea oil and gas drilling installations, oil pipelines, submarine cables, etc., leading to potential heavy casualties and economic losses. Submarine landslides can also cause huge waves and even tsunamis (Fine et al., 2005; Ni, 2009; Li, 2013).

5.1.3 Shallow gas

Shallow submarine gas usually refers to the gas accumulations in sediments less than 1,000 m below the sea floor (Davis, 1992). Shallow submarine gas is widely distributed throughout Chinese seaways. In some places, the oil and gas seedlings of the sea surfaces have a history of more than 100 years (He et al., 2000; He et al., 2010). Engineering hazards caused by shallow gas have also been reported frequently (Chen et al., 2010; Guo et al., 2013; Liu et al., 2019).

The interpretation of multichannel seismic data and the rich acoustic anomalies present in the data directly prove the existence of shallow gas in the study area. Seismic records show that the reflections between the layers of gas-bearing sediments are chaotic. The reflected waves with good continuity are suddenly interrupted, and the co-axial axis is hidden or disappears altogether, or the reflection is blurred. Further, the reflections are columnar, sac-like, and strip-like but not

rule-like. The southern part of the North Reef is mainly composed of shallow gas as indicated by diapir structures, faults, and gas chimneys (Figure 7A). Deep fluid or gas upwelling has occurred, part of which was captured by the Middle-Late Miocene reefs to form a reef trap (shown in the earthquake data as a tower tip mound reflection in the T_3 - T_5 interface). Part of the gas continued upwelling to the shallow stratum, and some gas was even released into the seawater. This process caused the interruption of the horizontal axis in the stratum, forming chaotic reflections in the shape of columns, mushrooms, etc. The surrounding and upper sedimentary layers generated numerous strong reflections. The top surface is wavy, clearly defined with the surrounding rock, and has clear upward warping traction characteristics (Figure 7D). The bright spots and scattered reflections on the section indicate that gas played an essential role in the middle stage of the formation of this type of structure. The natural gas and fluid permeability are related to the formation of these uplifts or mud diapirs. BSR (Bottom Simulating Reflector) are seen in the upper strata of the mud diapirs and gas chimneys (Figure 7C), and a blank band appears above the BSR, indicating gas hydrate accumulation in the mud diapirs in the peripheral seafloor sediments. At the top of the gas chimneys and mud diapirs, many shallow minor faults control the upward leakage of shallow gas, forming gas chimneys, and there is a pull-down phenomenon in the same internal direction axis (Figure 7B).

5.1.4 Active fracture

Active faults are one of the hazard types that require great attention when it comes to offshore engineering. The geophysical

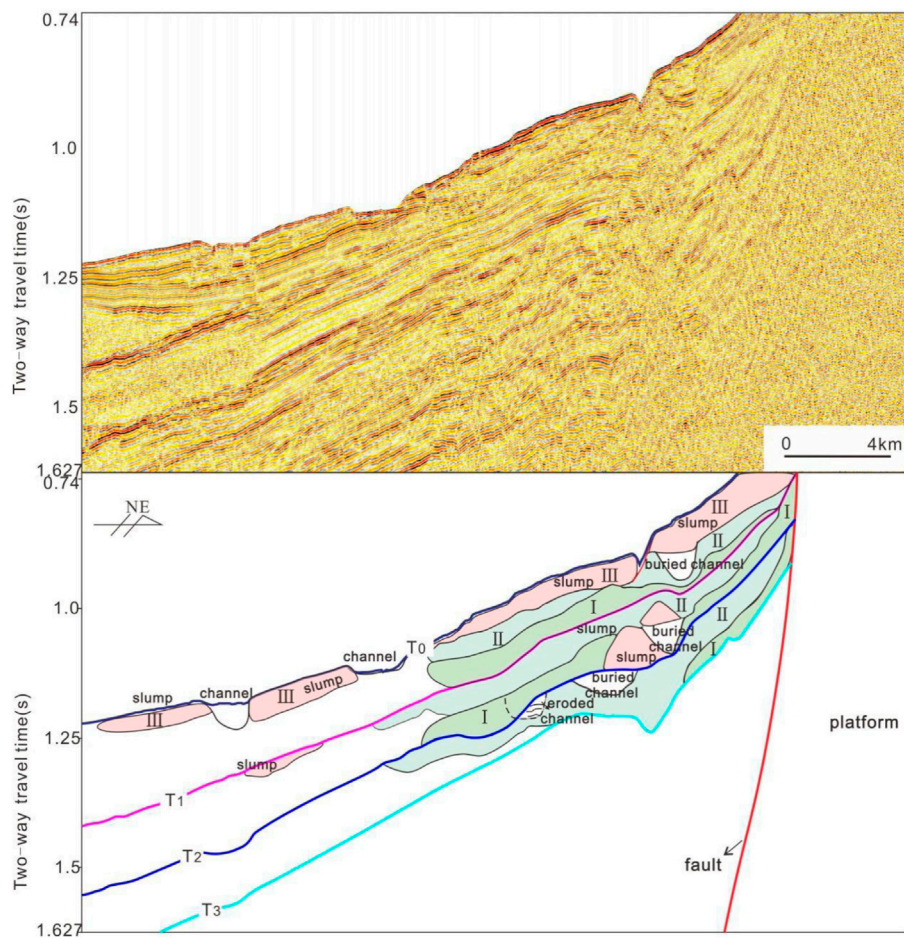


FIGURE 6
Landslides and ancient channel sediments of different stages in the northwest of Xuande Atoll.

data and the geological background of the study area indicate that the shallow faults in the study area were still active in the Quaternary, making them potentially quite dangerous. Some of the detrimental effects of these faults include the fact that they may directly affect offshore engineering activities. For example, when the drilling activity encounters a fault, it may lead to a stuck pipe and mud leakage (Ma and Chen, 2006). The seismic activity and stratum collapse caused by secondary faults are potential geological hazards.

The formation of the Xisha block was mainly controlled by the surrounding fault structures and affected by the multistage expansion of the South China Sea basin, forming the tectonic evolution characteristics of a “lower fault and upper depression.” There are many deep and large faults on the platform’s periphery, such as the Xisha Trough fault zone and the Binhai fault zone on the north side, the Ailaoshan-Honghe fault zone on the west side, and the Zhongsha Trough fault zone on the south side (Xu et al., 2010; Cao et al., 2014). A

series of normal faults with extensional shear properties are developed along these fault zones (Lin et al., 2009), and a series of normal faults are also developed in the transition zone between the Xisha block and the northwest sub-basin, indicating that the area has prominent extensional characteristics (Ding et al., 2009).

Many small shallow faults are developed in the study area in NE-NEE and NW directions. They are also mainly normal faults with a steep occurrence, vertical fault displacement of about 10m, and horizontal fault displacement of less. They are staggered T₁ (Quaternary stratigraphic bottom) seismic reflection interface and the seabed (Figure 11). In the single-channel seismic section, the faults are characterized by in-phase axis dislocation and distortion, different internal and external reflection patterns of the reflection wave groups on both sides of the fault, and sometimes an inconsistent thickness of the two plates. The faults are associated with volcanic activity, gas-bearing structures, and pockmarks.

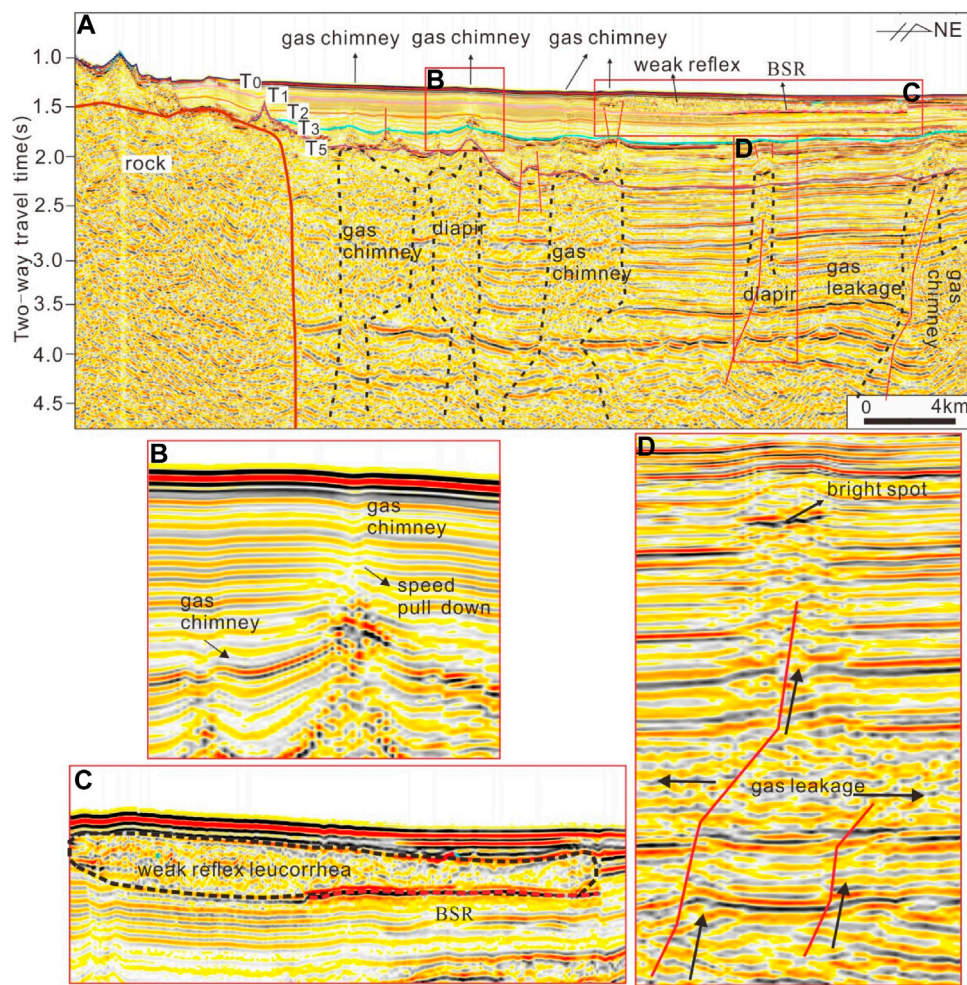


FIGURE 7

Schematic diagram of seismic profile of mud diapir and gas chimney at the edge of the platform (B). (C) and (D) are magnified views of corresponding parts in (A).

5.1.5 Submarine erosion of gullies (troughs) and canyons

Submarine scour gullies (troughs) are widely developed around the platforms. They are mainly distributed on the southern and eastern slopes of the Yongxing Platform, the southwest and southeast slopes of the Zhongjian North Platform, and the northwest and southern slopes of the Huaguang Platform (Figure 3). They are large or small and often occur in groups. The cross-section of the scour trough is mostly V-shaped and U-shaped, the wall of the valley side is relatively steep, and the sediments are collapsed (Figure 8), being controlled by the faults. Along the fault boundary, the sediments are continuously scoured by the current, denuded, and accumulate at the bottom of the valley for local deposition or transported and redeposited with the current. The current seafloor scour gullies have been affected by multiple factors,

such as hydrodynamic conditions, stability of the sediment layer, and sediment supply. The scour degree varies, with most water depths ranging from several meters to several hundred meters. On the southern side of the Xuande Platform in the study area, a series of east-west and north-south erosion grooves are developed on the slope (Figure 9). These grooves occur in water depths of 350 m–750 m; the cutting depth of the grooves ranges from 15 m to 40 m, and the width of the grooves mouths ranges from 110 m to 500 m. The grooves extend along the slope into deep water, nearly parallel to each other, forming a train of skirts around the reef.

There are more than six small and medium-sized canyons in the study area. The head of these small canyons generally has multiple branches and is connected with other geomorphic units, such as erosion and scouring grooves, which are in a “funnel” shape on the plane. The scales of these canyons are larger than

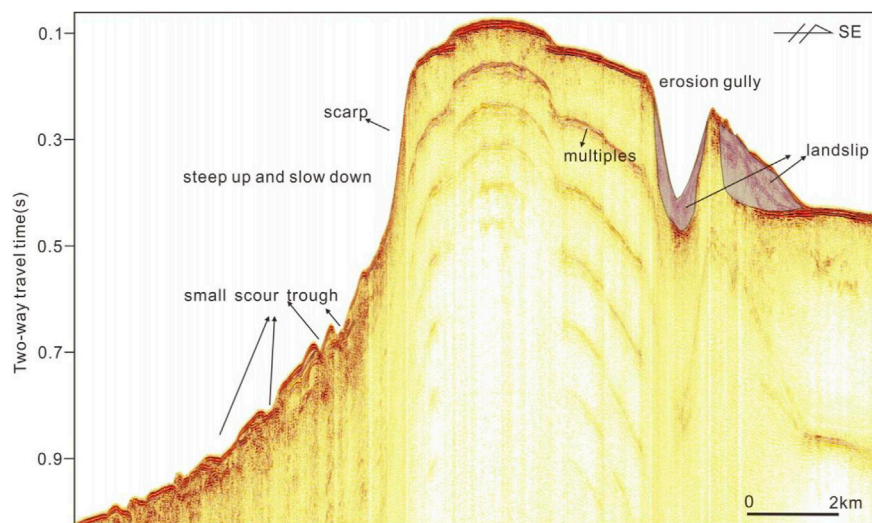


FIGURE 8
Scour trough phenomenon reflected on a single earthquake.

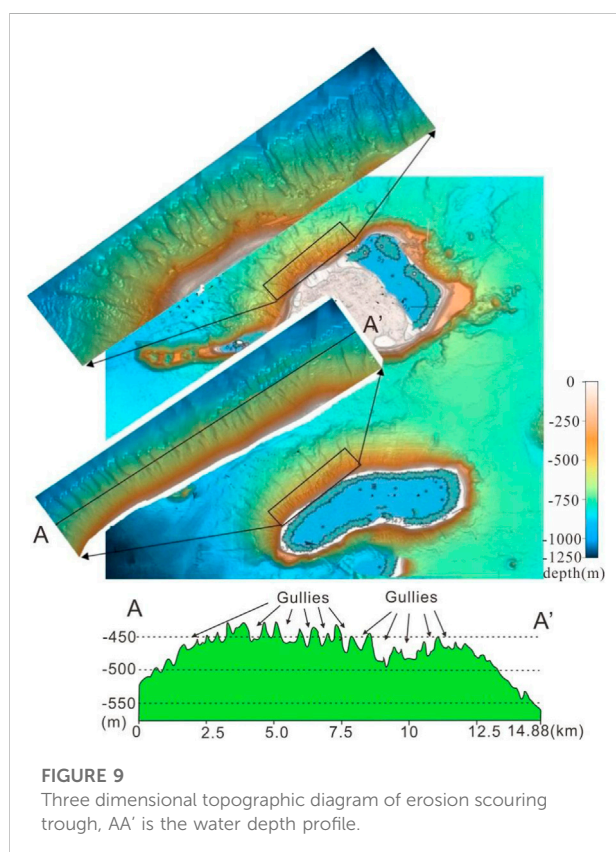


FIGURE 9
Three dimensional topographic diagram of erosion scouring trough, AA' is the water depth profile.

that of steep slope erosion grooves, with a length of up to 20 km and a width of about 600 m–1500 m. The cross section of the canyons is V-shaped, and the undercutting erosion depth is

generally 20 m–40 m. Generally, the erosion depth of the upper half of the canyons is deep, and the undercutting erosion depth of some small canyons in the south of the Huaguang Plateau can reach 150 m. The most typical canyon is the Yongle Canyon, located north of the East Island Platform (Li et al., 2017). The overall morphology of the Yongle canyon is several small canyons on the northeast side of the East Island platform converging into the main big canyon leading to the northwest sub-basin. The upstream slope of the Yongle Canyon is steep and varies greatly, and the channels around the atoll and the submarine landslide system are the transport channels of detrital materials in the source region. In the middle and lower reaches of the basin, the slope is gentle, the slope variation is slight, and the detrital material is mainly transported and merges into the erosion and collapse debris on both sides of the slope, forming a horn-shaped entrance basin in the northwest sub-basin (Wu and Qin, 2009).

The canyon area and scour trough are continually affected by erosion, a typical active geological hazard. The terrain changes are complex, and the unstable sediments on both sides of the valley slopes and valley shoulders cause fracturing and distortion of pipelines in the area and dumping of the foundation piles of drilling platforms. Also, the topographic conditions on both sides of the eroded valley/canyon can cause the strata on both sides to be deposited. Collapse or slip can occur, causing devastating damage to various constructions around it. Therefore, areas with eroded valleys/canyons should be avoided when choosing sites for engineering activities. In particular, the eroded valleys south of the Xuande Atoll, the west and southeast of the Middle North Sea Platform, the northwest of the Huaguang Reef, and the canyons on the northern and southern sides of the Dongdao

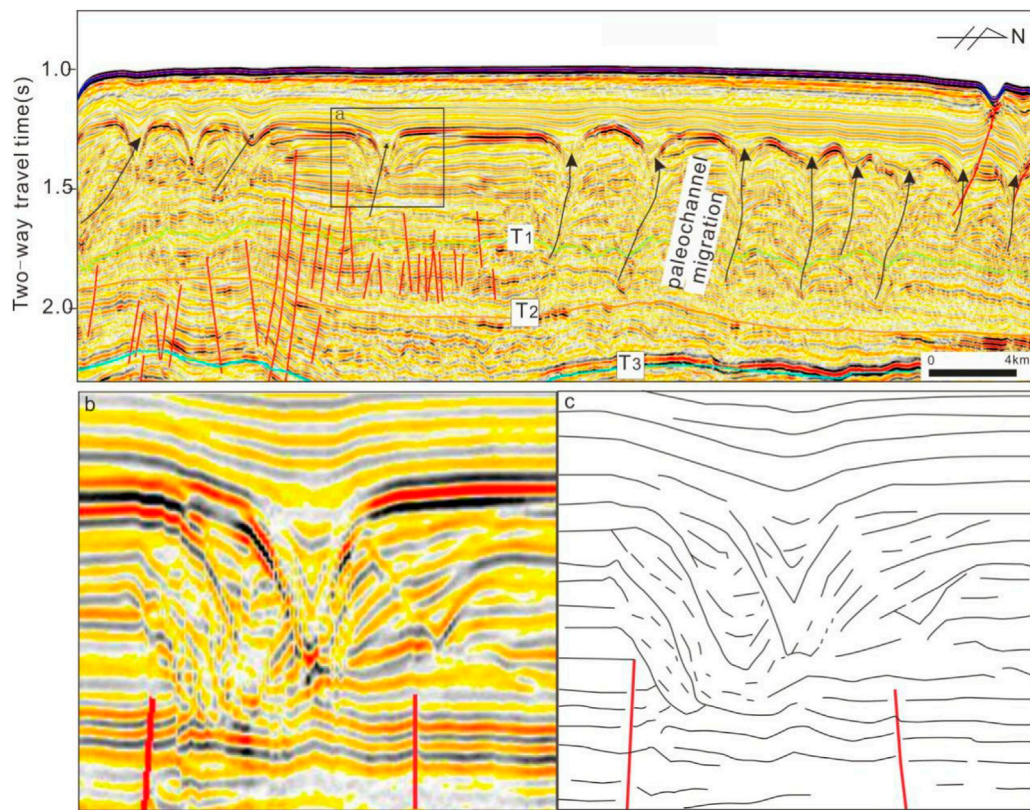


FIGURE 10

Seismic profile of buried paleochannel migration, where (B) is the enlarged part of (A), (C) is the fine description of the internal structure of (B)

Platform should be avoided when looking to create underwater engineering structures.

5.2 Destructive and inactive geological hazards

5.2.1 Buried palaeochannels

During the Wurm glacial stage of the Late Pleistocene, the global sea level generally dropped, the sea water retreated, and the continental shelf was exposed to land. Rivers and lakes of various scales developed. Since the Holocene, with the sharp rise in the sea level, the early channels sunk into the seabed, and most were buried under sediments of different thicknesses, forming ancient buried channels.

The paleochannels in the study area mainly developed between the T_0 to T_2 interface in the sediments from the Late Pliocene to the Late Pleistocene with NW-trending and NE-trends. Figure 10 shows that 12 continuously migrating paleochannels developed in the southwest corner of the Xisha area. The paleochannels in different periods are crisscrossed

vertically and horizontally, superimposed on each other, and show complex variations. Wave-like reflection interfaces can be seen at the bottom of the paleochannels, and chaotic discontinuous-relatively continuous reflections reflect the strata inside the ancient rivers. It shows that the study area in the Late Pliocene-Late Pleistocene was in an erosion and scouring stage and went through many stages of erosion-filling-re-erosion-refilling.

Paleochannel sediments are often complex and variable, and physical and mechanical properties vary significantly in the horizontal direction, such as particle size composition, sorting degree, density, compressive strength, and shear strength. The sediments and fillings of the paleochannels are mainly coarse clastic sand and gravel with large porosity, fast interlayer water circulation, and strong permeability. These could have easily been generated by long-term erosion, scour, and overburden loads in the strata (Kou, 1990; Chen and Li, 1993; Bao, 1995). Local collapse destroys the formation's original structure and causes basement instability. River sediments often contain a large amount of organic matter, which may form shallow gas.

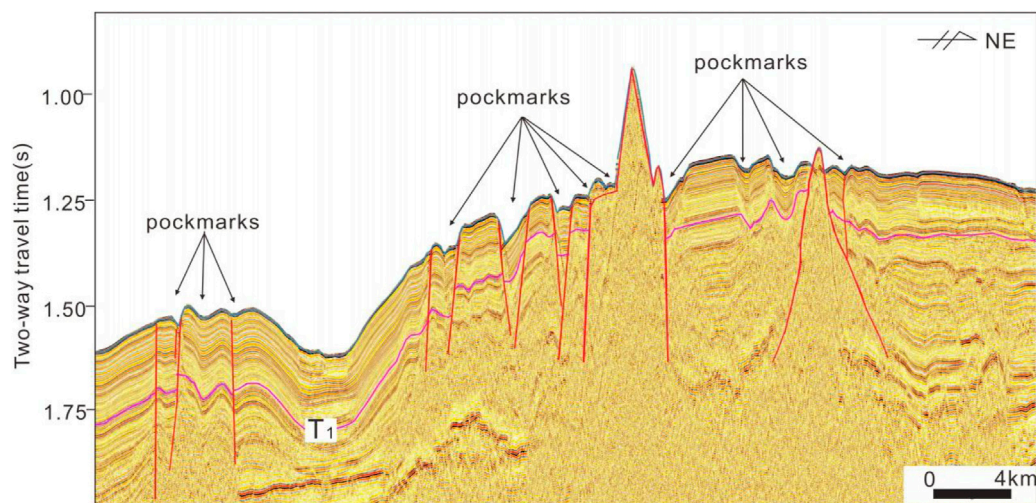


FIGURE 11
Active faults and Markeng recorded by single seismic profile.

This gas makes the area unsuitable for constructing offshore pile foundations and drilling platforms.

5.2.2 Seabed pockmarks

Submarine pockmarks are a negative seafloor topography formed by fluid and gas in formations leaking upward along migration channels and eroding the sediments on the seabed surface (Judd et al., 2007; Hovland et al., 2012; Luo et al., 2012; Riboulot et al., 2013; Riboulot et al., 2014; Andreassen et al., 2017). The continued escape of gas from a formation can cause sediments to collapse, creating pits on the seafloor surface. The results of multi-beam surveys show that large and small pits in the study area are highly developed, especially on the northwest side, where the scales are large. Multiple pits are distributed together to form a pockmark group. Four larger pockmarks groups are located on the east side of the Ganquan Plateau, the south side of the Xisha Trough, the south side of the Jinyin Valley, and the southwest side of the Xuande Atoll. This paper temporarily named them the Ganquan East Pockmark Group, the Xisha Trough South Pockmark Group, the Valley South Pockmarks Group, and the Xuande South Pockmarks Group. The strata in the pockmarks area are mainly characterized by weak or scattered local reflections (Figure 11), and a large number of normal faults are developed in the shallow part.

The Ganquan East Pockmark Group is the largest one in the study area (Figure 12). It is dumbbell-shaped (wide on both sides and narrow in the middle), with an area of about 1505 km². It is about 56.5 km long in the NS direction, 15–44 km wide in the EW direction, and has a water depth of 850–1250 m. There are three small pit groups arranged along

the NE direction in the Xisha Trough South Pockmark Group (with a total area of about 1409 km²), the westernmost of which is in the shape of a NE-direction strip, and the other two are irregular. The Valley South Pockmark Group is smaller, about 176.2 km², and a small oval-shaped depression is developed on the west side of the group. It is ~2.4 km long, 1.3 km wide, and 3.2 km² in area. The water depth in the depression is about 120 m; The Xuande South Pockmarks Group is in the shape of an irregular strip and is about 22.5 km long, 3–4 km wide, and 72.8 km² in area. Several small sea mounds are developed in the pockmark group.

It is generally thought that deep fluids (such as hydrocarbon gas, pore fluid, groundwater, etc.) migrate upward to shallow formations through migration channels (such as faults, unconformities, weak zones, etc.) and accumulate to form overpressure formations. When the pressure of the overlying formation decreases and the overpressure fluid in the lower part breaks through the seal, the fluid leaks. At the same time, the pore water in the formation is discharged from the pore space and transported to the seabed sediments, causing the relatively weak local seabed sedimentary formations to deform. The pore water also gradually erodes the local seabed formations, reducing the volume of sediments and forming pits (King and Maclean, 1970; Harrington, 1985; Scanlon and Knebel, 1989; Khandriche and Werner, 1995; Cathles et al., 2010). The pits in the study area are mainly of tectonic origin and have been generated due to faults, gas chimneys, mud volcanoes, mud diapirs, and other tectonic processes related to fluid activities. The undulating seabed topography in the area of the pockmark groups and the uneven settlement inside and outside the pockmarks can adversely affect cables and pipelines

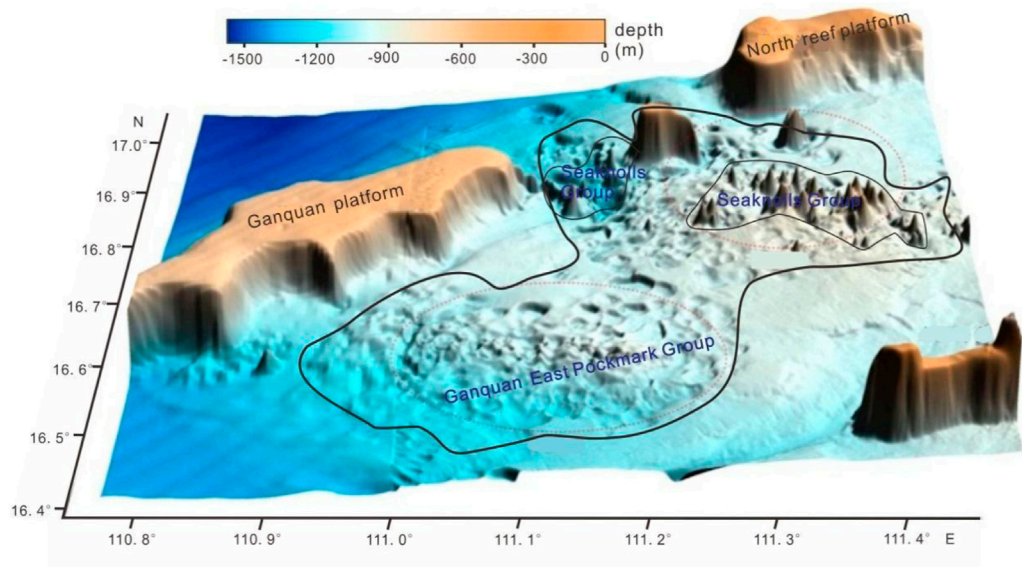


FIGURE 12
Three-dimensional topographic map of the Ganquan East Pockmark Group and Seaknolls Group.

TABLE 1 Geological classification of disasters in the Xisha Sea area.

Geological hazard type	Geological hazard factors
Destructive geological hazards with activity ability	Active fault, shallow gas, diapir, landslide, scarp, scouring trough, canyon
Destructive geological hazards without activity capacity	Buried palaeochannels, pockmarks, bioherms, mounds, volcanic structures

laid in the area, and, therefore, doing so should be treated with caution.

5.2.3 Submarine volcanoes

Existing studies have pointed out that in the northwest of the South China Sea, where the Xisha Sea area is located, after seafloor expansion, volcanic structures with small individual areas, large numbers, and apparent inherited activity became widely distributed (Zhang et al., 2014b). There is a concentrated distribution of Cenozoic volcanic activity in the area (Zhang et al., 2014b). Seismic profiles show about 10 volcanic structures in the southern part of the Xisha Sea area (Feng et al., 2017). According to our latest data, about 30 volcanic structures intrude into the Quaternary strata in the Xisha Sea area, even erupting out of the sea floor to form seamounts with different sizes and exposed areas ranging from 1.5 km² to 125 km². Volcanic structures are mainly manifested in the perforation of the seabed, typical low-frequency and strong reflections of the contour, internal chaos, discontinuous strong amplitude reflection characteristics or blank discontinuous weak reflection characteristics, and a main invasion of the Pliocene

and Pleistocene strata. In addition, a single volcanic structure has been found in the western edge, and central part of the Xisha area, and volcanic activity has invaded the surrounding Quaternary strata.

Active volcanoes have a strong disaster-causing effect, but most of the submarine volcanoes in the study area are no longer active, making them inactive geological hazards. The submarine volcanoes in the study area have had a noticeable transformation effect on the submarine topography, resulting in a considerable height difference between the volcanoes and the surrounding strata. The volcanoes have also dragged or disturbed the surrounding strata, resulting in the instability of the strata, making the area not conducive to laying large-scale pipelines or constructing platforms.

6 Conclusion

Based on the interpretation and analysis of geophysical data and from the perspective of geological hazards in the Xisha Sea area, the following conclusions are drawn:

- 1) Based on the interpretation of geophysical survey data, the geological hazards are divided into two categories: active and destructive geological hazards, such as active faults, shallow gas, diapirs, landslides, steep ridges, scour grooves, etc. The second comprises inactive geological hazards, such as buried ancient river channels, pits, etc.
- 2) The steep ridges are mainly located around the atolls or platforms. The average submarine slope of the scarps on the northwest side of the island reef area is about 4.6° , and the average submarine slope of the scarps on the southeast side is about 22° . Landslides are mainly developed in the west and southeast of the Yongxing Plateau and the west and south of the Yongle Plateau. There are seven medium and large slumps caused by gravity and faulting. Shallow gas is mainly developed in the southern part of the North Reef and mainly includes shallow gas indicated by diapirs, faults, and gas chimneys. The shallow faults in the study area are mainly steep normal faults. The paleochannels in the study area are mainly developed in the sediments of the Late Pliocene to the Late Pleistocene with NW and NE trends, and they underwent a multistage erosion-filling-re-erosion-refilling process. In the Xisha Sea area, there are four large pockmark groups, the Ganquan East Pockmark Group, the Xisha Trough South Pockmark Group, the Haigu South Pockmark Group, and the Xuande South Pockmark Group. They are mainly tectonic, including faults, gas chimneys, mud volcanoes, mud diapirs, and other structures related to fluid activities. Due to the influence of multiple factors, such as hydrodynamic conditions, the stability of sedimentary layers, and sediment supply, the scour valleys on the seafloor vary in terms of the scour degree. The degree of scouring varies from several meters to several hundred meters.
- 3) If engineering construction is to be carried out, hidden dangers should be identified before offshore construction, and measures should be taken to prevent harm to engineering infrastructure. To prevent geological disasters, engineering constructions should not be carried out in various shallow seabeds, especially active ones. Areas with geological hazards, such as the steep ridges around various atolls and platforms, landslides on the west and southeast sides of Yongxing Island, landslides in the west and south of Yongle Plateau, shallow gas in the southern part of the North Reef, active faults, mud diapirs, scour trough and canyon should be avoided when undertaking construction works in the area.

References

- Andreassen, K., Hubbard, A., Winsborrow, M., Patton, H., Vadakkepuliambatta, S., Plaza-Faverola, A., et al. (2017). Massive blow-out craters formed by hydrate-controlled methane expulsion from the Arctic seafloor. *Science* 356 (6341), 948–953. [J]. doi:10.1126/science.aal4500
- Bao, C. W. (1995). Buried ancient channels and deltas in the continental shelf area of the Pearl River Estuary. *Mar. Geol. Quat. Geol.* 15 (2), 25–34.

Data availability statement

The original contributions presented in the study are included in the article/supplementary material, further inquiries can be directed to the corresponding author.

Author contributions

JZ, writing-original draft, review, editing, drawing. HC, writing-review and editing. JC, writing-Seismic profile interpretation. SY, writing-multibeam interpretation, methodology. LG, writing-drawing. XH, writing-multibeam interpretation and interpretation. WD, writing-review. MS, writing-review.

Funding

This research was supported by the talent team introducing major special projects from the Guangdong Laboratory of Southern Marine Science and Engineering (Guangzhou) (GML2019ZD0201) and National Natural Science Foundation of China (91958212), the China Geological Survey Project (DD20221712, DD20221719, DD20190209, DD20190627).

Conflict of interest

The authors declare that the research was conducted in the absence of any commercial or financial relationships that could be construed as a potential conflict of interest.

Publisher's note

All claims expressed in this article are solely those of the authors and do not necessarily represent those of their affiliated organizations, or those of the publisher, the editors and the reviewers. Any product that may be evaluated in this article, or claim that may be made by its manufacturer, is not guaranteed or endorsed by the publisher.

Bao, C. W., and Jiang, Y. K. (1993). YK Types and characteristics of submarine potential geological hazards in China's offshore areas. *Tropical Ocean* 18 (3), 24–31.

Cao, J. H., Sun, J. L., Xu, H. L., and Xia, S. H. (2014). Seismological features of the littoral fault zone in the Pearl River Estuary. *Chin. J. Geophys.* 57 (2), 498–508.

- Cao, Y., Li, C. F., and Yao, Y. J. (2017). Thermal subsidence and sedimentary processes in the South China Sea Basin. *Marine Geology* 394, 30–38. doi:10.1016/j.margeo.2017.07.022
- Cathles, L. M., Su, Z., and Chen, D. F. (2010). The physics of gas chimney and pockmark formation, with implications for assessment of seafloor hazards and gas sequestration. *Mar. Petroleum Geol.* 27 (1), 82–91. doi:10.1016/j.marpetgeo.2009.09.010
- Chen, D. X., Wu, S. G., Wang, X. J., and Lv, F. (2011). Seismic expression of polygonal faults and its impact on fluid flow migration for gas hydrates formation in deep water of the South China Sea. *J. Geol. Res.* 2011, 1–7. doi:10.1155/2011/384785
- Chen, G. F., Chen, H. F., Hong, M., Guan, G. L., and Zhao, R. (2010). A brief discussion on the harm of harmful gases in Hangzhou Metro Tunnels and the prevention measures. *J. Railw. Eng.* 27 (5), 82–86.
- Chen, J. R., and Li, Y. H. (1993). Types and distribution of geological hazards in the South China Sea. *J. Geol.* 67 (1), 76–85.
- Chen, J. X., Guan, Y. X., Song, H. B., Yang, S. K., Geng, M. H., Bai, Y., et al. (2015). Distribution characteristics and geological implications of pockmarks and mud volcanoes in the northern and Western continental margins of the South China Sea. *Chin. J. Geophys.* 58 (3), 919–938. doi:10.6038/cjg20150319
- Chen, M., Xia, Z., Liu, W. T., He, J., and Ma, S. Z. (2021). Geohazards characteristics in the southeast of Xuande atoll, Xisha, south China sea. *J. Trop. Oceanogr.*. Available At: <https://kns.cnki.net/kcms/detail/44.1500.P.20210630.1525.004.html>.
- A. M. Davis (Editor) (1992). "Methane in marine sediments," 12, 1075–1264. *Cont. Shelf Res.* 10
- Ding, W. W., Li, M. B., Zhao, L. H., Ruan, A. G., and Wu, Z. L. (2009). Cenozoic tectono-sedimentary characteristics and extension model of the northwest sub-basin, south China sea. *Earth Sci. Front.* 16 (4), 147–156. [J].
- Du, W. B., Cai, G. Q., Huang, W. K., Chen, J. L., Nie, X., and Wang, X. M. (2021). Seismic reflection characteristics of Neogene carbonate platforms in the Xisha Sea area and their controlling factors. *Mar. Geol. Front.* 37 (1), 20–30.
- Feng, Y. C., Zhan, W. H., Sun, J., Yao, Y. T., Guo, L., and Chen, M. (2017). The formation mechanism and characteristics of volcanoes in the Xisha waters since Pliocene. *J. Trop. Oceanogr.* 36 (3), 73–79.
- Feng, Z. Q., Feng, W. K., Xue, W. J., Liu, Z. H., Chen, J. R., Li, W. F., et al. (1996). *Geological hazards and submarine engineering geological conditions in the northern South China Sea*. Nanjing, China: Hehai University Press, 10–100. [M].
- Fine, I. V., Rabinovich, A. B., Bornhold, B. D., Thomson, R. E., and Kulikov, E. A. (2005). The Grand Banks landslide-generated tsunami of November 18, 1929; preliminary analysis and numerical modeling. *Mar. Geol.* 215, 45–57. doi:10.1016/j.margeo.2004.11.007
- Gong, Z. S., and Li, S. T. (1997). *Analysis of continental margin basins and hydrocarbon accumulation in the northern South China Sea*. Beijing, China: Science Press, 10–70. [M].
- Guan, Y. X., Luo, M., Chen, L. Y., Wang, S. H., Yan, W., Wang, H. B., et al. (2014). Tracer study on the activity of submarine giant pits in the Western South China Sea. *Geochemistry* 43 (6), 628–639.
- Guo, A. G., Kong, L. W., Shen, L. C., Zhang, J. R., Wang, Y., Qin, J. S., et al. (2013). Study on the prevention and control measures of shallow gas hazard in subway construction. *Geotech. Mech.* 34 (3), 769.
- Hampton, M. A., Lee, H. J., and Locat, J. (1996). Submarine landslides. *Rev. Geophys.* 34 (1), 33–59. doi:10.1029/95rg03287
- Harrington, P. K. (1985). Formation of pockmarks by pore-water escape. *Geo-Marine Lett.* 5, 193–197. doi:10.1007/bf02281638
- He, J. X., Li, M. X., and Huang, B. J. (2000). Distribution of oil and gas seedlings and analysis of oil and gas exploration prospects in the northern slope of Yinggehai basin. *Nat. Gas. Geosci.* 11 (2), 1–9.
- He, J. X., Zhu, Y. H., Weng, R. N., and Cui, S. S. (2010). Characters of north—West mud diapirs volcanoes in south China sea and relationship between them and accumulation and migration of oil and gas. *Earth Science—Journal China Univ. Geosciences* 35 (1), 75–86.
- He, Q. X., and Zhang, M. S. (1986). *Xisha reef facies geology in China*. Beijing: Science Press, 1–182. [M].
- Hovland, M., Jensen, S., and Indreiten, T. (2012). Unit pockmarks associated with lophelia coral reefs off mid-Norway: More evidence of control by 'fertilizing' bottom currents. *Geo-Mar. Lett.* 32 (5–6), 545–554. doi:10.1007/s00367-012-0284-0
- Judd, A. G., and Hovland, M. (2007). *Seabed fluid flow: The impact of geology biology and the marine environment*. Cambridge, UK: Cambridge Univ Press. [M].
- Khandriche, A., and Werner, F. (1995). "Freshwater induced pockmarks in bay of eckernförde, western baltic[C]/Mojski JE," in Proceedings of the 3rd Marine Geological Conf, The Baltic (Warsaw: Prace Panstwowego Instytutu Geologicznego), 155–164.
- King, L. H., and Maclean, B. (1970). Pockmarks on the scotian shelf. *Geol. Soc. Am. Bull.* 81, 3141–3148. doi:10.1130/0016-7606(1970)81[3141:potss]2.0.co;2
- Kou, Y. Q. (1990). Paleochannel and its engineering geological evaluation of the northern continental shelf of the South China Sea. *Mar. Geol. Quat. Geol.* 10 (1), 37–45.
- Kuang, Z. G., Guo, Y. Q., Wang, L. L., Liang, J. Q., and Sha, Z. B. (2014). Discovery and evolution of late Miocene atoll system in Xisha Sea area. *Chin. Science:Earth Sci.* 44 (12), 2675–2688.
- Li, F. (1990). *Institute of oceanography, Chinese academy of Sciences marine science series (31 episodes)*. Beijing, China: Ocean Press, 25–49. [A]//Study on disastrous geology in the west of the South China Sea
- Li, Q., Wang, X., Ao, M., Gabrielson, E., Askin, F., Zhang, H., et al. (2013). Aberrant Mucin5B expression in lung adenocarcinomas detected by iTRAQ labeling quantitative proteomics and immunohistochemistry. *Clin. Proteomics* 6, 15–21. doi:10.1186/1559-0275-10-15
- Li, X. J., Wang, D. W., Wu, S. G., Wang, W. W., and Liu, G. (2017). Geomorphology of Sansha canyon: Identification and implication. *Mar. Geol. Quat. Geol.* 37 (3), 28–36.
- Li, X. L., Zhang, H. Y., Liu, G., Han, X. H., Qin, Y. P., and Wu, S. G. (2020). Seismic sequence and evolution model of isolated carbonate platform-A case from Yongle Atoll, Xisha Islands. *Mar. Geol. Quat. Geol.* 40 (5), 87–96.
- Lin, C. S., Tang, Y., and Tan, Y. H. (2009). Geodynamic mechanism of dextral strike-slip of the Western-edge faults of the South China Sea[J]. *Acta Oceanol. Sin.* 31 (1), 159–167.
- Liu, L. J., Fu, M. Z., Li, J. G., Li, X. S., Chen, Y. N., Gao, S., et al. (2014). Geologic hazards in the deep pipeline routing area of the Liwan 3-1 gas field in the South China Sea[J]. *Adv. Mar. Sci.* 32 (2), 162–174.
- Liu, S. Q., Liu, X. Q., Wang, S. J., and Guo, Y. G. (2002). Discussion on some problems in compilation of hazardous geological map (1:2000000) of South China Sea. *Chin. J. Geol. Hazard. Control* 13 (1), 17–20.
- Liu, Y. X., Zhan, W. H., and Lu, C. B. (1992). types, laws and Prevention Countermeasures of geological disasters along the coast of South China. *Trop. Ocean.* 11 (2), 46–53.
- Liu, Z. H. (1996). *Feng Zhiqiang, Feng Wenke, Xue Wanjun, et al. Geological hazards and submarine engineering geological conditions in the northern South China Sea*. Nanjing, China: Hehai University Press, 2–95. [M].Types and characteristics of potential geological disasters
- Liu, Z. Y., Han, Z., Su, B., Ma, Y. F., and Li, Y. G. (2019). Characteristics of harmful gases in shallow layer of subway engineering and advanced exhaust measures. *J. Undergr. Space Eng.* 15 (S1), 479–485.
- Locat, J., and Lee, H. J. (2002). Submarine landslides: Advances and challenges. *Can. Geotech. J.* 39 (1), 193–212. doi:10.1139/t01-089
- Luo, M., Wu, L. S., and Chen, D. F. (2012). Research status and progress of seabed pockmarks. *Mar. Geol. Front.* 28 (5), 33–42.
- Lv, B. Q., Xu, G. Q., Wang, H. G., and Zhao, H. M. (2002). sea floor spreading recorded by drowning events of cenozoic carbonate platforms in the South China sea. *Chin. J. Geol.* 37 (4), 405–414.
- Lv, C. L., Yao, Y. J., Wu, S. G., and Yao, G. S. (2011). Seismic responses and sedimentary characteristics of the Miocene wan'an carbonate platform in the southern south China sea. *Earth Science-Journal China Univ. Geosciences* 36 (5), 931–938.
- Ma, S. Z., and Chen, T. H. (2006). Marine geological hazards in the pearl river estuary. *Guangdong Geol.* 21 (4), 13–21.
- Ma, Y., Kong, L., Liang, Q. Y., Lin, J. Q., and Li, S. Z. (2017). Characteristics of hazardous geological factors on the Dongsha continental slope in the northern South China Sea. *Earth Sci. Front.* 24 (4), 102–111.
- Ma, Y., Li, S. Z., Xia, Z., Zhang, B. K., Wang, X. F., and Cheng, S. X. (2014). Characteristics of hazardous geological factors on shenhu continental slope in the northern south China sea. *Earth Science-Journal China Univ. Geosciences* 39 (9), 1364–1372.
- Ma, Y. B., Wu, S. G., Gu, M. F., Dong, D. D., Sun, Q. L., Lu, Y. T., et al. (2010). Seismic reflection characteristics and sedimentary model of carbonate platform in Xisha sea area. *J. Oceanogr. Ed.* 32 (4), 118–128.
- Ma, Y. B., Wu, S. G., Lv, F. L., Dongdong, D., Qiliang, S., Yintao, L., et al. (2011). Seismic characteristics and development of the Xisha carbonate platforms, northern margin of the South China Sea. *J. Asian Earth Sci.* 40, 770–783. doi:10.1016/j.jseas.2010.11.003
- Moscaredelli, L., Wood, L., and Mann, P. (2006). Mass-transport complexes and associated processes in the offshore area of Trinidad and Venezuela. *Am. Assoc. Pet. Geol. Bull.* 90 (710), 1059–1088. doi:10.1306/02210605052
- Moscaredelli, L., and Wood, L. (2008). New classification system for mass transport complexes in offshore Trinidad. *Basin Res.* 20 (1), 73–98. doi:10.1111/j.1365-2117.2007.00340.x

- Ni, D. (2009). Marine disasters and disaster reduction in the past decade. *Mar. Geol. Dyn.* 9, 96.
- Riboulot, V., Cattaneo, A., Sultan, N., Garziglia, S., Ker, S., Imbert, P., et al. (2013). Sea-level change and free gas occurrence influencing a submarine landslide and pockmark formation and distribution in deepwater Nigeria. *Earth Planet. Sci. Lett.* 375, 78–91. doi:10.1016/j.epsl.2013.05.013
- Riboulot, V., Thomas, Y., Berne, S., Jouet, G., and Cattaneo, A. (2014). Control of Quaternary sea-level changes on gas seeps. *Geophys. Res. Lett.* 41 (14), 4970–4977. doi:10.1002/2014gl060460
- Scanlon, K. M., and Knebel, H. J. (1989). Pockmarks in the floor of penobscot bay, Maine. *Geo-Marine Lett.* 9, 53–58. doi:10.1007/bf02262818
- Sun, Q. L., Wu, S. G., Cartwright, J., and Dong, D. (2012). Shallow gas and focused fluid flow systems in the pearl river mouth basin, northern south China sea. *Mar. Geol.* 315–318, 1–14. [J]. doi:10.1016/j.margeo.2012.05.003
- Wang, L., Wang, B., Li, J., Yu, K. Q., and Zhao, F. (2021). Morphology characteristics and formation mechanisms of submarine pockmarks in the northern Zhongjiannan Basin, South China Sea. *J. Trop. Oceanogr.* 40 (5), 71–84.
- Wei, X., Jia, C. Z., Meng, W. G., Zhu, Y. J., and Zhang, J. F. (2008). Discussion on the distribution of reefs and the direction of oil and gas exploration in the Xisha Sea area since Neogene. *Pet. Geophys. Explor.* 43 (3), 308–312.
- Wu, S. G., and Qin, Y. S. (2009). The research of deepwater depositional system in the northern South China Sea. *Acta Sedimentol. sin.* 27 (5), 922–930.
- Xu, H. L., Ye, C. M., Qiu, X. L., Sun, J. L., and Xia, S. H. (2010). Studies on the Binhai fault zone in the northern south China sea by the deep geophysical exploration and its seismogenic structure. *South China J. Seismol.* 30 (S), 10–18.
- Yang, S. X., Qiu, Y., and Zhu, B. D. (2015). *Atlas of geology and geophysics of the South China sea*. Tianjin, China: China Navigation Publications Press. [M].
- Yang, T. T., Lv, F. L., Wang, B., Fan, G. Z., Wang, X., Lu, Y. T., et al. (2011). Geophysical features and hydrocarbon exploration prospecting of reef in Xisha offshore. *Prog. Geophys* 26 (5), 1771–1778. doi:10.3969/j.issn.1004-2903
- Yang, Z., Wu, S. G., Lv, F. L., Wang, D. W., Wang, B., and Lu, Y. T. (2014). Evolutionary model and control factors of late Cenozoic carbonate platform in Xisha area. *Mar. Geol. Quat. Geol.* 34 (5), 47–55.
- Yang, Z., Zhang, G. X., Zhang, L., and Xia, B. (2016). Development and evolution of Neogene reef in Xisha Sea area and its controlling factors. *Pet. Exp. Geol.* 38 (6), 787–795.
- Yang, Z. L., Wang, B., Li, L., Li, D., Zhang, Y., and Sun, G. Z. (2020). Characteristics of pockmarks and their Genesis Zhongjian offshore area, South China Sea. *Mar. Geol. Front.* 36.
- Ye, J. L., Wei, J. G., Liang, J. Q., Lu, J., Lu, H., and Zhang, W. (2019). Complex gas hydrate system in a gas chimney, South China Sea. *Mar. Petroleum Geol.* 104, 29–39. doi:10.1016/j.marpetgeo.2019.03.023
- Ye, Y. C., Lai, X. H., Liu, D. J., and Tian, S. F. (2011). A preliminary study for hazard geology division in China Sea areas. *Chin. J. Geol. Hazard Control* 22 (4), 102–107.
- Zhang, B. K., Li, S. Z., Xia, Z., Ma, Y., Yu, S., and Wang, X. F. (2014a). Distribution of Cenozoic igneous rocks and its relation to submarine geological hazards in the deepwater area of the northern South China Sea. *Acta Oceanol. Sin.* 36 (11), 90–100.
- Zhang, Q., Wu, S. G., Lyu, F. L., Dong, D. D., Yan, Q. S., and Yang, Z. (2014b). The seismic characteristics and the distribution of the igneous rocks in the Northwestern slope of the south China Sea. *Geotect. Metallogenia* 38 (4), 919–938.
- Zhao, Q. (2010). *The sedimentary research about reef carbonatite in Xisha Islands waters*. Qingdao, China: Institute of Oceanology, Chinese Academy of Sciences, 1–158. [D].



OPEN ACCESS

EDITED BY
Zhigang Li,
Sun Yat-sen University, China

REVIEWED BY
Xiwu Luan,
Qingdao National Laboratory for Marine
Science and Technology, China
Junling Pei,
Chinese Academy of Geological
Sciences (CAGS), China

*CORRESPONDENCE
Guangzeng Wang,
✉ wangguangzeng@ouc.edu.cn
Yanhui Suo,
✉ suoyh@ouc.edu.cn

SPECIALTY SECTION
This article was submitted to Structural
Geology and Tectonics,
a section of the journal
Frontiers in Earth Science

RECEIVED 14 October 2022
ACCEPTED 29 November 2022
PUBLISHED 24 January 2023

CITATION
Zhan H, Wang G, Peng G, Suo Y, Wang P,
Du X, Zhou J, Li S and Zhu D (2023),
Cenozoic evolution of the Yangjiang-
Yitong'ansha fault zone in the northern
South China Sea: Evidence from 3D
seismic data.
Front. Earth Sci. 10:1070004.
doi: 10.3389/feart.2022.1070004

COPYRIGHT
© 2023 Zhan, Wang, Peng, Suo, Wang,
Du, Zhou, Li and Zhu. This is an open-
access article distributed under the
terms of the [Creative Commons
Attribution License \(CC BY\)](https://creativecommons.org/licenses/by/4.0/). The use,
distribution or reproduction in other
forums is permitted, provided the
original author(s) and the copyright
owner(s) are credited and that the
original publication in this journal is
cited, in accordance with accepted
academic practice. No use, distribution
or reproduction is permitted which does
not comply with these terms.

Cenozoic evolution of the Yangjiang-Yitong'ansha fault zone in the northern South China Sea: Evidence from 3D seismic data

Huawang Zhan^{1,2}, Guangzeng Wang^{1,2*}, Guangrong Peng³,
Yanhui Suo^{1,2*}, Pengcheng Wang^{1,2}, Xiaodong Du³, Jie Zhou^{1,2},
Sanzhong Li^{1,2} and Dingwei Zhu³

¹Frontiers Science Center for Deep Ocean Multispheres and Earth System, Key Lab of Submarine Geosciences and Prospecting Techniques, MOE and College of Marine Geosciences, Ocean University of China, Qingdao, China, ²Laboratory for Marine Mineral Resources, Qingdao National Laboratory for Marine Science and Technology, Qingdao, China, ³Shenzhen Branch, CNOOC China Limited, Shenzhen, Guangdong, China

The Yanjiang-Yitong'ansha Fault Zone (YYFZ) traverses the Pearl River Mouth Basin (PRMB) and plays an essential role in basin formation and hydrocarbon accumulation in the PRMB. Because of the lack of seismic data, its distribution, evolution, and effect on the basin evolution in the Cenozoic are poorly known. Based on a detailed interpretation of 3D multi-channel seismic data and previous research results, the YYFZ was identified and characterized. It comprises a series of NW-trending strike-slip faults that exhibit horsetail and en echelon structures in the map view and flower-like or Y-shaped structures in the profile view. By comprehensively analyzing the Paleogene migration of depocenters, activity characteristics of the YYFZ-related faults, and the relationships between faults and sedimentary sequences along the YYFZ, we propose the sinistral motion of the YYFZ initiated at about 35 Ma. The YYFZ served as a transfer zone during the intense rifting in the PRMB from 65 to 35 Ma. Then due to the combined effect of the Indian-Eurasian collision to the west, the Pacific subduction to the east, and the proto-SCS slab-pull to the south, it became a sinistral transtensional fault from 35 Ma to 16.5 Ma. Our results highlight the significant role of the NW-trending fault systems in the basin formation and the regional tectonic evolution of the PRMB.

KEYWORDS

sinistral motion, dynamic mechanism, Yangjiang-Yitong'ansha fault zone, Pearl River Mouth Basin, Cenozoic evolution

1 Introduction

As one of the largest marginal basins in the western Pacific region, the South China Sea (SCS) has been studied not only for its rich hydrocarbon and mineral resources but also for its unique tectonic location that makes it an ideal natural laboratory for studying and testing modes of lithospheric extension and breakup (Sun et al., 2016; Ye et al., 2020). The Pearl River Mouth Basin (PRMB) on the northern SCS is a Cenozoic sedimentary basin undergoing multiple extension episodes during the late Cretaceous to Oligocene. Faults in the PRMB, especially the strike-slip ones, significantly impact basin formation and hydrocarbon accumulation (Hou et al., 2008; Cao et al., 2014). Previous studies indicated that many regional strike-slip fault zones develop in the PRMB and control its tectonic configuration (Figure 1; Li et al., 2012; Cheng et al., 2012; Wang et al., 2014; Wang W et al., 2017; Wang et al., 2020; Wang et al., 2021; Wang et al., 2022; Mu et al., 2022; Zhou et al., 2022). However, its formation mechanisms remain controversial. Some authors referred to the PRMB as a transtensional basin triggered by widely distributed NE-

trending strike-slip faults (Xu and Zhang, 2000; Cheng et al., 2012; Li et al., 2012; Xu et al., 2014; Wang P et al., 2017; Mu et al., 2022; Zhou et al., 2022), whereas others proposed that the basin as a rift basin (Ho-Shing, 1990; Ge et al., 2020; Fu et al., 2021; Hao et al., 2021).

In the past few decades, the structural characterization of the PRMB has been one of the most studied targets (e.g., Shi et al., 2020; Huang et al., 2018; Zhang et al., 2021; Ye et al., 2020; Zhao et al., 2020; Hui et al., 2022; Ge et al., 2022). However, most of the studies mainly focus on the NE/NEE-trending faults since they control the basin's overall architecture (e.g., Liu et al., 2018; Ye et al., 2018, 2020; Zhao Y et al., 2018; Zhou et al., 2018; He et al., 2019; Zhou et al., 2019; Zhou et al., 2019; Ma B et al., 2020; Camanni and Ye, 2022; Suo et al., 2022). Less attention has been devoted to understanding the NW-trending ones, for example, the Yangjiang-Yitong'an-sha Fault Zone (YYFZ). Previous studies indicate that the YYFZ is an important NW-trending strike-slip fault zone influencing crustal structure, continent-ocean transition zone, basement lithology, sedimentary facies, Mesozoic tectonic environment, Cenozoic fault strike, and basin structure in the northern

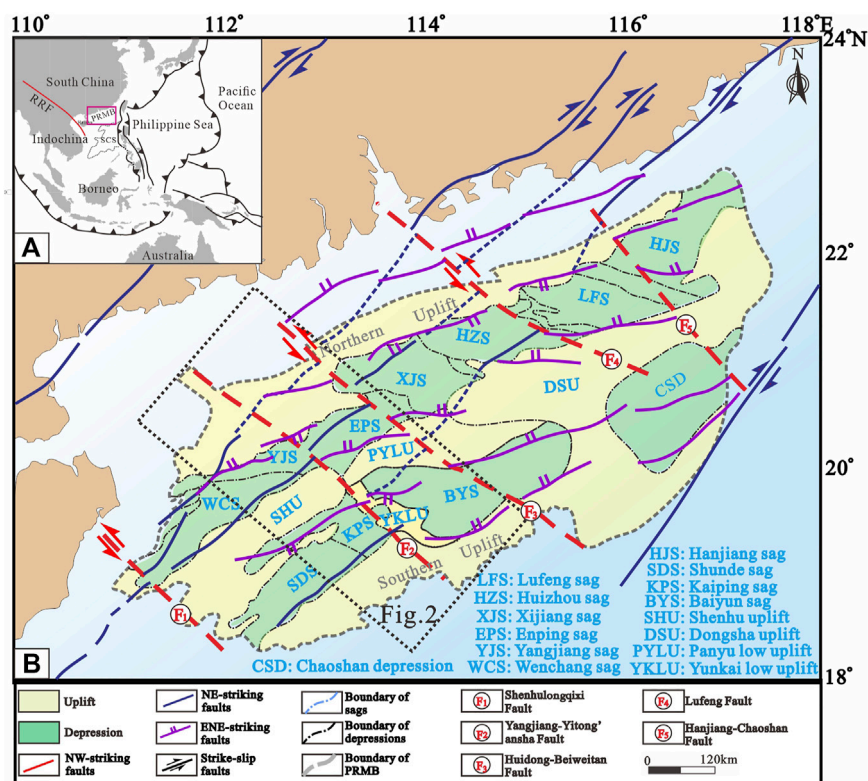


FIGURE 1

(A) Regional tectonic locations. (B) Structural units of the PRMB and the locations of regional strike-slip fault zone (modified after Zhu W et al., 2009; Zhu et al., 2021; Wang et al., 2020).

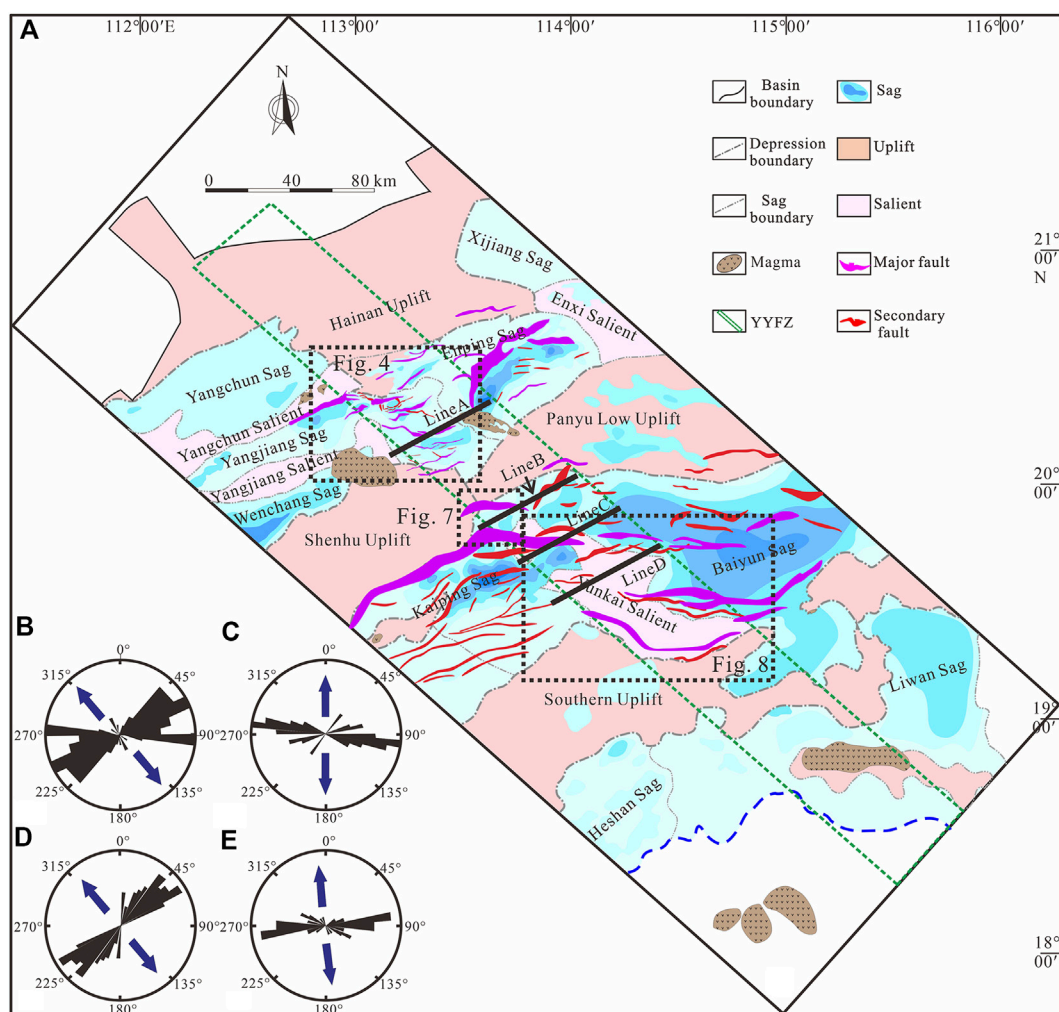


FIGURE 2

(A) Tectonic framework of the study area and the location of the YYFZ. (B–E) are the strike rose diagrams of major faults in the Yangjiang, Enping, Kaiping, and Baiyun sags, respectively.

SCS (Figure 2; Hu et al., 2009; Wang et al., 2006; Guo et al., 2016; Wei et al., 2011; Sun et al., 2008; Zhong et al., 2014; Liu et al., 2013; Cai et al., 2021; Sun et al., 2014; Zhu et al., 2017; Lu et al., 2011; Li et al., 2019). Owing to its specific geographical location, the YYFZ is an ideal site for investigating the NW-trending strike-slip fault zones.

The YYFZ, not often legible in shallow levels along its strike, has a complex geological history, and its origin and evolution likely had profound consequences on the formation of the PRMB (Mu et al., 2022; Wang et al., 2022). Previous research has shown that the YYFZ offset both basement gravity and magnetic anomaly belts and NE-trending faults in the PRMB and experienced marked sinistral motion during the Mesozoic (Zhou et al., 2006; Chen et al., 2005). However, limited by the low resolution of seismic data, its structural characteristics are still unclear, and its tectonic evolution remains controversial.

Some authors believed that the YYFZ only exhibits a tectonic transition zone in the Cenozoic (Zhong et al., 2014; Ma M et al., 2020). Some authors considered that it experienced sinistral movements throughout the Mesozoic (Zhou et al., 2006; Chen et al., 2005; Sun et al., 2009) and was subsequently reactivated as a dextral strike-slip fault during the Cenozoic (Chen et al., 2005; Lv et al., 2017). Besides, the YYFZ is generally considered as a major sinistral strike-slip fault since the Early Oligocene (Wang et al., 2013; Sun et al., 2014; Zhang et al., 2019; Cai et al., 2021; Liu X et al., 2021; Zhan et al., 2021; Zhang et al., 2021). Further, Li et al. (2019) have confirmed the YYFZ experienced sinistral transtensional deformation in the early Cenozoic, followed by dextral transtensional deformation from about 23.8 Ma to the present, based on the comparison of structural style and tectonic evolution history on both sides of the YYFZ. However, the following essential problems about the YYFZ had not been

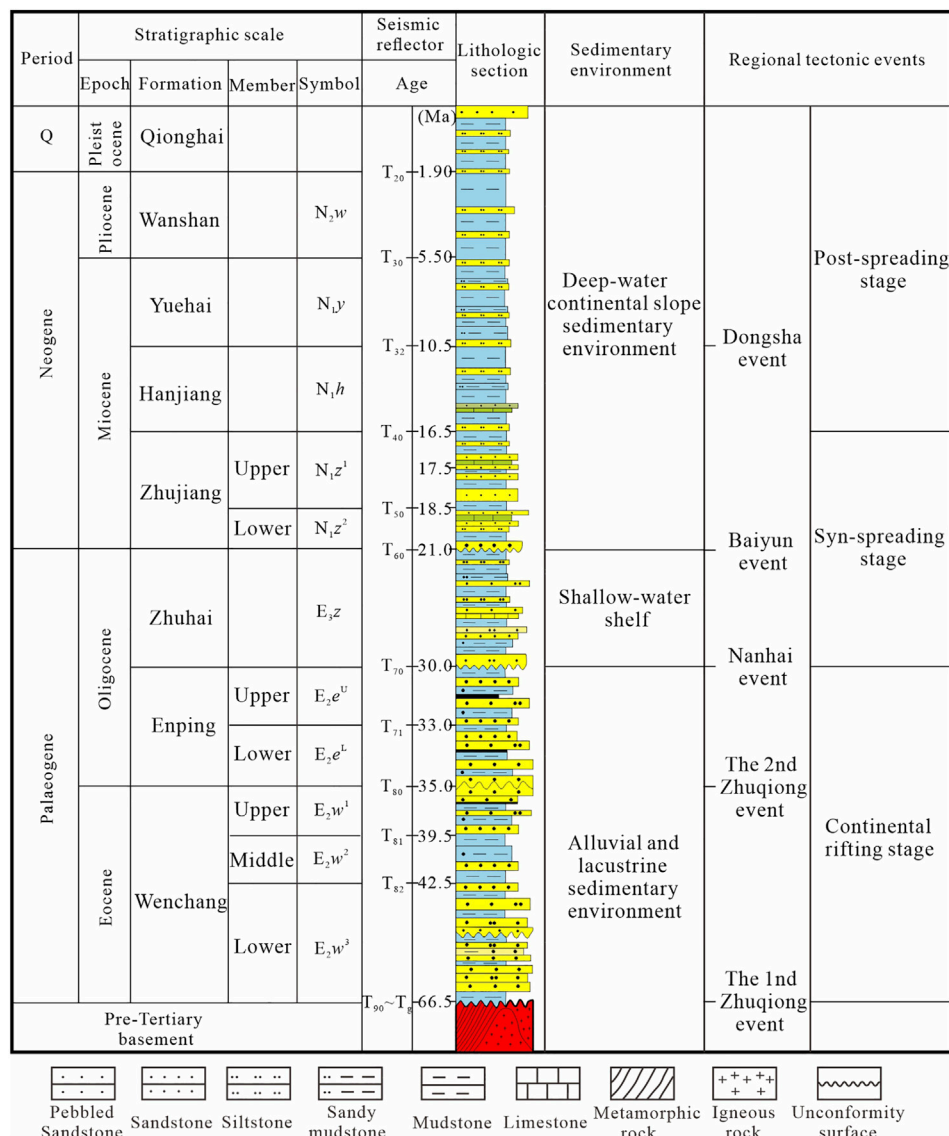


FIGURE 3

Comprehensive stratigraphic column of the PRMB showing major tectonic and depositional events (modified after Li H et al., 2014; Zhu W et al., 2009; Zhu et al., 2021; Zhang et al., 2021).

discussed clearly: 1) the structural features and initial activity of sinistral strike-slip faults, 2) the evolution history, 3) the control and influence of strike-slip fault on the evolution of the PRMB, and the driving mechanism in the Cenozoic.

In this study, we applied high-resolution 3D seismic data covering the western PRMB to investigate the YYFZ geometrical characteristics and discuss its Cenozoic evolution history. We also built a geodynamic model to reveal the influence of strike-slip fault on the evolution of the PRMB with some synchronous plate motions around the SCS in the Cenozoic. Our research has implications for understanding the complexity and diversity of faults in the PRMB and the

geological evolution of the basins, which would benefit petroleum exploration there.

2 Geological setting

The PRMB, with a total area of 175,000 km², is a long and wide ENE-trending graben located in the northern margin of SCS. Controlled by two groups of faults with NE and NW strikes, the basin presents a segmental and zonal structural framework in the NE and NW directions, respectively (Figure 1; Cheng et al., 2012; Zhong et al., 2014). From north to south, the basin can be

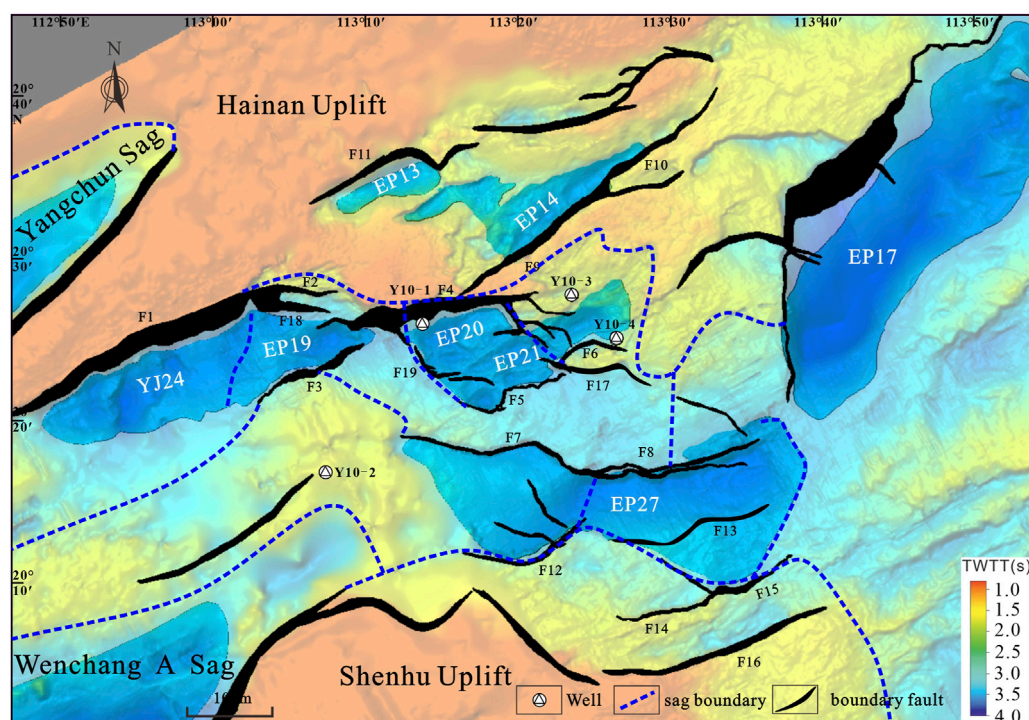


FIGURE 4

Secondary tectonic units of the Yangjiang Sag and adjacent areas (See Figure 2 for the location).

divided into five first-order structural units: the northern uplift zone, the northern depression zone, the central uplift zone, the southern depression zone, and the southern uplift zone (Xie et al., 2014; Wang P et al., 2017). The northern depression belt consists of the Zhu I Depression (Enping Sag, Xijiang Sag, Huizhou Sag, Lufeng Sag, and Hanjiang Sag) and the Zhu III Depression (Wenchang Sag, Yangchun Sag, Yangjiang Sag, Qionghai Sag, and Yangjiang low Uplift). The central uplift belt consists of Shenhu Uplift, Panyu low Uplift, and Dongsha Uplift from west to east. The central depression zone consists of the Zhu II Depression (Shunde Sag, Kaiping Sag, Yunkai low Uplift, and Baiyun Sag) and Chaoshan Depression. The Sag and Uplift in PRMB are mainly NE/ENE-trending. The faults developed in the PRMB during Cenozoic are mainly composed of NE-to EW-trending normal faults and NW-trending shear faults. The basin is divided into segments from west to east by NW-trending Qionghai, Yangjiang-Yitong, Huizhou, Huidong-Beiweitan, Raoping-Taixinan, Nanao-Taiwanxi faults (Chen et al., 2005).

The general stratigraphic column of the PRMB is shown in Figure 3. The Paleogene to Lower Oligocene strata consist of fluvial-lacustrine sediments in discrete rifts, among which the Eocene Wenchang and Enping Formations contain dark lacustrine mudstones that are primary source rocks for hydrocarbons in this area. Deposits in the Upper Oligocene

Zhuhai Formation are transitional (alternatively coastal and littoral) and contain both source rocks and reservoirs. Neogene strata consist of marine sediments that constitute a generally transgressive sequence. The Cenozoic strata comprised seven lithostratigraphic units (Figure 3). They are from the bottom to the top, the Shenhu (E_1s) Formation, the Wenchang (E_2w) Formation, the Enping (E_2e) Formation, Zhuhai (E_3z) Formation in the Paleogene and Zhujiang (N_1z) Formation, Hanjiang (N_2h) Formation, Yuehai (N_2y) Formation and Wanshan (N_2w) Formation in the Neogene. Nine high-amplitude seismic interfaces were recognized and tracked throughout the study area: the T_{30} , T_{32} , T_{40} , T_{60} , T_{70} , T_{80} , T_{90} , and T_g . These seismic interfaces correspond to lithostratigraphic interfaces standing for the second- and third-order sequence boundaries (Ye et al., 2018).

The NEE-trending Yangjiang Sag is bounded by the Yangchun Low Uplift to the north, the Shenhu Uplift to the south, the Wenchang Sag to the west, and the Enping Sag of Zhu I depression to the east (Figure 4). Separated by the Yangjiang Low Uplift, it can be divided into the west and east sag. The structure of the west sag is north-faulted and south-overlapped, while that of the east sag is relatively complex, represented by single half-grabens and composite half-grabens. From west to east, Yangjiang Sag is further subdivided into six subsags: the YJ

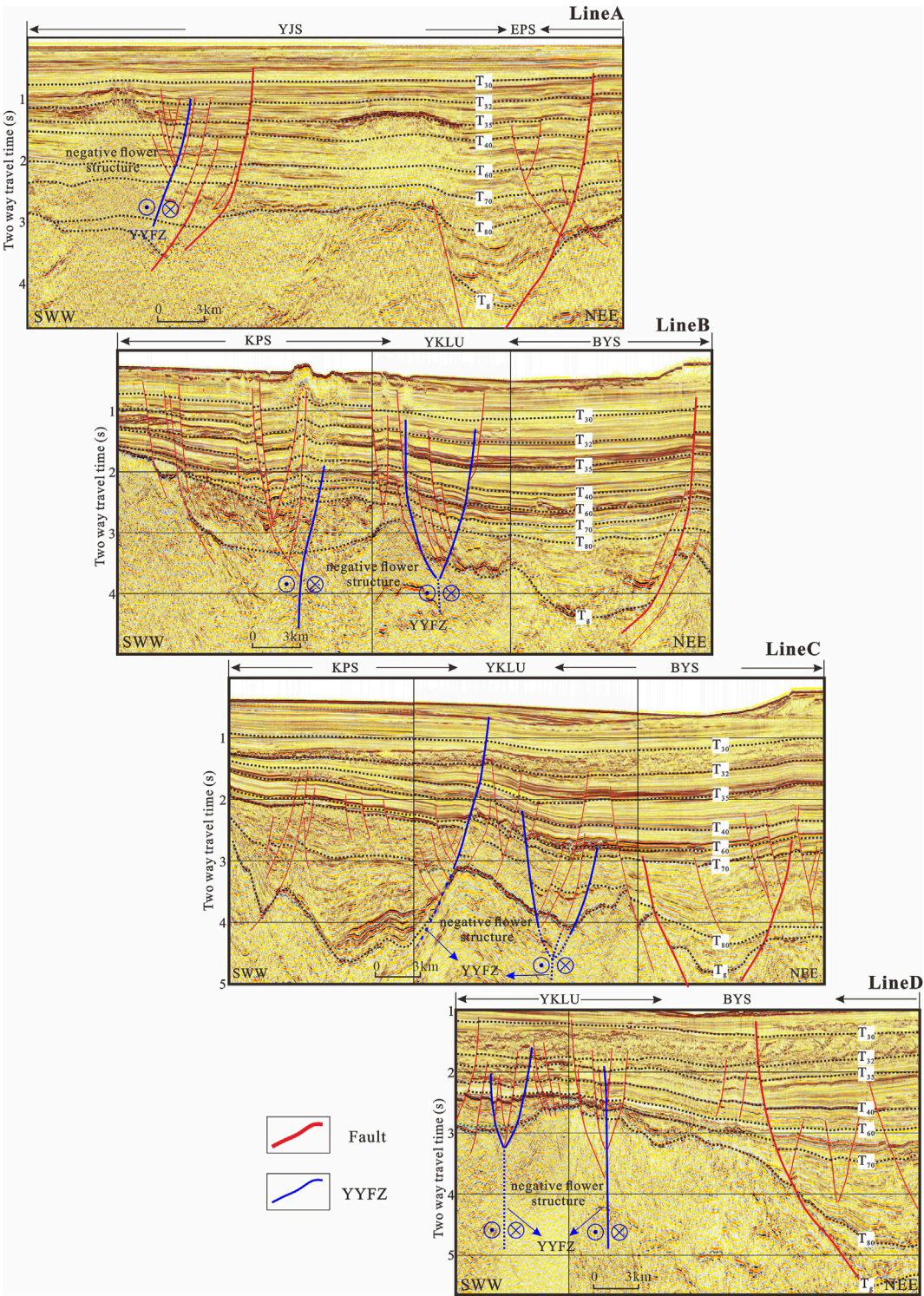


FIGURE 5
Structure, fault system, and stratum characteristics of the YYFZ. Profile locations are shown in Figure 2. The faults derived from the YYFZ terminate mainly in N_2W .

33, YJ 24, EP19, EP20, EP21, and EP27 subsags. The YJ33 and YJ24 subsags are bounded by the F_1 , the EP19 subsag is controlled by the F_2 and F_3 , the EP20 subsag is determined by the F_4 , the EP21 subsag is controlled by F_5 and F_6 , and the EP27 subsag is controlled by F_7 and F_8 . These boundary faults trend mostly NE-ENE and WNW.

3 Data and methods

Structural features and the spatial distribution of the YYFZ in the PRMB were analyzed through detailed seismic interpretation. All these 3D seismic and well data were acquired by the China National Offshore Oil Corporation (CNOOC) Shenzhen Branch and associated cooperative services companies over the past decades. The seismic profiles nearly cover the whole region of Yangjiang Sag, over 5,600 km². The bin size of the survey is 12.5 * 12.5 m. Inline seismic profiles are orientated NW, approximately perpendicular to the basin trend. Standard seismic interpretation workflows for the tectonic-stratigraphic analysis and magmatic body identifications were carried out in Geoframe Open Works (software). A stratigraphic framework was established by integrating 3D seismic and log data with VSP information from some typical wells. Due to its relatively integrated stratigraphic sequence, petroleum exploration boreholes were used to calibrate the Cenozoic strata. Twelve key seismic-stratigraphic boundaries have been identified and named following the nomenclature termed by the CNOOC as T_g (66.5 Ma), T_{82} (42.5 Ma), T_{81} (39.5 Ma), T_{80} (35 Ma), T_{71} (33 Ma), T_{70} (30 Ma), T_{60} (23 Ma), T_{50} (18.5 Ma), T_{40} (15.5 Ma), T_{32} (13.8 Ma), T_{30} (10.5 Ma) and T_{20} (5.5 Ma) (Figure 3). Fault dip and displacement values are calculated on the seismic profiles that cut across the fault (Huang and Liu, 2014). The time-depth conversion was performed using a second-order polynomial, $D=0.000274591t^2+0.72410996t+31.78776360$ (D-depth/m, t-TWT/ms), derived from boreholes within the study area.

The workflow includes the following steps: 1) identify and correlate seismic horizons; 2) generate time structural maps, seismic volume slices, and fault distribution maps during the different seismic reflectors; 3) observe the patterns of en echelon, feather-shaped, horsetail-shaped in map view; 4) observe the stacking patterns of flower-like or Y-shaped structures along the YYFZ; 5) systematically investigate the concomitant changes of depocenters; 6) calculate fault kinematics features; 7) conclude the initial time and evolutionary history of the YYFZ.

Fault geometry features were portrayed based on seismic sections covering the entire study area. Fault orientations are depicted in rose diagrams. Fault kinematics features and their tectonic evolution history were analyzed using 2Dmove software. The evolution history of the YYFZ can be constrained by growth strata and fault assemblage in the profile.

4 Results

The seismic sections across the YYFZ were selected to represent its structural characteristics in the Yangjiang Sag, the northern Kaiping Sag, and the Yunkai Low Uplift. As shown in Figure 5, the YYFZ mainly displays sub-vertical faults, Y-shaped or flower-like structures. In the Yangjiang Sag, the abovementioned structures were primarily observed between the interface T_{70} or T_{80} and T_{32} , while in the northern Kaiping Sag and the Yunkai Low Uplift, they were mainly between T_{80} and T_{32} with a few just between T_g and T_{60} (Figure 5).

4.1 Distribution patterns in map view

4.1.1 Yangjiang sag

Previous studies have suggested that the density of secondary faults can be used to constrain the relative intensity of faults (Huang et al., 2015). Here, we used fault patterns at different seismic reflectors to delineate the distribution and variations in secondary faults in different strata. In the deeper seismic reflectors (Figure 6A), the main faults formed simple NE- and ENE-trending alignments parallel or left-stepping en echelon structures. Subsequently, the formation of a fault system in the early stage may be related to extension, accompanied by slighter dextral transtensional. Besides, these faults only occur in the eastern section, which may be related to the YYFZ as a transfer zone. In contrast, in the middle seismic reflectors, the number, size, and distribution area of the ENE-trending fault become large. Broom-shaped structures and en echelon fault patterns were more extensively developed in the Yangjiang Sag (Figures 6B,C), suggesting that the strike slipping was more intense than in the early Middle Eocene. Meanwhile, a few EW- and WNW-trending faults arose in the sag, especially in its eastern part. The horsetail-shaped structures and right-stepping en echelon fault structure can be identified. The rose diagrams also show that strikes of newborn faults changed from the NE-ENE to the EW-WNW since the Late Eocene, implying a change in the extensional stress from NWN to N-S during the syn-rift stage. In the post-rift stage, the ENE- or NE-trending fault is less active. However, the abundant WNW- or EW-trending faults formed and cut off the pre-existing NE- or ENE-trending faults. These WNW-trending faulting assembled into right-stepping en echelon or horsetail-like patterns (Figure 6D).

The abovementioned characteristics reveal that the YYFZ experienced two tectonic episodes during the Cenozoic: 1) extensional deformation as a transfer zone during the Eocene and 2) sinistral transtensional deformation from the Oligocene to Neogene. Besides, the intensity of the dextral transtensional motion was weak during the early Middle Eocene. Still, it was

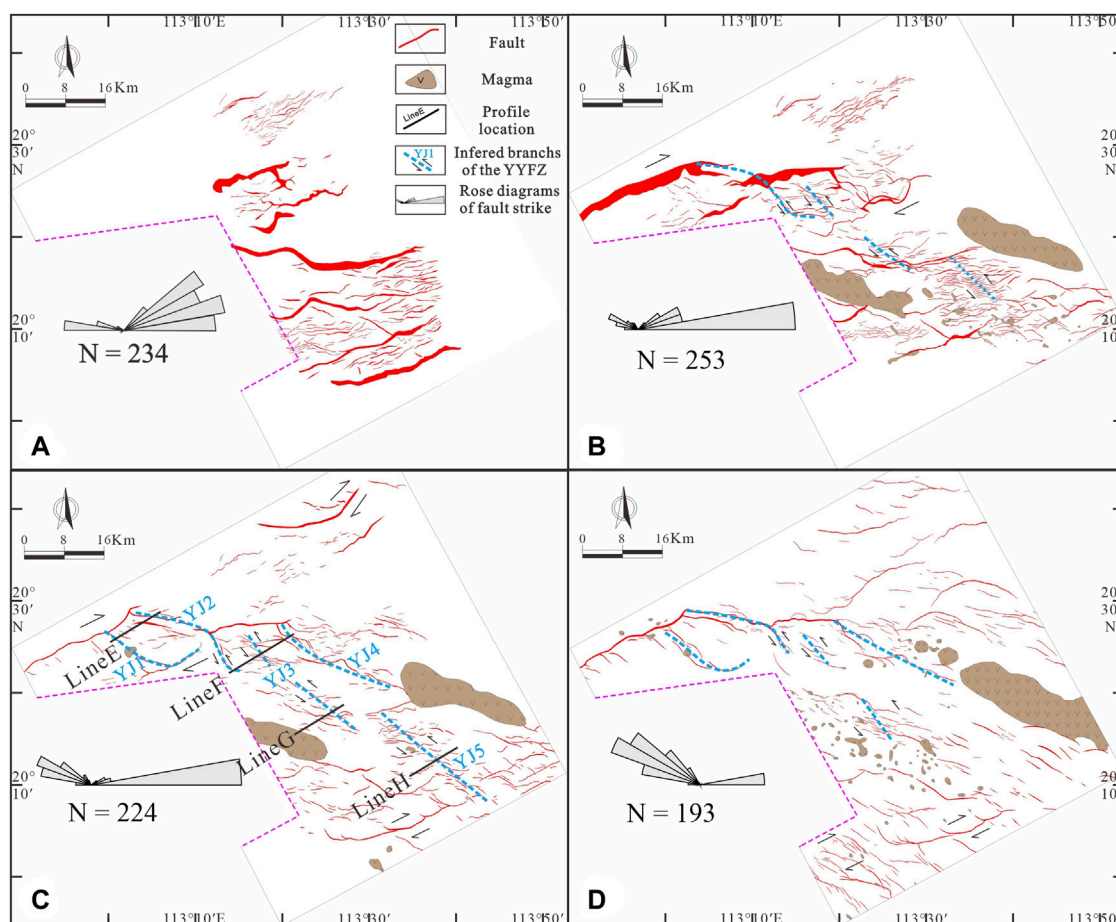


FIGURE 6
Fault patterns in different seismic reflectors of the Yangjiang Sag. (A)-T₈₂; (B)-T₈₀; (C)-T₇₀; (D)-T₄₀.

enhanced from the Middle Eocene to the Middle Miocene and became less active in the sag.

4.1.2 Northern kaiping sag

This study area is located in the Kaiping Sag, bounded by the Baiyun Sag to the east, Panyu low Uplift and Shenhu Uplift to the north, and the Yunkai low Uplift to the south (Figure 2). In the sag, the major faults are EW-trending and display simple parallel or right-stepping en echelon structures (Figure 2). Similarly, in the middle seismic reflectors (such as the T₇₀ interface), the fault distribution pattern in the northern Kaiping Sag also suggests that the boundary faults are composed of a series of NW- or EW-trending faults. However, they are not continuous and smaller, and display a right-stepping en echelon pattern (Figure 7).

4.1.3 Yunkai low uplift

The Yunkai Low Uplift, mainly distributed along the NW direction, is located in the tectonic transition zone from the Kaiping Sag in the west to the Baiyun Sag in the east (Figure 8).

Influenced by the YYFZ, the pre-existing faults experienced strike-slip reactivation, and the Uplift is characterized by WNW-trending right-stepping small-scale normal faults arranged in an echelon pattern (Figure 8). Therefore, to unravel the tectonic evolution of YYFZ, the fault patterns in different seismic reflectors of the Yunkai Low Uplift are carried out. The maps show that the dominant trend of faults in the study area mainly includes NWW/NW, EW, and ENE directions (Figure 9A), which show a clockwise rotation. During the Late Eocene to the Oligocene (corresponding to the T₈₀-T₇₀ in space, ~35–30 Ma in time), the main faults in the Yunkai Low Uplift were WNW/NW-trending and short with curved or sigmoidal features (Figure 9B). They were different from the NEE-trending main faults in the northern depression zone, such as the Yangjiang Sag. The horsetail- or right-stepping fault patterns in the Yunkai Low Uplift can be seen (Figures 9B,C), which suggests slighter sinistral transtension. Compared with the deeper sector, the number, size, and distribution area of the WNW-/NW-trending faults in the shallow seismic reflectors

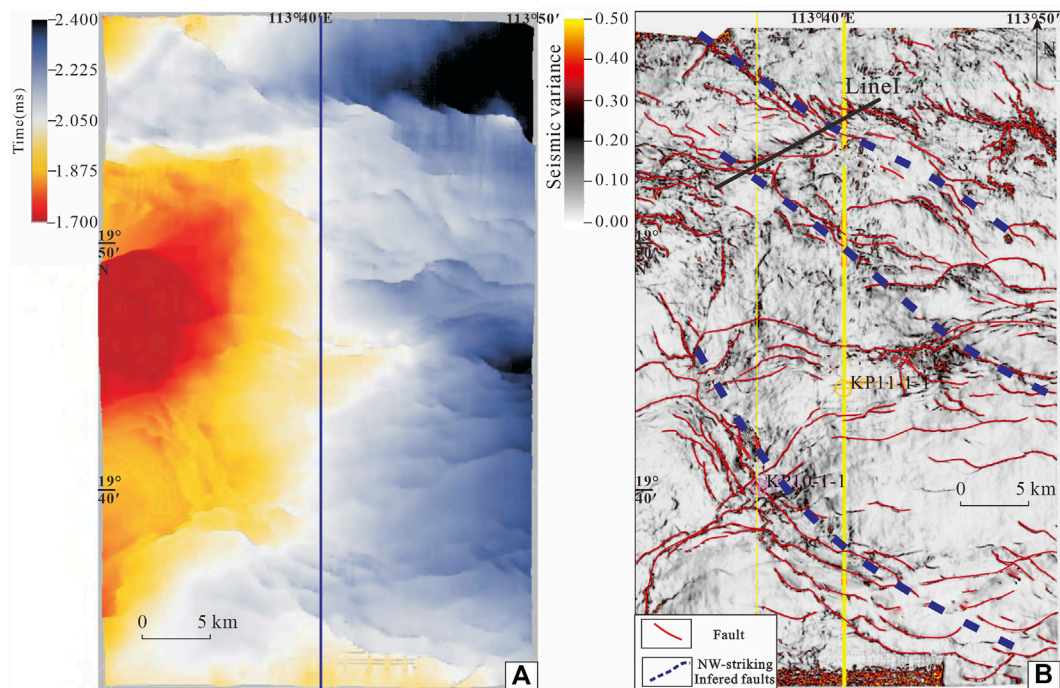


FIGURE 7
Distribution characteristics of fault plane combination along T_{70} in the northeastern part of the Kaiping Sag (Figure 2 shows figure location). (A). T_0 plane map; (B) Two-dimensional fracture plane distribution along the coherent attribute recognition (revised from Wang et al., 2021a; Wang et al., 2021b).

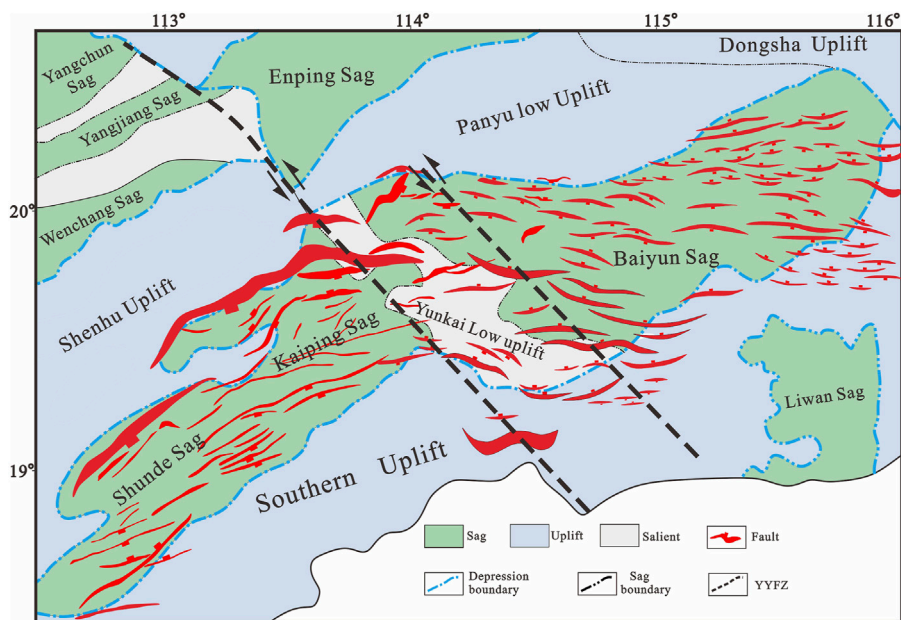


FIGURE 8
Structural units and fault pattern in the Zhu II Depression. The WNW- and E-W-trending secondary faults are assembled to produce an echelon fault pattern in the T_{80} interface. Figure location is shown in Figure 2 (revised from Wang et al., 2021).

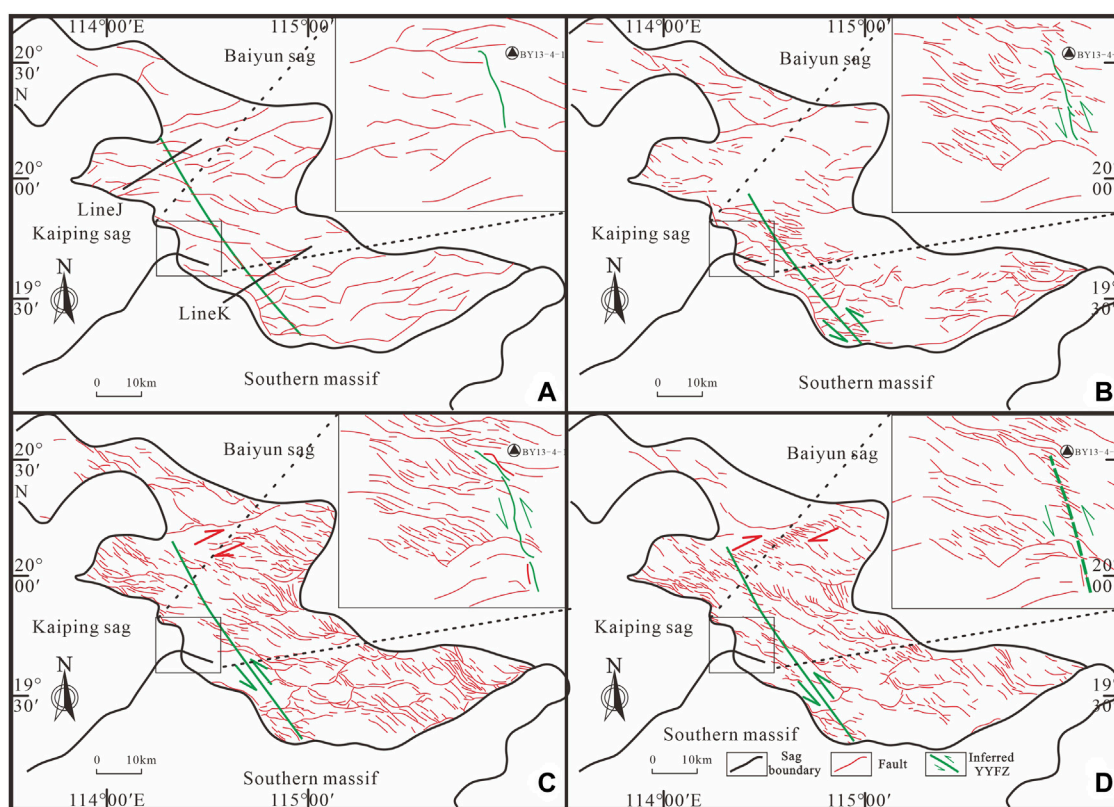


FIGURE 9
Fault patterns in different seismic reflectors of the Yunkai low uplift (revised from Sun et al., 2014; Yu et al., 2021). (A)– T_g ; (B)– T_{80} ; (C)– T_{60} ; (D)– T_{40} .

become smaller (Figures 9C,D). Besides, a group of NW-trending minor faults at the interface T_{40} exhibits a left-stepping en echelon pattern, suggesting ENE-trending dextral transtensional motion (Figure 9D).

Similarly, the strike-slip motion is evident in the BY13 area southwest corner of the Yunkai Low Uplift. During the early faulting, these NW-trending faults were reactivated as normal faults (Figure 9A). Compared with the T_g interface, the fault appears as discontinuous linear structures from the Late Eocene to the Early Miocene (T_{80} – T_{60} in space; Figures 9B,C). Meanwhile, these WNW-trending secondary faults developed along the NW-trending fault's right side and converged to the main faults. In comparison, the upper faults at interface T_{40} are composed of a series of WNW-trending faults, which present right-stepping en echelon arrangement (Figure 9D).

4.2 Structure styles in sections

4.2.1 Yangjiang sag

The profiles crossing the Yangjiang Sag indicate that the NE–NEE trending faults determine the structural framework of the

subbasin. As the main fault of the study area, the NEE-trending F_1 and F_4 faults present as a listric fault with a large offset. Notably, a series of WNW-trending secondary faults began to develop in the E_2 depositional stage. Some of them form flower-like or Y-shaped structures, indicating transtensional deformation characteristics.

To reveal the profile features of those WNW-trending secondary faults from north to south, we chose four SWW–NEE typical seismic profiles in the Yangjiang Sag (Figure 10, LineE–H). Profiles reveal that the NW-trending YJ1, YJ2, YJ3, YJ4, and YJ5 faults display a geometric feature similar to a steeply dipping listric fault in the lower part but a negative flower or Y-shaped structure in the upper part (this is, the lower listric upper flower structure) (Figure 10). These faults penetrate the T_{80} or T_g unconformity, terminate below the T_{32} (Figure 10), and control non-wedge-like sedimentation. Among those faults, the YJ2 fault in the north segment is mainly west dipping, and those in the south segment are mainly east dipping (Figure 10, LineE, and F), which display ribbon effect (Romeo et al., 2005) in space. Similarly, the YJ3 fault in the north segment is mainly east-dipping, and those in the south segment are mainly west-dipping (Figure 10, LineF, and G).

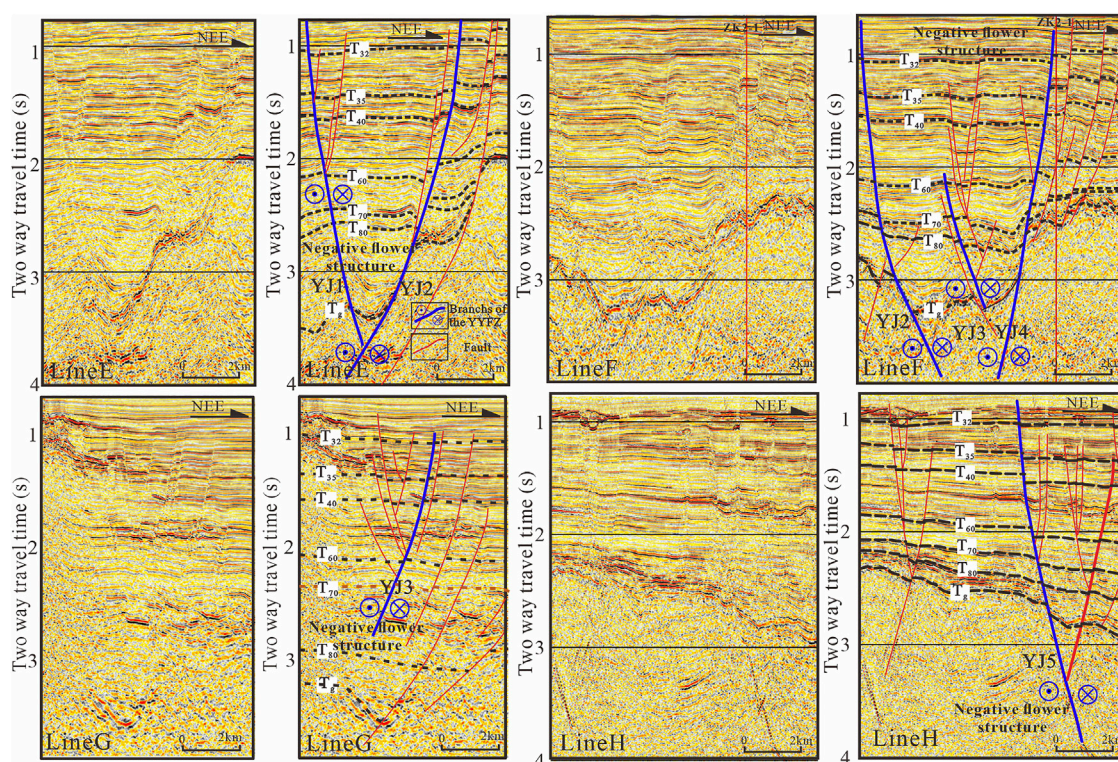


FIGURE 10

Interpreted seismic profiles showing fault intersections in the Yangjiang Sag. Profile locations are shown in Figure 6C. The profiles reveal that the NW-trending faults are characterized by flower-like structures that indicate they experienced transensional deformation.

4.2.2 Northern kaiping sag

The basement-involved faults in the northern Kaiping Sag are mainly planar or shovel-type faults at a high angle. Notably, a set of new normal faults began to develop during the depositional stage of E_2e . Some of them form flower-like or Y-shaped structures with main faults. Besides, magmatic diapirs intruded into the sedimentary cover of the basin along these faults and even erupted over the seabed. According to growth strata and fault assemblage in the profile (Figure 11, Line I), a displacement of normal fault or transtensional fault occurred in the basement-involved faults in the E_2e - E_3z depositional stage.

4.2.3 Yunkai low uplift

As the transition zone between the two sags, the Yunkai Low Uplift connects the Kaiping Sag and the Baiyun Sag with a slope and a faulted step zone, respectively (Figure 2). On the Yunkai Low Uplift, the Wenchang Formation is mostly eroded, directly overlain by the Enping Formation. Inside the Uplift, various scales of listric and planar normal faults develop. Several normal fault combinations display asymmetrical negative flower structures (Figure 11, Line J, and K). The deep layer structure is characterized by a listric fault through the T_g interface and developed upward across the T_{80} interface.

4.3 Characteristics of the sedimentary succession

Sequence thicknesses in different stages reveal three-stage depocenter migration, indicating two-stage structural transitions in the study area. There developed five independent depocenters during the depositional stage of E_2w , forming YJ24, EP19, EP20, EP21, and EP27 subsags, respectively (Figure 12A). In this period, these subsags were mainly controlled by the main faults (such as F_1 , F_4 , F_6 , and F_7) obviously, and the center of the E_2w sequence is distributed primarily in the east of the sag with the characteristics of thick in the east and thin in the west. However, during the depositional stage of E_2e^L , the depocenter migrated to the west Yangjiang Sag for the first time; the EP19 and YJ24 subsags presented, leading to thick in the west and thin in the east. Furthermore, from E_2e^L to E_3z , the study area presents a westward thickening slope and their depocenters are located along the NWW-trending faults and align in a right-stepping en echelon pattern, indicating that the NW-trending faults were sinistral during the depositional stage of E_2e^L - E_3z (Figures 12B-D). The depocenter migration is probably consistent with the intense activity of the strike-slip faults.

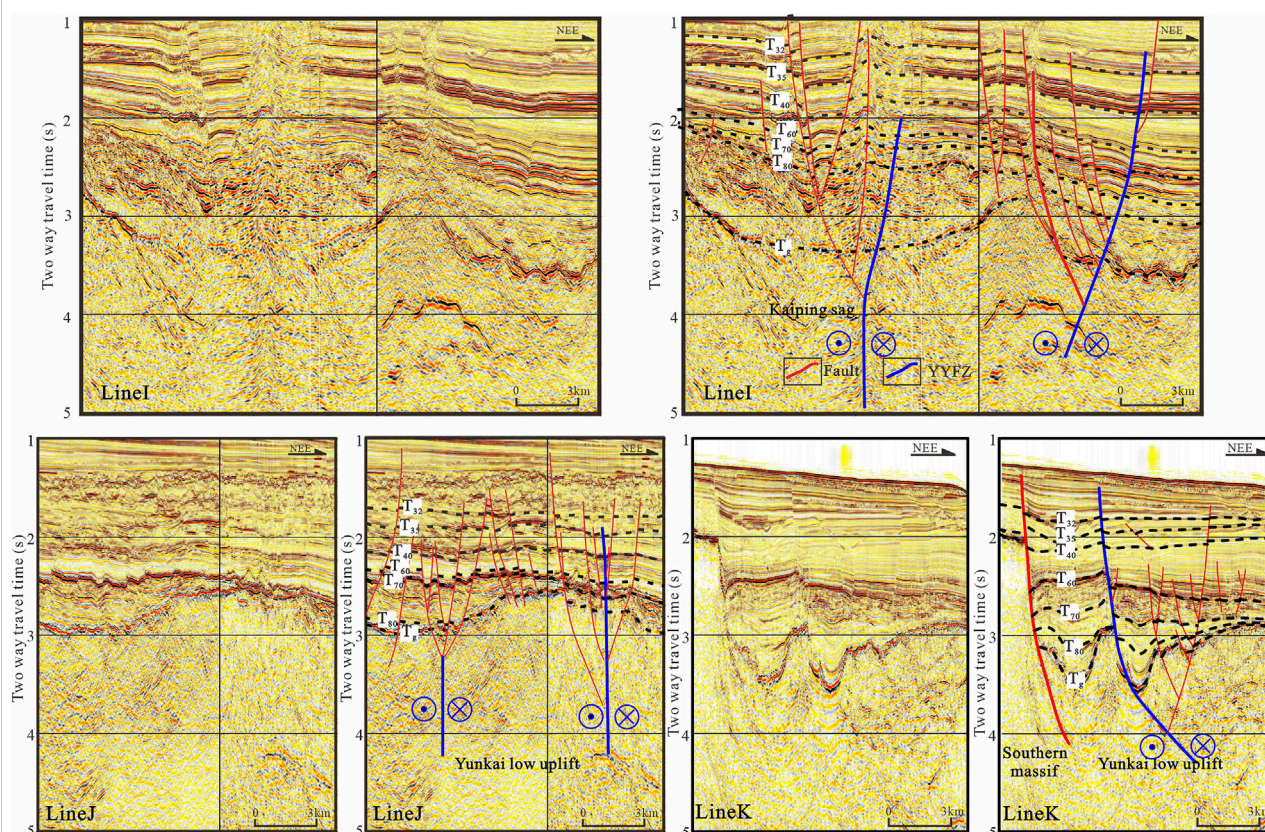


FIGURE 11

Seismic profiles show the geometry of the NW-trending faults in the northern Kaiping Sag and Yunkai low uplift. The location of seismic profiles Line I and Line J-K are demonstrated in Figures 8, 9, respectively. These faults are characterized by flower or Y-shaped structures.

Based on the analyses presented above, the residual thickness of E_{2w} , E_{2e} , and E_{3z} showed an obvious counter-clockwise rotation of the depocenter orientations from ENE to WNW in the Yangjiang Sag; a similar depocenter rotation also occurred in the Yunkai Low Uplift at the same time (Yu et al., 2021). Consequently, it indicates a clockwise rotation of the extension stress field from NW (in the E_{2w} depositional stage) to S-N (in the E_{2e} depositional stage), consistent with the stress field rotation in the PRMB (Hao et al., 2021).

5 Discussion

5.1 Initiation of the sinistral motion of the YYFZ

Several distinctive structures were used to identify the YYFZ in the PRMB. These structures include 1) a high-subvertical dip angle (Harding, 1990) or a Y-shaped structure governed by steeply dipping faults and a flower structure in cross-section (Harding, 1985; Cheng et al., 2017; Han et al., 2017), 2) the

abrupt changes of the thickness of the same lithologic stratigraphic unit, the sedimentary facies, and the formation occurrence across fault planes in the section (Ghalayini et al., 2014), 3) linear geometry, en echelon faults, pull-apart structures, and horsetail splays in the map view (Harding, 1985; McClay, 2001); dolphin (Graham et al., 1984) and ribbon effects (Romeo et al., 2005) in space. Previous results have shown that the blind fault and tectonic trend zones in sedimentary layers would inherit from pre-existing faults when suffering deformation (Bellahsen and Daniel, 2005; Wang et al., 2015). These pre-existing structures incline to show strike-slip deformation, accompanying many minor faults aligning in a parallel or en echelon arrangement (Liu Y et al., 2021). In this study, the YYFZ exhibited en echelon arrays of minor faults in the map view and flower-like or Y-shaped structures in the section. These small-scale normal faults are arranged in a right-stepping en echelon pattern on the T_{80} seismic interface, indicating that the YYFZ has a consistent initiation time (i.e., at about 35 Ma) and has the same overall kinematic framework. The fault plan arrangements suggest that these NW or WNW-trending faults had experienced sinistral

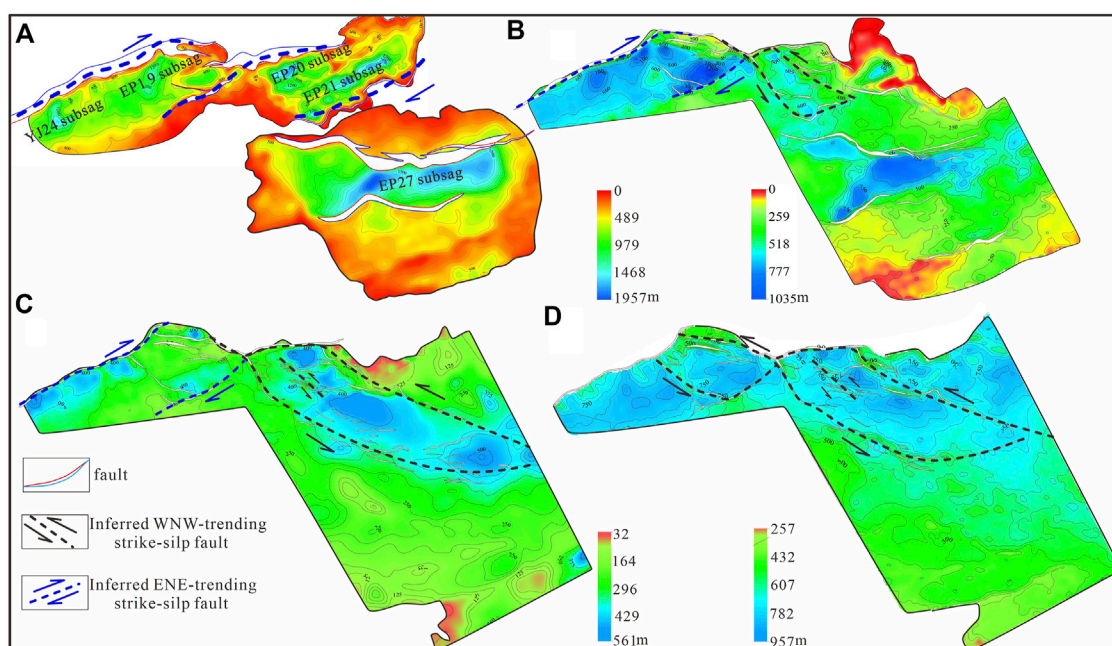


FIGURE 12

Sequence characteristics of different periods in the Yangjiang Sag area. (A), (B), (C), and (D) show the thickness of the E_2w , E_2e^L , E_2e^L , and E_3z Formation, respectively. Note the depocenter migration in (B) and (C).

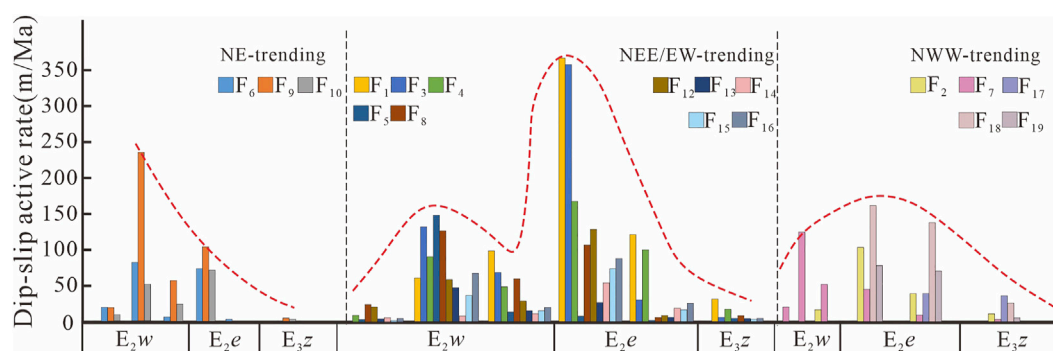


FIGURE 13

Average rates of active dip-slip faulting of main faults in the Yangjiang Sag.

strike-slip motion. Besides, the syn-depositional fault map of Paleogene shows that the E_2e^L sequence presents a thickening slope westward, and the depocenters are located in the NNW trending faults, which also confirms that the NNW-trending strike-slip faults began to slightly motion during the stage (Figure 12B). Based on the fault pattern in the BY13 area, Sun et al. (2014) indicated that the NNW-trending shear faults acted sinistrally about 32 Ma. Wang et al. (2013) also proposed that the sinistral transtensional activities occurred during the middle to early Oligocene, according to a comprehensive interpretation of seismic stratigraphic sequence and faults.

It is difficult to track the activity history because the strike-slip faults move along the strike (Yu et al., 2008). However, the activity of secondary faults derived from the main strike-slip faults can reveal the tectonic activity of strike-slip faults. By calculating the activity rate of main faults in the Yangjiang Sag during the Paleogene, the results reveal that the NE/ENE-trending normal faults activated during the depositional stage of E_2e and reached the peak stage during the period of the E_2e^L sequence. Meanwhile, the NNW-trending faults related to the YYFZ are active during the depositional stage of E_2e (Figure 13), which may also suggest that the YYFZ began to be active during the period.

As mentioned above, we suggest that all these fault bends or en echelon structures were induced by the sinistral strike-slip motion of the YYFZ, indicating that the sinistral slip of the YYFZ commenced at about 35 Ma.

5.2 Cenozoic evolutionary history of the YYFZ

Much previous work has shown that the Meso-Cenozoic evolution of the YYFZ was characterized by huge and significant sinistral motion (Zhan et al., 2021; Mu et al., 2022; Wang et al., 2022), whereas its Cenozoic evolutionary history is poorly known.

Evidence of the sense of motion from flower-like structures in the profile and en echelon arrangement in the plane along the YYFZ indicate that the Cenozoic sinistral motion occurred around 35 Ma. The fault pattern in the plane and the main fault cut through in the strata above marker T_{80} in the profile show that their remarkable formation period was during the depositional stage of E_2-E_{1z} ($T_{80}-T_{40}$ in space), indicating sinistral motion of the YYFZ during the period (Figures 5, 6). Remarkably, the change of tectonics stress regime and sediment provenance before and after the T_{80} reflection interface occurred in the PRMB (Tang et al., 2020), which is further validated by the fact that the EW-trending normal faults are primarily developed in the Yangjiang Sag (Figure 6B). Besides, combined with the sedimentary thickness data, the Yangjiang Sag is a strike-slip pull-apart superimposed area composed of multiple WNW-trending faults in the E_2-E_{3z} depositional stage, displaying en echelon arrangement itself to some extent as well (Figures 13B–D). These features strongly confirm that the YYFZ was active during these two periods. One further point should also be emphasized, although the depocenter appears not obvious in Neogene strata, some en echelon subsidiary faults are nevertheless still developed among shallow strata (Figure 6D), indicating that strike-slip motion still occurred during Neogene but has become much weaker.

The kinematics characteristics of the YYFZ in the Eocene remain controversial; some workers suggest that the YYFZ showed dextral displacement in the earlier faulting stage, which subsequently results in the boundary fault right laterally displaced (Lv et al., 2017); however, other authors proposed that the NW-trending pre-existing faults probably reactivated only as a transform zone under the NW-SE oriented stress field, regulating the differential tectonic deformation on both sides (Zhan et al., 2021; Shen et al., 2022). The transform zone is characterized by transform fault, which links different segments of extensional structural domains (Chen et al., 2011). Remarkably, the YYFZ in the Yangjiang Sag, as a transfer zone, accommodates the differential tectonic deformation on both sides (such as F_1 and F_6) during the depositional stage of E_2w . Moreover, the SW-NE-directed

seismic profiles cross YYFZ in the Yunkai Low Uplift show that the listric-shaped or flat-shaped faults and graben-like basins are primarily identified during the early Eocene to the middle Eocene, indicating that faults are mainly derived from the extensional activity.

Many investigations on the post-rift stage faults in the PRMB (Sun et al., 2014; Wu et al., 2014; Zhou et al., 2020) show that the number of subsidiary normal faults related to the sinistral shear of the YYFZ decreased greatly after 13.8 Ma and distributed more concentrated in NWW direction at shallow levels. Besides, the strike-slipping of the YYFZ controlled the distribution of magma activities in the western PRMB from 23.6–10 Ma, considering that nearly all the igneous rocks were distributed along the YYFZ (Li G et al., 2022).

According to the above discussions, we propose a new Cenozoic evolutionary history of the YYFZ (Figure 14). After a long period and significant sinistral motion during the Mesozoic, the YYFZ was reactivated as a transfer zone as a whole during 65–35 Ma. Besides, the principal deformation zone along the NE-trending strike-slip fault controlled the development of a series of Paleogene half-grabens (Cheng et al., 2012; Li et al., 2012; Wang W et al., 2017; Wang et al., 2020; Wang et al., 2021; Zhan et al., 2021). A sinistral shear with a component of extensional deformation from 35 to 16.5 Ma; meanwhile, the sinistral motion was most intense from 21 to 16.5 Ma. After 16.5 Ma, the SCS stopped the seafloor spreading, and the whole area entered a thermal subsidence period (Sun et al., 2008). In this period, the activity of YYFZ maintained the previous sinistral motion and the activity intensity decreased.

5.3 Implication for regional tectonic evolution and geodynamics of SCS

During the Paleogene (ca. 65–55 Ma), the Pacific plate subducted beneath the Eurasian continent and interacted with mantle materials, which probably resulted in slab retreat of the Pacific Plate and subsequently induced the initial rifting in PRMB (Allen et al., 1998; Liu et al., 2017; Ren, 2018; Wang et al., 2020; Wang et al., 2021). During this period, the rifting activities occurred only in the northern depression zone (Wenchang Sag in the Zhu III depression and Lufeng Sag of Zhu I depression), and the study area (the Yangjiang Sag and the Yunkai Low Uplift) was an uplift area. Subsequently, accompanied by the constant slab retreat of the Pacific Plate (Müller et al., 2008), several NE/ENE-trending syn-depositional faults widely developed in the PRMB during the early Eocene to the early middle Eocene (ca. 55–44 Ma), such as Yangjiang Sag, which exhibited listric-shaped or flat-shaped patterns on seismic profiles and dominated graben-like basins (Figure 15A).

During the late Middle Eocene to the Early Miocene (ca. 44–21 Ma), the Indian Plate continued to move northeastwards with a gradually declining plate velocity (Lee and Lawver, 1995;

Formation	Member	Age of the bottom(Ma)	Proposed evolution history of the YYFZ	Principle driving force	Evolutionary stage of the basin		
Quaternary	Q	1.9	sinistral shear with a component of extensional deformation	WNW-ward subduction of the Philippine Sea Plate & the extrusion of the Indochina Block	post-rift stage		
Wanshan	N ₂ w	5.5					
Yuehai	N ₁ y	10.5					
Hanjiang	N ₁ h	16.5	Stronger sinistral shear with a component of weak extensional deformation	Westward subduction of the Pacific Plate & the extrusion of the Indochina Block & the slab-pull system of the proto-SCS	Rift stage		
Zhujiang	N ₁ z	21	sinistral shear with a component of extensional deformation				
Zhuhai	E ₂ z	30					
Enping	E ₂ e	35	Transfer zone(with extensional deformation)				
Wenchang	E ₂ w	66.5					

FIGURE 14
Cenozoic evolution history of the YYFZ (revised from Huang et al., 2015).

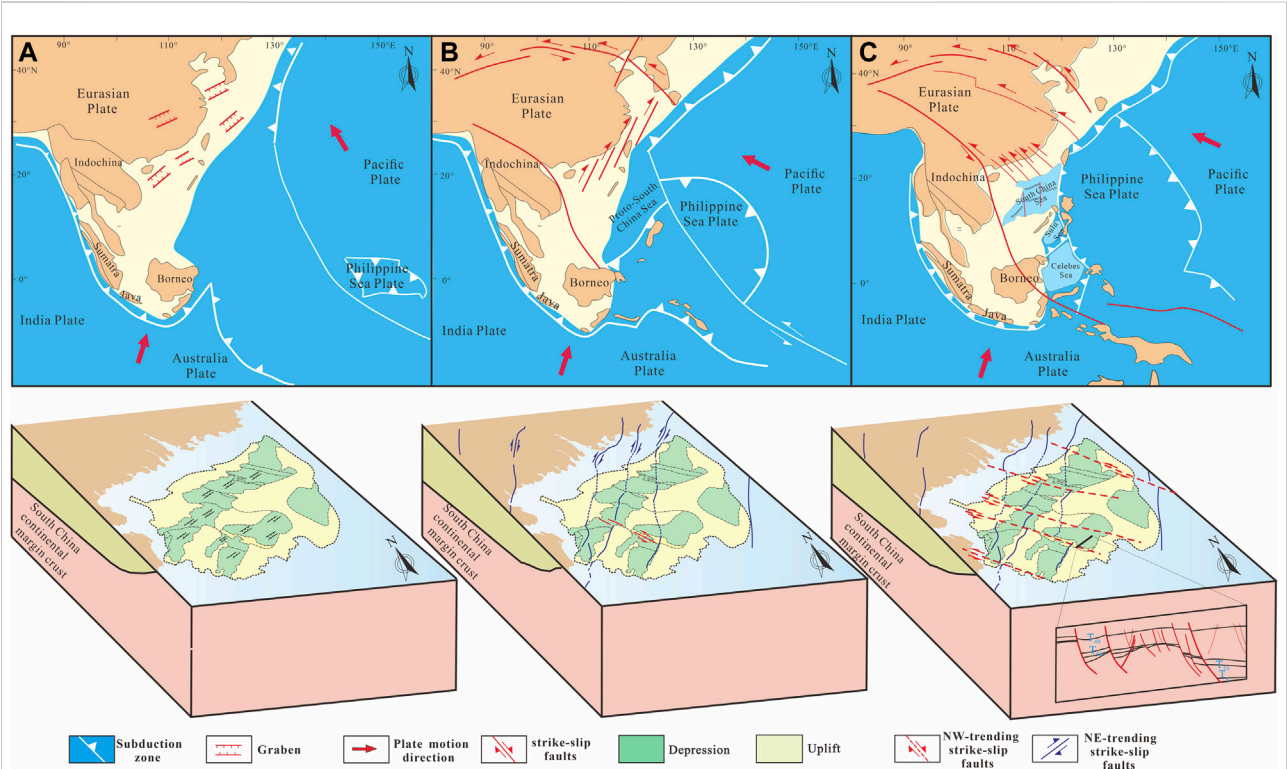


FIGURE 15
Simplified model showing three-stage extension and geodynamics in the Cenozoic PRMB (revised from Hall, 2012; Li S et al., 2022; Wang et al., 2022). (A)-55 Ma; (B)-35 Ma; (C)-20 Ma.

Torsvik et al., 2008). Simultaneously, to the east of the SCS, the subduction direction of the Pacific Plate changed from NNW to WNW, and the subduction velocity of the Pacific Plate to Eurasia increased from 38 mm/yr to 90 mm/yr (Northrup et al., 1995; Copley et al., 2010), to the south of the SCS, the S-directed slab-pull force of the proto-SCS began to affect the continental margin of the SCS. Eventually, the common effect among these three dynamic systems probably leads to a dextral trans-extensional stress field. Therefore, the NE-trending faults changed from normal to right-lateral strike-slip faults and were mainly active in the PRMB (Figure 15B; Wang et al., 2021). Besides, the dextral activity of the NE-trending fault has a

significant impact on the structure evolution of the PRMB (Mu et al., 2022; Zhou et al., 2022). Influenced by the dextral shear activity, the subsidence center of the Yangjiang Sag and the syn-depositional faults were primarily NEE-trending during this stage.

It is generally agreed that the Red River Fault (RRF) experienced an earlier sinistral deformation (e.g., Tapponnier et al., 1990; Leloup et al., 1995) and a later dextral movement (e.g., Clift and Sun, 2006; Sun et al., 2009; Sibuet et al., 2016). However, the timing of sinistral shear deformation is still a controversial topic. Most geologists suggested that the onset of the sinistral shearing activity along the Red River Fault occurred at ~35 Ma (Leloup et al., 1995; Sun et al., 2003; Clift and Sun, 2006; Liang et al., 2007; Zhu M et al., 2009; Zhao Z et al., 2018; Wang et al., 2019). However, some studies implied that the sinistral shearing deformation occurred much later, at 30–21 Ma (e.g., Cao et al., 2011; Liu et al., 2012, 2015; Tang et al., 2013). In this study, we suggest that the sinistral motion of the YYFZ has started since the formation of T_{80} interfaces (about 35 Ma), which is consistent with the initiation time of the RRF proposed by Lei et al. (2021). Thus, we infer that these faults probably have a consistent initiation time (at about 35 Ma).

At this moment, the Pacific Plate subducted beneath the Eurasia Plate with a high speed of 80 mm/yr to the east (Northrup et al., 1995); more importantly, the rapid extrusion of the Indochina block induced by the Indian-Asian collision occurred to the west (Lee and Lawver, 1995; Zhang et al., 2013; Guo et al., 2022; Wang et al., 2022). Besides, it is worth noting that the S-directed slab-pull force of the proto-SCS also plays an important role (Hall, 2013; Madon et al., 2013). Influenced by the joint action among these three dynamic systems and the secondary shear stress field triggered by the NE trending strike-slip fault (Zhou et al., 2022), the NW-trending faults in the northern SCS were reactivated subsequently, creating a series of en echelon arrays of minor faults and flower-like structures at depth (Zhang et al., 2019; Liu Y et al., 2021), where a conspicuous blind fault zone developed, similar to the NW-trending YYFZ in this study. Following the renewed north-south extension in the South China continental margin, the SCS spreading began at 34 Ma or 32 Ma (Li C.-F et al., 2014), resulting in the concentration of extensional stress sharply on the oceanic ridge.

After the Miocene (ca. 21–0 Ma), the SCS began to subduct along the Manila Trench and affect the adjacent tectonic domains (Gao et al., 2018). At the same time, the Philippine Plate was subducting in the WNW direction (Yan et al., 2022), and the Indian Plate continued to move northeastwards. The joint effect resulted in continuous sinistral motion of the NW-trending faults. In contrast, the NE-trending faults were not active or slightly active (Figure 15C). Above all, the three-stage evolution of the faults in the study area is an outcome of the basin evolution, which is closely associated with the movement of surrounding plates.

6 Conclusion

Based on the fault system maps and seismic profiles, we systematically investigated the development characteristics of the fault system in the western PRMB and can make the following conclusions:

1. A series of EW- and WNW-trending faults arose in the E_2 depositional stage, which exhibit horsetail and en echelon structures in the map view and flower-like or Y-shaped structures in the profile. Together with the response of depocenters in the Yangjiang Sag adjacent to the YYFZ, we suggest that the YYFZ have a consistent initiation time (i.e., at about 35 Ma).

2. Combined with the Cenozoic evolution of the PRMB, the Cenozoic activity of the YYFZ includes the following three stages: 1) 65–35 Ma, the YYFZ was a first-order transfer zone accommodating significant intraplate extensional deformation; 2) 35–16.5 Ma, the YYFZ displays as a sinistral strike-slip fault zone; 3) after 16.5 Ma, the activity of YYFZ maintained the previous sinistral motion and tended to be weakened.

3. The evolution of the PRMB in the late stage is affected by strike-slip reactivation along the YYFZ. This reactivation may be related to the joint action among the rapid extrusion of the Indochina block induced by the Indian-Asian collision to the west, the subduction of the Pacific Plate beneath the Asia continent to the east, and the slab-pull system of the proto-SCS to the south.

Data availability statement

The original contributions presented in the study are included in the article/supplementary material, further inquiries can be directed to the corresponding authors.

Author contributions

HZ processed the data, wrote the manuscript and designed the figures. GW and YS conceptualized the study and performed the analysis of the manuscript. GP, XD and DZ provided data sources and helped revise the manuscript. PW, JZ, and SL supervised the study. SL, PW, and GW acquired the funding.

Funding

This work was Financially supported by the Marine S&T Fund of Shandong Province for Pilot National Laboratory for Marine Science and Technology (Qingdao) (No. 2022QNLM050302), National Natural Science Foundation of China (Grant Nos. 42121005, 91958214, 42072235, 42002220), Shandong Provincial Natural Science Foundation (No. ZR2021ZD09), 111 Project (Grant No. B20048).

Conflict of interest

Authors GP, XD and DZ were employed by the Shenzhen Branch, CNOOC China Limited.

The remaining authors declare that the research was conducted in the absence of any commercial or financial relationships that could be construed as a potential conflict of interest.

References

- Allen, M. B., Macdonald, D. I. M., Xun, Z., Vincent, S. J., and Brouet-Menzies, C. (1998). Transtensional deformation in the evolution of the Bohai Basin, northern China. *SP 135*, 215–229. doi:10.1144/GSL.SP.1998.135.01.14
- Bellahsen, N., and Daniel, J. M. (2005). Fault reactivation control on normal fault growth: An experimental study. *J. Struct. Geol.* 27, 769–780. doi:10.1016/j.jsg.2004.12.003
- Cai, G., Zhang, X., Peng, G., Wu, J., Liu, B., Bai, H., et al. (2021). Neogene volcanism and tectonics along the yangjing-yitong'an-sha Fault Zone in the northern south China sea margin. *Geotect. Metallogenia* 45, 40–52. doi:10.16539/j.dgzzyckx.2021.01.004
- Camanni, G., and Ye, Q. (2022). The significance of fault reactivation on the Wilson cycle undergone by the northern South China Sea area in the last 60 Myr. *Earth-Science Rev.* 225, 103893. doi:10.1016/j.earscirev.2021.103893
- Cao, J., Xia, S., Sun, J., and Xu, H. (2014). Comparison of fault structure characteristics in the northern Pearl River Mouth Basin and its geological implication. *Prog. Geophys.* 29, 2364–2369. doi:10.6038/pg20140555
- Cao, S., Neubauer, F., Liu, J., Genser, J., and Leiss, B. (2011). Exhumation of the Diancang Shan metamorphic complex along the Ailao Shan-Red River belt, southwestern yunnan, China: Evidence from 40Ar/39Ar thermochronology. *J. Asian Earth Sci.* 42, 525–550. doi:10.1016/j.jseas.2011.04.017
- Chen, F., Wang, X., and Chen, Z. (2011). Analysis of transform structures in extensional fault depressions. *Geoscience* 25, 617–625. doi:10.3969/j.issn.1000-8527.2011.04.001
- Chen, H., Wu, X., Zhou, D., Wang, W., and Hao, H. (2005). Meso-cenozoic faults in Zhujiang River Mouth basin and their geodynamic background. *J. Trop. Oceanogr.* 24, 52–61. doi:10.3969/j.issn.1009-5470.2005.02.007
- Cheng, S., Li, S., Suo, Y., Liu, X., Yu, S., Dai, L., et al. (2012). Cenozoic tectonics and dynamics of basin groups of the northern South China Sea. *Mar. Geol. Quat. Geol.* 32, 79–93. doi:10.3724/SP.J.1140.2012.06079
- Cheng, X., Zhang, Q., Yu, X., Du, W., Liu, R., Bian, Q., et al. (2017). Strike-slip fault network of the Huangshi structure, SW Qaidam Basin: Insights from surface fractures and seismic data. *J. Struct. Geol.* 94, 1–12. doi:10.1016/j.jsg.2016.10.011
- Clift, P. D., and Sun, Z. (2006). The sedimentary and tectonic evolution of the Yinggehai-Song Hong basin and the southern Hainan margin, South China Sea: Implications for Tibetan uplift and monsoon intensification. *J. Geophys. Res.* 111, 1–28. doi:10.1029/2005JB004048
- Copley, A., Avouac, J.-P., and Royer, J.-Y. (2010). India-Asia collision and the Cenozoic slowdown of the Indian plate: Implications for the forces driving plate motions. *J. Geophys. Res.* 115, B03410. doi:10.1029/2009JB006634
- Fu, C., Li, S., Li, S., and Xu, J. (2021). Spatial and temporal variability of sediment infilling and episodic rifting in the north Pearl River Mouth basin, south China sea. *J. Asian Earth Sci.* 211, 104702. doi:10.1016/j.jseas.2021.104702
- Gao, J., Wu, S., Yao, Y., Chen, C., Song, T., Wang, J., et al. (2018). Tectonic deformation and fine structure of the frontal accretionary wedge, northern Manila subduction zone. *Chin. J. Geophys.* 61, 2845–2858. doi:10.6038/cjg2018L0461
- Ge, J., Zhao, X., Tan, M., Zhuo, H., Liu, C., and Jones, B. G. (2022). Sequence stratigraphy and depositional evolution of the north-eastern shelf (33.9–10.5 Ma) of the Pearl River Mouth basin, south China sea. *Mar. Petroleum Geol.* 141, 105697. doi:10.1016/j.marpetgeo.2022.105697
- Ge, J., Zhu, X., Zhao, X., Liao, J., Ma, B., and Jones, B. G. (2020). Tectono-sedimentary signature of the second rift phase in multiphase rifts: A case study in the Lufeng depression (38–33.9 Ma), Pearl River Mouth basin, south China sea. *Mar. Petroleum Geol.* 114, 104218. doi:10.1016/j.marpetgeo.2020.104218
- Ghalayini, R., Daniel, J.-M., Homberg, C., Nader, F. H., and Comstock, J. E. (2014). Impact of Cenozoic strike-slip tectonics on the evolution of the northern Levant Basin (offshore Lebanon): Cenozoic tectonics of the Levant basin. *Tectonics* 33, 2121–2142. doi:10.1002/2014TC003574
- Graham, S., McCloy, C., Hitzman, M., Ward, R., and Turner, R. (1984). Basin evolution during change from convergent to transform continental margin in central California. *Am. Assoc. Pet. Geol. Bull.* 68, 233–249. doi:10.1306/AD46A03-16F7-11D7-8645000102C1865D
- Guo, L. L., Li, S. Z., Zhao, S. J., Zhang, G. X., Suo, Y. H., Liu, H., et al. (2016). Final breakup of continental block and opening of oceanic lithosphere: Insights from deep crustal structure and tectonic evolution of the ocean-continent transition zone in the northern south China sea: OCT zone in the northern SCS. *Geol. J.* 51, 318–330. doi:10.1002/gj.2842
- Guo, X., Li, C., Gao, R., Li, S., Xu, X., Lu, Z., et al. (2022). The India-Eurasia convergence system: Late Oligocene to early Miocene passive roof thrusting driven by deep-rooted duplex stacking. *Geosystems Geoenvironment* 1, 100006. doi:10.1016/j.geogeo.2021.09.005
- Hall, R. (2012). Late Jurassic–Cenozoic reconstructions of the Indonesian region and the Indian Ocean. *Tectonophysics* 570–571, 1–41. doi:10.1016/j.tecto.2012.04.021
- Hall, R. (2013). Contraction and extension in northern Borneo driven by subduction rollback. *J. Asian Earth Sci.* 76, 399–411. doi:10.1016/j.jseas.2013.04.010
- Han, X., Deng, S., Tang, L., and Cao, Z. (2017). Geometry, kinematics and displacement characteristics of strike-slip faults in the northern slope of Tazhong uplift in Tarim basin: A study based on 3D seismic data. *Mar. Petroleum Geol.* 88, 410–427. doi:10.1016/j.marpetgeo.2017.08.033
- Hao, S., Mei, L., Shi, H., Paton, D., Mortimer, E., Du, J., et al. (2021). Rift migration and transition during multiphase rifting: Insights from the proximal domain, northern South China Sea rifted margin. *Mar. Petroleum Geol.* 123, 104729. doi:10.1016/j.marpetgeo.2020.104729
- Harding, T. P. (1990). Identification of wrench faults using subsurface structural data criteria and pitfalls. *Am. Assoc. Pet. Geol. Bull.* 74 (10), 1590e1609. doi:10.1306/OC9B2533-1710-11D7-8645000102C1865D
- Harding, T. P. (1985). Seismic characteristics and identification of negative flower structures, positive flower structures, and positive structural inversion. *Am. Assoc. Pet. Geol. Bull.* 69 (4), 582e600. doi:10.1306/AD462538-16F7-11D7-8645000102C1865D
- He, Y., Mei, L., Shi, H., Shu, Y., and Chen, Y. (2019). Structural characteristics and genetic model of the low-angle fault depression: a case in Enping Depression of Pearl River Mouth Basin. *Mar. Orig. Pet. Geol.* 23 (3), 73–81. doi:10.3969/j.issn.1672-9854.2018.03.008
- Ho-Shing, Y. (1990). The Pearl River Mouth basin: a rift basin and its geodynamic relationship with the southeastern Eurasian margin. *Tectonophysics* 183, 177–186. doi:10.1016/0040-1951(90)90415-5
- Hou, D., Pang, X., Xiao, J., Zhang, J., Shi, H., Wang, J., et al. (2008). Geological and Geochemical evidence on the identification of natural gas migration through fault system, Baiyun sag, Pearl River Mouth basin, China. *Earth Sci. Front.* 15, 81–87. doi:10.1016/S1872-5791(08)60041-X
- Hu, D., Zhou, D., Wu, X., He, M., Pang, X., and Wang, Y. (2009). Crustal structure and extension from slope to deepsea basin in the northern South China Sea. *J. Earth Sci.* 20, 27–37. doi:10.1007/s12583-009-0003-6
- Huang, K., Zhong, G., He, M., Liu, L., Wu, Z., and Liu, X. (2018). Growth and linkage of a complex oblique-slip fault zone in the Pearl River Mouth basin, northern south China sea. *J. Struct. Geol.* 117, 27–43. doi:10.1016/j.jsg.2018.09.002
- Huang, L., and Liu, C. (2014). Evolutionary characteristics of the sags to the east of Tan–Lu Fault Zone, Bohai Bay Basin (China): Implications for hydrocarbon

exploration and regional tectonic evolution. *J. Asian Earth Sci.* 79, 275–287. doi:10.1016/j.jseas.2013.09.031

Huang, L., Liu, C., and Kusky, T. M. (2015). Cenozoic evolution of the tan–Lu Fault Zone (east China)—constraints from seismic data. *Gondwana Res.* 28, 1079–1095. doi:10.1016/j.gr.2014.09.005

Hui, G., Zhang, P., Li, Z., Wang, W., Hu, L., Li, G., et al. (2022). Opening of the South China sea marginal basin: Insights from the tectonic evolution of the ENE-striking littoral Fault Zone. *Mar. Petroleum Geol.* 145, 105854. doi:10.1016/j.marpetgeo.2022.105854

Lee, T.-Y., and Lawver, L. A. (1995). Cenozoic plate reconstruction of the South China Sea region. *Tectonophysics* 235, 149–180. doi:10.1016/0040-1951(94)90022-1

Lei, C., Ren, J., Pei, J., Liu, B., Zuo, X., Liu, J., et al. (2021). Tectonics of the offshore Red River Fault recorded in the junction of the yinggehai and Qiongdongnan basins. *Sci. China Earth Sci.* 64, 1893–1908. doi:10.1007/s11430-020-9796-2

Leloup, P. H., Lacassin, R., Tapponnier, P., Schärer, U., Zhong, D., Liu, X., et al. (1995). The Ailao Shan-Red River shear zone (Yunnan, China), Tertiary transform boundary of Indochina. *Tectonophysics* 251, 3–84. doi:10.1016/0040-1951(95)00070-4

Li, C.-F., Xu, X., Lin, J., Sun, Z., Zhu, J., Yao, Y., et al. (2014). Ages and magnetic structures of the South China Sea constrained by deep tow magnetic surveys and IODP Expedition 349. *Geochem. Geophys. Geosyst.* 15, 4958–4983. doi:10.1002/2014GC005567

Li, G., Mei, L., Pang, X., Zheng, J., Ye, Q., and Hao, S. (2022). Magmatism within the northern margin of the South China Sea during the post-rift stage: An overview, and new insights into the geodynamics. *Earth-Science Rev.* 225, 103917. doi:10.1016/j.earscirev.2022.103917

Li, H., Chen, S., Zhang, Y., Niu, C., Zhang, K., Ye, Q., et al. (2014). Faults in the Zhu III depression of Pearl River Mouth basin and their control over hydrocarbon accumulation. *Mar. Geol. Quat. Geol.* 34, 115–124. doi:10.3724/SP.J.1140.2014.03115

Li, S., Suo, Y., Liu, X., Dai, L., Yu, S., Zhao, S., et al. (2012). Basin structural pattern and tectonic models of the South China sea: Problems, advances and controversies. *Mar. Geol. Quat. Geol.* 32, 35–53. doi:10.3724/SP.J.1140.2012.06035

Li, S., Suo, Y., Zhou, J., Wang, G., Li, X., Jiang, Z., et al. (2022). Tectonic evolution of the South China ocean-continent connection zone: Transition and mechanism of the Tethyan to the Pacific tectonic domains. *J. Geomechanics* 28. doi:10.12090/j.issn.1006-6616.20222809

Li, Y., Zhu, R., Liu, H., Qiu, X., and Huang, H. (2019). The cenozoic activities of yangjiang-yitongdong fault: Insights from analysis of the tectonic characteristics and evolution processes in Western Zhujiang (Pearl) River Mouth basin. *Acta Oceanol. Sin.* 38, 87–101. doi:10.1007/s13131-019-1477-x

Liang, H., Campbell, I. H., Allen, C. M., Sun, W., Yu, H., Xie, Y., et al. (2007). The Age of the Potassic Alkaline igneous rocks along the Ailao Shan-Red River shear zone: Implications for the onset Age of left-lateral shearing. *J. Geol.* 115, 231–242. doi:10.1086/510801

Liu, H., Mei, L., Shi, H., Shu, Y., Tian, W., and Ye, Q. (2018). Rift style controlled by basement attribute and regional stress in Zhu depression, Pearl River Mouth Basin. *Earth Sci.* 1–17. doi:10.3799/dqkx.2018.576

Liu, J., Chen, X., Wu, W., Tang, Y., Tran, M.-D., Nguyen, Q.-L., et al. (2015). New tectono-geochronological constraints on timing of shearing along the Ailao Shan-Red River shear zone: Implications for Genesis of Ailao Shan gold mineralization. *J. Asian Earth Sci.* 103, 70–86. doi:10.1016/j.jseas.2014.11.006

Liu, J., Tang, Y., Tran, M.-D., Cao, S., Zhao, L., Zhang, Z., et al. (2012). The nature of the Ailao Shan-Red River (ASRR) shear zone: Constraints from structural, microstructural and fabric analyses of metamorphic rocks from the Diancang Shan, Ailao Shan and Day Nui Con Voi massifs. *J. Asian Earth Sci.* 47, 231–251. doi:10.1016/j.jseas.2011.10.020

Liu, S., Gurnis, M., Ma, P., and Zhang, B. (2017). Reconstruction of northeast Asian deformation integrated with Western Pacific plate subduction since 200 Ma. *Earth-Science Rev.* 175, 114–142. doi:10.1016/j.earscirev.2017.10.012

Liu, X., Wu, J., Zhu, D., Suo, Y., Zhou, J., Wang, P., et al. (2021). Superimposition of strike-slip faults and pull-apart basins in the Pearl River Mouth basin: A case study from the eastern Yangjiang sag. *Geotect. Metallogenia* 45, 6–19. doi:10.16539/j.ddgyckx.2021.01.002

Liu, Y., Wu, Z., Liu, L., Yan, S., Hu, L., Ping, M., et al. (2021). Cenozoic structure and tectonics of north subbasins in Beibu Gulf basin, northern south China sea. *Tectonophysics* 812, 228912. doi:10.1016/j.tecto.2021.228912

Liu, Z., Wang, S., Yin, B., Zhang, Y., and Xiao, L. (2013). Nephrology in China. *Nat. Rev. Nephrol.* 35, 523–528. doi:10.1038/nrneph.2013.146

Lu, B., Wang, P., Zhang, G., Zhang, B., Sun, X., Li, W., et al. (2011). Basement structures of an epicontinental basin in the northern South China Sea and their significance in petroleum prospect. *Acta Pet. Sin.* 32, 580–587. doi:10.1007/s12182-011-0123-3

Lv, C., Zhang, G., and Yang, D. (2017). Differential structure and dynamic mechanism of Wenchang Formation in the Zhu depression of the Pearl River Mouth basin. *Earth Sci. Front.* 24, 333–341. doi:10.13745/j.esf.yx.2016-11-56

Ma, B., Qi, J., Chen, W., and Zhao, M. (2020). Fault interaction and evolution during two-phase rifting in the Xijiang sag, Pearl River Mouth basin, northern south China sea. *Geol. J.* 55, 1128–1147. doi:10.1002/gj.3474

Ma, M., Liu, C., Qi, J., Zhang, D., Zhang, S., Wang, J., et al. (2020). Cenozoic subsidence history of the Pearl River Mouth basin, northern south China sea. *Geol. J.* 55, 750–770. doi:10.1002/gj.3439

Madon, M., Kim, C. L., and Wong, R. (2013). The structure and stratigraphy of deepwater Sarawak, Malaysia: Implications for tectonic evolution. *J. Asian Earth Sci.* 76, 312–333. doi:10.1016/j.jseas.2013.04.040

Mcclay, K. (2001). Analog models of restraining stopovers in strike-slip fault systems. *AAPG Bull.* 85, 233–260. doi:10.1016/S0378-7753(00)00605-4

Mu, D., Peng, G., Zhu, D., Li, S., Suo, Y., Zhan, H., et al. (2022). Structure and formation mechanism of the Pearl River Mouth basin: Insights from multi-phase strike-slip motions in the Yangjiang sag, SE China. *J. Asian Earth Sci.* 226, 105081. doi:10.1016/j.jseas.2022.105081

Müller, R. D., Sdrolias, M., Gaina, C., and Roest, W. R. (2008). Age, spreading rates, and spreading asymmetry of the world's ocean crust: Digital Models of the World's Ocean Crust. *Geochem. Geophys. Geosyst.* 9, Q04006. doi:10.1029/2007GC001743

Northrup, C. J., Royden, L. H., and Burchfiel, B. C. (1995). Motion of the Pacific plate relative to Eurasia and its potential relation to Cenozoic extension along the eastern margin of Eurasia. *Geol.* 23, 719. doi:10.1130/0091-7613(1995)023<0719: motppr>2.3.co;2

Ren, J. (2018). Genetic dynamics of China offshore Cenozoic basins. *Earth Sci.* 43, 3337–3361. doi:10.3799/dqkx.2018.330

Romeo, I., Capote, R., and Anguita, F. (2005). Tectonic and kinematic study of a strike-slip zone along the southern margin of Central Onda Regio, Venus: Geodynamical implications for crustal plateaux formation and evolution. *Icarus* 175, 320–334. doi:10.1016/j.icarus.2004.11.007

Shen, M., Shan, X., Hao, G., Liu, P., Jia, P., Xu, C., et al. (2022). Structural difference and control mechanism of early Cenozoic depression in Yangjiang east sag, Pearl River Mouth Basin. *Earth Sci.* 1–23. doi:10.3799/dqkx.2022.078

Shi, H., Du, J., Mei, L., Zhang, X., Hao, S., Liu, P., et al. (2020). Huizhou Movement and its significance in Pearl River Mouth Basin, China. *Pet. Explor. Dev.* 47, 483–498. doi:10.1016/S1876-3804(20)60067-2

Sibuet, J.-C., Yeh, Y.-C., and Lee, C.-S. (2016). Geodynamics of the South China sea. *Tectonophysics* 692, 98–119. doi:10.1016/j.tecto.2016.02.022

Sun, W. (2016). Initiation and evolution of the South China sea: An overview. *Acta Geochim.* 35, 215–225. doi:10.1007/s11631-016-0110-x

Sun, Z., Xu, Z., Sun, L., Pang, X., Yan, C., Li, Y., et al. (2014). The mechanism of post-rift fault activities in Baiyun sag, Pearl River Mouth basin. *J. Asian Earth Sci.* 89, 76–87. doi:10.1016/j.jseas.2014.02.018

Sun, Z., Zhong, Z., Zhou, D., Pang, X., Huang, C., Chen, C., et al. (2008). Dynamics analysis of the Baiyun sag in the Pearl River Mouth basin, north of the South China sea. *Acta Geol. Sin.* 82, 73–83. doi:10.1111/j.1755-6724.2008.tb00326.x

Sun, Z., Zhou, D., Wu, S., Zhong, Z., Jiang, J., Fan, H., et al. (2009). Patterns and dynamics of rifting on passive continental margin from shelf to slope of the northern south China sea: Evidence from 3D analogue modeling. *J. Earth Sci.* 20, 136–146. doi:10.1007/s12583-009-0011-6

Sun, Z., Zhou, D., Zhong, Z., Zeng, Z., and Wu, S. (2003). Experimental evidence for the dynamics of the formation of the Yinggehai basin, NW South China Sea. *Tectonophysics* 372, 41–58. doi:10.1016/S0040-1951(03)00230-0

Suo, Y., Li, S., Peng, G., Du, X., Zhou, J., Wang, P., et al. (2022). Cenozoic basement-involved rifting of the northern South China Sea margin. *Gondwana Res.* doi:10.1016/j.gr.2022.02.017

Tang, X., Yang, S., and Hu, S. (2020). Provenance of the Paleogene sediments in the Pearl River Mouth basin, northern south China sea: Insights from zircon U-Pb and fission track double dating. *J. Asian Earth Sci.* 200, 104494. doi:10.1016/j.jseas.2020.104494

Tang, Y., Liu, J., Tran, M.-D., Song, Z., Wu, W., Zhang, Z., et al. (2013). Timing of left-lateral shearing along the Ailao Shan-Red River shear zone: Constraints from zircon U-Pb ages from granitic rocks in the shear zone along the Ailao Shan Range, western Yunnan, China. *Int. J. Earth Sci.* 102, 605–626. doi:10.1007/s00531-012-0831-y

Tapponnier, P., Lacassin, R., Leloup, P. H., Schärer, U., Dalai, Z., Haiwei, W., et al. (1990). The Ailao Shan/Red River metamorphic belt: Tertiary left-lateral shear between Indochina and south China. *Nature* 343, 431–437. doi:10.1038/343431a0

- Torsvik, T. H., Müller, R. D., Van der Voo, R., Steinberger, B., and Gaina, C. (2008). Global plate motion frames: Toward a unified model. *Rev. Geophys.* 46, RG3004. doi:10.1029/2007RG000227
- Wang, H., Cao, S., Li, J., Cheng, X., Lv, M., Manfred, B., et al. (2019). Cenozoic multi-metamorphism, shear deformation and geological significance of Ailaoshan high-grade metamorphic complex, Western Yunnan, China. *Acta Petrol. Sin.* 35, 2573–2596. doi:10.18654/1000-0569/2019.08.15
- Wang, J., Luan, X., He, B., Ran, W., Wei, X., Hu, Q., et al. (2021a). Study on the structural characteristics and dynamic mechanism of faults in the Kaiping sag of Zhujiang River Mouth basin. *Acta Oceanol. Sin.* 43, 41–53. doi:10.12284/hyxb2021082
- Wang, J., Luan, X., He, B., Ran, W., Zhang, H., and Yang, J. (2021b). Characteristics and genesis of faults in southwestern Pearl River Mouth basin, northern south China sea. *Earth Sci.* 46, 916–928. doi:10.3799/dqkx.2020.381
- Wang, J., Pang, X., Tang, D., Liu, B., and Xu, D. (2013). Transtensional tectonism and its effects on the distribution of sandbodies in the Paleogene Baiyun sag, Pearl River Mouth basin, China. *Mar. Geophys. Res.* 34, 195–207. doi:10.1007/s11001-013-9200-x
- Wang, P., Li, S., Guo, L., Zhao, S., Li, X., Wang, Y., et al. (2017). Opening of the South China sea (SCS): A joint effect of dextral strike-slip pull-apart and proto-SCS slab pull. *Earth Sci. Front.* 24, 294–319. doi:10.13745/j.esf.yx.2017-4-3
- Wang, P., Li, S., Suo, Y., Guo, L., Santosh, M., Li, X., et al. (2021). Structural and kinematic analysis of cenozoic rift basins in south China sea: A synthesis. *Earth-Science Rev.* 216, 103522. doi:10.1016/j.earscirev.2021.103522
- Wang, P., Li, S., Suo, Y., Guo, L., Wang, G., Hui, G., et al. (2020). Plate tectonic control on the formation and tectonic migration of Cenozoic basins in northern margin of the South China Sea. *Geosci. Front.* 11, 1231–1251. doi:10.1016/j.gsf.2019.10.009
- Wang, P., Suo, Y., Peng, G., Li, S., Du, X., Cao, X., et al. (2022). Three-stage extension in the cenozoic Pearl River Mouth basin triggering onset of the South China sea spreading. *Gondwana Res.* doi:10.1016/j.gr.2022.05.023
- Wang, T. K., Chen, M.-K., Lee, C.-S., and Xia, K. (2006). Seismic imaging of the transitional crust across the northeastern margin of the South China Sea. *Tectonophysics* 412, 237–254. doi:10.1016/j.tecto.2005.10.039
- Wang, W., Ye, J., Bidgoli, T., Yang, X., Shi, H., and Shu, Y. (2017). Using Detrital zircon Geochronology to constrain Paleogene provenance and its relationship to rifting in the Zhu 1 depression, Pearl River Mouth basin, south China sea. *Geochem. Geophys. Geosyst.* 18, 3976–3999. doi:10.1002/2017GC007110
- Wang, W., Zhou, W., Shan, X., and Liu, Y. (2015). Characteristics of hidden fault zone and its significance in geology in sedimentary basin. *J. Central South Univ.* 46, 2236–2243. doi:10.11817/j.issn.1672-7207.2015.06.035
- Wang, X., Yu, S., Gong, Y., Li, S., Liu, X., Ma, Y., et al. (2014). Extension of NE-trending faults in south China to northern south China sea continental shelf. *Geotect. Metallogenia* 38, 557–570. doi:10.16539/j.dgzycx.2014.03.005
- Wei, X., Ruan, A., Zhao, M., Qiu, X., Li, J., Zhu, J., et al. (2011). A wide-angle obs profile across the Dongsha uplift and chaoshan depression in the mid-northern South China sea. *China. J. Geophys.* 54, 3325–3335. doi:10.3969/j.issn.0001-5733.2011.12.030
- Wu, S., Gao, J., Zhao, S., Lüdmann, T., Chen, D., and Spence, G. (2014). Post-rift uplift and focused fluid flow in the passive margin of northern South China Sea. *Tectonophysics* 615–616, 27–39. doi:10.1016/j.tecto.2013.12.013
- Xie, H., Zhou, D., Li, Y., Pang, X., Li, P., Chen, G., et al. (2014). Cenozoic tectonic subsidence in deepwater sags in the Pearl River Mouth basin, northern south China sea. *Tectonophysics* 615–616, 182–198. doi:10.1016/j.tecto.2014.01.010
- Xu, J., Ben-Avraham, Z., Kelty, T., and Yu, H.-S. (2014). Origin of marginal basins of the NW Pacific and their plate tectonic reconstructions. *Earth-Science Rev.* 130, 154–196. doi:10.1016/j.earscirev.2013.10.002
- Xu, J., and Zhang, L. (2000). Genesis of cenozoic basins in northwest Pacific margin (2): Linked dextral pull apart basin system. *Oil Gas Geol.* 03, 185–190. doi:10.3321/j.issn:0253-9985.2000.03.001
- Yan, Q., Shi, X., Yuan, L., Yan, S., and Liu, Z. (2022). Tectono-magmatic evolution of the Philippine sea plate: A review. *Geosystems Geoenvironment* 1, 100018. doi:10.1016/j.geogeo.2021.100018
- Ye, Q., Mei, L., Shi, H., Du, J., Deng, P., Shu, Y., et al. (2020). The influence of pre-existing basement faults on the cenozoic structure and evolution of the proximal domain, northern south China sea rifted margin. *Tectonics* 39. doi:10.1029/2019TC005845
- Ye, Q., Mei, L., Shi, H., Shu, Y., Camanni, G., and Wu, J. (2018). A low-angle normal fault and basement structures within the Enping sag, Pearl River Mouth basin: Insights into late Mesozoic to early cenozoic tectonic evolution of the South China sea area. *Tectonophysics* 731, 1–16. doi:10.1016/j.tecto.2018.03.003
- Yu, C., Han, Q., Dong, D., Chen, S., and Yan, P. (2008). Estimation of cenozoic dextral strike-slip displacement of tan-Lu fault in laizhou Bay. *Nat. Gas. Geosci.* 19, 62–69. doi:10.11764/j.issn.1672-1926.2008.01.62
- Yu, Y., Zhang, T., Zhang, Z., Zhang, G., Zeng, J., Yang, H., et al. (2021). Structural characteristics and its Significances on hydrocarbon accumulation in the Yunkai low uplift, Pearl River Mouth basin. *Acta Geol. sinica- Engl. Ed.* 95, 21–29. doi:10.1111/1755-6724.14622
- Zhan, H., Cai, G., Zhang, Z., Wang, G., Li, Y., Suo, Y., et al. (2021). Paleogene Fault activity and basin controlling characteristics in the northern south China sea margin—a case study of the eastern Yangjiang sag. *Geotect. Metallogenia* 45, 20–39. doi:10.16539/j.dgzycx.2021.01.003
- Zhang, C., Wang, Z., Sun, Z., Sun, Z., Liu, J., and Wang, Z. (2013). Structural differences between the Western and eastern Qiongdongnan basin: Evidence of Indochina block extrusion and south China sea seafloor spreading. *Mar. Geophys. Res.* 34, 309–323. doi:10.1007/s11001-013-9187-3
- Zhang, G., Qu, H., Jia, Q., Zhang, L., Yang, B., Chen, S., et al. (2021). Passive continental margin segmentation of the marginal seas and its effect on hydrocarbon accumulation: A case study of the northern continental margin in south China sea. *Mar. Petroleum Geol.* 123, 104741. doi:10.1016/j.marpetgeo.2020.104741
- Zhang, Y., Qi, J., and Wu, J. (2019). Cenozoic faults systems and its geodynamics of the continental margin basins in the northern of South China Sea. *Earth Sci.* 44, 603–625. doi:10.3799/dqkx.2018.542
- Zhao, F., Alves, T. M., Xia, S., Li, W., Wang, L., Mi, L., et al. (2020). Along-strike segmentation of the South China Sea margin imposed by inherited pre-rift basement structures. *Earth Planet. Sci. Lett.* 530, 115862. doi:10.1016/j.epsl.2019.115862
- Zhao, Y., Ren, J., Pang, X., Yang, L., and Zheng, J. (2018). Structural style, formation of low angle normal fault and its controls on the evolution of Baiyun Rift, northern margin of the South China Sea. *Mar. Petroleum Geol.* 89, 687–700. doi:10.1016/j.marpetgeo.2017.11.001
- Zhao, Z., Sun, Z., Sun, L., Wang, Z., and Sun, Z. (2018). Cenozoic tectonic subsidence in the Qiongdongnan basin, northern south China sea. *Basin Res.* 30, 269–288. doi:10.1111/bre.12220
- Zhong, Z., Shi, H., Zhu, M., Pang, X., He, M., Zhao, Z., et al. (2014). A discussion on the tectonic-stratigraphic framework and its origin mechanism in Pearl River Mouth Basin. *China Offshore Oil Gas* 26, 20–29.
- Zhou, J., Li, S., Suo, Y., Zhang, L., Du, X., Cao, X., et al. (2022). NE-Trending transtensional faulting in the Pearl River Mouth basin of the northern south China sea margin. *Gondwana Res.* doi:10.1016/j.gr.2022.02.016
- Zhou, D., Wang, W., Wang, J., Pang, X., Cai, D., and Sun, Z. (2006). Mesozoic subduction-accretion zone in northeastern south China Sea inferred from geophysical interpretations. *Sci. China Ser. D* 49, 471–482. doi:10.1007/s11430-006-0471-9
- Zhou, W., Zhuo, H., Wang, Y., Xu, Q., and Li, D. (2020). Post-rift submarine volcanic complexes and fault activities in the Baiyun sag, Pearl River Mouth basin: New insights into the breakup sequence of the northern south China sea. *Mar. Geol.* 430, 106338. doi:10.1016/j.margeo.2020.106338
- Zhou, Z., Mei, L., Liu, J., Zheng, J., Chen, L., and Hao, S. (2018). Continentward-dipping detachment fault system and asymmetric rift structure of the Baiyun Sag, northern South China Sea. *Tectonophysics* 726, 121–136. doi:10.1016/j.tecto.2018.02.002
- Zhou, Z., Mei, L., Shi, H., and Shu, Y. (2019). Evolution of low-angle normal faults in the Enping sag, the northern south China sea: Lateral growth and vertical rotation. *J. Earth Sci.* 30, 1326–1340. doi:10.1007/s12583-019-0899-4
- Zhu, M., Graham, S., and McHargue, T. (2009). The Red River Fault zone in the yinggehai basin, south China sea. *Tectonophysics* 476, 397–417. doi:10.1016/j.tecto.2009.06.015
- Zhu, W., Huang, B., Mi, L., Wilkins, R. W. T., Fu, N., and Xiao, X. (2009). Geochemistry, origin, and deep-water exploration potential of natural gases in the Pearl River Mouth and Qiongdongnan basins, South China Sea. *Bulletin* 93, 741–761. doi:10.1306/02170908099
- Zhu, W., Shi, H., Huang, B., Zhong, K., and Huang, Y. (2021). Geology and geochemistry of large gas fields in the deepwater areas, continental margin basins of northern South China Sea. *Mar. Petroleum Geol.* 126, 104901. doi:10.1016/j.marpetgeo.2021.104901
- Zhu, W., Xie, X., Wang, Z., Zhang, D., Zhang, C., Cao, L., et al. (2017). New insights on the origin of the basement of the Xisha uplift, south China sea. *Sci. China Earth Sci.* 60, 2214–2222. doi:10.1007/s11430-017-9089-9



OPEN ACCESS

EDITED BY

Zhigang Li,
School of Earth Sciences and
Engineering, Sun Yat-sen University,
Zhuhai Campus, China

REVIEWED BY

Shang Xu,
China University of Petroleum, Huadong,
China
Yinhui Zuo,
Chengdu University of Technology,
China
Shaoze Zhao,
Chengdu University of Technology,
China

*CORRESPONDENCE

Leli Cheng,
✉ chengleli@yangtzeu.edu.cn

SPECIALTY SECTION

This article was submitted
to Marine Geoscience,
a section of the journal
Frontiers in Earth Science

RECEIVED 07 December 2022

ACCEPTED 06 February 2023

PUBLISHED 17 February 2023

CITATION

Xiong T, Cheng L, Guo D, Guan L, Jiang Q,
Zhangming H, Yin S and Chen G (2023),
Overpressure characteristics and
geological origin of the paleogene in
Baiyun Sag, Pearl River Mouth Basin.
Front. Earth Sci. 11:1118443.
doi: 10.3389/feart.2023.1118443

COPYRIGHT

© 2023 Xiong, Cheng, Guo, Guan, Jiang,
Zhangming, Yin and Chen. This is an
open-access article distributed under the
terms of the [Creative Commons
Attribution License \(CC BY\)](https://creativecommons.org/licenses/by/4.0/). The use,
distribution or reproduction in other
forums is permitted, provided the original
author(s) and the copyright owner(s) are
credited and that the original publication
in this journal is cited, in accordance with
accepted academic practice. No use,
distribution or reproduction is permitted
which does not comply with these terms.

Overpressure characteristics and geological origin of the paleogene in Baiyun Sag, Pearl River Mouth Basin

Ting Xiong^{1,2}, Leli Cheng^{3,4*}, Dongming Guo⁵, Lijun Guan²,
Qiangtao Jiang², Hu Zhangming^{1,6}, Senlin Yin⁴ and
Gongyang Chen⁴

¹School of Geosciences, Yangtze University, Wuhan, Hubei, China, ²Shenzhen Branch of CNOOC Ltd, Shenzhen, Guangdong, China, ³State Key Laboratory of Petroleum Resources and Prospecting, China University of Petroleum, Beijing, China, ⁴Institute of Logging Technology and Engineering, Yangtze University, Jingzhou, Hubei, China, ⁵China-France Bohai Geoservices Co Ltd, Tianjin, China, ⁶Geological Research Institute of Western Drilling Engineering Co Ltd, Kelamayi, Xinjiang, China

The accurate understanding of the origin of overpressure is the basis of formation pressure research and the core work of determining the distribution of formation pore pressure in drilling design. The deep water area of Baiyun Sag in the Pearl River Mouth Basin in the northern margin of the South China Sea has been proved to be a hydrocarbon rich depression. In recent years, overpressure has been encountered in the middle and deep layers, but the geological origin of the overpressure in the deep water area are still unclear. Therefore, the pore pressure profile of the Baiyun Sag was evaluated using the data of drilling and seismic velocity, and the relationship between overpressure and the generation mechanism was established. Most of the surrounding and shallow strata of Baiyun Sag show normal pressure, while the middle and deep strata generally show overpressure, with the maximum pressure coefficient up to 1.55. The overpressure zone mainly develops from the middle of Zhujiang Formation to the upper member of Enping Formation. The mudstone resistivity and density values of the two typical Wells deviated from the normal trend. The density showed a constant trend with the increase of depth, while the resistivity showed a certain degree of reversal. The upper layer of the overpressure zone showed abnormally high resistivity values, corresponding to the overgland and transition zone formed by high carbonate content. There is no obvious increase of porosity in the overpressured sandstone strata of Baiyun sag, which does not have the characteristics of undercompaction. The velocity in the overpressure section of the two Wells varies greatly, and the density is basically unchanged or slightly decreased. It is concluded that the overpressure is caused by fluid expansion from hydrocarbon-generation. The large-scale and long-term fluid expansion caused by hydrocarbon generation and expulsion of source rocks provides the power source for the formation of overpressure in Baiyun sag. The distribution of effective source rocks has a controlling effect on the distribution range of overpressure. The tight sandstone strata in the Zhuhai, Wenchang and Enping formations become the cover layer of the overpressure system in the longitudinal direction.

KEYWORDS

Pearl River Mouth Basin, Baiyun Sag, overpressure characteristics, controlling factors, overpressure origin

1 Introduction

Accurate understanding of formation pore pressure before opening the formation is an important part of reducing drilling risk and cost (Yassir and Bell, 1996). In drilling operations, proper drilling fluid density sequence is the core content of drilling design, and a clear formation pore pressure distribution is the premise of this work (Slavin and Smirnova, 1998). Depending on the sequence of drilling operations, formation pore pressure can be evaluated in two ways: monitoring and forecasting. Formation pressure monitoring generally starts from the comparison of Wells before drilling (Osborne and Swarbrick, 1997). The formation pressure is calculated in combination with the new dynamic data during drilling, which is used to adjust the drilling fluid performance and drilling strategy in real time (Hunt et al., 1994). Formation pressure prediction is to evaluate formation pressure using seismic and well drilled data in order to calculate formation pressure as accurately as possible before drilling (Hao et al., 2002). The prediction of formation pressure is generally based on the basic theories of Terzaghi and Biot theorem (Belonin and Slavin, 1998). Quantitative models such as Eaton method and Bowers method have been developed for pressure calculation, but these models are based on the premise of correctly understanding the causes of overpressure (Bowers G L, 1995; Luo and Vasseur, 1996; Peter et al., 2004; Lahann and Swarbrick, 2011; Zhao et al., 2018).

As for the research on the causes of overpressure, unbalanced compaction was believed to be the main reason for the formation of overpressure in the early stage, and then hydrocarbon generation expansion gradually came into people's view (Teige et al., 1999; Mark et al., 2009; Guo et al., 2010). The contribution of other causes of overpressure, especially the montmorillite-illite transformation, tectonic extrusion, pressure transfer, etc. to the formation of overpressure has been discovered and confirmed (Guo et al., 2011, 2012). The authors propose that the overpressure in the tensioning basin is mainly caused by unbalanced compaction and

hydrocarbon generation, which develop at different diagenetic stages and burial depths Xu et al., 2019a.

The deep water area of Baiyun Sag in the Pearl River Mouth Basin in the northern continental margin of the South China Sea is a hydrocarbon rich depression which has been proved by exploration practice (Figure 1) (Sun et al., 2011). It has the characteristics of hydrocarbon resources, which are both oil-gas generation and gas-dominated (Shi et al., 2007; Hu et al., 2021). In recent years, the Enping Formation has encountered overpressure in the middle and deep depths, but the distribution and geological origin of the overpressure in the deep water area are still unclear (Figure 2) (Li et al., 2012; Han et al., 2017). Due to the lack of offshore drilling data, unclear classification of overpressure causes and unclear response characteristics of LWD (Logging While Drilling) data, the prediction accuracy of pre-drilling overpressure in this area is low, and drilling accidents related to formation overpressure often occur in drilling practice, which not only affects the exploration results, but also causes considerable economic losses. Therefore, the pore pressure profile of the Enping Formation in the Baiyun Sag was evaluated using the data of well drilling and seismic velocity, and the relationship between overpressure and the generation mechanism was established.

2 Geologic setting

Located in the slope area of the northern continental shelf of the South China Sea, the Pearl River Mouth Basin is a Cenozoic passive continental margin extensional faulted basin, which is divided into five northeastern tectonic units from north to south, including the Northern Fault Step Zone and Depression Zone, the Central Uplift Zone, the Southern Depression Zone and Uplift Zone (Zhang et al., 2014). Each tectonic unit is further divided into several secondary depressions and low uplift, among which the Baiyun Sag in the south is the largest and deepest

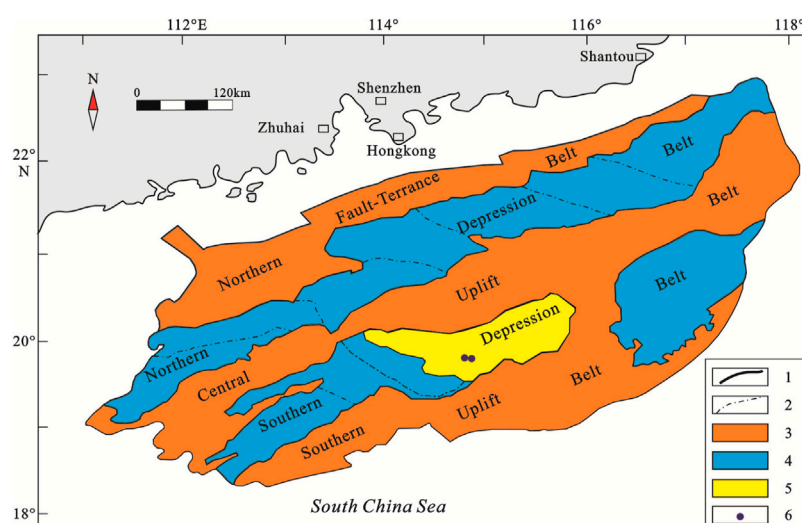


FIGURE 1

The Paleogene tectonic units of the Pearl River Mouth basin (adapted after Wang et al., 2017). 1 boundary of first-order tectonic unit, 2 boundary of second-order tectonic unit, 3 forward direction structure, 4 Negative direction structure, 5 Location of study area, 6 drilling wells position.

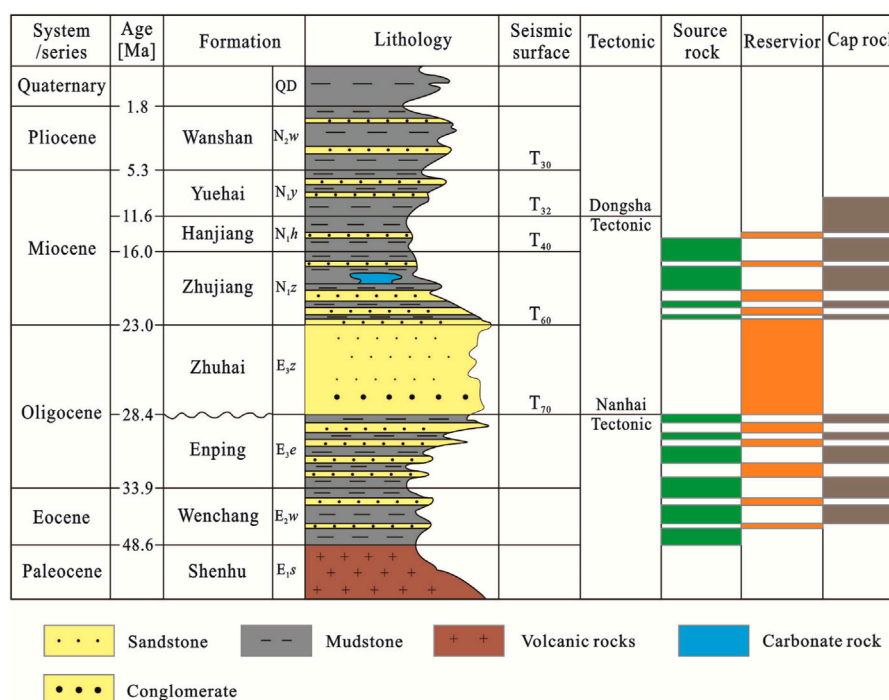


FIGURE 2
Stratigraphic column for the Baiyun Sag.

secondary depression. Influenced by the collision of Indo-Australian plate and Eurasian plate, subduction of Pacific plate and mantle plume arching, the Pearl River Mouth Basin is a Mesozoic and Cenozoic oil-bearing basin formed on the basement of Caledonian, Hercynian and Yanshanian folds (Wang et al., 2017). Baiyun Sag is located in the transition zone and upper slope area of the southwest Pearl River Mouth Basin (Figure 1) (Sun et al., 2014). It is a negative structural unit with long-term stable subsidence. In general, it is NEE trending, Panyu Low Uplift in the north, and adjacent to Shenhu Dark sand uplift and the second pearl depression in the west by a NW trending basement fault and magmatic activity zone. The east side is the Dongsha Uplift (Li et al., 2013a). Due to the downward slope of the depression facing the outlet of the Pearl River, there is sufficient supply of terrigenous sediments, and the lacustrine source rocks with large thickness are developed, and their deposition and filling are characterized by unilateral lateral transport of sediments. Therefore, the Cenozoic sedimentary filling characteristics of Baiyun Sag show the evolution law of “coarser lower and finer upper, from land to sea, from shallow water to deep water, and from over-compensation to under-compensation”. Baiyun Sag is located in the transitional zone between continental crust and oceanic crust (Zheng et al., 2012). The sedimentary basement is mainly medium-acid magmatic rocks, followed by metamorphic rocks and basic rocks. The crust thickness is relatively thin, generally ranging from 18 km to 28 km. The geothermal gradient is 31.5°C–41°C/hm, which belongs to the depression with high geothermal field (Han et al., 2017). The Baiyun Sag is mainly filled with the Eocene lacustrine sedimentary Wenchang Formation, the Lower

Oligocene fluvial lacustrine coal measure sedimentary Enping Formation, the Upper Oligocene shallow Marine shelf-delta sedimentary Zhuhai Formation, the Lower Miocene deep water continental slope-deep water fan sedimentary Zhujiang-Hanjiang Formation, Late Miocene Yuehai Formation, Pliocene Wanshan Formation and Quaternary (Li et al., 2012).

3 Pore pressure estimation methods

Using drilling and seismic data, we apply different methods to calculate or measure pore formation pressure.

3.1 Eaton's prediction method

The original Eaton method is a method to calculate formation pressure based on the normal compaction trend line proposed by Eaton in 1972. It is one of the most widely used formation pressure determination methods in petroleum industry. Eaton (1976) established the expression of the relationship between formation pore pressure and logging acoustic time difference based on the experience and theoretical analysis in the Gulf of Mexico and other areas. This relationship does not change with the lithology or depth. The principle is that the change of pressure gradient of overlying strata determines the relationship between the ratio of actual and normal trend values of observed compaction parameters and formation pore pressure (Eaton B A, 1976). In the face of different overpressure causes, the coincidence rate of calculation results can be improved by adjusting the index N . Its expression is:

$$\begin{aligned}
 P_p &= P_0 - (P_0 - P_h) \left(\frac{t_n}{t_0} \right)^N \\
 P_p &= P_0 - (P_0 - P_h) \left(\frac{V_0}{V_n} \right)^N \\
 P_p &= P_0 - (P_0 - P_h) \left(\frac{R_0}{R_n} \right)^N \\
 P_p &= P_0 - (P_0 - P_h) \left(\frac{C_n}{C_0} \right)^N \\
 P_p &= P_0 - (P_0 - P_h) \left(\frac{\rho_0}{\rho_n} \right)^N \\
 P_p &= P_0 - (P_0 - P_h) \left(\frac{dc}{dc_n} \right)^N
 \end{aligned}$$

where, P_p is the formation pore pressure; P_0 is the overburden pressure; P_h is normal hydrostatic pressure; t_n , V_n , R_n , C_n , ρ_n , d_{cn} are divided into the sonic time difference, sonic velocity, resistivity, electrical conductivity, density and dc index of the normal trend line of a certain depth of mud shale. t_0 , V_0 , R_0 , C_0 , ρ_0 , d_c are respectively measured sonic time difference, sonic velocity, resistivity, electrical conductivity, density and dc index of mud shale at a given depth. N is the Eaton index and the coefficient related to strata.

3.2 Bowers' prediction method

Bowers method was put forward by Bowers in 1995. It systematically considered the formation mechanism of mudstone's unbalanced compaction and other overpressures, and unified the other overpressure causes with the concept of pore fluid expansion (Dutta, 2002). Finally, the overpressure causes were summarized into two main factors: unbalanced compaction and pore fluid expansion. Since the uneven compaction of mudstone and pore fluid expansion show two opposite processes in the stress-strain curve of the sedimentation and overloading process, namely the sedimentation and overloading process and the unloading process, the sedimentation and overloading process is the process in which the vertical effective stress continues to increase or remain unchanged (Bowers GL, 2002). The relation curve of acoustic velocity and vertical effective stress of mudstone reflecting this process is called sedimentation and compaction curve. The unloading process refers to the process in which the vertical effective stress decreases. The unloading curve is the relationship between the acoustic velocity of mudstone and the vertical effective stress reflecting this process (Rmdhan and Gouly, 2011). The core of Bowers' method is that the overpressure caused by uneven compaction of mudstone should be determined by the compaction curve to determine the vertical effective stress, while the abnormal high pressure caused by pore fluid expansion should be determined by the unloading curve to determine the vertical effective stress. Then the effective stress theorem is used to calculate the formation pore pressure, that is, the overburden pressure and the vertical effective stress are used to determine the formation pore pressure. It is generally considered that this method does not require the establishment of a normal compaction trend line, but the process of establishing a loading curve is equivalent to the way of establishing a trend line.

Within the stress range of research significance, the original sedimentary loading curve of mudstone can be described as follows:

$$V = 5000 + A\sigma_{ev}^B$$

The unloading curve can be described as follows:

$$V = 5000 + A \left[\sigma_{\max} \left(\frac{\sigma_{ev}}{\sigma_{\max}} \right)^{\frac{1}{B}} \right]^B$$

where, V is the acoustic velocity of mudstone, σ_{ev} is the vertical effective stress, A and B are the relevant constant coefficients, σ_{\max} and V_{\max} are the maximum vertical effective stress and the corresponding acoustic velocity at the beginning of unloading, and U is the elastic-plastic coefficient of mudstone.

3.3 MDT method

The Modular Formation Dynamics Tester (Zhang et al., 2020) has become an indispensable part of formation testing projects in oil and gas Wells due to its superior testing performance and reliability. In the study area, MDT pressure sampling was performed in almost all evaluation Wells drilled with a certain hydrocarbon display. With the widespread application of MDT cable formation testing, a series of reservoir parameters can be obtained by scientific and reasonable analysis of pressure measurement data, such as formation pressure gradient, temperature gradient, and fluidity, which reflects the physical properties of the reservoir. In general, due to reservoir properties, it is not possible to measure all pressure points in MDT tests as effective points. Overpressure points, leakage points (seat seal failure) and dry points are often detected.

3.4 Abnormal drilling mud density and gas measurement

In the process of drilling, gas anomalies in gas logging are often the display of abnormally high pressure zones, including background gas, single root gas, aftereffect gas, drilling gas, and suction gas, etc. Therefore, the existence of overpressure can be predicted according to drilling fluid gas penetration and formation pressure can be judged in an auxiliary way. Tingay et al. (2013) summarized six principles for formation pressure determination by logging gas measurement:

- 1) If the background gas is normal and there is no gas infiltration from the borehole wall, P_p (pore pressure) < S_{wab} (swab pressure) < ESD (Equivalent Static Density) < ECD (equivalent circulating density);
- 2) If the background gas is normal and there is sporadic wall infiltration gas, $S_{wab} < P_p < ESD < ECD$;
- 3) If the background gas is normal and there is continuous borehole penetration gas, $S_{wab} < ESD < P_p < ECD$;
- 4) If the background gas increases and there is sporadic or continuous penetration into the wellbore, $S_{wab} < ESD < ECD < P_p$;
- (5) If there is a large increase in background gas and borehole infiltration gas cannot be identified, $S_{wab} < ESD < ECD < P_p$;

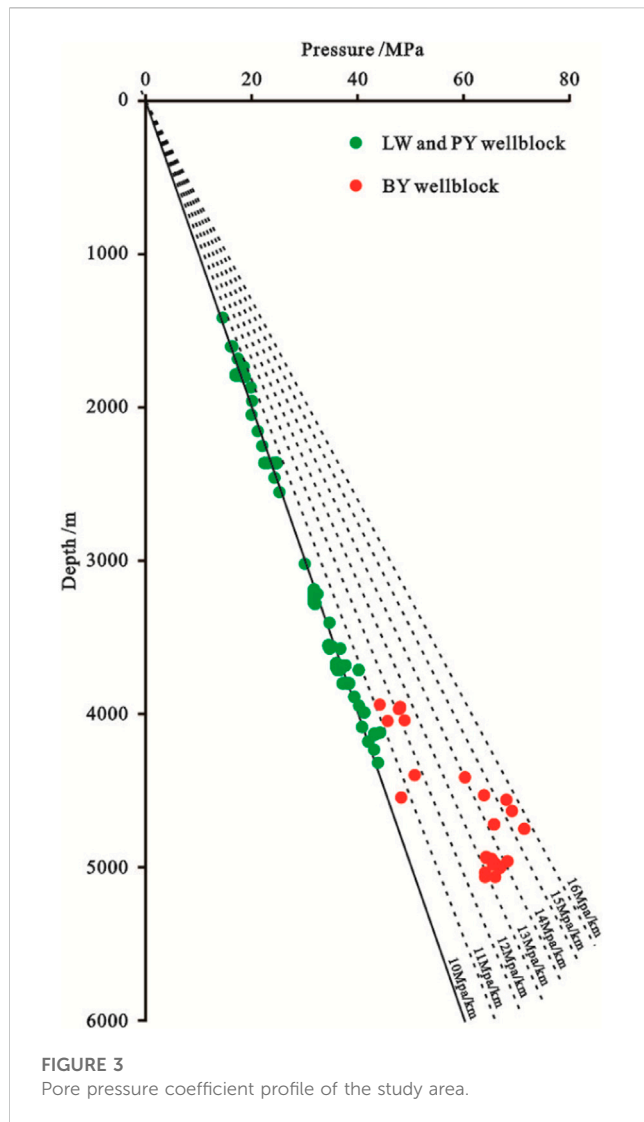


FIGURE 3
Pore pressure coefficient profile of the study area.

- 6) If there is a good correspondence between the decrease of gas total and the increase of ECD , then $P_p > ECD$.

4 Results interpretation

4.1 Characteristics of measured pressure

According to the results of MDT sampling analysis, the salinity of formation water in the study area ranges from 27,472 to 306,328 g/L, and the formation water is mainly of CaCl_2 type. The density of formation water is about 1,004–1,074 g/cm³, and the hydrostatic pressure gradient is 0.98–1.05 MPa/hm. The average value is about 1.02 MPa/hm. In this paper, pressure coefficient 1.2 is used as the boundary between normal pressure system and overpressure system. According to the statistics of 43 measured pressure values of seven Wells with MDT measured pressure data in Baiyun Sag, most of the measured pressure values in the periphery and shallow area of the sag are normal pressure, with pressure coefficient ranging from 0.9 to 1.0, while the deep area is generally

overpressure, with pressure coefficient exceeding 1.3 and up to 1.55 (Figure 3).

4.2 Characteristics of mudstone overpressure response

The measured MDT pressure can obtain the information of pressure and temperature of permeable rock strata, which can directly reflect the formation pressure state of the test interval. However, the longitudinal continuous pressure distribution profile of a large set of strata cannot be obtained, and it is generally difficult to obtain effective MDT data points in mudstone interval. Therefore, it is necessary to use geophysical logging data to study the longitudinal continuous response characteristics of overpressure in mudstone and sandstone intervals, and further identify the overpressure zone in combination with MDT testing of sandstone intervals (Bowers, 1995; Dutaa, 2002; Najibi et al., 2017). Previous studies have shown that the overpressure zone generally has the characteristics of low acoustic velocity, while the resistivity logging response to overpressure is complex, and the density logging presents abnormally low density values for the overpressure zone caused by undercompaction. According to the relationship between mudstone acoustic velocity, mudstone resistivity, density and other logging data and formation pore pressure calculation results (Figures 4, 5), the interface depth of the overpressure top in well BY01 is 3,550 m (Figure 4), and from the depth to the bottom hole 5,050 m, the mudstone acoustic velocity deviates from the normal compaction trend, resulting in abnormal low acoustic velocity. The overpressure system runs from the middle part of the Pearl River Formation to the top of the Enping Formation. At a depth of 4,625 m, the MDT measured formation pressure of sandstone in the middle section of Zhujiang Formation is 69.23 MPa, and the pressure coefficient is 1.54, which corresponds to the maximum pressure point estimated by mudstone acoustic velocity. The acoustic time difference of well BY02 (Figure 5) sandstone also deviates from normal compaction, and the amplitude is similar to or slightly smaller than mudstone. The interface depth of the overpressure top in well BY02 is 3,780 m. From the depth to the bottom hole of 5,120 m, the acoustic velocity of mudstone deviates from the normal compaction trend, resulting in abnormal high acoustic time difference. The overpressure system runs from the middle of Zhujiang Formation to the top of Enping Formation at a depth of 4,745 m, and the measured formation pressure value of MDT is 71.5 MPa and the pressure coefficient is 1.55. The pressure coefficient predicted by the maximum pressure position corresponding to the acoustic time difference of mudstone is about 1.56. The mudstone resistivity and density values of the two typical Wells deviated from the normal trend. The density showed a constant trend with the increase of depth, while the resistivity showed a certain degree of reversal. The upper layer of the overpressure zone showed abnormally high resistivity values, corresponding to the overgland and transition zone formed by high carbonate content. The overpressure logging response shows that the overpressure zone in Baiyun sag is mainly developed from the middle part of Zhujiang Formation to the upper part of Enping Formation.

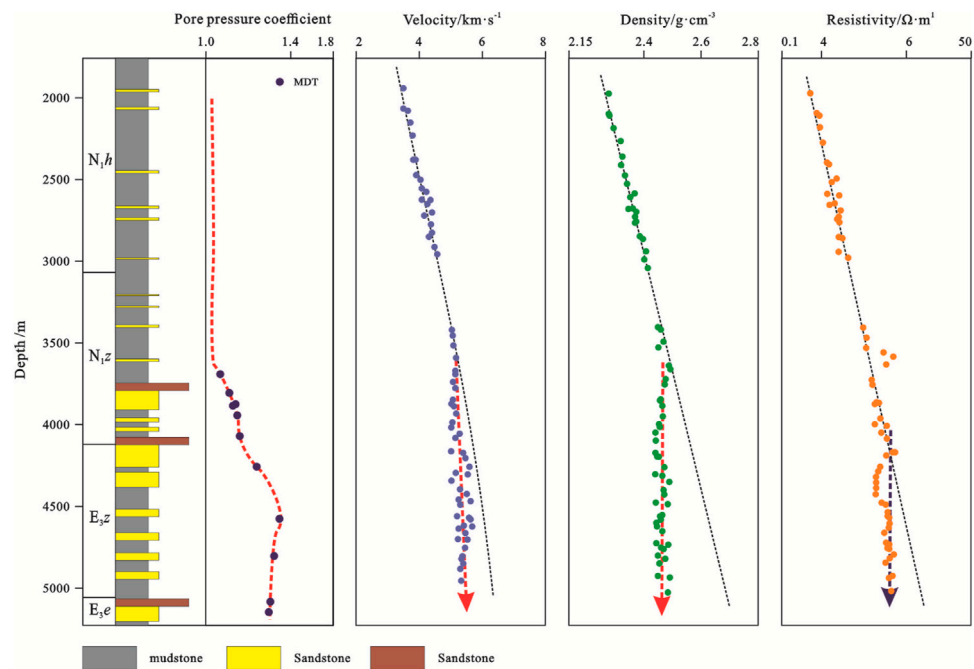


FIGURE 4
Calculation results of pore formation pressure and depth profiles of well-logging parameters, including velocity, density, resistivity and MDT data from Well BY01.

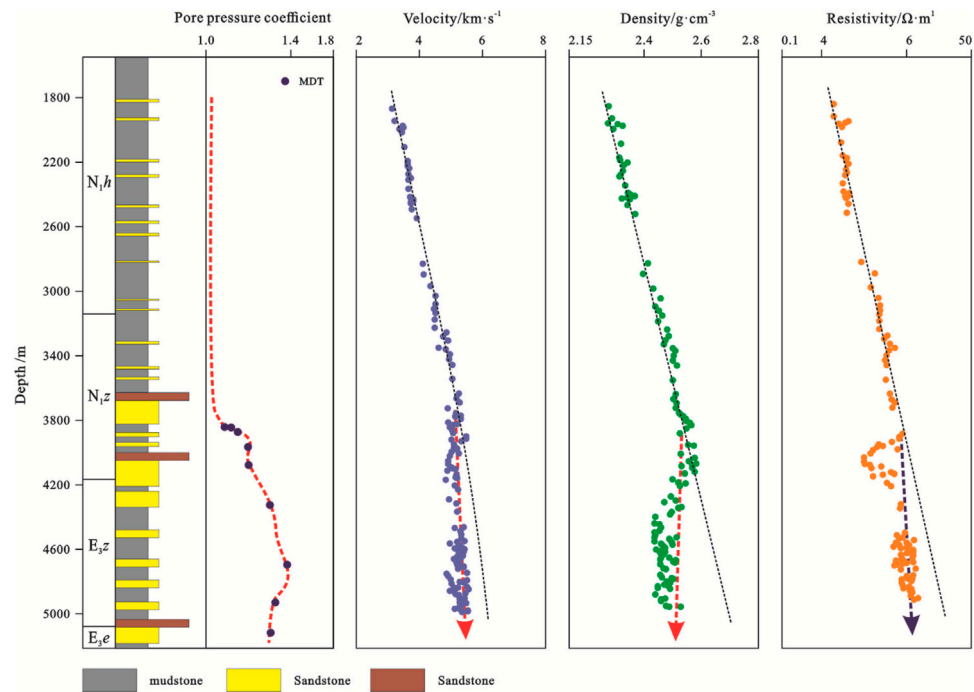


FIGURE 5
Calculation results of pore formation pressure and depth profiles of well-logging parameters, including velocity, density, resistivity and MDT data from Well BY02.

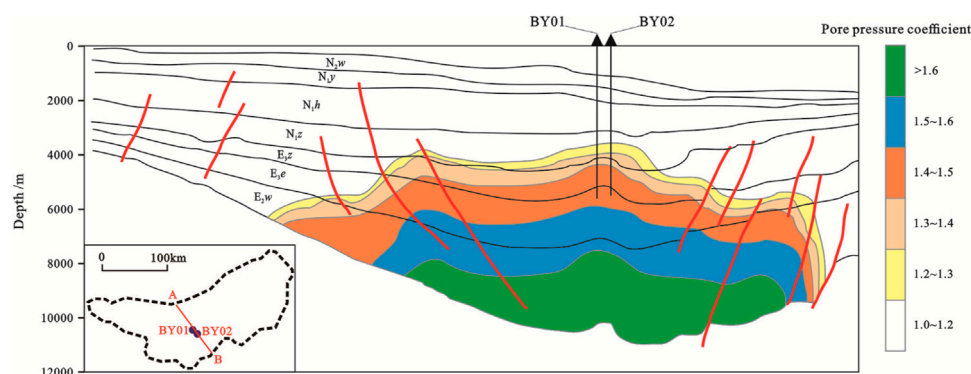


FIGURE 6
Profile distribution of pressure coefficient in Baiyun sag (Modified from Tian et al., 2020)

4.3 Pore pressure profile

The data of this study came from the MDT measured temperature and pressure data of seven Wells in Baiyun Sag. There were 53 measured pressure data, and the data points were concentrated in the depth range of 1,300–5,000 m. According to different horizons, Baiyun Sag is divided into four sets of overpressure systems: Zhujiang Formation, Zhuhai Formation, Enping Formation and Wenchang Formation (Figure 3, Figure 6). On the whole, the measured pressure in the shallow layer of Baiyun Sag is mainly normal pressure, and the pressure coefficient is mainly distributed in the range of 0.95–1.05, while there is overpressure in the middle and deep layer, and the pressure coefficient is greater than 1.3. Among them, the Pearl River Formation presents overpressure in some areas, and the pore pressure coefficient is up to 1.4. The formation of Zhuhai Formation presents overpressure in some areas, and the maximum pore pressure coefficient is about 1.5. The Enping Formation presents overpressure in most areas, and the maximum pore pressure coefficient can reach 1.6. It is speculated that overpressure is common in Wenchang Formation, and the maximum pore pressure coefficient is more than 1.6.

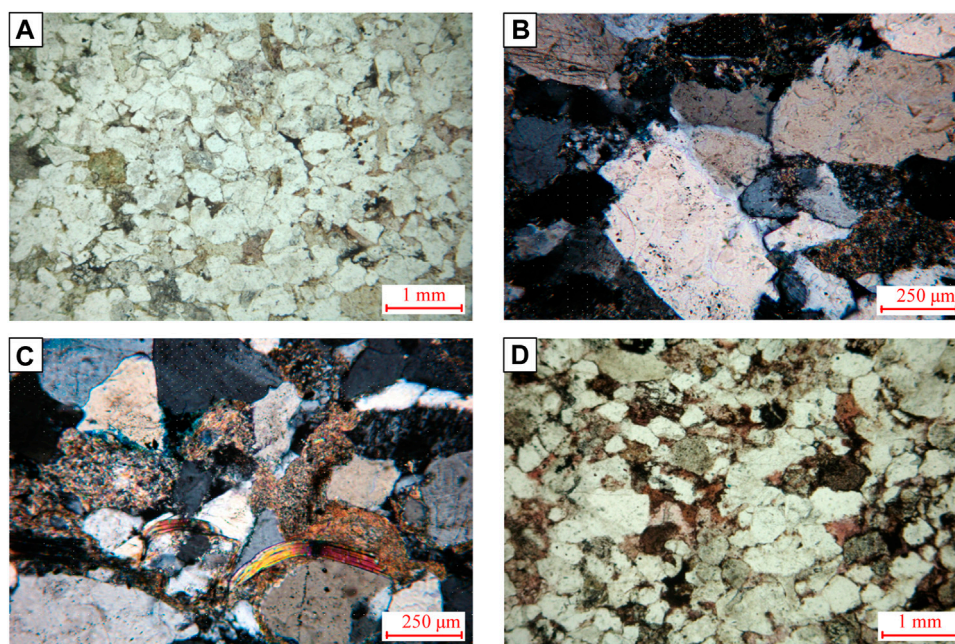
5 Discussion

5.1 Cause of overpressure in Baiyun Sag

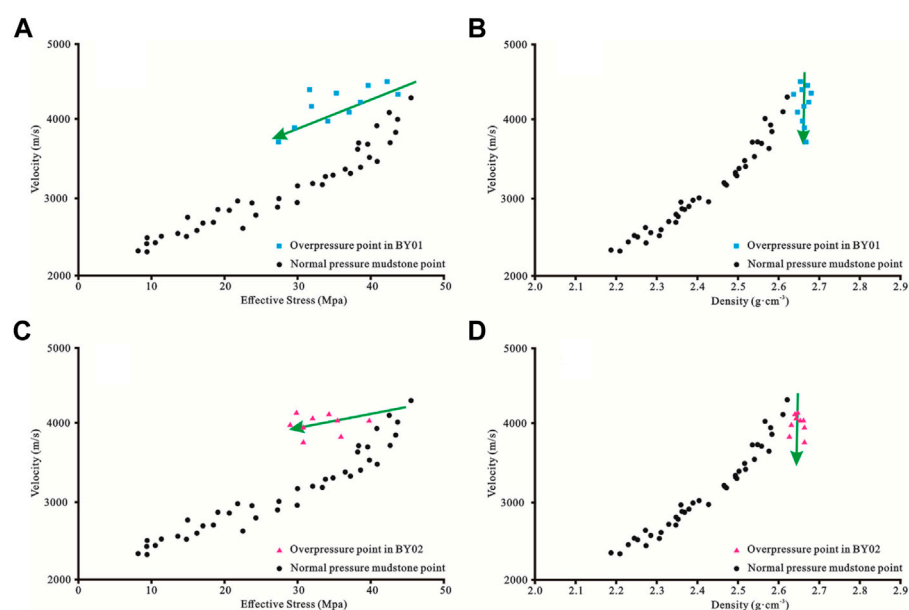
The stress action and fluid expansion in the process of rock compaction are two widely recognized overpressure formation mechanisms (Eaton, 1976; Guo et al., 2010), and the geological factors leading to the formation of overpressure usually include: tectonic extrusion, undercompaction, hydrocarbon generation, crude oil cracking, hydrothermal action, clay mineral dehydration, etc Xu et al., 2019b. Based on the analysis of geological conditions and geophysical parameters, it is concluded that the overpressure in the middle and deep Baiyun Sag does not have the characteristics of undercompaction, and the main cause of the overpressure is fluid expansion. The formation of undercompaction and overpressure usually requires high

deposition rate and large sets of mudstone deposition. However, the depositional environment of Zhuhai Formation in the BY well area of Baiyun Sag is continental shelf delta front, and the depositional environment of the upper member of Enping Formation is braided river delta plain, which lacks the development background of large sets of mudstone and does not have the geological conditions for the formation of undercompaction and overpressure. In addition, rock porosity and pore structure are the key parameters that reflect undercompaction and overpressure. No significant increase of porosity has been observed in sandstone strata in the overpressure section of Baiyun Sag. Thin section identification of reservoir rocks in the overpressure section shows that lineal contact and serrated contact are dominant among the grains (Figure 7A), or the physical properties are dense due to the filling of carbonate cements between grains (Figure 7B), reaching the middle diagenetic stage B. It does not have the characteristics of undercompaction.

Bowers. (1995) summarized the relationship between effective stress-velocity and effective stress-density in the overpressure section caused by undercompaction and fluid expansion, and pointed out that the overpressure caused by undercompaction was located on the stress loading curve, while the overpressure caused by fluid expansion was located on the upper part of the stress unloading curve. As indicated by the velocity-effective stress identification chart in this area, the overpressure section generally shows a tendency to deviate from normal compaction (Figures 8A, C), which is the cause of fluid expansion. Lahann and Swarbrick, (2011) proposed that the denson-velocity intersection diagram could distinguish the overpressure caused by dehydration of clay minerals from that caused by hydrocarbon-generation. The overpressure mudstone caused by dehydration of clay minerals showed a significant decrease in acoustic velocity and a slight increase in density, while the overpressure mudstone caused by fluid expansion caused by hydrocarbon-generation basically remained unchanged or slightly decreased in density. On the rate-density chart, the velocities in the overpressure section of the two Wells varied greatly, and the density remained basically unchanged or slightly decreased. It can also be concluded that the overpressure in the area was mainly caused by fluid expansion caused by hydrocarbon generation (Figures 8B, D).

**FIGURE 7**

Microscopic characteristics of sandstone reservoir in overpressure section (A) The sandstone appears to have low porosity under the microscope, BY01-2987m; (B,C) Concave-line contact between particles, BY01-3025m; (D) A large amount of carbonate cements are filled between particles, BY02-3231 m.

**FIGURE 8**

The genetic mechanism of overpressure is identified in Baiyun Sag, the plate according in Bowers (1995). (A,B) drop point results of Paleogene mudstone data in Well BY01. (C,D) drop point results of Paleogene mudstone data in Well BY02.

5.2 Control factors of overpressure distribution

According to the analysis of various geological conditions, the formation and distribution of overpressure in Baiyun Sag are affected by two factors.

- 1) Hydrocarbon generation and distribution range of source rocks. The Wenchang Formation is a semi-deep lacustrine source rock with TOC content of 0.9%–1.8%. The Enping Formation is dominated by transgressive/Marine source rocks with TOC content of 0.7%–5.4% and R_o of 1.8%–3.5% (about 200°C–260°C) (Mi et al., 2018). According to the results of

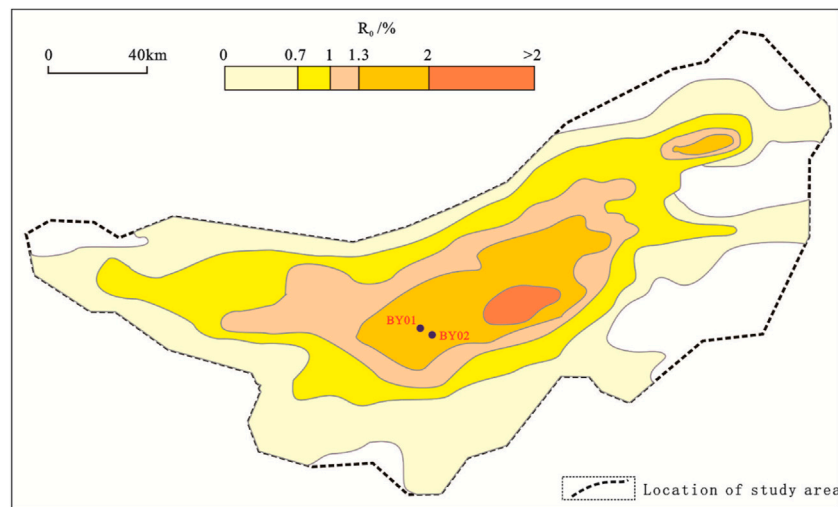


FIGURE 9
Contour map of maturity of organic matter in the Middle of Enping Formation, Baiyun Sag [Mi et al., 2018](#).

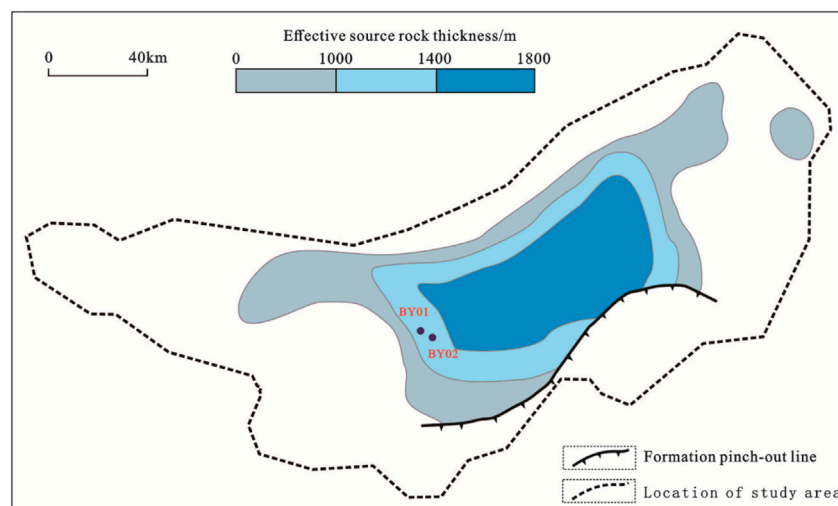


FIGURE 10
Isothickness map of Palaeogene effective source rocks in Baiyun Sag [Mi et al., 2018](#).

source rock thermal evolution simulation ([Zhang et al., 2014](#)), the Wenchang Formation entered the oil generation stage at 37 Ma, and the late high heat flow event led to the rapid gas generation stage since 16 Ma. Enping Formation also entered the stage of large-scale gas generation since 16 Ma ([Hu et al., 2021](#)). Due to the large burial depth and high geothermal gradient of the Wenchang Formation in Baiyun Sag, there is still potential for oil cracking gas on a large scale. The fluid expansion caused by hydrocarbon generation and expulsion in large-scale and long-term source rocks provides the power source for the formation of overpressure in Baiyun Sag. On the other hand, the Eocene Wenchang Formation and Enping Formation are the two main source rocks developed in Baiyun Sag ([Zhu et al., 2012](#); [Li et al., 2013b](#)), and the adjacent Zhujiang Formation and Shenhu

Formation received oil and gas migration and charging from the former, resulting in formation overpressure. It can be clearly seen on the plane ([Figures 9, 10](#)) that the area with the maximum organic matter maturity and effective thickness of the source rocks is consistent with the position with the highest formation pressure coefficient, indicating the control effect of the distribution of the source rocks on the overpressure distribution.

- 2) Formation and distribution of tight strata. Baiyun Sag is characterized by high variable geothermal temperature. With the increase of geothermal gradient, sandstone porosity and permeability decrease significantly ([Qing et al., 2018](#)). Previous analysis results of reservoir diagenesis and accumulation system showed that (citation), before the main

hydrocarbon charging of 13.8 Ma, the sandstone reservoir of Zhuhai Formation in the middle-high geothermal gradient area of Baiyun Sag had been generally diagenetic densification, and the remaining porosity was reduced from 22.8% to 11.9%, which formed an effective seal on the pressure system of the lower bed. It is not conducive to the expulsion of oil and gas generated by source rocks of Wenchang-Enping Formation. After this period, the deep sandstone reservoirs in Wenchang Formation and Enping Formation were also generally densified in the main accumulation period, which resulted in the poor outflow of oil and gas. Some drilling in Baiyun Sag reveals that the deep strata all have overpressure, the pressure state of sandstone and mudstone interval is closely related, and the overpressure of sandstone originates from mudstone. The overpressure of sandstone is usually the result of the transfer of overpressure fluid from mudstone to sandstone, and the overpressure amplitude in sandstone is usually smaller than or close to the overpressure amplitude in mudstone, which depends on the contact characteristics between sand and mudstone, the ability of fluid transfer and exchange, and the overpressure equilibrium time (Hao et al., 2002). Well BY01 is located in the center of the depression, and the sandstones in the nearly kilometer well section all contain gas. Since Zhuhai Formation, overpressure is common in the formation, and the sandstone reservoir has densification characteristics, while the overpressure top interface is in good consistency with the depth of the tight reservoir (Figures 4, 5), which confirms the sealing effect of the deep tight sandstone adjacent to the source rock.

Conclusion

- 1) Most of the surrounding and shallow strata of Baiyun sag show normal pressure, while the middle and deep strata generally show overpressure, with the maximum pressure coefficient of 1.55. The overpressure logging response shows that the overpressure zone in Baiyun Sag is mainly developed from the middle part of Zhujiang Formation to the upper part of Enping Formation. The mudstone resistivity and density values of the two typical Wells deviated from the normal trend. The density showed a constant trend with the increase of depth, while the resistivity showed a certain degree of reversal. The upper layer of the overpressure zone showed abnormally high resistivity values, corresponding to the overland and transition zone formed by high carbonate content.
- 2) The Zhujiang Formation in Baiyun Sag presents overpressure in some areas, and the pore pressure coefficient is up to 1.4. The formation of Zhuhai Formation presents overpressure in some areas, and the maximum pore pressure coefficient is about 1.5. The Enping Formation presents overpressure in most areas, and the maximum pore pressure coefficient can reach 1.6. It is speculated that overpressure is common in Wenchang Formation, and the maximum pore pressure coefficient is more than 1.6.
- 3) There is no obvious increase of porosity in the sandstone strata of the overpressured section of Baiyun Sag, and the thin section identification of the reservoir rocks of the overpressured section shows that the intergranular contact is mainly line contact and serrated contact, which reaches the middle petrogenesis stage B, and the sandstone does not have the characteristics of

undercompaction. According to the velocity density chart, the velocity of the overpressure section of the two Wells varies greatly, and the density is basically unchanged or slightly decreased. It is concluded that the overpressure in this area is mainly caused by fluid expansion caused by hydrocarbon-generation.

- 4) The large-scale and long-term fluid expansion caused by hydrocarbon generation and expulsion of source rocks provides a power source for the formation of overpressure in Baiyun Sag, and the distribution of effective source rocks has a controlling effect on the distribution range of overpressure. The sandstone reservoirs in Zhuhai Formation, Wenchang Formation and Enping Formation were generally densified before a large amount of oil and gas was generated, which resulted in the poor outflow of oil and gas, and these tight strata became the cover of overpressure system in the longitudinal direction.

Data availability statement

The datasets presented in this article are not readily available because The research data involved trade secrets. Requests to access the datasets should be directed to Leli Cheng, chengleli@yangtzeu.edu.cn.

Author contributions

TX completed the main processing and analysis work, LC established the framework and completed the paper writing, DG, LG, and QJ provided the data, HZ processed part of the data, SY and GC modified the paper and put forward useful suggestions.

Funding

This study was supported by the Foundation of State Key Laboratory of Petroleum Resources and Prospecting, China University of Petroleum, Beijing (No. PRP/open-2104).

Acknowledgments

The author acknowledges the support of operation geoscience team in Shenzhen Branch of CNOOC Ltd., for their technical input throughout the period of this research.

Conflict of interest

Authors TX, LG, QJ, were employed by Shenzhen Branch of CNOOC Ltd. Author GD was employed by China-France Bohai Geoservices Co Ltd. Author HZ was employed by Geological Research Institute of Western Drilling Engineering Co Ltd.

The remaining authors declare that the research was conducted in the absence of any commercial or financial relationships that could be construed as a potential conflict of interest.

Publisher's note

All claims expressed in this article are solely those of the authors and do not necessarily represent those of their affiliated

References

- Belonin, M. D., and Slavin, V. I. (1998). Abnormally high formation pressures in petroleum regions of Russia and other countries of the C. I. S. *AAPG Mem.* 70, 155–171. doi:10.1306/M70615C7
- Bowers, G. L. (2002). Detecting high overpressure. *Lead. Edge* 21 (2), 174–177. doi:10.1190/1.1452608
- Bowers, G. L. (1995). Pore pressure estimation from velocity data: Accounting for overpressure mechanisms besides undercompaction. *Int. J. Rock Mech. Min. Sci. Geomechanics Abstr.* 31, 276. doi:10.2118/27488-PA
- Dutta, N. C. (2002). Geopressure prediction using seismic data: Current status and the road ahead. *Geophysics* 67 (6), 2012–2041. doi:10.1190/1.1527101
- Eaton, B. A. (1976). Graphical method predicts geopressures worldwide. *World* 183 (1), 51–56. doi:10.1016/0038-092X(76)90080-3
- Guo, X., He, S., Liu, K., Song, G., Wang, X., and Shi, Z. (2010). Oil generation as the dominant overpressure mechanism in the cenozoic dongying depression, bohai bay basin, China. *AAPG Bull.* 94 (12), 1859–1881. doi:10.1306/05191009179
- Guo, X., He, S., Zheng, L., and Wu, Z. (2011). A quantitative model for the overpressure caused by oil generation and its influential factors. *Acta Pet. Sin.* 32 (3), 637–644. doi:10.7623/syxb201104011
- Guo, Z., Liu, Z., Lv, R., et al. (2012). Predrill prediction of formation pressure using seismic data in deep-water area of Baiyun Depression, northern South China Sea. *Oil Geophys. Prospect.* 47 (1), 126–132. (in chinese).
- Han, Y., Chen, Y., Yang, H., Wang, L., Shen, H., Guo, S., et al. (2017). Source to sink" of enping Formation and its effects on oil and gas exploration in baiyun sag, Pearl River Mouth basin. *china pet. Explor.* 22 (2), 25–34. (in chinese). doi:10.3969/j.issn.1672-7703.2017.02.003
- Hao, F., Zou, H., Ni, J., et al. (2002). Evolution of overpressured systems in sedimentary basins and conditions for deep. *oil/gas Accumul.* 27 (5), 20–28. (in chinese). doi:10.3321/j.issn:1000-2383.2002.05.022
- Hu, J., Long, Z., Huang, Y., Zhang, L., Hu, D., Wang, Y., et al. (2021). Tectono-thermal modelling of baiyun sag, pearl River Mouth basin, since cenozoic. *Chin. J. Geophys.* 64 (5), 1654–1665. (in chinese). doi:10.6038/cjg202100413
- Hunt, J. M., Whelan, J. K., Eglinton, L. B., et al. (1994). Gas generation-a major cause of deep Gulf Coast overpressure. *Oil Gas J.* 92 (29), 59–63. doi:10.2118/24117-PA
- Lahann, R. W., and Swarbrick, R. E. (2011). Overpressure generation by load transfer following shale framework weakening due to smectite diagenesis. *Geofluids* 11 (4), 362–375. doi:10.1111/j.1468-8123.2011.00350.x
- Li, Y., Fu, N., and Zhang, Z. (2013b). Hydrocarbon source conditions and origins in the deepwater area in the northern South China Sea. *Acta Pet. Sin.* 34 (2), 247–254. (in chinese). doi:10.7623/syxb201302006
- Li, Y., Zheng, R., Zhu, G., Boyu, G., and Xiaoqing, H. (2013a). Deep-water depositional features of Miocene Zhujiang Formation in baiyun sag, Pearl River Mouth basin. *Earth Sci. Frontiers* 87 (1), 197–210. (in chinese). doi:10.1111/1755-6724.12041
- Li, Y., Zheng, R., Zhu, G., et al. (2012). Deep-water tractive deposition in Zhujiang formation Baiyun sag, Zhujiang River Mouth Basin and its geological implications. *Acta Oceanol. Sin.* 34 (1), 127–135. (in chinese).
- Luo, X. R., and Vasseur, G. (1996). Geopressuring mechanism of organic matter cracking: Numerical modelling. *AAPG Bull.* 80 (6), 856–874. doi:10.1306/64ED88EA-1724-11D7-8645000102C1865D
- Mark, R. P., Richard, R. H., Richard, E. S., Swarbrick, R. E., Morley, C. K., and Damit, A. R. (2009). Origin of overpressure and pore pressure prediction in the Baram Province, Brunei. *AAPG Bull.* 93 (1), 51–74. doi:10.1306/08080808016
- Mi, L., Zhang, Z., Xiong, P., Liu, J., Zhang, B., Zhao, Q., et al. (2018). Main controlling factors of hydrocarbon accumulation in Baiyun Sag at northern continental margin of South China Sea. *Petroleum Explor. Dev.* 45 (5), 963–973. (in chinese). doi:10.1016/s1876-3804(18)30100-9
- Najibi, A. R., Ghafoori, M., Lashkaripour, G. R., and Asef, M. R. (2017). Reservoir geomechanical modeling: *In-situ* stress, pore pressure, and mud design. *J. Petroleum Sci. Eng.* 151, 31–39. doi:10.1016/j.petrol.2017.01.045
- Osborne, M. J., and Swarbrick, R. E. (1997). Mechanisms for generating overpressure in sedimentary basins: A reevaluation. *AAPG Bull.* 81 (6), 1023–1041. doi:10.1306/522B49C9-1727-11D7-8645000102C1865D
- Peter, V. R., Richard, H., and Peter, T. (2004). The origin of overpressure in the carnarvon basin, western Australia: Implications for pore pressure prediction. *Pet. Geosci.* 10, 247–257. doi:10.1144/1354-079302-562
- Qing, Y., Mei, L., Shi, H., Camanni, G., Shu, Y., Wu, J., et al. (2018). The Late Cretaceous tectonic evolution of the South China Sea area: An overview, and new perspectives from 3D seismic reflection data. *Earth-Science Rev.* 187, 186–204. doi:10.1016/j.earscirev.2018.09.013
- Rrmdhan, A. M., and Goulty, N. R. (2011). Overpressure and mudrock compaction in the lower kutai basin, Indonesia: A radical reappraisal. *AAPG Bull.* 95 (10), 1725–1744. doi:10.1306/02221110094
- Shi, W., Chen, H., Chen, C., Pang, X., and Zhu, M. (2007). Pressure evolution and hydrocarbon migration in the Baiyun sag, Pearl River Mouth basin, China. *Front. Earth Sci. China* 1 (2), 241–250. (in chinese). doi:10.1007/s11707-007-0030-5
- Slavin, V. I., and Smirnova, E. M. (1998). Abnormally high formation pressures: Origin, prediction, hydrocarbon field development, and ecological problems. *Abnorm. Press. hydrocarbon Environ.* 70, 105–114. doi:10.0000/PMID14070
- Sun, J., Zhan, W., and Qiu, X. (2011). Relationship between tectonic evolution and petroleum systems in baiyun sag, pearl river mouth basin. *Mar. Geol. Quat. Geol.* 31 (1), 101–108. (in chinese). doi:10.3724/sp.j.1140.2011.01101
- Sun, Y., Zhao, T., and Ke, Q. (2014). Numerical simulation of pverpressure of shallow water flow in baiyun sag of the northern south China sea. *Adv. Earth Sci.* 29 (9), 1055–1064. (in chinese). doi:10.11867/j.issn.1001-8166.2014.09.1055
- Teige, G. M. G., Hermanrud, C., Wensaas, L., and Nordgard Bolas, H. (1999). The lack of relationship between overpressure and porosity in North Sea and Haltenbanken shales. *Mar. Petroleum Geol.* 16 (4), 321–335. doi:10.1016/s0264-8172(98)00035-x
- Tian, L., Zhang, Z., Xiong, P., et al. (2020). Characteristics of overpressure development in the mid-deep strata of Baiyun sag and its new enlightenment in exploration activity. *China Offshore Oil Gas* 32 (6), 1–11. (in chinese).
- Tingay, M. R. P., Morley, C. K., Laird, A., Limpornpipat, O., Krisadasima, K., Pabchanda, S., et al. (2013). Evidence for overpressure generation by kerogen-to-gas maturation in the northern Malay Basin. *AAPG Bull.* 97 (4), 639–672. doi:10.1306/09041212032
- Wang, K., Zhang, G., Yang, H., et al. (2017). Thermal evolution of source rock and prediction of petroleum resources potential in Baiyun Depression, deep-water area of the northern South China Sea. *J. Trop. Oceanogr.* 36 (1), 25–34. (in chinese). doi:10.11978/2016047
- Xu, S., Hao, F., Xu, C., Zou, H., and Gao, B. (2019a). Seismic geomorphology and sedimentology of fluvial-dominated delta: Implications for the Neogene reservoirs, Offshore Bohai Bay Basin, China. *AAPG Bulletin* 103, 2399–2420. doi:10.1306/0130191522517122
- Xu, S., Hao, F., Xu, C., Zou, H., Zhang, X., Zong, Y., et al. (2019b). Hydrocarbon migration and accumulation in the northwestern Bozhong subbasin, Bohai Bay basin, China. *J. Pet. Sci. Eng.* 172, 477–488. doi:10.1016/j.petrol.2018.09.084
- Yassir, N., and Bell, J. S. (1996). Abnormally high fluid pressures and associated porosities and stress regimes in sedimentary basins. *SPE Form. Eval.* 11 (1), 5–10. doi:10.2118/28139-pa
- Zhang, G., Yang, H., Chen, Y., et al. (2014). The baiyun sag: A giant rich gas-generation sag in the deepwater area of the Pearl River Mouth basin. *Nat. Gas. Ind.* 34 (11), 11–25. (in chinese). doi:10.3787/j.issn.1000-0976.2014.11.002
- Zhang, X., Chen, H. H., Kong, L. T., and Long, Z. (2020). The coupling relationship between paleofluid pressure evolution and hydrocarbon-charging events in the deep of Biyang Depression, Central China. *Earth Sci.* 46 (5), 1769–1781. doi:10.3799/dqkx.2019.187
- Zhao, J., Li, J., and Xu, Z. (2018). Advances in the origin of overpressures in sedimentary basins. *Petroleum Res.* 3 (1), 1–24. (in chinese). doi:10.1016/j.ptlrs.2018.03.007
- Zheng, R., Ma, Q., Yang, B., et al. (2012). Characteristics of Miocene Zhujiang Formation submarine fan sandstone reservoirs in baiyun sag, Pearl River Mouth basin, China. *J. Chengdu Univ. Technol. Sci. Technol. Ed.* 39 (5), 455–462. (in chinese).
- Zhu, J., Shi, H., and Xiong, P. (2012). Origins and accumulation characteristics of hydrocarbons in eastern Baiyun Deepwater Area. *China Pet. Explor.* 17 (4), 20–28. (in chinese). doi:10.11764/j.issn.1672-1926.2012.02.213



OPEN ACCESS

EDITED BY

Rafael Almeida,
San Diego State University, United States

REVIEWED BY

Derman Dondurur,
Dokuz Eylül University, Türkiye
Wei Li,
South China Sea Institute of Oceanology
(CAS), China

*CORRESPONDENCE

Lyndon P. Nawanao Jr,
✉ lpnawanao@up.edu.ph

SPECIALTY SECTION

This article was submitted
to Marine Geoscience,
a section of the journal
Frontiers in Earth Science

RECEIVED 27 September 2022

ACCEPTED 31 January 2023

PUBLISHED 03 March 2023

CITATION

Nawanao LP Jr and Ramos NT (2023),
Frontal wedge variations and controls of
submarine landslides in the Negros–Sulu
Trench System, Philippines.
Front. Earth Sci. 11:1054825.
doi: 10.3389/feart.2023.1054825

COPYRIGHT

© 2023 Nawanao and Ramos. This is an
open-access article distributed under the
terms of the [Creative Commons
Attribution License \(CC BY\)](#). The use,
distribution or reproduction in other
forums is permitted, provided the original
author(s) and the copyright owner(s) are
credited and that the original publication
in this journal is cited, in accordance with
accepted academic practice. No use,
distribution or reproduction is permitted
which does not comply with these terms.

Frontal wedge variations and controls of submarine landslides in the Negros–Sulu Trench System, Philippines

Lyndon P. Nawanao Jr* and Noelynna T. Ramos

Geomorphology and Active Tectonics Research Laboratory, National Institute of Geological Sciences, University of the Philippines Diliman, Quezon City, Philippines

Frontal wedge characteristics provide clues to the efficiency of the overriding slab for large displacement during megathrust and upper-plate earthquakes, whereas submarine landslides along active margins may trigger or amplify tsunamis. The lack of clear precursors of submarine failures poses difficulty in monitoring and providing real-time alert warning systems. With that, delineating submarine features along active margins, their spatial distribution, and controls provide valuable information in identifying regions susceptible to large submarine landslides and tsunami hazard assessments. In this study, we performed terrain and morphometric analyses on 20 m resolution bathymetry data to map submarine landslides, submarine canyons, and lineaments in the forearc margin of the Negros–Sulu Trench System in the Philippines. Lineaments are distributed mainly along the frontal wedge, where previous seismic surveys revealed that the mapped ridges are morphotectonic expressions of thrust sediments. The morphological variations of the four frontal wedge segments were attributed to heterogeneous sediment influx, convergence rates, and subduction processes. More than 1,200 submarine landslides and their morphometric parameters were delineated, and exploratory spatial analyses indicate clustering and underlying controls. The tendencies of prolate submarine landslides (high L/W) to significantly cluster along submarine canyons while oblate morphologies (low L/W) along the frontal wedge reflect the different environments and geomorphological conditions to form these contrasting shapes. Ubiquitous small submarine landslides are mainly controlled by submarine canyon systems at relatively shallow depths of <2 km, where high sediment influx from inland sources preconditions instability. Large submarine landslides (>0.5 km³), on the other hand, are significantly most clustered where the Cagayan Ridge seamount collides and subsequently subducts beneath the northernmost frontal wedge. This suggests the dominant role of seamount subduction and related tectonic processes causing slope steepening to mainly induce large submarine landslides. This study unveiled how submarine landslides vary morphologically depending on their spatial, geomorphological, and tectonic controls in the active margin. This new information provides clues in identifying offshore areas susceptible to large submarine landslides that may induce damaging tsunamis in the Negros–Sulu Trench System as well as in other active margins of similar underlying controls.

KEYWORDS

frontal wedge, submarine landslides, Negros–Sulu Trench System, Sulu Sea, submarine canyons, exploratory spatial analyses

1 Introduction

Submarine landslides occur when driving stresses on sediment layers increase or when shearing resistance decreases and are mainly triggered and preconditioned by the following: earthquakes, slope steepening, volcanic eruptions, rapid loading causing overpressure, wave and tidal loading, rapid sediment loading, gas hydrates, fluid migration, and weak stratigraphic layers (Vanneste et al., 2013; Scarselli 2020; Watson et al., 2020). Moreover, submarine landslides can induce tsunamis. This occurs when seafloor vertical displacement is translated into the seawater column and is a function of submarine landslide volume, depth, acceleration, velocity, and fluid density (Harbitz et al., 2014; Yavari-Ramshe and Ataie-Ashtiani 2016; Løvholt et al., 2017; Baba et al., 2019). Complex triggering factors with no clear precursors are the main challenges in creating an effective real-time early-warning system for submarine landslide-driven tsunamis.

In the past, submarine landslides were overlooked to cause damaging tsunamis until the 1998 Papua New Guinea submarine slump. This event caused a 15 m wave height leading to more than 2,200 fatalities that reshaped the perspective on the impacts of submarine landslides (Heinrich et al., 2001; Tappin 2021). Advancements in seafloor mapping and tsunami modeling have also led to revisiting past tsunamis that were once attributed only to earthquakes. Tsunami modeling of the following events was found to either be amplified or mainly induced by an earthquake-triggered submarine landslide: 1908 Mw 7.1 Messina (12 m maximum tsunami, 80,000 fatalities) (Schambach et al., 2020), 1945 Mw 8.1 Makran (15 m, 4,000) (Rastgoftar and Soltanpour 2016), 1946 Ms 7.1 Aleutian (16 m, 167) (Fryer et al., 2004), 1964 Mw 9.2 Alaska (12 m, 131) (Parsons et al., 2014), 1992 Ms 7.5 Flores Island (26 m, 1,713) (Hidayat et al., 1995; Imamura et al., 1995), 1994 Mw 7.1 Mindoro (7 m, 78) (Ramirez et al., 2022), as well as the more recent 2011 Mw 9.0 Tohoku (40 m, 18,490) (Tappin et al., 2014) and 2018 Mw 7.5 Sulawesi (10 m, 2,000) (Takagi et al., 2019; Nakata et al., 2020) tsunami events.

The 1945 Makran, 1946 Aleutian, 1964 Alaska, 1992 Flores Island, and 2011 Tohoku tsunami events occurred along active margins, where subduction processes predominantly trigger submarine failures. Recent studies linked the distribution of submarine landslides in forearc basins to seismic loading, oversteepening of the frontal wedge, seamount subduction, and submarine canyon development (Mountjoy et al., 2009; Pedley et al., 2010; Watson et al., 2020). The frontal wedge is of particular interest as its configuration implicates the variability of subduction processes along the trench. This includes whether a trench segment undergoes accretion or erosion (e.g., Kao et al., 2000; Pedley et al., 2010; Armada et al., 2020) as well as the relationship between the frontal wedge morphometry and maximum tsunami wave heights for megathrust earthquakes (Qiu and Barbot 2022). The link between the frontal wedge and subsequent submarine landslides was also documented in other active margins including the Nankai Trough (Moore et al., 2019), Hikurangi Trough (Pedley et al., 2010), and Java Trench (Kopp et al., 2006). These studies highlight the role of variability in subduction processes along the trench and the consequent submarine slope failures.

Mapping both the frontal wedge and other submarine features as well as conducting exploratory spatial statistics can be significant

initial steps toward providing informed decisions in minimizing the impacts and inferring seafloor areas that are susceptible to tsunamigenic submarine landslides (e.g., Völker, 2010; Kawamura et al., 2012; Parsons et al., 2014; Watson et al., 2020; Gamboa et al., 2022).

The Philippines is an archipelago surrounded by subduction zones with the potential to generate strong to great earthquakes that can trigger submarine landslides. Despite its active seismicity and tectonics, the Negros–Sulu Trench System (NSTS) remains understudied, and its submarine geomorphological features are poorly constrained. In this study, we mapped the frontal wedge variations, submarine canyons, lineaments, and submarine landslides in the active margin of the Sulu Sea using high-resolution multibeam bathymetry data. Furthermore, this study aims to infer the controls of submarine landslides through their morphometric parameters and exploratory spatial analyses. For the first time, the morphological characteristics of these submarine features in the NSTS are examined in detail, with a particular focus on the morphological variations and spatial distribution of submarine landslides.

2 Sulu Sea tectonic setting and historical tsunamis

The NSTS is an active margin where the Sulu Sea subducts beneath the Philippine Mobile Belt (PMB). This marginal basin is enclosed by the Zamboanga Peninsula and the islands of Sulu, Panay, Negros, and Palawan. The Sulu Sea is divided into four major tectonic terranes: northwest Sulu basin (NWS), Cagayan Ridge (CR), southeast Sulu basin (SES), and the accretionary prism (AP) along the NSTS (Rangin, 1989). The Palawan Microcontinental Block (PCB) terrane occupies north of the Sulu Sea. The NWS has thicker crust (>10 km) than the SES (6 km), and between these two sediment-filled sub-basins is the Cagayan Ridge seamount composed of basalt, tuff, and andesite (Rangin and Silver 1990) (Figure 1). GPS surveys revealed that this trench system generally has low convergence rates (<60 mm yr⁻¹) (Rangin et al., 1999; Simons et al., 1999). Two prominent models suggest that the Sulu Sea was formed due to back-arc rifting from the subduction of either the proto-South China Sea along the Cagayan Arc (e.g., Bellon & Rangin, 1991; Rangin & Silver, 1991; Schlüter et al., 2001; Liu et al., 2014) or the Celebes Sea along the Sulu and Zamboanga Peninsula Arc (Rangin, 1989; Hall 2002, 2013, 2012; Lai et al., 2021).

Since 1589, three historical tsunamigenic earthquakes occurred along the NSTS: 1897 Ms 7.5, 1925 Ms 6.8, and 1948 Ms 8.2 events (Bautista et al., 2012). The 1897 earthquake event had an epicenter near the Zamboanga Peninsula and generated up to a 6 m tsunami that widely affected the coastal areas in the Sulu Sea. The basin-wide distribution and maximum tsunami wave height for a Ms 7.5 earthquake pose questions regarding its mechanism. Whether this event was a tsunami earthquake or triggered by a submarine landslide is still unknown. On the other hand, the 1925 and 1948 earthquake events generated a tsunami of up to 2 m that only affected southeastern Negros and Panay islands, respectively. The 1948 event is distinct among the three as its epicenter is inland. The rupture parameters of these tsunamigenic earthquakes, however, are still poorly constrained.

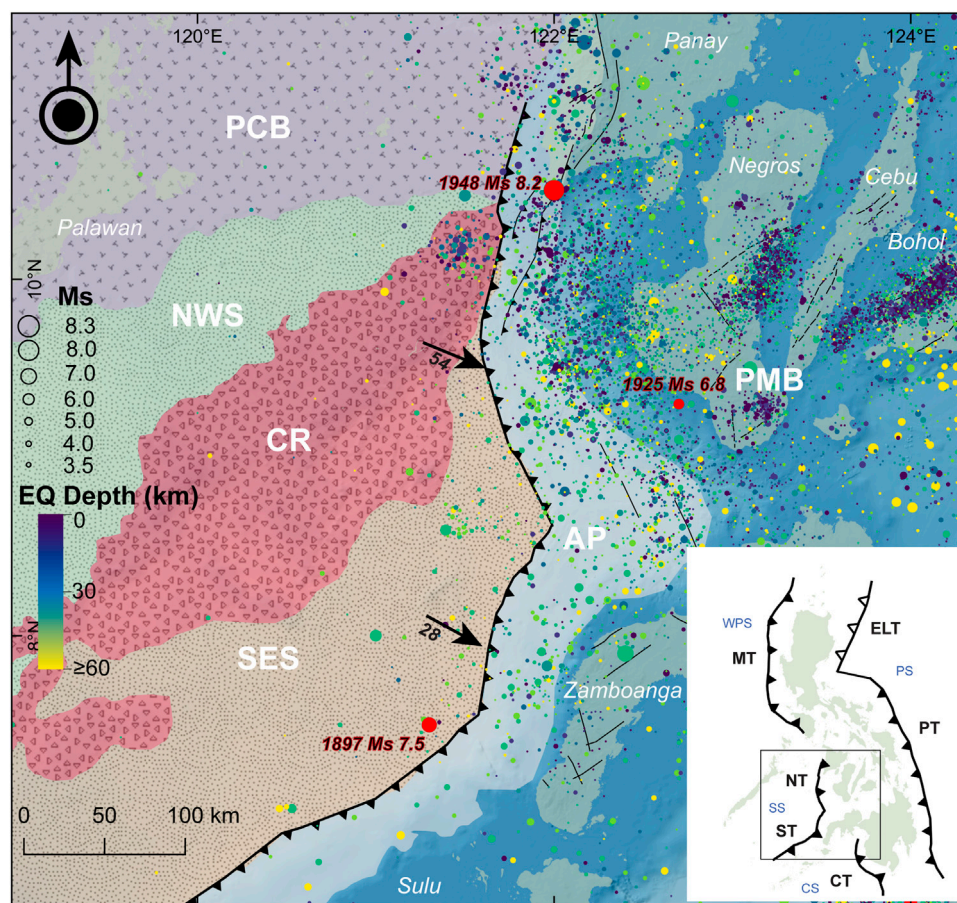


FIGURE 1

The Sulu Sea Basin and nearby tectonic features. Major tectonic terranes in the Sulu Sea include the northwest Sulu basin (NWS), Cagayan Ridge (CR), southeast Sulu basin (SES), and accretionary prism (AP) along the Negros–Sulu Trench System (NSTS). The Palawan Microcontinental Block (PCB) consists of continent-derived lithologies rifted from the eastern Eurasian margin, while the arc-derived Philippine Mobile Belt (PMB) comprises the rest of the archipelago (modified from Rangin, 1989). Arrows indicate the velocity vectors (mm yr^{-1}) from continuous GPS campaigns (1994–1996) across the Philippines (Rangin et al., 1999; Simons et al., 1999). Red circles indicate the epicenter of the three historical tsunamigenic earthquakes in the Sulu Sea (Bautista et al., 2012). The onshore faults, lineaments (black lines), and catalog (1589–2020) of surface-wave magnitude (Ms) earthquakes (EQ) are from PHIVOLCS. The inset map shows the location of the Sulu Sea (SS) and the other surrounding basins (West Philippine Sea, WPS; Cotabato Sea, CS; Philippine Sea, PS) and trenches (Manila Trench, MT; Negros Trench, NT; Sulu Trench, ST; Cotabato Trench, CT; Philippine Trench, PT; East Luzon Trough, ELT).

3 Materials and methods

3.1 Delineating submarine landslides and their morphological parameters, submarine canyons, and lineaments

The bathymetry data of the National Mapping and Resource Information Authority (NAMRIA) has a 20 m resolution and a depth accuracy of 1 m. These were collated from the multibeam bathymetric surveys in the Sulu Sea between 1999 and 2018 by the NAMRIA and the Naval Oceanographic Office (NAVOCEANO, United States). Terrain analyses were applied to the bathymetry data including slope, roughness, and hillshade. Slope was derived using the algorithm of Horn (1981). By showing both the slope and depth through transparency adjustments, submarine landslides, canyons, and lineaments were mapped. To delineate submarine

canyons, drainage extraction algorithms in ArcGIS were utilized including *flow direction* and *flow accumulation*.

The submarine landslides were mapped based on the following key morphological features: head scarp (scar) characterized by a relatively steep slope at the top of the landslide, arcuate or concave morphology of the landslide area, and the presence of mass transport deposits (MTDs) at the toe of the landslide (Watson et al., 2020). Majority of the mapped landslides, however, are based mainly on head scarp and arcuate morphologies due to the rare occurrence of MTDs observed. The apparent rare occurrence of MTDs is attributed to the resolution of the bathymetry and the low preservation of these deposits once disintegrated. Interactive 2D cross-sectional profiles in QGIS also aided in recognizing the concave morphology of submarine landslides, especially at smaller scales. The submarine landslides are further categorized into four levels (1–4) of confidence scale (Watson et al., 2020) based on the presence of key morphological features of submarine landslides (Figure 2).

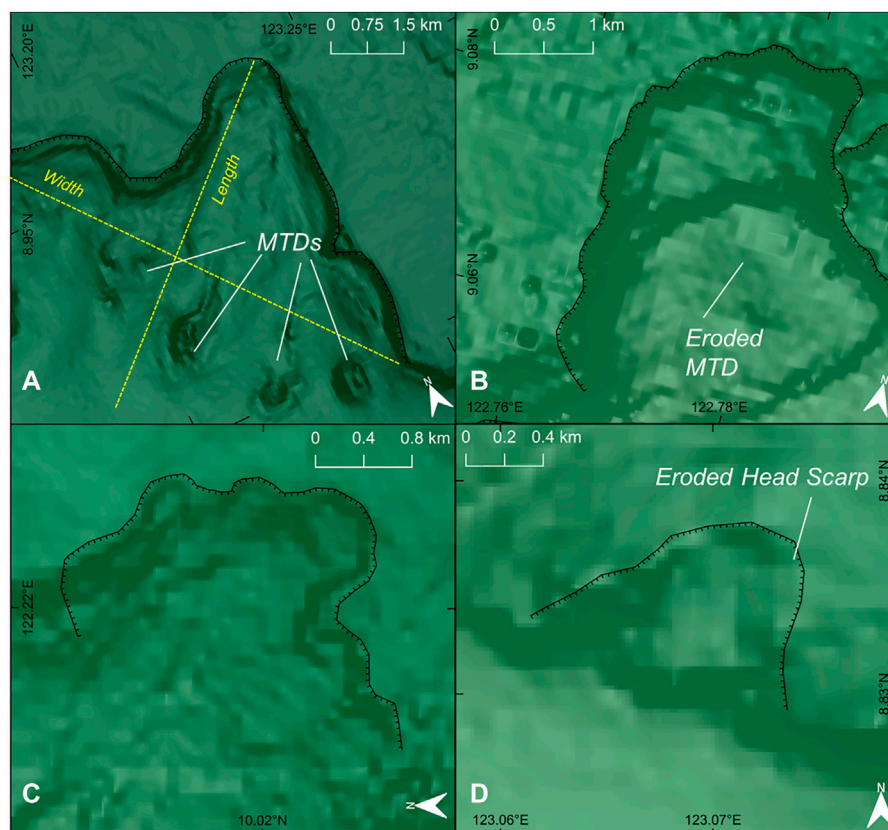


FIGURE 2

Landslide morphometric parameters (length, width, MTDs, head scarp) and confidence classification based on Watson et al. (2020). **(A)** Category 1: well-defined head scarp, arcuate morphology, and MTD at the toe. **(B)** Category 2: well-defined head scarp and arcuate morphology, eroded to no clear indication of MTDs. **(C)** Category 3: presence of head scarps, although eroded, and arcuate morphology. No MTDs. **(D)** Category 4: Heavily eroded headscarps and no MTDs but with arcuate morphology; these are mainly small submarine landslides limited by the bathymetry resolution.

Table 1 shows the delineated morphometric parameters of submarine landslides modified after Gamboa et al. (2022) and Watson et al. (2020). Volume, in particular, was estimated by first creating a pre-landslide digital elevation model (DEM) similar to the methods of Gamboa et al. (2022). The pre-landslide DEM is estimated by sampling elevations around the perimeter of the landslide and applying a multi-level b-spline interpolation at a larger 100 x 100 m raster grid. Volume is calculated based on the surface difference between the pre-landslide DEM as the top surface and the present bathymetry data as the base. Figure 3 shows a sample of the modeled pre-landslide surface and the present scarp morphology for volume calculation.

3.2 Statistical analyses of submarine features

Two-dimensional (2D) histograms were applied among the morphometric parameters to infer correlations. Ripley's L function (Ripley 1977) was calculated through the *spatstat* package in R to determine whether the distribution of submarine landslides has significant clustering across different distance scales.

The L function is a linear transformation of the K function expressed in distance and calculated by:

$$L(r) = \sqrt{\frac{K(r)}{\pi}} = \sqrt{\frac{A \sum_{i=1}^n \sum_{j=1, j \neq i}^n k(i, j)}{\pi n(n-1)}} \quad (1)$$

where A = area of the bathymetry coverage, n = total number of mapped submarine landslides, r = distance, and $k(i, j)$ is the weighting factor for edge detection. A neighboring (j) submarine landslide is included in the summation when its distance from the reference submarine landslide (i) is $\leq r$. The centroid of each submarine landslide served as an input point. Observed $L(r)$ greater than the expected values indicate significant clustering, whereas lower observed $L(r)$ suggest dispersion. A total of 999 permutations were run to calculate the confidence interval (CI) envelope of the $L(r)$ signifying complete spatial randomness.

Kernel density analysis was performed in ArcGIS to estimate the 2D probability density distribution (Silverman 1986) of the delineated submarine landslides, submarine canyons, and lineaments. The distribution of earthquakes (1589–2020) from the Philippine Institute of Volcanology and Seismology (PHIVOLCS) was also included in the kernel estimation. Kernel

TABLE 1 Delineated morphometric parameters of submarine landslides modified from Gamboa et al. (2022) and Watson et al. (2020).

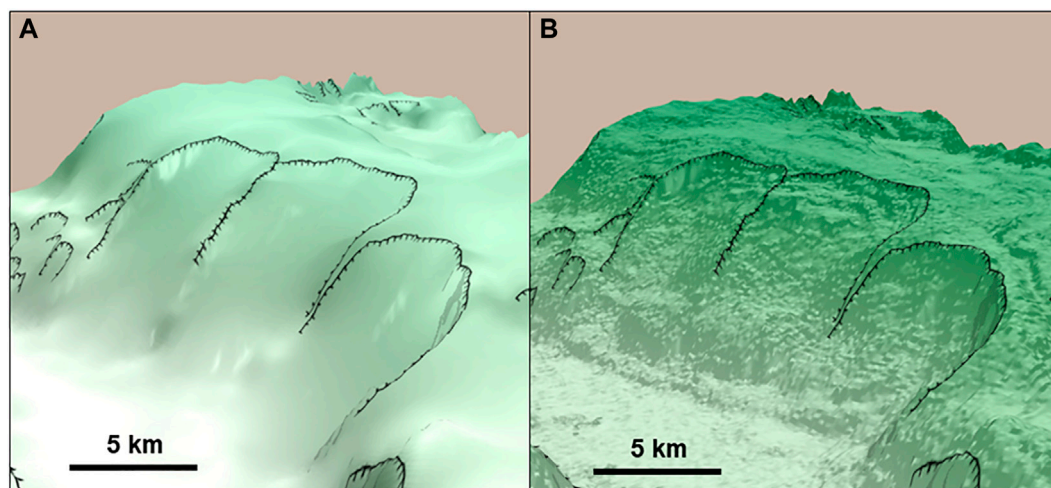
Parameter	Description
Minimum depth (top depth)	Submarine landslide depth (km) of the head scarp
Maximum depth	Submarine landslide depth (km) of the toe
Mean depth	Mean depth (km) within the landslide area
Height	Difference between the maximum and minimum depths (km)
Head scarp length	Length (km) of the landslide head scarp
Area	Area of the landslide polygon (km ²)
Length	Landslide length perpendicular to the contour and flow direction (km)
Width	Landslide width, i.e., the widest distance within the landslide area perpendicular to the length (km)
L/W	Length-to-width ratio
Maximum slope	Highest slope within the submarine landslide area, typically along the head scarp (°)
Mean slope	Mean slope within the submarine landslide area (°)
Volume	Estimated volume (km ³) of the submarine landslide based on the difference between the surface of the modeled pre-landslide and present landslide DEM
Distance from trench	The shortest distance of the submarine landslide from the trench (km)
Distance from submarine canyon	The shortest distance of the submarine landslide from a submarine canyon (km)

density can provide insights into the intensity variation, spatial correlation among submarine features, and underlying processes that may be linked to the distribution of submarine landslides. These kernel densities are further evaluated through correlation matrices of the raster bands between submarine landslides and submarine canyons, lineaments, and earthquakes.

To examine statistically significant clusters of relatively large- and small-volume submarine landslides, we identified their spatial distribution using the Getis-Ord (G_i^*) statistic (Getis and Ord 1992) that calculates the z-score and equivalent p -values of each submarine landslide:

$$G_i^*(d) = \frac{\sum_{j=1}^n w_{i,j} x_j - \bar{x} \sum_{j=1}^n w_{i,j}}{s \sqrt{\frac{n \sum_{j=1}^n w_{i,j}^2 - \left(\sum_{j=1}^n w_{i,j}\right)^2}{n-1}}} \quad (2)$$

where G_i^* = z-score, x_j = volume, $w_{i,j}$ = weighting factor based on the spatial relationship of i and j neighbors at distance d , \bar{x} = mean sample volume, and s = volume standard deviation among neighbors. The *optimized hot spot analysis* in ArcGIS based on Getis-Ord assigns a fixed distance d based on the first peak clustering (=14.3 km). Submarine landslides were then grouped into seven: one that belongs to null groups (1), three that belong to significant clusters of high values at 99% confidence interval (CI) (2), 95% CI (3), 90% CI (4), and three that belong to significant clusters of low values at 99% CI (5), 95% CI (6), and 90% CI (7). These groups are then compared based on select morphometric parameters using boxplots. In addition to volume, another morphometric parameter that was calculated with G_i^* is the length-to-width ratio (L/W) to explore significant clusters of prolate (high L/W) and oblate (low L/W) submarine landslides relative to the flow direction. Altogether, these exploratory spatial analyses aim to

**FIGURE 3**

Three-dimensional (3D) perspective of the modeled pre-landslide and the present surface of the submarine landslides. (A) The modeled pre-landslide is calculated based on the multi-level b-spline calculation at a coarser 100 x 100 m resolution around the perimeter of the submarine landslide that represents the intact slope. (B) The present surface DEM serves as the base, whereas the modeled pre-landslide is the top surface for estimating the slump volume.

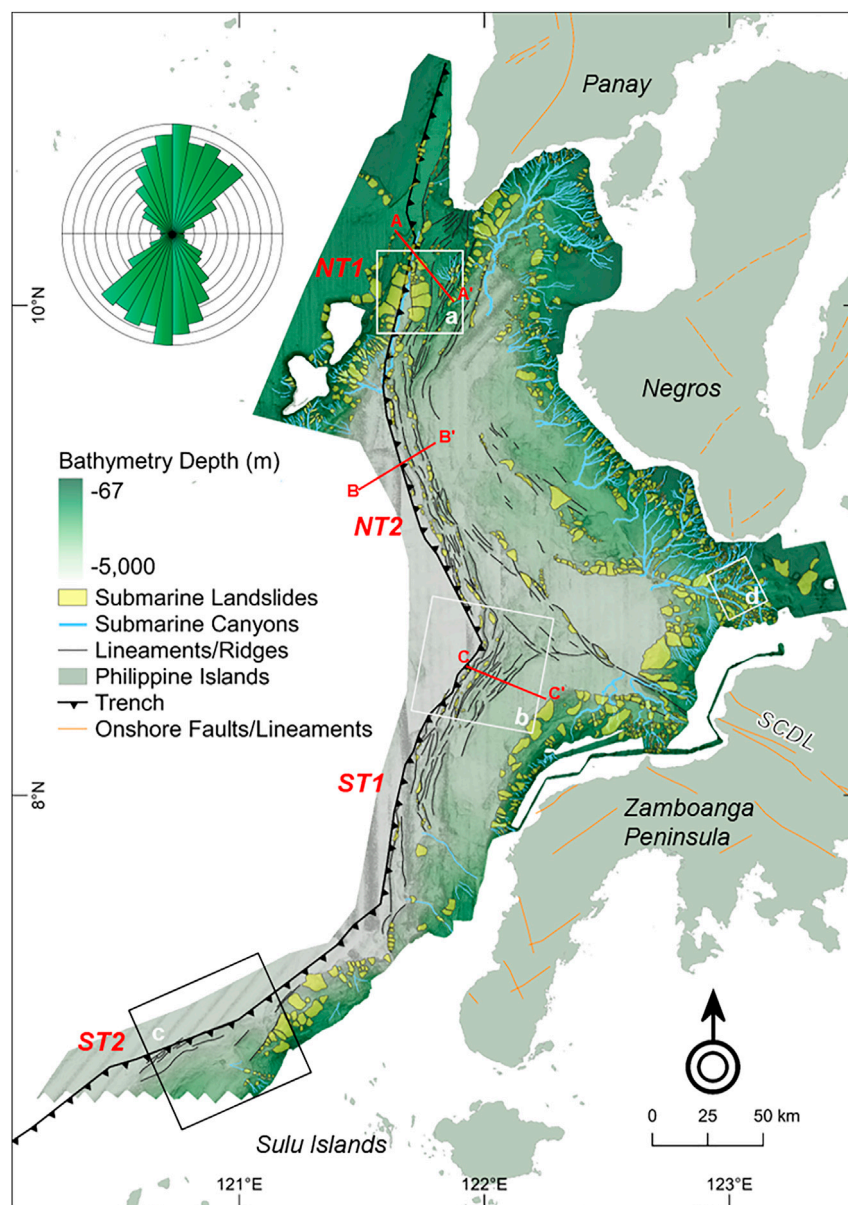


FIGURE 4

Submarine landslides, submarine canyons, and lineaments mapped in the active margin of the NSTS. Rose diagram shows the general northerly trend of the lineaments. Four segments (NT1, NT2, ST1, ST2) were delineated based on the orientation and width variations of the frontal wedge. Squares a–d show the locations of representative submarine features in Figure 5. Red lines are transects of seismic reflection profiles from Schlüter et al. (1996) (Figure 6). The northwest-trending lineaments mapped offshore of Zamboanga Peninsula are inferred to be an extension of the Sindangan–Cotabato–Daguma Lineament (SCDL) in western Mindanao Island (orange lines = onshore faults/lineaments from PHIVOLCS).

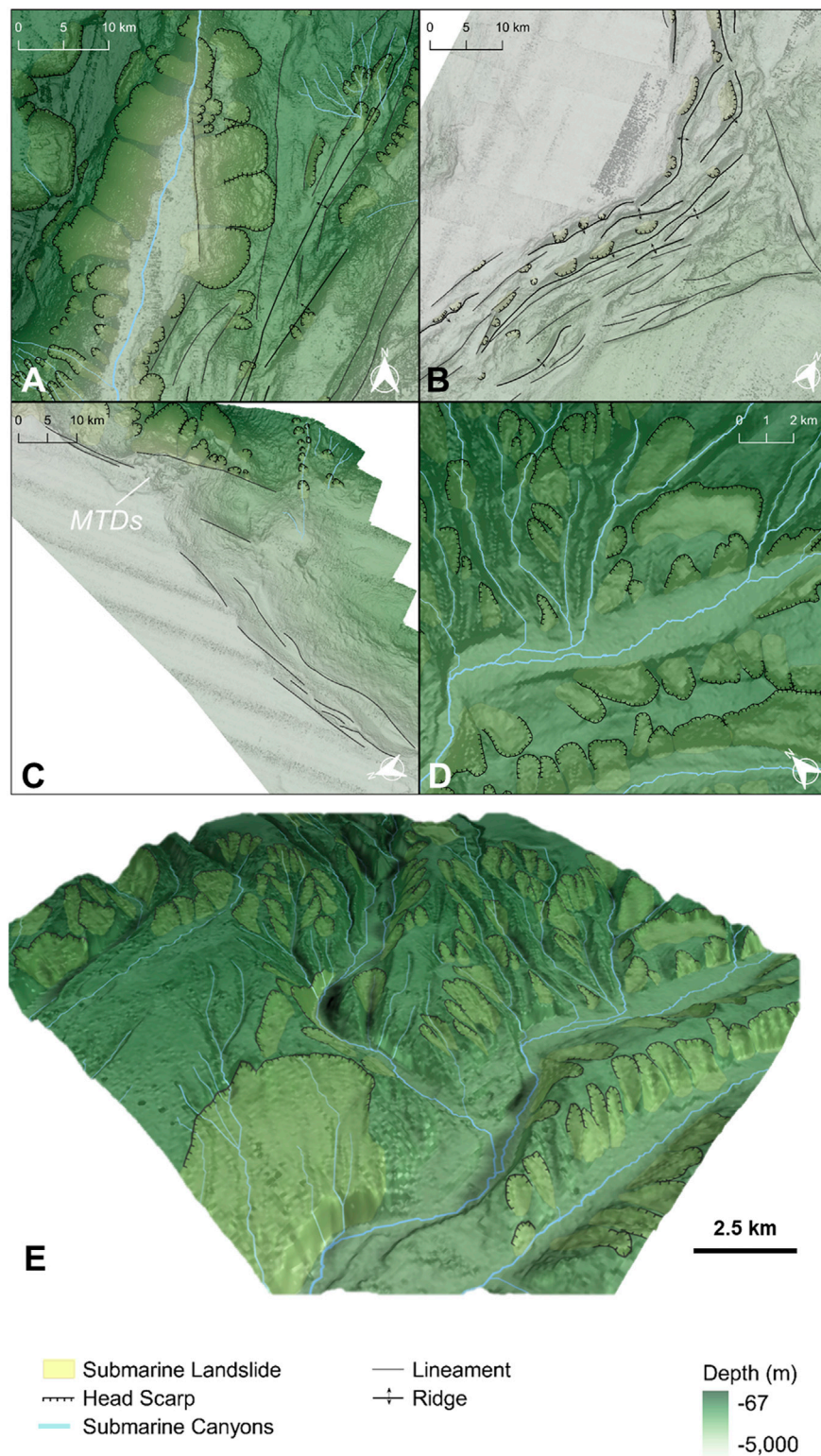
unravel spatial patterns, providing insights into the occurrence and controls of submarine landslides in the NSTS.

4 Results

4.1 Submarine landslides, submarine canyons, lineaments, and frontal wedge variations

A total of 1,214 submarine landslides were mapped (Figure 4) with 64.7% under category 4, 31.6% category 3,

3.1% category 2, and 0.6% category 1. The multitude of categories 3 and 4 reflects the limitation of the bathymetry resolution in readily discerning head scarp and arcuate morphologies but without traces of MTDs. Large networks of submarine canyons were mapped between Negros Island and Zamboanga Peninsula and between Panay and Negros islands. Submarine gullies develop at the shelf edge of about 180 m below sea level and interconnect with larger submarine canyons at deeper portions as slope abruptly increases (Figures 5D, E). Lineaments are mainly situated along the frontal wedge, occurring as parallel ridges, with the majority following a north-to-northeast trend. In addition, the northwest-trending

**FIGURE 5**

Close-up view of the mapped submarine features (see Figure 4 for their location). **(A)** Large submarine landslides along the steep frontal wedge of the northern NT segment (NT1) and steep bathymetry of the colliding Cagayan Ridge (CR) in the west. Between the frontal wedge and the CR is a deeply incised submarine canyon that is parallel to the trench. **(B)** Prominent deformation front and associated submarine features of the frontal wedge in the northern ST segment (ST1). **(C)** Poorly developed frontal wedge, submarine canyons, and submarine landslides in the southern ST segment (ST2). **(D)** Well-developed networks of submarine canyons and associated submarine landslides offshore of southern Negros island. **(E)** Three-dimensional perspective of submarine landslides in Figure 5D.

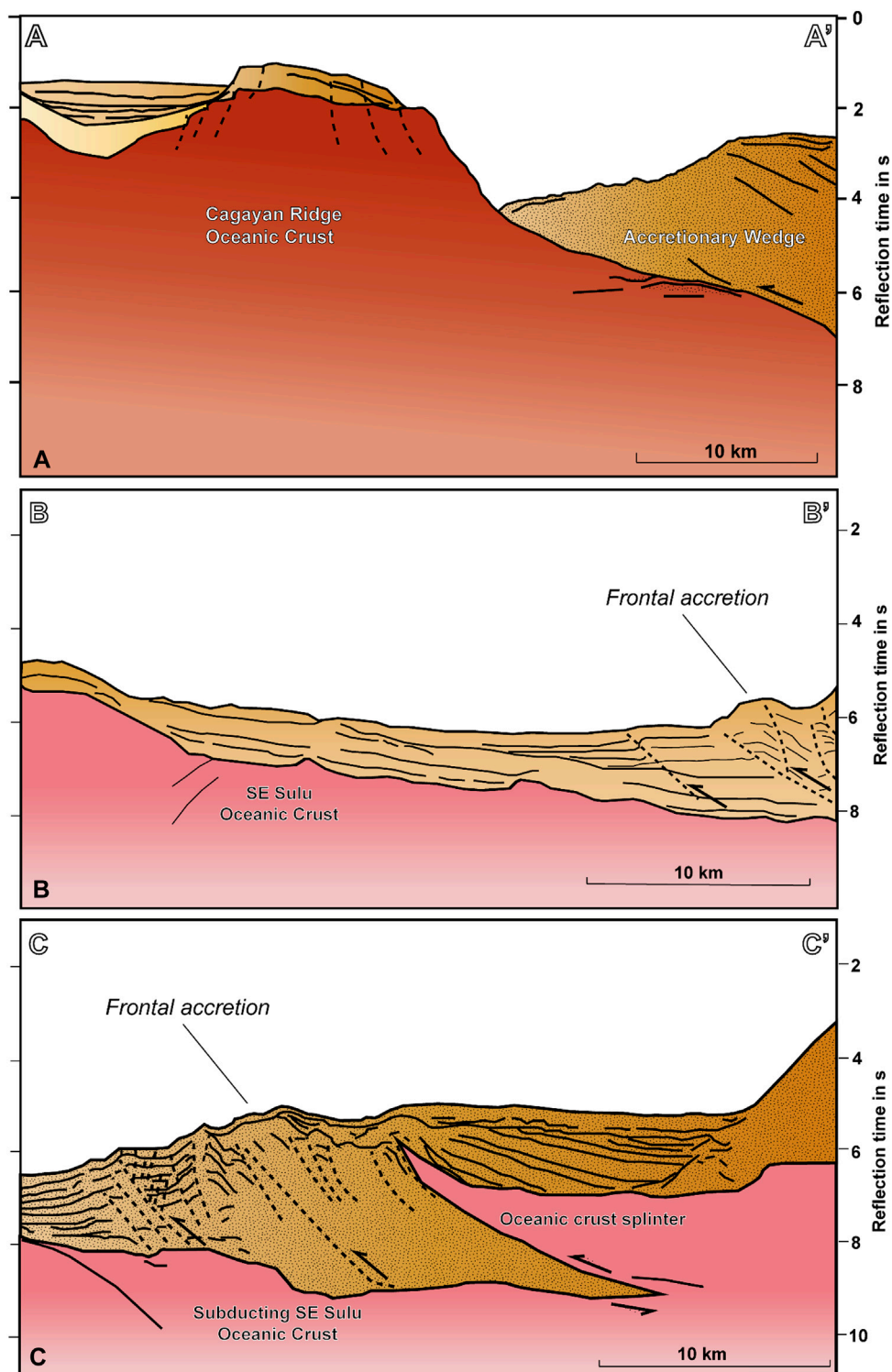


FIGURE 6

Interpreted seismic reflection profiles (as shown in Figure 4) perpendicular to the frontal wedge (adapted from Schlüter et al., 1996 with permission from Elsevier). **(A)** (Line SO 49-16) Collision and subduction of the Cagayan Ridge seamount beneath the northern accretionary prism. **(B)** (Line SO 49-09) Reverse faults associated with the frontal accretion of sediments in the southern Negros Trench segment (NT2). **(C)** (Line SO 49-06) Dense high-angle reverse faults associated with frontal accretion in the northern Sulu Trench segment (ST1), manifested by dense lineaments and ridges as shown in Figure 5B. The identified oceanic splinter is linked to intense thrusting and folding along this segment.

lineaments offshore of Zamboanga Peninsula are inferred to be an extension of the Sindangan–Cotabato–Daguma Lineament (SCDL) (Pubellier et al., 1996) (Figure 4).

Interpreted seismic reflection profiles (Figure 6) by Schlüter et al. (1996) across the trenches revealed that these mapped frontal ridges are seafloor manifestations of accreted trench sediments thrust by

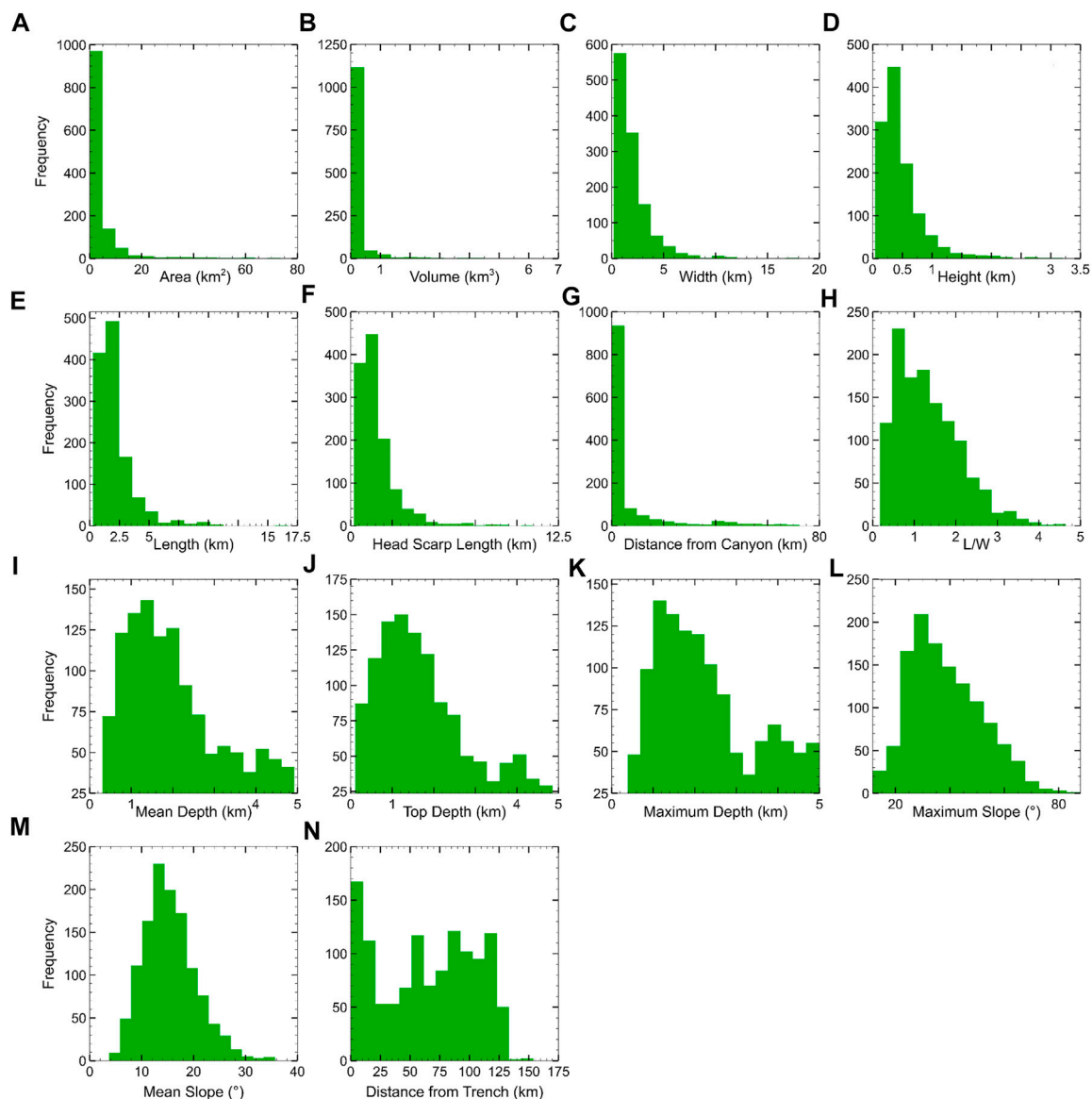


FIGURE 7

Histograms of submarine landslide morphometric parameters. (A) Area, (B) volume, (C) width, (D) height, (E) length, (F) head scarp length, and (G) distance from submarine canyons follow a power-law distribution, reflecting the ubiquitous small submarine landslides. (H) L/W ratio, (I–K) depth, and (L, M) slope show a positively skewed binomial distribution. On the other hand, the (N) distance from the trench has an irregular distribution.

reverse faults. Profile A–A' shows the collision and subsequent subduction of the Cagayan Ridge beneath the northern Negros Trench forearc. In profiles B–B' and C–C', the décollement and subduction of the southeast Sulu Sea along the frontal wedge are shown. Notably, profile C–C' also depicts a crustal splinter that is associated with intense thrusting and folding along this segment.

Four segments were delineated based on frontal wedge variations: (1) The northern Negros Trench (NT1) is northeast trending (15° azimuth) and transects between 10.86°N and 9.76°N with a length of about 126 km. This segment is bounded by the Cagayan Ridge seamount chain and southern Panay Island. Its frontal wedge has a maximum width of about 30 km and steepens subvertically northward. (2) The southern Negros Trench (NT2) is northwest trending (azimuth 340°), with a

length of 131 km and a maximum width of 15 km. (3) The northern Sulu Trench (ST1) is northeast trending (azimuth 19°) with a length of 146 km and a frontal wedge width of 20 km. (4) Lastly, the southern Sulu Trench (ST2) segment is east-northeast trending (azimuth 61°) with a length of about 170 km. Unlike the other segments, ST2 has a poorly developed frontal wedge with subparallel lineaments.

4.2 Morphometry of submarine landslides

Morphometric parameters that are size-dependent, i.e., area, volume, width, height, length, and head scarp length, all follow a power-law distribution with ubiquitous low values (Figures 7A–F).

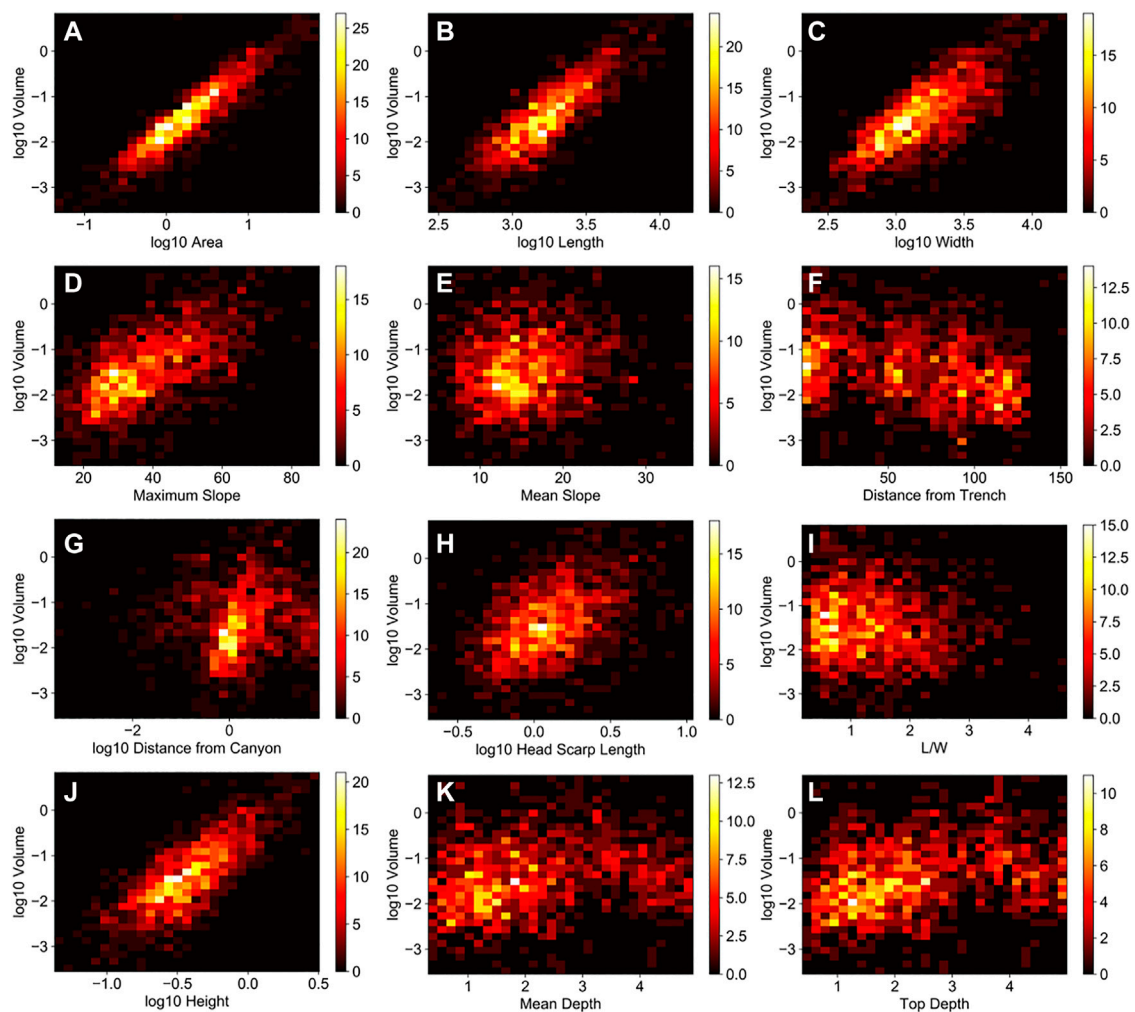


FIGURE 8

2D histograms of submarine landslide parameters with respect to volume (refer to Figure 7 for units). Size-dependent parameters such as (A) area, (B) length, (C) width, (H) head scarp length, and (J) height show a positive correlation with volume. The (D) maximum slope also shows a positive trend with volume. Other parameters (E–L) have a weak association with volume, but an apparent inverse trend can be observed with (F) distance from the trench and (I) L/W. Volume is observed to increase with (K, L) depth up to around 3 km and then shifts to a negative trend toward 5 km depth.

The distance from the submarine canyon also follows the same distribution. On the other hand, L/W, maximum slope, and mean, top, and maximum depth have skewed binomial distributions that peak around 1.4–1.8 km. Of the 1,214 submarine landslides, 78% have an area and volume of $<5 \text{ km}^2$ and 0.5 km^3 , respectively (Figure 7). The mean area and volume are 1.8 km^2 (median = 4.0 km^2) and 0.03 km^3 (median = 0.18 km^3), respectively. The average maximum slope is 38° , and the majority (23%) of distances from the trenches were $<20 \text{ km}$. On the other hand, 77% of submarine landslides are less than 5 km away from submarine canyons.

Area, volume, length, width, distance from submarine canyons, head scarp length, and height were scaled logarithmically in the 2D histogram to normalize highly skewed power-law distributions. A base of 10 was arbitrarily chosen for the logarithmic normalization. Figure 8 and Figure 9 show the 2D histogram correlation relative to the volume and L/W, respectively, among morphometric parameters. Area, length, width, headscarp length, and height show positive correlations with volume as these are typically size-dependent. The

maximum slope is also positively correlated with volume. Although the plots were highly scattered, an apparent inverse trend is observed between volume and the distance from the trench and L/W. Top and mean depths show an apparent positive trend where volume increases with depth up to around 3 km and then shifts to an inverse pattern toward 5 km depth. For L/W correlations, the rest of the parameters have highly scattered plots, except for the apparent negative trend with respect to area, width, maximum slope, and distance from submarine canyons. In addition, an apparent positive trend is observed between length and L/W.

4.3 Spatial distribution and correlation of submarine features

Ripley's L function (Figure 10) shows higher observed $L(\hat{L}_{\text{obs}(r)})$ than the expected ($\hat{L}_{\text{theo}(r)}$) values, indicating a non-random distribution and clustering at a wide range of distances. This is

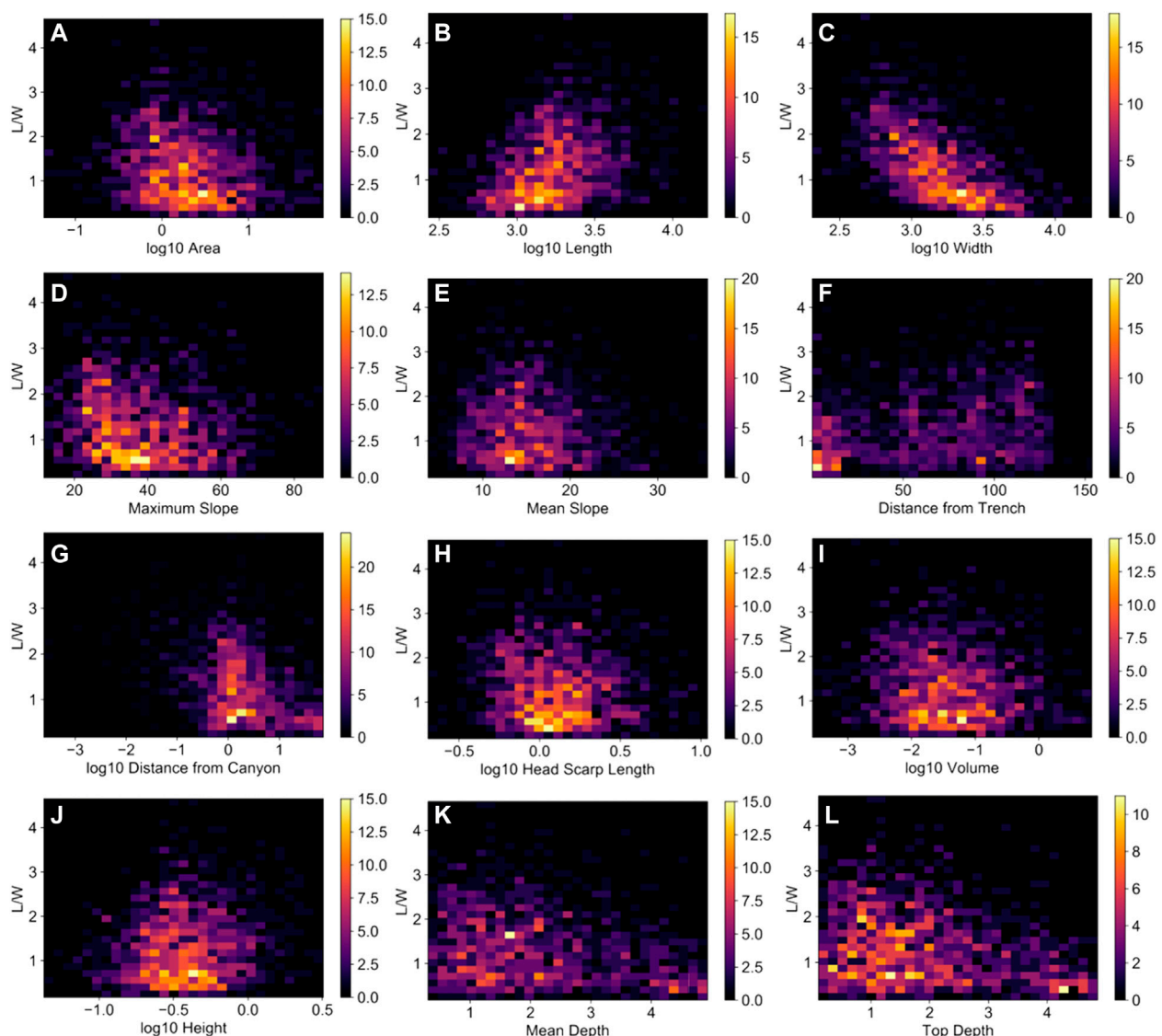


FIGURE 9

2D histograms of submarine landslide parameters with respect to the L/W (refer to Figure 7 for units). Majority of the parameters have highly scattered plots (E, F, H, I, J, K, L), although (A) area, (C) width, (D) maximum slope, and (G) distance from the submarine canyon show an apparent inverse trend. In addition, an apparent positive trend is observed in (B) length and L/W.

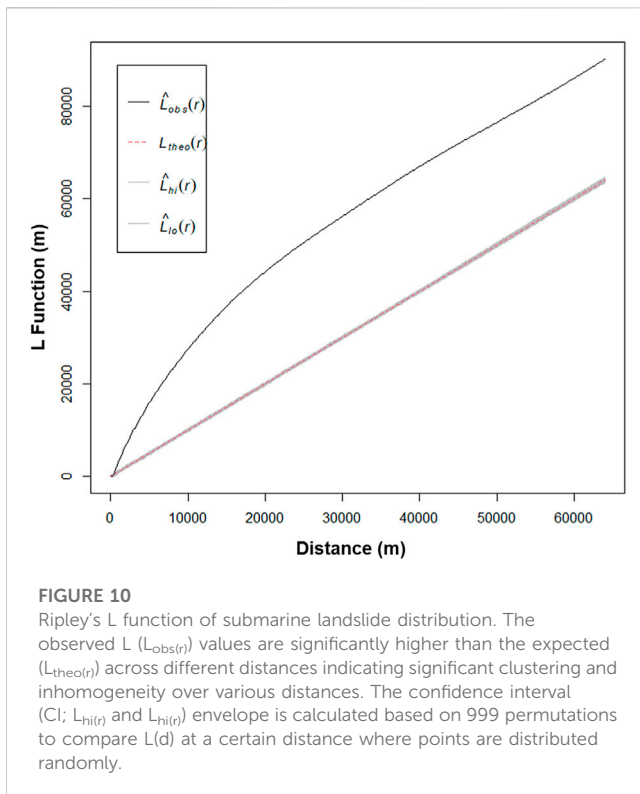
exemplified by the inhomogeneous kernel density of submarine landslides in Figure 11A. The highest intensity distribution of submarine landslides is located offshore between southeastern Negros Island and northern Zamboanga Peninsula, as well as between southern Panay and southwestern Negros islands. Submarine canyons also have a similar distribution to submarine landslides (Figure 11C), whereas lineaments (Figure 11B) are concentrated in the frontal wedge of the trench. Matrix correlation among kernel densities including earthquakes reveals that submarine canyons have the highest correlation (0.76) with the distribution of submarine landslides.

Regions with significant clusters of high and low volume and L/W based on Getis-Ord statistics are shown in Figure 12. Significantly large-volume ($>0.5 \text{ km}^3$) submarine landslides are clustered offshore of southern Panay Island as well as offshore

southeastern Negros, Zamboanga Peninsula, and Sulu islands. On the other hand, those with a significantly small volume ($<0.05 \text{ km}^3$) are concentrated where the highest probability density of submarine landslides and canyons occurs (Figures 11A,C, respectively). Significantly high L/W submarine landslides (Figure 12B) are clustered along areas with high kernel density of submarine canyons (Figure 11C). Those with significantly low L/W are clustered along the frontal wedge and abyssal plains.

4.4 Significant clusters of high and low volume and L/W

Significant clusters of submarine landslides were grouped based on the degree of statistical significance (% CI), while their depth and



slope parameters were plotted in boxplots (Figure 13). Significant clusters of large-volume submarine landslides (90%, 95%, and 99% CI) have a wide interquartile range (IQR) of top and mean depths (Figures 13A, B), whereas significantly small-volume (90% and 95% CI) submarine landslides have a narrow IQR around 1–2 km depths. An opposite trend is observed for those with significantly high and low L/W ratios (Figures 13E, F). Submarine landslides with high L/W ratios (90%, 95%, 99% CI) have high distribution occurring at shallower depths, whereas those with low L/W ratios (90%, 95%, 99% CI) occur at deeper levels with a wider IQR. In terms of slope, those with significantly high volume have generally steeper mean and maximum slope than those with significantly low volume (Figures 13C, D). On the other hand, groups in terms of L/W have a similar range of mean slope (Figure 13G), but the maximum slope decreases with higher L/W ratios (Figure 13H).

5 Discussion

5.1 Frontal wedge variations along the NSTS

The well-developed frontal wedge of the three segments (NT1, NT2, ST1) of the NSTS is linked to relatively high sedimentation rates of this active margin demonstrated by dense networks of submarine canyons (i.e., conduits of inland clastic deposits) and low overall convergence rates (54 mm yr⁻¹, NT; 28 mm yr⁻¹, ST) based on previous GPS surveys (Rangin et al., 1999; Simons et al., 1999). High sediment influx and slow convergence rates (<60 mm yr⁻¹) are conducive conditions in developing accretionary margins and frontal wedge (e.g., Huene and Scholl, 1991; Lallemand et al., 1994; Clift and Vannucchi 2004; Simpson

2010). In addition, morphological variations of the frontal wedge along the NSTS are attributed to the heterogeneity of sediment distribution from nearby islands and variability of convergence rates and forearc deformation. NT1, NT2, and ST1 segments are relatively closer to Panay, Guimaras, Negros, and Zamboanga Peninsula. These segments are presumed to receive higher sediment influx due to larger land areas than the ST2 segment which is closer to the smaller Sulu Group of Islands (Figure 1). Similar findings along the northern segments of both the Manila (Armada et al., 2020) and Japan (Tsuru et al., 2002; Kodaira et al., 2017) trenches also attributed the well-developed accretionary prism to higher sedimentation influx than the southern segments.

Another variation observed on the trench segments is their steepness, most notably on NT1, which is marked by an oversteepened frontal wedge. While well-developed frontal wedges have been correlated to high sediment influx and slow convergence rates, oversteepening is mainly driven by seamount subduction. These bathymetric highs cause intense uplift, deformation, and thrust faulting of the overriding plate inducing steepening and erosion (Yang et al., 2022). Examples of these frontal wedge oversteepening include segments of the Hikurangi Trough (Pedley et al., 2010), Java Trench (Masson et al., 1990), Middle America Trench (Hühnerbach et al., 2005), and Nankai Trough (Bangs et al., 2006; Moore et al., 2019). Similarly, the collision and subsequent subduction of the northeastern portion of the Cagayan Ridge along NT1 presumably induce oversteepening of the frontal wedge as well as its orientation change to the northeast.

The characteristics of the four trench segments based on frontal wedge variations provide essential information not only on the potential impacts of submarine landslides but also for modeling future megathrust tsunami scenarios. Furthermore, the width of the frontal wedge is indicative of its tsunami hazard potential as tsunami run-ups of shallow megathrust ruptures have been correlated to the width of the frontal wedge (Qiu and Barbot 2022). This is further emphasized by historical records where great offshore earthquakes occur mostly along accretionary prisms with thick sediment cover (Bilek and Lay 2018).

5.2 Controls of submarine landslide distribution

Exploratory spatial analyses revealed non-random and significant clustering of submarine landslides in which ubiquitous and small-volume landslides are controlled predominantly by submarine canyon systems. These conduits of terrestrial sedimentation influx induce overloading and instability of prolate precondition slope failures. In addition, significant clustering of prolate (high L/W) submarine landslides coincides with the distribution of submarine canyon systems. The resemblance of prolate morphology to submarine canyons implies that these prolate submarine landslides influence the development of submarine canyon networks. Small submarine landslides may eventually interconnect forming incisions for sediment transportation (Baztan et al., 2005; Micallef et al., 2012). This relationship between prolate submarine landslides and submarine canyons is further supported by the apparent inverse trend between L/W and the distance from submarine canyons (Figure 9F). These

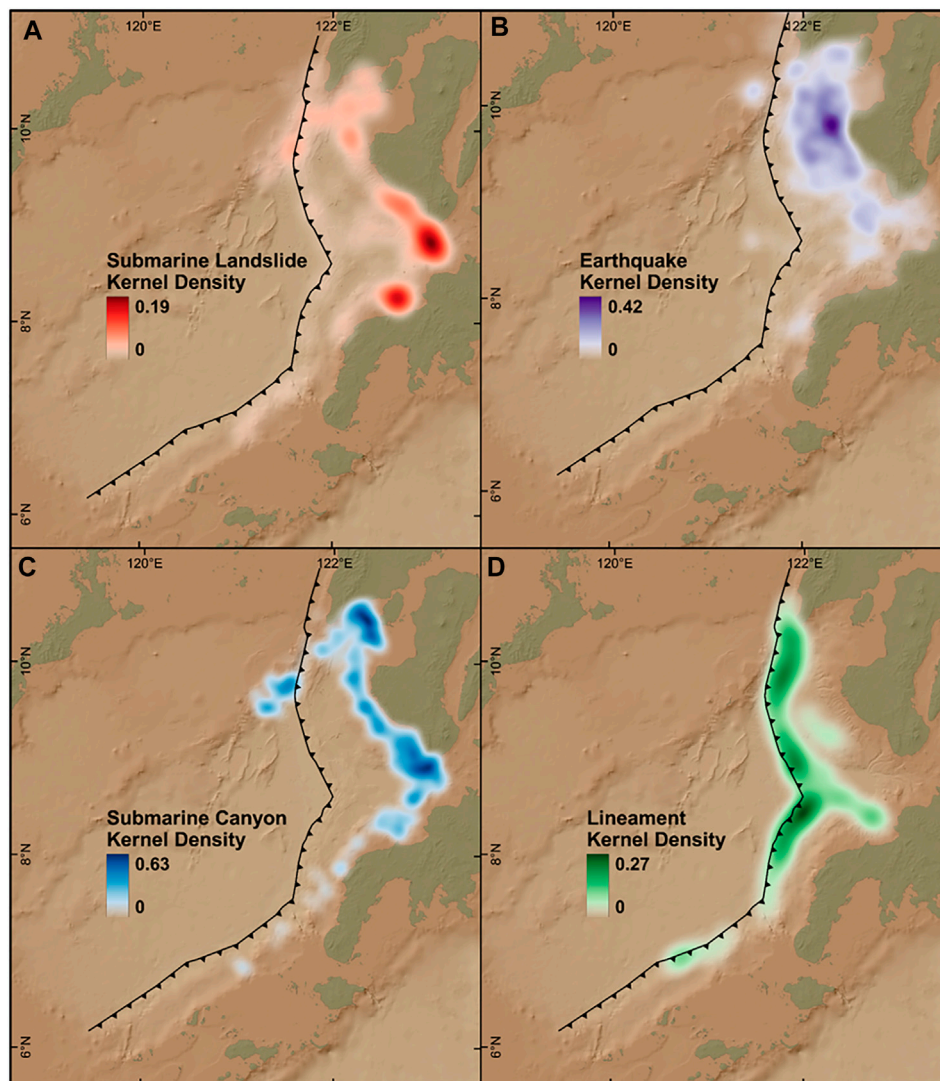


FIGURE 11

Kernel density variations (per km²) of (A) submarine landslides, (B) earthquakes, (C) submarine canyons, and (D) lineaments across the NSTS.

Earthquake kernel density is distributed mainly along the Negros Trench segments, whereas that of lineaments along the frontal wedge. Matrix band correlations showed that submarine canyons have the highest correlation to submarine landslide distribution of 0.76, followed by earthquakes (0.46) and then lineaments (0.20).

clustered submarine landslides with high L/W are prevalent in relatively shallower depths around 1–3 km where submarine canyons typically form. On the other hand, significant clusters of oblate (low L/W) submarine landslides mainly occur along the frontal wedge and in abyssal plains (Figure 12B). This is due to the subparallel and steep ridges along the frontal wedge that are suitable morphotectonic structures to form oblate submarine landslides.

While small landslides are mainly controlled by submarine canyons, large ones are significantly clustered along steep slopes and at varying depths. Most notably, the NT1 frontal wedge is marked by the densest cluster of large submarine landslides. As discussed in Section 5.1, this segment has an oversteepened and wide frontal wedge linked to the collision and subsequent subduction of Cagayan Ridge seamounts. Thus, we associate the seamount

subduction and subsequent slope oversteepening as dominant preconditioning factors for the occurrence of large submarine landslides along this segment. Modeling of seamount subduction beneath the accretionary prism, in its initial stage, resulted to oversteepening of the frontal wedge, reactivation of frontal thrust faults, and large submarine landslides (Dominguez et al., 2000; Ruh 2016; Morgan and Bangs 2017). This is supported by other accretionary prisms where seamount subduction underlies large submarine landslides (e.g., Hühnerbach et al., 2005; Pedley et al., 2010). While it is unclear what causes the clustering of large submarine landslides in other portions, the role of nearby fault structures (e.g., SCDL), intense tectonic deformation and fully subducted seamounts, together with sediment overloading could all play complex roles to induce steepening. Nonetheless, the identified regions with clusters of large submarine landslides

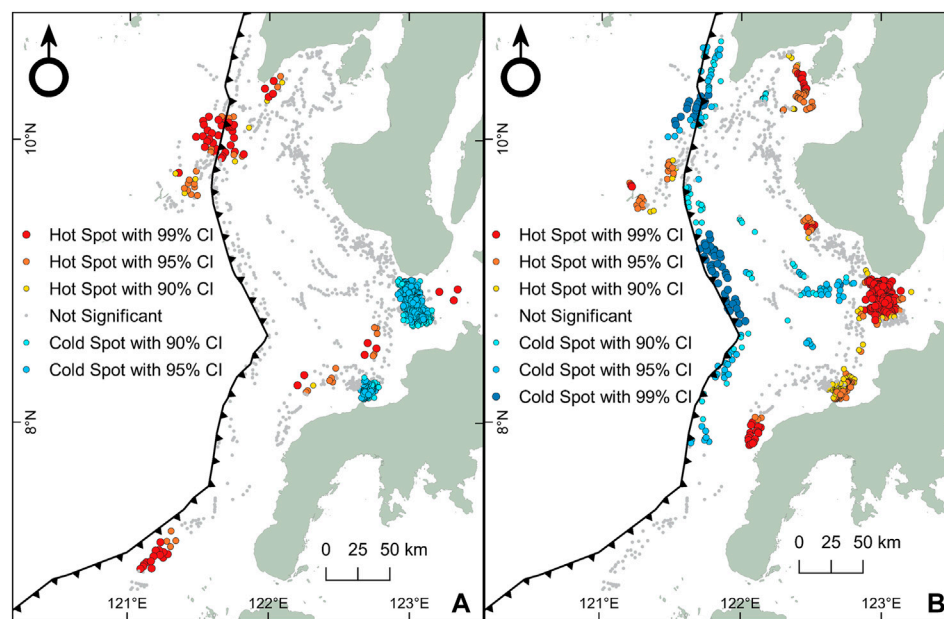


FIGURE 12

Getis-Ord (G_i^*) analysis of submarine landslide distribution with respect to volume and L/W. (A) Significant clusters of large-volume submarine landslides (red dots) are found in different regions of the active margin, but the densest clusters are in the northern NT segment (NT1), where collision with the Cagayan Ridge occurs. Significant clusters of small-volume submarine landslides (blue dots) are located offshore of Negros Island and Zamboanga Peninsula, corresponding to areas with the densest submarine canyon systems (Figure 11A). (B) Significant clusters of high L/W (red dots) are also in regions with dense submarine canyon systems. On the other hand, the frontal wedge and abyssal plain host significant clusters of low L/W (blue dots).

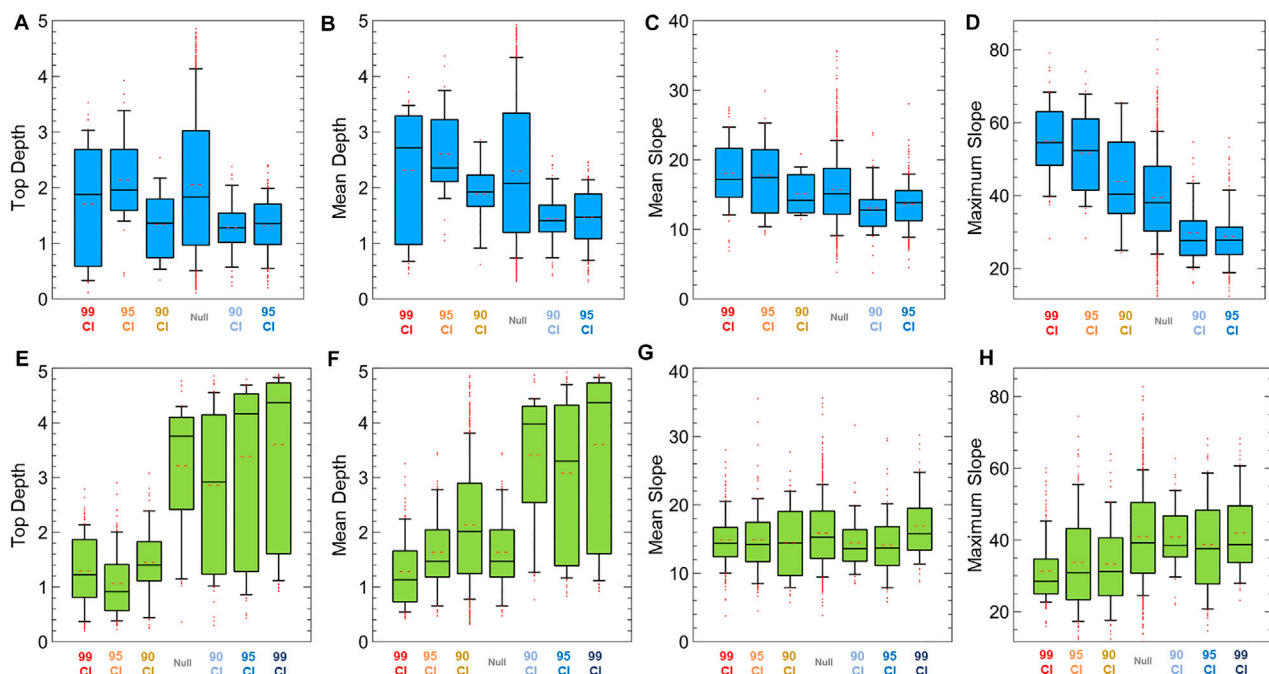


FIGURE 13

Boxplots showing the depth and slope of submarine landslides that are grouped based on the G_i^* statistic (blue boxplots, based on volume; yellow green, based on L/W) in Figure 13 (red hue, hot spots; blue hue, cold spots). Red dots indicate the outliers, while broken lines inside the interquartile range (IQR) show the mean value. (A–D) Box plots based on the volume show that significant clusters of large submarine landslides have depths with wide IQR (0.1–4 km), while small ones are in a narrow IQR of about 0.1–2 km. Mean slope (C) tends to concentrate between 10° and 30° with slightly lower values for significantly small-volume submarine landslides. (D) Maximum slope showed a positive association with clusters of significantly large-volume submarine landslides, whereas small-volume landslides have a lower maximum slope. (E–H) Clusters of significantly high L/W occur in shallower depths and slightly lower slopes than those of significantly low L/W.

provide significant insights into modeling landslide-driven tsunamis, where the estimated volume is highly correlated with potential tsunami wave height (Sabetti and Heidarzadeh 2022).

This study highlights the dominant role of submarine canyon systems due to high sediment influx and subduction-induced oversteepening to precondition slope instability. As the slope becomes unstable, gravity and earthquakes can readily trigger submarine failures along active margins (Masson et al., 2006; Scarselli 2020). The possible presence of gas hydrates may also be involved as they occur along margins with high sedimentation influx (e.g., Gee et al., 2007; Mountjoy et al., 2014; Crutchley et al., 2016). Thus, we recommend dense seismic reflection surveys to further map the underlying structures and their variations across the active margin in detail. In addition, the current resolution of bathymetry data is inadequate to map even smaller (m-scale) submarine landslides. This has been shown by the absence of significant clusters of small submarine landslides at 99% CI. As bathymetry resolution has been a common limitation in mapping submarine landslides (e.g., Gazioglu et al., 2005; Watson et al., 2020; Gamboa et al., 2022), higher-resolution multibeam bathymetry surveys will further improve the characterization of submarine geomorphological features.

6 Conclusion

Four frontal wedge segments were delineated in the NSTS, with varying widths, lengths, and associated morphotectonic features. These variations are linked to the disparity of convergence rates along the trench, subduction processes, and heterogeneous distribution of sediments from inland sources. A total of 1,214 submarine landslides and their morphometric parameters along this active margin were delineated. Prolate submarine landslides (high L/W) tend to form in submarine canyons, whereas oblate morphologies (low L/W) generally occur along the frontal wedge and abyssal plains. These opposing submarine landslide morphologies reflect their different environments and geomorphological conditions.

Ubiquitous small submarine landslides are mainly controlled by submarine canyon systems where high sediment influx from inland sources preconditions instability. These small-volume submarine landslides also occur in relatively shallow depths of about 1–2 km and generally have a lower mean and maximum slope. On the other hand, seamount subduction and related tectonic processes that induce oversteepening play dominant role to precondition large submarine landslides. This study revealed the influence of spatial, geomorphological, and tectonic controls to the morphological variations of submarine landslides in the active margin. Furthermore, the identified regions with clustered large submarine landslides and the segments of the NSTS provide essential information in modeling fault and submarine failure-driven tsunamis and identification of highly exposed coastal areas. This study also demonstrates the use of morphological and exploratory spatial analyses to elucidate underlying controlling factors and to evaluate the hazard potential of areas with limited geological and geophysical datasets.

Data availability statement

The original contributions presented in the study are included in the article/supplementary material, further inquiries can be directed to the corresponding author.

Author contributions

LN and NR contributed to the conceptualization and structure of the study. LN wrote the first draft of the manuscript and performed the terrain and statistical analyses. Both authors contributed to the manuscript writing and revision and have read and approved the submitted version.

Funding

This study is supported by the 2022 NIGS Research Grant “Investigating the frontal wedge characteristics and geological controls of submarine landslides in the Negros–Sulu Trench System”, funded by the University of the Philippines Diliman and “Investigation and Numerical Modeling of Philippine Tsunamis Based on Historical, Geomorphological, and Geological Evidence of Past Earthquakes Investigation and Numerical Modeling of Philippine Tsunamis” (No. 4233), funded by the Department of Science and Technology (DOST) through the DOST–Philippine Council for Industry, Energy, and Emerging Technology Research and Development (DOST-PCIEERD).

Acknowledgments

The authors would like to acknowledge the Philippine National Mapping and Resource Information Authority (NAMRIA) for providing multibeam bathymetry data, as well as the PHIVOLCS for the seismicity and onshore fault data. We are grateful to Editor RA and reviewers DD and WL for their insightful comments that have greatly improved the content and structure of the manuscript. We also thank D. Gamboa for providing valuable insights in the parameterization of submarine landslides in this study. The ArcGIS Pro software was utilized through the academic license acquired by the University of the Philippines Diliman. We would also like to acknowledge the following open-source libraries, software, and processing tools that were used in this study: Veusz, Jupyter, spatstat (R), and Python libraries: Matplotlib, NumPy, Pandas, and math; QGIS plug-ins: Profile Tool, Qgis2threejs, and Volume Calculation Tool.

Conflict of interest

The authors declare that the research was conducted in the absence of any commercial or financial relationships that could be construed as a potential conflict of interest.

Publisher's note

All claims expressed in this article are solely those of the authors and do not necessarily represent those of their affiliated

References

- Armada, L. T., Hsu, S. K., Dimalanta, C. B., Yumul, G. P., Doo, W. B., Yeh, Y. C., et al. (2020). Forearc structures and deformation along the Manila trench. *J. Asian Earth Sci.* 194, 100036. doi:10.1016/j.jaesx.2020.100036
- Baba, T., Gon, Y., Imai, K., Yamashita, K., Matsuno, T., Hayashi, M., et al. (2019). Modeling of a dispersive tsunami caused by a submarine landslide based on detailed bathymetry of the continental slope in the Nankai Trough, southwest Japan. *Tectonophysics* 768, 228182. doi:10.1016/j.tecto.2019.228182
- Bangs, N. L. B., Gulick, S. P. S., and Shipley, T. H. (2006). Seamount subduction erosion in the Nankai Trough and its potential impact on the seismogenic zone. *Geology* 34 (8), 701–704. doi:10.1130/G22451.1
- Bautista, M. L. P., Bautista, B. C., Joan, S., and Narag, I. (2012). *Philippine tsunamis and seiches (1589–2012)*.
- Baztan, J., Berné, S., Olivet, J. L., Rabineau, M., Aslanian, D., Gaudin, M., et al. (2005). Axial incision: The key to understand submarine canyon evolution (in the western gulf of lion). *Mar. Petroleum Geol.* 22 (6–7), 805–826. doi:10.1016/j.marpetgeo.2005.03.011
- Bellon, H., and Rangin, C. (1991). Geochemistry and isotopic dating of cenozoic volcanic arc sequences around the Celebes and Sulu seas. *Proc., Sci. Results, ODP, Leg 124, Celebes Sulu Seas* 124, 321–338. doi:10.2973/odp.proc.sr.124.163.1991
- Bilek, S. L., and Lay, T. (2018). Subduction zone megathrust earthquakes. *Geosphere* 14 (4), 1468–1500. doi:10.1130/GES01608.1
- Clift, P., and Vannucchi, P. (2004). Controls on tectonic accretion versus erosion in subduction zones: Implications for the origin and recycling of the continental crust. *Rev. Geophys.* 42 (2). doi:10.1029/2003RG000127
- Crutchley, G. J., Mountjoy, J. J., Gorman, A. R., Pecher, I. A., and Henrys, Stuart A. (2016). Submarine slope instabilities coincident with shallow gas hydrate systems: Insights from New Zealand examples. *Submar. Mass Movements Their Consequences. Adv. Nat. Technol. Hazards Res. Vol. 41*. Cham: Springer, 401–409. doi:10.1007/978-3-319-20979-1_40
- Dominguez, S., Malavieille, J., and Lallemand, S. E. (2000). Deformation of accretionary wedges in response to seamount subduction: Insights from sandbox experiments. *Tectonics* 19 (1), 182–196. doi:10.1029/1999TC900055
- Fryer, G. J., Watts, P., and Pratson, L. F. (2004). Source of the great tsunami of 1 april 1946: A landslide in the upper aleutian forearc. *Mar. Geol.* 203 (3–4), 201–218. doi:10.1016/S0025-3227(03)00305-0
- Gamboa, D., Omira, R., and Pedro, T. (2022). Spatial and morphometric relationships of submarine landslides offshore west and southwest iberia. *Landslides* 19 (2), 387–405. doi:10.1007/s10346-021-01786-3
- Gazioğlu, C., Yücel, Z. Y., and Doğan, E. (2005). Morphological features of major submarine landslides of marmara Sea using multibeam data. *J. Coast. Res.* 21 (4), 664–673. doi:10.2112/03-0060.1
- Gee, M. J. R., Uy, H. S., Warren, J., Morley, C. K., and Lambiasi, J. J. (2007). The Brunei slide: A giant submarine landslide on the north west borneo margin revealed by 3D seismic data" 246: 9–23. doi:10.1016/j.margeo.2007.07.009
- Getis, A., and Ord, J. K. (1992). The analysis of spatial association by use of distance statistics. *Geogr. Anal.* 24 (3), 189–206. doi:10.1111/j.1538-4632.1992.tb00261.x
- Hall, R. (2002). Cenozoic geological and plate tectonic evolution of SE asia and the SW pacific: Computer-based reconstructions, model and animations. *J. Asian Earth Sci.* 20 (4), 353–431. doi:10.1016/S1367-9120(01)00069-4
- Hall, R. (2013). Contraction and extension in northern borneo driven by subduction rollback. *J. Asian Earth Sci.* 76, 399–411. doi:10.1016/j.jaesx.2013.04.010
- Hall, R. (2012). Late jurassic–cenozoic reconstructions of the Indonesian region and the Indian ocean. *Tectonophysics* 570–571, 5701–57141. doi:10.1016/j.tecto.2012.04.021
- Harbitz, C. B., Finn, L., and Hilmar, B. (2014). Submarine landslide tsunamis: How extreme and how likely? *Nat. Hazards* 72 (3), 1341–1374. doi:10.1007/s11069-013-0681-3
- Heinrich, P. H., Piatanesi, A., and Hébert, H. (2001). Numerical modelling of tsunami generation and propagation from submarine slumps: The 1998 Papua New Guinea event. *Geophys. J. Int.* 145 (1), 97–111. doi:10.1111/j.1365-246X.2001.00336.x
- Hidayat, D., Barker, J. S., and Satake, K. (1995). Modeling the seismic source and tsunami generation of the december 12, 1992 Flores island, Indonesia, earthquake. *Pure Appl. Geophys. PAGEOPH* 144 (3–4), 537–554. doi:10.1007/BF00874382
- Horn, B. K. P. (1981). Hill shading and the reflectance map. *Proc. IEEE* 69 (1), 14–47. doi:10.1109/proc.1981.11918
- Huene, Roland von, and Scholl, David W. (1991). Observations at convergent margins concerning sediment subduction, subduction erosion, and the growth of continental crust. *Rev. Geophys.* 29 (3), 279. doi:10.1029/91RG00969
- Hühnerbach, V., Masson, D. G., Bohrmann, G., Bull, J. M., and Weinrebe, W. (2005). Deformation and submarine landsliding caused by seamount subduction beneath the Costa Rica continental margin - new insights from high-resolution sidescan sonar data. *Geol. Soc. Spec. Publ.* 244, 195–205. doi:10.1144/GSL.SP.2005.244.01.12
- Imamura, F., Gica, E., Takahashi, T., and Shuto, N. (1995). Numerical simulation of the 1992 Flores tsunami: Interpretation of tsunami phenomena in northeastern Flores island and damage at babi island. *Pure Appl. Geophys. PAGEOPH* 144 (3–4), 555–568. doi:10.1007/BF00874383
- Kao, H., Huang, G. C., and Liu, C. S. (2000). Transition from oblique subduction to collision in the northern Luzon arc-taiwan region: Constraints from bathymetry and seismic observations. *J. Geophys. Res. Solid Earth* 105 (B2), 3059–3079. doi:10.1029/1999jb900357
- Kawamura, K., Sasaki, T., Kanamatsu, T., Sakaguchi, A., and Ogawa, Y. (2012). Large submarine landslides in the Japan Trench: A new scenario for additional Tsunami generation. *Geophys. Res. Lett.* 39 (5), 3–7. doi:10.1029/2011GL050661
- Kodaira, S., Nakamura, Y., Yamamoto, Y., Obana, K., Gou, F., No, T., et al. (2017). Depth-varying structural characters in the rupture zone of the 2011 tohoku-oki earthquake. *Geosphere* 13 (5), 1408–1424. doi:10.1130/GES01489.1
- Kopp, H., Flueh, E. R., Petersen, C. J., Weinrebe, W., Wittwer, A., and Meramex Scientists (2006). The Java margin revisited: Evidence for subduction erosion off Java. *Earth Planet. Sci. Lett.* 242 (1–2), 130–142. doi:10.1016/j.epsl.2005.11.036
- Lai, C. K., XiaoXia, P., Hall, R., Meffre, S., Tsikouras, B., Balangué-Tarriela, M. I. R., et al. (2021). Cenozoic evolution of the Sulu Sea arc-basin system: An overview. *Tectonics* 40 (2), 1–26. doi:10.1029/2020TC006630
- Lallemand, S. E., Schnürle, P., and Malavieille, J. (1994). Coulomb theory applied to accretionary and nonaccretionary wedges: Possible causes for tectonic erosion and/or frontal accretion. *J. Geophys. Res. Solid Earth* 99 (B6), 12033–12055. doi:10.1029/94JB00124
- Liu, W. N., Li, C. F., Li, J., Fairhead, D., and Zhou, Z. (2014). Deep structures of the palawan and Sulu Sea and their implications for opening of the South China sea. *Mar. Petroleum Geol.* 58 (PB), 721–735. doi:10.1016/j.marpetgeo.2014.06.005
- Løvholt, F., Stein, B., Laberg, J. S., Kim, J., and Noel, B. (2017). Some giant submarine landslides do not produce large tsunamis. *Geophys. Res. Lett.* 44 (16), 8463–8472. doi:10.1002/2017GL074062
- Masson, D. G., Harbitz, C. B., Wynn, R. B., Pedersen, G., and Løvholt, F. (2006). Submarine landslides: Processes, triggers and hazard prediction. *Philosophical Trans. R. Soc. A Math. Phys. Eng. Sci.* 364 (1845), 2009–2039. –39. doi:10.1098/rsta.2006.1810
- Masson, D. G., Parson, L. M., Milsom, J., Nichols, G., Sikumbang, N., Dwiyanto, B., et al. (1990). Subduction of seamounts at the Java Trench: A view with long-range sidescan sonar. *Tectonophysics* 185 (1–2), 51–65. doi:10.1016/0040-1951(90)90404-V
- Micallef, Aaron, J Mountjoy, Joshu, Canals, Miquel, and Lastras, Galderic (2012). "Deep-seated bedrock landslides and submarine canyon evolution in an active tectonic margin: Cook strait, New Zealand," in *Submarine mass movements and their consequences. Yujiro ogawa, roger urgeles, david mosher, jason chaytor, and michael strasser, 201–12*. Editors Yasuhiro Yamada, Kiichiro Kawamura, and Ken Ikehara (Dordrecht: Springer Netherlands). doi:10.1007/978-94-007-2162-3_18
- Moore, G. F., JasonLackey, K., Strasser, M., and Yamashita, M. 2019. "Submarine landslides on the Nankai Trough accretionary prism (offshore central Japan)." 247–259. doi:10.1002/9781119500513.ch15
- Morgan, J. K., and Bangs, N. L. (2017). Recognizing seamount-forearc collisions at accretionary margins: Insights from discrete numerical simulations. *Geology* 45 (7), 635–638. doi:10.1130/G38923.1
- Mountjoy, J. J., Barnes, P. M., and Pettinga, J. R. (2009). Morphostructure and evolution of submarine canyons across an active margin: Cook strait sector of the Hikurangi margin, New Zealand. *Mar. Geol.* 260 (1–4), 45–68. doi:10.1016/j.margeo.2009.01.006
- Mountjoy, J. J., Pecher, I., Henrys, S., Crutchley, G., Barnes, P. M., and Plaza-Faverola, A. (2014). Shallow methane hydrate system controls ongoing, downslope sediment transport in a low-velocity active submarine landslide complex, Hikurangi margin, New Zealand. *Geochem. Geophys. Geosystems* 15 (11), 4137–4156. doi:10.1002/2014GC005379

- Nakata, K., Katsumata, A., and Muhari, A. (2020). Submarine landslide source models consistent with multiple tsunami records of the 2018 palu tsunami, Sulawesi, Indonesia. *Earth, Planets Space* 72 (1), 44. doi:10.1186/s40623-020-01169-3
- Parsons, T., Geist, E. L., Ryan, H. F., Lee, H. J., Haeussler, P. J., Lynett, P., et al. (2014). Source and progression of a submarine landslide and tsunami: The 1964 great Alaska earthquake at valdez. *J. Geophys. Res. Solid Earth* 119 (11), 8502–8516. doi:10.1002/2014JB011514
- Pedley, K. L., Barnes, P. M., Pettinga, J. R., Lewis, K. B., and Lewis, K. B. (2010). Seafloor structural geomorphic evolution of the accretionary frontal wedge in response to seamount subduction, poverty indentation, New Zealand. *Mar. Geol.* 270 (1–4), 119–138. doi:10.1016/j.margeo.2009.11.006
- Pubellier, M., Quebral, R., Aurelio, M., and Rangin, C. (1996). Docking and post-docking escape tectonics in the southern Philippines. *Geol. Soc. Spec. Publ.* 106 (106), 511–523. doi:10.1144/GSL.SP.1996.106.01.32
- Qiu, Q., and Barbot, S. (2022). Tsunami excitation in the outer wedge of global subduction zones. *Earth-Science Rev.* 230, 104054. doi:10.1016/j.earscirev.2022.104054
- Ramirez, A. B. G., Ramos, N. T., Nawanao, L. P. J., Mangahas-Flores, R. Z., Narag, I. C., Baba, T., et al. (2022). An earthquake-triggered submarine mass failure mechanism for the 1994 Mindoro tsunami in the Philippines: Constraints from numerical modeling and submarine geomorphology. *Front. Earth Sci.* 10, 1–20. doi:10.3389/feart.2022.1067002
- Rangin, C., and Silver, E. (1990). Geological setting of the Celebes and Sulu seas. *Proc. Ocean Drill. Program Initial Rep.*, 124. Ocean Drilling Program. doi:10.2973/odp.proc.ir.124.103.1990
- Rangin, C., and Silver, E. A. (1991). Neogene tectonic evolution of the celebes-sulu basins: New insights from leg 124 drilling. *Proc. Ocean Drill. Program Scientific Results*. 124. Ocean Drilling Program, 51–63. doi:10.2973/odp.proc.sr.124.122.1991
- Rangin, C. (1989). The Sulu Sea, a back-arc basin setting within a neogene collision zone. *Tectonophysics* 161 (1–2), 119–141. doi:10.1016/0040-1951(89)90307-7
- Rangin, C. X., Mazzotti, S., Pubellier, M., Aurelio, M., Walpersdorf, A., and Quebral, R. (1999). Plate convergence measured by GPS across the sundaland/Philippine Sea plate deformed boundary: The Philippines and eastern Indonesia, 296–316.
- Rastgoftar, E., and Soltanpour, M. (2016). Study and numerical modeling of 1945 makran tsunami due to a probable submarine landslide. *Nat. Hazards* 83 (2), 929–945. doi:10.1007/s11069-016-2356-3
- Ripley, B. D. (1977). Modelling spatial patterns. *J. Stat. Soc.* 39=39 (2), 172–192. Available at: <https://www.jstor.org/stable/2984796>. doi:10.1111/j.2517-6161.1977.tb01615.x
- Ruh, J. B. (2016). Submarine landslides caused by seamounts entering accretionary wedge systems. *Terra nova*. 28 (3), 163–170. doi:10.1111/ter.12204
- Sabeti, R., and Heidarzadeh, M. (2022). A new empirical equation for predicting the maximum initial amplitude of submarine landslide-generated waves. *Landslides* 19 (2), 491–503. doi:10.1007/s10346-021-01747-w
- Scarselli, N. (2020). Submarine landslides – architecture, controlling factors and environments. A summary. *Regional geology and tectonics: Principles of geologic analysis*. BV. doi:10.1016/b978-0-444-64134-2.00015-8
- Schambach, L., Grilli, S. T., Tappin, D. R., Gangemi, M. D., and Barbaro, G. (2020). New simulations and understanding of the 1908 Messina tsunami for a dual seismic and deep submarine mass failure source. *Mar. Geol.* 421, 106093. doi:10.1016/j.margeo.2019.106093
- Schlüter, H. U., Block, M., Hinz, K., Neben, S., Seidel, D., and Djajadihardja, Y. (2001). Neogene sediment thickness and miocene basin-floor fan systems of the Celebes Sea. *Mar. Petroleum Geol.* 18 (7), 849–861. doi:10.1016/S0264-8172(01)00027-7
- Schlüter, H. U., Hinz, K., and Block, M. (1996). Tectono-stratigraphic terranes and detachment faulting of the South China sea and Sulu Sea. *Mar. Geol.* 130 (1–2), 39–78. doi:10.1016/0025-3227(95)00137-9
- Silverman, B. W. (1986). *Density estimation for statistics and data analysis*. Boston, MA: Springer US. doi:10.1007/978-1-4899-3324-9
- Simons, W. J. F., Ambrosius, B. A. C., Noomen, R., Angermann, D., Wilson, P., Becker, M., et al. (1999). Observing Plate motions in S.E. Asia: Geodetic results of the GEODYSSSEA project. *Geophys. Res. Lett.* 26 (14), 2081–2084. doi:10.1029/1999GL900395
- Simpson, G. D. H. (2010). Formation of accretionary prisms influenced by sediment subduction and supplied by sediments from adjacent continents. *Geology* 38 (2), 131–134. doi:10.1130/G30461.1
- Takagi, H., Pratama, M. B., Kurobe, S., Esteban, M., Aránguiz, R., and Ke, B. (2019). Analysis of generation and arrival time of landslide tsunami to palu city due to the 2018 Sulawesi earthquake. *Landslides*. March: 983–91. doi:10.1007/s10346-019-01166-y
- Tappin, D. R., Stephan, T. G., Harris, J. C., Geller, R. J., Masterlark, T., Kirby, J. T., et al. (2014). Did a submarine landslide contribute to the 2011 Tohoku tsunami? *Mar. Geol.* 357, 344–361. doi:10.1016/j.margeo.2014.09.043
- Tappin, D. R. (2021). Submarine landslides and their tsunami hazard. *Annu. Rev. Earth Planet. Sci.* 49 (1), 551–578. doi:10.1146/annurev-earth-063016-015810
- Tsuru, T., Park, J.-O., Miura, S., Kodaira, S., Kido, Y., and Hayashi, T. (2002). Along-Arc structural variation of the plate boundary at the Japan trench margin: Implication of interplate coupling. *J. Geophys. Res. Solid Earth* 107 (B12), ESE 11–1–ESE 11–15. doi:10.1029/2001jb001664
- Vanneste, M., Forsberg, C. F., Glimsdal, S., Harbitz, C. B., Issler, D., Kvalstad, T. J., et al. (2013). Submarine landslides and their consequences: What do we know, what can we do? *Landslide Sci. Pract. Complex Environ.* 5, 5–17. doi:10.1007/978-3-642-31427-8_1
- Völker, D. J. (2010). A simple and efficient GIS tool for volume calculations of submarine landslides. *Geo-Mar. Lett.* 30 (5), 541–547. doi:10.1007/s00367-009-0176-0
- Watson, S. J., Mountjoy, J. J., and Crutchley, G. J. (2020). Tectonic and geomorphic controls on the distribution of submarine landslides across active and passive margins, eastern New Zealand. *Geol. Soc. Lond. Spec. Publ.* 500 (1), 477–494. doi:10.1144/SP500-2019-165
- Yang, G., Si, G., Tong, L., Li, H., Lindagato, P., and Zeng, R. (2022). The effect of seamount chain subduction and accretion. *Geol. J.* 57 (7), 2712–2734. doi:10.1002/gj.4435
- Yavari-Ramshe, S., and Ataie-Ashtiani, B. (2016). Numerical modeling of subaerial and submarine landslide-generated tsunami waves—recent advances and future challenges. *Landslides* 13 (6), 1325–1368. doi:10.1007/s10346-016-0734-2



OPEN ACCESS

APPROVED BY
Frontiers Editorial Office,
Frontiers Media SA, Switzerland

*CORRESPONDENCE
Lyndon P. Nawanao Jr,
✉ lpnawanao@up.edu.ph

SPECIALTY SECTION
This article was submitted
to Marine Geoscience,
a section of the journal
Frontiers in Earth Science

RECEIVED 05 March 2023
ACCEPTED 07 March 2023
PUBLISHED 21 March 2023

CITATION
Nawanao LP Jr and Ramos NT (2023),
Corrigendum: Frontal wedge variations
and controls of submarine landslides in
the Negros-Sulu Trench
system, Philippines.
Front. Earth Sci. 11:1180022.
doi: 10.3389/feart.2023.1180022

COPYRIGHT
© 2023 Nawanao and Ramos. This is an
open-access article distributed under the
terms of the [Creative Commons
Attribution License \(CC BY\)](#). The use,
distribution or reproduction in other
forums is permitted, provided the original
author(s) and the copyright owner(s) are
credited and that the original publication
in this journal is cited, in accordance with
accepted academic practice. No use,
distribution or reproduction is permitted
which does not comply with these terms.

Corrigendum: Frontal wedge variations and controls of submarine landslides in the Negros-Sulu Trench system, Philippines

Lyndon P. Nawanao Jr* and Noelynna T. Ramos

Geomorphology and Active Tectonics Research Laboratory, National Institute of Geological Sciences, University of the Philippines Diliman, Quezon City, Philippines

KEYWORDS

frontal wedge, submarine landslides, Negros–Sulu Trench system, Sulu Sea, submarine canyons, exploratory spatial analyses

A Corrigendum on

[Frontal wedge variations and controls of submarine landslides in the Negros-Sulu Trench system, Philippines](#)

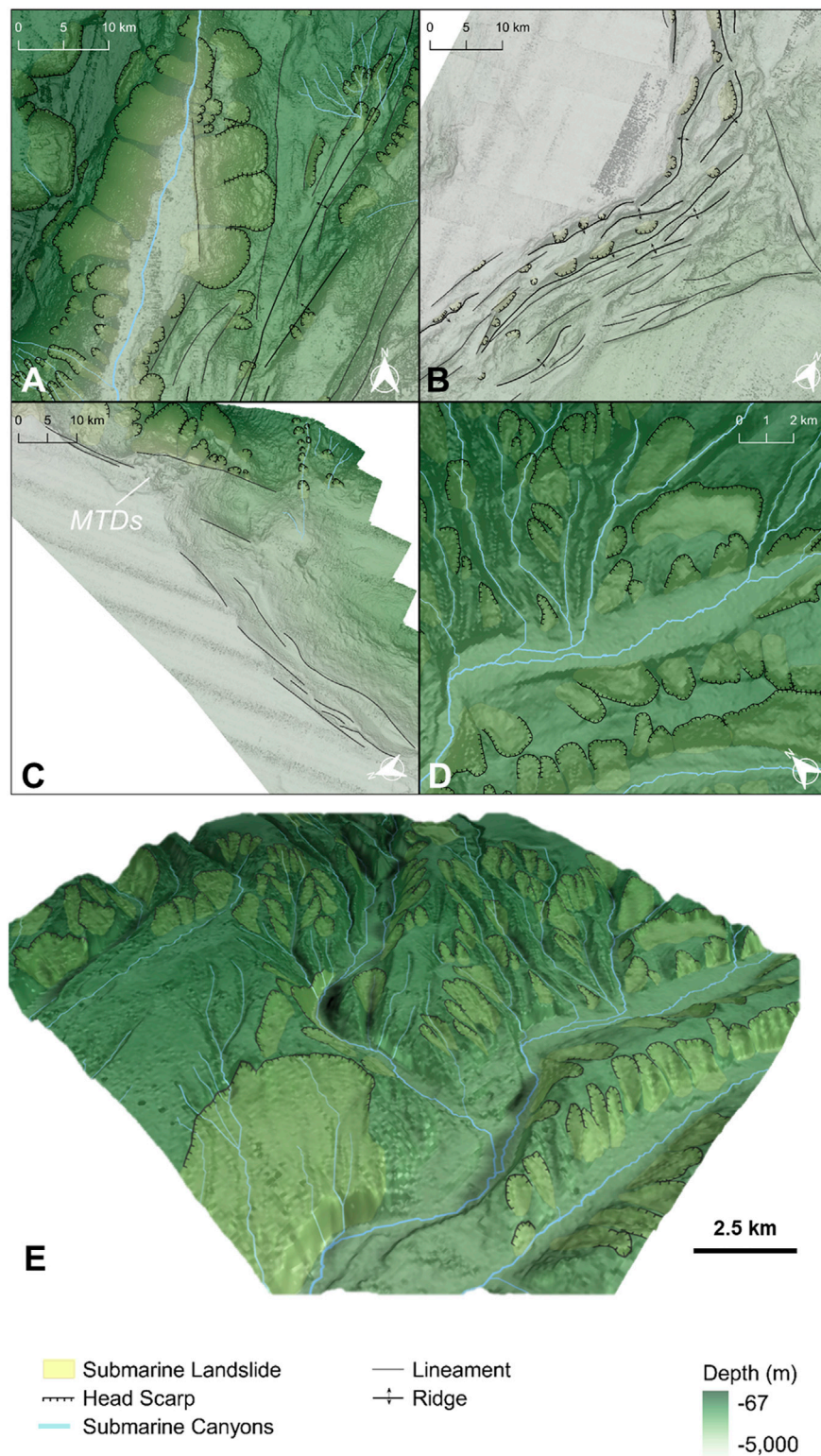
by Nawanao LP and Ramos NT (2023). *Front. Earth Sci.* 11:1054825. doi: [10.3389/feart.2023.1054825](#)

In the published article, there was an error in [Figure 5](#) as published. An older version of the figure was used. The revised [Figure 5](#) has updated subfigures B, C, and D, which are located in squares b–d in Figure 4. The corrected [Figure 5](#) and its caption appear below.

The authors apologize for this error and state that this does not change the scientific conclusions of the article in any way. The original article has been updated.

Publisher's note

All claims expressed in this article are solely those of the authors and do not necessarily represent those of their affiliated organizations, or those of the publisher, the editors and the reviewers. Any product that may be evaluated in this article, or claim that may be made by its manufacturer, is not guaranteed or endorsed by the publisher.

**FIGURE 5**

Close-up view of the mapped submarine features (see Figure 4 for their location). **(A)** Large submarine landslides along the steep frontal wedge of the northern NT segment (NT1) and steep bathymetry of the colliding Cagayan Ridge (CR) in the west. Between the frontal wedge and the CR is a deeply incised submarine canyon that is parallel to the trench. **(B)** Prominent deformation front and associated submarine features of the frontal wedge in the northern ST segment (ST1). **(C)** Poorly developed frontal wedge, submarine canyons, and submarine landslides in the southern ST segment (ST2). **(D)** Well-developed networks of submarine canyons and associated submarine landslides offshore of southern Negros Island. **(E)** Three-dimensional perspective of submarine landslides in Figure 5D.



OPEN ACCESS

EDITED BY

Xunhua Zhang,
Qingdao Institute of Marine Geology
(QIMG), China

REVIEWED BY

Jianhui Jin,
Fujian Normal University, China
Qi Su,
Beijing Normal University, China

*CORRESPONDENCE

Ruonan Tian,
✉ 20rntian@stu.edu.cn
Zhongping Lai,
✉ zhongping_lai@stu.edu.cn

SPECIALTY SECTION

This article was submitted to Marine
Geoscience,
a section of the journal
Frontiers in Earth Science

RECEIVED 04 November 2022

ACCEPTED 30 March 2023

PUBLISHED 11 April 2023


CITATION

Zhong J, Liu B, Ou Y, Tian R, Shan J, Xu Y,
Wang F, Abbas M, Zhang K and Lai Z
(2023), An erosive neritic area of Shantou
in coastal NE South China Sea since at
least MIS 5 revealed by OSL dating
of cores.
Front. Earth Sci. 11:1089946.
doi: 10.3389/feart.2023.1089946

COPYRIGHT

© 2023 Zhong, Liu, Ou, Tian, Shan, Xu,
Wang, Abbas, Zhang and Lai. This is an
open-access article distributed under the
terms of the [Creative Commons
Attribution License \(CC BY\)](https://creativecommons.org/licenses/by/4.0/). The use,
distribution or reproduction in other
forums is permitted, provided the original
author(s) and the copyright owner(s) are
credited and that the original publication
in this journal is cited, in accordance with
accepted academic practice. No use,
distribution or reproduction is permitted
which does not comply with these terms.

An erosive neritic area of Shantou in coastal NE South China Sea since at least MIS 5 revealed by OSL dating of cores

Jiemei Zhong¹, Bohui Liu¹, Yang Ou¹, Ruonan Tian^{1*},
Jingxiang Shan¹, Yantian Xu², Feng Wang¹, Mahmoud Abbas ¹,
Ke Zhang³ and Zhongping Lai^{1*}

¹Institute of Marine Sciences, Guangdong Provincial Key Laboratory of Marine Disaster Prediction and Prevention, Shantou University China, and Southern Marine Science and Engineering Guangdong Laboratory (Zhuhai), Zhuhai, China, ²School of Geography and Tourism, Jiaying University, Meizhou, China, ³Guangdong Provincial Key Laboratory of Geodynamics and Geohazard, School of Earth Science and Engineering, Sun Yat-sen University, Guangzhou, China

The neritic region of the Chaoshan plain is located on the northeastern (NE) boundary of the South China Sea (SCS). Despite the extensive research on the stratigraphic architecture and sedimentary processes within the Chaoshan plain, the neighboring neritic area remains largely unexplored. In this study, we provide a new set of ages on seventeen quartz optically stimulated luminescence (OSL) dating results from four cores (SY2-2, SY3-1, SY3-2, and HS02) to investigate the regional chronostratigraphy and sedimentology of the area. The samples were collected at depths ranging from 0.6 to 73.5 m and yielded ages ranging from 4.9 ± 0.3 ka to $>139 \pm 28$ ka. Sedimentation thickness from cores SY3-2, SY2-2, and HS02 is less than 4.2 m, 5.5 m, and 6.4 m, respectively, since at least Marine Isotope Stage (MIS) 5, and the Holocene sediments of core SY3-2 are less than 4.2 m thick. The preservation state of the sediments in the area is poor since at least 83.6 ka, indicating an intensified erosion in the neritic region of the northeastern South China Sea (NESCO) since at least MIS 5. This erosion may have been caused by fluvial incision resulting from sea-level decline during the last glacial period, as well as strong transportation caused by coastal currents.

KEYWORDS

OSL dating, drilling cores, Chaoshan plain, South China sea, sedimentary environment

1 Introduction

The continental shelf is a vital component in sedimentation and the land-sea interaction, holding significant geological information such as changes in sea level, tectonic activity, and sedimentary processes (Li et al., 2014; Wang et al., 2019; Qin et al., 2023; Wang et al., 2023). The eastern continental shelf of China is abundant in Quaternary sediments with thicknesses exceeding 10 m since the Holocene (Wang et al., 2020). For instance, the Holocene sediments thicknesses recorded from core samples in the Bohai Sea and the south Yellow Sea are around 15 and 13 m thick, respectively (Liu et al., 2010; Lan et al., 2018; Chen et al., 2020; Long et al., 2022). Studies on the inner shelf of the East China Sea have mainly yielded a paleoclimate record since the Last Deglaciation, with thickness of the Holocene sediments approximately 20 m

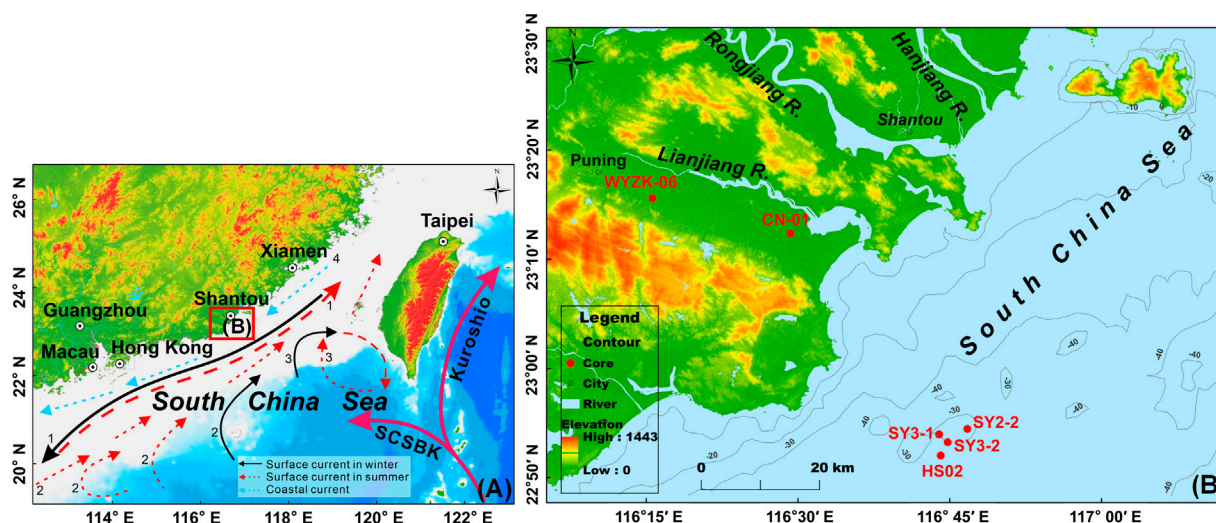


FIGURE 1

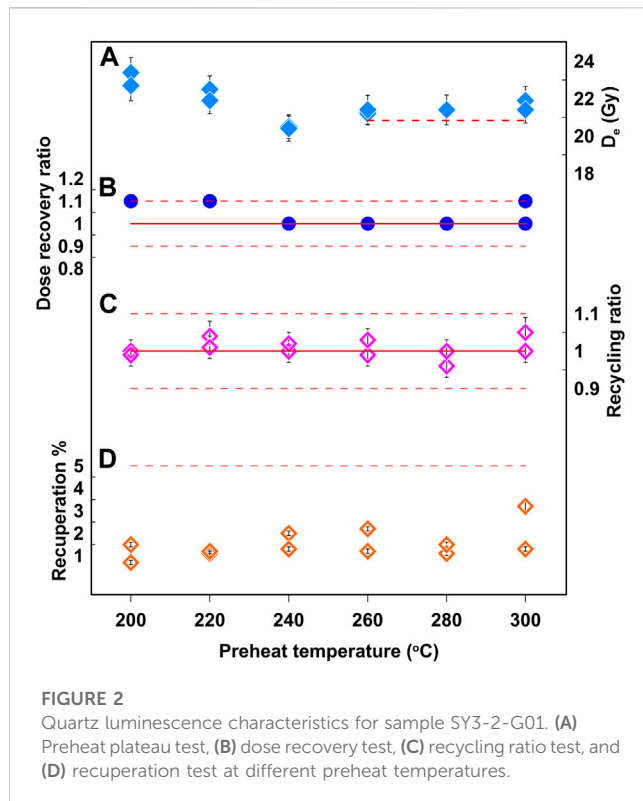
Location of the Chaoshan Plain, its neritic area, and core sites. (A) General map of the northern SCS and its significant surface circulations. The Chaoshan Plain and its adjacent neritic area are outlined by a solid red line rectangle. The surface circulations in the northern SCS were adapted from Zhang et al. (2022). The SCSBK abbreviation denotes the SCS Branch of Kuroshio, and the black numbers represent major modern surface currents, as follows: 1: Guangdong Coastal Current, 2: SCS Warm Current, 3: Loop Current, and 4: Coastal Current. (B) The major area of the Chaoshan Plain, include the Lianjiang River, Hanjiang River, and Rongjiang River plains. Four cores (SY3-1, SY3-2, SY2-2, and HS02) were obtained from the neritic area of the Lianjiang River plain. Core WYZK-06 was from Song et al. (2012), and core CN-01 was from Tang et al. (2018). Base maps from <http://www.gscloud.cn/> and <https://www.ngdc.noaa.gov/mgg/global/global.html>.

thick (Xu et al., 2009; Zheng et al., 2010). The thickness of the Holocene deposits in from the northern South China Sea (SCS) are around 10 m (Wang et al., 2020). The sedimentation characteristics of these regions revealed that aggradation was the dominant process in the eastern continental shelf of China since the Holocene. The Chaoshan Plain is located in southeastern China and borders the northeastern South China Sea (NCS). The Quaternary deposits in the Chaoshan plain reach a maximum thickness of about 141 m (Chen W., 1984; Song et al., 2012). Several investigations on the Quaternary sediments have been conducted in the Chaoshan plain using multi proxy dating techniques (Chen G., 1984; Li et al., 1987; Li et al., 1988; Zong, 1992; Zheng and Li, 2000; Song et al., 2012; Tang et al., 2018; Zhong et al., 2022). On the contrary, core and chronological data from the adjacent neritic area are limited. The lack of information on sedimentary structures and ages in the area has hindered thorough comprehension of the sedimentary evolution of the Chaoshan region. It remains unclear how many transgressive layers have formed in this area since the Holocene and whether aggradation or incision has been the dominant process since that time. Additionally, the contribution of the sea-level changes and/or tectonic activities on sedimentary process are still debated. The present study employed the optically stimulated luminescence (OSL) dating method to determine the age of the Quaternary sediments from four cores in the neritic area of the Lianjiang River plain, namely, SY2-2, SY3-1, SY3-2, and HS02. The chronological data obtained from these cores will provide an opportunity to understand the timing of the deposition of the Quaternary sediments and factors that led to its formation in the region.

2 Geological setting and sample collection

The SCS is located at the intersection of Eurasia, India-Australia, and the Philippine Sea plates, and is considered as the largest marginal sea in East Asia (Xia et al., 2020). The Chaoshan plain is lying at the NCS and composed of three major sub-plains, the Lianjiang River plain, the Rongjiang River plain, and the Hanjiang River plain (Figure 1). The Lianjiang River plain extends to about 50 km inland, with a drainage area of up to 838.5 km² and water discharge amounts of approximately 587 million m³/yr (Tang et al., 2018). It characterized by warm-and-wet zone influenced by the East Asian summer monsoon (EASM), with an annual temperature of 22.3°C on average and annual precipitation from 1800 to 2,100 mm (Tang et al., 2018). Differential uplifting–subsidence movement from the Neogene to the early Quaternary has changed the Lianjiang River plain into a faulted basin (Chen W., 1984). Therefore, the Lianjiang River plain has a large accommodation space for the Quaternary deposition, and the thickness of sedimentary sequences reaches up to 141 m (Chen W., 1984; Li et al., 1987; Wang et al., 1997).

Four borehole cores were obtained by rotary drilling from the neritic area of the Lianjiang River plain (Figure 1), i.e., HS02 (116°44'6.51" E, 22°52'10.67" N), SY3-1 (116°43'56.05" E, 22°54'7.07" N), SY3-2 (116°43'57.32" E, 22°54'6.44" N), and SY2-2 (116°46'44.2" E, 22°54'37.36" N). The drilling sites are at an altitude that ranging between 29 and 34 m below mean sea level (bmsl), and core lengths range from 95.15 m to 95.35 m. Details of core lithology are shown in Supplementary Table S1. Seventeen OSL samples were collected from cores SY2-2, SY3-1, SY3-2, and HS02. Despite the



sampling difficulties that prevented high-resolution sampling, this limitation does not affect the scientific discussion presented in our study.

3 OSL dating

3.1 Samples pretreatment

Seventeen OSL samples were treated with 10% HCl and 30% H₂O₂ successively to remove carbonates and organic materials. Wet sieving was utilized to obtain coarse-grained fractions (90–125 μm) according to availability. 90–125 μm fractions were treated with 40% HF for ~40 min to remove feldspar and washed with 10% HCl for about 30 min to remove the fluoride precipitation generated during etching. The purity of quartz fractions was tested by the infrared stimulated luminescence (IRSL) signals.

3.2 D_e determination

90–125 μm quartz fractions were mounted on the center (5 mm diameter) of 9.7-mm diameter stainless-steel discs using silicone oil for equivalent dose (D_e) measurements. Irradiation, preheating, and OSL measurements were conducted on a Risø TL/OSL-DA-20 reader equipped with a ⁹⁰Sr/⁹⁰Y beta source and blue LEDs (λ = 470 ± 20 nm) (Botter-Jensen et al., 1999). All quartz signals were stimulated at 130 °C for 40 s and recorded by an EMI 9235QA

photomultiplier tube fitted with a 7.5-mm Hoya U-340 filter. The D_e in this study was measured by the SAR-SGC method (Lai and Ou, 2013), a combination of single aliquot regenerative dose (SAR) protocol (Murray and Wintle, 2000) and standard growth curve (SGC) method (Roberts and Duller, 2004; Lai, 2006). The preheat for natural and regenerative dose signals was 260 °C for 10 s (Wintle and Murray, 2006), and the preheat for test doses response was 220 °C for 10 s. Preheat plateau test and dose recovery test results from this study and neighboring Pearl River Delta showed that preheat temperature at 260 °C for 10 s was appropriate for dating (Xu et al., 2020; Lin et al., 2022; Xu et al., 2022; Lin et al., 2023). For samples SY3-2-G01, SY3-2-G02, SY3-2-G03, and those from core SY2-2, 6 aliquots were measured using the SAR protocol, and 12 aliquots were measured for the natural L_N/T_N measurement. Given the saturation of the OSL signal in samples from cores SY3-2 and SY2-2, the D_e value of samples SY3-2-G04, SY3-2-G05, and samples from cores SY3-1, HS02 were determined based solely on the natural L_N/T_N measurement to expedite the measurement process. After eliminating any obvious statistical outliers, the final D_e value for a sample was calculated.

3.3 Quartz luminescence characteristics

Tests including the preheat plateau, dose recovery, recycling ratio, and recuperation were conducted on sample SY3-2-G01 to examine the suitability of luminescence properties for the SAR protocol (Wintle and Murray, 2006).

The preheat plateau test was conducted with a preheat temperature ranging from 200 °C to 300 °C with an interval of 20 °C for 10 s and cut-heat temperatures kept at 220 °C for 10 s, using a heating rate of 5 °C/s. Twelve aliquots (two aliquots per preheat temperature) were measured at each temperature point. The results indicate a preheat plateau between 260 °C to 280 °C (Figure 2A).

The dose recovery test is to examine whether the D_e measurement protocol can recover a known laboratory dose (Wintle and Murray, 2006). Ideally, the measured dose is in agreement with the given laboratory dose (Wintle and Murray, 2006). The dose recovery test was applied to twelve natural aliquots of sample SY3-2-G01. The given laboratory dose is 20.83 Gy. The measured average D_e value at the 260 °C preheat temperature was 21.3 Gy, resulting in the ratio of dose recovery of 1.02 (Figure 2B). The results are within 10% of the natural dose, indicating that the SAR protocol can recover a laboratory dose.

Recycling ratio and recuperation tests are mainly examining whether no obvious thermal transfer was present and whether sensitivity changes could be well corrected in the measurement (Wintle and Murray, 2006). Research showed that a reliable D_e value can preferably meet two requirements including recuperation < 5% and the recycling ratio within 0.9–1.1 (Wintle and Murray, 2006). The average recycling ratio for sample SY3-2-G01 at the 260 °C preheat temperature was 1.01 (Figure 2C), indicating that the sensitivity changes were well corrected. The recuperation for sample SY3-2-G01 at the 260 °C preheat temperature was 1.7% (Figure 2D), suggesting that no

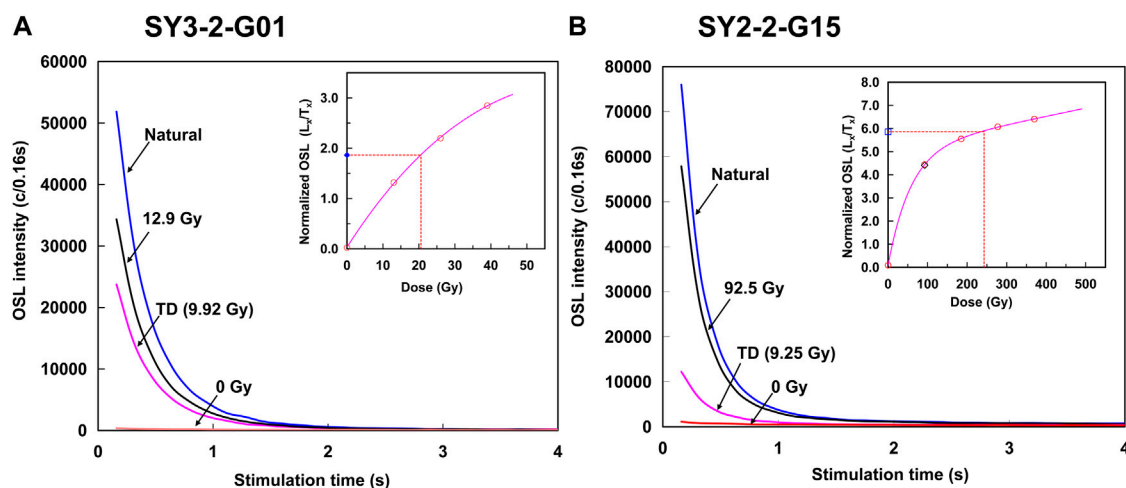


FIGURE 3
OSL decay and growth curves of samples (A) SY3-2-G01 and (B) SY2-2-G15 in the neritic area of the Lianjiang River plain.

obvious thermal transfer was present. Besides, the accepted D_e aliquots for each sample in this study matched the criteria of recycling ratios between 0.9 and 1.1 and recuperation ratios $<5\%$.

3.4 Dose rate measurement

Inductively coupled plasma mass spectrometry (ICP-MS) was used for measuring uranium (U) and thorium (Th). Inductively coupled plasma/optical emission spectrometry (ICP/OES) was utilized for determining potassium (K). The cosmic ray dose was calculated depending on the depth, altitude, and geomagnetic latitude of each sample. The moisture content was estimated to be $25\% \pm 5\%$ for all OSL samples, considering the variation of moisture content within the burial period in the study region. The dose rates and final ages were calculated on the website program DRAC (Durcan et al., 2015).

4 OSL dating results and discussion

4.1 Sediment ages of cores

Representative decay and growth curves of samples SY3-2-G01 and SY2-2-G15 are shown in Figure 3. The decay curves show that OSL intensity decreasing rapidly during the first second of stimulation toward background levels, indicating that the OSL signals are dominated by the fast component in these samples (Wintle and Murray, 2006). The well-fitted growth curves show that the combined SAR–SGC protocol is appropriate for all the samples in this study. Our quartz OSL results from the four cores are listed in Table 1 and can be shown in Figure 4, with ages ranging from 4.9 ± 0.3 ka to 139 ± 28 ka. Quartz OSL signal

saturation could be observed in sixteen samples, with D_e exceeding 190 Gy, indicating that the obtained dating results are regarded as minimum ages (Lai, 2010; Murray et al., 2021; Long et al., 2022; Xu et al., 2022).

The D_e is usually saturates at ~ 150 Gy, resulting in age underestimation for sediments over 50 ka (Buylaert et al., 2007; Lai, 2010; Timar-Gabor et al., 2011; Lai and Fan, 2014; Chapot et al., 2016). Underestimation of quartz OSL age is common in coastal deposits. OSL and thermally transferred OSL (TT-OSL) signals of quartz samples from the coastal plain of Israel demonstrated that the upper limit of quartz D_e from Nilotic origin is close to 140 Gy (Faershtein et al., 2019). In the western Bohai Sea (China), the D_e values of quartz OSL samples are >200 Gy, resulting in ages saturation at >80 ka (Long et al., 2022). Core HPQK01 in the Pearl River Delta also showed that quartz OSL ages ranging from 125 ± 18 ka to 58 ± 6 ka are considered as minimum ages due to the OSL signal saturation >150 Gy (Xu et al., 2022). Age underestimation of fine quartz ($11\text{--}44\text{ }\mu\text{m}$) from the Lianjiang River plain occurred on samples older than ~ 130 ka (Tang et al., 2018). Our results suggest that the quartz OSL ages older than ~ 60 ka are underestimated as a result of signal saturation (~ 180 Gy).

4.2 Poor preservation of the late Quaternary sediments

The OSL dating results obtained from core sediments in the neritic area of the Lianjiang River plain suggest that the timing of deposition is between 4.9 ± 0.3 ka and $>83.6 \pm 6.5$ ka, with sedimentation thickness of less than 6.4 m since at least MIS 5 (Figure 4). The sediment thickness in the inner Lianjiang River plain is at least 80 m since MIS 5, which gradually decreases to less than 20 m thick in the outer Lianjiang River plain (Song et al., 2012; Tang et al., 2018) (Figure 5). In the neritic area of the

TABLE 1 OSL dating results from cores SY3-1, SY3-2, SY2-2, and HS02, in the neritic area of the Lianjiang River plain.

Sample ID	Depth (m)	Grain size (μm)	Aliquot number	Moisture (%)	U (ppm)	Th (ppm)	K (%)	Dose rate (Gy/ka)	De (Gy)	Age (ka)
SY3-1-G02	19.1	90–125	3 ^a	25 \pm 5	3.2 \pm 0.16	14.22 \pm 0.71	2.06 \pm 0.21	2.98 \pm 0.17	321 \pm 16	>107.6 \pm 8.2
SY3-2-G01	0.6	90–125	4 ^b + 10 ^a	25 \pm 5	5.07 \pm 0.25	15.57 \pm 0.78	2.08 \pm 0.21	3.57 \pm 0.18	17.6 \pm 0.5	4.9 \pm 0.3
SY3-2-G02	4.8	90–125	4 ^b + 8 ^a	25 \pm 5	2.25 \pm 0.11	11.29 \pm 0.56	1.97 \pm 0.2	2.66 \pm 0.15	222 \pm 12	>83.6 \pm 6.5
SY3-2-G03	6.5	90–125	6 ^b + 6 ^a	25 \pm 5	1.79 \pm 0.09	9.47 \pm 0.47	1.84 \pm 0.18	2.36 \pm 0.14	229 \pm 18	>97.1 \pm 9.6
SY3-2-G04	10.2	90–125	5 ^a	25 \pm 5	3.9 \pm 0.2	16.92 \pm 0.85	2.16 \pm 0.22	3.37 \pm 0.18	239 \pm 41	>71 \pm 12.7
SY3-2-G05	14.4	90–125	7 ^a	25 \pm 5	4.1 \pm 0.2	15.75 \pm 0.79	2.25 \pm 0.22	3.39 \pm 0.18	243 \pm 33	>71.7 \pm 10.4
SY2-2-G15	5.45	90–125	6 ^b + 5 ^a	25 \pm 5	2.27 \pm 0.11	9.47 \pm 0.47	1.75 \pm 0.18	2.39 \pm 0.14	236 \pm 23	>98.9 \pm 11.1
SY2-2-G14	14.95	90–125	6 ^b + 7 ^a	25 \pm 5	2.97 \pm 0.15	13.79 \pm 0.69	2.21 \pm 0.22	3.05 \pm 0.17	227 \pm 16	>74.6 \pm 6.8
SY2-2-G13	19.55	90–125	6 ^b + 4 ^a	25 \pm 5	4.05 \pm 0.2	14.72 \pm 0.74	2.01 \pm 0.2	3.12 \pm 0.17	402 \pm 69	>129 \pm 23
SY2-2-G12	28.45	90–125	6 ^b + 5 ^a	25 \pm 5	3.46 \pm 0.17	13.18 \pm 0.66	2.23 \pm 0.22	3.09 \pm 0.18	312 \pm 30	>101 \pm 11.3
SY2-2-G10	43.35	90–125	2 ^b + 5 ^a	25 \pm 5	3.78 \pm 0.19	10.2 \pm 0.51	1.64 \pm 0.16	2.52 \pm 0.13	334 \pm 20	>133 \pm 11
SY2-2-G09	47.75	90–125	2 ^b + 4 ^a	25 \pm 5	3.81 \pm 0.19	18 \pm 0.9	2.17 \pm 0.22	3.36 \pm 0.18	335 \pm 26	>99.7 \pm 9.4
SY2-2-G07	64.05	90–125	3 ^b + 6 ^a	25 \pm 5	3.17 \pm 0.16	14.24 \pm 0.71	1.96 \pm 0.2	2.87 \pm 0.16	334 \pm 28	>117 \pm 12
SY2-2-G03	73.45	63–125	6 ^b + 5 ^a	25 \pm 5	3.59 \pm 0.18	17.62 \pm 0.88	2.59 \pm 0.26	3.63 \pm 0.21	506 \pm 96	>139 \pm 28
HS02-G01	6.4	90–125	9 ^a	25 \pm 5	2.7 \pm 0.14	11.73 \pm 0.59	2.06 \pm 0.21	2.82 \pm 0.16	233 \pm 27	>82.6 \pm 10.6
HS02-G02	10.5	90–125	4 ^a	25 \pm 5	3.18 \pm 0.16	14.65 \pm 0.73	2.11 \pm 0.21	3.07 \pm 0.17	197 \pm 38	>64.2 \pm 13
HS02-G03	12.7	90–125	3 ^a	25 \pm 5	2.93 \pm 0.15	13.47 \pm 0.67	2.21 \pm 0.22	3.03 \pm 0.17	249 \pm 11	>82.1 \pm 6

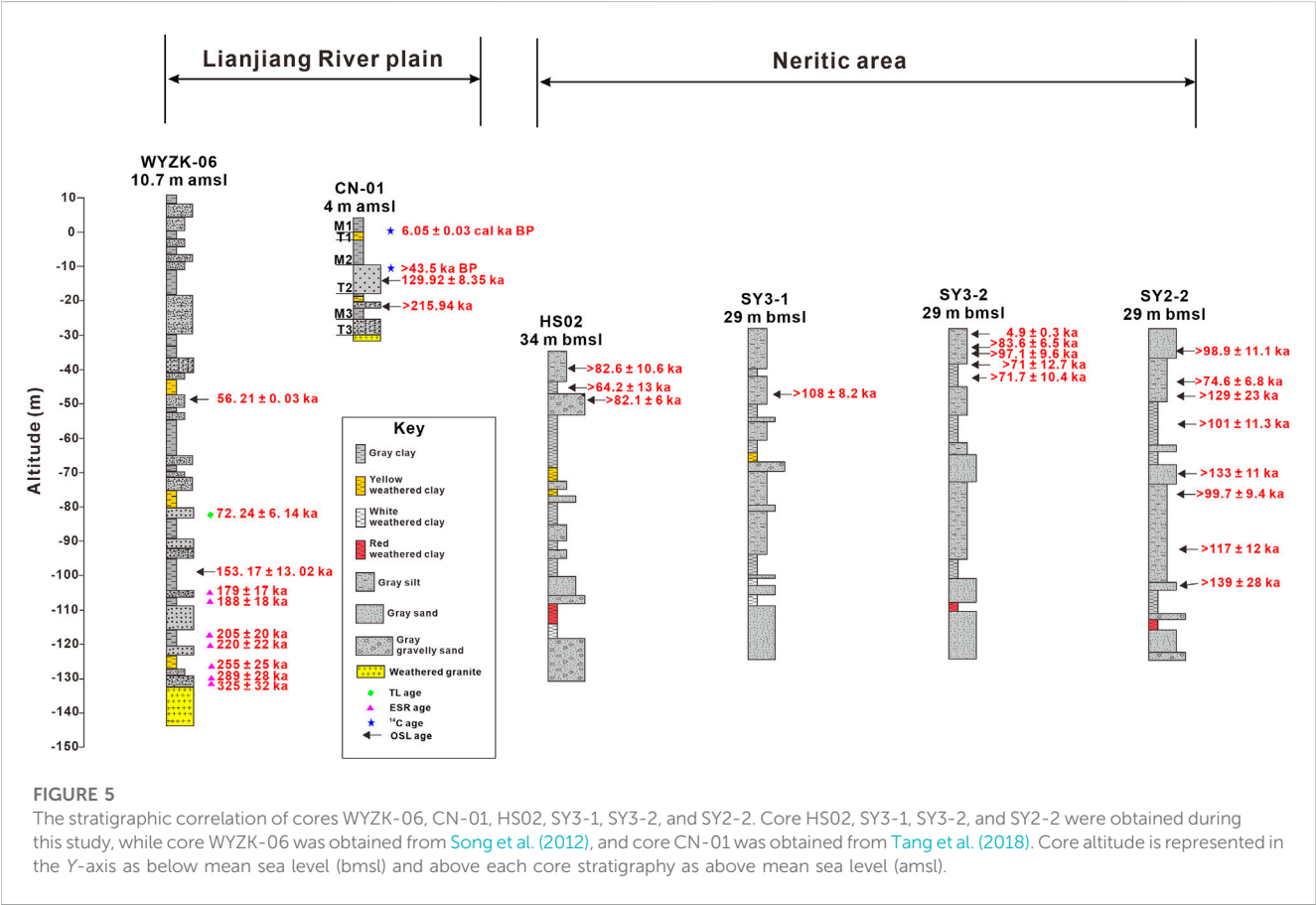
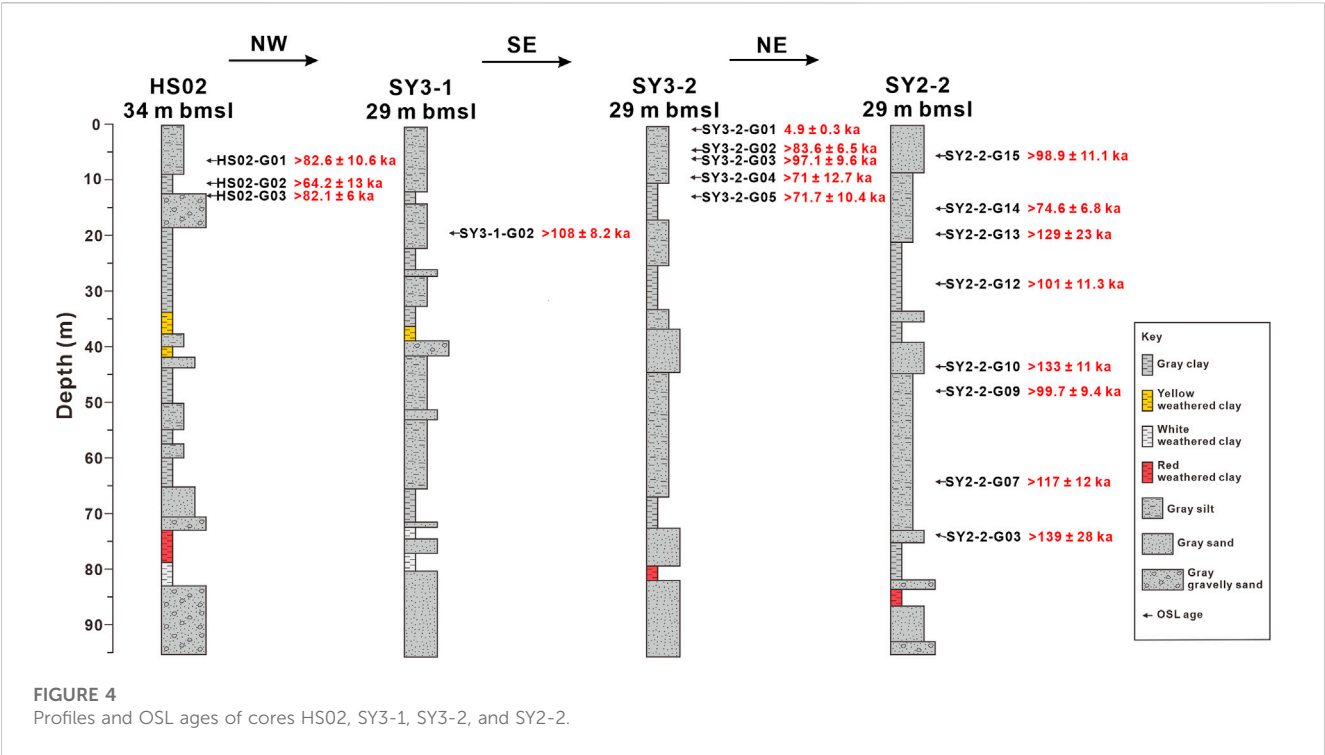
a Numbers of aliquots measured using the standard SGC, method.

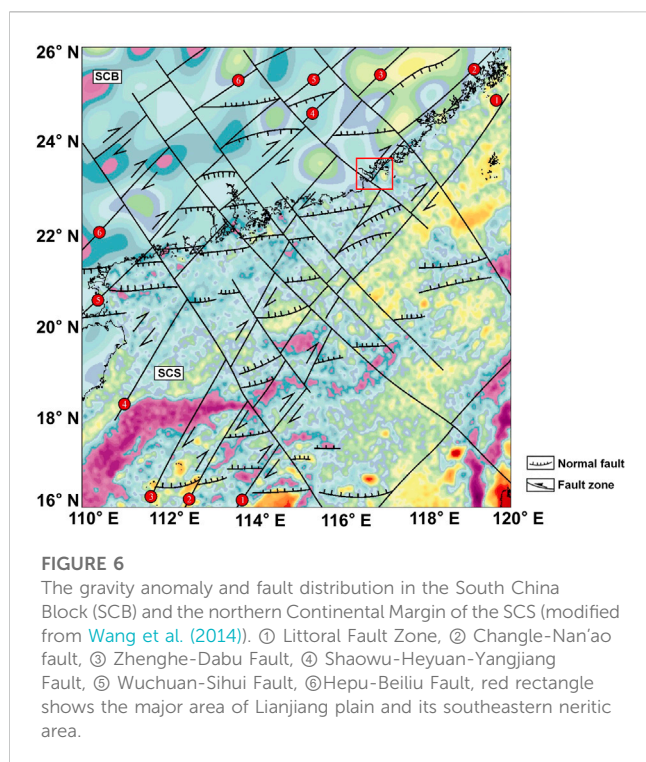
b Numbers of aliquots measured using the standard SAR, method.

Lianjiang River plain, the Holocene sediments are around the same thickness as those in the outer Lianjiang River plain, less than 4.2 m (Tang et al., 2018) (Figure 5). However, core sediments at depths of 12.9 m, 18 m, and 19.4 m were dated to 1,442 \pm 65 cal a BP, 11,712 \pm 508 cal a BP, and 9,321 \pm 221 cal a BP, respectively, indicating that nearly 20 m thick of the Holocene sedimentation formed in the neritic area between the Chaoshan plain and Nanao Island (Sun et al., 2007). The Bohai Sea and the China Sea contain the Holocene sediments that are more than 12 m thick (Liu et al., 2017; Long et al., 2022), while they are thinner in the SCS, around 10 m (Wei et al., 2015; Wang et al., 2020). The neritic area of the Lianjiang River plain has comparatively poor conditions for sedimentary

preservation. The preservation of the late Quaternary sediments in the Lianjiang River plain is still debated. Some studies attributed it to tectonic activities, while others suggested the corresponding of the sea-level variations (Song et al., 2012; Tang et al., 2018).

The South China Block comprises four NE-trending faults, namely, the Littoral, Changle-Nan'ao, Zhenghe-Dabu, and Shaowu-Heyuan-Yangjiang faults (Figure 6) (Sun et al., 2014; Wang et al., 2014). Of these faults, the Littoral and Changle-Nan'ao faults are active since the Quaternary, and have a significant impact on the Lianjiang River plain and its neritic area (Xu et al., 2010; Wang et al., 2014). These faults have influenced sedimentary evolution and paleo-depositional



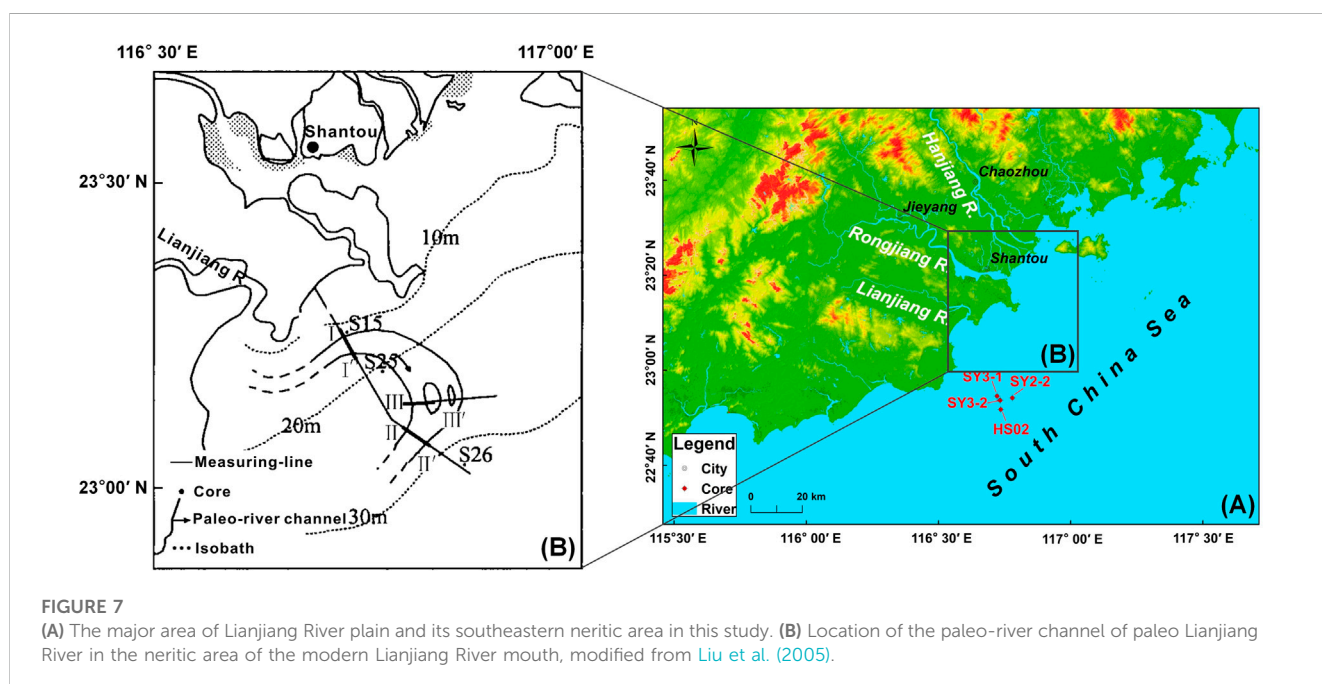


environments, resulting in accumulation and transportation of the Quaternary along the faults (Sun et al., 2007).

However, the southeastern neritic area of the Lianjiang River plain is under intense interaction of the SCS and Lianjiang River. Global sea level declined since the end of the last interglacial period and reached the maximum at ca. 130 m bmsl during the last glacial maximum (LGM; ca. 30–20 ka) (Hanebuth et al., 2006; Hodgson et al., 2006; Lambeck et al., 2014; Spratt and Lisiecki, 2016). Low-stand sea level led to the incision of the Lianjiang

River and the exposure of the continental shelf in the northern SCS (Wei et al., 2015; Xu et al., 2019). A series of buried paleochannels extending from the southeastern neritic area of the Lianjiang River plain to approximately 25 km offshore were discovered and considered as the paleo-Lianjiang River (Figure 7) (Liu et al., 2005). The cores in this study are located at the southern part of the paleo-channels of the Lianjiang River, where they likely experienced fluvial incision during the last glacial period. Lan et al. (1991) demonstrated that the medium coarse sands in the Taiwan Shoal were mainly transported by the currents from the coastal region of southeastern China during 10–20 ka BP based on the ^{14}C dating. Sediments from the core sites were largely transported to the Taiwan Shoal by the Hanjiang diluted water and Guangdong Coastal Currents (Figure 1A), resulting in limited sediments in the neritic area of the Lianjiang River plain (Lan et al., 1991; Lian and Li, 2011). Studies have shown that terrigenous sediments can be transported and spread by oceanic currents once they enter continental margins (Liu et al., 2008; Liu Z. et al., 2016; Zhang et al., 2022). For instance, the sediment from the Pearl River is predominantly transported southwestward via coastal currents, while Taiwan-derived sediments are among the principal contributors in the NESCS due to the influence of deep-water currents and surface currents that vary seasonally (Liu Z. et al., 2016; Zhang et al., 2022). Therefore, fluvial incision during the last glacial period and strong transportation by coastal currents may result in poor preservation of sediments since at least 83.6 ka in the study area.

The Chaoshan plain neritic area experienced poor sediment preservation since MIS 5, while other regions experienced transgressions and regressions resulting in more than 30 m thick of deposition. Studies from the Bohai Sea, the western South Yellow Sea, and the East China Sea have revealed evidence of sea-level changes and their impact on sedimentary processes (Liu J. et al., 2016; Liu et al., 2017; Wang et al., 2019; Wang et al., 2020; Long et al.,



2022). Further research indicated that sea-level changes were identified as the primary control for sedimentation on the northeastern SCS, with Kuroshio intrusion being responsible for the transport of Taiwan-derived sediment during the late Quaternary (Zhang et al., 2022). In summary, the sedimentary processes in the eastern continental shelf of China were mainly influenced by sea-level changes.

5 Conclusion

In this study, we used quartz OSL technique to date the Quaternary sediments from cores SY2-2, SY3-1, SY3-2, and HS02 in the neritic area of the Lianjiang River plain. Seventeen dates ranged from 4.9 ± 0.3 ka to $>139 \pm 28$ ka. Except for SY3-2-G01, all samples were considered minimum ages due to De saturation (>190 Gy). Our findings reveal that the sediments have been poorly preserved for at least 83.6 ka, with a sedimentation thickness since at least MIS 5 of less than 6.4 m and Holocene sediments of less than 4.2 m. This study has shown that erosion has occurred in the neritic area of the Lianjiang River plain in the NESCS since at least MIS 5 due to fluvial incision caused by low sea levels during the last glacial period and strong coastal currents.

Data availability statement

The original contributions presented in the study are included in the article/Supplementary Material, further inquiries can be directed to the corresponding authors.

Author contributions

JZ: data curation, visualization, writing-original draft. BL: data curation, investigation. YO: data curation, investigation. RT: data curation. JS: data curation, investigation. YX: writing-reviewing and editing. FW: data curation, investigation. MA: reviewing and editing. KZ: investigation. ZL: conceptualization, methodology,

supervision, funding acquisition, reviewing, and editing. All authors contributed to the article and approved the submitted version.

Funding

This research was supported by the Natural Science Foundation of Guangdong Province (2023A1515012926), the National Natural Science Foundation of China (Grants No. 41877438), the STU Scientific Research Start-Up Foundation for Talents (NTF19003, NTF20006), and Innovation and Entrepreneurship Project of Shantou (2021112176541391).

Acknowledgments

We thank Qinjing Shen and Xiaolin Xu for the helpful discussions.

Conflict of interest

The authors declare that the research was conducted in the absence of any commercial or financial relationships that could be construed as a potential conflict of interest.

Publisher's note

All claims expressed in this article are solely those of the authors and do not necessarily represent those of their affiliated organizations, or those of the publisher, the editors and the reviewers. Any product that may be evaluated in this article, or claim that may be made by its manufacturer, is not guaranteed or endorsed by the publisher.

Supplementary material

The Supplementary Material for this article can be found online at: <https://www.frontiersin.org/articles/10.3389/feart.2023.1089946/full#supplementary-material>

References

- Bøtter-Jensen, L., Duller, G. A. T., Murray, A. S., and Banerjee, D. (1999). Blue light emitting diodes for optical stimulation of quartz in retrospective dosimetry and dating. *Radiat. Prot. Dosim.* 84, 335–340. doi:10.1093/oxfordjournals.rpd.a032750
- Buylaert, J. P., Vandenberghe, D., Murray, A. S., Huot, S., De Corte, F., and Van den Haute, P. (2007). Luminescence dating of old (>70 ka) Chinese loess: A comparison of single-aliquot OSL and IRSL techniques. *Quat. Geochronol.* 2 (1), 9–14. doi:10.1016/j.quageo.2006.05.028
- Chapot, M. S., Roberts, H. M., Duller, G. A. T., and Lai, Z. P. (2016). Natural and laboratory TT-OSL dose response curves: Testing the lifetime of the TT-OSL signal in nature. *Radiat. Meas.* 85, 41–50. doi:10.1016/j.radmeas.2015.11.008
- Chen, G. (1984). Quaternary fault block movement in Chao-Shan Plain. *South China J. Seismol.* 4 (4), 001–018. (in Chinese). doi:10.13512/j.hndz.1984.04.001
- Chen, W. (1984). Several features for the development of sedimentary basin in Chaoshan area, Guangdong province. *South China J. Seismol.* 4 (2), 20–30. (in Chinese). doi:10.13512/j.hndz.1984.02.004
- Chen, X., Li, R., Lan, X., and Xu, X. (2020). Late quaternary stratigraphic sequence and depositional response in the Western Bohai Sea. *Earth Sci.* 45 (7), 2684–2696. (in Chinese with English abstract). doi:10.3799/dqkx.2020.014
- Durcan, J. A., King, G. E., and Duller, G. A. (2015). Drac: Dose rate and age calculator for trapped charge dating. *Quat. Geochronol.* 28, 54–61. doi:10.1016/j.quageo.2015.03.012
- Faershtein, G., Porat, N., and Matmon, A. (2019). Natural saturation of OSL and TT-OSL signals of quartz grains from Nilotic origin. *Quat. Geochronol.* 49, 146–152. doi:10.1016/j.quageo.2018.04.002
- Hanebuth, T. J. J., Saito, Y., Tanabe, S., Vu, Q. L., and Ngo, Q. T. (2006). Sea levels during late marine isotope stage 3 (or older?) reported from the Red River delta (northern Vietnam) and adjacent regions. *Quat. Int.* 145–146, 119–134. doi:10.1016/j.quaint.2005.07.008
- Hodgson, D. A., Verleyen, E., Squier, A. H., Sabbe, K., Keely, B. J., Saunders, K. M., et al. (2006). Interglacial environments of coastal east Antarctica: Comparison of MIS 1 (Holocene) and MIS 5e (last interglacial) lake-sediment records. *Quat. Sci. Rev.* 25 (1–2), 179–197. doi:10.1016/j.quascirev.2005.03.004
- Lai, Z. (2010). Chronology and the upper dating limit for loess samples from Luochuan section in the Chinese Loess Plateau using quartz OSL SAR protocol. *J. Asian Earth Sci.* 37 (2), 176–185. doi:10.1016/j.jseas.2009.08.003

- Lai, Z., and Fan, A. (2014). Examining quartz OSL age underestimation for loess samples from Luochuan in the Chinese Loess Plateau. *Geochronometria* 41 (1), 57–64. doi:10.2478/s13386-013-0138-1
- Lai, Z., and Ou, X. (2013). Basic procedures of optically stimulated luminescence (OSL) dating. *Prog. Geogr.* 32 (5), 683–693. (in Chinese with English abstract). CNKI: SUN:DLKJ.0.2013-05-003.
- Lai, Z. (2006). Testing the use of an OSL standardised growth curve (SGC) for determination on quartz from the Chinese Loess Plateau. *Radiat. Meas.* 41 (1), 9–16. doi:10.1016/j.radmeas.2005.06.031
- Lambeck, K., Rouby, H., Purcell, A., Sun, Y., and Sambridge, M. (2014). sea level and global ice volumes from the last glacial maximum to the Holocene. *Proc. Natl. Acad. Sci. U. S. A.* 111 (43), 15296–15303. doi:10.1073/pnas.1411762111
- Lan, D., Zhang, W., Chen, C., and Xie, Z. (1991). Preliminary study on age and origin of medium-coarse sands in Taiwan Shoal. *Taiwan Strait* 10 (2), 156–161. (in Chinese with English abstract). CNKI:SUN:TWHX.0.1991-02-009.
- Lan, X. H., Ri-Hui, L. I., Chen, X. H., Qin, Y. C., Wang, Z. B., and Bei-Bei, M. I. (2018). Study of sedimentary geochemistry in the western Bohai Sea since late pleistocene. *Adv. Mar. Sci.* 1, 67–78. (in Chinese with English abstract).
- Li, G., Li, P., Liu, Y., Qiao, L., Ma, Y., Xu, J., et al. (2014). Sedimentary system response to the global sea level change in the East China Seas since the last glacial maximum. *Earth-Science Rev.* 139, 390–405. doi:10.1016/j.earscirev.2014.09.007
- Li, P., Huang, Z., Zong, Y., and Zhang, Z. (1987). *Hanjiang Delta*. Beijing: Ocean Press. (in Chinese).
- Li, P. R., Huang, Z. G., and Zong, Y. Q. (1988). New views on geomorphological development of the Hanjiang River Delta. *Acta Geogr. Sin.* 55 (1), 19–34. (in Chinese). doi:10.11821/xb198801003
- Lian, Y. K., and Li, Y. (2011). Grain size characteristics and transport trend in the Taiwan Bank. *J. Oceanogr. Taiwan Strait* 30 (1), 122–127. (in Chinese with English abstract). doi:10.3969/j.issn.1000-8160.2011.01.018
- Lin, P., Song, Y., Zhan, W., Tian, R., Wang, Z., Xu, X., et al. (2023). Late Pleistocene to Holocene sedimentary history in the Pearl River Delta revealed by OSL and radiocarbon dating. *Catena* 224, 106972. doi:10.1016/j.catena.2023.106972
- Lin, P., Xu, X., Yan, C., Luo, L., and Lai, Z. (2022). Holocene sedimentary of the Pearl River Delta in South China: OSL and radiocarbon dating of cores from zhuai. *Front. Mar. Sci.* 2260. doi:10.3389/fmars.2022.1031456
- Liu, A., Lü, W., and Cai, F. (2005). A buried meandering river of late quaternary off Shantou city, Guangdong province. *Oceanol. Limnologia Sinica* 36 (2), 104–110. (in Chinese with English abstract). CNKI:SUN:HYFZ.0.2005-02-001.
- Liu, J., Saito, Y., Kong, X., Wang, H., Wen, C., Yang, Z., et al. (2010). Delta development and channel incision during marine isotope stages 3 and 2 in the Western South Yellow Sea. *Mar. Geol.* 278 (1), 54–76. doi:10.1016/j.margeo.2010.09.003
- Liu, J., Wang, H., Wang, F., Qiu, J., Saito, Y., Lu, J., et al. (2016). Sedimentary evolution during the last ~1.9Ma near the Western margin of the modern Bohai Sea. *Palaeogeogr. Palaeoclimatol. Palaeoecol.* 451, 84–96. doi:10.1016/j.palaeo.2016.03.012
- Liu, S., Mi, B., Fang, X., Li, X., Pan, H.-J., Chen, M.-T., et al. (2017). A preliminary study of a sediment core drilled from the mud area on the inner shelf of the East China Sea: Implications for paleoclimatic changes during the fast transgression period (13 ka B.P.–8 ka B.P.). *Quat. Int.* 441, 35–50. doi:10.1016/j.quaint.2016.09.057
- Liu, Z., Tuo, S., Colin, C., Liu, J. T., Huang, C.-Y., Selvaraj, K., et al. (2008). Detrital fine-grained sediment contribution from Taiwan to the northern South China Sea and its relation to regional ocean circulation. *Mar. Geol.* 255 (3), 149–155. doi:10.1016/j.margeo.2008.08.003
- Liu, Z., Zhao, Y., Colin, C., Stattegger, K., Wiesner, M. G., Huh, C.-a., et al. (2016b). Source-to-sink transport processes of fluvial sediments in the South China Sea. *Earth-Science Rev.* 153, 238–273. doi:10.1016/j.earscirev.2015.08.005
- Long, Z., Wang, Z., Tu, H., Li, R., Wen, Z., Wang, Y., et al. (2022). OSL and radiocarbon dating of a core from the Bohai Sea in China and implication for Late Quaternary transgression pattern. *Quat. Geochronol.* 70, 101308. doi:10.1016/j.quageo.2022.101308
- Murray, A., Arnold, L. J., Buylaert, J.-P., Guérin, G., Qin, J., Singhvi, A. K., et al. (2021). Optically stimulated luminescence dating using quartz. *Nat. Rev. Methods Prim.* 1 (1), 72. doi:10.1038/s43586-021-00068-5
- Murray, A. S., and Wintle, A. G. (2000). Luminescence dating of quartz using an improved single-aliquot regenerative-dose protocol. *Radiat. Meas.* 32 (1), 57–73. doi:10.1016/S1350-4487(99)00253-X
- Qin, Y.-C., Wang, Z., Jiang, X., Zhang, X., and Luan, X. (2023). Quantitative sediment provenance of the northwestern East China Sea: Evidence for tidal current-driven offshore transport and paleogeographic implications. *Geomorphology*, 108668. doi:10.1016/j.geomorph.2023.108666
- Roberts, H., and Duller, G. A. (2004). Standardised growth curves for optical dating of sediment using multiple-grain aliquots. *Radiat. Meas.* 38 (2), 241–252. doi:10.1016/j.radmeas.2003.10.001
- Song, Y., Chen, W., Pan, H., Zhang, Z., He, Z., Chen, X., et al. (2012). Geological age of Quaternary series in Lianjiang plain. *J. Jilin Univ.(Earth Sci. Ed.)* 42, 154–161. (in Chinese with English abstract). doi:10.13278/j.cnki.jjuese.2012.s1.040
- Spratt, R. M., and Lisiecki, L. E. (2016). A Late Pleistocene sea level stack. *Clim. Past* 12 (4), 1079–1092. doi:10.5194/cp-12-1079-2016
- Sun, J.-I., Xu, H.-I., Wu, P., Wu, Y.-b., Qiu, X.-I., and Zhan, W.-h. (2007). Late Quaternary sedimentological characteristics and sedimentary environment evolution in sea area between Nan'ao and Chenghai, eastern Guangdong. *J. Trop. Oceanogr.* 26, 30–36. (in Chinese with English abstract). doi:10.3969/j.issn.1009-5470.2007.03.005
- Sun, X. M., Zhang, X. Q., Zhang, G. C., Lu, B. L., Yue, J. P., and Zhang, B. (2014). Texture and tectonic attribute of Cenozoic basin basement in the northern South China Sea. *Sci. China Earth Sci.* 57 (6), 1199–1211. doi:10.1007/s11430-014-4835-2
- Tang, Y., Zheng, Z., Chen, C., Wang, M., and Chen, B. (2018). Evolution of the Lian River coastal basin in response to Quaternary marine transgressions in Southeast China. *Sediment. Geol.* 366, 1–13. doi:10.1016/j.sedgeo.2018.01.003
- Timar-Gabor, A., Vandenberghe, D. A. G., Vasiliniuc, S., Panaitiu, C. E., Panaitiu, C. G., Dimofte, D., et al. (2011). Optical dating of Romanian loess: A comparison between silt-sized and sand-sized quartz. *Quat. Int.* 240 (1), 62–70. doi:10.1016/j.quaint.2010.10.007
- Wang, F., Wang, F., Zhang, W., Xu, S., and Lai, Z. (2023). A novel machine learning fingerprinting method using sparse representation for provenance detection in delta sediments. *Catena* 227, 107095. doi:10.1016/j.catena.2023.107095
- Wang, J. H., Zheng, Z., and Wu, C. Y. (1997). Sedimentary facies and paleoenvironmental evolution of the late quaternary in the Chaoshan Plain, east Guangdong. *Acta Scintiarum Nat. Univ. Sunyatseni* 36 (1), 95–100. (in Chinese with English abstract). CNKI:SUN:ZSDZ.0.1997-01-019.
- Wang, L., Li, G., Xu, J., Liu, Y., Qiao, L., Ding, D., et al. (2019). Strata sequence and paleochannel response to tectonic, sea-level, and Asian monsoon variability since the late Pleistocene in the South Yellow Sea. *Quat. Res.* 92 (2), 450–468. doi:10.1017/qua.2019.29
- Wang, X. F., Yu, S., Gong, Y. H., Li, S. Z., Liu, X., Ma, Y., et al. (2014). Extension of NE-trending faults in South China to northern South China sea continental shelf. *Geotect. Metallogenia* 38 (3), 557–570. (in Chinese with English abstract).
- Wang, Z., Zhang, J., Mei, X., Chen, X., Zhao, L., Zhang, Y., et al. (2020). The stratigraphy and depositional environments of China's sea shelves since MIS5 (74–128) ka. *Geol. China* 47 (5), 1370–1394. (in Chinese with English abstract).
- Wei, C., Zhang, K., Yu, Z., and Qiu, Y. (2015). Correlation of stratigraphic sequences between the Pearl River Delta and its offshore continental shelf since the late pleistocene. *Acta Sedimentol. Sin.* 33 (4), 714–723. (in Chinese with English abstract).
- Wintle, A. G., and Murray, A. S. (2006). A review of quartz optically stimulated luminescence characteristics and their relevance in single-aliquot regeneration dating protocols. *Radiat. Meas.* 41 (4), 369–391. doi:10.1016/j.radmeas.2005.11.001
- Xia, S., Zhou, P., Zhao, D., and Cao, J. (2020). Seismogenic structure in the source zone of the 1918 M7.5 NanAo earthquake in the northern South China Sea. *Phys. Earth Planet. Interiors* 302, 106472. doi:10.1016/j.pepi.2020.106472
- Xu, F., Li, A., Xiao, S., Wan, S., Liu, J., and Zhang, Y. C. (2009). Paleoenvironmental evolution in the inner shelf of the East China Sea since the last deglaciation. *Acta Sedimentol. Sin.* 27, 118–127. (in Chinese with English abstract).
- Xu, H. L., Ye, C. M., Qiu, X. L., Sun, J. L., and Xia, S. H. (2010). Studies on the binhai Fault Zone in the northern South China sea by the deep geophysical exploration and its seismogenic structure. *South China J. Seismol.* 30, 10–18. (in Chinese with English abstract).
- Xu, X., Li, H., Tang, L., Lai, Z., Xu, G., Zhang, X., et al. (2020). Chronology of a Holocene core from the Pearl River delta in southern China. *Front. Earth Sci.* 8, 262. doi:10.3389/feart.2020.00262
- Xu, X., Zhong, J., Huang, X., Li, H., Ding, Z., and Lai, Z. (2022). Age comparison by luminescence using quartz and feldspar on core HPQK01 from the Pearl River Delta in China. *Quat. Geochronol.* 71, 101320. doi:10.1016/j.quageo.2022.101320
- Xu, Y. T., Lai, Z. P., and Li, C. A. (2019). Sea-level change as the driver for lake formation in the Yangtze Plain - a review. *Glob. Planet. Change* 181, 102980. doi:10.1016/j.gloplacha.2019.102980
- Zhang, C., Yang, S., Huang, X., Dou, Y., Li, F., Xu, X., et al. (2022). Sea level change and Kuroshio intrusion dominated Taiwan sediment source-to-sink processes in the northeastern South China Sea over the past 244 kyrs. *Quat. Sci. Rev.* 287, 107558. doi:10.1016/j.quascirev.2022.107558
- Zheng, Y., Zheng, H., and Wang, K. (2010). History of sea level change since last glacial: Reflected by sedimentology of core from East China Sea inner shelf. *J. Tongji Univ.* 38 (9), 1381–1386. (in Chinese with English abstract).
- Zheng, Z., and Li, Q. (2000). Vegetation, climate, and sea level in the past 55,000 years, Hanjiang Delta, Southeastern China. *Quat. Res.* 53 (3), 330–340. doi:10.1006/qres.1999.2126
- Zhong, J., Ling, K., Yang, M., Shen, Q., Abbas, M., and Lai, Z. (2022). Radiocarbon and OSL dating on cores from the Chaoshan delta in the coastal South China Sea. *Front. Mar. Sci.* 9. doi:10.3389/fmars.2022.1030841
- Zong, Y. Q. (1992). Postglacial stratigraphy and sea-level changes in the han River Delta, China. *J. Coast. Res.* 8 (1), 1–28. Available at: <https://www.jstor.org/stable/4297948>.



OPEN ACCESS

EDITED BY

Rafael Almeida,
San Diego State University, United States

REVIEWED BY

Yan Qiu,
Guangzhou Marine Geological Survey,
China
Wenhuan Zhan,
South China Sea Institute of Oceanology
(CAS), China

*CORRESPONDENCE

Cong Chen,
✉ chenc66@mail.sysu.edu.cn

[†]These authors have contributed equally
to this work

SPECIALTY SECTION

This article was submitted to Quaternary
Science, Geomorphology and
Paleoenvironment,
a section of the journal
Frontiers in Earth Science

RECEIVED 31 December 2022

ACCEPTED 05 April 2023

PUBLISHED 21 April 2023

CITATION

Chen Z, Wang W, Huang P, Tang Y,
Wang J, Zeng Q and Chen C (2023), Soft-
sediment deformation structures of
mottled clay in Huizhou Quaternary
basin, coastal South China.
Front. Earth Sci. 11:1135335.
doi: 10.3389/feart.2023.1135335

COPYRIGHT

© 2023 Chen, Wang, Huang, Tang, Wang,
Zeng and Chen. This is an open-access
article distributed under the terms of the
[Creative Commons Attribution License
\(CC BY\)](https://creativecommons.org/licenses/by/4.0/). The use, distribution or
reproduction in other forums is
permitted, provided the original author(s)
and the copyright owner(s) are credited
and that the original publication in this
journal is cited, in accordance with
accepted academic practice. No use,
distribution or reproduction is permitted
which does not comply with these terms.

Soft-sediment deformation structures of mottled clay in Huizhou Quaternary basin, coastal South China

Zhen Chen^{1,2†}, Wen Wang^{3†}, Ping Huang², Yongjie Tang¹,
Jing Wang⁴, Qiang Zeng² and Cong Chen^{1*}

¹School of Earth Sciences and Engineering, Sun Yat-sen University, Zhuhai, China, ²GDZD Institute on Deep-Earth Sciences, Guangzhou, China, ³Nonferrous Metals Geological Bureau of Guangdong Province 935 Battalion, Huizhou, China, ⁴Museum and History Museum of Sun Yat-sen University, Guangzhou, China

Tectonically induced liquefaction and the resulting soft-sediment deformation structure (SSDS) can provide useful information on paleo-earthquakes, which is vital for the assessment of geohazard susceptibility in tectonically active regions. In this study, we combined sedimentary and chronological methods to reveal the detailed characteristics of the mottled clay in the Huizhou Quaternary Basin. The dating results suggest that mottled clay usually developed during the late Pleistocene, overlying the fluvial deposit or embedding homogeneous aeolian yellow silt. Mottled clay has a typical bimodal frequency distribution with modal sizes at 5 and 80–90 μm , which are identical to those of the yellow silt and the underlying fluvial sand, respectively. Micro-X-ray fluorescence mapping revealed high concentrations of Fe and Si in the red and white fraction, respectively. In addition, the red fraction of mottled clay has a high hematite content, similar to loess-like yellow silt, whereas the white fraction and the underlying fluvial sediments are dominated by goethite. This sedimentary evidence together suggests that the mottled clay could be an admixture of aeolian yellow silt and the underlying fluvial sand. Furthermore, diverse deformed structures (e.g., fragmented structures, sand veins, sand dykes and flame structures) were observed in mottled clay. Therefore, we suggest that the mottled clay structure in the Huizhou Basin is a product of liquefaction-induced SSDS. Tectonic activity was considered to have triggered the liquefaction and SSDS, which is supported by the close spatial relationship between the mottled clay and regional faults. We propose that the SSDS of mottled clay could be a potential indicator of paleo-earthquakes in the coastal Quaternary basins of the northern South China Sea.

KEYWORDS

soft-sediment deformation, mottled clay, tectonic activity, late Pleistocene, Huizhou basin, South China

1 Introduction

Tectonic-induced liquefaction and resulting soft-sediment deformation structure (SSDS) that was preserved in the geological record, are commonly used to derive information (e.g., intensity and recurrence intervals) of paleo-earthquake, and are thus vital for the assessment of geohazard susceptibility in tectonically active regions (Allen, 1986; Deev et al., 2009; Qiao et al.,

2017; Liang et al., 2018; Tuttle et al., 2019; Üner et al., 2019). For example, a compilation of historical earthquakes that occurred during the last millennium and the related liquefaction in Italy permitted the establishment of an empirical relationship between the magnitude and distance of liquefaction (Galli, 2000). An integrated method was applied to provide information on the seismic shaking intensity recorded in lacustrine sediments at sites where it was difficult to conduct research by excavating trenches owing to their rough topography, strong erosion, or the absence of co-seismic ruptures (Zhong et al., 2022). In particular, paleo-earthquakes in the late Quaternary are actively researched because their potential risk to contemporary urban growth and safety in habitations, which have been successfully identified, for instance, in Ecuador (Hibsch et al., 1997), Kyrgyzstan (Gladkov et al., 2016), and Brazil (Rossetti et al., 2017), mostly based on liquefaction and SSDS features in the deposit profiles. However, in addition to earthquakes, liquefaction-induced SSDS can also be triggered by other factors, such as water waves, rapid sediment accumulation, groundwater movement, ice-wedges, and meteorites (Owen and Moretti, 2011; Su et al., 2022). Therefore, correctly determining the trigger for liquefaction-induced SSDS is fundamental for interpreting information on paleo-earthquake. A methodology and criteria for analyzing SSDS and distinguishing the triggers have been proposed, involving sedimentological, paleoenvironmental and tectonic contexts (Owen and Moretti, 2011).

In the coastal region of the northern South China Sea (SCS), there are many Quaternary basins, such as the Pearl River Delta (PRD), Lianjiang Plains, Hanjiang Delta and Fujian coastal basins, the emergence of which is generally related to the regional neo-tectonic activity (Chen et al., 2002; Yao et al., 2013). Previous studies have also revealed geological evidence of late Quaternary fault activity (e.g., Song et al., 2001; Tang et al., 2011). For example, a sedimentary layer younger than 23 ka was cut off by a normal fault with a fault-throw of 53 cm at the Xilingang Site in the PRD (Tang et al., 2011). Several historical earthquake events are also documented (Wei et al., 2000). This implies that the PRD with a dense population and economic activity is tectonically active. Moreover, most Quaternary basins are filled with several to dozens of meters of loose, water-saturated silt and sand, consisting mainly of fluvial, marine and aeolian sediments (Wang et al., 2018a; Tang et al., 2018). Tectonic and sedimentary features generally favor the development of liquefaction (Owen and Moretti, 2011). However, tectonic activity-induced liquefaction and related SSDS in the PRD remain poorly understood. Mottled clay, which exhibits a mixed yellow, red and white color, broadly developed in these coastal Quaternary basins and is primary regarded as a weathering product of the underlying fluvial/marine sediments (Huang, 1982; Li et al., 1984). Later, Wang et al. (2018b) suggested an aeolian origin of the mottled clay rather than a weathering product based on sedimentary and geochemical analyses, and proposed that the mottled structure was formed by post-sedimentary modification of oxidation. Recently, we studied a series of drilling cores derived from the Huizhou Basin (HZB) in the eastern PRD and found diverse deformed structures in the mottled clay sediments, implying a potential liquefaction origin of the mottled structure.

In this study, we combined sedimentary and chronological methods, including lithological feature, grain size analysis, micro-X-ray fluorescence (μ -XRF) scanning, diffuse reflectance spectroscopy (DRS) analysis, and accelerator mass spectrometry

radiocarbon dating (AMS ^{14}C), to reveal detailed characteristics of mottled clay in the drilling cores derived from the HZB. We further discuss the origin of the mottled structures, which are possibly liquefaction-induced SSDS triggered by regional neo-tectonic activity during the late Pleistocene.

2 Geological settings

The Pearl River, one of the longest watercourses in southern China, includes three major tributaries (i.e., the Xijiang River, Beijiang River and Dongjiang River), and its delta (the PRD) is the largest Quaternary plain in the coastal northern SCS (Figure 1A). The HZB situated in the eastern PRD is an alluvial basin of the middle Dongjiang River, ranging from 114°20' to 114°40' E and 22°50' to 23°10' N. The evolution of the Huizhou Basin was mostly controlled by the SW-NE and NW-SE faults, that is, the Huizhou Fault to the west, Lianghua Fault to the east, the Zijin-Boluo Fault and Tonghu Fault to the north, and the Lianhuashan Fault to the south (Figure 1B) (Li et al., 2020, 2021). The Zijin-Boluo and Tonghu faults belong to the same regional fault zone, with a length of approximately 20 km, striking NE, inclining SE and dipping 40°–60°. The Lianhuashan Fault is part of the Wuhua-Shenzhen Fault zone, striking NE and inclining NW. The Huizhou Fault is approximately 20 km long, striking NW, inclining NE and dipping 65°–75°. All five faults are normal faults (BGMGRP, 1988), and are considered as being active. The bedrock of the HZB consist mainly of Jurassic and Cretaceous igneous rock and sandstone, which have an unconformity contact with the overlying unconsolidated late Quaternary sediments. At present, the HZB experiences a subtropical monsoonal climate, with a mean annual temperature of 21.9°C, summer temperature of 27.9°C and winter temperature of 14.5°C, respectively, between 1954 and 2006 AD (Li et al., 2008).

3 Material and methods

3.1 Drilling cores

In this study, 12 cores (Table 1) were drilled in the HZB during April-May 2022 to reveal the features of Quaternary sediments in the basin. Combined with three published drilling cores, the lithological chart shows that the Quaternary sediments are generally approximately 15–25 m thick, and the overall succession can be divided into three units from the bottom to the top based on the lithology as follows (Figure 2): 1) Unit I, Q_3^a fluvial sediment; the lithology is grayish white to yellow gravel sand, sand or clay sand, underlain by weathered pre-Cenozoic bedrock. The thickness of this unit is generally larger than 10 m. 2) Unit II, Q_3^b aeolian sediment, mostly consists of loess-like silt, with occasional mottled clay. The thickness of this unit varies in the basin, mostly between 2 and 10 m. 3) Unit III, Q_4 fluvial or marsh sediments; it mainly consists of gray to yellow coarse to fine sand, silt and clay. The organic carbon content of this unit is generally higher than that of Unit I. In particular, a mottled clay structure with 1–5 m thick was found in seven of the 12 drilling cores in the HZB. The mottled clay exhibits a mixed yellow, red and grey-white color, and the bright clay generally shows vein- and/or

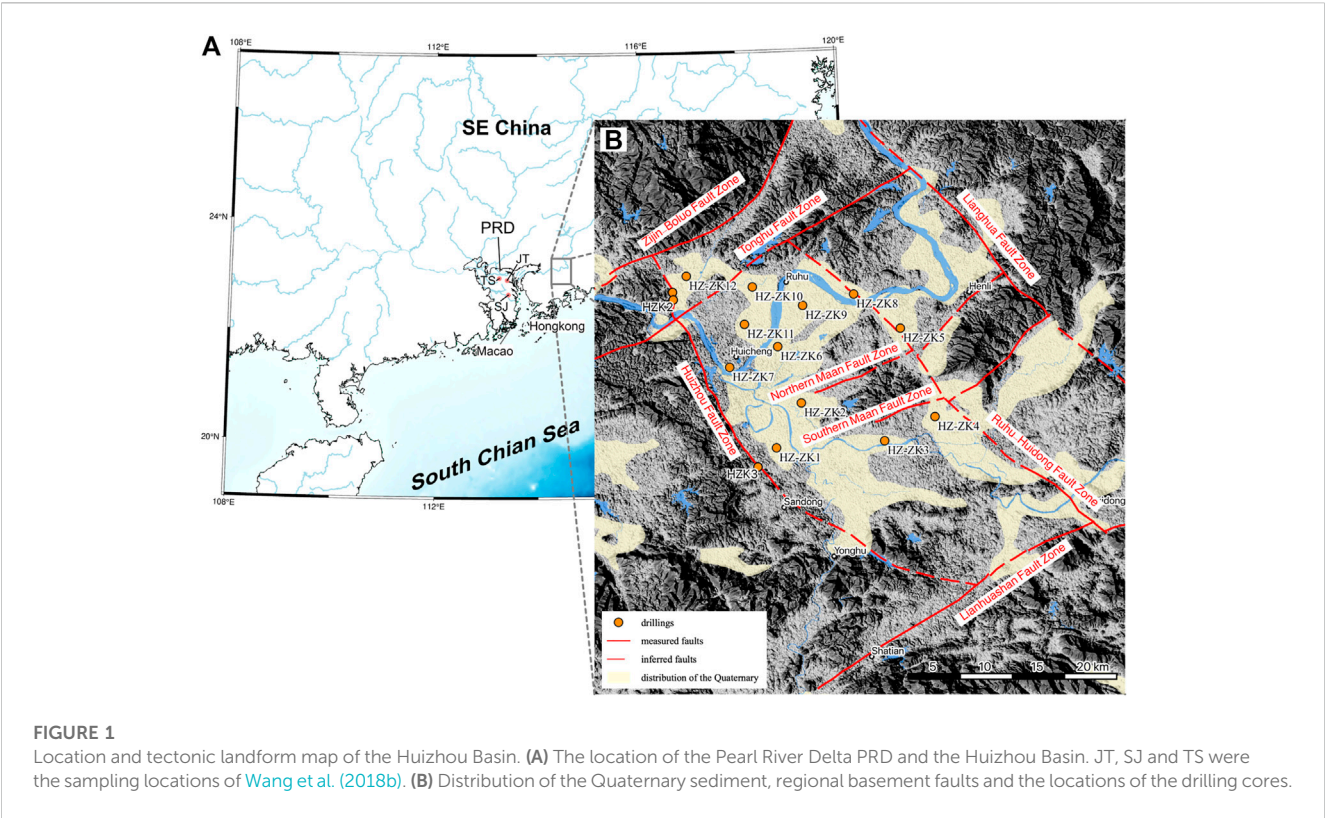


TABLE 1 Locations of the drilling cores in the Huizhou Basin.

Core ID	Longitude (E)	Latitude (N)	Elevation (m)	Mottled clay
HZ-ZK01	114° 27' 02.3448"	23° 01' 51.4574"	11.7	No
HZ-ZK02	114° 28' 19.3890"	23° 04' 10.9721"	11.6	No
HZ-ZK03	114° 32' 37.8219"	23° 02' 13.6413"	15.5	No
HZ-ZK04	114° 35' 13.9168"	23° 03' 28.5875"	15.9	Yes
HZ-ZK05	114° 33' 26.3536"	23° 08' 03.1127"	15.0	Yes
HZ-ZK06	114° 27' 06.0229"	23° 07' 05.7405"	11.1	Yes
HZ-ZK07	114° 24' 36.9448"	23° 06' 01.1982"	14.2	No
HZ-ZK08	114° 31' 01.4063"	23° 09' 48.9913"	13.2	No
HZ-ZK09	114° 28' 23.1944"	23° 09' 13.6555"	10.7	Yes
HZ-ZK10	114° 25' 47.2292"	23° 10' 10.8851"	12.0	Yes
HZ-ZK11	114° 25' 22.8159"	23° 08' 14.7721"	11.7	Yes
HZ-ZK12	114° 22' 22.2858"	23° 10' 43.8220"	10.7	Yes

flame-like vertical structures intruding into yellow/red sediments (Figure 3B). The deformation features were clearly distinguished from the underlying loess-like silt or fluvial sand deposits (Figure 3). The normal aeolian sediment is homogeneous in color and grain size (Figure 3A), and fluvial sand deposits present pronounced horizontal features (e.g., laminae).

3.2 AMS ¹⁴C dating

To constrain the age of the Quaternary stratigraphy in the HZB, we collected ten samples from the drilling cores for AMS ¹⁴C dating. Bulk organic sediment samples were pretreated using the standard acid-base-acid (ABA) method and analyzed at the

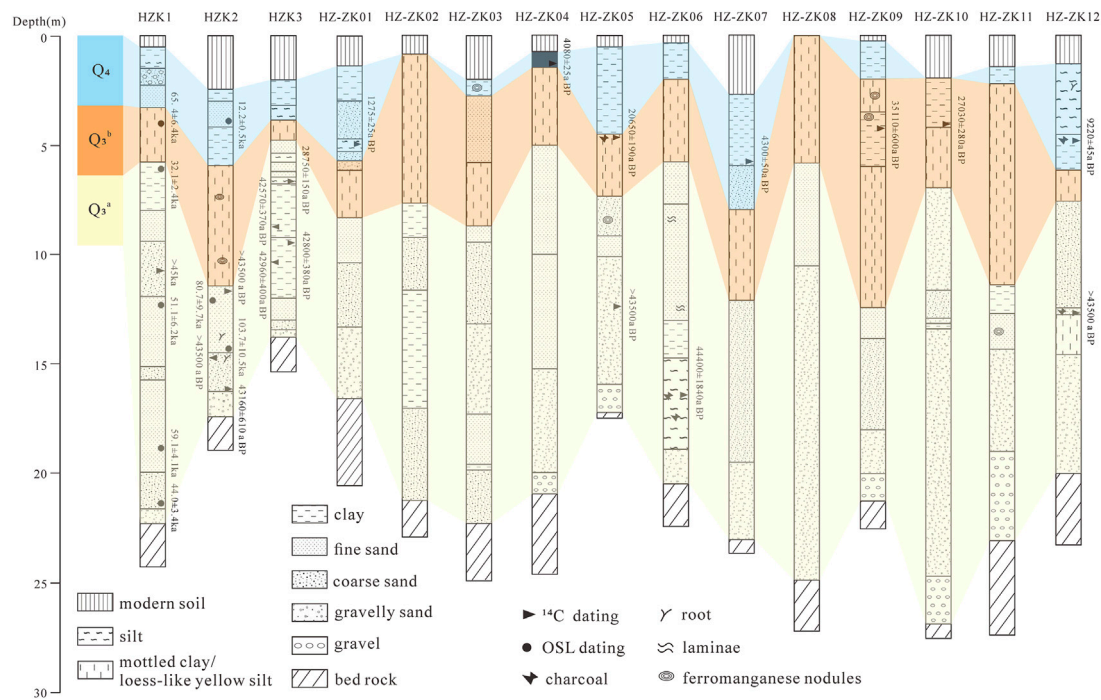


FIGURE 2 Comparison chart of the drilling cores in the Huizhou Basin. Cores HZK1-3 are according to Li et al. (2021). AMS ¹⁴C and OSL dating results are also indicated.

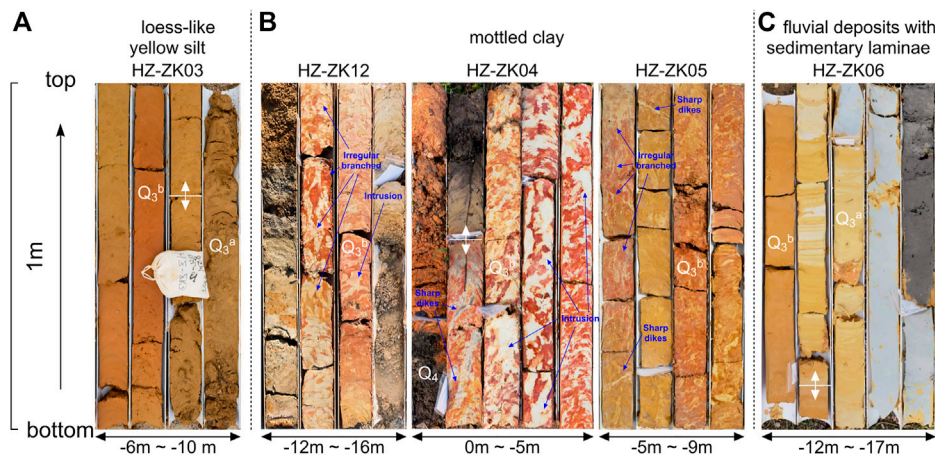


FIGURE 3 Photograph of different lithological layers in the Huizhou Basin. (A) Homogeneous loess-like yellow silt. (B) Mottled clay, exhibiting a yellow, red and grey-white mixed color and vertical structure. (C) Fluvial sand deposit with horizontal features.

Qingdao National Laboratory for Marine Science and Technology, China. The dates were then calibrated to calendar years (i.e., cal BP) using the IntCal20 Data Sets (Reimer et al., 2020) (Table 2). Additionally, the optically stimulated luminescence (OSL) dates provided in a previous study (Li et al., 2021) were combined to constrain the age of the lower fluvial deposit (Figure 2), which is generally beyond the dating limit of the AMS ¹⁴C method.

3.3 μ -XRF, DRS and grain size analysis

In this study, we conducted μ -XRF and DRS analysis to reveal detailed geochemical element and iron oxide features of mottled clay structure in the HZB. Three thin sections of mottled clay structure (10 cm in diameter and dozens of centimeters in length) (Table 3) were collected for μ -XRF scanning, using an M4 Plus Micro Area X-Ray Fluorescence Analyzer at Guangzhou Tuoyan Analytical Technology Co. Ltd. The

TABLE 2 AMS¹⁴C dating results of the late Pleistocene sediments in the Huizhou Basin.

Sample no.	Depth (m)	Material	Radiocarbon age (a BP)	Calibrated age (2σ, cal a BP)
HZ-ZK01- ¹⁴ C-01	4.81	organic sediment	1275 ± 25	1131–1284
HZ-ZK04- ¹⁴ C-01	1.25	organic sediment	4080 ± 25	4444–4478
HZ-ZK05- ¹⁴ C-01	4.85	charcoal	20650 ± 190	24254–25303
HZ-ZK05- ¹⁴ C-02	12.35	charcoal	-	-
HZ-ZK06- ¹⁴ C-01	16.44	charcoal	44400 ± 1840	43429–51403
HZ-ZK07- ¹⁴ C-01	5.71	charcoal	4300 ± 50	4655–5038
HZ-ZK09- ¹⁴ C-01	4.30	organic sediment	35110 ± 600	39108–41369
HZ-ZK10- ¹⁴ C-01	4.10	organic sediment	27030 ± 280	30474–31692
HZ-ZK12- ¹⁴ C-04	4.90	organic sediment	9220 ± 45	10249–10504
HZ-ZK12- ¹⁴ C-02	12.70	charcoal	-	-

TABLE 3 Sampling information and analysis methods.

Sample ID	Drilling core	Depth (m)	Lithological	Method
XRF-01	HZ-ZK04	3.30–3.60	mottled clay	μ-XRF
XRF-02	HZ-ZK05	6.05–6.20	mottled clay	μ-XRF
XRF-03	HZ-ZK12	13.30–13.35	mottled clay	μ-XRF
UV-01	HZ-ZK03	7.50	loess-like yellow silt	DRS
UV-02	HZ-ZK12	13.36	red fraction of mottled clay	DRS
UV-03	HZ-ZK12	13.40	white fraction of mottled clay	DRS
UV-04	HZ-ZK06	13.50	fluvial sand	DRS
GS-01	HZ-ZK06	2.70	loess-like yellow silt	grain size
GS-02	HZ-ZK06	3.50	mottled clay	grain size
GS-03	HZ-ZK06	4.50	mottled clay	grain size
GS-04	HZ-ZK06	5.50	mottled clay	grain size
GS-05	HZ-ZK06	8.50	loess-like yellow silt	grain size
GS-06	HZ-ZK06	13.80	fluvial sand	grain size
GS-07	HZ-ZK06	15.80	fluvial sand	grain size
GS-08	HZ-ZK06	17.80	fluvial sand	grain size
GS-09	HZ-ZK06	18.40	fluvial sand	grain size

instrument is equipped with a 20 μm diameter polycapillary X-ray lens and two X-Flash silicon drift detectors and operated at a voltage of 50 kV and a current of 300 μA. The scanning was carried out at a 20 μm spot size, 5 ms acquisition time and 35 μm points distance. Original data were processed using M4 tornado software to analyze the spectral peak information, and derive the element surface distribution map.

Four samples with different lithologies (Table 3) were ground in an agate mortar and passed through a 200-mesh sieve prior to DRS analysis. In particular, the red and white fractions of mottled clay were separated into two separate samples. DRS analysis was conducted using a Perkin Elmer (U.K.) ultraviolet-visible near-infrared spectrophotometer with a wavelength range of 175–3,300 nm at the Instrumental Analysis &

Research Center of Sun Yat-sen University. Data for the visible light range of 400–700 nm were collected at 1 nm intervals and used as the first-order derivative of the peak height mapping.

Furthermore, we collected samples from different lithological layers of core HZ-ZK06 for grain size analysis. The grain size was determined using a Malvern (U.K.) Mastersizer 2000 laser particle size instrument (measurement error <2%). Prior to measurement, the samples were pretreated with 10% H₂O₂ and 10% HCl to remove organic matter and carbonates, respectively. Then samples were washed with distilled water, sieved through a 1,000 μm mesh, and dispersed with 0.05 mol/L sodium hexametaphosphate (NaPO₃)₆ solution. Before the analysis, the samples were placed in an ultrasonic vibrator for 20 min.

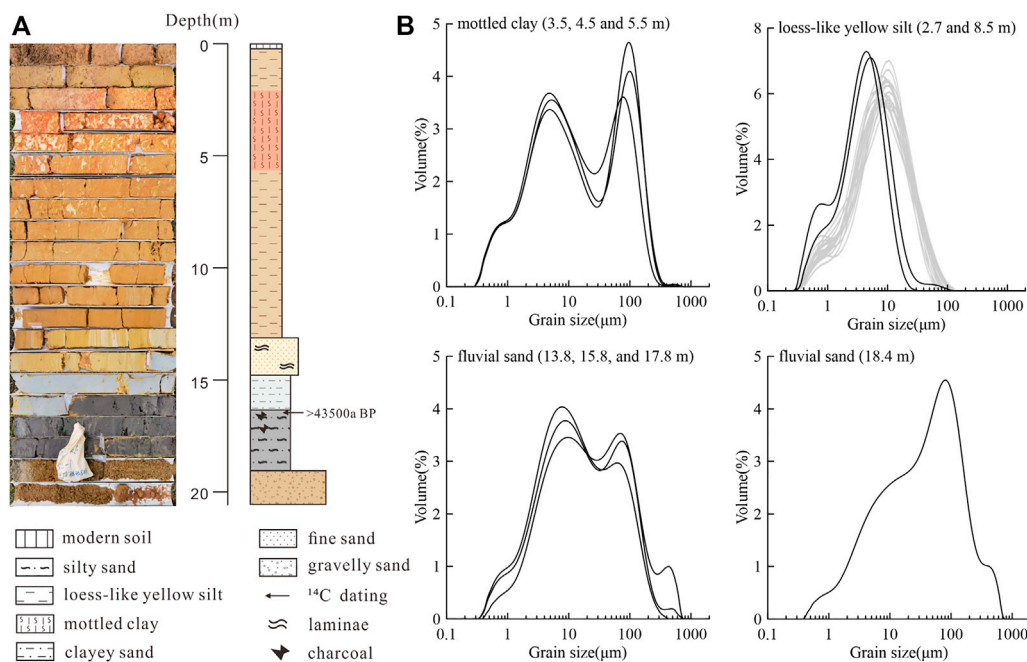


FIGURE 4

Lithology and grain size distribution of core HZ-ZK06. (A) Photography and lithology of core HZ-ZK06. (B) Grain size frequency distribution of different lithological layers from core HZ-ZK06. The frequency distribution of loess-like yellow silt in the Pearl River Delta is also shown (grey lines) (Wang et al., 2018b).

4 Results

4.1 Dating results

The results suggest that the unconsolidated sediment in the HZB has mostly developed since the late Pleistocene, directly overlying the weathered pre-Cenozoic bedrock. The radiocarbon dating results of the samples from HZ-ZK01, HZ-ZK04, HZ-ZK07, and ZH-ZK12 suggest that the uppermost Unit III (fluvial or marsh sediments) was mostly deposited during the Holocene (Table 2). The ages of the samples from Unit II (aeolian sediment) ranged between 20 and 35 ka BP, which is consistent with the ages of the yellow silt in the PRD. Wang et al. (2018a, b) demonstrated that the aeolian deposits found in most Quaternary basins of Southeast China developed during the Last Glacial period and were predominantly deposited during the Last Glacial Maximum (LGM). However, the ages of the underlying fluvial sediments (Unit I) exceeded the beyond the ¹⁴C dating limit of the AMS ¹⁴C method. A previous study using the OSL dating method (Li et al., 2021) suggests that Unit I could be older than 103 ± 10.5 ka (Figure 2).

4.2 Grain size characteristics

Grain size analysis is one of the most popular methods used for the analysis of sediments and helps determine the transport agents and sedimentary environment (Xu et al., 1992). The grain size distribution characteristics of the samples from core HZ-ZK06 generally became finer from the bottom to the top (Figure 4B). Specifically, the frequency distribution curves of the fluvial deposits have a unimodal or

multimodal form biased towards the coarse-grain end. The primary modal size of the lower fluvial sample (18.4 m) was around 85 μm, while those of the upper fluvial samples (13.8, 15.8, and 17.8 m) were around 75 and 9 μm, respectively. The yellow silt samples (2.7 and 8.5 m) present a uniform unimodal distribution with a fine tail and sharp kurtosis. The modal size of yellow silt is about 5 μm. The curves of yellow silt in the HZB decreased abruptly at the coarse-grained end and more gradually at the fine-grained end, similar to those of the loess-like yellow silt in the PRD (Figure 4B) and typical Chinese loess (Wang et al., 2018a). However, the modal size of yellow silt in the HZB is finer than those in the PRD (~16 μm), indicating wind sorting and decreasing transporting capacity. Nevertheless, our results suggest that the yellow silt in the HZB shares a common sedimentary type (aeolian) with loess-like yellow silt in the PRD and typical loess in China.

The mottled clay in core HZ-ZK06 occurred as an interbed within a thick layer of homogeneous yellow silt (Figure 4A), showing a deformation structure. The frequency distribution curves of the samples have a typical bimodal distribution, with a primary modal size of 80–90 μm and a secondary modal size of about 5 μm. Interestingly, the two distinct modal sizes were identical to those of the yellow silt and underlying fluvial sand, respectively. The finer part (<20 μm) of the curves is also similar with the curves of yellow silt. This implies that the mottled clay may be an admixture of fluvial sand and yellow silt.

4.3 μ-XRF element mapping

μ-XRF is a non-destructive method offering excellent spatial resolution and high sensitivity for small geochemical element

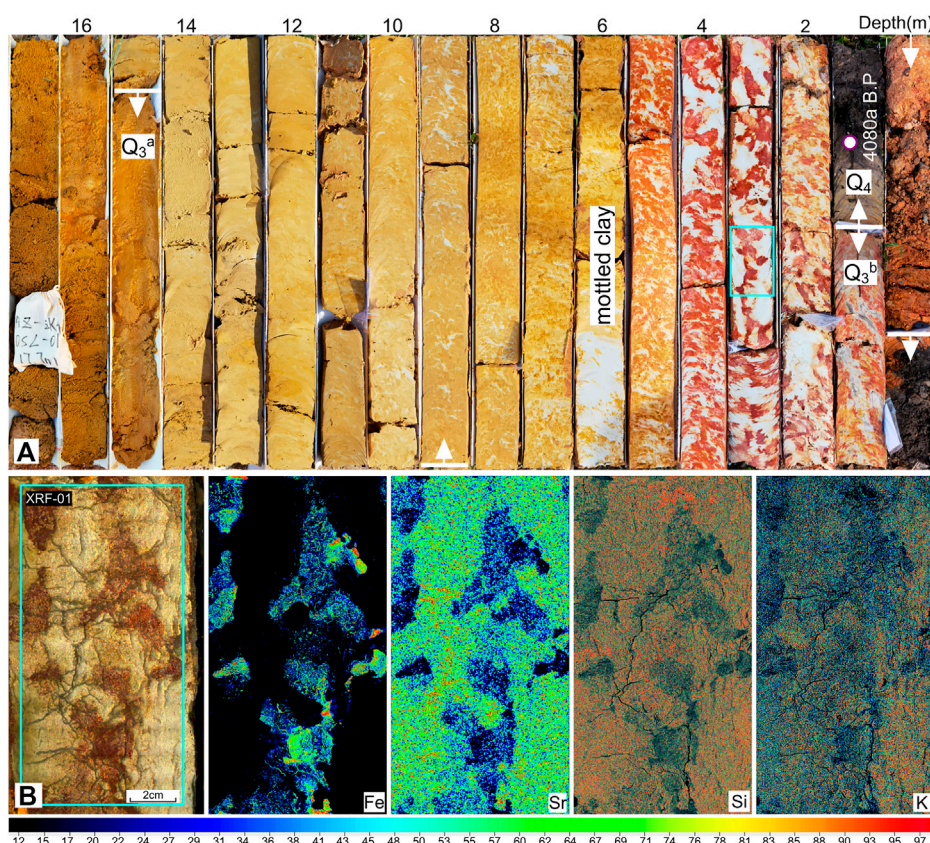


FIGURE 5

Photograph (A) and μ -XRF element mapping of mottled clay structure (B) of core HZ-ZK04. The mottled clay shows a fragmented structure in the spatial distribution of elements.

concentrations (Hoehnel et al., 2018). In this study, three thin sections of mottled clay showed a heterogeneous spatial distribution of geochemical elements. Generally, the red/yellow fraction of the mottled clay had high concentrations of Fe and Cr, whereas the gray/white fraction had high Si, Al and K concentrations (Figure 5, Figure 6, Figure 7). In particular, the visual structures of samples can be characterized by the varying concentrations of Fe, because the redness of the sediment is dominantly controlled by the type and concentration of iron oxides (Sun et al., 2011). Moreover, the core HZ-ZK04 sample showed a fragmented structure in the spatial distribution of elements (Figure 5B). In core HZ-ZK05, a small white sand vein was characterized by extremely low Fe concentrations, intruding into yellow silt with high Fe concentrations (Figure 6B).

4.4 DRS characteristics

Discriminating iron oxides is of great environmental significance; for example, they are indicators of the sedimentary environment (Zhang et al., 2009). In the subtropical region, hematite and goethite are the two main iron oxide minerals (Wang et al., 2018b), the contents of which in the sediment can be obtained from the DRS first-order derivative curves. The characteristic peak of hematite is typically observed at a wavelength of 565 nm, whereas

goethite has two characteristic peaks at 535 and 435 nm (Deaton and Balsam, 1991; Ji et al., 2002). In general, goethite tends to be enriched in wet environments, whereas large amounts of hematite reflect dry environments (Cornell and Schwertmann, 2003; Balsam et al., 2004).

In this study, two peaks at wavelengths of 565 and 435 nm were presented in the loess-like yellow silt (UV-01) and the red fraction of mottled clay (UV-02) samples (Figure 8). The peak at 565 nm is substantially greater than that at 435 nm, which indicates that hematite predominates over goethite in the loess-like yellow silt and the red fraction of mottled clay. Due to overall low iron content as revealed by μ -XRF analysis (Figures 5–7), the DRS curve of the white fraction of mottled clay (UV-03) is relatively flat, and three peaks could be discerned at 435, 505 and 555 nm, respectively (Figure 8). The hematite peak at 565 nm is usually offset to 555 or 575 nm after being affected by the Fe content, and the characteristic peak of goethite at 535 nm is often biased toward 505 nm (Deaton and Balsam, 1991; Ji et al., 2002). Therefore, the white fraction of the mottled clay contained both goethite and hematite, with the former being higher than the latter. The DRS curve of the fluvial sand (UV-04) shows two peaks at 435 and 505 nm, indicating the predominance of goethite. Overall, the curves of the loess-like yellow silt and the red fraction of mottled clay (UV-01 and UV-02) share a similar pattern with high hematite content, indicating a relatively dry sedimentary environment (i.e., aeolian

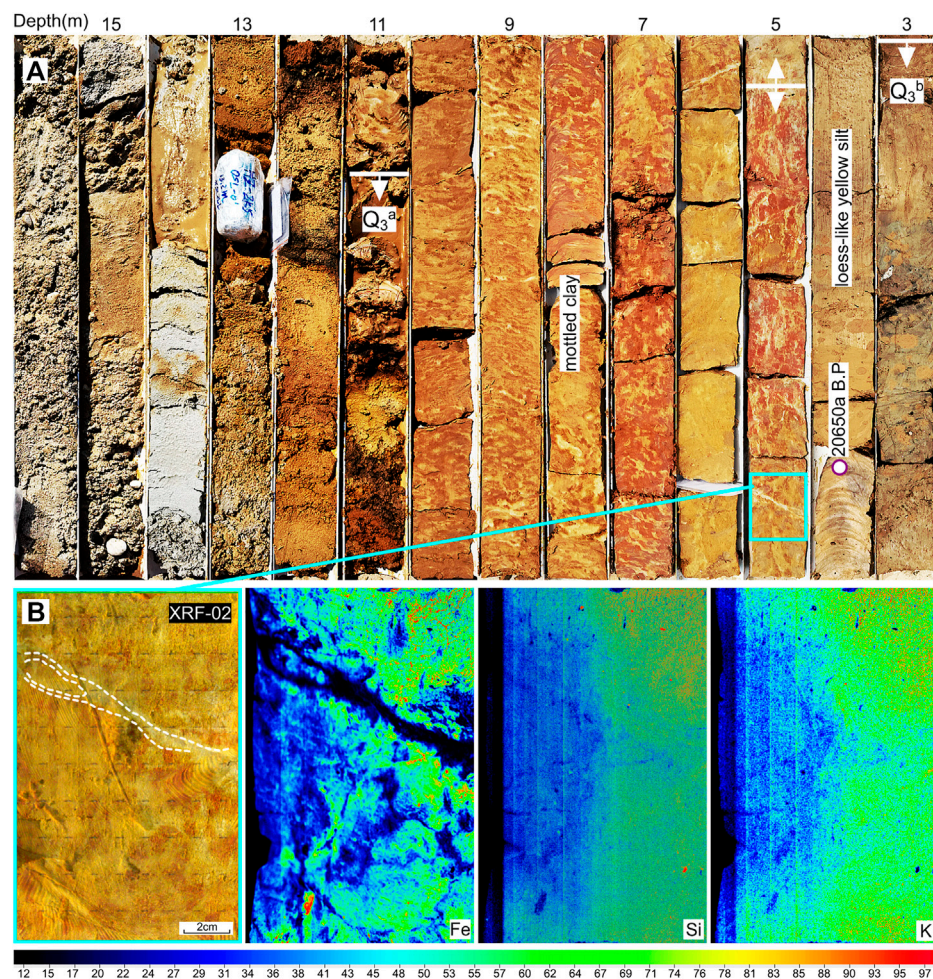


FIGURE 6
Photograph (A) and μ -XRF element mapping of mottled clay structure (B) of core HZ-ZK05. The sand vein is characterized by low Fe concentrations.

deposit). In contrary, samples of the white fraction of the mottled clay and fluvial sediment were predominantly goethite, reflecting a typical aquatic environment.

5 Discussion

5.1 Identification of the soft-sediment deformation structure

Mottled clay is primarily regarded as a weathering product of underlying fluvial/marine sediments (Huang, 1982; Li et al., 1984). Based on the evidences from grain size, mineral, and geochemical composition, Wang et al. (2018b) suggested no obvious weathering transition relationship between mottled clay and its underlying sediments, and proposed that the mottled structure was formed by post-sedimentary oxidation modification of homogeneous aeolian dust accumulated during the last glacial period, under the hot and humid conditions of the Holocene epoch. However, in the HZB, the mottled clay layer was not always overlaid with the Holocene organic-rich sediments. Instead, it is also overlaid with

late Pleistocene fluvial sand (e.g., in core HZ-ZK12, Figure 7), or occurs as an interbed within the thick layer of homogeneous yellow silt (Figure 4A). Therefore, we suggest that the mottled clay is neither a post-sedimentary oxidation product of the loess-like yellow silt, nor a weathering product of the underlying fluvial/marine sediments. Alternatively, μ -XRF element mapping shows that the red/white fraction of mottled clay has a different geochemical composition (Figures 5–7). Two major components of grain size (5 and 80–90 μ m) are identical to the modal sizes of the yellow silt and the underlying fluvial sand, respectively (Figure 4B). In addition, the red fraction of mottled clay had a high hematite content, similar to loess-like yellow silt, whereas the white fraction and the underlying fluvial sediments were dominated by goethite (Figure 8). These two types of iron oxides refer to opposite sedimentary environments (i.e., dry vs. wet conditions), implying that the accumulation of these two fractions was asynchronous. Furthermore, there are diverse deformed structures in the mottled clay, such as fragmented structures (Figure 5B), sand veins (Figure 6B), sand dykes (Figure 7B) and flame structure. The degree of deformation also increases upwards in mottled clay, which is a common characteristic of liquefaction-related

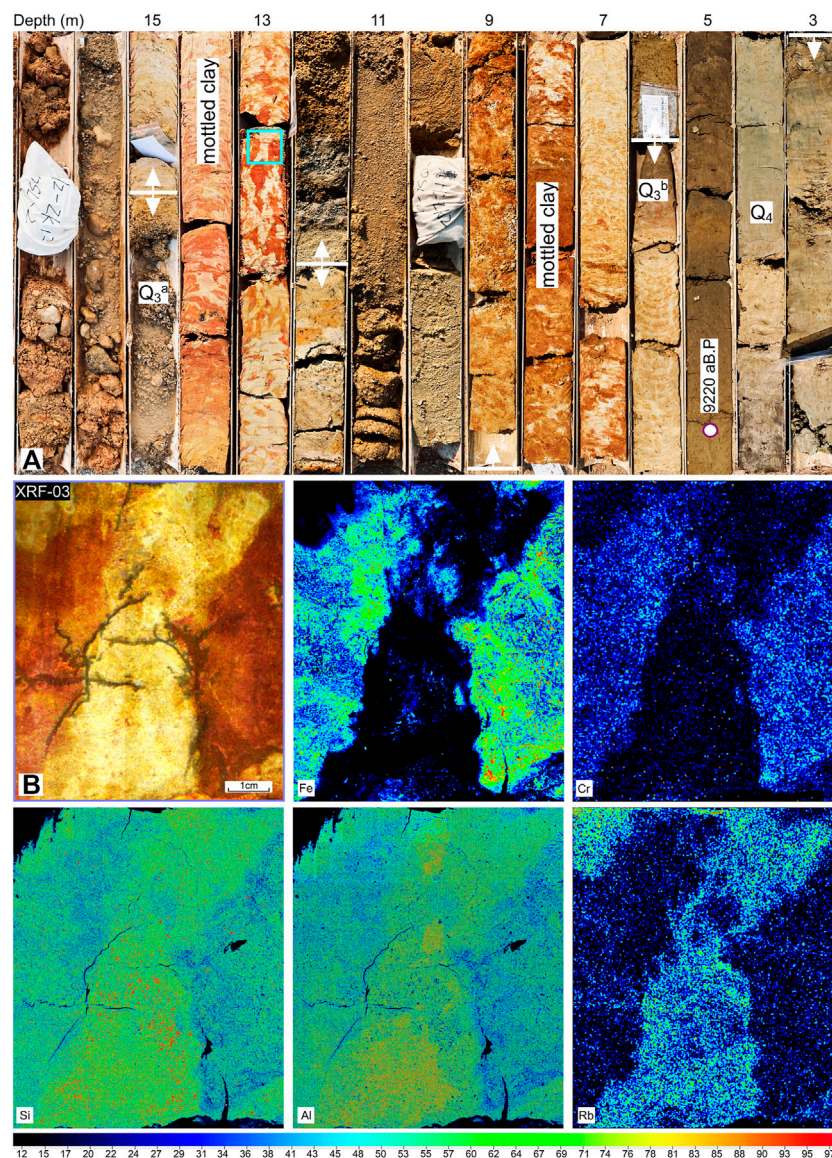


FIGURE 7
Photograph (A) and μ -XRF element mapping of mottled clay structure (B) of core HZ-ZK12.

deformations (Owen and Moretti, 2011). Therefore, we suggest that the mottled clay structure in the HZB is a product of liquefaction-induced SSD, which produced an admixture of aeolian yellow silt and underlying fluvial sand.

Several key factors of sediment characteristics, including grain size, porosity, saturation, permeability barrier, overburden pressure, and sediment history strongly influence susceptibility to liquefaction (Owen and Moretti, 2011). In most cases, liquefaction develops in loose, water-saturated silt or fine sand without previous liquefaction. A higher overburden pressure could also decrease the potential for liquefaction, such that most liquefaction develops in sediment with a small buried depth (generally less than 5 m) (Obermeier, 1996). In HZB, the underlying fluvial sand is mostly fine, loose, and water-saturated. In the other hand, the overlying yellow silt layer could act as a permeability barrier, leading to an increase in the pore-fluid

pressure. These sedimentary characteristics of the HZB generally promote the development of liquefaction. Moreover, the fluvial sand and aeolian yellow silt are significantly different in many sedimentary characteristics, such as grain size, iron oxides, and geochemical (Figures 4–8), which favors the preservation of liquefaction-induced SSDs.

5.2 Triggers for the liquefaction and related SSDS

Liquefaction-induced SSDS can be triggered by many factors, which can be categorized into two types (Owen and Moretti, 2011). The first type is directly associated with sedimentation processes and termed autogenic or internal triggers and includes groundwater

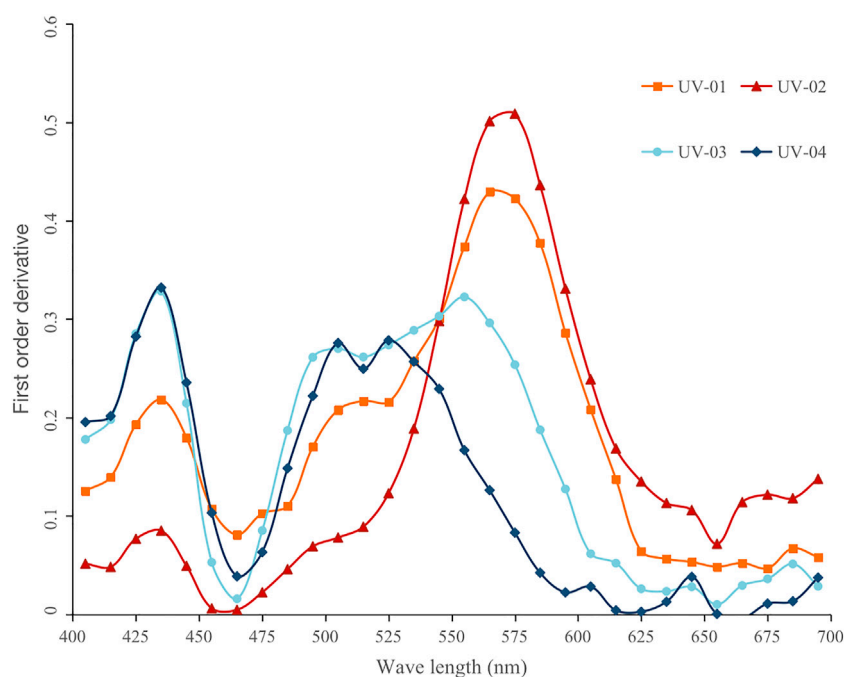


FIGURE 8

DRS first order derivative curves of different lithological samples in the Huizhou Basin. Samples of UV-01 to UV-04 refer to the loess-like yellow silt, the red fraction of mottled clay, the white fraction of mottled clay and fluvial sand, respectively.

fluctuations, water flows/waves, rapid sediment loading, tidal shear, tsunamis and permafrost thawing. Other triggers such as earthquakes, meteorite impacts and volcanic eruptions act as external agents (Su et al., 2022), and are referred to as allogenic triggers. Regarding the liquefaction-induced SSDS of mottled clay in the HZB, some triggers could be eliminated by exclusion. First, meteorite impacts and volcanic eruptions can be ruled out, because such events could produce unique geomorphological formations and sedimentary deposits, which have not been found in the study region since the late Pleistocene. The high hematite content in the red fraction of mottled clay indicates a relatively dry sedimentary environment, and in some cases, a mottled clay structure occurs interbedded with aeolian yellow silt (e.g., core HZ-ZK06), which together exclude an underwater sedimentary environment and thus possible triggers of water flows/waves and tidal shear. Third, the Lianhuashan Mountains situated between the HZB and the northern SCS (Figure 1B) could be a barrier weakening the influence of tsunamis and storm surges. Finally, paleotemperature reconstruction from a nearby maar lake indicates a drop of about 6 °C during the Last Glacial Maximum, a period of maximum glacier extent since the late Pleistocene, compared to modern annual temperature (Chu et al., 2017). Considering the present subtropical climate with hot conditions (e.g., 14.5 °C in winter) (Li et al., 2008), the freeze-thaw process was not likely the trigger that led to the formation of SSDS in the mottled clay layer of the HZB.

Instead, liquefaction-induced SSDS in the mottled clay layer of the HZB were interpreted as tectonic activity -induced after consideration of all other possible trigger agents. As a subsidence basin controlled by active faults (Figure 1B), the HZB has

experienced tectonic activity since the late Pleistocene. For example, a normal fault cutting a peat bed dated at 33.59 ± 0.16 ka BP was found in the Huizhou fault zones (unpublished data). After homogeneous aeolian dust accumulation, seismic shaking led to a sudden increase in pore-water pressure and triggered the liquefaction of the underlying fluvial sediments. The excessive pore pressure water and sand mixture upwelled and intruded into the overlying loess-like yellow silt layer. This intrusion deformed the homogeneous aeolian layer, formed vertical structures (e.g., sand vein), and resulted in an admixture of aeolian silt and fluvial sand as revealed by the results of grain size, DRS and μ -XRF analysis. Moreover, the spatial distribution of the mottled clay layer is highly related to regional faults (Figure 9). For example, most cores with mottled clay layers were concentrated in the communicating zone of the Tonghu and Huizhou faults, where a historical earthquake of 4 occurred in October 1590 (Wei et al., 2000). The spatial relationship between the mottled clay layers and regional faults strongly supports the suggestion of tectonic activity -induced liquefaction and SSDS. Notably, the formation of mottled clay structures in the different cores did not occur during a single seismic event. Generally, seismic events tend affect surface sediments (e.g., Shao et al., 2020). Multiple deformed layers in the vertical direction (e.g., two layers in core HZ-ZK12) reflect the repetition of paleo-earthquakes since the late Pleistocene in the HZB.

Seismically induced liquefaction and SSDS are usually recorded in lacustrine (e.g., Becker et al., 2002; Fan et al., 2022), fluvial (e.g., Suter et al., 2011; Rossetti et al., 2017) and aeolian (e.g., Moretti, 2000; Brand and Maithel, 2020) sediments. In the upper Senne area of Northwest Germany, seismically triggered SSDS in mixed alluvial

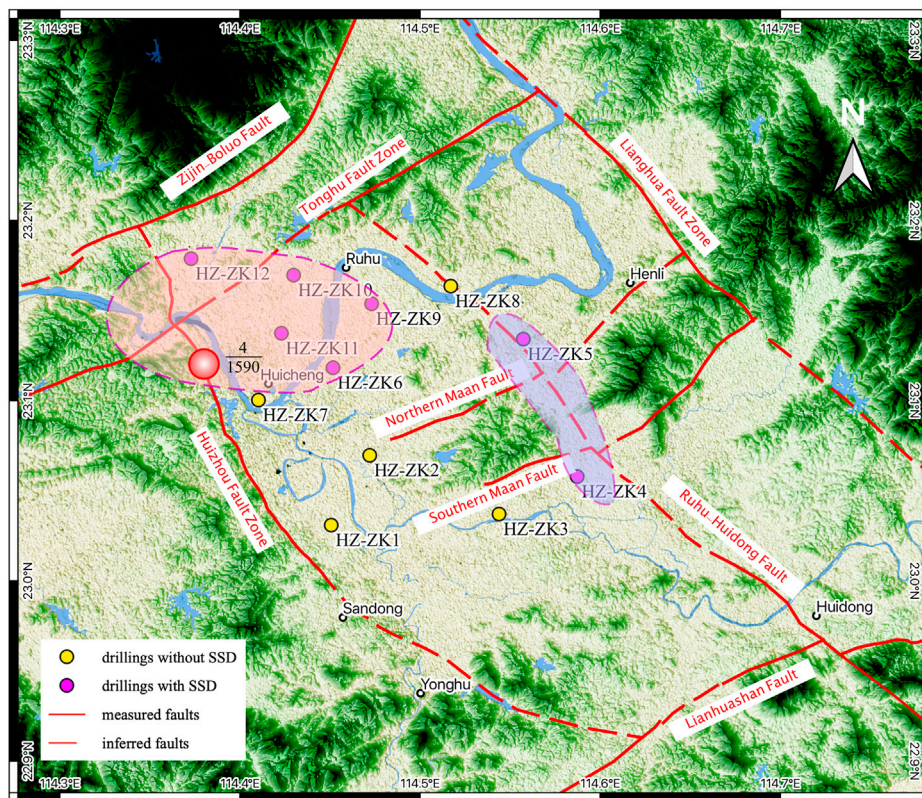


FIGURE 9

Spatial distribution of mottled clay layer in the Huizhou Basin. There is a close spatial relationship between mottled clay and regional faults.

and aeolian deposits that accumulated during the Last Glacial were also recognized (Brandes and Winsemann, 2013). Two outcrops from the Senne area consist mainly of alluvial deposits, overlain by several-meter-thick aeolian deposits, similar to the lithological succession of late Quaternary sediments in the HZB. Different types of SSDs, including closely spaced low offset normal faults, ball-and-pillow structures, flame structures, sills and irregular sedimentary intrusions, dikes, and sand volcanoes, were identified based on a detailed sedimentological analysis (Brandes and Winsemann, 2013). In the coastal region of the northern SCS, aeolian yellow silt broadly developed during the Last Glacial period in coastal basins, mostly underlain by late Pleistocene fluvial or alluvial deposits. This lithological succession is susceptible to seismically induced liquefaction. Therefore, the SSDs of the mottled clay layer could be a potential indicator of paleo-earthquakes in the coastal region of the northern SCS.

6 Conclusion

Tectonically induced liquefaction and the resulting SSDs are of great significance in long-term research on paleo-earthquakes in tectonically active regions. In this study, we combined age dating, grain size analysis, μ -XRF element mapping and DRS measurement to characterize the mottle clay structure in the

HZB. The results indicate that mottle clay is an admixture of aeolian yellow silt and underlying fluvial sands, originating from liquefaction-induced SSDs during the late Pleistocene. After considering possible trigger agents, tectonic activity was considered to have trigger liquefaction and SSDs, which is supported by the close spatial relationship between mottled clay and regional faults. The SSDs of mottled clay could be a potential indicator of paleo-earthquakes in the coastal region of the northern South China Sea.

Data availability statement

The original contributions presented in the study are included in the article/Supplementary Material, further inquiries can be directed to the corresponding author.

Author contributions

ZC: Conceptualization, Methodology, Investigation, Writing—original draft, Writing—review and editing, Funding acquisition. WW: Methodology, Investigation, Writing—review and editing, Funding acquisition. PH: Methodology, Investigation, Writing—review and editing. YT: Methodology,

Investigation. JW: Methodology. QZ: Conceptualization, Methodology, Investigation, Writing–review and editing. CC: Conceptualization, Methodology, Investigation, Writing–original draft, Writing–review and editing, Funding acquisition.

Funding

This work was supported by the China Postdoctoral Science Foundation (Grant No. 2021M703659), 2021 Urban Geological Investigation of Huizhou City, Guangdong Province, China (Grant No. GDJR2021066), and Special Fund for Special Project of Geological Hazard Control, Guangdong Province, China (Grant No. 2017201).

Acknowledgments

The authors are grateful to Xibing Yang, Yuanxiao Huang, Huilin Niu and Jinlong Zhang from the Non-ferrous Metals Geological Bureau of Guangdong Province 935 Battalion for their assistance in the field.

References

- Allen, J. R. L. (1986). Earthquake magnitude–frequency, epicentral distance, and soft-sediment deformation in sedimentary basins. *Sediment. Geol.* 46, 67–75. doi:10.1016/0037-0738(86)90006-0
- Balsam, W., Ji, J. F., and Chen, J. (2004). Climatic interpretation of the Luochuan and Lingtai loess sections, China, based on changing iron oxide mineralogy and magnetic susceptibility. *Earth Planet. Sci. Lett.* 223, 335–348. doi:10.1016/j.epsl.2004.04.023
- Becker, A., Davenport, C. A., and Giardini, D. (2002). Palaeoseismicity studies on end-Pleistocene and Holocene lake deposits around Basle, Switzerland. *Geophys. J. Int.* 149, 659–678. doi:10.1046/j.1365-246X.2002.01678.x
- Brand, L., and Maithel, S. (2020). Small-scale soft-sediment deformation structures in the cross-bedded Coconino Sandstone (Permian; Arizona, United States); Possible evidence for seismic influence. *Front. Earth Sci.* 9, 723495. doi:10.3389/feart.2021.723495
- Brandes, C., and Winsemann, J. (2013). Soft-sediment deformation structures in NW Germany caused by Late Pleistocene seismicity. *Int. J. Earth Sci.* 102, 2255–2274. doi:10.1007/s00531-013-0914-4
- Bureau of Geology and Mineral Resources of Guangdong Province (BGMGRP) (1988). Regional Geology of Guangdong Province. Beijing: Geological Publishing House.
- Chen, G. N., Zhang, K., Li, L. F., Shao, R. S., Zhuang, W. M., and Lin, X. M. (2002). Development of the Pearl River Delta in SE China and its relations to reactivation of basement faults. *J. Geosci. China* 14 (1), 17–24.
- Chu, G. Q., Sun, Q., Zhu, Q. Z., Shan, Y. B., Shang, W. Y., Ling, Y., et al. (2017). The role of the Asian winter monsoon in the rapid propagation of abrupt climate changes during the last deglaciation. *Quat. Sci. Rev.* 177, 120–129. doi:10.1016/j.quascirev.2017.10.014
- Cornell, R. M., and Schwertmann, U. (2003). *The iron oxides: Structure, properties, reactions, occurrences, and uses*. Weinheim: Wiley VCH.
- Deaton, B. C., and Balsam, W. L. (1991). Visible spectroscopy: A rapid method for determining hematite and goethite concentration in geological materials. *J. Sediment. Petrol.* 61, 628–632. doi:10.1306/D4267794-2B26-11D7-8648000102C1865D
- Deev, E. V., Zolnikov, I. D., and Gus'kov, S. A. (2009). Seismites in quaternary sediments of southeastern altai. *Russ. Geol. Geophys.* 50 (6), 546–561. doi:10.1016/j.rgg.2008.10.004
- Fan, J. W., Xu, H. Y., Shi, W., Guo, Q. Q., Zhang, S. Q., Wei, X. T., et al. (2022). A ~28-kyr continuous lacustrine paleoseismic record of the intraplate, slow-slipping Fuyun Fault in Northwest China. *Front. Earth Sci.* 10, 828801. doi:10.3389/feart.2022.828801
- Galli, P. (2000). New empirical relationships between magnitude and distance for liquefaction. *Tectonophysics* 324, 169–187. doi:10.1016/S0040-1951(00)00118-9
- Gladkov, A. S., Lobova, E. U., Deev, E. V., Korzhnikov, A. M., Mazeika, J. V., Abdieva, S. V., et al. (2016). Earthquake-induced soft-sediment deformation structures in Late Pleistocene lacustrine deposits of Issyk-Kul lake (Kyrgyzstan). *Sediment. Geol.* 344, 112–122. doi:10.1016/j.sedgeo.2016.06.019
- Hibsch, C., Alvarado, A., Yepes, H., Perez, V. H., and Sébrier, M. (1997). Holocene liquefaction and soft-sediment deformation in quito (Ecuador): A paleoseismic history recorded in lacustrine sediments. *J. Geodyn.* 24, 259–280. doi:10.1016/S0264-3707(97)00010-0
- Hoehnel, D., Reimold, W. U., Altenberger, U., Hofmann, A., Mohr-Westheide, T., Özdemir, S., et al. (2018). Petrographic and Micro-XRF analysis of multiple archean impact-derived spherule layers in drill core CT3 from the northern Barberton Greenstone Belt (South Africa). *J. Afr. Earth Sci.* 138, 264–288. doi:10.1016/j.jafrearsci.2017.11.020
- Huang, Z. G. (1982). *Formation and evolution of the Pearl River Delta of China*. Guangzhou Branch, Guangzhou: Popular Science Press.
- Ji, J. F., Balsam, W., Chen, J., and Liu, L. W. (2002). Rapid and quantitative measurement of hematite and goethite in the Chinese loess-paleosol sequence by diffuse reflectance spectroscopy. *Clay Clay Min.* 50, 208–216. doi:10.1346/000986002760832801
- Li, P. R., Huang, G., Zhang, Z. Y., and Li, K. H. (1984). Quaternary stratigraphy in the zhujiang delta. *Sci. Geogr. Sin.* 4 (2), 133–142.
- Li, M. H., Cui, S. P., Wu, N. K., Zhang, Z. F., Fan, S. J., and Yang, L. (2008). The characteristics of temperature change of Huizhou in the past half century. *J. Trop. Meteorol.* 24 (4), 435–440.
- Li, J. H., Cawood, P. A., Ratschbacher, L., Zhang, Y. Q., Dong, S. W., Xin, Y. J., et al. (2020). Building Southeast China in the late Mesozoic: Insights from alternating episodes of shortening and extension along the Lianhuashan fault zone. *Earth-Sci. Rev.* 201, 103056. doi:10.1016/j.earscirev.2019.103056
- Li, Y. H., Guo, L. T., and Yan, Y. X. (2021). Earthquake hazard evaluation of Huizhou fault and its adjacent area. *Seismol. Geomagn. Obs. Res.* 42 (1), 48–60. doi:10.3969/j.issn.1003-3246.2021.01.008
- Liang, L. J., Dai, F. C., Jiang, H. C., and Zhong, N. (2018). A preliminary study on the soft-sediment deformation structures in the late Quaternary lacustrine sediments at Tashkorgan, northeastern Pamir, China. *Acta Geol. sin.-engl. Ed.* 92 (4), 1574–1591. doi:10.1111/1755-6724.13644
- Moretti, M. (2000). Soft-sediment deformation structures interpreted as seismites in middle-late Pleistocene aeolian deposits (Apulian foreland, southern Italy). *Sediment. Geol.* 135, 167–179. doi:10.1016/S0037-0738(00)00070-1
- Obermeier, S. F. (1996). Use of liquefaction-induced features for paleoseismic analysis — an overview of how seismic liquefaction features can be distinguished from other features and how their regional distribution and properties of source sediment can be used to infer the location and strength of Holocene paleo-earthquakes. *Eng. Geol.* 44, 1–76. doi:10.1016/S0013-7952(96)00040-3
- Owen, G., and Moretti, M. (2011). Identifying triggers for liquefaction-induced soft-sediment deformation in sands. *Sediment. Geol.* 235, 141–147. doi:10.1016/j.sedgeo.2010.10.003
- Qiao, X. F., Li, H. B., Su, D. C., He, B. Z., Tian, H. S., Guo, X. P., et al. (2017). *Soft-sediment deformation structures*. Beijing: Geological Publishing House.

Conflict of interest

The authors declare that the research was conducted in the absence of any commercial or financial relationships that could be construed as a potential conflict of interest.

Publisher's note

All claims expressed in this article are solely those of the authors and do not necessarily represent those of their affiliated organizations, or those of the publisher, the editors and the reviewers. Any product that may be evaluated in this article, or claim that may be made by its manufacturer, is not guaranteed or endorsed by the publisher.

Supplementary material

The Supplementary Material for this article can be found online at: <https://www.frontiersin.org/articles/10.3389/feart.2023.1135335/full#supplementary-material>

- Reimer, P. J., Austin, W. E. N., Bard, E., Bayliss, A., Blackwell, P. G., Bronk Ramsey, C., et al. (2020). The IntCal20 Northern Hemisphere radiocarbon age calibration curve (0–55 cal kBP). *Radiocarbon* 62, 725–757. doi:10.1017/RDC.2020.41
- Rossetti, D. F., Alves, F. C., and Valeriano, M. M. (2017). A tectonically-triggered late Holocene seismite in the southern Amazonian lowlands, Brazil. *Braz. Sediment. Geol.* 358, 70–83. doi:10.1016/j.sedgeo.2017.07.003
- Shao, Z. F., Zhong, J. H., Howell, J., Hao, B., Luan, X. W., Liu, Z. X., et al. (2020). Liquefaction structures induced by the M5.7 earthquake on May 28, 2018 in Songyuan, Jilin Province, NE China and research implication. *J. Palaeogeogr.* 9, 3. doi:10.1186/s42501-019-0053-3
- Song, F. M., Wang, Y. P., Li, C. Y., Chen, W. G., and Zhao, H. M. (2001). New insight into the Quaternary activity of Wuguishan southern piedmont fault in Zhujiang Delta. *Seismol. Geol.* 23 (4), 521–526.
- Su, D. C., Sun, A. P., Li, Z. L., Chen, S. Y., and Wu, Z. J. (2022). Origin of soft-sediment deformation structures in Nihewan Basin. *J. Palaeogeogr.* 11 (3), 332–359. doi:10.1016/j.jop.2022.05.002
- Sun, Y. B., He, L., Liang, L. J., and An, Z. S. (2011). Changing color of Chinese loess: Geochemical constraint and paleoclimatic significance. *J. Asian Earth Sci.* 40, 1131–1138. doi:10.1016/j.jseas.2010.08.006
- Suter, F., Martínez, J. I., and Vélez, M. I. (2011). Holocene soft-sediment deformation of the Santa Fe-Sopetrán Basin, northern Colombian Andes: Evidence for pre-Hispanic seismic activity? *Sediment. Geol.* 235, 188–199. doi:10.1016/j.sedgeo.2010.09.018
- Tang, Y. K., Chen, G. N., Peng, Z. L., and Zhang, K. (2011). Late quaternary tectonics of the Pearl River Delta, SE China: Evidence from Xilingang. *Geodin. Acta* 24 (3–4), 133–139. doi:10.3166/ga.24.133-139
- Tang, Y. J., Zheng, Z., Chen, C., Wang, M. Y., and Chen, B. S. (2018). Evolution of the Lian River coastal basin in response to Quaternary marine transgressions in Southeast China. *Sediment. Geol.* 366, 1–13. doi:10.1016/j.sedgeo.2018.01.003
- Tuttle, M. P., Wolf, L., Hartleb, R., and Mayne, P. W. (2019). Paleoliquefaction studies and the evaluation of seismic hazard. *Geosciences* 9 (7), 311. doi:10.3390/geosciences9070311
- Üner, S., Özsayın, E., and Selçuk, A. S. (2019). Seismites as an indicator for determination of earthquake recurrence interval: A case study from erciş fault (eastern anatolia-Turkey). *Tectonophysics* 766, 167–178. doi:10.1016/j.tecto.2019.06.010
- Wang, J., Chen, Z., Gao, Q. Z., Grapes, R., Peng, Z. L., and Chen, G. N. (2018a). Late Pleistocene loess-like deposits in the coastal area of south China. *Catena* 167, 305–318. doi:10.1016/j.catena.2018.04.032
- Wang, J., Chen, Z., Gao, Q. Z., and Chen, G. N. (2018b). New research on the origin of mottled clay in Quaternary basins in the coastal area of south China. *Aeolian Res.* 32, 170–180. doi:10.1016/j.aeolia.2018.02.006
- Wei, B. L., Chen, R. F., and Huang, R. H. (2000). *Seismotectonic map of Guangdong Province*. Beijing: Seismological Press.
- Xu, X., He, C. H., and Shen, Z. D. (1992). *Research methods of quaternary environment*. Guiyang: Guizhou Science and Technology Press.
- Yao, Y. T., Zhan, W. H., Liu, Z. F., Zhang, Z. Q., Zhan, M. Z., and Sun, J. (2013). Neotectonics and its relations to the evolution of the Pearl River Delta, Guangdong, China. *J. Coast. Res.* 66 (1), 1–11. doi:10.2112/SI_66_1
- Zhang, W. G., Yu, L. Z., Zheng, L. M., Ji, X. M., Zhou, J. F., Wang, L. M., et al. (2009). East Asian summer monsoon intensity inferred from iron oxide mineralogy in the Xiashu Loess in southern China. *Quat. Sci. Rev.* 28, 345–353. doi:10.1016/j.quascirev.2008.10.002
- Zhong, N., Jiang, H. C., Li, H. B., Su, D. C., Xu, H. Y., Liang, L. J., et al. (2022). The potential of using soft-sediment deformation structures for quantitatively reconstructing paleo-seismic shaking intensity: Progress and prospect. *Environ. Earth Sci.* 81, 408. doi:10.1007/s12665-022-10504-8

Frontiers in Earth Science

Investigates the processes operating within the major spheres of our planet

Advances our understanding across the earth sciences, providing a theoretical background for better use of our planet's resources and equipping us to face major environmental challenges.

Discover the latest Research Topics

[See more →](#)

Frontiers

Avenue du Tribunal-Fédéral 34
1005 Lausanne, Switzerland
frontiersin.org

Contact us

+41 (0)21 510 17 00
frontiersin.org/about/contact

